

200 CITE 0787

1

AGARD-CP-451

AGARD-CP-451

AD-A218 094

AGARD

ADVISORY GROUP FOR AEROSPACE RESEARCH & DEVELOPMENT

TRIEUX-ARDECHE - 63000 MONTPELLIER - FRANCE

AGARD CONFERENCE PROCEEDINGS No.451

Stability and Control of Tactical Missile Systems

DISTRIBUTION STATEMENT A

Approved for public release
Distribution Unlimited

DTIC
ELECTE
MAY 15 1989
S D

NORTH ATLANTIC TREATY ORGANIZATION



DISTRIBUTION AND AVAILABILITY
ON BACK COVER

89 5 15 092

AGARD-CP-451

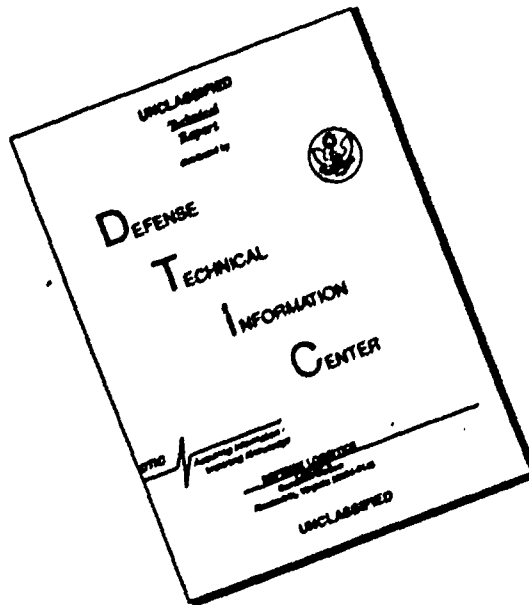
NORTH ATLANTIC TREATY ORGANIZATION
ADVISORY GROUP FOR AEROSPACE RESEARCH AND DEVELOPMENT
(ORGANISATION DU TRAITE DE L'ATLANTIQUE NORD)

AGARD Conference Proceedings No.451

STABILITY AND CONTROL OF
TACTICAL MISSILE SYSTEMS

Descript. For	
MS. 000001	<input checked="" type="checkbox"/>
MS. 000002	<input type="checkbox"/>
MS. 000003	<input type="checkbox"/>
MS. 000004	<input type="checkbox"/>
MS. 000005	<input type="checkbox"/>
MS. 000006	<input type="checkbox"/>
MS. 000007	<input type="checkbox"/>
MS. 000008	<input type="checkbox"/>
MS. 000009	<input type="checkbox"/>
MS. 000010	<input type="checkbox"/>
MS. 000011	<input type="checkbox"/>
MS. 000012	<input type="checkbox"/>
MS. 000013	<input type="checkbox"/>
MS. 000014	<input type="checkbox"/>
MS. 000015	<input type="checkbox"/>
MS. 000016	<input type="checkbox"/>
MS. 000017	<input type="checkbox"/>
MS. 000018	<input type="checkbox"/>
MS. 000019	<input type="checkbox"/>
MS. 000020	<input type="checkbox"/>
MS. 000021	<input type="checkbox"/>
MS. 000022	<input type="checkbox"/>
MS. 000023	<input type="checkbox"/>
MS. 000024	<input type="checkbox"/>
MS. 000025	<input type="checkbox"/>
MS. 000026	<input type="checkbox"/>
MS. 000027	<input type="checkbox"/>
MS. 000028	<input type="checkbox"/>
MS. 000029	<input type="checkbox"/>
MS. 000030	<input type="checkbox"/>
MS. 000031	<input type="checkbox"/>
MS. 000032	<input type="checkbox"/>
MS. 000033	<input type="checkbox"/>
MS. 000034	<input type="checkbox"/>
MS. 000035	<input type="checkbox"/>
MS. 000036	<input type="checkbox"/>
MS. 000037	<input type="checkbox"/>
MS. 000038	<input type="checkbox"/>
MS. 000039	<input type="checkbox"/>
MS. 000040	<input type="checkbox"/>
MS. 000041	<input type="checkbox"/>
MS. 000042	<input type="checkbox"/>
MS. 000043	<input type="checkbox"/>
MS. 000044	<input type="checkbox"/>
MS. 000045	<input type="checkbox"/>
MS. 000046	<input type="checkbox"/>
MS. 000047	<input type="checkbox"/>
MS. 000048	<input type="checkbox"/>
MS. 000049	<input type="checkbox"/>
MS. 000050	<input type="checkbox"/>
MS. 000051	<input type="checkbox"/>
MS. 000052	<input type="checkbox"/>
MS. 000053	<input type="checkbox"/>
MS. 000054	<input type="checkbox"/>
MS. 000055	<input type="checkbox"/>
MS. 000056	<input type="checkbox"/>
MS. 000057	<input type="checkbox"/>
MS. 000058	<input type="checkbox"/>
MS. 000059	<input type="checkbox"/>
MS. 000060	<input type="checkbox"/>
MS. 000061	<input type="checkbox"/>
MS. 000062	<input type="checkbox"/>
MS. 000063	<input type="checkbox"/>
MS. 000064	<input type="checkbox"/>
MS. 000065	<input type="checkbox"/>
MS. 000066	<input type="checkbox"/>
MS. 000067	<input type="checkbox"/>
MS. 000068	<input type="checkbox"/>
MS. 000069	<input type="checkbox"/>
MS. 000070	<input type="checkbox"/>
MS. 000071	<input type="checkbox"/>
MS. 000072	<input type="checkbox"/>
MS. 000073	<input type="checkbox"/>
MS. 000074	<input type="checkbox"/>
MS. 000075	<input type="checkbox"/>
MS. 000076	<input type="checkbox"/>
MS. 000077	<input type="checkbox"/>
MS. 000078	<input type="checkbox"/>
MS. 000079	<input type="checkbox"/>
MS. 000080	<input type="checkbox"/>
MS. 000081	<input type="checkbox"/>
MS. 000082	<input type="checkbox"/>
MS. 000083	<input type="checkbox"/>
MS. 000084	<input type="checkbox"/>
MS. 000085	<input type="checkbox"/>
MS. 000086	<input type="checkbox"/>
MS. 000087	<input type="checkbox"/>
MS. 000088	<input type="checkbox"/>
MS. 000089	<input type="checkbox"/>
MS. 000090	<input type="checkbox"/>
MS. 000091	<input type="checkbox"/>
MS. 000092	<input type="checkbox"/>
MS. 000093	<input type="checkbox"/>
MS. 000094	<input type="checkbox"/>
MS. 000095	<input type="checkbox"/>
MS. 000096	<input type="checkbox"/>
MS. 000097	<input type="checkbox"/>
MS. 000098	<input type="checkbox"/>
MS. 000099	<input type="checkbox"/>
MS. 000100	<input type="checkbox"/>
MS. 000101	<input type="checkbox"/>
MS. 000102	<input type="checkbox"/>
MS. 000103	<input type="checkbox"/>
MS. 000104	<input type="checkbox"/>
MS. 000105	<input type="checkbox"/>
MS. 000106	<input type="checkbox"/>
MS. 000107	<input type="checkbox"/>
MS. 000108	<input type="checkbox"/>
MS. 000109	<input type="checkbox"/>
MS. 000110	<input type="checkbox"/>
MS. 000111	<input type="checkbox"/>
MS. 000112	<input type="checkbox"/>
MS. 000113	<input type="checkbox"/>
MS. 000114	<input type="checkbox"/>
MS. 000115	<input type="checkbox"/>
MS. 000116	<input type="checkbox"/>
MS. 000117	<input type="checkbox"/>
MS. 000118	<input type="checkbox"/>
MS. 000119	<input type="checkbox"/>
MS. 000120	<input type="checkbox"/>
MS. 000121	<input type="checkbox"/>
MS. 000122	<input type="checkbox"/>
MS. 000123	<input type="checkbox"/>
MS. 000124	<input type="checkbox"/>
MS. 000125	<input type="checkbox"/>
MS. 000126	<input type="checkbox"/>
MS. 000127	<input type="checkbox"/>
MS. 000128	<input type="checkbox"/>
MS. 000129	<input type="checkbox"/>
MS. 000130	<input type="checkbox"/>
MS. 000131	<input type="checkbox"/>
MS. 000132	<input type="checkbox"/>
MS. 000133	<input type="checkbox"/>
MS. 000134	<input type="checkbox"/>
MS. 000135	<input type="checkbox"/>
MS. 000136	<input type="checkbox"/>
MS. 000137	<input type="checkbox"/>
MS. 000138	<input type="checkbox"/>
MS. 000139	<input type="checkbox"/>
MS. 000140	<input type="checkbox"/>
MS. 000141	<input type="checkbox"/>
MS. 000142	<input type="checkbox"/>
MS. 000143	<input type="checkbox"/>
MS. 000144	<input type="checkbox"/>
MS. 000145	<input type="checkbox"/>
MS. 000146	<input type="checkbox"/>
MS. 000147	<input type="checkbox"/>
MS. 000148	<input type="checkbox"/>
MS. 000149	<input type="checkbox"/>
MS. 000150	<input type="checkbox"/>
MS. 000151	<input type="checkbox"/>
MS. 000152	<input type="checkbox"/>
MS. 000153	<input type="checkbox"/>
MS. 000154	<input type="checkbox"/>
MS. 000155	<input type="checkbox"/>
MS. 000156	<input type="checkbox"/>
MS. 000157	<input type="checkbox"/>
MS. 000158	<input type="checkbox"/>
MS. 000159	<input type="checkbox"/>
MS. 000160	<input type="checkbox"/>
MS. 000161	<input type="checkbox"/>
MS. 000162	<input type="checkbox"/>
MS. 000163	<input type="checkbox"/>
MS. 000164	<input type="checkbox"/>
MS. 000165	<input type="checkbox"/>
MS. 000166	<input type="checkbox"/>
MS. 000167	<input type="checkbox"/>
MS. 000168	<input type="checkbox"/>
MS. 000169	<input type="checkbox"/>
MS. 000170	<input type="checkbox"/>
MS. 000171	<input type="checkbox"/>
MS. 000172	<input type="checkbox"/>
MS. 000173	<input type="checkbox"/>
MS. 000174	<input type="checkbox"/>
MS. 000175	<input type="checkbox"/>
MS. 000176	<input type="checkbox"/>
MS. 000177	<input type="checkbox"/>
MS. 000178	<input type="checkbox"/>
MS. 000179	<input type="checkbox"/>
MS. 000180	<input type="checkbox"/>
MS. 000181	<input type="checkbox"/>
MS. 000182	<input type="checkbox"/>
MS. 000183	<input type="checkbox"/>
MS. 000184	<input type="checkbox"/>
MS. 000185	<input type="checkbox"/>
MS. 000186	<input type="checkbox"/>
MS. 000187	<input type="checkbox"/>
MS. 000188	<input type="checkbox"/>
MS. 000189	<input type="checkbox"/>
MS. 000190	<input type="checkbox"/>
MS. 000191	<input type="checkbox"/>
MS. 000192	<input type="checkbox"/>
MS. 000193	<input type="checkbox"/>
MS. 000194	<input type="checkbox"/>
MS. 000195	<input type="checkbox"/>
MS. 000196	<input type="checkbox"/>
MS. 000197	<input type="checkbox"/>
MS. 000198	<input type="checkbox"/>
MS. 000199	<input type="checkbox"/>
MS. 000200	<input type="checkbox"/>
MS. 000201	<input type="checkbox"/>
MS. 000202	<input type="checkbox"/>
MS. 000203	<input type="checkbox"/>
MS. 000204	<input type="checkbox"/>
MS. 000205	<input type="checkbox"/>
MS. 000206	<input type="checkbox"/>
MS. 000207	<input type="checkbox"/>
MS. 000208	<input type="checkbox"/>
MS. 000209	<input type="checkbox"/>
MS. 000210	<input type="checkbox"/>
MS. 000211	<input type="checkbox"/>
MS. 000212	<input type="checkbox"/>
MS. 000213	<input type="checkbox"/>
MS. 000214	<input type="checkbox"/>
MS. 000215	<input type="checkbox"/>
MS. 000216	<input type="checkbox"/>
MS. 000217	<input type="checkbox"/>
MS. 000218	<input type="checkbox"/>
MS. 000219	<input type="checkbox"/>
MS. 000220	<input type="checkbox"/>
MS. 000221	<input type="checkbox"/>
MS. 000222	<input type="checkbox"/>
MS. 000223	<input type="checkbox"/>
MS. 000224	<input type="checkbox"/>
MS. 000225	<input type="checkbox"/>
MS. 000226	<input type="checkbox"/>
MS. 000227	<input type="checkbox"/>
MS. 000228	<input type="checkbox"/>
MS. 000229	<input type="checkbox"/>
MS. 000230	<input type="checkbox"/>
MS. 000231	<input type="checkbox"/>
MS. 000232	<input type="checkbox"/>
MS. 000233	<input type="checkbox"/>
MS. 000234	<input type="checkbox"/>
MS. 000235	<input type="checkbox"/>
MS. 000236	<input type="checkbox"/>
MS. 000237	<input type="checkbox"/>
MS. 000238	<input type="checkbox"/>
MS. 000239	<input type="checkbox"/>
MS. 000240	<input type="checkbox"/>
MS. 000241	<input type="checkbox"/>
MS. 000242	<input type="checkbox"/>
MS. 000243	<input type="checkbox"/>
MS. 000244	<input type="checkbox"/>
MS. 000245	<input type="checkbox"/>
MS. 000246	<input type="checkbox"/>
MS. 000247	<input type="checkbox"/>
MS. 000248	<input type="checkbox"/>
MS. 000249	<input type="checkbox"/>
MS. 000250	<input type="checkbox"/>
MS. 000251	<input type="checkbox"/>
MS. 000252	<input type="checkbox"/>
MS. 000253	<input type="checkbox"/>
MS. 000254	<input type="checkbox"/>
MS. 000255	<input type="checkbox"/>
MS. 000256	<input type="checkbox"/>
MS. 000257	<input type="checkbox"/>
MS. 000258	<input type="checkbox"/>
MS. 000259	<input type="checkbox"/>
MS. 000260	<input type="checkbox"/>
MS. 000261	<input type="checkbox"/>
MS. 000262	<input type="checkbox"/>
MS. 000263	<input type="checkbox"/>
MS. 000264	<input type="checkbox"/>
MS. 000265	<input type="checkbox"/>
MS. 000266	<input type="checkbox"/>
MS. 000267	<input type="checkbox"/>
MS. 000268	<input type="checkbox"/>
MS. 000269	<input type="checkbox"/>
MS. 000270	<input type="checkbox"/>
MS. 000271	<input type="checkbox"/>
MS. 000272	<input type="checkbox"/>
MS. 000273	<input type="checkbox"/>
MS. 000274	<input type="checkbox"/>
MS. 000275	<input type="checkbox"/>
MS. 000276	<input type="checkbox"/>
MS. 000277	<input type="checkbox"/>
MS. 000278	<input type="checkbox"/>
MS. 000279	<input type="checkbox"/>
MS. 000280	<input type="checkbox"/>
MS. 000281	<input type="checkbox"/>
MS. 000282	<input type="checkbox"/>
MS. 000283	<input type="checkbox"/>
MS. 000284	<input type="checkbox"/>
MS. 000285	<input type="checkbox"/>
MS. 000286	<input type="checkbox"/>
MS. 000287	<input type="checkbox"/>
MS. 000288	<input type="checkbox"/>
MS. 000289	<input type="checkbox"/>
MS. 000290	<input type="checkbox"/>
MS. 000291	<input type="checkbox"/>
MS. 000292	<input type="checkbox"/>
MS. 000293	<input type="checkbox"/>
MS. 000294	<input type="checkbox"/>
MS. 000295	<input type="checkbox"/>
MS. 000296	<input type="checkbox"/>
MS. 000297	<input type="checkbox"/>
MS. 000298	<input type="checkbox"/>
MS. 000299	<input type="checkbox"/>
MS. 000300	<input type="checkbox"/>
MS. 000301	<input type="checkbox"/>
MS. 000302	<input type="checkbox"/>
MS. 000303	<input type="checkbox"/>
MS. 000304	<input type="checkbox"/>
MS. 000305	<input type="checkbox"/>
MS. 000306	<input type="checkbox"/>
MS. 000307	<input type="checkbox"/>
MS. 000308	<input type="checkbox"/>
MS. 000309	<input type="checkbox"/>
MS. 000310	<input type="checkbox"/>
MS. 000311	<input type="checkbox"/>
MS. 000312	<input type="checkbox"/>
MS. 000313	<input type="checkbox"/>
MS. 000314	<input type="checkbox"/>
MS. 000315	<input type="checkbox"/>
MS. 000316	<input type="checkbox"/>
MS. 000317	<input type="checkbox"/>
MS. 000318	<input type="checkbox"/>
MS. 000319	<input type="checkbox"/>
MS. 000320	<input type="checkbox"/>
MS. 000321	<input type="checkbox"/>
MS. 000322	<input type="checkbox"/>
MS. 000323	<input type="checkbox"/>
MS. 000324	<input type="checkbox"/>
MS. 000325	<input type="checkbox"/>
MS. 000326	<input type="checkbox"/>
MS. 000327	<input type="checkbox"/>
MS. 000328	<input type="checkbox"/>
MS. 000329	<input type="checkbox"/>
MS. 000330	<input type="checkbox"/>
MS. 000331	<input type="checkbox"/>
MS. 000332	<input type="checkbox"/>
MS. 000333	<input type="checkbox"/>
MS. 000334	<input type="checkbox"/>
MS. 000335	<input type="checkbox"/>
MS. 000336	<input type="checkbox"/>
MS. 000337	<input type="checkbox"/>
MS. 000338	<input type="checkbox"/>
MS. 000339	<input type="checkbox"/>
MS. 000340	<input type="checkbox"/>
MS. 000341	<input type="checkbox"/>
MS. 000342	<input type="checkbox"/>
MS. 000343	<input type="checkbox"/>
MS. 000344	<input type="checkbox"/>
MS. 000345	<input type="checkbox"/>
MS. 000346	<input type="checkbox"/>
MS. 000347	<input type="checkbox"/>
MS. 000348	<input type="checkbox"/>
MS. 000349	<input type="checkbox"/>
MS. 000350	<input type="checkbox"/>
MS. 000351	<input type="checkbox"/>
MS. 000352	<input type="checkbox"/>
MS. 000353	<input type="checkbox"/>
MS. 000354	<input type="checkbox"/>
MS. 000355	<input type="checkbox"/>
MS. 000356	<input type="checkbox"/>
MS. 000357	<input type="checkbox"/>
MS. 000358	<input type="checkbox"/>
MS. 000359	<input type="checkbox"/>
MS. 000360	<input type="checkbox"/>
MS. 000361	<input type="checkbox"/>
MS. 000362	<input type="checkbox"/>
MS. 000363	<input type="checkbox"/>
MS. 000364	<input type="checkbox"/>
MS. 000365	<input type="checkbox"/>
MS. 000366	<input type="checkbox"/>
MS. 000367	<input type="checkbox"/>
MS. 000368	<input type="checkbox"/>
MS. 000369	<input type="checkbox"/>
MS. 000370	<input type="checkbox"/>
MS. 000371	<input type="checkbox"/>
MS. 000372	<input type="checkbox"/>
MS. 000373	<input type="checkbox"/>
MS. 000374	<input type="checkbox"/>
MS. 000375	<input type="checkbox"/>
MS. 000376	<input type="checkbox"/>
MS. 000377	<input type="checkbox"/>
MS. 000378	<input type="checkbox"/>
MS. 000379	<input type="checkbox"/>
MS. 000380	<input type="checkbox"/>
MS. 000381	<input type="checkbox"/>
MS. 000382	<input type="checkbox"/>
MS. 000383	<input type="checkbox"/>
MS. 000384	<input type="checkbox"/>
MS. 000385	<input type="checkbox"/>
MS. 000386	<input type="checkbox"/>
MS. 000387	<input type="checkbox"/>
MS. 000388	<input type="checkbox"/>
MS. 000389	<input type="checkbox"/>
MS. 000390	<input type="checkbox"/>
MS. 000391	<input type="checkbox"/>
MS. 000392	<input type="checkbox"/>
MS. 000393	<input type="checkbox"/>
MS. 000394	<input type="checkbox"/>
MS. 000395	<input type="checkbox"/>
MS. 000396	<input type="checkbox"/>
MS. 000397	<input type="checkbox"/>
MS. 000398	<input type="checkbox"/>
MS. 000399	<input type="checkbox"/>
MS. 000400	<input type="checkbox"/>
MS. 000401	<input type="checkbox"/>
MS. 000402	<input type="checkbox"/>
MS. 000403	<input type="checkbox"/>
MS. 000404	<input type="checkbox"/>
MS. 000405	<input type="checkbox"/>
MS. 000406	<input type="checkbox"/>
MS. 000407	<input type="checkbox"/>
MS. 000408	<input type="checkbox"/>
MS. 000409	<input type="checkbox"/>
MS. 000410	<input type="checkbox"/>
MS. 000411	<input type="checkbox"/>
MS. 000412	<input type="checkbox"/>
MS. 000413	<input type="checkbox"/>
MS. 000414	<input type="checkbox"/>
MS. 000415	<input type="checkbox"/>
MS. 000416	<input type="checkbox"/>
MS. 000417	<input type="checkbox"/>
MS. 000418	<input type="checkbox"/>
MS. 000419	<input type="checkbox"/>
MS. 000420	<input type="checkbox"/>
MS. 000421	<input type="checkbox"/>
MS. 000422	<input type="checkbox"/>
MS. 000423	<input type="checkbox"/>
MS. 000424	<input type="checkbox"/>
MS. 000425	<input type="checkbox"/>
MS. 000426	<input type="checkbox"/>
MS. 000427	<input type="checkbox"/>
MS. 000428	<input type="checkbox"/>
MS. 000429	<input type="checkbox"/>
MS. 000430	<input type="checkbox"/>
MS. 000431	<input type="checkbox"/>
MS. 000432	<input type="checkbox"/>
MS. 000433	<input type="checkbox"/>
MS. 000434	<input type="checkbox"/>
MS. 000435	<input type="checkbox"/>
MS. 000436	<input type="checkbox"/>
MS. 000437	<input type="checkbox"/>
MS. 000438	<input type="checkbox"/>
MS. 000439	<input type="checkbox"/>
MS. 000440	<input type="checkbox"/>
MS. 000441	<input type="checkbox"/>
MS. 000442	<input type="checkbox"/>
MS. 000443	<input type="checkbox"/>
MS. 000444	<input type="checkbox"/>
MS. 000445	<input type="checkbox"/>
MS. 000446	<input type="checkbox"/>
MS. 000447	<input type="checkbox"/>
MS. 000448	<input type="checkbox"/>
MS. 000449	<input type="checkbox"/>

DISCLAIMER NOTICE



THIS DOCUMENT IS BEST QUALITY AVAILABLE. THE COPY FURNISHED TO DTIC CONTAINED A SIGNIFICANT NUMBER OF PAGES WHICH DO NOT REPRODUCE LEGIBLY.

THE MISSION OF AGARD

According to its Charter, the mission of AGARD is to bring together the leading personalities of the NATO nations in the fields of science and technology relating to aerospace for the following purposes:

- Recommending effective ways for the member nations to use their research and development capabilities for the common benefit of the NATO community;
- Providing scientific and technical advice and assistance to the Military Committee in the field of aerospace research and development (with particular regard to its military application);
- Continuously stimulating advances in the aerospace sciences relevant to strengthening the common defence posture;
- Improving the co-operation among member nations in aerospace research and development;
- Exchange of scientific and technical information;
- Providing assistance to member nations for the purpose of increasing their scientific and technical potential;
- Rendering scientific and technical assistance, as requested, to other NATO bodies and to member nations in connection with research and development problems in the aerospace field.

The highest authority within AGARD is the National Delegates Board consisting of officially appointed senior representatives from each member nation. The mission of AGARD is carried out through the Panels which are composed of experts appointed by the National Delegates, the Consultant and Exchange Programme and the Aerospace Applications Studies Programme. The results of AGARD work are reported to the member nations and the NATO Authorities through the AGARD series of publications of which this is one.

Participation in AGARD activities is by invitation only and is normally limited to citizens of the NATO nations.

The content of this publication has been reproduced
directly from material supplied by AGARD or the authors.

Published March 1989

Copyright © AGARD 1989
All Rights Reserved

ISBN 92-835-0494-1



*Printed by Specialised Printing Services Limited
40 Chigwell Lane, Loughton, Essex IG10 3TZ*

PREFACE

With recent advances in missile seekers and processors, and in the analysis of missile dynamics motions and the associated control subsystem designs, missile manoeuvre envelopes have significantly expanded. It was therefore appropriate and timely that the stability and controllability of such missiles be examined. This symposium has provided a forum for the interchange of ideas, and discussions of the different techniques currently involved in dealing with the various aspects of this subject. The presentation covered a wide selection of topics, from prediction, simulation and test, through to a look at current development experience. The subject of the symposium was deliberately limited to tactical missiles, encompassing air-to-air, air-to-ground, and ground-to-air, but not ballistic missiles.

* * *

Grâce aux progrès réalisés récemment dans les domaines des têtes chercheuses, et des processeurs intégrés aux missiles, ainsi que dans l'analyse des mouvements dynamiques des missiles et dans la conception des sous-systèmes de commande associés, les domaines d'évolution des missiles ont pu être considérablement élargis.

Le Panel a donc estimé pertinent et opportun d'examiner la stabilité et la manoeuvrabilité de tels missiles.

Le présent symposium a servi de forum pour un échange d'idées sur ce sujet et a permis des discussions sur les différentes techniques mises en oeuvre à l'heure actuelle pour résoudre les problèmes posés par les divers aspects de cette question.

Les présentations ont couvert une large gamme de sujets tels que la prévision, la simulation et les essais, pour en terminer par un aperçu des développements en cours. Le sujet du symposium a été intentionnellement limité aux missiles tactiques, du type air-air, air-sol et sol-air, à l'exclusion des missiles balistiques.

FLIGHT MECHANICS PANEL OFFICERS

Chairman: Dr Ing. A.Filisetti
Director
Combat Aircraft Group
Aeritalia
10146 Turin
Italy

Deputy Chairman: Mr R.C.A'Harrah
O.C.N.R.
Code OOJDL
800 N Quincy Street
BCT/1
Virginia 22217-5000
USA

TECHNICAL PROGRAMME COMMITTEE

Mr F.Mary
Sous-Directeur
Recherche & Développement
Aérospatiale
37 Boulevard de Montmorency
75781 Paris Cedex 16
France

Mr S.R.Metres
Assistant Director
AFWAL-FI
Wright-Patterson Air Force Base
Ohio 45433
USA

HOST NATION COORDINATORS

Colonel D.Kaya
Ministry of National Defence
Department of R & D
(ARGE)
Ankara
Turkey

Dr F.Ozek
TUBITAK
Konya Yolu
Beşevler
Bahçelievler
Ankara
Turkey

PANEL EXECUTIVE

Mr M.K.Foster
AGARD/OTAN
7 rue Ancelle
92200 Neuilly-sur-Seine
France

ACKNOWLEDGEMENT

The Flight Mechanics Panel wishes to express its thanks to the Turkish National Delegates to AGARD for the invitation to hold this meeting in Ankara, Turkey and for the facilities and personnel which made this meeting possible.

Le Panel du Mécanique du Vol tient à remercier les Délégués Nationaux de la Turquie auprès de l'AGARD de leur invitation à tenir cette réunion à Ankara ainsi que des installations et du personnel mis à sa disposition.

CONTENTS

	Page
PREFACE	iii
PANEL OFFICERS	iv
	Reference
Keynote Address: THE PRESENT STATUS AND THE FUTURE OF MISSILE AERODYNAMICS by J.N.Nielsen	K
PREVISION DE LA STABILITE AERODYNAMIQUE DES MISSILES par J.Champigny	1
Paper 2 withdrawn	
PREDICTION OF STABILITY DERIVATIVES FOR MISSILES USING THE HUSSE PANEL CODE by L.Fornasier and P.D'Espiney	3
MISSILE DATCOM: ENHANCEMENTS FOR DESIGN APPLICATIONS by J.E.Jenkins and W.B.Blake	4
THE EFFECT OF INTERDIGITATION ANGLE ON THE AERODYNAMIC CHARACTERISTICS OF A REPRESENTATIVE CANARD CONFIGURATION AT SPEEDS UP TO MACH 5.5 by P.G.C.Herring	5*
PREDICTION OF DYNAMIC DERIVATIVES by H.Fuchs	6
PREDICTION OF TACTICAL MISSILE DYNAMICS by L.E.Ericsson	7
VORTEX INDUCED CHARACTERISTICS OF MISSILES IN UNSTEADY MANEUVERS by M.R.Mendenhall and S.C.Perkins, Jr	8
Paper 9 not available at time of printing	
AEROELASTIC TAILORING PROCEDURE FOR CONTROLLING FIN HINGE MOMENTS by M.F.E.Dillenius and S.C.McIntosh, Jr	10
LATERAL REACTION JET CONTROL OF TACTICAL MISSILES by A.Machell	11*
ALTERNATIVE POLAR HOMING STRATEGIES by M.S.Gate and R.S.Randall	12
HOW TO CONTROL UNSTABLE MISSILE AIRFRAMES: METHODOLOGY AND LIMITATIONS by A.Gazzina	13
PIF-PAF CONTROL OF TACTICAL MISSILES by B.Lazure	14*
GYROMETRE LASER TRIAXIAL MINIATURISE par S.Petit	15
NEW TEST TECHNIQUES TO EVALUATE NEAR FIELD EFFECTS FOR SUPERSONIC STORE CARRIAGE AND SEPARATION by W.C.Sawyer, R.L.Stallings, Jr, F.J.Wilcox, Jr, A.B.Blair, Jr, W.J.Monta and E.B.Plentovich	16
REMOTE CONTROL MISSILE MODEL TEST by J.M.Allen, D.S.Shaw and W.C.Sawyer	17

* Printed in classified publication CP 451 (Supplement)

	Reference
WIND TUNNEL TESTS: THE ROLE OF THE MODEL by S.Mazzuca and B.Piacentini	18
IDENTIFICATION OF STABILITY AND CONTROL PARAMETERS OF A BRILLIANT AMMUNITION. <i>WASSER-UND-ERDE-ROKETS</i> by K.-F.Doherr, G.Lehmann and H.Schilling	19
VALIDATION OF MISSILE SIMULATION by W.Bub	20
INVESTIGATIONS OF THRUST VECTOR CONTROL FOR HIGH-ALPHA PITCHOVER by A.O.Danielson and R.B.Dillinger	21
A STRUCTURED SINGULAR VALUE APPROACH TO MISSILE AUTOPILOT ANALYSIS II by G.A.Hewer, R.Klabunde and C.Kenney	22
ANALYSIS AND TESTING OF A HIGH PERFORMANCE AIR-AIR MISSILE by G.L.Stevens	23
MARGINAL RELEASE DISTURBANCES ON ADVANCED MISSILES by R.Deslandes	24
AEROELASTIC ANALYSIS OF MISSILE CONTROL SURFACES WITH STRUCTURAL NON-LINEARITY by D.Sepahy	25
Paper 26 withdrawn	
EXPERIENCE GAINED IN THE IMPROVEMENT OF THE ASPIDE AERODYNAMIC CONFIGURATION FOR THE SURFACE TO AIR ROLE by S.Mazzuca	27
WINGED VERSUS WINGLESS MISSILE AIRFRAMES by A.Gazzina and S.Mazzuca	28
Paper 29 withdrawn	
APPLICATION OF MODERN AERODYNAMIC CONTROL TO FUTURE AIR TO AIR MISSILES by P.Letang	30*

THE PRESENT STATUS AND THE FUTURE OF MISSILE AERODYNAMICS

Jack N. Nielsen
 Chief Scientist
 NASA Ames Research Center
 Moffett Field, California 94035, U.S.A.

SUMMARY

This paper reviews some recent developments in the state of the art in missile aerodynamics. Among the subjects covered are (1) Tri-service/NASA data base, (2) wing-body interference, (3) nonlinear controls, (4) hypersonic transition, (5) vortex interference, (6) airbreathers, supersonic inlets, (7) store separation problems, (8) correlation of missile data, (9) CFD codes for complete configurations, (10) engineering prediction methods, and (11) future configurations. Throughout the paper, suggestions are made for future research and development to advance the state of the art of missile aerodynamics.

SYMBOLS

a	body radius at wing position
AR	aspect ratio
b	span, wing tip to wing tip
C_A	axial force coefficient
C_{ξ}	rolling moment coefficient
$C_{\xi\delta}$	effective dihedral, negative for stability
C_m	pitching moment
C_{NF}	normal force coefficient of fin
C_{NF}^*	value of C_{NF} at $\bar{\alpha}_\xi$ and $\bar{\theta}_\xi$ for wing alone
C_n	yawing moment coefficient
$C_{n\delta}$	directional stability, positive for stability
D	drag of missile configuration
K_B	$N_B(W)/N_W$, body lift interference parameter for $\delta_f = 0$
K_W	$N_W(B)/N_W$, wing lift interference parameter for $\delta_f = 0$
K_ϕ	constant used to express change in fin angle of attack caused by α_B coupling
k_1	$b/(1 \tan \alpha)$
k_2	$M_\infty \sin \alpha$, cross-flow Mach number
k_3	$(\tan \alpha)/AR$
k_w	lift interference parameter for control; $N_W(B)/N_W$ with $\alpha_B = 0$, $\alpha_w = \delta_f$
L/D	configuration lift-drag ratio
l	length of missile configuration
M_∞	freestream Mach number
M_C, M_n	Mach number normal to body axis
M_ξ	local Mach number at a point in a flow
\bar{M}_ξ	average Mach number across exposed span of fin
N	configuration normal force

K-2

$N_{B(W)}$	normal force on body caused by presence of wing
N_W	normal force on wing alone (wing alone = two fins joined at root chord)
$N_{W(B)}$	normal force of wing in the presence of body
q_∞	freestream dynamic pressure
q_x	local dynamic pressure
\bar{q}_x	average value of q_x across exposed span of fin
r	radial distance of point from body longitudinal axis
r, ϕ	polar coordinates in crossflow plane
s, s_m	distance from body longitudinal axis to tip of fin
y	lateral distance from body longitudinal axis in plane of fins
$(\bar{x}/c)_F$	distance of fin center of pressure from leading edge of root chord nondimensionalized by fin root chord
α	angle of attack of undeflected fin, $\alpha_C \cos \phi$
α_C	angle of attack of missile body
α_{eq}	equivalent angle of attack, Eq. (5)
α_x	local angle of attack at a point in flow
$\bar{\alpha}_x$	average angle of attack across exposed span of fin
δ_f	angular deflection of fin from zero position
$\delta_1, \delta_2, \delta_3, \delta_4$	deflection of fin 1, etc.
ϕ	roll angle of right fin from its horizontal position, positive clockwise
λ	taper ratio of fin, ratio of tip chord to root chord at wing-body juncture
β	sideslip angle, $\beta = \alpha_C \sin \phi$ or $\sin \beta = \sin \alpha_C \sin \phi$ for large α_C
θ_C	semi-apex angle of cone
A_{jj}	an interference factor slightly less than unity associated with deflection of fin j

1. INTRODUCTION

In the six years since the last AGARD meeting on missile aerodynamics in Trondheim, Norway in 1982, much has happened. The purposes of the present paper are to describe the recent developments in missile aerodynamics, and to suggest areas where future research could be fruitful.

The emphasis in the paper is on the U.S. experience in stability and control of tactical missiles. The aerodynamic problems are discussed in generic terms so that reference to particular missiles is not necessary.

The paper covers theory, experiment, and engineering prediction, but not radar cross-section. The papers of the 1982 AGARD meeting are to be found in Ref. 1.

2. OVERVIEW

Among the aerodynamic requirements for tactical missiles are range, maneuverability, and speed. These requirements can be contradictory depending on the specific application. The search for range has led to much work on airbreathing missiles. As a consequence, there is an interest in noncircular, non-rolling missiles. The desire for maneuverability has led to operation at high angles of attack, which, in turn, has created serious stability and control problems. At the same time, the use of airbreathers puts definite angle-of-attack limits under which the engines will operate, and in this regard, range and maneuverability are in conflict.

The trend toward higher speeds has brought with it new problems in hypersonic aerodynamics such as wing-body interference effects and unusual vortex behavior. In addition, there are the questions of transition and turbulence at hypersonic speeds which are important in many applications.

Methods of calculating the aerodynamics of missiles have been improved and recent developments have increased the accuracy of the Euler equations for calculating missile flow fields. An engineering method for the design of missiles has been produced in MISSILE DATACOM (Ref. 31).

Also an engineering design code which works to high angles of attack, Missile III, has been developed based on an extensive Tri-service/NASA data base (ref. 2).

3. TRI-SERVICE/NASA DATA BASE

The Tri-service/NASA data base is being considered at this point because many nonlinear aerodynamic phenomena are illustrated by data from this source. The basic body for the systematic tests consisted of a cylindrical body with an ogive nose 3.0 calibers long for a total body length of 12.5 calibers. A series of fins (Fig. 1) ranging in aspect ratio from 0.25 to 4.0 was tested in a tail cruciform arrangement with the body over the angle of attack and Mach number range (shown in Fig. 2). The radius to semispan ratio was maintained constant at 0.5. The configurations were all tested over the roll-angle range and, in some of the tests, the fins were deflected as much as $\pm 40^\circ$ about their hinge lines.

Six component force-and-moment data were taken for the configurations and normal force, root-bending moment, and hinge moment were measured for each fin.

These data form the basis of a prediction method for cruciform missile aerodynamic characteristics, and are incorporated into a code called Missile III (Ref. 2). In addition, Refs. 3-5 make use of the Tri-service/NASA data base.

4. WING-BODY INTERFERENCE

Wing-body interference has been an important subject for decades. At high angles of attack it has an effect on the total normal force developed by a missile and its maneuverability. For moderate angles of attack, and subsonic to moderate supersonic Mach numbers methods for predicting interference between mid-wing and circular bodies are well known. This interference for the wing is measured by a parameter defined by

$$K_W(B) = \frac{N_W(B)}{N_W} \quad (1)$$

Here $N_W(B)$ is the normal force on the undeflected wing divided by the normal force of the wing alone at the same angle of attack. For the normal force carried over onto the body from the wing, an analogous ratio K_B is defined as follows:

$$K_B = \frac{N_B(W)}{N_W} \quad (2)$$

The data of the Tri-service/NASA data base are sufficient to see the effect of compressibility on the values of K_W and K_B . In the range of angle of attack and Mach number cited above, both parameters are functions of α/s only. What happens to the value of these parameters at higher values of angle of attack and Mach number has been reported in Ref. 3 based on the Tri-service/NASA data base.

The value of K_W and K_B/K_W have been extracted from the data base for $M_\infty = 2.5, 3.5$, and 4.5 , and for angles of attack up to 40° . These are tabulated in Ref. 3 for seven fin planforms varying in aspect ratio and taper ratio. Sufficient information is contained in the reference to determine the normal-force coefficients for the entire configurations.

Plots of K_W versus α are shown in Fig. 3 for aspect ratio 2 wings as functions of Mach number and taper ratio. The effects of taper ratio are small, but the effects of angle of attack are large. For small angles of attack, K_W tends toward the slender-body value, but at high angles of attack it moves toward one or thereabouts. Thus the favorable body interference on the fins tends to disappear at high angles of attack for all Mach numbers. This result is compatible with the simple method of finding loading on bodies at high angles of attack by using Newtonian impact pressure on all surfaces facing the air-stream and assuming vacuum pressure (0) on the leeward surfaces. On page 509 of reference 12 it is seen that the cross-flow Mach number correlates K_W for different Mach numbers.

A series of curves for K_B/K_W is shown in Fig. 4 in the same format as Fig. 3. The values of K_B at low α tend generally toward the slender body value of 0.55 or lower. There is a fair amount of scatter in the data. At high angles of attack ($\alpha \geq 20^\circ$), the value of K_B tends to small values, indicating a loss of lift carryover from the fins to the body for Mach numbers from 2.5 to 4.5.

In connection with the value of K_B/K_W , these values pertain to the short afterbody lengths of the present configuration. These lengths are not uniform. The length of the afterbody probably can have a significant effect on K_B . This problem is a good one for further work, possibly using an Euler code.

Another problem which needs future attention: where is the center-of-pressure location for the lift carryover onto the body from the fin?

5. NONLINEAR CONTROL EFFECT

The control type that will be of interest here is the all-movable control which rotates about a hinge line perpendicular to the body. This information about all-movable controls is also true to a considerable extent about other controls, such as wraparound fins and retractable fins. Extensive measurements were made as a function of M_∞ , α , δ , λ , and AR of all-movable fin normal force, root bending moment, and fin hinge moment. Some interesting effects were found in the Tri-service data base as described in Ref. 4.

Because of the variation in local flow conditions about a body of revolution at high angle of attack as a function of roll angle, the effectiveness of the fin in producing normal force will vary greatly between the leeward and windward fins. The local quantities affecting the fin normal force are the upwash angle, dynamic pressure, and Mach number. As examples of how the effectiveness of a fin in producing normal force varies with M_∞ and ϕ , consider Fig. 5 (taken from Ref. 4). For $\phi = 90^\circ$, the fin is on the windward meridian and for $\phi = -90^\circ$, the fin is on the leeward meridian. Examining the $M_\infty = 4.5$ case first, we note that for constant ϕ , increases in fin deflection from -40° to $+40^\circ$ are always accompanied with increase in fin normal force. At $M_\infty = 2$ there is a peak normal force below $\delta = 40^\circ$ for $\phi > -20^\circ$. Thus there is a fin stall.

A second interesting feature is that at $\phi = 90^\circ$, a given fin deflection produces more change in normal force than it does at $\phi = -90^\circ$. This effect is particularly noticeable at $M = 4.5$ where the fin on the leeward meridian is operating almost in a vacuum.

It is possible to correlate the data of Fig. 5 by accounting for the local Mach number, dynamic pressure, and upwash angle.* These local quantities are determined by using an Euler code to calculate the body alone flow field. The average value of these quantities over the span of the fin is determined in accordance with the following formula

$$\bar{M}_k = \frac{1}{s_m - a} \int_a^{s_m} M_k(\phi, r) dr \quad (3)$$

with analogous formulas for $\bar{\alpha}_k$ and \bar{q}_k . Using the values of \bar{M}_k and $\bar{\alpha}_k$ to define a uniform flow, we find the value of C_{NF}^* in this parallel flow from analysis or wing-alone data. The predicted value of C_{NF} is then given as follows:

$$C_{NF} = C_{NF}^* k_w \frac{\bar{q}_k}{q_\infty} \quad (4)$$

Conversely, the measured value of C_{NF} can be used to calculate k_w . The value of k_w should correlate the fin normal-force data for all roll angles and fin deflections for a given Mach number. Such a correlation is shown in Fig. 6 by using the data of Fig. 5. For the $M_\infty = 2.0$ results, good correlation is obtained for all the data except the $\delta_2 = +40^\circ$ data near $\phi = 0^\circ$. These data represent a stall condition on the fin as observed in Fig. 5. For $M_\infty = 4.5$, the data correlate well. For ϕ between -90° and -60° the flow is separated, and Euler equation solutions to evaluate \bar{M}_k , $\bar{\alpha}_k$, and \bar{q}_k do not give accurate results. Thus k_w is not approximately unity as expected.

The question of hinge moments of all-movable controls at large α and/or large M_∞ is also of interest. Sufficient data exist in the Tri-service/NASA data base to form the basis of a hinge-moment prediction method. All of the data are for fins having double-wedge sections of varying thickness ratios. A preliminary method for estimating hinge moments at transonic speed is advanced in Ref. 7.

With regard to pitching moment, knowledge of fin normal force and hinge moment is sufficient to determine the fin contribution to missile pitching moment.

6. TRANSITION AT HYPERSONIC SPEED

Transition from laminar to turbulent flow in missile boundary layers will have large effects on the vortical separated flow field about the missile at high angle of attack, as well as on the heat transfer to the missile itself. It is important to keep in mind that present methods for predicting the location of hypersonic transition can be very inaccurate and this can lead to serious errors in predictions.

*The flow angle in a streamwise plane normal to the fin planform.

Because of the reduced emphasis on hypersonics over the last 15 years, transition research for hypersonic flow has lagged that for lower Mach number flow (Ref. 8). There is a significant lack of information on the effects on transition of three-dimensional flow, real gases, shock waves, and pressure gradients. This void must be filled for the design of future hypersonic missiles and aircraft. In the meantime an interim empirical approach to boundary-layer transition at high Mach numbers is suggested in Ref. 8.

A somewhat fuller discussion on hypersonic boundary-layer transition prediction is given in Ref. 9. It contains some thoughts on how to predict transition on bodies characterized by a blunt nose, an early frustum, and a frustum.

It is clear that much research must be done before prediction of hypersonic transition can be put on a sound basis. Until reasonable correlation between wind tunnel and flight data at hypersonic speed is achieved, one must be cautious in using wind tunnel data.

7. VORTEX INTERFERENCE

Control problems on missiles caused by vortices can occur in several ways. We first consider the classical case of asymmetric vortex separation on bodies of revolution at high angles of attack, which can occur if the cross-flow Mach number is subsonic. (This is a necessary condition for asymmetric separation, but alone it is not a sufficient one.) A correlation is presented in Fig. 7 as taken from Ref. 10 of the maximum side force coefficient caused by asymmetric body vortex separation for bodies of revolution. It can be seen that the asymmetric side force is negligible if the cross-flow Mach number is highly subsonic or supersonic of about $M_c > 0.8$. Asymmetric separation vortices are not to be confused with a Karman vortex strut which can occur with symmetric separation.

A necessary condition for the existence of side force at zero sideslip is that the angle of attack be less than a critical value which depends on Mach number. In Fig. 8 the region of possible asymmetric side force is indicated. It is noted in Fig. 7 that bluntness reduces the cross-flow Mach number above which asymmetric side force does not exist.

It is clear that if a nonrolling missile is to operate in a region of vortex asymmetry, the controls must have enough power to handle the side force developed by asymmetric vortices.

Another effect with which the missile controls must cope is vortex switching in which the side force quickly changes sign. It is hoped, however, that this severe requirement can be avoided by making the missile antisymmetric in some way so that vortex switching does not occur. However, *means of avoiding vortex switching still need investigation in a wind tunnel which does not have a strong asymmetry itself both for the rolling and nonrolling cases.*

The interference associated with symmetric-body vortices still exists at hypersonic speeds. Little is known about the strength and position of vortices at such speeds. For the present, the prediction methods for lower speeds must be used. *A combined experimental-theoretical investigation should be made of vortex behavior at hypersonic speeds and large angles of attack.* One question of interest is: since density is very low on the leeward surfaces at high α and high Mach number, are the vortex-induced forces significant for body vortex effects or for wing vortex effects on the tail?

It is possible with existing tools to conduct an inquiry into hypersonic vortices, and by using an Euler code, to calculate the entire flow field if the body separation lines are known. This was demonstrated in Ref. 11 for the symmetric vortices on a body of revolution at $M = 3$ and $\alpha = 15^\circ$. The calculation uses the separation-line position as input and imposes the boundary condition that the velocity vector is tangent to the separation line. To carry out the suggested work requires first determining the body separation lines experimentally for symmetric body vortices at a hypersonic Mach number. One can then carry out the Euler calculations to determine the entire flow field. It can then be seen if the cross-flow field can be well represented by two concentrated vortices using the Biot-Savart law in the cross-flow plane.

One of the variables that might influence the position of the onset of separation is the location of transition, especially at high altitude. *The flow condition for the onset of symmetric vortex separation at hypersonic speeds needs to be measured for bodies of revolution.* It is not clear that the axial position of separation is necessarily behind the position for the onset of transition so that laminar separation could occur.

Transition at hypersonic speed is thus of possible importance for vortex formation, besides being important for heat transfer.

8. AIRBREATHERS; SUPERSONIC INLETS

Rocket-powered missiles have specific impulses which are a small fraction of those for turbojets, ramjets, or scramjets. Turbojets are limited to a Mach number of about 2 because of the pressure and temperature effects on the rotating structure of gas-turbine engines, whereas the static structures of ramjets and scramjets can stand much higher Mach numbers.

The specific impulse of the power package influences the size and weight of a missile for a given payload and range. The chart of specific impulse versus free-stream Mach number shown in Fig. 9 (from Ref. 12) demonstrates the superiority of ramjets and scramjets for hypersonic missiles. It also depicts the range of operation of the next generation of missiles.

Other than the TALOS and BOMARC, long since out of service, there are no airbreathing tactical missiles in the U.S. military inventory. However, a large amount of research has been done since World War II on airbreathing propulsion for supersonic missile airframes. Because of the reduction in weight and size for a given payload or range, it is strange that more airbreathing missiles have not seen service.

Airbreathing missiles are for the most part of the bank-to-turn kind rather than the rolling kind. If the angle required for the flow to turn into a supersonic inlet at high angle of attack exceeds a certain value (dependent on Mach number), the flow will not turn into the inlet and the inlet will "unstart." For bank-to-turn missiles putting the inlet on the bottom of the body yields higher inlet pressures as the angle of attack increases. A ramjet is less sensitive to initial flow nonuniformities than is a turbojet engine. Accordingly, a ramjet with the inlet on the bottom surface appears to be a likely candidate for a hypersonic maneuvering missile. The skid-to-turn missile is seen to deteriorate in performance as the angle of attack increases. An example of a ramjet in normal service is the Sea Dart of the Royal British Navy.

In accordance with the purpose of this paper, future problems need to be identified where possible. Inlet technology presents a ripe area for innovation and invention for hypersonic propulsion. *One area where future efforts should yield a good payoff is the application of computational fluid dynamics to inlet design.* Some preliminary efforts in this direction using an Euler code have been promising. The code also determines the inlet contribution to the stability of the missile.

A few years ago McMillan et al. made a detailed survey of the available information on airbreathing inlets (Refs. 13 and 14). The papers contain descriptions of the inlets tested, the testing parameters ranges, and the kinds of measurements made.

9. STORE-SEPARATION PROBLEMS

Many tactical missiles are carried and released by aircraft. During their release they can encounter destabilizing forces and moments caused by the aircraft flow field which can be the most severe in their operating range. A possibility exists of missiles even striking the aircraft.

Most missiles are mounted on external racks and pods and operate well up into the transonic speed range. However, at high transonic speeds they frequently become unstable when released. At supersonic speeds they have so much drag that new methods of carrying and releasing the stores are necessary.

For supersonic aircraft a number of new carriage techniques have been suggested. The methods include mounting the store flush with the bottom of the fuselage (tangential carriage) and semi-submerging the missile in a cutout of the airplane. These methods will significantly reduce the supersonic drag. Another method which has a number of benefits is storing the missile internally to reduce its drag. As an approximation, the missile drag coefficient is the airplane drag coefficient times the internal volume used by the missile divided by the total internal volume of the aircraft, a figure which is a small fraction of the airplane drag. There are no radar cross-section effects created by the missile, except at launching the missile.

The design of cavities for containing missiles at supersonic speeds has been extensively investigated by R. L. Stallings of NASA-Langley (Ref. 15). It is important that the cavity not become a Helmholtz resonator when its cover is removed to separate the missile. This phenomenon is a function of cavity depth-to-length ratio, Mach number, and Reynolds number. Also the pitching moment on the missile should be nose down to have a clear separation of the store from the aircraft. The missile may be given a downward linear velocity and initial angular velocity to aid separation. It is important that a supersonic aircraft be able to separate its missiles at subsonic and supersonic speeds.

Computational fluid dynamics finds use in the study of missile launching from aircraft at both transonic and supersonic speeds. Panel methods can now model complete airplanes. Missiles can also be included in the calculation. In Ref. 16 Deslandes has applied an Euler code at transonic and supersonic speeds to predict carriage loads on external stores using zonal decomposition. In Ref. 17, Dougherty, Benek, and Steger apply overlapping grids to solve by iteration for the interference field between several bodies at transonic speed. These authors have just scratched the surface of possibilities for the application of CFD to missile-airplane interference. *Much remains to be done.* Eventually CFD should largely replace experiment in this application.

While Euler codes give good solutions for many aircraft interference problems, some problems are Reynolds-number dependent so that the Navier-Stokes equations may be called for. Such problems may include missiles at transonic speeds where flow separation occurs because of the close proximity of the stores. Also, open cavities might require the Navier-Stokes equations in certain instances. *The field is open for further research.*

10. CORRELATION OF MISSILE DATA

While methods exist for calculating the complete flow field about many missile configurations, such calculations are costly and often of unknown accuracy. Engineering prediction methods based on data correlation plus analysis offer a cheaper and faster way of prediction in many cases. Methods for cruciform missiles and planar missiles exist but would benefit from further development.

We now discuss two correlation methods that are useful in engineering prediction methods before describing the methods themselves.

The equivalent angle-of-attack concept (Ref. 18) has been very useful in helping to predict the normal force and center-of-pressure location of a fin in the presence of a body. It has also been useful in predicting the amount of normal force carried over onto the body. We will describe the concept here with minimal mathematics and refer the reader to Ref. 19 for the details.

A fin mounted on a circular body is subject to flow normal to its planform from at least four sources: (a) body angle of attack, (b) fin deflection, (c) sideslip, and (d) vortices. The equation connecting these quantities (without control deflection) is

$$\tan \alpha_{eq_i} = K_W \tan \alpha_C \cos \phi_i + \frac{4}{AR} K_\phi \sin \alpha_C \cos \alpha_C \sin \phi_i \cos \phi_i + \tan(\Delta \alpha_v) \quad (5)$$

Adding in control deflection, we have

$$\alpha_{eq_i} = \alpha_{eq_i} + \sum_{j=1}^{j=4} \Lambda_{ij} \delta_j$$

where Λ_{ij} is approximately unity for $j = i$ and a small fraction for $j \neq i$. Here $(\Delta \alpha_v)$ is the average angle of attack induced normal to the fins by the body or other vortices. The basic assumption here in determining the resulting angle of attack of the fin is that the velocities normal to the fin are linearly additive (Fig. 10). We do not add component normal forces but use the tangent addition theorem on the component normal velocities. If the normal-force curve of the fin alone is linear, then we could add normal-force components. However, by the present method, nonlinear wing alone normal-force curves can be used. The normal force of the fin in the presence of the body corresponds to that for the wing alone at $\alpha_W = \alpha_{eq}$. Data in Ref. 20 show excellent correlation of both $C_{N(F)}$ and $(\bar{x}/c)_F$ versus α_{eq} for data from several sources. Further refinement of Equation (5) considers the induced normal velocity at a given fin caused by the deflections of the other fins through the Λ_{ij} coefficients. It is also possible to linearize Equation (5) and get good results in the moderate angle-of-attack range. An example of the correlation of fin normal force achieved by α_{eq} is shown in Fig. 11.

The other method of correlation which is useful for missile aerodynamic methods is due to Sychev (Ref. 21) as adapted by Hensch (Ref. 6). Hensch has shown how the modified similarity of Sychev can be used to correlate the normal force and center-of-pressure position for wings and bodies up to high angles of attack, assuming a supersonic cross-flow Mach number.[‡] The normal force and pitching moment for a slender configuration are given by the following set of equations.

$$\frac{C_N}{\sin^2 \alpha} = f_1(k_1, k_2) \quad (6)$$

$$\frac{C_m}{\sin^2 \alpha} = g_1(k_1, k_2) \quad (7)$$

where

$$k_1 = \frac{b/l}{\tan \alpha} \quad k_2 = M_\infty \sin \alpha \quad (8)$$

Introducing a third parameter

$$k_3 = \frac{\tan \alpha}{AR} = \frac{\text{constant}}{k_1} \quad (9)$$

the normal-force coefficient and center-of-pressure location turn out to be

$$\frac{C_N}{AR \sin \alpha \cos \alpha} = f_2(k_2, k_3) \quad (10)$$

$$\frac{\bar{x}}{l} = g_2(k_2, k_3) \quad (11)$$

[‡]This assumption turns out to be unnecessary for some reason.

Hemisch applied the results to a systematic series of sharp delta wings tested by Miller and Wood* (Ref. 22). He first plotted the position for the various data points in the k_2, k_3 plane as shown in Fig. 12. Four regions were found which corresponded to four types of delta-wing flow. It is then shown that two fins with the same values of k_2 and k_3 yield the same pressure coefficients in the form $C_p/\sin^2 \alpha$ versus y/s . This assumes similar airfoil shapes.

A simplification was found for the wings of the Stallings-Lamb data (Ref. 23) consisting of wings varying in aspect ratio from 0.25 to 4.0 and with taper ratios of 0, 0.5, and 1.0. An accurate data correlation was found in the form

$$\frac{C_N}{AR \sin \alpha \cos \alpha} = A \frac{\tan \alpha}{AR}^B \quad (12)$$

where

$$A = A(M_\infty \sin \alpha); \quad B = B(M_\infty \sin \alpha) \quad (13)$$

Hemisch found that three families of sharp-edged wings and two families of smooth bodies had normal force curves as represented by Equations (12) and (13). It was also possible to correlate the center-of-pressure position of wings alone as curves of \bar{y}/s versus α/AR with $M_\infty \sin \alpha$ as a parameter.

11. CFD CODES FOR COMPLETE CONFIGURATIONS

It is often of interest to calculate the pressure or flow field for a complete missile or for a missile in the presence of an airframe. Various codes exist in the United States for this purpose. The codes vary in their speed, range of applicability, and the partial differential equation being solved among other ways. Four codes are compared in Fig. 13. These four codes are: (1) PANAIR (Ref. 24), (2) TRANAIR (Ref. 25), (3) DEMON (Ref. 26), and (4) SWINT (Ref. 27).

PANAIR (Ref. 24) is a code intended to solve the linear aerodynamic theory (the Glauert-Prandtl equation) for complete configurations of some complexity. Although developed for airplane use, it can easily be adapted to a missile in flight. It can also handle a separating missile still within the influence of the airplane.

PANAIR can be used through the subsonic and supersonic speed range except in the nonlinear transonic range. For this purpose, TRANAIR was created for application to aircraft in the nonlinear transonic region (Ref. 25). It is applicable to missiles. The code solves the full potential equation for the entire flow field. It can be adapted to apply to an airplane-store combination.

DEMON (Ref. 26) is a supersonic panel program based on the Glauert-Prandtl rule. However, nonlinear compressibility effects are accounted for in an engineering approximation. It handles both body and fin vortices, and it is applicable when calculating interference between missiles and airplanes.

Finally, SWINT (Ref. 27) is a supersonic marching code based on the Euler equations. It employs a grid with radial lines from a center somewhere in the body. The radial lines in the cross-flow plane are allowed to intersect the surface of the missile only once. This limits its application to a class of missile configurations. The important aspect of SWINT is that it is based on the Euler equations which handle nonlinear compressibility effects precisely.

There are gaps in the application of the foregoing codes. The difficulty in some cases, which is due to the mesh of the Euler code just discussed, can be overcome, and this problem is a good one for future work. At the same time, it might also be modified to handle multiconnected regions. If the Mach number in the marching direction becomes subsonic, the Euler code "blows up" (this usually occurs at some limiting angle of attack). A method for handling small regions of embedded subsonic flow with the Euler equation would be of interest.

All the codes have been or can be adjusted to account for vortices in an engineering fashion. The rigorous treatment of the vortices awaits a Navier-Stokes code to handle the vortices from first principles. There are a number of Euler solvers besides SWINT for solving flow problems of supersonic missiles. In fact, four different Euler solvers have been compared by Priolo, Wardlaw, and Solomon in Ref. 28. SWINT has a number of shortcomings including geometric limitations, occasional instability in calculation, use of special means at leading edges, trailing edges and tips, inability to reproduce sharp shock discontinuities, and use of artificial viscosity. MUSE is an extension of SWINT to handle fin thickness and more general geometrics. ZEUS E is a first-order code using the Gudonov method while ZEUS H is a second-order code using the Gudonov method. The Gudonov method can remove most of the instabilities occurring in SWINT. It does not need artificial viscosity nor special procedures; it gives sharp discontinuities associated with shocks. While these advances improve Euler codes, further advances are needed to handle viscous effects in a rotational inviscid way.

A supersonic panel code has been coupled with a NASTRAN code to determine static aeroelastic forces and moments as well as deformed shapes. This work has been accomplished by Dillenius et al. and is

*Miller and Woods obtained similar results using different parameters.

reported in Ref. 29. The combined program has been provided with an optimizing capability. One application under consideration is how to design a fin to minimize hinge moments. McIntosh and Dillenius have written an aeroelastic tailoring procedure for reduction of fin hinge moments. The code (Ref. 30) makes use of McIntosh and Dillenius' DEMON code.

12. ENGINEERING PREDICTION METHODS

It is not economical and, in certain cases, not currently possible to calculate the aerodynamic characteristics of complete tactical missiles using CFD. Therefore, much preliminary design is done by engineering prediction methods. Many companies have their own engineering-prediction methods which are not in the public domain. However, there are several engineering methods that are in the public domain and which we will discuss: (a) MISSILE DATCOM (Ref. 31), (b) MISSILE III (Ref. 32), and (c) Schindel's Code (Ref. 33).

We are discussing MISSILE DATCOM for purposes of completeness and comparison. MISSILE DATCOM is a collection of empirical, semiempirical, and theoretical methods mostly applicable to ordinary missiles. An "ordinary" missile is defined as either a planar or cruciform missile with an axisymmetric body. Two pairs of fins are included which are in line or are interdigitalized by 45°. We will not discuss the methodology which is described in Ref. 31.

MISSILE DATCOM was used to predict the coefficients C_N , C_M , and C_A for a large number of missile configurations. The tolerances allowable in the predictions were:

$$C_N: \pm 20\%$$

$$C_M: \pm 20\% \text{ or } 25\% L$$

$$C_A: \pm 10\% \text{ or } \pm 2 C_D/C_A \cos \alpha$$

At $\alpha \leq 20^\circ$, the method fell within the tolerances 60% of the time; for $\alpha \leq 40^\circ$, 40% of the time. Clearly the method is not a high- α method. For closely coupled wings and tails, it does not handle wing-body interference well; however, this matter can be rectified. It is not well adapted to handling α - δ coupling of all-movable fins or to handling asymmetric ϕ settings well, or the effects of α and M on K_B and K_W . Reference 3 gives systematic data sufficient for updating the effects of α and M on K_W and K_B .

The next computer code, MISSILE III, supplements DATCOM in some instances. It utilizes a newly available systematic Tri-service/NASA data base previously described. It covers the Mach range 0.6 to 4.5, fin aspect ratio from 0.25 to 4.0, angles of attack up to 45°, and arbitrary roll angles. It contains also a set of data for systematic variations of ϕ and δ , for a number of fins over an α and M range. These data are sufficient to handle α - δ coupling as well as δ_1 - δ_2 coupling, assuming this latter quantity is small. The program's disadvantage is that it does not handle drag.

The data were taken at $a/s = 0.5$. For $a/s = 0$ there is no wing-body interference so that $K_W = 1$ and $K_B = 0$. For other a/s ratios, a linear interpolation is made between $a/s = 0$ and 0.5 for K_W and K_B as is approximately true from slender-body theory. This assumption has never been clearly investigated and would be a worthwhile subject of future research. The generalization of $a/s = 0.5$ data to any a/s gives the data base an additional parameter of freedom. Also the effects of putting a wing and tail on a missile are handled by providing a wing-tail interference method in the program. In these ways, the applicability of the data base is vastly expanded.

It is clear that anything that can be accomplished with MISSILE III could also be added to MISSILE DATCOM.

A number (6) of suggestions for the extension of MISSILE III are included in Ref. 32.

In Ref. 33 Schindel has produced a computer code for preliminary design and screening of missile airframes. Its virtues are that it is fast and applicable to waveriders. It also includes a plotting routine for the results.

13. SOME FUTURE CONFIGURATIONS

As a result of future trends in tactical missiles, a number of new concepts are being advanced to fill the needs. These configurations include waveriders, noncircular bodies, airbreathing engines, etc. We will examine a number of these future configurations.

Consider first the waverider which is now receiving much attention. Figure 14 illustrates a waverider at its design point. It is the type of waverider known as a caret wing. Its upper surface consists of two triangular planes joined at a hinge line. At the design condition, the hinge line is parallel to the freestream direction, and no pressure exists on the upper surfaces. In the chordwise direction, the airfoil sections are all wedge sections of a uniform wedge angle. The flow under the wing is all parallel flow at oblique shock pressure. The region between the bottom of the waverider and a plane containing the apex and wing tips is at uniform pressure. We thus know its lift/drag ratio from oblique shock theory.

Waveriders have higher L/D ratios at hypersonic speeds than the usual cruciform missiles by about a factor of 2. Waveriders were seriously considered for designs of hypersonic aircraft by Kucheman (Ref. 34) and his associates in England about 25 years ago. It is only recently that waveriders have been given serious attention for hypersonic tactical missiles.

A large variety of waverider configurations is possible (Schindel, Ref. 35). The use of waveriders as missiles presents a series of aerodynamic problems such as adding a propulsion system, controls, and a radome to the basic waverider, hopefully without seriously degrading $(L/D)_{\max}$. It is clear that considering the large number of waverider configurations and the above aerodynamic problems, a large and fruitful opportunity exists for research and development in this field.

An interesting study in the optimization of hypersonic waveriders is given in Ref. 36. In this study, a class of waveriders was optimized for maximum L/D ratio considering skin friction and blunt leading-edge drag. At $M = 6$ an L/D over 8 was calculated and at $M = 25$ an L/D of about 4.5 was calculated.

One virtue of the conical waverider is that its center of pressure remains constant at supersonic speed as long as the flow is attached. Of interest is how much the L/D is degraded by adding the necessary components to make it into an airplane.

With the introduction of airbreathing missiles to achieve range, it becomes possible to use non-circular bodies which do not roll continuously. This possibility opens up the design space and allows increased performance and increased stability and control. While rocket powered cruciform missiles usually use skid-to-turn maneuverability, airbreathers utilize bank-to-turn maneuvering. Possible advantages claimed in the use of noncircular bodies include higher lift, better storage, improved carriage, better separation, and improved stability and control.

A nonplanar missile on a noncircular body represents an interesting new design possibility which can have different stability and control than the usual cruciform missile. A few examples with noncircular bodies are now presented.

A circular body can develop rolling moments by skin friction but they are of small magnitude. It thus has zero effective dihedral, C_{z_B} . A noncircular body under sideslip can have rolling moment and side force as a result of pressure forces, yielding finite values of C_{z_B} and C_{n_B} . Figure 15 shows the effective dihedral and directional stability of an elliptical body as compared to a circular one of the same area distribution. Note that the elliptical body has good effective dihedral while the circular body has neutral stability. Both bodies have poor directional stability, but the elliptical body is less unstable than the circular body and will thus require a smaller vertical fin.

Many investigations have advanced configurational ideas for improved hypersonic missiles (Refs. 37-39). A number of these configurations discussed in Ref. 37 have flat tops and are presented in Fig. 16. The maximum L/D ratios are presented there for both flat top and flat bottom orientations. The difference in maximum L/D between the two orientations is not very large. It is thus possible to provide volume below the wing to house the engine. Also, the positive pressure gives the engine more thrust. The maximum L/D ratios shown in Fig. 16 are below the empirical limit given by Kucheman in Ref. 34.

$$\left(\frac{L}{D}\right)_{\max} = \frac{4(M+3)}{M} \quad (14)$$

The stability and control characteristics of monoplanes with elliptical bodies generally provides a good balance between longitudinal and lateral-directional stabilities. Too low a profile, looking normal to the body in the horizontal plane, reduces the directional stability. It also causes unporting of controls at high deflections with an attendant loss of control.

Hunt and his coworkers (Ref. 38) have studied hypersonic missile airframes capable of housing a scramjet engine. The studies showed engine/airframe integration to be a significant problem for this class of missiles. Also the engine can have a significant effect on the missile's stability and control. In Ref. 39 Spearman analyzes the aerodynamics of some unconventional missiles and considers their applicability to certain missions. The classes of missiles considered are: (1) delta-wing bodies (Fig. 17), (2) ring-parasol wing bodies (Fig. 18), and (3) monoplane missile with circular/elliptical body (Fig. 19). Spearman's objective was to indicate the types of mission suitable for various configurations. The requirements for various missions include full load carrying capability, low drag, low detectability, ease of carriage and stowage, low cost, etc.

Spearman's candidate for a tactical penetrator capable of high speed, low-altitude overflight with downward spray of warhead fragments is the thick delta wing and a semi-conical body with delta wings. This configuration, being small and slender, is hard to detect. High-speed, high-altitude concepts with good aerodynamic efficiency for volume and range are a possible approach to strategic penetration. The parasol wing concept appears to be applicable to this mission. It provides high-lift capability at low angle of attack by utilizing favorable interference flow fields.

A monoplane wing in connection with an elliptical body is a good candidate for a maneuvering missile such as required in air defense or air combat missions. Its high L/D makes it a good candidate for longer range air-to-surface missions.

In this section we have considered four general categories of missile types: (a) waveriders, (b) flat-top monoplane missiles, (c) missiles designed for scramjet propulsion, and (d) missiles suitable for particular missions. Although a number of stability and control problems have been mentioned in connection with these missile types, a great amount of research and development will be required in the future.

A detailed discussion of waveriders is to be found in Ref. 35 and of bank-to-turn missiles with non-circular bodies in Ref. 40.

14. CONCLUDING REMARKS

In this paper a wide range of subjects in missile aerodynamics has been covered from a general point of view. Certain subjects such as aerodynamic heating, drag, radar cross-section, and real gas effects have been neglected because of space limitations or classification restrictions. The first two subjects are well covered by chapters IX and X in the book "Tactical Missile Aerodynamics," Vol. 104, AIAA Series Progress in Astronautics and Aeronautics.

15. ACKNOWLEDGMENT

I am grateful to Dr. Michael Hensch, who reviewed the document and made a number of helpful suggestions.

REFERENCES

1. "Missile Aerodynamics," AGARD-CP-336, Restricted NATO, presented at the Fluid Dynamics Panel Symposium, Sept. 20-22, 1982, Trondheim, Norway.
2. Lesieur, D. J., Mendenhall, M. R., Nazario, S. M., and Hensch, M. J., "Aerodynamic Characteristics of Cruciform Missiles at High Angles of Attack," AIAA Paper 87-0212, 1987.
3. Nielsen, J. N., "Supersonic Wing-Body Interference at High Angles of Attack with Emphasis on Low Aspect Ratios," AIAA Paper 86-0568, 1986.
4. Hensch, M. J. and Nielsen, J. N., "Extension of Equivalent Angle-of-Attack Method for Nonlinear Flow Fields," *J. Spacecraft and Rockets*, Vol. 22, No. 3, pp. 304-308, May-June 1985.
5. Lesieur, D. J., Mendenhall, M. R., Nazario, S. M., and Hensch, M. J., "Prediction of the Aerodynamic Characteristics of Cruciform Missiles Including Effects of Roll Angle and Control Deflection," NEAR TR-360, 1987.
6. Hensch, M. J., "Engineering Analysis of Slender-Body Aerodynamics Using Sychev Similarity Parameters," AIAA Paper 87-0267, 1987. (To be presented in *J. Aircraft*, 1988.)
7. Nielsen, J. N., Goodwin, F. K., and Dillenius, M. F. E., "Prediction of Cruciform All-Movable Control Characteristics at Transonic Speeds," NEAR TR-321, 1984.
8. Reshotko, E., Bushnell, D. M., and Cassidy, M. D., "Report of the Task Force on Boundary Layer Transition," NASP TM-1007, 1987.
9. Stetson, K. F., "On Predicting Hypersonic Boundary Layer Transition," AFWAL-TM-87-160-FIMG, March 1987.
10. Wardlaw, A. B., Jr. and Morrison, A. M., "Induced Side Forces at High Angles of Attack," NSWC/WOL/TR 75-17, 1975.
11. Klopfer, G. H. and Nielsen, J. N., "Euler Solutions of the Body Vortices of Tangent Ogive Cylinders at High Angles of Attack and Supersonic Speeds," AIAA Paper 81-0361, 1981. Also NEAR TR-130.
12. Tactical Missile Aerodynamics, Progress in Astronautics and Aeronautics, Vol. 104, Martin Summerfell, Series Editor in Chief, Chapter 4, Inlets, by A. M. Thomas, Jr., the Marquand Co., Van Nuys, Calif., pp. 129-167.
13. McMillan, O. J., Perkins, S. C., Jr., Perkins, E. W., and Kuhn, G. D., "Data Base for the Prediction of Airbreathing Missile Airframe/Propulsion System Interference Effects (I)," NWC TP-6136, 1980, Limited Distribution. (Prepared under Contract N60530-78-C-0098 (Confidential Report).)

14. Perkins, Stanley C., Jr. and McMillan, O. J., "A Handbook of Experimental Data for the Effects of Inlet Systems on Airbreathing Missile External Aerodynamics (U)," NWC TP-6147, 1982, Limited Distribution. (Prepared under Contract N60530-78-C-0201.) Vol. 1, Overview and Summary (U) (Confidential); Vol. 2, Configuration Data: Inlet Type Effects (U) (Unclassified, but Limited Distribution); Vol. 3, Data Classified by Inlet Type, Part 1 (U) (Confidential); Vol. 3, Data Classified by Inlet Type, Part 2 (U) (Confidential).
15. Stallings, R. L., "Store Separation from Cavities at Supersonic Flight Speeds," *Journal of Spacecraft and Rockets*, Vol. 20, pp. 129-132, March-April 1983.
16. Deslandes, Ronald, "Zonal Decomposition: An Advanced Concept for Euler Codes in Order to Predict Carriage Loads of Non-Trivial External Store Configurations," Paper No. 2, AGARD CP-389, 1986.
17. Dougherty, F. C., Benek, J. A., and Steger, J. L., "On the Application of Chimera Grid Schemes to Store Separation," AGARD CP-389, 1986.
18. Smith, C. A., Nielsen, J. N., and Hemsch, M., "Prediction of Aerodynamic Characteristics of Banked Cruciform Missiles at High Angles of Attack," AIAA Paper 79-0024, 1979.
19. Hemsch, M. and Nielsen, J., "The Equivalent Angle-of-Attack Concept for Engineering Analysis," Chpt. XI, "Tactical Missile Aerodynamics," Vol. 104, *Progress in Astronautics and Aeronautics*, AIAA, 1986.
20. Hemsch, M. J. and Nielsen, J. N., "Equivalent Angle of Attack Method for Estimating Nonlinear Aerodynamics of Missile Fins," *J. Spacecraft and Rockets*, Vol. 20, pp. 356-362, July-August 1983.
21. Sychev, V. V., "Three-Dimensional Hypersonic Gas Flow Past Slender Bodies at High Angles of Attack," *J. Appl. Math. and Mech.*, Vol. 24, pp. 286-306, 1960.
22. Miller, R. S. and Wood, R. M., "Leeside Flow Over Delta Wings at Supersonic Speeds," NASA TP-2430, 1985.
23. Stallings, R. L., Jr. and Lamb, M., "Wing-alone Aerodynamics Characteristics for High Angles of Attack at Supersonic Speeds," NASA TP-1889, 1981.
24. Derbyshire, T. and Sidwell, K. W., "PANAI Summary Document," NASA CR-3250, 1982.
25. Samant, S. S., Bussioletti, J. E., Johnson, F. T., Burkhart, R. H., Everson, B. L., Melvin, R. G., Young, D. P., Erickson, L. L., Madson, M. D., and Woo, A. C., "TRANAIR: A Computer Code for Transonic Analysis of Arbitrary Configuration," AIAA Paper 87-0034, 1987.
26. Dillenius, Marnix F. E., "Aerodynamic Predictions Using Supersonic Paneling Methods Accounting for Vorticity and Nonlinear Effects," AIAA Paper 86-0569, 1986.
27. Wardlaw, A. B., Priolo, F. J., and Solomon, J. M., "A Multiple-Zone Method for Supersonic Tactical Missiles," NSWC TR 85-484, 1986.
28. Priolo, F. J. and Wardlaw, A. B. Jr., "A Comparison of Inviscid Computational Methods for Supersonic Tactical Missiles," AIAA Paper 87-0113, 1987.
29. Dillenius, M. F. E., Perkins, S. C., Jr., and Lesieutre, D. J., "Modified NWCOM-NSTRN and Supersonic Store Programs for Calculating NASTRAN Forces Acting on Missiles Attached to Supersonic Aircraft," NEAR TR 369, 1987.
30. McIntosh, S. C., Jr. and Dillenius, M. F. E., "Aeroelastic Tailoring Procedure for Reduction of Fin Hinge Moments," NEAR 374, 1987.
31. Vukelich, S. R. and Jenkins, J. E., "MISSILE DATACOM: Aerodynamic Predictions of Conventional Missiles Using Component Build-up Techniques," AIAA Paper 84-0388, 1984.
32. Lesieutre, D. J., Mendenhall, M. R., Nazario, S. M., and Hemsch, M. J., "Prediction of the Aerodynamic Characteristics of Cruciform Missiles Including Effects of Roll Angle and Control Deflection," NEAR TR-360, 1986.
33. Schindel, L. H., "A Preliminary Design and Screening Process for Missile Airframe Configurations," AIAA Preprint 87-0211, 1987.
34. Kucheman, D., *The Aerodynamic Design of Aircraft*, Pergamon Press, Oxford, pp. 448-510, 1978.
35. Schindel, L., *Waveriders*, Chpt. 6 in "Tactical Missile Aerodynamics," AIAA *Progress in Astronautics and Aeronautics*, Vol. 104, 1986.

36. Bowcutt, K. G., Anderson, J. D., and Capriotti, D., "Viscous Optimized Hypersonic Waveriders," AIAA Paper 87-0272, 1987.
37. Krieger, R. J., Gregoire, J. E., Hood, R. F., Eiswirth, E. A., and Taylor, M. L., "Aerodynamic Configured Missile Development--Final Report," Vols. 1-5, AFWAL-TR-80-3071, 1980.
38. Hunt, J. L., Johnston, P. J., Cabbage, J. M., Dillon, J. L., Richie, C. G., and Marcum, D. C., Jr., "Hypersonic Airbreathing Missile Concepts Under Study at Langley," AIAA Paper 82-0316, 1982.
39. Spearman, M. L., "Unconventional Missile Concepts from Consideration of Varied Mission Requirements," AIAA Preprint 84-0076, 1984.
40. Jackson, C. M., Jr. and Sawyer, W. C., "Bodies with Noncircular Cross Sections and Bank-to-Turn Missiles," Chpt. V, pp. 168-187, in "Tactical Missile Aerodynamics," Vol. 104 in AIAA Series "Progress in Astronautics and Aeronautics."

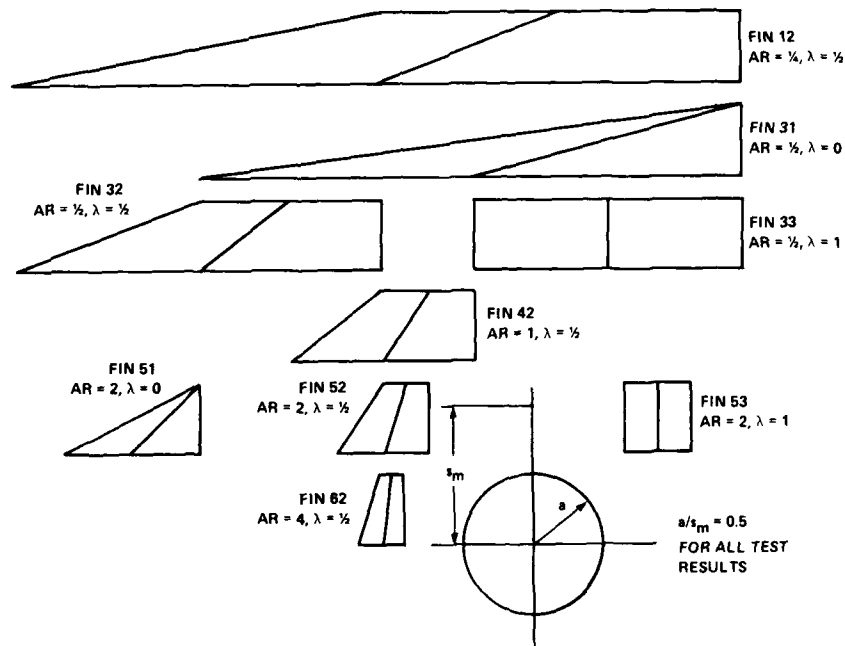


Figure 1 - Test fin geometrics.

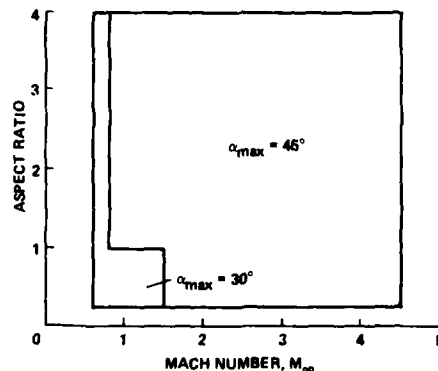


Figure 2 - Mach number and aspect ratio ranges and maximum angle of attack for Tri-service data base.

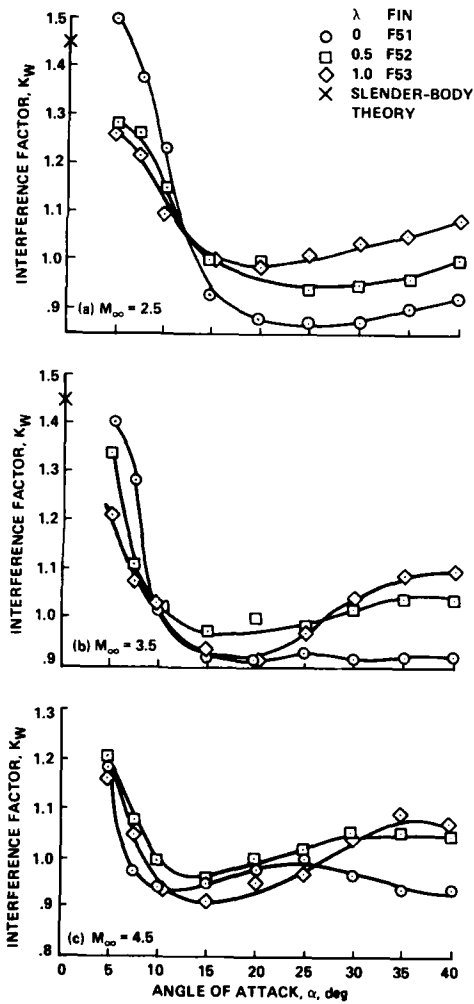


Figure 3 - Effect of taper ratio on interference factor K_W for aspect ratio 2 fins.

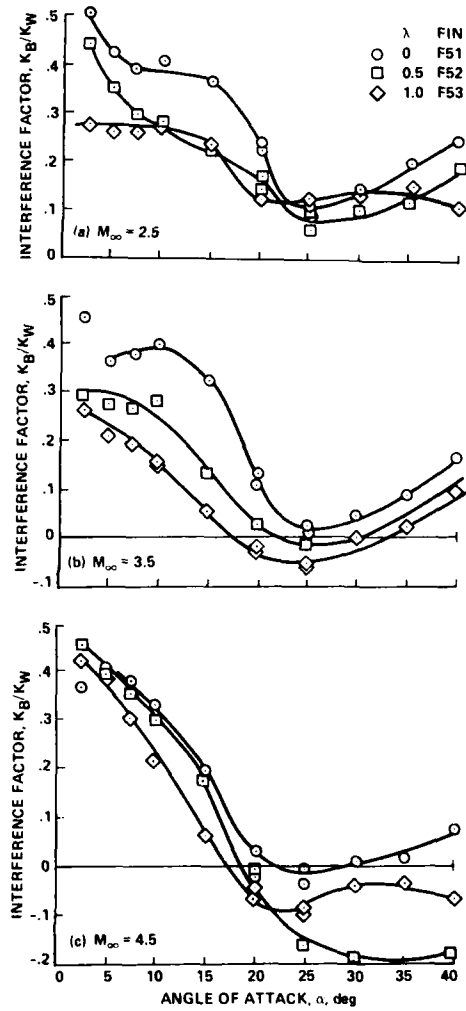


Figure 4 - Effect of taper ratio on K_B/K_W for aspect ratio 2 fins.

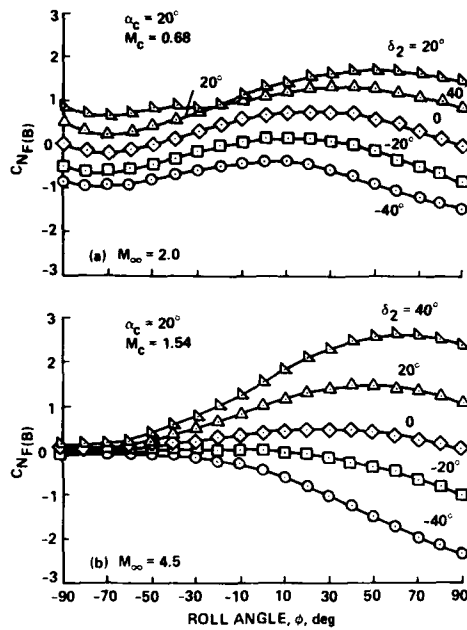


Figure 5 - Effect of roll angle and fin deflection on the normal force generated by fin F2.

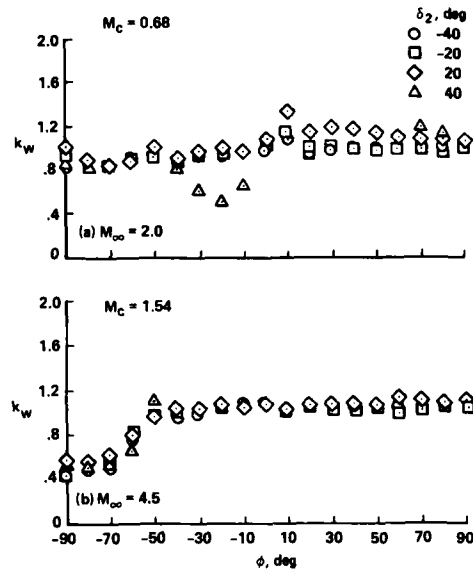


Figure 6 - Effect of roll angle and control deflection on k_w for all-movable controls.

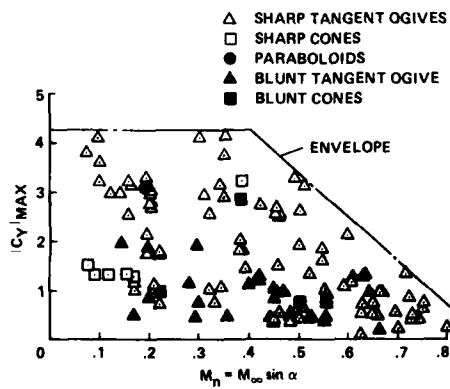


Figure 7 - Effect on crossflow Mach number on the sideforce of cones, tangent ogives, and paraboloids.

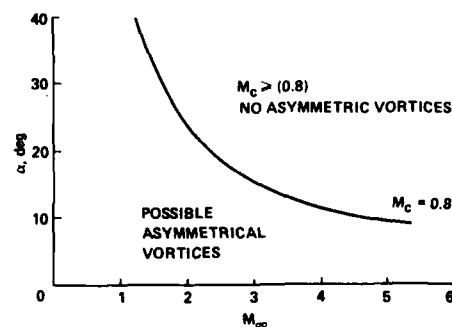


Figure 8 - Boundary between symmetric separation and asymmetric separation for body of revolution.

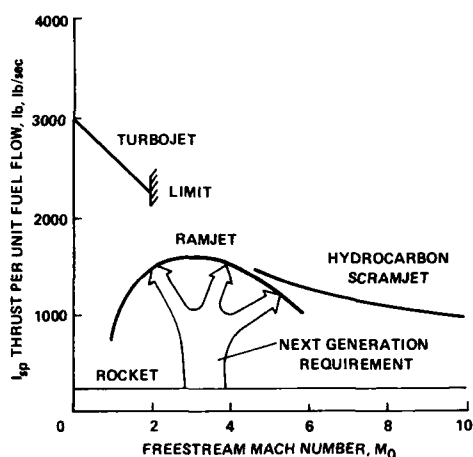
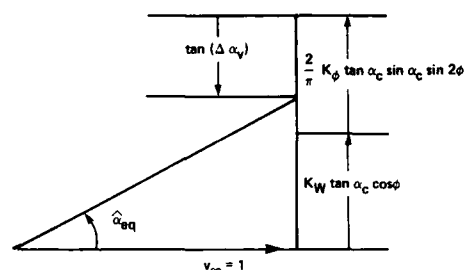


Figure 9 - Specific thrusts of various propulsion means.



$$\tan \hat{\alpha}_{eq} = K_W \tan \alpha_c \cos \phi + \frac{2}{\pi} K_\phi \tan \alpha_c \sin \alpha_c \sin 2\phi + \tan (\Delta \alpha_v)$$

Figure 10 - Addition of velocity components normal to fin defining equivalent angle of attack.

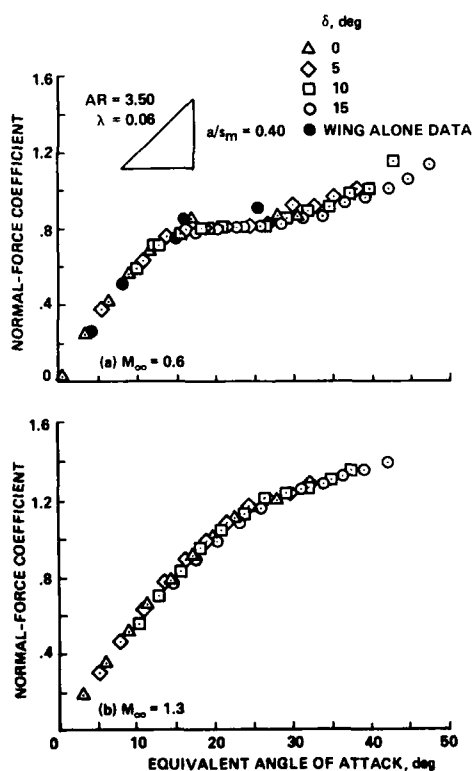


Figure 11 - Correlation of normal force coefficients with the equivalent angle of attack for moderate aspect ratio fin.

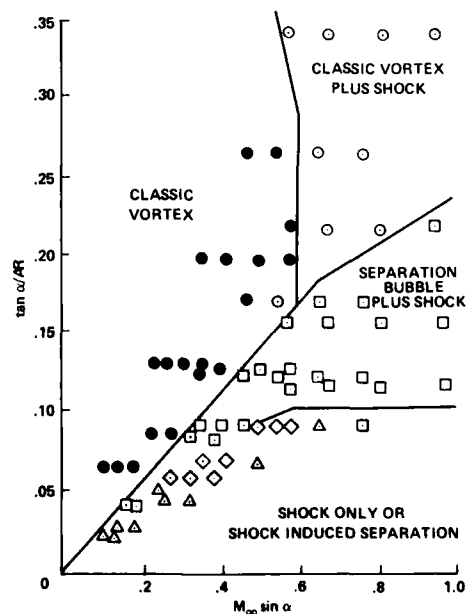


Figure 12 - Classification of Miller-Wood delta wing flow field data using the Sychev similarity parameters.

	PANAIR	TRANAIR	DEMON III	SWINT
PANEL OR FIELD	PANEL	FIELD	PANEL	FIELD
BASIC EQUATION	GLAUERT - PRANDTL	FULL POTENTIAL	GLAUERT - PRANDTL	EULER
MACH NUMBER RANGE	-0.9 1.2-2.5	0.6-0.95	$M > 1.1$	$M > 1$
BODY VORTICES	NO	NO	YES	NO
WING-TAIL INTERFERENCE	MUST INPUT VORTEX POSITION	MUST INPUT VORTEX POSITION	YES	?

Figure 13 - Characteristics of computer codes for calculating the loading on missiles or aircraft.

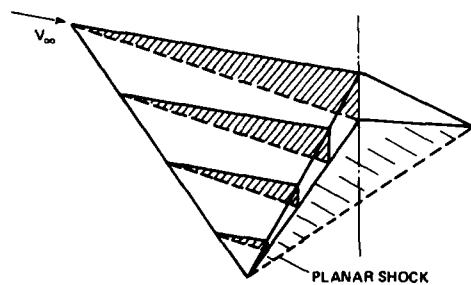


Figure 14 - Sketch of a simple waverider, a caret wing.

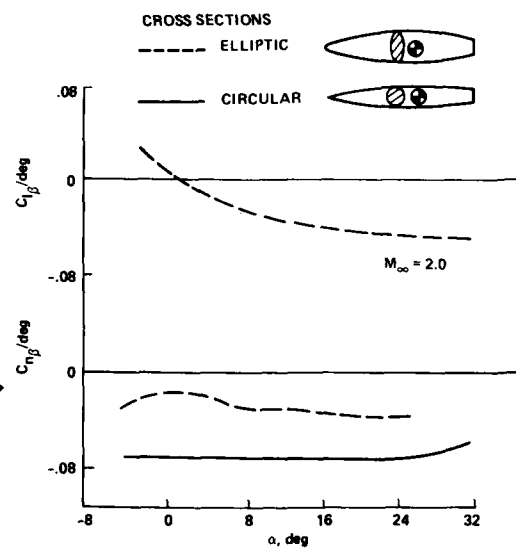


Figure 15 - Comparisons of effective dihedral and directional stabilities between Sear-Haack bodies of circular and elliptical cross section.

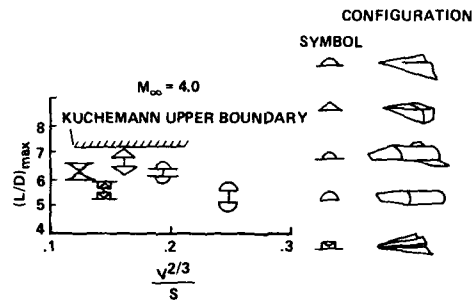
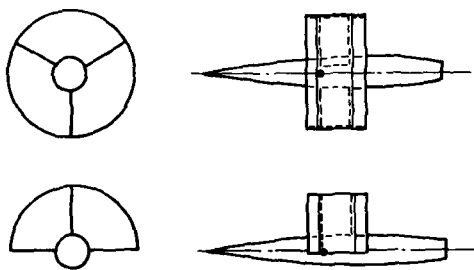
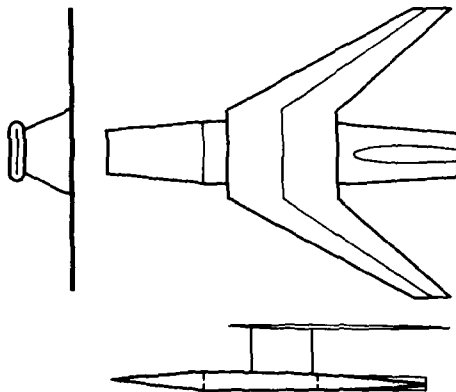


Figure 16 - Shape effects on maximum lift-drag ratios both right side up and upside down.

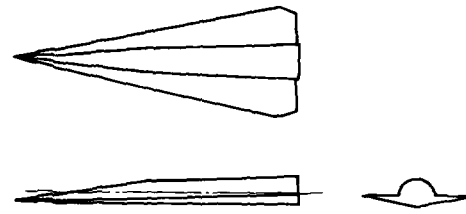


(a) RING-WING-BODY CONCEPTS

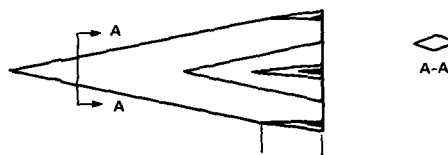


(b) FLAT BODY WITH SWEEPED PARASOL WING

Figure 18 - Ring wing-body and parasol wing-body concepts of Spearman.

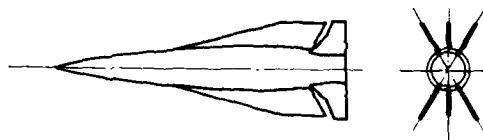


(a) SEMICONICAL BODY WITH DELTA WINGS

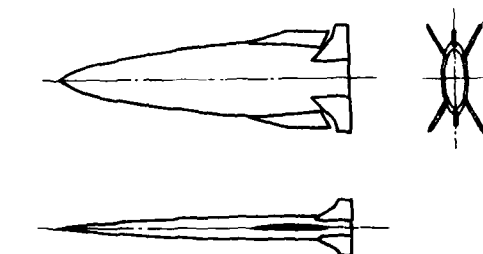


(b) THICK DELTA WING CONCEPT

Figure 17 - Some delta wing-body concepts of Spearman.



(a) MONOPLANAR MISSILE WITH CIRCULAR BODY



(b) MONOPLANAR MISSILE WITH ELLIPTICAL BODY

Figure 19 - Monoplane missiles with circular or elliptical bodies.

PREVISION DE LA STABILITE AERODYNAMIQUE DES MISSILES

Par

P. CHAMPIGNY

Office National d'Etudes et de Recherches Aérospatiales (ONERA)
B.P. N° 72 - 92322 CHATILLON CEDEX (France)RESUME

Le développement de missiles sol-air et air-air de plus en plus performants du point de vue manoeuvrabilité (facteur de charge et temps de réponse) nécessite une connaissance affinée des coefficients aérodynamiques et en particulier de ceux relatifs à leur stabilité.

Dans ce cadre, l'objet de cette communication est de comparer l'intérêt des diverses méthodes de calcul disponibles pour la prévision de la stabilité d'un missile, et aussi d'exposer les problèmes posés par la détermination expérimentale de cette stabilité.

ABSTRACT

The development of new surface to air and air to air missiles with improved maneuverability in term of load factor or time lag requires a better prediction of the aerodynamic coefficients mainly those related to the static stability.

Within this context, this paper presents examples of stability predictions based on several theoretical methods. This paper also underlines experimental problems for the evaluation of the static stability from wind-tunnel tests.

1 - INTRODUCTION

Le développement de missiles de plus en plus performants du point de vue manoeuvrabilité, vitesse de vol, portée, nécessite une connaissance de plus en plus fine des coefficients aérodynamiques, ceci pour des configurations de missiles de plus en plus complexes.

Pour l'ingénieur aérodynamicien, deux voies sont possibles : les méthodes de calcul ou les essais en soufflerie.

Si en phase finale de développement, les essais en soufflerie sont nécessaires pour confirmer les estimations faites en avant-projet, mais surtout pour établir un modèle aérodynamique complet, il n'en est pas de même lors d'une étude de faisabilité, eu égard à leur coût et à leur temps de réponse trop long.

Le recours à des méthodes de calcul est donc indispensable, et ces méthodes devront être capables d'évaluer rapidement les coefficients aérodynamiques avec suffisamment de précision, et pour des configurations très variées.

L'objet de cette communication est de faire une revue de ces moyens de prédiction des coefficients aérodynamiques, et plus particulièrement de la stabilité, tout en essayant de faire ressortir leurs domaines d'application et leurs limitations actuelles.

2 - CRITERES DE PRECISION

Avant d'exposer les différentes méthodes d'évaluation des coefficients aérodynamiques, que ce soit d'un point de vue théorique ou expérimental, il convient de fixer des critères de précision afin de pouvoir juger de la validité des méthodes employées.

L'incertitude admissible sur les coefficients aérodynamiques est évidemment fonction de la précision recherchée sur les performances du missile. Ainsi, plutôt que fixer a priori une précision sur les coefficients aérodynamiques, celle-ci sera déduite des écarts de performances admissibles pour le missile considéré.

KRIEGER et WILLIAMS [1] ont ainsi établi des relations entre ces performances, les dimensions du missile, le guidage, etc..., et les coefficients aérodynamiques. A titre d'exemple, le tableau n° 1 expose les principaux critères de performances pris en considération par ces auteurs, ainsi que les coefficients aérodynamiques les concernant. En particulier, on peut noter que le coefficient de moment de tangage, autrement dit la stabilité du missile, est un paramètre très influent.

Tableau 1 - Performances et coefficients aérodynamiques (traduit de [1]).

PERFORMANCES	COEFFICIENTS AERODYNAMIQUES
. Portée en croisière stabilisée . Portée en vol balistique . Rayon de virage instantané . Taux de virage instantané . Facteur de charge instantané . Temps de réponse . Altitude de croisière . Capacité d'accélération . Décélération en manoeuvre	CA, CN CA CN,CY CN,CY CN Cm _g Cm CN _x , CA CN, CA
DEFINITION DE LA CONFIGURATION	
. Dimensions des gouvernes . Dimensions des dérives . Dièdre des voilures . Dimensions des voilures . Braquage des gouvernes . Position du centre de gravité	Cm Cn Cl CN Cm Cm
PILOTAGE	
. Stabilité longitudinale . Stabilité en roulis . Stabilité en lacet . Couplage lacet-roulis	Cm _x , Cm _g Cl _p , Cn _p , Cl _g Cl _r , Cn _p , Cn _g Cn _g , Cl _g

En pratique, il est très difficile de se donner une règle générale pour ces critères, compte tenu du type de pilotage utilisé et de la grande variété des missions envisagées. De plus, la précision recherchée sera différente selon que l'on se trouve au stade de l'avant-projet (ce qui intéresse les méthodes de calcul) ou en phase de développement (pour les essais en soufflerie).

Néanmoins, pour ce qui concerne la prévision de la stabilité aérodynamique, les précisions généralement recherchées sur la position du centre de poussée et sur l'efficacité des gouvernes sont :

	ΔX_{cp}	$\frac{\Delta C_{m_g}}{C_{m_g}}$
Avant-projet	0,5 D	
Méthodes de calcul	(3 % L)	20 %
Phase de développement	0,1 à 0,5 D	
Essais en soufflerie		5 à 10 %

3 - MESURE DE LA STABILITE EN SOUFFLERIE

Lors de la phase finale de développement, les coefficients aérodynamiques sont généralement déduits d'essais en soufflerie, ce qui permet d'avoir un modèle aérodynamique très complet et assez précis.

Il faut cependant souligner que les mesures en soufflerie ne sont pas toujours représentatives de la réalité, notamment la stabilité qui peut être affectée par exemple par :

- l'influence du support de la maquette,
- la présence en vol d'un jet propulsif,
- l'écart entre les nombres de Reynolds en soufflerie et en vol,
- la souplesse du missile réel.

3.1 - Influence du dard et du jet propulsif

En soufflerie, le montage le plus couramment utilisé pour mesurer les caractéristiques aérodynamiques de maquettes de missiles est du type "dard". Si ce montage ne crée pratiquement aucune interaction en supersonique, il n'en est pas de même en subsonique. Par exemple il est bien connu que la traînée de culot est modifiée, mais de plus lorsque le missile est en incidence, l'écoulement sur tout l'arrière-corps est altéré par la présence du dard et la stabilité du missile est donc modifiée.

De même, si le missile est en phase propulsée, il est bien évident que la présence d'un jet propulsif, en particulier si la tuyère est très sous-détendue, viendra elle aussi modifier la stabilité.

A titre d'exemple, la figure 1 met en évidence ces influences sur la portance d'un arrière-corps de missile empenné classique. Pour cet exemple, les écarts sur la stabilité du missile à 20° d'incidence atteignent 0,5 D.

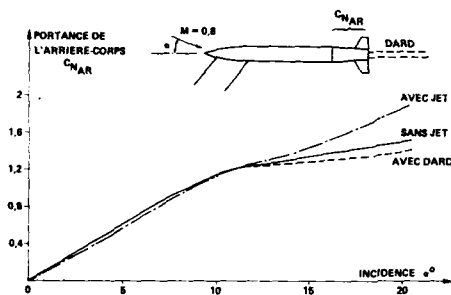


Fig. 1 - Influence du dard et du jet propulsif sur la stabilité (essais ONERA).

3.2 - Influence du nombre de Reynolds

Pour certains missiles très élancés, la contribution du fuselage à l'aérodynamique globale est très importante, or il est reconnu qu'en incidence l'écoulement tourbillonnaire qui s'établit sur un fuselage dépend du nombre de Reynolds, en particulier aux faibles nombres de Mach [2].

Il s'ensuit des variations de la force normale de l'ordre de 100 % à 40° d'incidence et des écarts de stabilité d'environ 1D (figure 2).

Des gouvernes placées à l'arrière d'un tel fuselage verront leur portance et leur efficacité modifiées par ces structures tourbillonnaires très différentes en fonction du nombre de Reynolds, et la stabilité du missile complet pourra aussi varier d'environ 1 D.

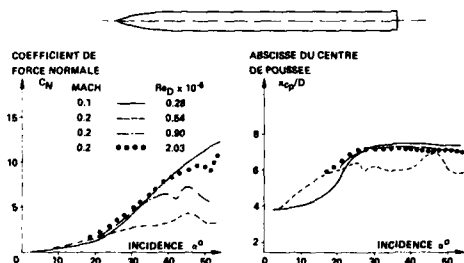


Fig. 2 - Influence du nombre de Reynolds sur la portance et la stabilité d'un fuselage.

3.3 - Influence de la souplesse du missile

Le dernier problème qui sera évoqué ici, concerne certains types de missile, comme les "Air-Air", qui ont des fuselages de plus en plus élancés ($L > 20 D$) et qui, pour des contraintes de poids utilisent des structures légères constituées par exemple de matériaux composites. On se trouve alors en présence de missiles relativement souples, qui, sous l'effet des forces aérodynamiques se déforment. Leur stabilité et leur manœuvrabilité pourront ainsi être notablement réduites, comme le montre l'exemple de la figure 3 [3].

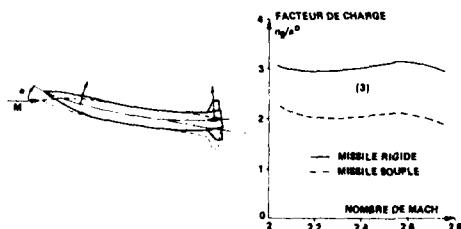


Fig. 3 - Influence de la souplesse du missile sur sa manœuvrabilité.

4 - METHODES DE CALCUL

En aérodynamique des missiles, deux principaux types de méthodes sont utilisés :

- les méthodes semi-empiriques,
- les méthodes numériques.

Les méthodes semi-empiriques, simples à mettre en oeuvre et très rapides, sont le plus couramment utilisées lors de la phase d'avant-projet. Elles sont basées sur des théories simples (choc-détente, corps élanés, potentiel linéarisé ...) ou sur des banques de données. Le calcul du missile complet s'effectue en considérant chaque élément séparément (fuselage, ailes, gouvernes ...) puis les interactions entre ces éléments.

De nombreux codes de calcul, développés chez tous les industriels et les organismes de recherche ont fait l'objet de nombreuses publications ; une revue de ces codes est donnée dans la référence [4].

La plupart de ces codes sont adaptés à des configurations de missiles conventionnels (fuselage cylindrique, voilures cruciformes), mais pour des configurations plus complexes telles que celles relatives aux missiles aérobie, l'emploi de méthodes numériques devient indispensable.

Parmi celles-ci, citons les méthodes de singularités, subsonique ou supersonique, d'ordre faible ou élevé, qui ne nécessitent qu'une définition surfacique de l'obstacle.

Enfin, compte tenu des progrès réalisés ces dernières années sur les schémas numériques, les algorithmes de calcul, les techniques de maillage et la puissance des ordinateurs, les méthodes basées sur la résolution des équations d'Euler sont de plus en plus utilisées pour le calcul des coefficients globaux des missiles [4], [5].

Quelques exemples d'applications de ces méthodes, telles qu'elles sont utilisées à l'ONERA, vont être maintenant présentés.

4.1 - Méthodes semi-empiriques

4.1.1 - Programme "MISSILE" (ONERA)

Ce code de calcul, développé dans les années 80, permet de traiter des configurations simples du type : fuselage cylindrique muni de 1 ou 2 séries de voilures cruciformes alignées ou croisées. Une extension en cours permettra prochainement de prendre en compte des fuselages munis de prises d'air latérales (application aux missiles aérobie).

Le domaine de validité de ce programme de calcul est approximativement :

- Mach : $0 < M < 4$
- Incidence : $0 < \alpha < 25^\circ$
- Roulis : $0 < \theta < 360^\circ$
- Braquage : $0 < \delta < 20^\circ$

Il permet de calculer tous les coefficients aérodynamiques globaux à l'exception du coefficient de traînée, ainsi que les efforts sur les voilures.

Les méthodes de calcul relatives à chaque élément constituant l'ensemble "MISSILE" (fuselage, aile avant, aile arrière) ainsi que celles relatives aux interactions entre ces éléments sont précisées dans le tableau n° 2.

En outre, ce programme utilise le concept d'incidence équivalente développé par NIELSEN [6], qui permet de bien décrire les non-linéarités des coefficients aérodynamiques en fonction de l'incidence et du roulis.

Pour des configurations simples, type fuselage + gouvernes, la prédiction du gradient de force normale et de la stabilité à incidence nulle est, en général, excellente (figure 4). Elle l'est un peu moins pour des missiles munis de 2 séries de voilures, en particulier lorsque celles-ci sont coplanaires et proches l'une de l'autre (figure 5).

En incidence, les évolutions de la force normale et de la position du centre de poussée sont également bien reproduites par le calcul (figures 6 et 7), en particulier grâce à l'utilisation du concept d'incidence équivalente.

Enfin, la figure 8 montre un exemple de prédiction d'efficacité de gouvernes ; pour tout le domaine de Mach considéré, l'accord calcul-expérience est satisfaisant.

A partir des nombreuses confrontations calcul-expérience effectuées à l'ONERA, on peut estimer que la précision d'une telle méthode est de l'ordre de :

$$\begin{array}{ll} \text{portance} & : \quad \frac{\Delta C_N}{C_N} < 10 \% \qquad \text{stabilité} \quad \Delta x_{cp} < 0,5 D \\ \text{efficacité de} & \quad \frac{\Delta C_{m_g}}{C_{m_g}} < 20 \% \\ \text{gouvernes} & \end{array}$$

pour des temps de calcul de quelques secondes.

Tableau 2 - Méthodes de calcul utilisées par le code "MISSILE".

		M < 1	M > 1
F U S E L A G E	Gradient force + foyer	Banque de données (DFVLR, Data sheets)	
	Portance tourbillonnaire	Théorie de l'écoulement transversal $C_{dc} = f(M, ReD, \alpha)$	
A I L E S	Gradient force + foyer	Théorie de la Surface portante	Théorie linéarisée
	Portance Tourbillonnaire	Méthode semi-empirique (ONERA)	
I N T E R A C T I O N S	Fuselage → aile	Théorie des corps élancés $K_A = f(r/s, M \sin \alpha)$ $K_O = f(r/s)$	
	Braquage Gouvernes	Théorie des corps élancés $\Delta_{ij} = f(r/s, M)$	
	Tourbillons Fuselage	Méthode semi-empirique + Théorie de la ligne tourbillon	
	Aile avant → Aile arrière	Théorie de la ligne tourbillon	
	Aile → Fuselage	Théories des corps élancés, linéarisée	

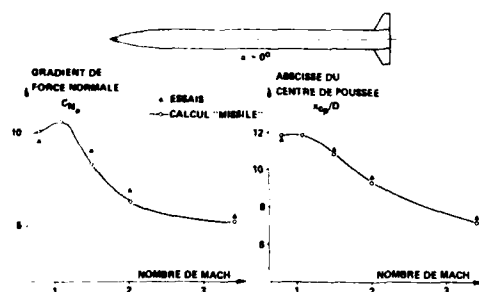
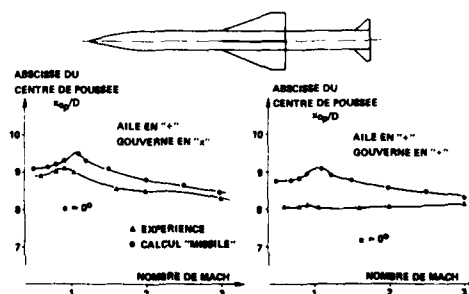


Fig. 4 - Portance et stabilité d'une configuration fuselage + gouverne. Comparaison calcul "MISSILE" - expérience.

Fig. 5 - Stabilité d'une configuration "aile-gouverne". Comparaison calcul "MISSILE" - expérience.



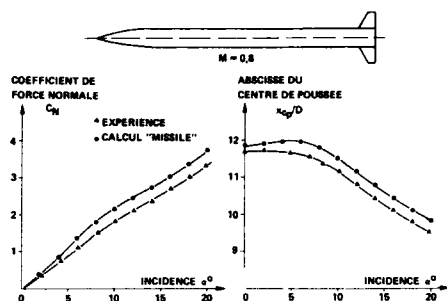


Fig. 6 - Portance et stabilité d'une configuration fuselage + gouverne à $M = 0.8$. Comparaison calcul "MISSILE" - expérience.

Fig. 7 - Portance et stabilité d'une configuration "canard" à Mach 2. Comparaison calcul "MISSILE" - expérience.

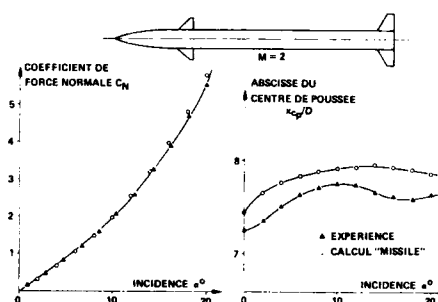
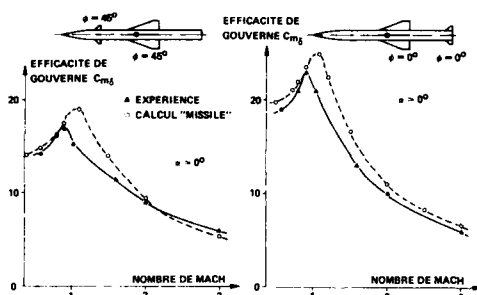


Fig. 8 - Efficacités de gouvernes. Comparaison calcul "MISSILE" - expérience.

4.1.2 - Programmes HABP - SHABP

Les nouveaux projets de missile mettant en jeu le vol à grande vitesse suscitent depuis quelques années une activité de recherche croissante et, au stade de l'avant-projet, il n'est plus possible d'utiliser des moyens de prédiction tels que ceux décrits précédemment, valables pour des formes simples et jusqu'à des nombres de Mach supersoniques peu élevés.

Il faut alors utiliser les méthodes spécifiques des écoulements hypersoniques, telles que celles regroupées dans les programmes HABP [7] et SHABP [8] (Hypersonic et Supersonic - Hypersonic - Arbitrary - Body - Program) développés à la Douglas Aircraft Company.

Ces programmes ont été conçus comme des outils d'ingénieur, c'est-à-dire autour de méthodes approchées ou empiriques simples (voir tableau n° 3), faibles consommatrices en temps de calcul, adaptées à des géométries variées et aux différents régimes d'écoulement rencontrés en supersonique élevé et hypersonique.

Il faut noter que le domaine d'application de chaque méthode est cependant limité, et que le choix de la méthode à utiliser est quelquefois délicat [9].

Par contre, l'avantage de ces codes est de pouvoir traiter des formes tridimensionnelles arbitraires par décomposition en éléments simples, sur lesquels un maillage surfacique est constitué.

En ce qui concerne les missiles à proprement parler, ils représentent le type de configurations pour lequel la prévision des coefficients aérodynamiques par "SHABP" reste la plus délicate, en particulier en incidence car l'écoulement peut être fortement influencé par un ensemble de phénomènes qui ne sont pas ou difficilement pris en compte par le calcul, tels que décollements, présence de tourbillons, interférence entre éléments, etc... De plus, tous ces phénomènes deviennent de plus en plus importants au fur et à mesure que le nombre de Mach diminue.

Tableau 3 - Méthodes de calcul utilisées par "SHABP".

$\vec{n} \cdot \vec{V} < 0$	$\vec{n} \cdot \vec{V} > 0$
ZONE D'IMPACT	ZONE D'OMBRE
. NEWTON MODIFIE	. NEWTON (KP = 0)
. NEWTON MODIFIE PRANDTL-MEYER	. NEWTON MODIFIE PRANDTL-MEYER
. DIEDRE TANGENT	. DETENTE DE PRANDTL-MEYER
. DIEDRE TANGENT EMPIRIQUE	. ACM EMPIRIQUE
. CONE TANGENT EMPIRIQUE	
. CONE INCLINE	. CONE INCLINE
. PETITES PERTURBATIONS (VAN DYKE)	. PETITES PERTURBATIONS (VAN DYKE)
. FORCES TANGENTIELLES SUR CORPS EMOUSSES	
. CHOC DETENTE	. CHOC DETENTE
. REGIME LIBRE MOLECULAIRE	. REGIME LIBRE MOLECULAIRE
. COEFFICIENT DE PRESSION CONSTANT DONNE	. COEFFICIENT DE PRESSION CONSTANT DONNE
. HANKEY EMPIRIQUE (SURFACE PLANE)	
. AILE DELTA EMPIRIQUE	
. DARLEM BUCK MODIFIE	
. ONDES EXPLOSIVES	. PRESSION DE CULOT

Pour des configurations de missiles volant en régime supersonique ou hypersonique, c'est-à-dire pour des configurations élancées, les méthodes généralement utilisées sont :

- Fuselage : "cône tangent empirique" pour les zones d'impact et méthode "ACM" pour les zones d'ombre
- Voilures : "dièdre tangent" ou "cône tangent" pour les zones d'impact et "Prandtl-Meyer" pour les zones d'ombre

Un exemple d'application de ces méthodes à un fuselage de section lenticulaire muni de 4 gouvernes est présenté figures 9 et 10. La comparaison avec l'expérience montre que la prédiction de la force normale est excellente sur toute la plage d'incidence considérée ($\alpha \leq 15^\circ$) et que la stabilité est prévue à mieux de 2 % près. Un tel calcul nécessite environ 20 secondes CPU sur un CYBER 170-855.

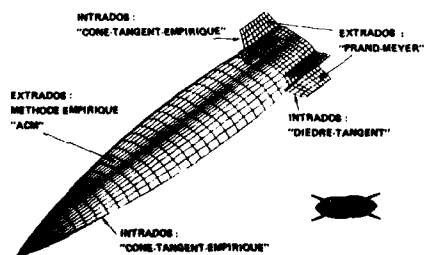


Fig. 9 - Calcul "SHABP". Exemple de maillage et méthodes utilisées.

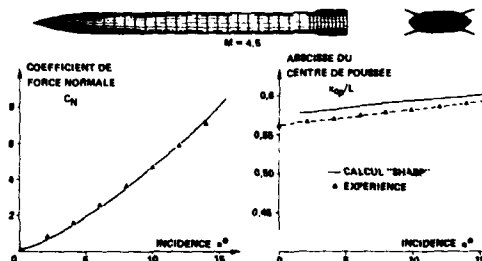


Fig. 10 - Missile de section lenticulaire. Comparaison calcul "SHABP" - expérience.

4.2 - Méthodes numériques

Comme nous l'avons vu précédemment, ces méthodes sont les seules capables de traiter des configurations complexes, mais elles sont aussi très utiles pour déterminer les répartitions de charge (nécessaires aux calculs de structure) ou les caractéristiques locales de l'écoulement autour du missile.

Actuellement, les méthodes de calcul les plus employées au stade industriel sont basées soit sur les équations d'Euler, soit sur l'équation du potentiel linéarisé. Pour résoudre cette dernière équation, on utilise la technique des distributions de singularités sur la surface de l'obstacle d'où le nom de méthode de singularités.

Par rapport aux méthodes de singularités qui ne nécessitent qu'une discrétisation de la surface de l'obstacle, les codes "Euler" sont de ce point de vue moins souples d'emploi car ils ont besoin d'une discrétisation de tout l'espace entourant l'obstacle et donc de techniques de maillages tridimensionnels.

Par contre, les équations d'Euler permettent de traiter des écoulements avec ondes de choc, nappes tourbillonnaires et éventuellement zones décollées.

Il faut par ailleurs noter que toutes ces méthodes numériques nécessitent des ordinateurs puissants et qu'elles conduisent à des temps de calcul beaucoup plus élevés que les méthodes semi-empiriques, ce qui les rend peu compatibles avec des études paramétriques.

4.2.1 - Méthodes de singularités

L'ONERA dispose actuellement de deux codes de singularités permettant de traiter des écoulements aussi bien subsoniques que supersoniques.

Le premier code "USSAERO" développé par WOODWARD [10] utilise des singularités d'ordre faible. Le fuselage est discrétisé par une répartition surfacique de sources d'intensité constante et les ailes par des tourbillons et des sources à variation linéaire dans le sens de l'écoulement amont.

Les nombreux calculs effectués sur des configurations de missiles classiques, de missiles à fuselage non circulaire et de missiles aérobie, nous ont permis de constater les limitations de ce code.

Une grande sensibilité au maillage apparaît en supersonique lorsque les configurations sont complexes, ou lorsque les formes des sections de fuselage varient beaucoup dans le sens de l'écoulement.

De plus, il y a un manque de liberté dans le choix :

- de la position des sillages des surfaces portantes, ce qui restreint leur position les unes par rapport aux autres ;
- de l'inclinaison des facettes qui ne peuvent pas, en supersonique, être inclinées d'un angle supérieur à celui de l'angle de Mach, ce qui exclut par exemple la représentation d'entrées d'air.

Toutefois, compte tenu de la simplicité relative de ce code et des temps de calcul modérés, son emploi est intéressant pour des configurations simples, telles que celle de la figure 11.

Cette configuration a été modélisée avec un maillage de (22 x 7) facettes pour le demi-fuselage et (6x6) facettes pour chaque gouverne. Un balayage en Mach a été effectué sur cette configuration et les résultats obtenus, au niveau du gradient de force normale et du point d'application du centre de poussée sont en très bon accord avec l'expérience (figure 11). Chaque calcul (Mach, incidence) demande l'équivalent de 1 mm CPU sur un CYBER 170-855.

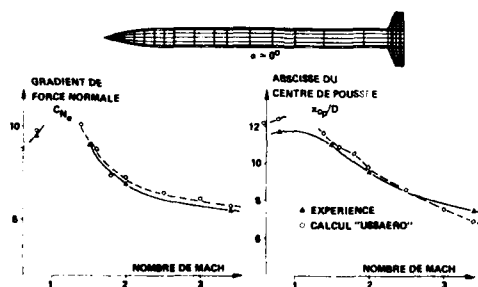


Fig. 11 - Portance et stabilité d'une configuration fuselage + gouverne. Comparaison calcul "USSAERO" - expérience.

Pour combler les défauts rencontrés avec le code USSAERO, l'ONERA a acquis le code HISSS aux termes d'un accord de collaboration avec MBB.

Ce code, développé par L. FORNASIER [11], utilise des singularités d'ordre élevé (variation quadratique de doublet et variation linéaire de source sur chaque facette) permettant ainsi d'assurer la continuité de la solution sur tout le corps. Ceci est particulièrement important lorsque l'on cherche à traiter des configurations complexes comme celle de la figure 12 (missile aérobie avec quatre prises d'air circulaires).

En supersonique, du fait de la nature de l'équation à traiter (équation des ondes), deux problèmes

peuvent conduire à une dégradation des résultats. Ces problèmes liés à la propagation des ondes dans tout l'espace proviennent :

- des ondes virtuelles qui se forment à l'intérieur des corps épais et qui en se réfléchissant sur les parois intérieures et entre elles, viennent perturber la solution extérieure ;
- du non évanouissement à distance des perturbations dues aux discontinuités d'intensité de singularités entre facettes.

Si le second problème est résolu par l'ordre élevé de l'intensité des singularités, le premier l'est par l'utilisation dans ce code, d'une répartition de singularités mixtes (source + doublet) sur la surface des corps, dont les intensités sont obtenues par une double condition aux limites (potentiel de perturbation nul à l'intérieur $\psi_i = 0$ et vitesse totale extérieure tangentielle à la paroi $\vec{V} \cdot \vec{n} = 0$).

Parmi les nombreuses applications de ce code faites à l'ONERA [12], un exemple de résultat relatif à un missile aérobie est présenté figures 12, 13 et 14. La configuration a été modélisée avec un maillage de 1426 facettes, entrées d'air incluses. On impose à l'écoulement entrant dans les prises d'air d'être uniforme et d'avoir un nombre de Mach égal à celui à l'infini amont.

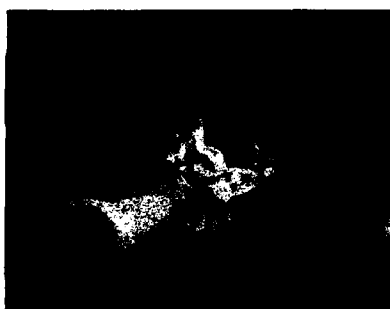


Fig. 12 - Missile aérobie. Pressions pariétales obtenues avec le code "HISST".

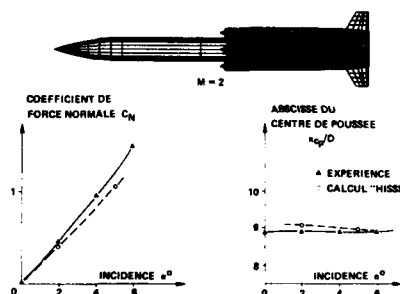


Fig. 13 - Portance et stabilité d'un missile aérobie à $M = 2$. Comparaison calcul "HISST" - expérience.

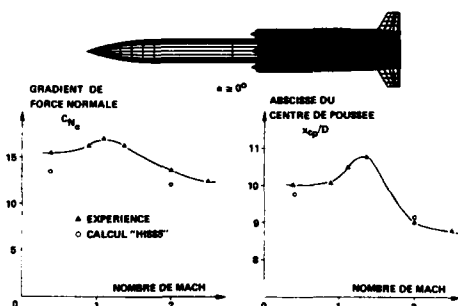


Fig. 14 - Portance et stabilité d'un missile aérobie. Comparaison calcul "HISST" - expérience.

La répartition de K_p obtenue pour un vol à Mach 2 et 5° d'incidence (figure 12) illustre la complexité de l'écoulement. La comparaison avec les essais montre que le coefficient de force normale et la position du centre de poussée sont bien prévus (figure 13). A noter cependant que l'écart sur la force normale s'accroît à forte incidence ; il résulte de la non-prise en compte des effets tourbillonnaires dans ces méthodes linéaires.

Un calcul effectué en subsonique ($M = 0,4$) a également permis de constater un bon accord avec l'expérience (figure 14).

Il faut noter que le principal inconvénient de ce code est l'importance de son temps de calcul ; pour la configuration présentée, constituée de 1426 facettes, chaque calcul (M fixé) nécessite environ 4h CPU de CRAY XMP en supersonique et 1h 30 mn en subsonique.

4.2.2 - Code "Euler"

Une méthode de calcul d'écoulements supersoniques par résolution des équations d'Euler instationnaires a été étudiée et développée à l'ONERA par BORREL et MONTAGNE [14].

Suivant les idées de VAN LEER, ces auteurs ont mis au point un schéma explicite décentré, précis au second ordre, de type MUSCL [13], qui par sa robustesse et sa précision est bien adapté au calcul d'écoulements présentant de fortes discontinuités.

Par ailleurs, une procédure numérique de "marche en espace" permettant d'obtenir des gains en temps de calcul, a été développée dans les zones purement supersoniques.

La discrétisation des équations d'Euler est réalisée suivant une formulation conservatrice de type volumes finis, et les conditions aux limites peuvent être traitées par flux ou par relations de compatibilité.

Sur ces bases et dans une optique industrielle, un programme de calcul "FLU3C" a été mis en oeuvre en collaboration avec l'AEROSPATIALE afin de traiter des missiles réels [15].

Dans ce code, la génération de maillages tridimensionnels est effectuée au moyen de préprocesseurs souples d'emploi et rapides, utilisant un mailleur bidimensionnel. Ce mailleur est dérivé du programme GRAPE selon les travaux de STEGER et SORENSON [16]. L'acquisition de la forme du missile peut être fournie soit par des outils de CAO, soit par des formulations analytiques.

Le premier exemple de calcul présenté est relatif à une configuration schématique de missile : fuselage + ailes + gouvernes. A partir du maillage surfacique de la figure 15, le domaine de calcul compris entre le corps et le choc frontal issu du nez du missile est discrétisé par environ 260 000 points. Un tel calcul nécessite de l'ordre de 40 mn CPU de CRAY XMP pour chaque incidence.

La figure 16 donne un aperçu des répartitions de pression sur le corps du missile pour $\alpha = 10^\circ$ et 20° .

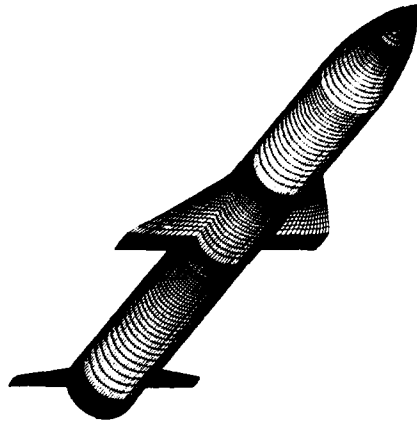


Fig. 15 — Maillage d'une configuration fuselage-aile-gouverne pour calcul Euler "FLU3C".



Mach 2, incidence 10°



Mach 2, incidence 20°

Fig. 16 — Configuration fuselage-aile-gouverne.
Pressions pariétales obtenues par calcul Euler "FLU3C".

Ces visualisations permettent entre autres de bien mettre en évidence les zones du fuselage interactionnées par les voilures.

Au niveau des efforts globaux, la figure 17 montre que la prédiction de la force normale et de la stabilité est excellente sur tout le domaine d'incidence.

Le deuxième exemple considéré ici, concerne une application industrielle de ce code au calcul du missile ASTER de l'AEROSPATIALE (figure 18).

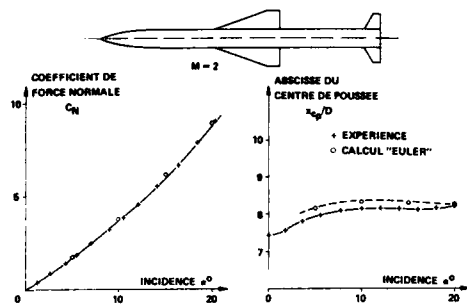


Fig. 17 - Portance et stabilité d'un missile classique.
Comparaison calcul "Euler" - expérience.

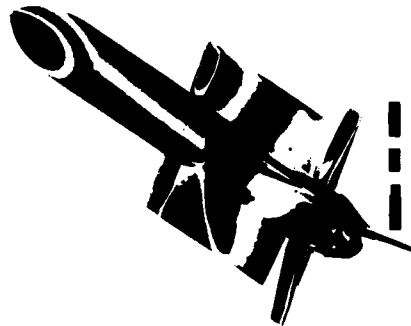


Fig. 18 - Missile ASTER. Pressions pariétales obtenues par
calcul Euler "FLU3C". $M = 2,5 - \alpha = 12^\circ - \phi = 22,5^\circ$.

Pour les différentes configurations géométriques considérées dans cette famille de missiles, les comparaisons calcul-expérience sont en bon accord (figure 19), ce qui met en évidence l'intérêt d'une telle méthode de calcul pour le dimensionnement de formes complexes.

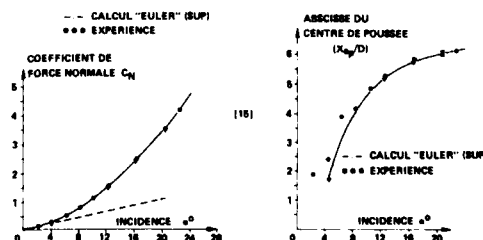
Comme nous venons de le voir, les méthodes "EULER" sont bien adaptées à ces configurations de missiles présentant une aérodynamique fortement non-linéaire. Ainsi, les ondes de choc et les nappes tourbillonnaires issues des arêtes vives des voilures sont généralement bien représentées. De même, il est possible, moyennant un traitement local, de capter les zones tourbillonnaires issues de surfaces lisses, comme celles prenant naissance sur un fuselage en incidence. Pour cela, il suffit par exemple d'introduire une condition de Kutta-Joukowski le long d'une presmée ligne de décollement, de façon à ce que le vecteur vitesse près de la paroi prenne la direction de la ligne de décollement.

Cette technique a été introduite par l'AEROSPATIALE dans un autre code EULER [15] et les résultats obtenus montrent que la portance tourbillonnaire et l'évolution du centre de poussée d'un fuselage à forte incidence peuvent ainsi être bien prédites (figure 20).

CONFIGURATION	MACH	INCIDENCE	DCN/CN (%)	$\Delta X_{cp}/D$
1	2	5	9 %	0,4
1	2	10	2 %	0,45
1	2,6	5	3 %	0,1
2	2,6	5	1 %	0,15
3	2,6	5	3 %	0,20
4	2,6	5	4 %	0,20
5	2,6	5	0,4 %	0,15
6	2,6	5	4 %	0,15
1	2,6	10	4 %	0
3	2,6	10	2 %	0,05

Fig. 19 - Exemples de précision obtenus avec le code
Euler "FLU3C" (référence Aérospatiale).

Fig. 20 - Portance et stabilité d'un fuselage (ogive-cylindre) à $M = 2,8$. Comparaison calcul "Euler" avec
décollement - expérience.



5 - CONCLUSIONS

Une revue des différentes méthodes de prédiction de la stabilité aérodynamique des missiles a été effectuée.

Les essais en soufflerie restent encore le moyen le plus fiable pour estimer les coefficients aérodynamiques mais ils ne sont pas toujours représentatifs de la réalité. Compte tenu des précisions recherchées, les effets du montage, d'un jet propulsif, du nombre de Reynolds, ou de la souplesse du missile sont quelquefois non négligeables.

Au stade de l'avant-projet, les essais ne sont cependant pas envisageables pour faire les études paramétriques car trop coûteux et demandant des délais trop importants.

Il est alors nécessaire de disposer d'une panoplie de méthodes de calcul, allant des plus simples comme les méthodes semi-empiriques, aux plus sophistiquées, méthodes de singularités ou "Euler". Chaque méthode a ses avantages et ses inconvénients, et est adaptée à des situations particulières.

On peut noter que :

- les méthodes semi-empiriques, très rapides, sont bien adaptées aux missiles conventionnels, et permettent de prendre assez bien en compte les effets non-linéaires ;
- les méthodes de singularités sont d'emploi assez limité en particulier en incidence de par leur caractère linéaire ; pour traiter des configurations complexes l'emploi de singularités d'ordre élevé est nécessaire, mais les temps de calcul sont alors importants ;
- les méthodes basées sur la résolution des équations d'Euler sont de plus en plus attrayantes bien que leur coût reste encore élevé.

REFERENCES

- [1] - KRIEGER R.J., WILLIAMS J.E.
Accuracy Criteria for Evaluating Supersonic Missile Aerodynamic Coefficient Predictions.
AIAA paper 81-1894, August 1981.
- [2] - CHAMPIGNY P.
Reynolds Number Effect on the Aerodynamic Characteristics of an Ogive-Cylinder at High Angles of Attack.
AIAA paper 84-2176, August 1984.
- [3] - CRONVICH L.L.
Missile Aerodynamics.
John Hopkins APL Technical Digest. Vol. 4. July-September 1983.
- [4] - LACAU R.G.
An Introduction to Tactical Missile Aerodynamics.
AGARD -FDP - VKI Special course on "Missile Aerodynamics", April 1987.
- [5] - KLOPPER G.H., NIELSEN J.N.
Computational Fluid Dynamic Applications to Missile Aerodynamics.
AGARD CP 336, 1982.
- [6] - HEMSCH M.J., NIELSEN J.N.
Equivalent Angle of Attack Method for Estimating Non-linear Aerodynamics of Missile Fins.
Journal of Spacecraft and Rockets. Vol. 20, July-August 1983.
- [7] - GENTRY A.E.
Hypersonic Arbitrary Body Program (version MARK II). Vol I, II.
Douglas Aircraft Company. Report DAC 56080 (April 1968).
- [8] - GENTRY A.E. and Al.
The Mark IV Supersonic Hypersonic Arbitrary Body Program. Volumes I, II, III.
Douglas Aircraft Company. Report AFFDL-TR 73-159.
- [9] - LECUYER M.
Prévision des coefficients aérodynamiques de véhicules hypersoniques par les codes HABP et SHABP. Comparaisons avec l'expérience.
AAAF Poitiers 1987. Papier N° 13. ONERA TP 1987-184.
- [10] - WOODWARD F.A.
An Improved Method for the Aerodynamic Analysis of Wing-body-tail configuration in Subsonic and Supersonic Flow.
NASA CR-2228-1973.
- [11] - FORNASIER L.
HISSS. A Higher-order Subsonic - Supersonic Singularity Method for Calculating Linearized Potential Flow.
AIAA Paper 84-1646, June 1984.
- [12] - FORNASIER L., d'ESPINAY P.
Prediction of Stability Derivatives for Missiles Using the HISSS panel code.
AGARD FNP Symposium on "The Stability and Control of Tactical Missiles". Turkey, May 1988.

- [13] - BORREL M., MONTAGNE J.L.
Numerical Study of a Non-centered Scheme with Applications to Aerodynamics.
AIAA paper N° 85-1497.
- [14] - BORREL M., MONTAGNE J.L., DIET J., GUILLEN Ph., LORDON J.
Méthode de calcul d'écoulements supersoniques autour de missiles tactiques à l'aide d'un schéma décentré.
La Recherche Aérospatiale (à paraître).
- [15] - LORDON J., GUILLEN P., LACAU R.G.
Calcul d'écoulements supersoniques autour de missiles tactiques.
AAAF. 23ème Colloque d'Aérodynamique Appliquée. Modane, novembre 1986.
- [16] - STEGER J.L., SORENSON R.L.
Automatic Mesh Point Clustering Near a Boundary in grid Generation with Elliptic Partial Differential Equation.
J. Comp. Phys. Vol. 33, p. 405-410 (1979).

PREDICTION OF STABILITY DERIVATIVES FOR MISSILES USING THE HISSS PANEL CODE

L. Fornasier
Messerschmitt-Bölkow-Blohm GmbH, FE122
Postfach 80 11 60
8000 München 80, Federal Republic of Germany

P. D'Espiney
Office National d'Etudes et de Recherches Aéronautiques (ONERA)
92322 Châtillon Cedex (France)

SUMMARY

The investigation of the applicability of a higher order panel method code to the aerodynamic analysis of missile configurations is the object of the paper. In a cooperative work between MBB and ONERA, the HISSS code - developed by MBB for the analysis of attached, subsonic and supersonic flow about complex aircraft configurations - has been used for calculating a large variety of different missile geometries, including classical configurations, non-circular bodies and air-breathing configurations. Accuracy and limitations of the present theoretical approach are evaluated and discussed by comparison of calculated results with wind tunnel data available at ONERA. It is concluded that the method can be successfully used for the analysis of very complex missile geometries at both subsonic and supersonic Mach numbers, provided that the flow conditions prevent violation of the underlying linearized potential theory.

1. INTRODUCTION

An advanced panel method has been developed at MBB for the calculation of linearized potential flows about three-dimensional configurations at subsonic and supersonic speeds [1],[2]. The method - called HISSS, an acronym which means Higher-order Subsonic Supersonic Singularity method - uses non-constant surface singularity distributions which, together with enforcement of mixed external/internal boundary conditions, allow to overcome the numerical instability problems induced by the propagation and reflection of Mach waves at supersonic speeds [3]. The code has been extensively applied to complex fighter-type aircraft configurations producing results which compare well with experimental data provided that the flow conditions prevent violation of the assumptions implicit in the linearized potential flow model [4].

The flexibility of panel methods in the modelling of complex geometries coupled with the capability to compute detailed flow characteristics make of them an attractive tool even in the analysis of missile configurations, filling the gap between semiempirical methods and more exact - but even more expensive - CFD methods such as Euler or Navier-Stokes codes. Of particular interest is the application to missile configurations of novel design which feature non-circular bodies, air-breathing engines and unconventional arrangements of lifting and control surfaces. The semiempirical methods - which rely on experimental databases gathered from classical configurations - cannot be properly used for such more complicated configurations. Moreover, detailed surface pressures obtained by panel method calculations can be usefully used for preliminary analysis of structural loads.

When considering the range of applicability of panel methods to missiles, two main aspects must be considered. In comparison to aircraft configurations, missile geometries are more slender and therefore violation of linearized potential assumptions is delayed to higher Mach numbers. On the other side, presence of very low aspect ratio lifting surfaces featuring sharp, highly swept leading edges attached to bodies of high fineness ratios promotes significant flow separation phenomena even at relatively low flow angularities, which in turn induce large non-linearities in the aerodynamic characteristics.

A cooperative work is currently underway at MBB and ONERA aimed at evaluating the capabilities and the limitations of the present method with respect to the prediction of missile longitudinal stability characteristics. To this purpose, wind tunnel data gathered by ONERA on several varieties of models at different subsonic and supersonic flow conditions [5],[6], have been used for comparison with the results obtained by the release B4 of the HISSS code. An account of the results so far obtained are presented here.

The paper is organized as follows. In the Section 2 the background theory and a schematic description of the numerical method is given, more detailed information being provided in [7]. The Section 3 deals with the applications of the method and the relevant comparisons with the wind tunnel data: classical missile configurations are discussed in para 3.1, non-circular bodies are treated in 3.2 and air-breathing missiles are considered in 3.3. Final remarks conclude the paper.

2. THE NUMERICAL METHOD

2.1 Background theory

It is well known that a unique advantage of the panel methods in the analysis of geometrically complex configurations lies in the necessity to discretize only the surface of the configuration of interest, whereas codes relying on Finite Difference or Finite Element algorithms require the definition of an additional computational mesh in the external flowfield. This property derives from the existence of the Green's theorem which allows to transform the second order, partial derivative Laplace equation

$$\phi_{xx} + \phi_{yy} + \phi_{zz} = 0 \quad (1)$$

describing the velocity perturbation potential in incompressible flows into the equivalent integral form

$$\phi(x,y,z) = \frac{1}{4\pi} \iint_S \left\{ -\frac{\sigma}{r} + \mu \frac{\partial}{\partial n} \left(\frac{1}{r} \right) \right\} dS. \quad (2)$$

Here σ and μ are respectively source and doublet singularities distributed over the boundary surface S enclosing the configuration of interest, r is the distance from the field point $P(x,y,z)$ to the point Q lying on S and $\partial/\partial n$ is the normal derivative of S at the point Q . Uniqueness of ϕ is guaranteed inside the domain whenever either the function ϕ itself (Dirichlet's problem) or its normal derivative $\partial\phi/\partial n$ (Neumann's problem) are known over the surface S . Perturbation velocity components are then computed by differentiating ϕ with respect to the coordinates of P , i.e.

$$v(x,y,z) = \frac{1}{4\pi} \iint_S \left\{ -\sigma \text{grad} \frac{1}{r} + \mu \text{grad} \frac{\partial}{\partial n} \left(\frac{1}{r} \right) \right\} dS. \quad (3)$$

Although in general equations (2) and (3) must be solved numerically, analytical solutions can be derived, provided that the surface S and the singularity distributions σ and μ be expressed in polynomial form. In the panel method approach, the solution is achieved by dividing the boundary surface S into elements (panels) carrying singularity distributions of parameterized shape which approximate the actual σ and μ distributions over S . The values of the singularity parameters are then determined by enforcement of the boundary conditions at a set of surface points (control points), whose number must be equal to the number of unknown singularities. Once the σ and μ distributions are determined, eq. (3) can be used to evaluate the induced flowfield by summing up the contributions of all panels. The energy equation can then be used to derive pressure data from velocity values. Finally forces and moments acting on the configuration surface are derived from integration of pressure and of momentum.

A formal identity with (2) exists at supersonic speed for the case $M_\infty = \sqrt{2}$, provided that the geometrical distance r and the normal at the surface n be replaced by the hyperbolic distance r_h and the conormal \tilde{n} defined as follows:

$$r = (r_x, r_y, r_z), \quad r_h = (-r_x, r_y, r_z) \quad (4)$$

and

$$n = (n_x, n_y, n_z), \quad \tilde{n} = (-n_x, n_y, n_z). \quad (5)$$

The solution for any other intermediate Mach number is obtained from the relevant fundamental solution by applying Goethert's similarity rule. Since the numerical solution can not be more accurate than the governing equation, assumptions under which the equation (1) or its supersonic counterpart are derived restrict the range of validity of the method. Existence of a velocity potential implies inviscid, irrotational steady-state flow. Further assumptions necessary to linearize the compressible potential equation along the x-axis postulate that the perturbation in this direction be small in comparison to the freestream velocity and that the freestream Mach number be neither too large nor close to one. The first assumption is locally violated in stagnation regions while the latter excludes applicability of this method to the transonic and hypersonic regimes.

The first numerical implementation of this theory date back to about thirty years ago [8] and since that time a variety of different codes have been developed. Most of them, however, are restricted to the calculation of subsonic flows while only a handful of codes are applicable to supersonic flows [9],[10],[11],[12]. The discrepancy can be explained as follows. Historically, incompressible flows have been studied first. Neglecting the viscous effects, these flows are governed by the Laplace equation (1), which is very well suited for the solution by the singularity technique. Once the equations of mass and of momentum are linearized, the extension from the incompressible to the subsonic case is very straightforward, requiring only the introduction of an affine transformation (Goethert's similarity rules). In supersonic flow, the linearization of the equations lead to the solution of a wave equation. Application of the singularity technique to this type of equation is much more difficult, involving the calculation of integrals whose integrand function becomes singular. Not only the mathematical effort necessary to derive the analytical expressions is bigger, but also the stability of the numerical scheme becomes more critical. Essentially, two problems arise, both of them being originated by the hyperbolic character of the governing equation at supersonic speeds. Due to the mechanism peculiar to the wave propagation, numerical influences just

like physical disturbances do not decay with distance from the generating source but propagate unattenuated along the characteristic lines throughout the whole domain of dependence. Therefore, the effect of the singular term induced into the perturbation velocity by a finite doublet strength at panel edges is transported into the computational domain by the Mach waves originated at the edges. Unless the doublet distributions are made continuous over the whole boundary surface - in which case the contributions from two adjacent panels cancel exactly each other - a false perturbation is felt by control points lying close to these Mach lines. As a result, severe local numerical instabilities can appear, which make the results extremely sensitive to random combination of panel spacings, control point locations and freestream Mach numbers. The other problem is related to the property of singularity distributions to propagate disturbances not only into the flowfield but also into virtual domains, like interiors of closed volumes. In this way, flow perturbations are transmitted directly through internal volumes instead of being convected along the external surface. Once generated, such internal waves become trapped within the closed volume and multiple reflections take place which induce unrealistic oscillations in the external pressure distributions. As a consequence, supersonic calculations require control of both the external and the internal flow characteristics.

In the PAN AIR higher order panel method [9], these problems are avoided using panels carrying both source and doublet singularities, and by making the doublet distribution continuous over the entire configuration. In this way, significant improvements can be achieved in solution quality, at the expense, however, of increased coding complexity and of larger computing requirements.

2.2 Brief description of the HISSS Code.

HISSS is a higher order panel method developed at the Theoretical Aerodynamic Dept. of MBB following the PAN AIR approach [9]. The code uses distributions of piecewise linear sources and quadratic doublets for the numerical solution of the subsonic and supersonic linearized potential flow equations about arbitrary three-dimensional configurations. The configuration is modelled by networks of panels located over the actual surface and carrying a specified singularity distribution (source, doublet or composite, i.e. source and doublet) whose unknown strengths are determined by imposing appropriate boundary conditions at a discrete set of control points. A variety of different types of boundary condition specification are available. All the results presented in this paper have been obtained using networks of composite panels and applying a mixed internal/external specification over the impermeable parts of the configuration. A condition of zero normal velocity at the surface has been applied to the external flow, and the perturbation potential has been set to zero on the interior of the configuration to suppress the propagation of internal Mach waves at supersonic speeds. Because of the supersonic requirement to ensure continuity of the doublet distributions over the whole configuration, the surface must be modelled without generating any gaps at network edges. Since the corner points of a panel do not lie - in general - on a planar surface, continuity of the geometry within a network is maintained by subdividing each panel into planar subpanels. Each of these subpanels carries a quadratic doublet distribution which allow to ensure continuity of the singularity strength throughout each network. Continuity of doublet strength across networks is obtained by enforcement of a matching algorithm at control points lying along the network edges.

Vorticity generated at the configuration surface is carried downstream by using special networks carrying doublet distributions which are constant streamwise and constant in the transverse direction. Unlike other methods - as [10],[11], in which the trailing vorticity is implicitly taken into account in the integration scheme - the wake geometry must be here modelled by the user. This feature offers the possibility to investigate the effect of different wake positionings on the local and global aerodynamic characteristics.

Of particular interest for supersonic calculations past air-breathing missile configurations is the capability of the method to calculate 'superinclined' panels [9], i.e. elements whose surface is more inclined to the freestream velocity than the (asymptotic) Mach angle. Due to the special pattern assumed by the Mach waves leaving the surface of such panels, boundary conditions cannot be specified on their upstream face so that they can not be used to model solid portions of the configuration. Instead, they can be used to influence the downstream flowfield by - for example - absorbing oncoming flow perturbations capturing or simulating jet effluxes. In this investigation superinclined panels have been used to close the engine inlets at supersonic speeds for preventing the propagation of disturbances into the interior of the configurations.

Initially developed on the VAX 11/780 computer system, the numerical code is currently implemented on various IBM and CDC scalar processor machines. With minor modifications the code has been transferred to the CRAY-XMP and SIEMENS VP200 vector computers, where substantial gains in computing times have been obtained in the calculation of large configurations through vectorization of the LU decomposition algorithm used for inverting the linear equation system. HISSS is connected to a system of ancillary programs which have been 'ad hoc' developed for the post-processing of the output results. An interface program exists for generating the input data of the panelling from a CATIA geometry database.

3. COMPARISON OF NUMERICAL RESULTS WITH EXPERIMENTAL DATA.

The investigation of the capabilities and limitations of HISSS with respect to the prediction of the aerodynamic characteristics of missiles has been carried out for one classical configurations (axisymmetrical bodies bearing different cruciform arrangements of wings and rear-mounted control surfaces), for two configurations featuring a body of non-circular cross section, and for two air-breathing configurations. Essentially, the normal force coefficient C_N and the position of its application point X_{cp} have been considered as main parameters in the comparison of the numerical results with the experimental data. For three configurations - ogive-cylindrical body in isolation, one lenticular-shaped body and one air-breathing missile configuration - the calculated surface pressures have been compared with the relevant measured values. Availability of detailed experimental pressures for the lenticular body allowed to compare the distribution of the local normal forces along the longitudinal axis for the Mach = 2.0 case.

All the configurations investigated have been modelled using networks of composite panels for representing the actual shape of the solid surfaces. Thus, the same singularity arrangement has been used for all configuration components, avoiding the artificial distinction between lifting and non-lifting parts (wing-like and body-like components in the terminology of [9] and [10]) and the need to define a lift-carry-over model. The combination of boundary conditions reputed to give the best results has been prescribed for all the cases presented herein. This is the condition of zero normal component of the total velocity at the surface wetted by the flow ($V_n = 0$) together with the condition of zero perturbation potential on the interior ($\phi_i = 0$).

A different modelling has been used at the base of the configurations. Clearly a physically correct simulation of the flow at the base of a missile is out of the realm of a (linearized) potential flow model; the simplified treatment followed here is aimed at limiting the negative influence of an improper modelling on the global stability characteristics. It is argued that for most of the body geometries at low to moderate angles of attack, the flow separates in the vicinity of the base and that the resulting vortex shedding takes place at the base contour. Neglecting the details of the downstream evolution of this vortex sheet, the essential feature of the base flowfield is the smooth flow-off of the streamlines which leave the body surface in a direction (nearly) parallel to the freestream velocity. Such type of flow can be simulated by fitting an annular wake to body and closing the base using a source network. The source strengths are then determined by the interior Dirichlet condition (i.e. $\phi_i = 0$) while the absence of doublets on the base implies automatically the desired condition of zero tangential component for the perturbation velocity. At supersonic speeds, the modelling has been omitted for the bases located at the back end of the configurations, since no influence can be transmitted upstream.

In the air-breathing configurations, the intakes have been close using networks of composite panels. At subsonic speeds, one of the two boundary conditions is used for determining the inlet mass-flux while the other the usual condition $\phi_i = 0$. These panels become superinclined at supersonic speeds and in this case both boundary conditions are used for cancelling the perturbations of the oncoming flow which would, otherwise, deteriorate the downstream solution.

As mentioned in the previous section, the geometry of the wakes shed from the trailing edges of the lifting surfaces and at the base contour must be defined by the user as part of the configuration specification. In fact the position of the wake(s) is - within the frame of potential theory - a part of the problem specification and not - as in Euler and Navier-Stokes methods - an output result. In a correct modelling, a wake surface should be everywhere force-free, which implies that the wake vorticity should be aligned to the local velocity. In practice, very seldom the initial guess for the wake location yields this property so that the right wake position should be found iteratively. In general, the influence of the geometry of a wake is quite negligible on the component from which it is shed (it is null at supersonic speeds) but the effects can and usually do become important for downstream components lying close to the wake sheet. In this investigation, the relocation of the wing wake was done manually for the most critical configuration, the classical missile featuring the coplanar cruciform arrangement for wings and control surfaces. The results show clearly the potential benefits which could be gained by the incorporation of an automatic wake relaxation process in the present code.

3.1 Classical missile configuration.

Extensive experimental data have been gathered on a wind tunnel model representative of a classical missile configuration. The body of the model is of modular construction, allowing the mounting of a set of cruciform wings and control fins in different orientations. Tests have been performed at both subsonic and supersonic speeds, yielding a considerable bulk of data, a part of which have been used for the comparisons presented herein.

Isolated body.

The whole configuration consists of an axisymmetric body of total length equal to 15 diameters, made up of a forward ogive of length 3 diameters faired into a cylinder of constant circular section. It has been modelled using one composite network of 210 panels for representing the surface of the body, one network for the base and one wake network attached to the base contour. For supersonic calculations the base and the wake networks have been omitted. The comparison of the evolution of the lift slope $C_{L\alpha}$ and of the center of pressure XCP/D in the interval between Mach No.s 0.40 and 3.0 is presented in figure 1. The experimental evolution with the Mach number is well reproduced by the calculations for both characteristics, with the noticeable exception of the small region close to Mach number equal to 1.0. Quantitatively, the figure shows that the calculations underestimate systematically the lift by about 15%, while the predicted point of application of the normal force at small angle of attack is shifted about one diameter upstream of the measured value. This discrepancy is due to the generation - in the experiments - of non linear characteristics induced by flow separations along the body sides which develop vortical lift. The non-linear lift becomes particularly significant at higher angles of attack - figure 2 - but the boundary layer development and the incipient separation present even at lower angles makes quite impossible to define a 'fair' linear slope to be used for comparison with the calculations. Moreover, due the length of the body - the position of the center of pressure is very sensible to small variations of the longitudinal pressure distributions. In fact, the comparison of the pressure coefficients C_p acting on the symmetry plane show a very good agreement between HISSS and experiments at Mach number equal to 2.0, α equal to 0.0 and 2.0 degrees of angle of attack, figure 3. Only at higher incidences, $\alpha = 10$ degs., the effect of the vortical separation is visible on the leeside pressures downstream of the ogive (section X/D = 3.0).

Body and cruciform wings.

This configuration consists of the body previously analysed, to which a cruciform wing set is fixed in a '+' orientation, figure 4. The lifting surfaces have a leading edge sweep of 70.42 degrees, a straight trailing edge and features a double-wedge section of 5% thickness. The intersection between the wing leading edge and the body is located at the section X/D = 6.14. The root chord has a length equal to 3.43 body diameters, the total span measures 2.971 diameter. The panelling used for this configuration is shown in figure 4. For symmetry reasons, only the half of the configuration lying in the space $y > 0$ has been modelled. Two networks have been used for representing the upper and lower surface of each wing to which a network consisting of a single row of panels has been added at the tip for separating completely the inner from the outer domain. The wake shed from the horizontal wings is located in the $x = 0$ plane. Since sideslip cases had not been considered here, the wakes of the vertical wings have been omitted. The panelling of the body used in the analysis of the isolated characteristics has been rearranged, increasing the panel density in the afterbody region and introducing separate networks for the upper and lower surface downstream of the wing leading edge. It is to note that downstream of the wing trailing edge the network split must be introduced for picking up the potential jump carried by the inner leg of the wake network. At subsonic cases, the base of the configuration has been modeled according to the specifications of the section 2.2.

A good agreement with the experimental longitudinal characteristics has been obtained for this configuration, figure 5. The evolution of the normal coefficient slope show has been predicted within 10% of the experimental value while the accuracy achieved in the calculation of the location of the center of pressure lies within 0.20 diameter length. The next two figures show the lift and the center of pressure location in function of the angle of attack. At Mach equal to 2.0, figure 6, the normal force is well predicted up to about 5 degrees of incidence. Although at higher angles of attack non linear lift is obtained in the experiments, the position of the center of pressure remains nearly constant and very close to the calculated value. Stronger lift non-linearities are observable at the Mach 0.80 case, figure 7, so that the validity of the lift predictions is reduced to very low incidences (approximately up to 2.0 degrees). The downstream shift of the center of pressure is again very limited, so that the HISSS prediction is acceptable up to higher incidences (the difference amounts about one half of diameter at $\alpha = 15.0$ degs.).

Integration of the pressure distributions acting on the vertical wings confirmed that the contribution of these configuration components is practically negligible to all global coefficients but axial force. Since this characteristic has not been considered in this analysis, the modelling of vertical surfaces has been sometimes omitted in the analysis of the following configurations.

Body with cruciform wings and control fins in coplanar arrangement.

This configuration is obtained mounting four control surfaces at the rear of the previous body/wing combination (orientation in '+'). The fins - having a leading edge sweep of 24.16 degrees and a simple-wedge section of 8% thickness - are fixed to the body with their straight trailing edge in line to the base of the missile. Two panellings of different panel densities have been used for modelling the configuration. The panelling used first is shown in figure 8. It has a relatively small number of panels considered the complexity of the configuration, obtained using a rather sparse definition of the lifting surfaces and of the body in longitudinal direction and omitting the modelling of the vertical surfaces. This model has been used for investigating the effect of different positionings of the wing wake with respect to the rear control surfaces. In fact, due to

the coplanar arrangement of the surfaces, the proper simulation of downwash characteristics induced by the wing wake onto the fin flowfield was expected to play a critical role for predicting the fin stability contribution. Essentially two different types of wake modelling have been tested, see bottom of figure 8. In the first one, the panels of the wake are located in the horizontal plane and their trailing edges about the leading edge of the fin. In this way, the doublet of the wake is connected to the doublet distributions of the upper and lower surfaces of the fin. In the second model, the location assumed by the physical wake at positive angles of attack is schematically simulated by rotating the panels along the wing trailing edge wake of an angle ϵ upwards. In this modelling, a network of constant doublets is used to connect the inner leg of the wing wake to the body side, thus avoiding the generation of a vortex line at the free edge of the wake. The analysis of the comparison between results and experiments, figure 9 and 10, demonstrates clearly that:

- the numerical results are very sensitive to the particular modelling used; in particular at Mach = 0.80 the variation induced on the location of the center of pressure is about two diameters;

- the downwash relevant to the connected-wake modelling is too large causing a strong underestimation of the fin lift;

- better agreement with the experiments is obtained when the wake passes over the fin surface; in principle, using a proper combination of inclination angles ϵ and angles of attack it would be possible to simulate the dependency of the center of pressure location from the incidence. In practice, the calculations were limited to two inclination angles equal to $\epsilon = 2.0$ and 5.0 degrees.

Simulation of control deflection.

A finer panelling scheme has been then defined using the best wing wake modelling emerged from the preliminary investigation, i.e. a wing wake passing over the fin surface with an inclination $\epsilon = 2.0$ degrees. This model has been used to investigate the simulation of pitch control characteristics obtained by deflecting the horizontal fin of an angle $\delta = 10$ degrees. Two different modellings have been tested. In HISSS, geometrical transformations of a whole network is achieved by specification of appropriate values for parameters controlling translations, rotations about any user-oriented axis and scaling factors. In addition, a special restart option allows to run the code in the variational analysis mode, by which the effects due to geometrical variations from a 'datum' configuration at the same Mach number can be computed in an economical way by simply updating the right-hand-side of the linear system only and reusing the aerodynamic influence coefficient and the inverted matrix already computed for the baseline. Incremental lift and pitching moment computed using this option compare well with experimental data at Mach 2.0 but overestimate control power at Mach .80. Inspection of the individual contributions of the control surfaces and of the body indicated that while at supersonic speed the interference lift induced on the body is small, the amount of lift carry over predicted at subsonic speeds builds up almost exactly the difference between calculated and measured incremental pitching moments, as can be seen in the following table.

Mach	$\Delta C_{m_{exp}}$	$\Delta C_{m_{calc}}$	$\Delta C_{m_{fin}}$	$\Delta C_{m_{body}}$
0.80	5.27	6.58	5.01	1.50
2.00	2.92	3.16	2.98	0.18

Comparison of experimental vs. calculated pitching moment increments at $\alpha = 0$ degree corresponding to a fin deflection of $\delta = 10$ degrees

It was conjectured that the connection between the doublet distributions of the fin and the body implied by this modelling be not compatible to the physical flow conditions of the wind tunnel model. Here, due to the circular shape of the body, a gap exists between the body surface and the deflected surface, causing a flow leakage from the higher to the lower pressure regions which eventually develops into a counter-rotating vortex. The sum of these phenomena induces a loss of control power over the value obtainable preserving geometrical continuity between the fixed and the movable parts. Therefore, a second series of calculations has been carried out for the Mach 0.80 case, modelling the control surface in its actual deflected position and simulating the gap by closing the inner side of the fin by a separate network, figure 11. Figure 12 presents the comparison of the results obtained using the 'sealed' and the 'unsealed' modellings with the experimental values. It can be seen that although the 'unsealed' curves now lie below the wind tunnel data, the discrepancy between theory and experiments has been significantly reduced by the refined modelling.

Body with cruciform wings and fins in non-coplanar arrangement.

This configuration is obtained from the previous one by rotating the fin set 45 degrees about the body axis thus obtaining an orientation in 'x', figure 13. Hence, the geometry of each component is identical to that of the previous configuration. The panelling of half configuration is made up of 16 networks representing the solid surfaces, three wake networks and one base network. Here again, the vertical wings have been omitted. Due to the angular displacement of wings and fins, no significant interference between the wing wake and the control surfaces should be expected at low angles of attack. Therefore, the wake shed from the wing is modelled here in the horizontal plane.

The lift characteristics of this configuration are very well predicted at Mach equal to 2.0, figure 14. As usual at subsonic speeds, the stronger non-linearities deteriorate the agreement between experiments and numerical results at incidences already beyond $\alpha = 2.0$ degrees, figure 15. With respect to the center of pressure, its location is well predicted for both Mach numbers at angles of attack up to 5.0 degrees. At $\alpha = 2$ deg.s experimental and theoretical values are practically coincident.

3.2 Missile configurations with non axisymmetrical body.

This section considers the application of HISSS to the analysis of non axisymmetrical bodies. Calculation of this type of configuration requires the capability to represent an arbitrary three-dimensional surface. Hence simpler methods, based on use of line singularities for simulating body effects, cannot be used for such configurations. Moreover, panelling irregularities occurring in the fitting of double curvature surfaces with flat quadrilaterals are very likely to promote numerical instabilities at supersonic speeds, as already mentioned in section 2.1. Therefore the present configurations can be considered as a first benchmark for evaluating the arbitrary geometry capability of the present method.

A lenticular body featuring four winglets in the afterbody region has been studied first, figure 16. The configurations has been modelled using a total number of 886 panels distributed over 16 networks (without body base and wake networks). Calculations have been carried out for two subsonic Mach numbers - Mach 0.60 and 0.80 - and three supersonic Mach numbers - Mach 1.4, 2.0 and 3.0 -. Smooth pressure distributions have been obtained for all flow conditions, confirming the favourable effects of the use of higher order singularities. The figure 17 shows the isobar pattern computed at the case Mach 2.0, $\alpha = 5.0$ degrees of angle of attack. The comparison of the global lift characteristics, figure 18, however reveals that only for the Mach 2.0 case a good agreement is achieved, while the subsonic predictions are underestimated by about 20 % with respect to the experimental values. Surprisingly, the location of the center of pressure is adequately predicted in the whole range of Mach numbers. Comparison of the variations with the angle of attack - presented in figures 19 and 20 for Mach number 2.0 and 0.60 - confirms the presence of large non-linearities in the experimental lift characteristics.

The availability of detailed surface pressure measurements for a quite similar configuration, figure 21, gave the opportunity to analyse the differences between theory and experiments in more details. This configuration was tested without rear tails. The planform and the side view resemble the silhouette of a surfing board, but the frontal view reveals the presence of a sharp edge, running longitudinally along the side of the body. Initially, the configuration was modelled in the usual way, using two composite networks to represent the upper and the lower surface of the body. Due to the absence of the lift produced by the winglets, the first results compared very bad with experiments, showing a strong underestimation of the lift characteristics and a completely false position for the center of pressure, figure 22. Clearly, the lift generated on such configuration is in large part due to the formation of vortical phenomena at the sharp side edge. In fact, at this location the cross flow separates into vortices, even at low incidences, which roll up and interfere with the upper surface flow, generating a vortical lift. An exploratory test to model this type of flow was made by introducing a lateral wake downstream of the position of the largest body width. In spite of the simplicity of this modelling - in practice only the side smooth flow-off condition was introduced without any attempt to model the actual shape of the vortical sheet - a significant increment in the lift characteristics was obtained together with a favourable rearward shift of the center of pressure. Improvements in the predictions are particularly encouraging at supersonic speeds, where the modelling with lateral wake show a good agreement with experimental data at low incidences, figure 23.

Comparison of surface pressures can be use to gain further insight into the flow phenomena by which lift is generated on such configuration. At subsonic speeds, the effects of the body vortices influence the whole flowfield, whilst at supersonic speeds the influences can be transmitted only downstream. Hence, comparison of the experimental flowfield with the calculations corresponding to no separation conditions allows to trace back the formation and the longitudinal progression of the separation-induced vortices. The comparison of the local normal force distribution along the longitudinal axis is given in figure 24. At $\alpha = 2$ deg.s, the distribution computed by the present method agrees well with the measurements, indicating that no separation still occurs. At $\alpha = 5$ degrees, the two curves show a departure at a longitudinal position equal to about 40% of the total body length. At $\alpha = 10$ degrees the differences extend to more than 80% of the total length. It is to note that the HISSS distributions - in according to linearized theory - exhibit a negative local lift for the region downstream of the longitudinal section having the maximum cross sectional area.

3.3 Air-breathing configurations.

Consideration of possible use of ram-jet engines for tactical missile of the next generation is drawing increasing interest, leading to the definition of configurations of unconventional architecture featuring one or more external air intakes. Due to the complexity of the resulting geometries and to the influence of the inlet(s) on the overall aerodynamic characteristics of the configuration, application of the classical predictions methods available to the missile community is very difficult [13],[14]. The arbitrary geometry capability of the present method has been identified as a key benefit potential for improving the efficiency of the theoretical estimates of air-breathing missiles. So far, two configurations have been analysed.

Body with rectangular intakes.

This configuration consists of an ogive-cylinder body to which a cruciform set of four rectangular intakes is fixed on the cylindrical part, figure 25. In the wind tunnel model, the frontal face of the intakes is fitted with a plate inclined toward the body surface. A circular hole in the plate allows the oncoming air to enter the inlet. However, since the capture area is smaller of the frontal area of the intakes, at supersonic speeds a detached shock system forms ahead of the intakes, which decelerates locally the stream to subsonic speeds allowing the refused mass-flux to turn around the intakes. Presence of bow shocks cannot be treated within linearized potential theory. Instead, the inlet flow has been simulated in HISS using superinclined panels which swallow the whole stream tube intercepted by intakes. Consequently, the predicted flowfield in the inlet region does not show the two recompression shocks clearly detectable in the experimental pressure distributions measured along two azimuthal cuts passing between the intakes, figure 26. Better comparison is obtained in the regions upstream and downstream of the intakes, especially on the lower side of the configuration, as shown by the comparisons of figure 27 where the circumferential pressures of the pressure tap sections number 10, 14 and 16 have been considered. In general, the pattern of the inlet-induced shocks is not very sensitive to the angle of attack so that - at least at low incidences - for symmetry reasons the effects on the overall aerodynamic characteristics is not too strong. This explains the still reasonable agreement of results with experiments shown in figure 28.

Body with rear fins and conical intakes.

The architecture of this configuration is very complex. A cruciform set of four air intakes of circular shapes are faired into the body. Downstream, the intake fairings evolve into a rectangular shape. Four lifting surfaces are fixed to the intake fairings with their trailing edge aligned to the body base. The configuration has been modeled in detail using a total number of 1426 panels distributed over 78 networks, figure 29. The modelling of the air intakes includes the boundary layer diverter between the lower cowl and the body surface, and the conical spike ahead of the capture area. Boundary conditions specified on the networks used to close the intake prescribe no flow-through at the subsonic case, while at supersonic speeds only a flow-through condition is possible on the superinclined barrier.

Calculations have been made for Mach numbers equal to 0.4 and 2.0. The predictions for the normal force slope and the position of the center pressure at low angles of attack are in good agreement with the experimental data, figure 30. The figure 31 presents the variations with the angle of attack for the Mach 2.0 case. Considering the complexity of the configuration, the agreement of the location of the center of pressure is excellent. As already observed in the analysis of more conventional configurations, section 3.1, the lift curve is underestimated of less than 10%.

The isobars calculated for the case Mach 2.0, $\alpha = 5$ degrees of angle of attack are displayed in figure 32. It is possible to identify four main flow regions. In the portion of the body upstream of the intakes, cross flow effects are predominant. In the mid-body region, compression waves originating at the conical spikes and at the inlet lips propagate along the body surface. More downstream, a strong expansion occurs in the diverging channel between the intake fairings. Due to the weak inclination of the characteristic lines at this Mach number, the interference of the lifting surfaces on the body pressure is limited to a small region in proximity to the base. Globally, in spite of the geometrical complexity of the configuration, the computed pressures appear to have a character in accordance with the expected properties of the physical flow, giving confidence in the useability of the code as primary numerical tool for the preliminary analysis of aerodynamic loads on very complicated configurations, such as the present one.

4. CONCLUDING REMARKS

In a cooperative effort between MBB and ONERA, the applicability of a higher order panel method code to the aerodynamic analysis missile configurations has been investigated. The code - developed at the Theoretical Aerodynamic Dept. of the Military Aircraft and Helicopter Division of MBB for calculating attached, subsonic and supersonic flows about complex aircraft configurations - has been used herein for modelling several types of geometries representative of modern tactical missile configurations. The arbitrary geometry capability of the method allowed - for each type of missile architecture considered - the definition in the mathematical modelling of all the configurational details deemed to be essential for the achievement of the desired level of accuracy. The advantages offered by use of higher order singularities coupled with the specification of appropriate combination of external and internal boundary conditions over low order panel methods were clearly demonstrated in the enhanced stability of the numerical results, which, above all, do not deteriorate at supersonic Mach numbers. In particular, the geometrical complexity of air-breathing configurations does not hamper the quality of the results obtainable by the present method at supersonic speeds.

Experimental data available at ONERA have been used for validating the present results. Since the code solves the linearized potential flow equations, the accuracy of the results decreases rapidly outside of the range of linear flow. For missile configurations, non-linearities induced by formation and subsequent rolling up of vortices are stronger than those induced by transonic compressibility effects. As a consequence, applicability of the present method is much more limited in angle of attack range than in Mach number envelope. In practice, the panel method predictions can be used only at very low angles of attack. The actual range within which an acceptable agreement with experiments is obtained is strongly configuration dependent. For winged and/or finned configurations the range of applicability is restricted to $\alpha < 5.0$ degrees of angle of attack. In this range, the normal force is computed within 5 to 10 % of the experimental value. With respect to the static longitudinal stability, the position of the center of pressure is predicted within 0.5 to 1 body diameter. In general, accuracy of supersonic predictions is better than at subsonic Mach numbers. Characteristics of isolated bodies are very difficult to predict with such an inviscid code since, in practice, almost all the lift generated at angle of attack is due to separation phenomena. However, modelling of a vortex sheet introduced manually at the separation line of a non circular body allowed to appreciate the benefit potential of the incorporation of the modelling of separated vortices into the present code.

In conclusion, the use of the code 'as it is' is limited to the calculation of the aerodynamic characteristics of missile configurations at very small angles of attack. Coupling with boundary layer calculation - already possible in the latest HISSS release -, implementation of automatic wake relaxation procedures and modelling of separated vortical sheets would greatly enhance the present angle of attack capability of the method.

ACKNOWLEDGEMENT

Part of the MBB contribution has been sponsored by the German Ministry of Defense, contract T/Rf41/E0010/E1410.

Part of the ONERA contributions has been sponsored by French Official Services.

REFERENCES

- [1] Fornasier, L., "HISSS - A Higher-order Subsonic/supersonic Singularity Method for Calculating Linearized Potential Flow", AIAA Paper 84-1646, 1984.
- [2] Fornasier, L., "Linearized Potential Flow Analysis of Complex Aircraft Configurations by HISSS, a Higher-order Panel Method", AIAA Paper 85-281, 1985.
- [3] Fornasier, L., "Treatment of Supersonic Configurations by an Updated Low-Order Method", J. of Aircraft, Vol. 21, Apr. 1984.
- [4] Fornasier, L., and Heiss, S., "Application of HISSS Panel Code to a Fighter Aircraft Configuration at Subsonic and Supersonic Speeds", AIAA Paper 87-2619.
- [5] Unpublished Wind Tunnel Data from ONERA.
- [6] N.N., "Missiles Aerobies - Mesures des Coefficients aerodinamiques et mesures de pression", Proces verbal SAE/20/87/E57/PV13, 1987.
- [7] Fornasier, L., "HISSS - A Higher-order Panel Method for Subsonic and Supersonic Attached Flow about Arbitrary Configurations", in Notes on Numerical Fluid Mechanics, Vol. 21, Vieweg Verlag, Braunschweig/Wiesbaden, 1988.
- [8] Hess, J.L., and Smith, A.M.O., "Calculation of Non-lifting Potential Flow about Arbitrary Three-dimensional Bodies", Douglas Aircraft Report No. E.S. 40622, 1962.
- [9] Ehlers, F.E., et al., "A Higher Order Panel Method for Linearized Supersonic Flow", NASA CR-3062, 1979.
- [10] Woodward, F. A., "An Improved Method for the Aerodynamic Analysis of Wing-Body-Tail Configurations in Subsonic and Supersonic Flow", Nasa CR-2228, 1973.
- [11] Hoeijmakers, H.W.M., "A Panel Method for the Determination of the Aerodynamic Characteristics of Complex Configurations in Linearized Subsonic or Supersonic Flow", NLR Report 80124 U, 1981.
- [12] Youngren, H.H., 'QUADPAN', Lecture in AIAA Professional Study Seminar on Aerodynamic Analysis Using Panel Methods, 1985.
- [13] Champigny, P., "Problemes lies a l'aerodynamique externe des missiles aerobies", AGARD-CP-336 on Missile Aerodynamics, 1982.
- [14] Mortel, P., et al., "Calcul d'écoulements supersoniques autour de missiles tactiques", Proceed.s of the 23^{eme} Colloque d'aerodynamique appliquee, AAAP, 1986.

FIGURES

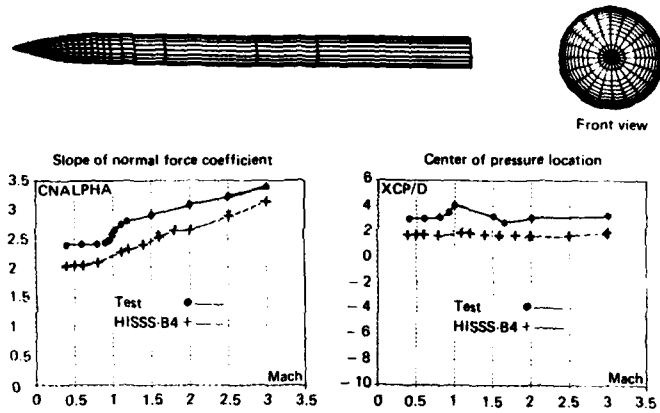


Figure 1 - Comparison of variation of longitudinal characteristics with Mach number for the isolated body configuration.

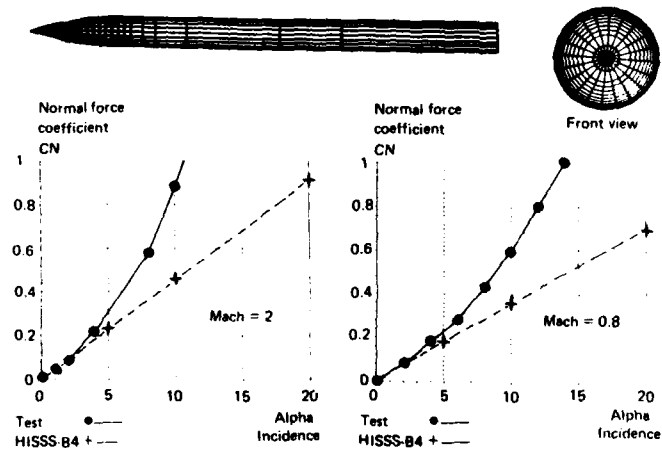


Figure 2 - Comparison of variation of lift characteristics with angle of attack at Mach 0.80 and 2.0 for the isolated body.

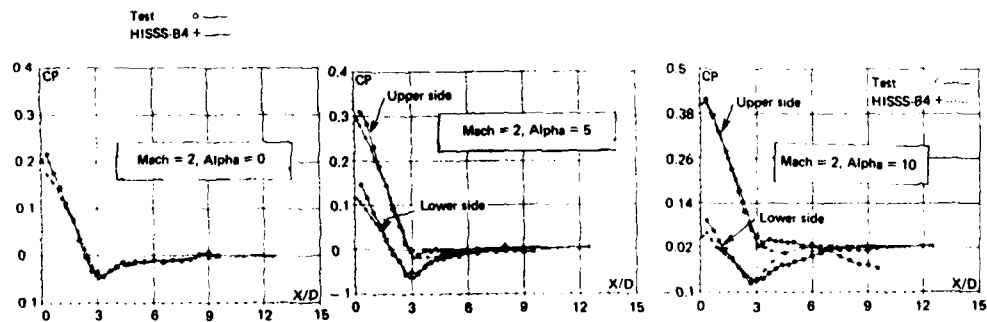


Figure 3 - Comparison of variation of longitudinal pressures with angle of attack at Mach 2.00 for the isolated body.

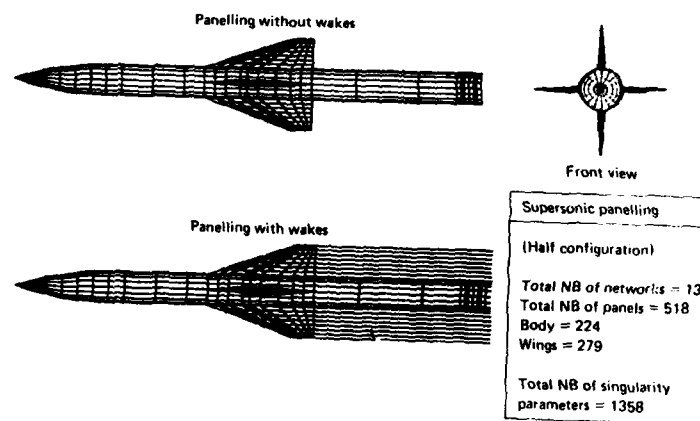


Figure 4 - Panelling scheme of the body with cruciform wings.

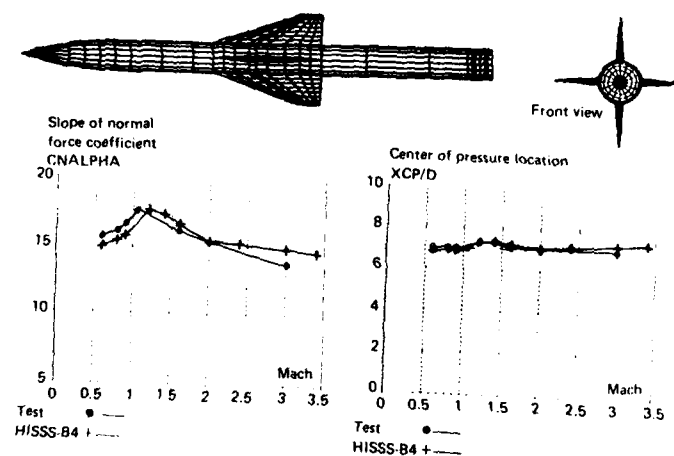


Figure 5 - Comparison of variation of longitudinal characteristics with Mach number for the body with cruciform wings configuration.

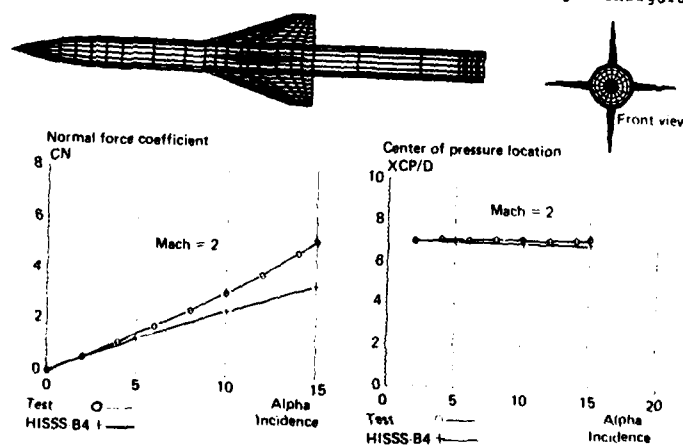


Figure 6 - Comparison of variation of longitudinal characteristics with angle of attack at Mach 2.0 for the body-wing configuration.

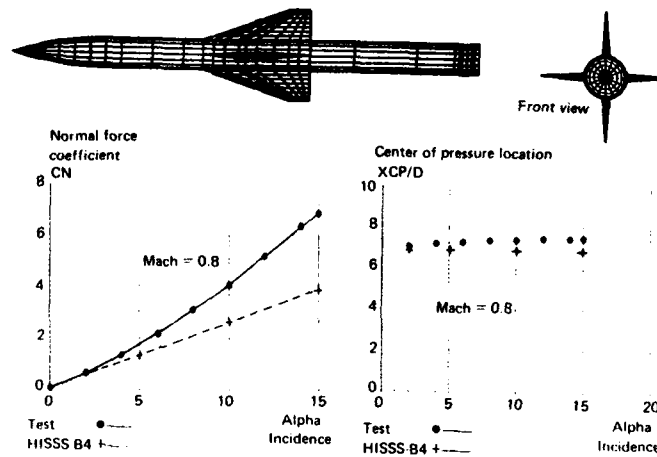


Figure 7 - Comparison of variation of longitudinal characteristics with angle of attack at Mach 0.80 for the body-wing configuration.

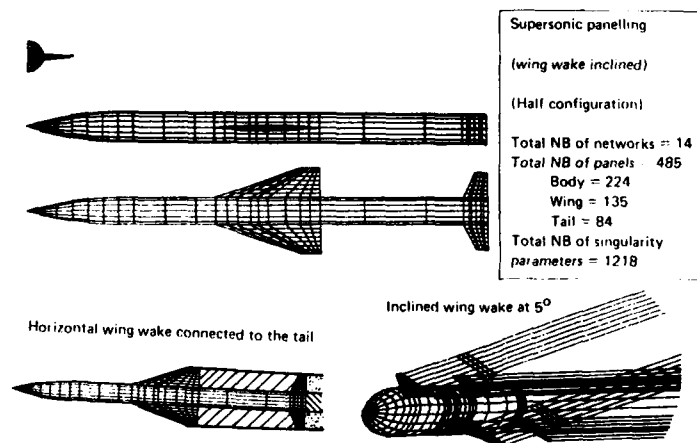


Figure 8 - Panelling scheme of the body with coplanar cruciform wings and fins configuration.

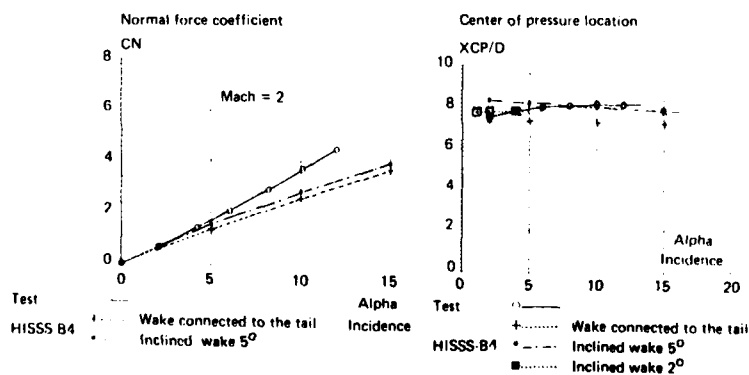


Figure 9 - Comparison of variation of longitudinal characteristics with angle of attack at Mach 2.0 for the body-wing-fin configuration (coplanar arrangement).

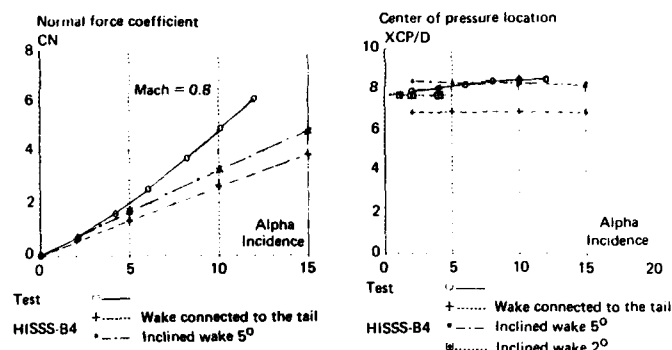


Figure 10 - Comparison of variation of longitudinal characteristics with angle of attack at Mach 0.80 for the body-wing-fin configuration (coplanar arrangement).

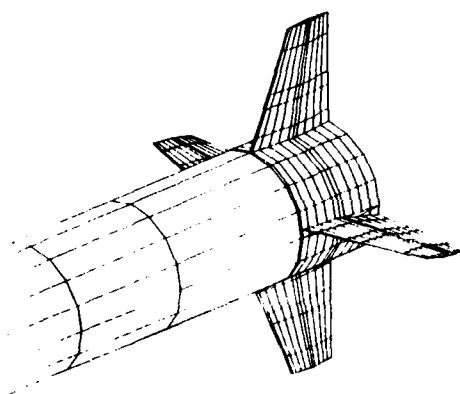


Figure 11 - Panelling scheme of the control surface deflected $\delta=10$ deg.s upward (detail).

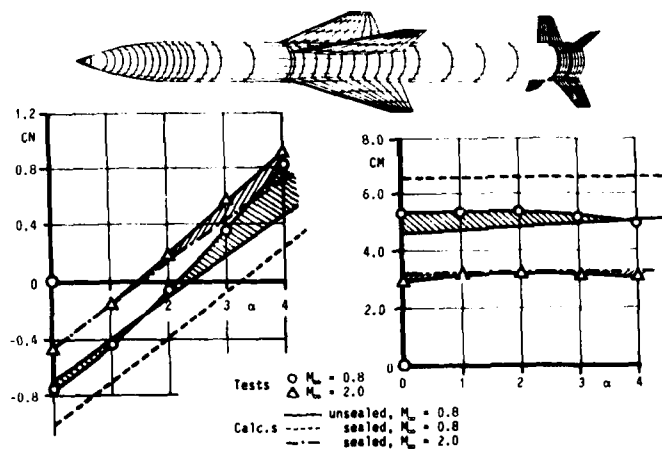


Figure 12 - Comparison of variation of pitch control characteristics with angle of attack at Mach 0.80 and 2.0.

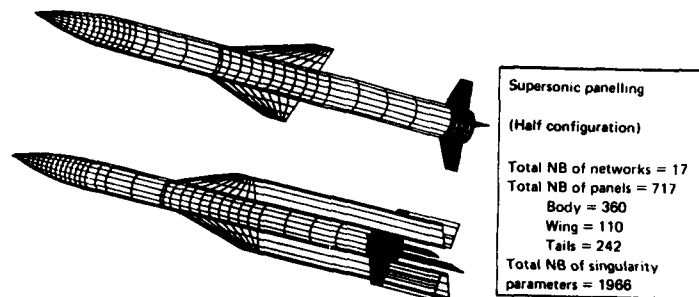


Figure 13 - Panelling scheme of the body with non-coplanar wings and fins configuration.

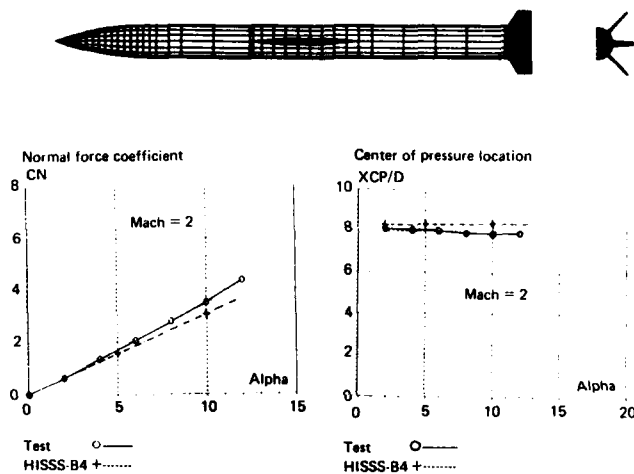


Figure 14 - Comparison of variation of longitudinal characteristics with angle of attack at Mach 2.0 for the body-fin-wing configuration (non-coplanar arrangement).

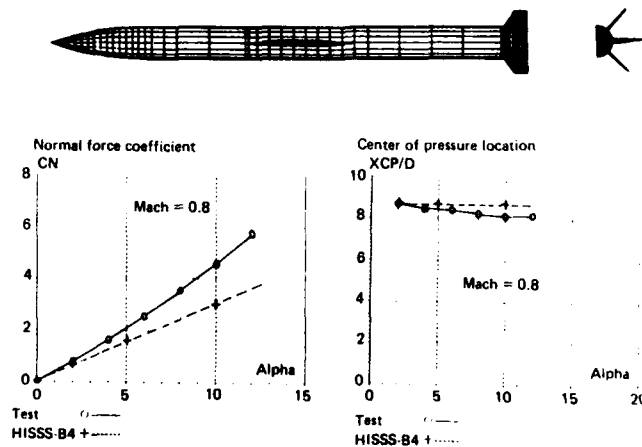


Figure 15 - Comparison of variation of longitudinal characteristics with angle of attack at Mach 0.80 for the body-fin-wing configuration (non coplanar arrangement).

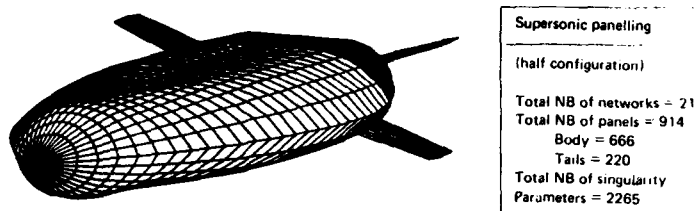


Figure 16 - Panelling scheme of the non circular body with rear winglets.

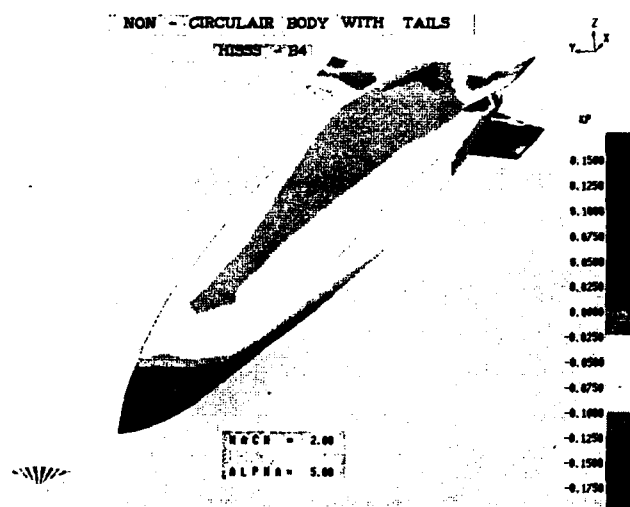


Figure 17 - Pattern of computed surface pressures at Mach 2.0, $\alpha = 5.0$ deg.s for the non-circular body with rear winglets.

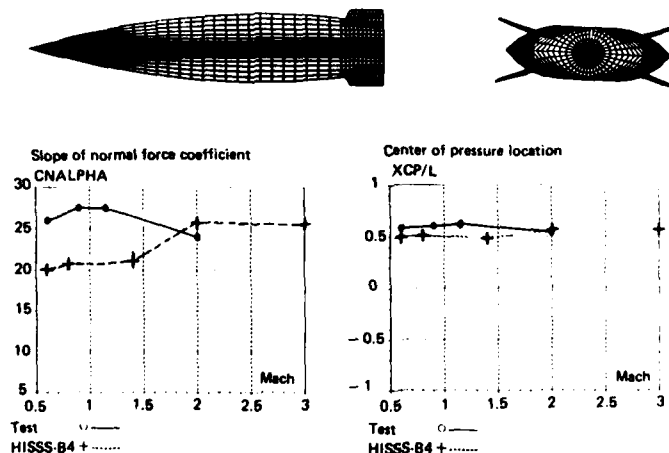


Figure 18 - Comparison of variation of longitudinal characteristics with Mach number for the non-circular body with rear winglets.

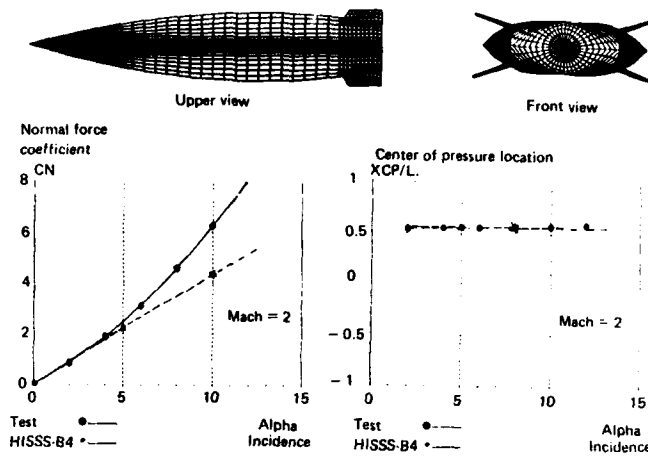


Figure 19 - Comparison of variation of longitudinal characteristics with angle of attack at Mach 2.0 for the non-circular body with rear winglets.

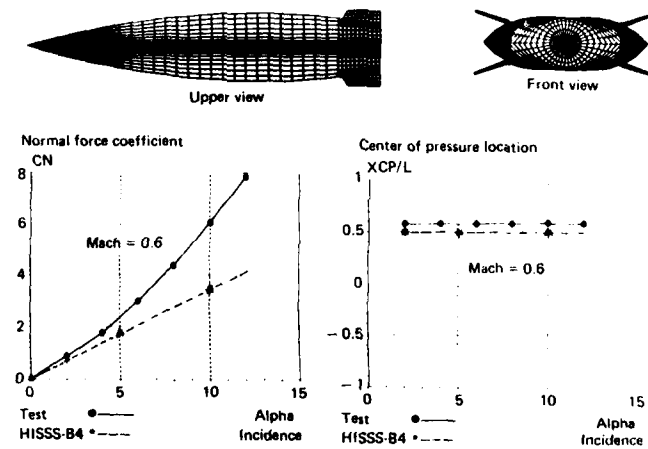


Figure 20 - Comparison of variation of longitudinal characteristics with angle of attack at Mach 0.60 for the non-circular body with rear winglets.

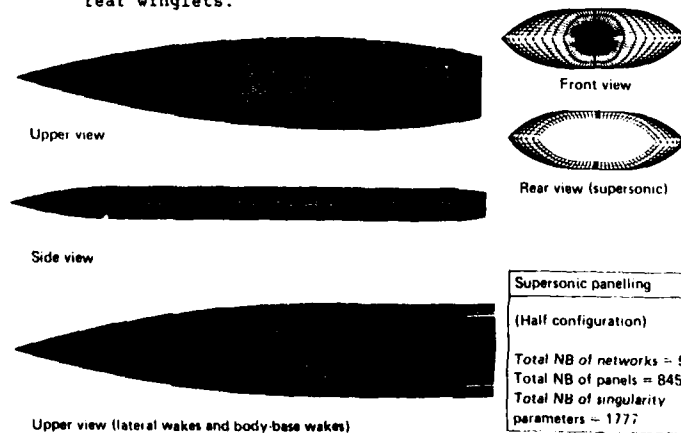


Figure 21 - Panelling scheme of the non-circular body configuration.

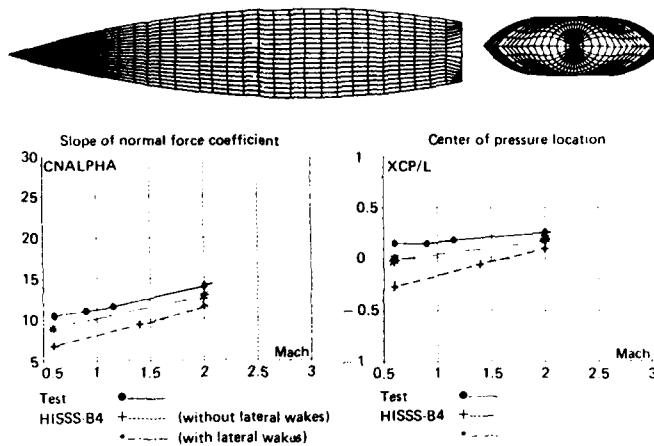


Figure 22 - Comparison of variation of longitudinal characteristics with Mach number for the non-circular configuration.

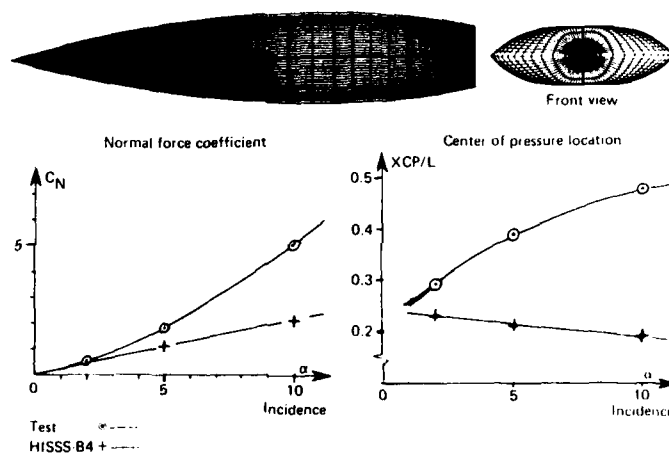


Figure 23 - Comparison of variation of longitudinal characteristics with angle of attack at Mach 2.0 for the non-circular body.

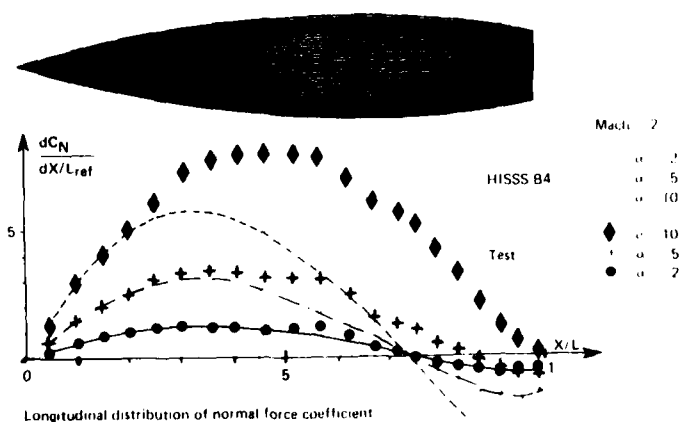


Figure 24 - Comparison of variation of longitudinal distribution of local normal load with angle of attack at Mach 2.0 for the non-circular body.

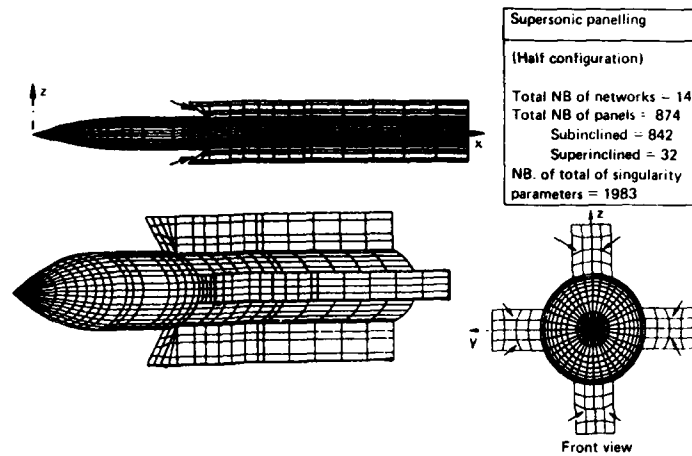


Figure 25 - Panelling scheme of the air-breathing body configuration with rectangular intakes.

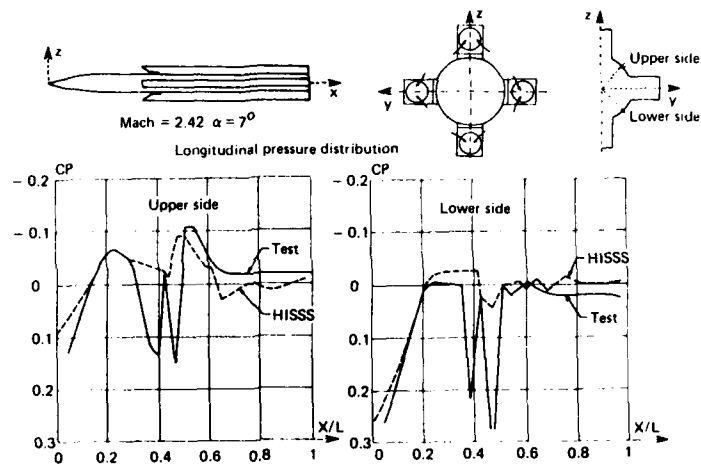


Figure 26 - Comparison of longitudinal pressures at Mach 2.42, $\alpha = 7^\circ$. deg.s for the air-breathing isolated body.

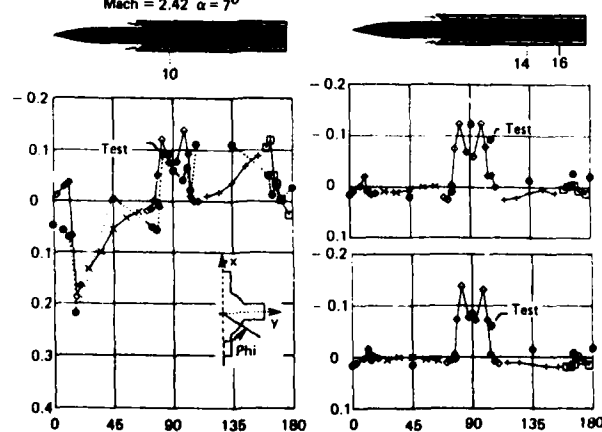


Figure 27 - Comparison of circumferential pressures at Mach 2.42, $\alpha = 7^\circ$. deg.s for the air-breathing isolated body.

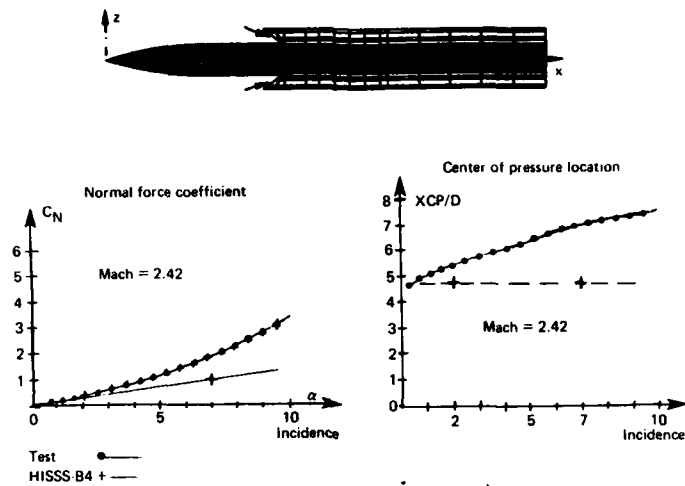


Figure 28 - Comparison of variation of longitudinal characteristics with angle of attack at Mach 2.42 for the air-breathing body.

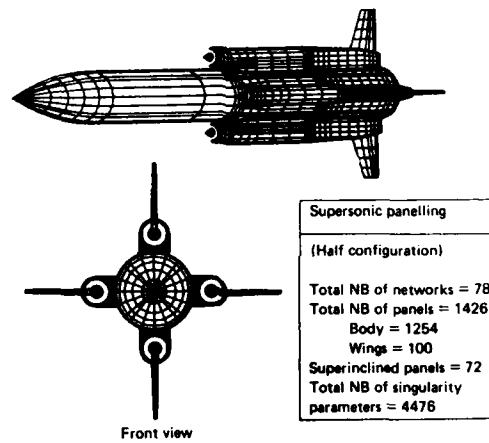


Figure 29 - Panelling scheme of the air-breathing missile configuration.

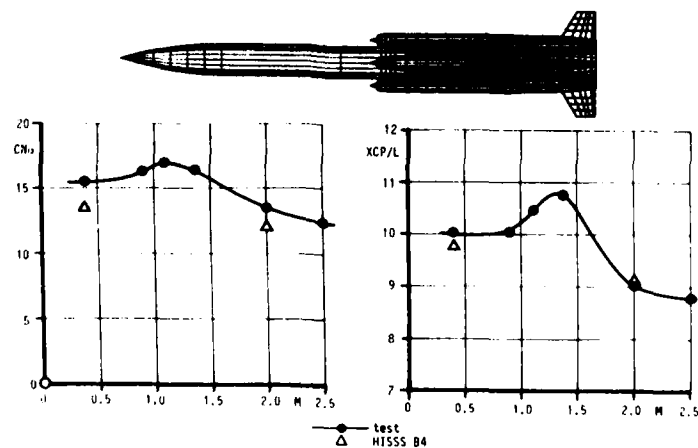


Figure 30 - Comparison of variation of longitudinal characteristics with Mach number for the air-breathing missile configuration.

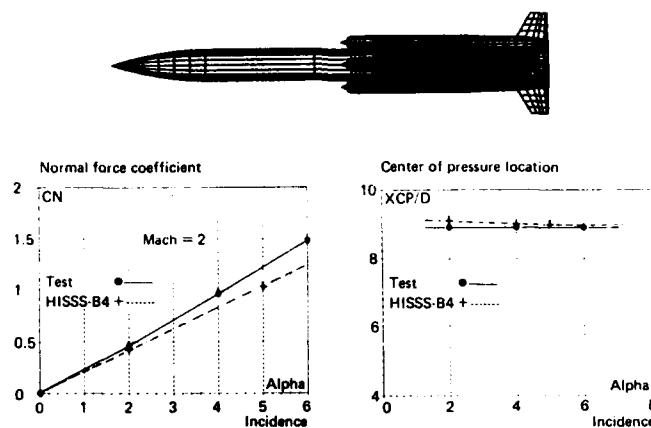


Figure 31 - Comparison of variation of longitudinal characteristics with angle of attack at Mach 2.0 for the air-breathing missile.

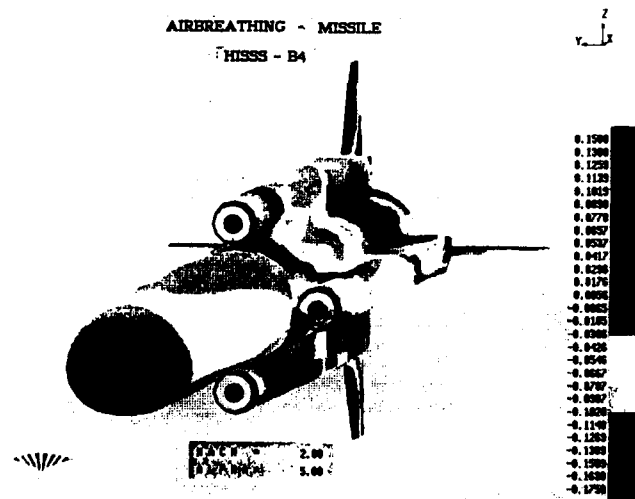


Figure 32 - Isobar pattern of surface pressures computed for the air-breathing missile at Mach 2.0, $\alpha = 5.0$ degs.

MISSILE DATCOM: ENHANCEMENTS FOR DESIGN APPLICATIONS

by

Jerry E. Jenkins and William B. Blake
 U.S. Air Force Wright Aeronautical Laboratories (FIGC)
 Wright-Patterson Air Force Base, Ohio 45433
 U.S.A.

SUMMARY

Missile Datcom, a stability and control prediction code tailored to conceptual and preliminary design applications, has been developed. The program uses a component build-up approach based on the equivalent angle-of-attack concept. Simple vortex models are employed to allow for rapid and economical analyses. Two novel enhancements for design application that have been incorporated into the code are:

a) Experimental data substitution. Accuracy improvements are attained by permitting the user to substitute experimental data for Missile Datcom predictions during the component build-up process. Its use is appropriate when more accurate data are available for vehicle components or for partial configurations.

b) Configuration incrementing. This allows a user to more accurately investigate the effects of geometry changes on an existing configuration. In this case, experimental data for the complete baseline configuration are used to "correct" Missile Datcom predictions for the modified vehicle.

Problem areas, in many cases related to vortex modeling, can degrade accuracy for some types of configurations. These are examined in the light of selected theory-to-test correlations. Finally, current efforts to improve existing methods and to develop new methods are briefly reviewed.

LIST OF SYMBOLS

C_l Rolling moment coefficient, Rolling moment/ $q_\infty S_d$
 C_m Pitching moment coefficient, Pitching moment/ $q_\infty S_d$
 C_N Normal force coefficient, Normal force/ $q_\infty S$
 (aeroballistic axis system)
 $C_{N'}$ Normal force coefficient, Normal force/ $q_\infty S$
 (fin axis system)
 C_n Yawing moment coefficient, Yawing moment/ $q_\infty S_d$
 d Reference length
 K_B Fin-body carryover factor
 K_F Body-fin carryover factor
 k_F Body-fin incidence factor
 K_p Potential contribution calibration factor
 K_v Viscous contribution calibration factor
 K_ϕ Roll angle correction factor
 q_∞ Free stream dynamic pressure
 S Reference area

Subscripts

B Body contribution
 F Fin contribution
 FB Fin in presence of body contribution
 exp Experimental value
 th Theoretical value
 p Potential increment
 v Viscous increment

Greek

α_b Body axis angle-of-attack
 α Total angle-of-attack
 β_b Body axis sideslip angle
 λ Adjacent fin interference factor
 ϵ Total aerodynamic roll angle

1. INTRODUCTION

Since 1960, when the development of a comprehensive missile prediction code (Missile Datcom) was seriously contemplated at the Air Force Flight Dynamics Laboratory, a virtually continual stream of papers detailing its development progress and interim capabilities has been published in the open literature. Aerodynamic methods selected for implementation in Missile Datcom are summarized in [1], which also includes a discussion of their limitations and of proposed method extensions. More detail on various aspects of method selection and development can be found in [2-6]. As will be evident from an examination of these references, the McDonnell Douglas Corporation (notably S.R. Vukelich) was responsible for the development of Missile Datcom under contract with the Flight Dynamics Laboratory.

The current paper will very briefly summarize the earlier work. Its major emphasis will be on aspects not previously covered in detail such as: (a) the synthesis procedure for total configuration aerodynamics (given component data), (b) provisions for using experimental data to get improved predictions, (c) lateral-directional results, including control-surface interference effects, and (d) activities currently underway to alleviate known deficiencies.

2. DEVELOPMENT OVERVIEW

From the beginning, the intent was to provide a prediction capability that would address relevant configuration and flight condition parameters. Equally important, Missile Datcom was also to be compatible with conceptual and preliminary design accuracy requirements, design-cycle time constraints, and experience levels of typical analysts. Critiques, such as Williams [7], of commonly used codes were used extensively to establish an efficient approach to this problem. The development philosophy and method selection criteria, summarized by Vukelich and Jenkins [8], are reviewed below.

Useful preliminary design codes must successfully combine the features of rapid turnaround, applicability over a wide range of design parameters, and good accuracy. Previous codes were primarily (1) empirical codes that gave highly accurate results over the rather limited parameter space encompassed by their defining data base or (2) "research-oriented" codes with input requirements and output that were excessive for design applications. Neither adequately addressed the designer's needs. However, the aggregate of these codes contained a nucleus of well-documented and accepted methods. Thus, a code based on the "component build-up" approach, relying heavily on existing methodology, could be developed. Component build-up codes offer all of the features needed in the preliminary design environment (Figure 1), although at the expense of the rather complex program logic required to blend numerous component and synthesis methods into a cohesive whole.

Over 300 candidate methods were screened during the Missile Datcom Feasibility Study [9]. Methods applicable to tactical missiles received primary emphasis, with secondary emphasis given to projectiles and ordnance. Factors considered in the screening process included the theoretical basis for the method, range of validity, complexity, compatibility with other methods, and accuracy. An important aspect of the accuracy assessments was the use of criteria developed by Krieger and Williams [10]. These criteria express the allowable error for a given aerodynamic parameter (e.g., axial force) as a function of the tolerances placed on vehicle performance requirements (e.g., range). Thus methods giving acceptable accuracy for early trade-off studies could be selected without unduly compromising speed. The criteria used for static longitudinal characteristics are given below.

Coefficient	Error Allowed	Design Parameter (error)
C_N	$\pm 20\%$	Range ($\pm 10\%$) Load Factor ($\pm 20\%$)
C_m	$\pm 20\%$ or $\pm 2\% L$	Fin Area ($\pm 20\%$) Center of Gravity ($\pm 2\%L$)
C_A	$\pm 10\%$ or $\pm .2 C_p /$ ($C_A \cos \alpha$)	Range ($\pm 10\%$) Turn Deceleration ($\pm 20\%$)

Candidate methods, identified in the feasibility study, were examined in detail during the actual development program. The selection process is depicted in Figure 2. A large data base was assembled for this purpose, allowing approximately 800 body-alone, 78 fin-alone, and 278 complete missile configuration "comparisons" to be carried out using the selected methodology. (An angle-of-attack sweep generates one "comparison" for each non-trivial aerodynamic coefficient.) Final method selections for axisymmetric missiles are shown in Figures 3, 4, and 5. Longitudinal predictive error for the "conventional" missile category is shown in Figure 6.

The computer code was developed using a top-down structured format, for ease of maintenance. In many cases, it was possible to obtain the methods shown in Figures 3-5 from existing codes, thus eliminating expensive debugging. Several codes were drawn on heavily, including the Naval Surface Weapons Center Aeroprediction Code (NSWCAP) [11], the Missile series of codes developed by Nielsen Engineering and Research (NEAR) [12-13], and the USAF Digital Datcom [14]. Each of these codes offers additional unique capabilities, which the reader is encouraged to investigate. All of these codes are maintained and upgraded on a continuing basis.

3. SYNTHESIS OF CONFIGURATION AERODYNAMICS

Automated techniques for improving prediction accuracy, given relevant experimental data, are discussed in Section 4. However, a cursory knowledge of the Missile Datcom aerodynamic synthesis procedure is essential to an understanding of the experimental data options. A brief review of the "equivalent angle-of-attack" concept and the vortex models used in Missile Datcom will be presented.

All "internal" calculations of Missile Datcom are performed in the total angle of attack - aerodynamic roll coordinate system. This system is commonly known as the "aeroballistic axis system" (Figure 7). Body-axis angle of attack and sideslip angle are transformed to total angle of attack and roll angle through the following relations:

$$\alpha = \tan^{-1}[(\tan \alpha_b)^2 + (\tan \beta_b)^2]^{1/2} \quad (1)$$

$$\phi = \tan^{-1}[\tan \theta_b / \tan \alpha_b] \quad (2)$$

This axis system is also used in the following discussion.

Equivalent Angle-of-Attack Concept

The basis for the synthesis procedure is the "equivalent angle-of-attack" method described by Hemsch, Nielsen, et al [15]. It is a non-linear extension of the method developed by Pitts, Nielsen, and Kaattari [16]. The equivalent angle of attack is defined as that angle of attack for the isolated fin (no interference effects) which results in a force (normal to the fin) identical to the one actually generated in the missile flow field. Fin axial force and moment are also assumed to correlate directly with the equivalent angle of attack as defined above. Each individual panel has its own associated equivalent angle of attack. The first step in the procedure is to determine the equivalent angle of attack for an undeflected fin,

$$\tan \alpha_{eq_{\delta=0}} = K_F \tan \alpha \sin \phi - FK_F \tan \alpha \sin \phi \cos \phi + \tan \alpha_{vortices} \quad (3)$$

The first two terms on the right-hand side of equation (3) represent the effects of body upwash and bank angle, respectively. The last term represents the effects of external vortices, i.e. those shed from the forebody and upstream fins. This equation is depicted schematically in Figure 8.

Next, the effects of deflection and interference from adjacent panels in the same set are added, yielding the overall equivalent angle of attack,

$$\tan \alpha_{eq_{\delta}} = \tan \alpha_{eq_{\delta=0}} + K_F [\tan(\alpha_{eq_{\delta=0}} + \delta) - \tan \alpha_{eq_{\delta=0}}] + \sum_{j=2}^n (A_j \delta_j) \quad (4)$$

so that

$$\alpha_{eq_{\delta}} = \tan^{-1}(\tan \alpha_{eq_{\delta}}) \quad (5)$$

With the exception of the vortex terms (to be discussed below), the equivalent angle of attack is a function only of configuration geometry.

Computed values for each panel's alpha-equivalent are then used to interpolate predicted fin-alone normal-force and axial-force characteristics. These calculations are carried out in a local coordinate system attached to the fin in question. Thus, the "local" panel forces must be resolved into the missile-axis system,

$$C_{N_F} = C_{N'_F} \cos \delta \sin \phi \quad (6)$$

where

$$C_{N'_F} = C_{N'_F}(\alpha_{eq})$$

This result represents, in the missile-axis system, the total force on a single fin in the presence of the body. To obtain the total configuration normal force, fin-onto-body carryover and isolated-body results are added to the sum of the individual fin contributions,

$$C_N = C_{N_B} + \sum_{sets} C_{N_{FB}} \quad (7)$$

where

$$C_{N_{FB}} = (1 + K_B/K_F) \sum_{fins} C_{N_F}$$

For missiles with multiple fin sets (up to four sets are permitted), calculations must proceed from front to back since the strength of the vortex shed by each fin must reflect the alpha-equivalent contribution of all upstream external vortices. Moment coefficients are computed directly from the forces and computed center-of-pressure locations, e.g.

$$C_m = C_{m_B} - \sum_{sets} C_{N_{FB}} (x_{cp}) \quad (8)$$

where x_{cp} is measured from the moment reference point.

A flow chart of the aerodynamic synthesis procedure is shown in Figure 9. Although not shown explicitly, "fin in the presence of body" computations include alpha-equivalent increments due to forebody vortices.

Clearly, the equivalent angle-of-attack concept requires accurate predictions for the isolated fin normal-force characteristics. Missile Datcom uses the methods of the USAF Datcom [17] and the R.A.S. Data Sheets [18] to compute panel-alone normal force. These methods are semi-empirical in nature, and are valid up to 90 degrees angle of attack. Stoy and Vukelich [6] made extensive fin-alone comparisons for a wide variety of fin planform and Mach numbers, and found excellent agreement in all cases. A typical result from their study is presented in Figure 10.

Vortex Modeling

Missile Datcom uses a very simple model for both body and fin vortices and their effects on downstream fins (Figure 11). More sophisticated models are available, but they are computationally intensive, resulting in increased cost and turnaround time. An improved body vortex model is currently

being implemented into Missile Datcom as an option (see Section 6), to allow for improved predictions when cost and speed are not driving factors compared to accuracy requirements.

Body vortices are modeled as a pair of concentrated vortex filaments. Their "separation point", downstream trajectory, and strengths are determined using empirical charts developed by Hemsch et al [19]. The method is based on tests of various nose shapes mounted on a cylindrical afterbody, at both subsonic and supersonic conditions.

Fin vortices are also modeled as single vortex filaments; i.e., the roll-up process is not modeled. These are shed from the centroid of the fin-load distribution, as determined from charts based on vortex lattice theory. Fin vortices are assumed to track downstream along the free-stream velocity vector. Stoy and Vukelich [6] studied the effects of alternate linear tracking schemes (using single vortex filaments) on both longitudinal and lateral-directional prediction accuracy for conventional configurations. Longitudinal characteristics were quite insensitive to the tracking angle relative to the free-stream. Lateral effects were insensitive to tracking angle at low alpha, but significant deviations were observed above 10 to 15 degrees alpha. Perhaps the most serious limitation of this simple model is that mutual interactions between body and fin vortices as they move downstream are not treated.

Missile Datcom computes the load on downstream fins by estimating the equivalent angle-of-attack increment due to the vortices. A series of charts, due to Pitts et al [16], is used to compute a vortex-interference factor as a function of vortex strength and position in the fin cross-flow plane. The interference factors are then transformed into equivalent angle-of-attack increments. This process is repeated for each vortex affecting a given fin (see again Figure 9). These are summed, as indicated in equation (3), to give the overall fin alpha-equivalent due to vortices.

With this simple model, vortices can track to positions that intersect downstream fins, leading to anomalous predictions [20]. Therefore, Missile Datcom enforces a minimum separation between vortex filaments and fins, based on the work of Spreiter and Sacks [21]. In the crossflow plane, it is also possible for a vortex from a windward fin to track to a position inside or above the body at high angles of attack. If either of these occurs, Missile Datcom sets the vortex strength to zero. This violates the Helmholtz law of vorticity, but is physically realistic in that the vortex is absorbed by the boundary layer along the body. (The Helmholtz law is predicated on inviscid flow.)

4. ENHANCEMENTS FOR DESIGN APPLICATIONS

As indicated above, Missile Datcom method selection was biased toward conceptual design by applying accuracy criteria tailored to these applications. However, provisions have also been made to address the needs of later analyses. The basic idea is to improve final prediction accuracy with previously obtained experimental data. Two quite different means for accomplishing this are provided (credit for the development of both options belongs to S.R. Vukelich of the McDonnell Douglas Corporation). The first is called "experimental data substitution" and the second is termed "configuration incrementing". Each is discussed separately below.

Experimental Data Substitution

With this input option, experimental data for any configuration component, or "partial" configuration (working from the nose to the aft end), may be input as shown below.

Components for which Data can be Substituted:

Body Alone	Body + Fin Set 1
Fin Set 1 (single isolated panel)	Body + Fin Sets 1-2
Fin Set 2 (single isolated panel)	Body + Fin Sets 1-2-3
Fin Set 3 (single isolated panel)	Body + Fin Sets 1-2-3-4
Fin Set 4 (single isolated panel)	

Data may be substituted for any of the six components of force and moment. Angles of attack, center-of-gravity location, or reference quantities corresponding to the existing data may differ from those desired in the final results. Missile Datcom automatically interpolates the data and compensates for any center-of-gravity shift or reference area change. A center-of-gravity position transfer will be done only if data are supplied for both a moment and the corresponding force; i.e. if either pitching moment and normal force or yawing moment and side force are provided.

The process is illustrated in Figure 12. When the experimental data substitution option is used, the "increment flag" will be turned off. Analysis begins with $K = 1$, the most forward set of fins, and proceeds aft until all sets have been considered ($K = NSETS$). Aerodynamic characteristics for the K 'th stage of the configuration build-up are computed before checking for the presence of experimental data corresponding to that configuration. If data are input, the calculated values are replaced by the experimental ones. These experimental values will then be used in lieu of computed results and will impact results higher in the synthesis hierarchy (subsequent values of K). Configuration synthesis proceeds exactly as shown in Figure 9, with the exception that some of the values used in equations (6), (7), and (8) are experimental rather than predicted.

The effects of body-alone, body-fin, or isolated-fin data substitution are shown below for a missile with two fin sets. Body or body-fin data input affects only those coefficients for which test data were supplied; e.g., normal force input will impact output normal force, and no other coefficient in the output. The exception to this rule is that static coefficient input does have an effect on dynamic derivative output. Substitution of fin-alone data has a quite different result. Only two aerodynamic parameters (normal and axial force) will have any effect on subsequent computations. Especially noteworthy is that all output parameters will be affected by the inclusion of normal-force data. The changes in downstream fin characteristics arise from equivalent angle-of-attack changes due to differences in the vortex strength

of the upstream fin (which is proportional to panel normal force). Unfortunately, isolated fin data are not commonly available.

Unfortunately, isolated fin data are

Affects		Experimental Data Input For					Body-Fin 1				
		C _N	C _m	C _A	C _Y	C _l	C _N	C _m	C _A	C _Y	C _l
Body	C _N	X	-	-	-	-	-	-	-	-	-
	C _m	-	X	-	-	-	-	-	-	-	-
	C _A	-	-	X	-	-	-	-	-	-	-
	C _Y	-	-	-	X	-	-	-	-	-	-
	C _l	-	-	-	-	X	-	-	-	-	-
	C _l	-	-	-	-	-	X	-	-	-	-
** C _{N₀}	C _{N₀}	X	-	-	-	-	-	-	-	-	-
	C _{m₀}	-	X	-	-	-	-	-	-	-	-
Body-Fin 1	C _N	X	-	-	-	-	X	-	-	-	-
	C _m	-	X	-	-	-	-	X	-	-	-
	C _A	-	-	X	-	-	-	-	X	-	-
	C _Y	-	-	-	X	-	-	-	-	X	-
	C _l	-	-	-	-	X	-	-	-	-	X
	C _l	-	-	-	-	-	X	-	-	-	-
** C _{N₀}	C _{N₀}	X	-	-	-	-	X	-	-	-	-
	C _{m₀}	-	X	-	-	-	-	X	-	-	-
Body-Fin 1-Fin 2	C _N	X	-	-	-	-	X	-	-	-	-
	C _m	-	X	-	-	-	-	X	-	-	-
	C _A	-	-	X	-	-	-	-	X	-	-
	C _Y	-	-	-	X	-	-	-	-	X	-
	C _l	-	-	-	-	X	-	-	-	-	X
	C _l	-	-	-	-	-	X	-	-	-	-
** C _{N₀}	C _{N₀}	X	-	-	-	-	X	-	-	-	-
	C _{m₀}	-	X	-	-	-	-	X	-	-	-

- = No effect
X = Always affected
** = q and α derivatives each given

Affects		Data Input For		Fin 1		Fin 2	
		C _N	C _A	C _N	C _A	C _N	C _A
Fin 1	C _N	X	-	-	-	-	-
	C _m	X	-	-	-	-	-
	C _A	* X	-	-	-	-	-
	C _Y	✓	-	-	-	-	-
	C _l	✓	-	-	-	-	-
	C _l	✓	-	-	-	-	-
** C _{N₀}	C _{N₀}	X	-	-	-	-	-
	C _{m₀}	X	-	-	-	-	-
Body-Fin 1	C _N	X	-	-	-	-	-
	C _m	X	-	-	-	-	-
	C _A	* X	-	-	-	-	-
	C _Y	✓	-	-	-	-	-
	C _l	✓	-	-	-	-	-
	C _l	✓	-	-	-	-	-
** C _{N₀}	C _{N₀}	X	-	-	-	-	-
	C _{m₀}	X	-	-	-	-	-
Body-Fin 1-Fin 2	C _N	X	-	X	-	X	-
	C _m	X	-	X	-	X	-
	C _A	* X	-	* X	-	* X	-
	C _Y	✓	-	✓	-	✓	-
	C _l	✓	-	✓	-	✓	-
	C _l	✓	-	✓	-	✓	-
** C _{N₀}	C _{N₀}	X	-	X	-	X	-
	C _{m₀}	X	-	X	-	X	-

* = Only affected for $M < 1.4$
✓ = β derivatives affected

The experimental data substitution option can be used to improve the accuracy of parametric analyses commonly encountered in design. For example, tail-fin aspect ratio parametrics can be studied based on preliminary wind-tunnel results (provided that fin-off characteristics are known). This option can also be used to synthesize results from other, more accurate, prediction techniques that have been applied to selected components.

For a sample application of the technique, consider data presented by Graves [22] on a circular missile with two fin sets (Figure 13). Body-alone, wing-body, tail-body, and wing-body-tail data were obtained for this configuration. Missile Datcom predictions for the complete configuration at Mach 2.96 are given in Figures 14 and 15. Both predictions are within the preliminary-design accuracy criterion given in Section 2 (the error in pitching moment at high-alpha corresponds to a c.p. error of 1.5% body length). However, accuracy requirements get more stringent later in the design cycle and the high-alpha trends have not been captured. As shown in Figures 16 and 17, the reason for the discrepancy is that both wing-body normal force and pitching moment are overpredicted at angles of attack greater than ten degrees. Substitution of experimental normal-force and pitching-moment data for the wing-body combination results in a significant improvement in both predictions (Figures 14 and 15). Improvements of this order can be expected if there are no significant errors in the vortex-interference calculations.

Configuration Incrementing

In the design environment, the direct substitution procedure described above has limited applicability. It depends on having data, or better estimates, for components or partial configurations identical to those of the configuration being analyzed. Furthermore, vortex-interference computations will be affected only if panel-alone data are provided. A far more common design tactic is to modify or "correct" experimental data on a configuration similar (but not identical) to the configuration of interest.

Configuration incrementing automates this procedure. Two operations are performed: (1) a geometric description of a configuration and experimental data corresponding to this configuration are used to "calibrate" the prediction methods, and (2) Missile Datcom derived predictions for the configuration of interest are then adjusted (based on the calibration increments and factors calculated in step one). Only those aerodynamic coefficients for which data are supplied (for Configuration 1) will be affected in the final result (Configuration 2 output). The remainder will be Missile Datcom "theoretical" results, or possibly a combination of the two for derived quantities such as configuration center-of-pressure location. For example, if only pitching-moment data were input, Configuration 2 pitching-moment results would be

incremented, but normal force would be a theoretical result and center of pressure would be the quotient of the two.

As in most design activities, the application of such a procedure is likely to be more art than science. Missile Datcom represents the first attempt at integrating this capability within a prediction code. Therefore, a critical look at the implementation is in order.

The computational sequence is shown in Figure 12. In contrast to the experimental-data substitution option, experimental data is read only for the complete configuration ($K = \text{NSETS}$). To ensure valid results, "Case 2" geometry should contain exactly the same number of fin sets as "Case 1" and other differences between the two configurations should be relatively small.

A brief summary of the procedure, using pitching moment computations as the example, will be presented (normal force is incremented in the same manner). In this discussion, the subscript "exp" indicates the experimental data input for the original configuration, while the subscript "th" denotes theoretical (Missile Datcom) predictions. The subscript "1" indicates the original configuration, for which calibration factors are determined, and the subscript "2" indicates values for the desired configuration.

First, the zero-alpha shift between predicted and test values for Configuration 1 is determined,

$$\Delta C_{m_o} = C_{m_{exp,1}} - C_{m_{th,1}} \quad (9)$$

The pitching-moment coefficient is then divided into potential (linear) and viscous (nonlinear) components, using the technique Allen and Perkins [23] developed for the analysis of body forces and moments,

$$C_{m_{tot}} = C_{m_p} + C_{m_v} \quad (10)$$

where

$$C_{m_{pth,1}} = 0.5(C_{m_\alpha})_{th,1}[\sin(2\alpha)\cos(\alpha/2)] \quad (11)$$

and

$$C_{m_{vth,1}} = C_{m_{totth,1}} - C_{m_{pth,1}} \quad (12)$$

Next, calibration factors are determined for the potential and viscous terms,

$$K_p = [(C_{m_\alpha})_{exp,1}] / [(C_{m_\alpha})_{th,1}] \quad (13)$$

and

$$K_v = [(C_{m_{exp,1}} - \Delta C_{m_o}) - K_p(C_{m_p})_{th,1}] / [(C_{m_v})_{th,1}] \quad (14)$$

The moment-curve slopes in equations (11) and (13) are the "linear" values, taken at zero angle of attack. Hence, K_p is a constant, while K_v is a function of angle of attack. Note that the technique may be sensitive to the experimental value of the zero-alpha slope; therefore high-quality data is essential (transferred to a moment center well removed from the configuration c.p. for pitching moment). Similarly, the predicted pitching moment for Configuration 2 is broken into potential and viscous increments,

$$C_{m_{pth,2}} = 0.5(C_{m_\alpha})_{th,2}[\sin(2\alpha)\cos(\alpha/2)] \quad (15)$$

$$C_{m_{vth,2}} = C_{m_{totth,2}} - C_{m_{pth,2}} \quad (16)$$

Now the calibration factors, from equations (13) and (14), are applied to these increments, and the zero-alpha moment shift is added, to give the final, incremented result,

$$C_{m_{tot,2}} = K_p(C_{m_p})_{th,2} + K_v(C_{m_v})_{th,2} + \Delta C_{m_o} \quad (17)$$

In the incrementing process described above, the "potential" and "viscous" contributions are computed directly from total-configuration characteristics. However, Missile Datcom predictions for the total configuration are based on the synthesis of fin-alone and body-alone characteristics, each of which consists of potential and viscous components. Hence, equation (8) can be re-written as

$$C_m = (C_{m_B} + C_{m_v}) + \sum_{sets} [(1+K_B/K_F) \sum_{fins} (C_{m_Fp} + C_{m_Fv})] \quad (18)$$

or

$$C_m = \left[C_{m_B} + \sum_{sets} [(1+K_B/K_F) \sum_{fins} C_{m_Fp}] \right]_p + \left[C_{m_B} + \sum_{sets} [(1+K_B/K_F) \sum_{fins} C_{m_Fv}] \right]_v \quad (19)$$

We can now see the motivation for calculating separate correction factors for the potential and viscous terms. The form of this equation is identical to that of equation (10).

Note that the total-configuration potential term, as given by equation (11), will not precisely match the first term of equation (19). This is because the fin-plus-interference contribution will not, in general, exhibit the assumed body-like variation. However, in the limit as configuration differences approach zero, incrementing will produce the correct result; i.e., the right-hand side of equation (17) reduces to Configuration 1 experimental values if both configurations are identical.

Incrementing implicitly assumes that predictive errors for the "configuration of interest" are consistent with those of the "calibrating configuration". Thus, quite misleading results could be obtained if configuration differences grossly alter the relative magnitudes of the body, fin-alone, and interference contributions.

A typical use of the procedure might be to assess the effect of an increase in tail fin area, given data for the complete baseline configuration. An air-slewed missile is presented as an example of this application. The missile (Figure 18) was tested with two differing tail-fin planforms [24]. Data used for this example, both for incrementing and for interpreting the results, were read from the plots of pitching moment and normal force presented in reference [20]. Because of the small size of these figures there may be as much as $\pm .5\%$ body length error in the experimental c.p. locations shown in Figures 12 and 13.

The conduit/strakes were modeled (in the Missile Datcom input) as very low-aspect ratio fins to ensure that the vortex-interference due to these protuberances was taken into account. Both the Missile Datcom prediction and the experimental data for the small-fin (baseline) configuration center of pressure are shown in Figure 19. The predictions show a qualitatively correct forward c.p. shift with increasing angle of attack, but are consistently 5 to 8% body length aft of the experimental results (compared to the accuracy criterion of 2%).

Shown in Figure 20 are Missile Datcom center-of-pressure predictions for the large tail fin, without incrementing (solid curve), and by incrementing (dashed curve). The center-of-pressure was not incremented directly, rather, the configuration normal force and pitching moment were incremented. The calculated center-of-pressure location is the ratio of the final incremented results. The theoretical predictions are in error by roughly the same amount as for the small-fin case (5% body length). The incremented prediction is significantly improved, and is within the accuracy criterion over most of the angle of attack range.

5. LATERAL-DIRECTIONAL EVALUATIONS

The vortex interference modeling currently in Missile Datcom (reviewed in Section 3) is very basic. The accuracy of lateral-directional predictions (even for conceptual design) can be questioned, since these predictions are particularly sensitive to vortex interference effects. Indeed, Williams et al [1] reported that, in the angle-of-attack range of 0 to 20 degrees, only 60% of total configuration lateral-directional comparisons met the accuracy criteria (compared to a success rate of 86% for longitudinal comparisons). The acceptability level rises to 75% if rolling-moment correlations are removed.

Given that fin-alone characteristics are well predicted, a critical look at the contributors to the interference effects is warranted. Therefore, cases where interference effects dominate are of particular interest. One such case is a canard-controlled missile tested by Blair [25,26] and shown in Figure 21. The missile was tested with the forward (canard) fins in the plus (+) orientation and the aft fins in either the (+) or (x) orientation. Force and moment data were taken with roll, yaw, and pitch control deflections, with and without tail-fins.

Positive roll commands (right "wing" down) were generated by deflecting the left horizontal canard panel five degrees trailing-edge down and the right horizontal canard panel five degrees trailing-edge up. As seen in Figure 22, the tail-off rolling-moment predictions are high by about 20-30% across the angle-of-attack range. This is probably due to the simplicity of the method used for estimating fin lateral center of pressure. The method is a function of the fin-span to body-diameter ratio only, and gives values that only vary from 0.416 to 0.424 of the fin span. An improved method is now being developed (see Section 6) that will include the effects of fin planform, Mach number, and angle of attack.

For the plus-tail configuration, the addition of the tails results in negative values for the resultant rolling moment (roll reversal). This is caused by the canard-vortex induced loads on the tail fins. Induced effect decreases above ten degrees angle of attack, but the prediction remains largely unchanged. This may be the result of mutual interaction among the vortices, which Missile Datcom ignores. For the x-tail (Figure 23), roll reversal is also evident at low angles of attack. The induced effect is highest in the 6-8 degree alpha range, where the vortices pass over the upper tail fins. Missile Datcom does pick up this effect, but again misses the behavior above ten degrees angle of attack.

A sketch of the predicted flow field is given in Figure 24. The locations and strengths of the canard vortices relative to the plus-tail planform at three angles of attack are shown. An asymmetry in vortex strength is evident as the angle of attack increases. This arises from the differential deflection; i.e., because (neglecting interference effects) the left canard fin "sees" an angle of attack of $(\alpha + 5)$, while the right fin "sees" an angle of attack of $(\alpha - 5)$. Hence the normal force and vortex strength for the left fin are greater than those for the right fin. The induced angles of attack at the tail fins (roughly 1.5 degrees at zero alpha) are small relative to the five degree control deflection. However, four fins contribute to the adverse rolling moment, compared to only two contributing to the commanded moment. In addition, the area of a tail fin is roughly three times the canard fin area, so the induced rolling moment is greater than the commanded moment, and roll reversal occurs.

Predictions of yawing moment induced by a roll command are presented in Figures 25-26. Missile Datcom predicts the tail-off values to be zero at all angles of attack, while the data show small positive yawing moments at the higher angles of attack. Again, interactions between the canard and body vortices are the probable cause. When the tails are added, Missile Datcom predicts a small positive induced yawing moment with increasing angle of attack. This levels off above ten degrees angle of attack. These moments are a consequence of the difference in the canard vortex strengths, which increase with angle of attack. This strength-differential induces positive side-forces on the upper tail fins, which generate small yawing moments. The plus-tail data show almost no effect except at the higher angles of attack. The x-tail data show a trend in qualitative agreement with the prediction.

Interference effects are also important for missiles with close-coupled fin sets. However, in these cases, the absence of a vortex roll-up model in Missile Datcom is expected to be the dominant source of error. In order to assess the impact of this deficiency, comparisons with data generated by Lamb [27] for a missile with close-coupled tail fins (Figure 27) are presented. Triform tail fins were tested in several orientations relative to the wings.

Directional stability correlations with two tail orientations are presented in Figure 28. Tail A has two fins in the horizontal plane with the third mounted vertically on top, as shown in Figure 27. Tail B, on the other hand, is an "inverted-Y" configuration. As expected, Tail B shows a significant improvement in directional stability at low angles of attack; however, its advantage steadily decreases with angle of attack. Missile Datcom predictions for both tails are in excellent agreement with the data at zero alpha. As angle of attack increases, the predicted directional stability for the inverted-Y tail is consistently greater than measured, while Tail A comparisons are acceptable over the complete alpha range.

Note that the horizontal tail fins on Tail A can make no contribution to the body-axis yawing moment. Thus, given the good agreement across the angle-of-attack range, we may conclude that the wing-vortex induced effects on vertical-fin side-force are predicted fairly well. On the other hand, there are significant errors in the predicted behavior of the downward-canted fins on Tail B. Since we have excellent agreement with data at zero alpha, (where wing-induced vorticity is small), the degradation in accuracy must represent poorly predicted interference effects. Since this is an extremely close-coupled configuration, a vortex-sheet representation for wing shed vorticity would be more realistic than a filament model. Apparently a discrete model is an adequate approximation if the actual vorticity is spread along a plane perpendicular to a fin; this is not so if the sheet is more nearly parallel to the fin.

Lateral stability results, shown in Figure 29, are consistent with the discussion presented in the previous paragraph. Excellent agreement with data at zero alpha was obtained. In this case all three fins, in either tail configuration, contribute to rolling moment (although the contributions for Tail B cancel at zero alpha). Thus, predictions for both deviate from experiment with increasing angle of attack. The degradation is expected to be worse for Tail A since the horizontal fins are always in closer proximity to the wing vortex system.

6. METHOD IMPROVEMENT ACTIVITIES

Work is currently underway to improve the predictive capability of Missile Datcom. Specific methods that address seven problem areas are being developed. This work is subdivided into two categories: replacement of deficient methods (4 cases), and addition of completely new methods (3 cases). The work, sponsored by AFWAL, is being performed by McDonnell Douglas Astronautics Company and Nielsen Engineering and Research (NEAR).

Revised Methods

(a) Fin-Alone Center of Pressure

The method currently contained in Missile Datcom for fin center of pressure is based on the strip theory result from reference [16]. Lateral c.p. is a function of only the fin-span to body-diameter ratio, and gives values that vary only from 0.416 to 0.424 of the fin span. The discrepancies in the tail-off rolling-moment predictions presented in Section 5 were traced to inadequacies in this method.

A recently completed series of wind tunnel tests, jointly sponsored by the U.S. Army, Navy, and Air Force, has yielded a very large data base on the control effectiveness and hinge moments of all-movable fins. The fin geometries and test conditions are summarized below.

Tri-Service Data Base Summary

Aspect Ratio	.25,.5,1,2,4	Angle of Attack	0-30, transonic
Taper Ratio	0,.5,1.0		0-45, supersonic
Mach Number	0.6-4.5	Roll Angle	0-180
		Deflection Angle	0-40

Empirical correlations are being developed by NEAR from this data base, as functions of aspect ratio, taper ratio, Mach number, deflection angle, roll angle, and C_N . These correlations will replace both the lateral and longitudinal c.p. methods, and should improve hinge-moment, pitching-moment and rolling-moment predictions.

(b) Subsonic/Transonic Forebody Drag

In the early phases of the development effort, it was decided to emphasize methods applicable to tactical missiles, especially at supersonic speeds. As a result, the subsonic and transonic methods suffered in their range of applicability. Using a guided projectile data base, Mikhail [28] compared the NSWCAP [11] and Missile Datcom prediction codes, and concluded that both gave "poor estimates" in the subsonic/transonic speed regimes. At these speeds, the Missile Datcom method for drag (as well as normal force and pitching moment) is restricted in application to conical or tangent ogive nose shapes. It is not applicable to arbitrary nose shapes, such as ellipsoids or conically tipped hemispheres. This method will be replaced by McDonnell Douglas with a series of tables, valid for a wide variety of nose shapes, that will be generated using a transonic Euler code.

(c) Body Vorticity

The existing method for estimating body vorticity effects was discussed in Section 3. Briefly, a pair of vortex filaments are shed and tracked using charts derived from experimental data. A more realistic approach is the "vortex cloud" model, developed by Mendenhall and Perkins [29]. Using this technique,

discrete vortices are shed along a series of crossflow planes, which start near the body nose. A single vortex is shed at each plane, and is tracked to the next crossflow plane, where it can affect the pressure distribution and separation point for the next vortex. The vortices are free to interact with each other as they move downstream. The method has been shown to give good predictions at high angles of attack, and is valid for non-circular body cross-sections. Because this new method is computationally intensive compared to the existing method, it will be included in the code for use on an optional basis.

(d) Improved Inlet Pressure Distribution Method

The final phase of the initial Missile Datcom development effort incorporated a method to predict the effects of inlets (external surface effects only) on missile stability and control. A simplified paneling technique was incorporated for inlet modeling. This method was found to give good predictions at high supersonic speeds, but poor estimates at low supersonic speeds. The problem has been traced to deficiencies in the pressure distribution estimates on the aft portion of the inlet. Alternate prediction methods will be investigated by McDonnell Douglas to alleviate these difficulties.

New Methods

(a) Exhaust-Plume Effects

Exhaust-plume effects are currently ignored in Missile Datcom. These can alter the flow field near the base of the missile, changing the base drag, and seriously degrade the effectiveness of fins located near the nozzle. An enhanced version of the base-flow model method based on the work of Addy [30] and White [31] will be used to predict the location of flow separation on the vehicle afterbody. The model will be modified by McDonnell Douglas to provide a force- and moment-prediction capability that accounts for plume-induced changes in fin effectiveness.

(b) Arbitrary Cambered Bodies

The arbitrary body method currently in Missile Datcom was developed by Beall [32]. It is based on the application of an "added-mass" concept to slender-body theory. Non-circular bodies are treated by finding equivalent circular bodies based on the added apparent mass of the non-circular body cross-section. The method provides predictions for normal-force-curve slope, pitching-moment-curve slope, and axial force at zero angle of attack. However, body-camber effects, which create non-zero values for both normal force and pitching moment at zero angle of attack, are not addressed. Therefore, the current method will be replaced by a new technique, based on the approach of Allen and Perkins [23]. Families of cross-sectional shapes (elliptic, triangular, etc.) will be defined. Linear theory will be used to calculate the normal-force and pitching-moment coefficients and slopes at zero angle of attack. A two-dimensional Navier-Stokes code will then be used to generate crossflow drag coefficients for these shapes. These results will be merged with the existing data base, to give a set of tables from which viscous contributions to the normal force and pitching moment will be determined.

(c) Inlet Additive Forces and Moments

Inlet "additive" forces and moments are not currently computed in Missile Datcom. These forces and moments act on the streamtube captured by the inlet, and are important to thrust-drag accounting procedures. Additive forces appear in both wind-tunnel model measurements with "flow-through" inlets and in flight on missiles with an air-breathing propulsion system. They can become significant at off-design operating conditions. NEAR will develop the Missile Datcom method based on the work of Dillenius [33]. A modified supersonic panel method is used to estimate the minimum additive force (which occurs at maximum mass-flow). The maximum additive force occurs for a fully blocked inlet and is estimated by assuming that the pressure on the inlet face is equal to the stagnation value. Finally, a linear variation with mass-flow ratio is assumed to exist between the minimum additive force and the maximum value.

7. CONCLUSIONS

Earlier studies, which focused on the longitudinal predictive accuracy of Missile Datcom, have shown that the program is a reliable low-cost tool for preliminary design of conventional tactical missiles. The current paper has addressed issues pertaining to design applications and has taken a critical look at anticipated problem areas. These include vortex-interference effects on lateral-directional stability and close-coupled configurations. Specific conclusions are:

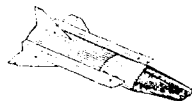
- (1) When appropriate component build-up data are available, significant improvements in prediction accuracy can be achieved with the experimental data substitution option.
- (2) Configuration incrementing is also an effective means for increasing accuracy. This technique has more general applicability than direct substitution since only complete configuration data on the baseline is needed. However, care should be taken to ensure that deviations in geometry from the baseline are not "excessive". Good quality data, especially at low alpha, is essential and moment reference points should be chosen to avoid zero or small values for zero-alpha slopes.
- (3) Missile Datcom does an adequate job of predicting the interference effects due to asymmetric control deflections at low-to-moderate angle of attack. Similar results can be expected for asymmetric flight conditions. Methods which account for the mutual interaction among vortices would extend applicability to higher angles of attack at the expense of longer running times.
- (4) Alternate vortex models are needed to adequately predict close-coupled configuration lateral and directional stability characteristics, even at moderate angle of attack.

(5) Development of new and improved methodology, which is currently underway, will significantly alleviate previously noted discrepancies. This is especially true for vortex-induced interference effects at angle of attack and for rolling moment prediction inaccuracies due to fin center-of-pressure errors. The new methods will also extend the range of applicability to include some unconventional configurations.

8. REFERENCES

1. Williams, J. E., Vukelich, S. R., and Stoy, S. L., "Prediction of Missile Aerodynamic Characteristics Using Component Build-up Techniques," NAECON 87-388, May 1987.
2. Vukelich, S. R. and Jenkins, J. E., "Development of a Missile Datcom Handbook and Computer Program," AGARD Symposium on Missile Aerodynamics, September 1982, Trondheim, Norway.
3. Vukelich, S. R. and Jenkins, J. E., "Missile Datcom Status Report: Body- and Fin-Alone Methodology," AIAA 83-0181, January 1983.
4. Vukelich, S. R. and Jenkins, J. E., "Missile Datcom: Aerodynamic Prediction of Conventional Missiles Using Component Build-up Techniques," AIAA 84-0388, January 1984.
5. Vukelich, S. R., "Aerodynamic Prediction of Elliptically-Shaped Missile Configurations Using Component Methodology," AIAA Paper 85-0271, January 1986.
6. Stoy, S. L., and Vukelich, S. R., "Extension of the Equivalent Angle of Attack Prediction Method," AIAA 84-0311, January 1984.
7. Williams, J. E., "Evaluation of Supersonic Missile Aerodynamic Prediction Techniques," AIAA 82-0375, January 1982.
8. Vukelich, S. R. and Jenkins, J. E., "Evaluation of Component Buildup Methods for Missile Aerodynamic Predictions," *Journal of Spacecraft and Rockets*, Vol. 19, No. 6, November-December 1982.
9. Vukelich, S. R., Development Feasibility of Missile Datcom," AFWAL TR-81-3130, October 1981.
10. Krieger, R. J., and Williams, J. E., "Accuracy Criteria for Evaluating Supersonic Missile Aerodynamic Coefficient Predictions," AIAA 82-0390, January 1982.
11. Devan, L., and Mason, L. A., "Aerodynamics of Tactical Weapons to Mach Number 8 and Angle of Attack 180 Degrees," NSWC TR 81-358, September 1981.
12. Nielsen, J. N., Hemach, M. J., and Smith, C. A., "A Preliminary Method for Calculating the Aerodynamic Characteristics of Cruciform Missiles to High Angles of Attack Including Effects of Roll Angle and Control Deflection," ONR CR215-226-4F, November 1977.
13. Lesieur, D. J., Mendenhall, M. R., Nazario, S. M., and Hemach, M. J., "Prediction of the Aerodynamic Characteristics of Cruciform Missiles Including Effects of Roll Angle and Control Deflection," NEAR TR 360, August 1987.
14. Williams, J. E., and Vukelich, S. R., "The USAF Stability and Control Digital Datcom," AFWAL TR-79-3032, April 1979.
15. Hemach, M. J., and Nielsen, J. N., "The Equivalent Angle-of-Attack Concept for Engineering Analysis," Chapter XI, *Tactical Missile Aerodynamics*, AIAA Progress in Astronautics and Aeronautics, Vol. 104, 1986.
16. Pitts, W. C., Nielsen, J. N., and Kaattari, G. E., "Lift and Center of Pressure of Wing-Body-Tail Combinations at Subsonic, Transonic, and Supersonic Speeds," NACA TR 1307, 1959.
17. Hoak, D. E., et al, "USAF Stability and Control Datcom," AFWAL TR-81-3048, October 1980 (Revised 1978).
18. Royal Aeronautical Society, "Data Sheets", 1966.
19. Hemach, M. J., Nielsen, J. N., and Dillenius, M. F. E., "Method for Calculating Induced Rolling Moments for Cruciform Canard Missiles at Angles of Attack up to 20 Degrees," NWC TP 5761, May 1975.
20. Gur, I., Shinar, J., and Rom, J., "A Model for the Evaluation of Induced Rolling Moments and Side Forces in Slender Cruciform Canard Configurations at Small Angles of Incidence," *Israel Journal of Technology*, Vol. 14, 1976, pp. 74-86.
21. Spreiter, J. R., and Sacks, A. H., "The Rolling-up of the Trailing Vortex Sheet and Its Effect on the Downwash Behind Wings," *Journal of the Aerospace Sciences*, January 1951.
22. Graves, E. B., "Aerodynamic Characteristics of a Monoplanar Missile Concept With Bodies of Circular and Elliptical Cross Section," NASA TM 74079, December 1977.
23. Allen H. J., and Perkins, E. W., "A Study of Effects of Viscosity on Flow over Slender Inclined Bodies of Revolution," NACA TR 1048, 1951.
24. Baker, D. C., "Aerodynamic Characteristics of a 1/3-Scale Air-Slewed Missile at Mach Numbers From 0.4 to 4.3," AEDC TR-73-141, August 1973.

25. Blair, A. B. Jr., "Remote Control Canard Missile with a Free-Rolling Tail Brake Torque System," AIAA 81-0146, January 1981.
26. Blair, A. B. Jr., "Wind Tunnel Investigation at Supersonic Speeds of a Remote-Controlled Canard Missile With a Free-Rolling Tail Brake Torque System," NASA TP 2401, March 1985.
27. Lamb, M., "Stability and Control Characteristics of a Monoplanar Missile Configuration With Triform Tail-Fin Arrangements at Mach Numbers From 1.70 to 2.86," NASA TM 83223, December 1981.
28. Mikhail, A. G., "Application and Assessment of Two Fast Aerodynamic Prediction Codes for a Class of Guided Projectiles," AIAA 85-4085, October 1985.
29. Mendenhall, M. R., and Perkins, S. C. Jr., "Vortex Cloud Model for Body Vortex Shedding and Tracking," Chapter XII, Tactical Missile Aerodynamics, AIAA Progress in Astronautics and Aeronautics, Vol 104, 1986.
30. Addy, A. L., "Analyses of the Axisymmetric Base-Pressure and Base-Temperature Problem with Supersonic Interacting Free Stream Nozzle Flows Based on the Flow Model of Korst, et al," U.S. Army Missile Command, RD TR-69-14, February 1970.
31. White, R. A., "The Calculation of Supersonic Axisymmetric Afterbody Flow with Jet Interference and Possible Flow Separation," Aeronautical Research Institute of Sweden, TN AU-912, 1974.
32. Beall, B., "Application of Slender Body Theory to Missiles with Arbitrary Shape Cross Sections," AIAA 86-0488, January 1986.
33. Dillenius, M. F. E., and Kierstead, M. M., "Panel Methods Applied to Supersonic Inlets Alone and to Complete Supersonic Air Breathing," NASA CR 3979, May 1986.



METHODOLOGY	COMPONENT BUILD-UP	PANELING	CFD
GEOMETRY	CONVENTIONAL	ARBITRARY	ARBITRARY
ACCURACY	GOOD	VARIABLES	GOOD
COST	LOW	HIGH	VERY HIGH
PARAMETRICS	EASY	DIFFICULT	DIFFICULT
TEST DATA USE	YES	NO	NO
PRIMARY USE	CONFIGURATION SCREENING	DETAILED DESIGN	POINT DESIGN

Figure 1. Aerodynamic Method Comparison

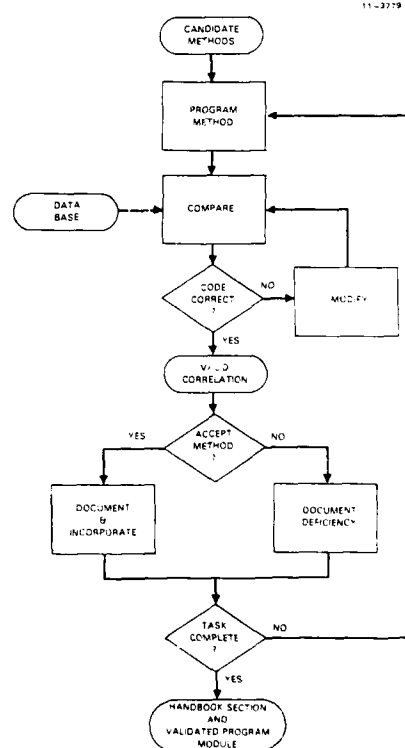


Figure 2. Method Selection Process

	SUBSONIC M < 0.8	TRANSONIC 0.8 < M < 1.2	SUPERSONIC M > 1.2
C_{NB} C_{DB} (INNOV CYLINDER)	MSE TR WE 7-87-88 AND WE 12-88/70 ^a		
C_{NB} C_{DB} (BOATTAILS)	NWC TR 81-156 ^a		NWC TR 81-156 (HYBRID/DOSEI)
C_{NB} C_{DB} (FLARES)	AMCP 708-280 ^a		
η	MODERN DEVELOPMENTS IN FLUID DYNAMICS (GOLDSTEIN) ^a	AEOC TR 75-124 ^a	(VALUE OF UNITY ASSUMED)
C_{DE}	NASA TR D-6996 AND AEOC TR 75-124 ^a		
SKIN FRICTION	BLASIUS + TRANSITION ^a + VAN DRIEST II		
PRESSURE DRAG - NOSE CYLINDER	FLUID DYNAMIC DRAG (HOFERER)		(NOT APPLICABLE)
PRESSURE DRAG - BOATTAILS	DTNROD/ASED-80/10 ^a		
PRESSURE DRAG - FLARES	AMCP 708-280 ^a		
WAVE DRAG-NOSE - CYLINDER	NWC TR 80-346		NWC TR 81-156 (HYBRID/DOSEI)
WAVE DRAG BOATTAILS	(NOT APPLICABLE)		
WAVE DRAG FLARES	AMCP 708-280 ^a		
BASE DRAG CYLINDERS	NASA TR R100 ^a		NWC TR 81-156 ^a (HYBRID/DOSEI)
BASE DRAG BOATTAILS	NWC TR 81-156 ^a		
BASE DRAG FLARES	AMCP 708-280 ^a		

^a EMPIRICAL METHOD

Figure 3. Axisymmetric Body Aerodynamic Methods

11-4784
1-20-84

	SUBSONIC $M < 0.8$	TRANSONIC $0.8 < M < 1.2$	SUPERSONIC $M > 1.2$
CARRY-OVER INTERFERENCE	NACA 1307		AIAA JOURNAL, JUN/AUG 1982
BODY VORTICES STRENGTH/TRACKING	NWC TP-5761 ^a		
WING VORTICES STRENGTH/TRACKING	NACA 1307		
PANEL LOADS	AIAA PAPER 77-1153		

^a EMPIRICAL METHOD

Figure 5. Configuration Synthesis Methods

CONFIGURATION	NUMBER COMPARISONS	WITHIN ACCURACY
FIN ALONE	78	91%
HARPOON	14	71%
ARMY GENERALIZED	6	83%
NASA TMX-2531	3	100%
AIM-9L	10	100%
LFRED	43	89%
MAVERICK	7	43%
HIGH-ALPHA BT	84	95%
GOMILLION	111	95%
TOTAL/AVERAGE	366	86%

Figure 6. Longitudinal Predictive Accuracy

	SUBSONIC M < 0.8	TRANSONIC 0.8 < M < 1.2	SUPERSONIC M > 1.2
AIRFOIL SECTION AERODYNAMICS	WEBER ANALYSIS (CONFORMAL MAPPING) AND R & B 2918, APC R & B 2076		(NOT REQUIRED)
C _{NB}	DATCOM 4.1.3.2	R & S DATA SHEETS	DATCOM 4.1.3.2
C _{DB}	DATCOM 4.1.4.2		
C _{ND}	DATCOM 4.1.3.3, 4.1.3.4		
C _{NB(D)}	ENGINEERING METHOD (NONLINEAR AT PLATFORM CENTROID)		
SKIN FRICTION	BLASIUS + TRANSITION ^a + VAN DRIEST II		
PRESSURE DRAG	FLUID DYNAMIC DRAG (HOFERER)		(NOT APPLICABLE)
WAVE DRAG	(NOT APPLICABLE)	LINEAR FAIRING FROM M = 1.05	NWL TR 3018 (USED TO M = 1.05)
LEADING-EDGE BLUNTNESS DRAG	DATCOM 4.1.5.1 ^a		NWL TR 2708 ^a
TRAILING-EDGE DRAG	NWL TR 2708 ^a		
C _{A(0)}	DATCOM 4.1.5.2		(INVARIANT)

^a EMPIRICAL METHOD

Figure 4. Fin-Alone Aerodynamic Methods

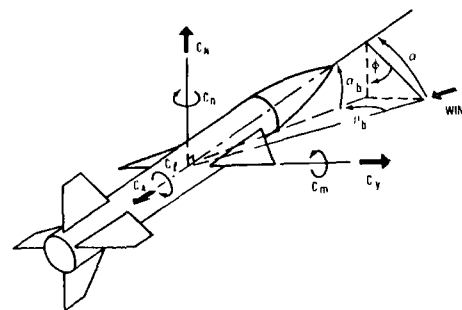


Figure 7. Aeroballistic Axis System

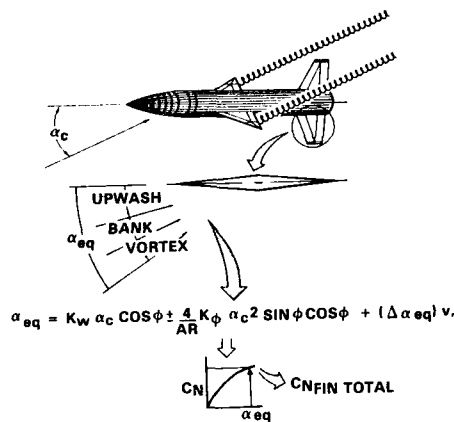


Figure 8. Contributors to Alpha-Equivalent

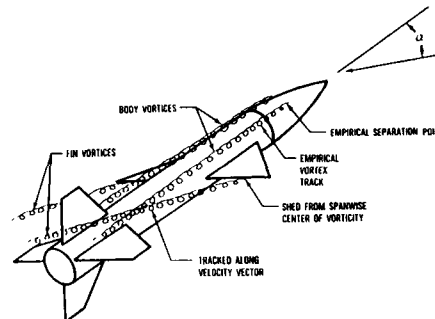


Figure 11. Missile Datcom Vortex Model

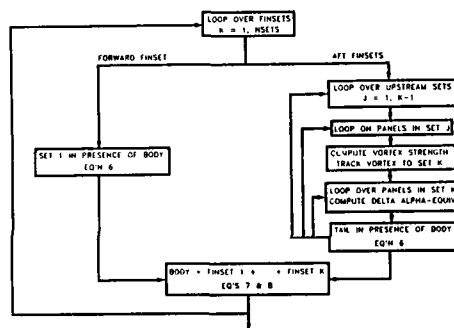


Figure 9. Aerodynamic Synthesis

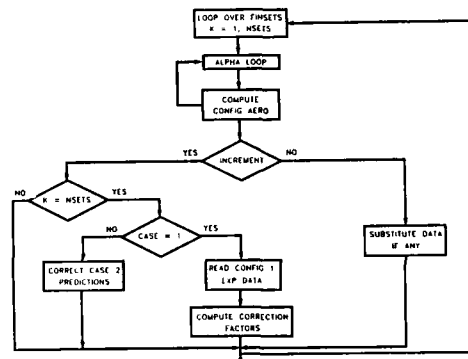


Figure 12. Data Substitution Options

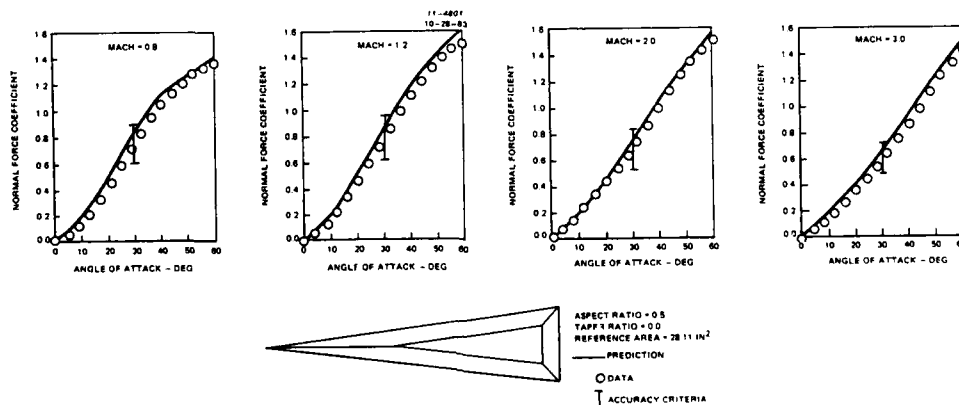


Figure 10. Fin-Alone Normal Force Data Comparison

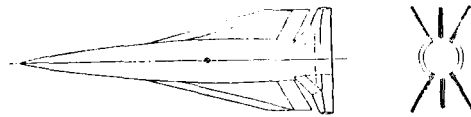


Figure 13. Graves Circular Body

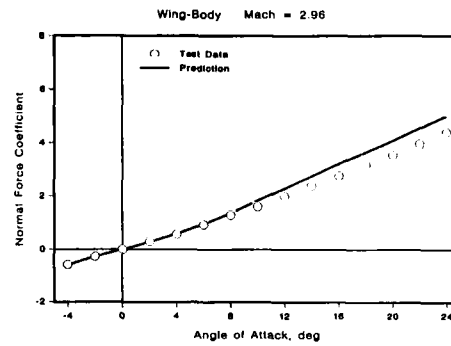


Figure 16. Wing-Body Normal Force

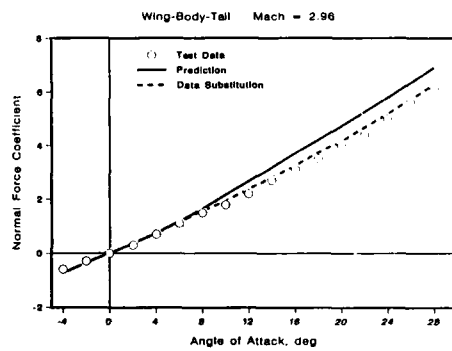


Figure 14. Normal Force Data Substitution

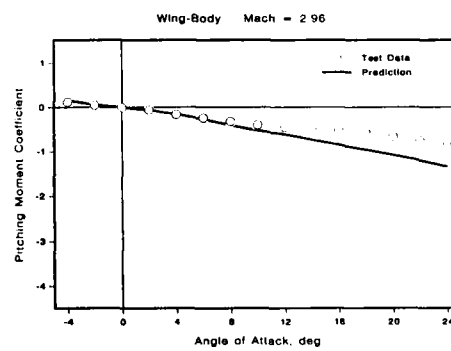


Figure 17. Wing-Body Pitching Moment

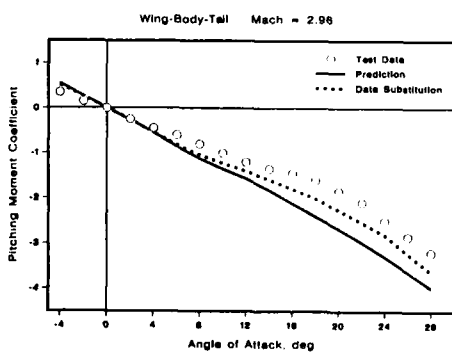


Figure 15. Pitching Moment Data Substitution

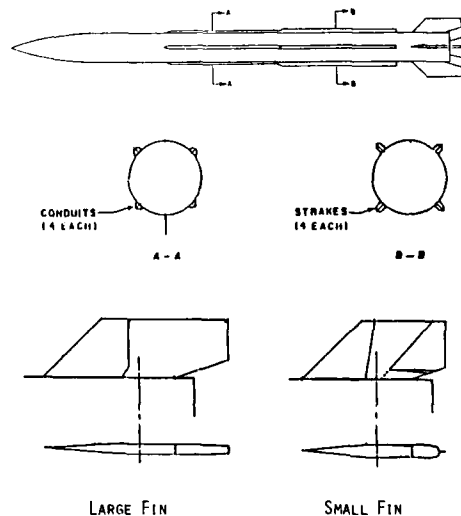


Figure 18. Air-Slewed Missile

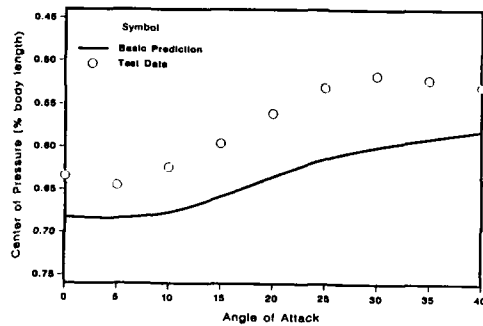


Figure 19. Small Fin Configuration c.p.

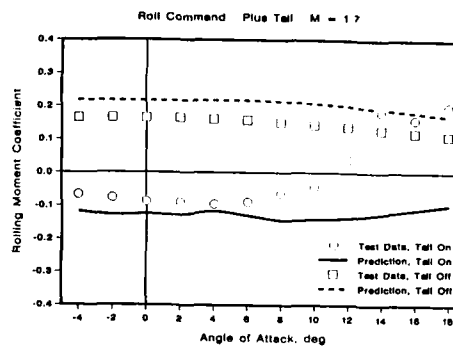


Figure 22. Rolling Moment Coefficient Prediction

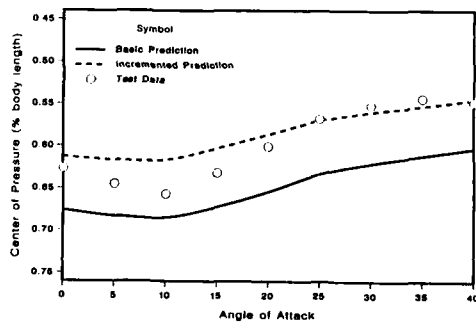


Figure 20. Large Fin Incremented Result

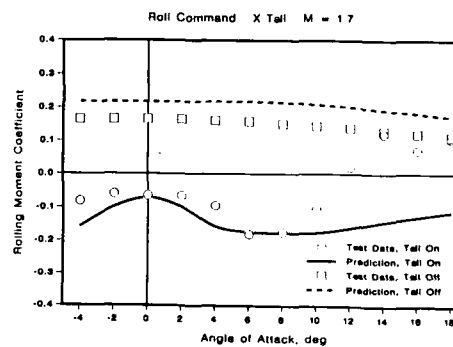


Figure 22. Rolling Moment Coefficient Prediction

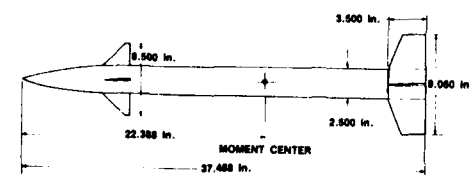
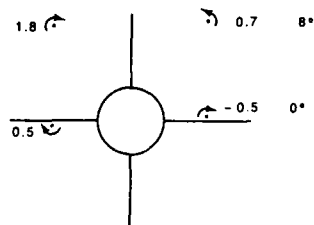


Figure 21. Canard Controlled Missile

$$\Gamma = 2.8 \quad \alpha = 16^\circ$$



Γ = NONDIMENSIONAL
VORTEX STRENGTH
 α = ANGLE OF ATTACK

Figure 24. Predicted Vortex Positions at Tail

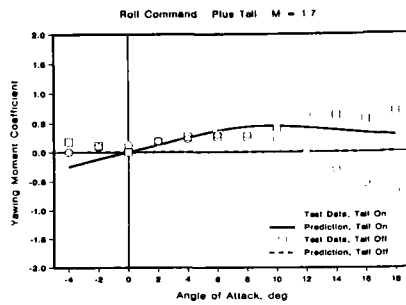


Figure 25. Yawing Moment Coefficient Prediction

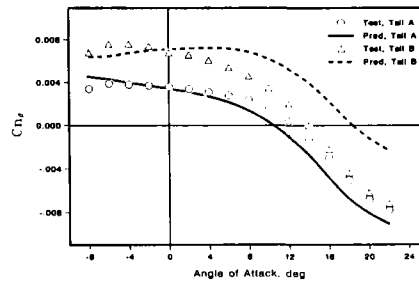


Figure 28. Directional Stability Comparisons

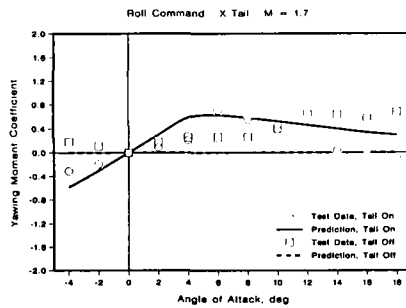


Figure 26. Yawing Moment Coefficient Prediction

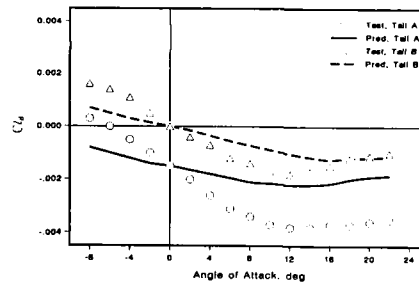


Figure 29. Lateral Stability Comparisons

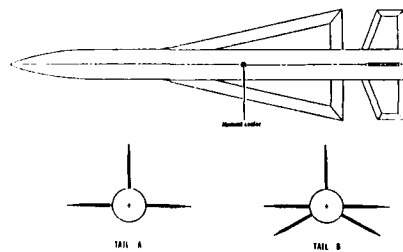


Figure 27. Close-Coupled Triform Tail Configuration

PREDICTION OF DYNAMIC DERIVATIVES

by

Heinz Fuchs

Dornier GmbH, Abt. BF20, Postfach 1420, D-7990 Friedrichshafen, FRG

SUMMARY

The prediction methodology of dynamic derivatives is presented as derived from semiempirical calculation procedures like 'USAF Stability and Control Datcom' in combination with some modifications necessary for tactical missile configurations at higher angles-of-attack. The main subject is the longitudinal stability derivatives and the roll damping derivativum. A comparison of theoretical and experimental results is presented where different dynamic wind tunnel test equipments are explained including the data evaluation theory. Some aspects of modification of the present linear data evaluation method to nonlinear terms at high angles-of-attack are shown with an example of a fighter aircraft configuration using the MOD test rig in the Dornier wind tunnel.

NOTATION

A [deg]	amplitude
C_{Dc} [-]	cross flow drag coefficient
$C_{m_{\alpha}}$ [1/rad]	$\frac{\partial C_m}{\partial \alpha}$ pitching moment slope
$C_{Z_{\alpha}}$ [1/rad]	Z-force slope

Dynamic derivatives:

C_{l_p} [1/rad]	$\frac{\partial C_l}{\partial p}$ roll damping derivativum
C_{m_q} [1/rad]	pitch damping derivativum
C_{n_r} [1/rad]	yaw damping derivativum
$C_{m_{\alpha}}, C_{Y_r}, C_{Z_{\alpha}}, C_{Z_q}, C_{Z_{\dot{q}}}$	1st order derivativa
$C_{m_{\alpha\dot{\alpha}}}, C_{Z_{\alpha\dot{\alpha}}}, C_{Z_{\alpha\ddot{q}}}, C_{Z_{q\dot{q}}}$	2nd order derivativa

all dyn. derivativa use q_{∞} for reference e.g. $C_{m_q} = \frac{\partial M}{\partial q} \frac{V_{\infty}}{S l^2 q_{\infty}}$

c_l [-]	lift curve distribution	q_{∞} [N/m ²]	dyn. press. $\frac{1}{2} \rho_{\infty} V_{\infty}^2$
c_p [-]	pressure coefficient	R_{eD} [-]	$\frac{V_{\infty}}{\nu}$, Reynolds number
D [m]	caliber, ref. length	s [m]	wing span
f [Hz]	frequency	t [s]	time
g [m/s ²]	earth grav. acceleration	V_{∞} [m/s]	free stream velocity
K [kg/m]	constant eq. 2.1	u, v, w [m/s]	velocity com. (aircr. fixed)
k_1 [$\frac{s}{deg}$]	factors of $\Delta \alpha = f(\Delta \theta)$	X, Y, Z [N]	comp. of aerod. force (aircr. fixed)
k_2 [$\frac{1}{deg^2}$]		$x_{c.g.}$ [m]	center of gravity position
L, M, N [Nm]	comp. of aerod. moment (aircraft fixed)	α [deg]	angle-of-attack
L [N]	aerod. lift	β [deg]	angle-of-sideslip
l [m]	ref. length (= D for missiles, = l_{μ} for aircr.)	δ_N / δ_F [deg]	nose- and trailing edge defl. angle
l_{μ} [m]	mean aerod. chord length	ϵ_C [deg]	canard angle
M [-]	Mach number	n [deg]	elevator angle to trim
m [kg]	mass	θ [deg]	pitch angle
p, q, r [rad/s]	comp. of aerod. angular velocity (aircr. fixed)	ν [m ² /s]	kinematic viscosity
		ρ_{∞} [kg/m ³]	free stream density of air
		ω^* [-]	reduced frequency
		Δ	small perturbation values

Superscripts:

- ① linear
- ①① nonlinear
- ① 1st order
- ② 2nd order } terms
- derivativum wrt time
- multipl. by $1/V_{\infty}$

Subscripts:

- sin sin-terms } of Fourier
- cos cos-terms } Series
- o initial value
- = free stream conditions

1. INTRODUCTION

The dynamic derivatives of aerodynamic force and moment with respect to the independent variables of flow acceleration like angular velocity components $\dot{\omega} = (p, q, r)$ i.e. $C_{Z_q}, C_{m_q}, C_{Y_r}, C_{n_r}, C_{l_p}$ become more and more important with all types of agile flight vehicles. Accelerated flight manoeuvres also cause derivatives of the rate-of-change of the angle-of attack and angle-of-sideslip. These derivatives become of flight mechanical relevance with all curved flight paths flown through.

The need for the verification of appropriate prediction methods for dynamic derivatives is evident from the engineering progress in modern missile and fighter aircraft mission requirements of advanced manoeuvrability. The specifications of the guidance and control systems also define the requirements.

Various theoretical and semiempirical prediction methods are at hand in the national or industrial research institutes. Likewise, the experimental wind tunnel test rigs are important prediction tools. In FR Germany they are available at the DFVLR test facilities or the aircraft industries. Today, main emphasis is also placed to improvements of the prediction methods at the high angle-of-attack range.

2. DYNAMIC STABILITY DERIVATIVES

Definition, Classification and Application to Unsteady Motion

The dynamic derivatives are per definitionem the partial derivatives of an aerodynamic function (like lift-function L) with respect to independent flow variables, especially to the variables combined with the acceleration of the fluid flow.

Following the definitions of [1] the simplifying assumption is useful that an aerodynamic function L is only a function of the instantaneous values of the variables u, v, w, p, q, r and possibly of the derivatives of these variables with respect to time. This is the common assumption of a quasi-stationary approach of aerodynamic functions which is valid for attached-flow conditions and for motions of the missile which are sufficiently slow. With the assumptions above, function L is steady and multiple derivatives exist. Let us now consider a Taylor series expansion of the aerodynamic function L with respect to small perturbations $\Delta u, \Delta \dot{u}, \Delta w, \Delta \dot{w}, \Delta q, \Delta \dot{q}$ (planar case) up to quadratic order (see equation A.1 of Appendix).

Some of the terms of eq. A.1 are vanishing small. From $L = Ku^2$ it follows

$$\left. \begin{aligned} \frac{\partial L}{\partial u} \Delta u &= 2 Ku \Delta u = 2L \frac{\Delta u}{u} \ll 1 \\ \frac{\partial^2 L}{\partial u \partial w} \Delta u \Delta w &= 2 \frac{\partial L}{\partial w} \Delta w \frac{\Delta u}{u} \ll 1 \end{aligned} \right\} \text{eq. (2.1)}$$

The terms of $\Delta u \Delta q$ and Δu^2 are vanishing for the same reason as well as the terms containing $\Delta \dot{u}$.

Introducing the angle of attack $\Delta \alpha$ by

$$\frac{\partial L}{\partial w} \Delta w = \frac{1}{V_\infty} \frac{\partial L}{\partial \alpha} \Delta \alpha = \frac{\partial L}{\partial \alpha} \Delta \alpha \quad \text{eq. (2.2)}$$

the following terms of the Taylor series remain:

$$\begin{aligned} L(u+\Delta u, w+\Delta w, q+\Delta q, \dot{q}+\Delta \dot{q}) &= L(u, w, q, \dot{q}) + \\ &\frac{\partial L}{\partial \alpha} \Delta \alpha + \frac{\partial L}{\partial q} \Delta q + \frac{\partial L}{\partial \dot{q}} \Delta \dot{q} + \frac{1}{2} \frac{\partial^2 L}{\partial \alpha^2} \Delta \alpha^2 + \frac{1}{2} \frac{\partial^2 L}{\partial q^2} \Delta q^2 + \frac{1}{2} \frac{\partial^2 L}{\partial \dot{q}^2} \Delta \dot{q}^2 + \frac{\partial^2 L}{\partial \alpha \partial q} \Delta \alpha \Delta q \\ &\quad + \frac{\partial^2 L}{\partial \alpha \partial \dot{q}} \Delta \alpha \Delta \dot{q} \end{aligned} \quad \text{eq. (2.3)}$$

In an analogous way the lateral terms of an equivalent Taylor series are obtained assuming function L to be dependent from the variables $v, p, r, \dot{v}, \dot{p}, \dot{r}$.

What terms of aerodynamic coefficients are derived from eq. (A.1) and eq. (2.3) is determined by phenomenological experience. Especially the question where the Taylor series can be truncated without loss of significant accuracy is determined by the experimental and free flight experience. By this reason, a lot of terms of equations (A.1) and (2.3) can be omitted because they are neglectably small.

On the other hand the physical significance of higher order terms cannot be predicted a priori in all cases of applications so some higher order terms are usually truncated because of insurmountable difficulties of their precise determination.

Function L of eq. 2.3 may be identified by the aerodynamic Z-force or the aerodynamic pitching moment M . If eq. 2.3 is written in dimensionless form the coefficients of the power series turn into the dynamic derivatives e.g. $C_{Z_q}, C_{Z_{\dot{q}}}$ etc. according to the list of notation.

We distinguish between 'damping derivatives', 'cross derivatives' and 'cross-coupling derivatives'.

The damping derivatives are defined by the rule that each vector component of the force $\vec{F} = (X, Y, Z)$ or the moment $\vec{M} = (L, M, N)$ is differentiated with respect to the same corresponding vector component of $\dot{\omega} = (p, q, r)$ i.e. $C_{Z_q}, C_{l_p}, C_{m_q}, C_{n_r}$ etc.

The cross derivatives are defined by cross-wise correlations of the vector components but with cross-wise relations between longitudinal and lateral components excluded, i.e. C_{l_r} or C_{n_p} .

The cross-coupling derivatives are defined by cross-wise correlations between the vector components of the function and its derivativum combined with a cross-wise correlation of longitudinal and lateral components i.e. C_{l_q} , C_{m_r} , C_{m_p} , C_{n_q} (see schematic of Fig. 2.1).

The dynamic derivatives represent the aerodynamic response to nonstationary motion. The meaning of the dynamic derivatives are shown by the examples of either quasistationary flight curves (like looping) or other nonstationary motions shown in Fig. 2.2. The last type of pitching motions of Fig. 2.2 represents the type which is usually found at wind tunnel test equipments for the measurement of dynamic derivatives. Because this mode combines the rate of change of the angle-of-attack with that of the longitudinal attitude, it is normally not possible to separate both the derivativa with respect to q and $\dot{\alpha}$.

3. METHODS OF THEORETICAL PREDICTION OF DYNAMIC DERIVATIVES

3.1 Existing Methods and Range of Applicability

Besides of the semi-empirical methods (cf. next section) there are some other theoretical approaches: First the indicial function concept derived from the fundamental works of M. Tobak [2].

The advantages of this method are the contributions to the downwash effects from forward positioned wings to after positioned tails and the usefulness of the theory with respect to the rate of change of the angle-of-attack. This is due to the idea of the theory in considering the aerodynamic response to instantaneous changes of the conditions determining the aerodynamic properties at steady flow. Disadvantages are that the theory is derived from potential theory. In recent years there were extensions of the theory to more general assumptions (see Tobak, Schiff [3]). Schneider [4] and Schneider-Nikolitsch [5] applied the indicial function concept especially to missile configurations.

A panel-procedure for the prediction of unsteady airloads was developed at the NLR, Netherland (see [6]). This method has the advantage to be applied for complex configurations because of its flexibility with the representation of geometrical surfaces by panel discretization. The characteristics of the unsteady panel method is that each panel contains a time-varying source distribution. Its solutions can be found in terms of integrals over the source distribution on the surface of the configuration. The integral equations are reduced to a set of algebraic equations similar to the well-known steady panel procedures. In doing so, the strengths of the source distributions are defined by applying boundary conditions of an harmonic oscillating body surface.

This reveals the disadvantages of such procedures with its confinement to the linear angle-of-attack range and also the difficulties in the modeling of wakes. Therefore, the powerful tool of this procedure is in its application to aeroelasticity and flutter problems of rather high frequencies and small amplitudes.

3.2 Semiempirical Method According to 'USAF Stability and Control DATCOM'

3.2.1 Longitudinal Derivatives

A computer program, designated DYNAM, has been developed by Dornier for several years to calculate the longitudinal dynamic derivatives. The program follows the DATCOM-methods [7] which have been extended to moderate and higher angles-of-attack by introduction of the α -dependencies of the static components.

In general, the DATCOM method for calculation of the dynamic derivatives is a semi-empirical method which treats the individual missile components separately. Subsequently, the contributions of the individual components like body and wings are summed up in order to determine the total result of the whole missile configuration. This procedure is quite similar to the DATCOM-methods of the static aerodynamic coefficients.

The method of constructing the total result by the contributions of the different missile components implies that the mutual interference effects between the various missile components can be treated in an analogous way to the treatment of the static aerodynamic coefficients. This is a fundamental assumption of the methods described in DATCOM and is also used in DYNAM. The mutual interference factors which are calculated in the static theory can be transferred to program DYNAM via the input data without changing them (an additional option of DYNAM is to calculate them).

The DATCOM-methods for calculation of the dynamic derivatives are based on lifting-surface theory for the wing contributions and subsonic speeds and linearized theory for supersonic speeds. The body derivatives are determined by slender-body-theory. Thus for low-aspect ratio wings - as usually found at missile configurations - the origin DATCOM-methods are restricted to small angles-of-attack.

This means that the DATCOM formulae are confined to attached flow conditions whereas separate flow phenomena are not included in the theory.

At Dornier, the DATCOM method was extended in such a way that all dependencies on the angle-of-attack were introduced wherever such dependencies exist in the terms describing the theory. By this way, the influence of the angle-of-attack was introduced by the function of the lift curve slope $C_{Z_\alpha} = C_{Z_\alpha}(Ma, \alpha, n)$ and the slope of the moment curve $C_{m_\alpha} = C_{m_\alpha}(Ma, \alpha)$. The movement of the aerodynamic center $x_{a.c.}$ with the change of the angle-of-attack was also included.

Within this paper it is not the place to reproduce all DATCOM-formulae of dynamic derivatives, the user is referenced to [7] and [8].

Wing part contributions are within all speed ranges composed according to

$$\left. \begin{aligned} C_{Z_q}^{(1)}(\eta, \alpha) &= (C_{Z_q}^{(1)} + \frac{\bar{x}(\eta, \alpha)}{l}) (C_{Z_\alpha}^{(1)}(\eta, \alpha) - C_{X_\alpha}(\eta, \alpha)) \\ C_{Z_q}^{(n)}(\eta, \alpha) &= (C_{Z_q}^{(n)} + \frac{\bar{x}(\eta, \alpha)}{l}) C_{Z_\alpha}^{(n)}(\eta, \alpha) \end{aligned} \right\} \text{eq. (3.1)}$$

\bar{x} is the distance between the point-of-rotation of angular velocity q and the aerodynamic center of the wing, positive if a.c. of the wing is after the point of rotation.

Eq. (3.1) shows another basic principle of general mechanics, namely the splitting of a pure rotational motion into a translational and a rotational part. The motion of a wing with point of rotation apart from wing-a.c. is splitted into the rotation about the wing-a.c. position and a corresponding translational motion of the $x_{a.c.}$ -point. The calculation of the dynamic derivatives is also splitted into these parts where the rotation of the wing about its $x_{a.c.}$ -position is the wing-alone part $C_{Z_\alpha}^{(1)}$.

One main attribute of these methods is that the calculation of dynamic derivatives is reduced to static terms like C_{Z_α} . Therefore, these methods can also be updated by use of experimental results for the lift curve slopes so that - as a rule - an increase of accuracy can be realized.

In order to qualify the wing-alone contributions, different other methods were also used (e.g. slender body theories by Nielsen [1] and Burhan [9], lifting surface theory by Garner [10], Otto [11] and Gersten [12], see Fig. 3.1).

3.2.2 Roll Damping Derivative

With missile aerodynamics the roll damping derivative C_{l_p} is of interest for often the correct work of the seeker section (esp. for TV-imaging, radar- or IR-seeker) requires some restriction to the rolling rate.

The theories of DATCOM only define a roll damping coefficient of wing sections but not for bodies alone.

The physical phenomenon of the roll-damping is a change of the wing lift distribution induced by the roll-rate. The roll-rate p causes an asymmetric lift distributions as schematically shown in Fig. 3.2. At the wing side which is moved downward an additional increment of lift is induced according to the incremental increase of the angle-of-attack $\Delta\alpha = \arctan(\frac{p}{2V})$. At the wing tip moved upward a corresponding decrease of the lift distribution is induced. Assuming attached flow conditions, this change of the lift distribution causes a rolling moment ΔC_l which acts against the initial rolling motion.

The DATCOM subsonic method is a potential theory based on Bird [13] and Young [14], for supersonic speeds it follows data sheets [15], Harmon and Jeffreys [16] and Malvestuto et.al. [17].

3.3 Cross-flow Method for the q-Derivatives at High Angles-of-Attack

Since the results of the DATCOM-method are partly in poor agreement with test results of the high angle-of-attack range, some improvements of the calculation method were looked for at Dornier. From the work of Jorgensen [18] the cross-flow theory is known to be a useful tool for the prediction of static aerodynamic forces of missile bodies in the nonlinear α -range.

At Dornier, this theory was extended to the dynamic derivatives with respect to q as it is outlined in [19] and [20].

For cylindrical bodies the equations

$$\left. \begin{aligned} C_{N_q} &= -\frac{A}{\pi} C_{D_c} \sin \alpha \left[\left(\frac{x_u}{D} \right)^2 - \left(\frac{x_l}{D} \right)^2 \right] \\ C_{m_q} &= -\frac{B}{\pi} C_{D_c} \sin \alpha \left[\left(\frac{x_u}{D} \right)^3 - \left(\frac{x_l}{D} \right)^3 \right] \end{aligned} \right\} \text{eq. (3.2)}$$

were derived with x_u, x_l as the distances from c.g. to top or rear end. The theory was extended to complete configurations [20] making use of the cross flow wake induced normal force and proved to be a powerful tool.

4. EXPERIMENTAL METHODS FOR THE PREDICTION OF DYNAMIC DERIVATIVES

4.1 Overview

The dynamic test rigs used in FR Germany are shown with missile test results in the next section. Besides of the MFD-balance and the MOD test rig they are all of the 1 dof-type. Important multi-dof dynamic test rigs are

in Canada: the forced-oscillation apparatus MKI
at NAE, Ottawa
and the NAE Dynamic Calibrator
(see [21] and [22])

- in U.S.A.: different oscillation apparatus of
AEDC, Tullahoma
and NASA Langley
- in U.K. : forces oscill. 3 dof-app.
of RAE Bedford

4.2 Dynamic Test Rigs Used in the Different Aerodynamic Laboratories of FR Germany

4.2.1 The MFD Test-Rig of the DFVLR Braunschweig

The first German dynamic apparatus for oscillatory motion was the Multi-degree-of-Freedom Derivative Balance (MFD) for sting mounted models in the 3 m low-speed wind tunnels of DFVLR (see [23], [24]).

Installation of the MFD apparatus in the closed test section of the low-speed wind tunnel at DFVLR Braunschweig is shown in Fig. 4.1. The main features of the mechanical system are a flexible sting with two bending flexures in line, which allow combined pitch and plunge motions in the longitudinal plane.

The support system allows inclination of the total system to angles of attack up to 40 degrees. The MFD apparatus was used with a stainless steel missile model (D = 120 mm, mass m = 22 kg).

4.2.2 The TRAD Apparatus of DFVLR Göttingen

Since 1979 a high-load dynamic derivative balance (German abbreviation TRAD) has been developed for use in the 1 m transonic wind tunnel at DFVLR-AVA Göttingen. A description of the test rig is given in [25], a similar 1 dof dynamic balance was developed at FFA, Bromma, Sweden, (see [26]). Main features of this forced-oscillation apparatus are:

- 1 dof oscillation at fixed amplitude in pitch, yaw or roll
- high rigidity against static loads
- direct parallel measurement of displacement and total static and dynamic loads on the model
- analog data reduction with special vector component resolvers and online data transfer to central computer.

The setup for tests in the pitching mode is sketched in Fig. 4.2. For oscillation mode see Fig. 4.3. The one degree amplitude of oscillation is prescribed by an eccentricity at the tip of a rotating shaft with in the hollow sting. The shaft is driven by a five-phase step motor, selected for its ability to maintain constant speed at alternating torque.

The TRAD balance was used with a light weight missile mode (D = 50 mm, mass m = 1.55 kg). The oscillation in roll is conducted by an additional sting connected with the driving motor (maximum roll amplitude is 2 deg).

4.2.3 Free-Oscillation Apparatus of DFVLR Cologne

The principle of the free-oscillation derivative balance of DFVLR Cologne is shown in Fig. 4.4. The apparatus is specially designed for damping measurements on missiles in the 0,6 m blow-down trisonic wind tunnel at subsonic and supersonic speeds up to Ma = 3,0 (see [27]).

The model is strut-mounted on a removeable cross flexure, the stiffness of which is appropriate to the model inertia. The free-oscillation motion in pitch is initiated by a tripping device, which is hydraulically pushed into the rear end of the model, deflecting it to the starting position. The time history of the model motion is taken from strain gauges glued to the cross flexure. The stiffness and damping derivatives are evaluated from the response data using Fourier transforms and spectral analysis.

The tests were conducted with a stainless steel manufactured model of a body diameter of D = 28 mm.

4.2.4 The "Mobile Oscillation Derivativa Balance" MOD

The "mobile oscillation derivativa balance" MOD is a dynamic test rig of a two dof-motion of forced oscillation type. The MOD was developed in a joint cooperation of the aircraft industries Dornier and the former VFW-Fokker with DFVLR and the flight technics institute of the TH Darmstadt (see [28] and [29]). One main feature is that MOD is transportable thus to be useful in various low speed wind tunnels.

Four types of motion (plunging, pitching, yawing and rolling) can independently be excited. Figure 4.5 shows the test setup with the support and the driving rod of the pitch and roll mode.

The vertical sting is mountable at a curved guide rail of the support for high angle-of-attack applications. The evaluation method is based upon 1st order Fourier analysis or regression theory (see [29]). With Fourier analysis the prescribed oscillation $\theta(t)$ is expanded according to

$$\theta(t) = \theta_{\sin}^{\textcircled{1}} \sin \omega t + \theta_{\cos}^{\textcircled{1}} \cos \omega t \quad \text{eq. (4.1)}$$

as well as the aerodynamic response $M(t)$

$$M(t) = M_{\sin}^{\textcircled{1}} \sin \omega t + M_{\cos}^{\textcircled{1}} \cos \omega t \quad \text{eq. (4.2)}$$

By the common used assumption

$$M(t) = f_0 + f_1 \dot{\theta}(t) + f_2 \ddot{\theta}(t) \quad \text{eq. (4.3)}$$

which means that the aerodynamic response is proportional to the elongation itself (stiffness derivatives) and to the velocity of the motion (damping derivatives), one is able to derive two algebraic equations for the unknown derivatives which are easily solved.

5. MISSILE TEST RESULTS AND COMPARISON WITH THEORETICAL PREDICTION

5.1 Missile Configurations

For dynamic wind tunnel tests at different Mach numbers and with different test rigs two tail-controlled missiles were selected (configurations see Fig. 5.1). They are composed of a cylindrical body of revolution with 17 calibers body length, blunt base and ogival nose, a cruciform wing and a cruciform tail, both in the plus position. Wing and tail are congruent in geometric shape with a scale factor of two. The lifting surfaces of the wind tunnel models were constructed from flat plates of 2 % profile thickness with wedge angles of 20 degs normal to all outer edges (see also [19]).

5.2 Free-Oscillation Results up to Ma = 3.0

Results of pitching moment damping of configuration RFL 122 obtained by the free oscillation apparatus at DFVLR Cologne are shown in Fig. 5.2.

The reduced frequency ω^* of the model varied from 0.006 to 0.025 and the Reynolds number Re_D from 0.4 Mio to 1.5 Mio depending on Mach number. The variation of the measured results with angle of attack is small at subsonic speeds whereas at supersonic speeds a considerable variation is to be found (for more details see [19].)

5.3 Forced-Oscillation Results at Transonic Speeds

5.3.1 Longitudinal Results

The stiffness and the damping derivatives of normal force and pitching moment were measured at the Mach numbers 0.7/0.9/1.05/1.2 with angles of attack up to 30 degs. The oscillation frequencies varied from 3 to 19 Hz corresponding to the reduced frequencies $\omega^* = 0.004/0.008/0.016/0.020$. The Reynolds number was $Re_D = 0.4$ Mio. A BL strip was positioned 2.5 D behind the nose tip. A comprehensive overview of the longitudinal results is to be found in [19] and [20]. The center of rotation D was at 10.872 D behind the nose at all tests. The measured dynamic derivatives are then transformed to a rotation axis at $x_{c.g.} = 10.5$ D to which all results shown in the figures are referred to. Some typical results are shown in Fig. 5.3 in comparison to free-oscillation measurements and theoretical predictions.

At every test point (defined by Mach number, angle of attack and reduced frequency) up to four independent measurements were made to detect the scatter of the resultant derivatives. The spread of the results in the order of 5 % of the maximum value was too small to be drawn. Therefore, the figures given in this paper show averaged values for each reduced frequency.

The angle of attack has large influence on all dynamic derivatives measured with the TRAD. At high angles-of-attack the configuration shows complicated flow conditions with line vortex shedding of body and vortex interaction phenomena observed in the water tunnels of Dornier [30] and VKI/Belgium [31]. For the general aspects of nonlinear effects at the high angle-of-attack range with respect to unsteady aerodynamics see also [32] and [33].

The influence of reduced frequency is almost negligible at $\alpha = 0$ deg and more pronounced at higher α , especially for configuration RFL 122 (see Fig. 5.3). The trend of the ω^* -influence is different for both configurations. The body-tail configuration RFL 102 shows a decrease with increased ω^* , whereas the reverse tendency holds if the cross wing is added.

On the whole, all results show that the extension of the pure DATCOM-methods by the cross-flow method (cf. sec. 3.3) considerably improves the theoretical predictions.

5.3.2 Lateral Results

For example, the roll-damping derivativum C_{l_p} of config. RFL 122 is shown for $M = 0.88$ and $\omega^* = 0.004$ and 0.012 (see Fig. 5.4 and ref. [34].)

The theoretical and experimental results are in quite good agreement even at higher angles of attack. The measured values represent the sum $C_{l_p} + C_{l_p} \sin \alpha$, which turn into the pure C_{l_p} -value at $\alpha = 0$ deg. At $\alpha = 30$ degs the measured results show a considerable scatter but the accumulation points give a reasonable tendency of the results. At each angle-of-attack four independent measurements were conducted and each result is drawn in the figures by a separate symbol. The scattering of the results at high angles-of-attack reveal the difficulty to measure a pure lateral derivativum like the roll damping when cross-coupling effects occur.

6. LONGITUDINAL DERIVATIVES AT HIGH ANGLES-OF-ATTACK

6.1 Oscillations in Pitch Near Stall Conditions

Various investigations describe the physical phenomena and the problems evaluating aerodynamic forces of configurations which are undergoing large amplitude pitching oscillations at high angles-of-attack (for example see [35], [36], [37]).

At higher angles-of-attack α_0 , where a configuration is just approaching stall conditions, forced oscillations of large amplitudes will create complicated flow-field patterns including oscillating separation bubbles or regions alternating between separation and reattachment of the flow.

During the upstroke of the harmonic oscillation, at the leading edge suction side of the wing separating vortices are normally created growing with increasing pitch angle. During the downstroke phase of the oscillation, at least partial reattachment of the flow occurs. Such a cycle of the harmonic oscillation also reveals some sort of hysteresis loops of characteristic variables which are measured.

The main features of publications in this field (see the papers quoted above) are investigations of the phenomenological flow description by means of flow visualization (e.g. dye layer or laser light sheet techniques) also including the measurement of c_p -coefficient as function of time.

The investigations shown in the present paper were confined to the apparatus and methods of the dynamic test rig MOD without use of flow visualization devices. Thus, the time history of the overall aerodynamic forces is recorded by a 6 component DMS strain gauge balance whatever flowfield pattern cycle will belong to.

6.2 Problems of Linear Evaluation Methods at High Angles-of-Attack

The static C_Z -curve (and the pitch-moment curve) of the Dornier fighter aircraft configuration versus the angle-of-attack is shown in Fig. 6.1. It is a typical function with linear slope at low α 's and strong curvature and drop of C_Z at stall conditions.

When a pitching motion experiment is conducted with large amplitudes (e.g. $A = \pm 5.25$ deg) according to $\theta(t) = \alpha_0 + A \sin \omega t$ with $\alpha_0 = 24$ deg it yields to a variation of θ of $18.75 \text{ deg} \leq \theta(t) \leq 29.25 \text{ deg}$.

The original evaluation method of the MOD dynamic test rig is derived from the linear lift curve slope assumption, using

$$C_Z(t) = C_{Z_0}(\alpha_0) + C_{Z_\alpha} \Delta\alpha(t) + C_{Z_{\dot{\alpha}}} \dot{\Delta\alpha}(t) + C_{Z_{\ddot{\alpha}}} \ddot{\Delta\alpha}(t) \quad \text{eq. (6.1)}$$

Thus, a nonlinear term $C_{Z_{\alpha^2}}(\Delta\alpha)^2$ is omitted as well as higher order terms of dynamic derivative coefficients (sect. 4.2.4). Besides, the simple assumption

$$\Delta\alpha(t) = \Delta\theta(t) + k_1 \Delta\dot{\theta}(t) \quad \text{eq. (6.2)}$$

of the oscillation induced overall angle-of-attack $\Delta\alpha$ is introduced.

From these assumptions, it can be concluded that the linear data evaluation procedure is - at high angles-of-attack - at best applicable to small amplitude oscillations (i.e. $A \sim \pm 1$ deg) whereas in the case of large amplitudes some extensions of the method seems to be needed.

6.3 Approach of an Evaluation Method with Nonlinear Terms Included

As shown above, one of the main shortcomings of the linear method is the lack of terms $C_{Z_{\alpha^2}}$ and $C_{m_{\alpha^2}}$ in the Taylor series of the Z-force and moreover the lack of some second order dynamic derivative like the mixed type $C_{Z_{\alpha\dot{\alpha}}}$ or the acceleration term $C_{Z_{\ddot{\alpha}}}$.

Therefore, a new approach was tried where the series expansion of C_Z according to eq. 2.3 was assumed. Thus, the additional set $C_{Z_{\alpha^2}}$, $C_{Z_{\dot{\alpha}^2}}$, $C_{Z_{\alpha\dot{\alpha}}}$ and $C_{Z_{\ddot{\alpha}}}$ of aerodynamic coefficients is included.

Furthermore, the correlation between the oscillation induces angle-of-attack $\Delta\alpha$ and the prescribed angle-of-attitude $\Delta\theta$ is extended by a term $k_2 \Delta\theta^2$

$$\Delta\alpha(t) = \Delta\theta(t) + k_1 \Delta\dot{\theta}(t) + k_2 \Delta\theta^2 \quad \text{eq. (6.3)}$$

where the coefficient k_2 is not a priori known but has to be determined by an additional condition.

The change of θ with time is given by

$$\theta(t) = \theta_0 + \Delta\theta(t)$$

and

$$\Delta\theta(t) = \theta_{\sin} \sin \omega t + \theta_{\cos} \cos \omega t = a \sin(\omega t + \phi) \quad \text{eq. (6.4)}$$

This function may also be expressed in complex notation

$$\Delta\theta = \Delta\theta_R + i \Delta\theta_I$$

with

$$\Delta\theta_R = a \cos(\omega t + \phi), \quad \Delta\theta_I = a \sin(\omega t + \phi)$$

The measured overall force $Z(t)$ during one oscillation cycle is expanded into a 2nd order Fourier series:

$$\Delta Z(t) = \Delta Z_0(t) + \Delta Z_{\cos}^{(1)} \cos \omega t + \Delta Z_{\cos}^{(2)} \cos 2\omega t + i (\Delta Z_{\sin}^{(1)} \sin \omega t + \Delta Z_{\sin}^{(2)} \sin 2\omega t) \quad \text{eq. (6.5)}$$

In general, the evaluation method of the dynamic test rig by Fourier analysis is based upon the expression of the independent Taylor series variables $\Delta\alpha$, $\Delta q = \Delta\theta$, $\Delta\dot{\alpha}$, $\Delta\dot{q}$, $(\Delta\alpha)'$, $\Delta\alpha\Delta q$ and $(\Delta q)'$ by the assumptions eq. 6.3 and eq. 6.5, subsequently setting up the identities of equivalent right and left hand side terms of the power series. This adequate relationship between both side coefficients leads to a linear system of equations with the static and dynamic derivatives as unknown variables.

Thus, a system of 5 equations is set up (absolute-, $\sin \omega t$ -, $\cos \omega t$ -, $\sin 2\omega t$ -, $\cos 2\omega t$ -terms) with the 7 'unknown' variables C_{Z_α} , $C_{Z_{\alpha'}}'$, C_{Z_q} , $C_{Z_{\dot{\alpha}}}$, $C_{Z_{\dot{q}}}$, $C_{Z_{\alpha q}}$ and $C_{Z_{q'}}'$.

The unfavourable situation of too many unknowns at a too small number of equations is overcome by introducing the static derivatives C_{Z_α} , $C_{Z_{\alpha'}}'$ from parallel static measurements adding these contributions to the right-hand sides.

The set of equations and its structure is shown in eq. A.2 and table A.3, Appendix. It is important that the $\dot{\alpha}$ -derivatives are defined by the second order terms $\sin 2\omega t$, $\cos 2\omega t$.

The additional assumption, that during one loop the mean absolute value of the Z-force should not be altered (i.e. the absolute term should vanish) leads to:

Real part:

$$a_{11} k_R C_{Z_\alpha} + [a_{12} + a_{13} (k_R - k_I)] C_{Z_{\alpha'}} = 0$$

Imaginary part:

$$a_{21} k_I C_{Z_\alpha} + [a_{22} + a_{23} (k_R k_I - k_I^2)] C_{Z_{\alpha'}} = 0$$

(coefficients a_{ij} see Append. eq. A.4).

Near stall conditions ($C_{Z_\alpha} \approx 0$) eq. 6.6 has a unique solution $k_2 = k_R + i k_I$.

} eq. (6.6)

6.4 A Fighter Aircraft Configuration Test at the MOD in the Dornier Windtunnel

6.4.1 Test Conditions

During tests from late 1986 to the mid of 1987 predesign configurations of the Eurofighter have been investigated at the MOD test rig. A light weight composite aircraft model (mass of 9 kg) has been built (aluminum spars plus CFK covers) with a flat plate wing during phase I and a profiled wing for phase II (see Fig. 6.2). According to trim, variable canard deflections ($\epsilon_C = 10/20$ deg) and leading- and trailing edge flaps ($\delta_H/\delta_F = 0/0$ deg, $36/20$ deg) were modeled. The MOD dynamic test rig demands an under-fuselage sting support but the static aerodynamics were compared with rearward base area sting support results (small differences for $25 \text{ deg} \leq \alpha \leq 35 \text{ deg}$).

Tests were conducted with pitch motion frequencies f of $0.89 \leq f \leq 3.27$ ($0.05 \leq \omega^* \leq 3.27$, $\omega^* = \frac{1}{V_\infty} \frac{V_\infty}{\omega}$). Values of $\omega^* = 0.3$ were obtained by decreasing V_∞ from $V_\infty \approx 47 \text{ m/s}$ to 28 m/s ($Re \sim 1.36 \cdot 10^6$ and $8 \cdot 10^5$). Angular motions $\theta(t) = \theta_0 + A \sin \omega t + B \cos \omega t$ were prescribed ($\theta_0 = 0/6/12/18/24/30$ deg and $A = 5.25/2.5/1.42$ deg). Friction effects of the eccentric drive cause small values B . (For test setup see photograph Fig. 6.3).

6.4.2 Test Results

Figure 6.4 shows lift- and pitching moment curves for $\theta_0 = \alpha_0 = 24$ deg and $A = \pm 2.5$ deg. A second order Fourier approximation is plotted in comparison to the scattering original signals. The obvious phase shifting of the aerodynamic response (to smaller times) relative to the motion is characteristic. During the upstroke phase, the induced Z-force loss is much smaller than the gain during the downstroke phase.

The asymmetric Z-force response also indicates a non-symmetric induced $\Delta\alpha$ -distribution as assumed by factor k_2 of eq.(6.3).

A comparison of the linear and the nonlinear data evaluation is shown in Fig. 6.5. The new approach suggests relative higher absolute $\dot{\alpha}$ -derivatives at smaller frequencies ω^* . Similar results are shown by the pitch moment derivatives (see Fig. 6.6).

The effects outlined above are even more evident at the high-amplitude oscillations with $A = \pm 5.25$ deg and $\alpha_0 = 24$ deg. A systematic nonlinearity of the Z-force and pitching moment curves is obtained characterized by the deviation of the measured signals from the 1st order Fourier approximation (Fig. 6.7). The

corresponding data evaluation results are drawn in Fig. 6.8 and Fig. 6.9. An example of the induced angle-of-attack history $\Delta\alpha(t)$ accord. to eq.(6.3) is shown in Fig. 6.10.

Relevant investigations of others ([35], [36]) report that even at very low reduced frequencies no quasi-steady states were achieved in the 3 dim. case. Furthermore, at high reduced frequencies, the pitching wing changed to downstroke before the separation vortices reached the fully developed stage.

This could be an explanation for the result of decreasing $\dot{\alpha}$ -derivativa amount at higher u^* near stall conditions.

In other words, it is assumed that the growing separation bubbles flowing downstream and inducing the effects of $\dot{\alpha}$ can fully influence at low frequency pitch rates, whereas at high frequencies they cannot be established fast enough to follow the oscillating model contour.

7. CONCLUSION

As shown, there are various methods available for the determination of dynamic derivatives of missiles and aircrafts. For the linear angle-of-attack range, theory seems more or less well established and sufficiently accurate predictions can be obtained by numerical or experimental methods. Within the theoretical field, the semiempirical methods can be updated by available static aerodynamic values whereas Panel- or Euler-methods have the advantage of a larger applicability to variable geometry of the configurations.

The theoretical attempts to the research in high angle-of-attack derivatives should necessarily be continued for the insight in the physical phenomena is partly still incomplete. There, the data evaluation methods of dynamic test rigs certainly are of particular interest.

8. REFERENCES

- [1] J. Nielsen
Missile Aerodynamics, Mc Graw-Hill Book Comp., New York, 1960, pp. 397-401 and pp. 409-416
- [2] M. Tobak
The use of the indicial function concept in the analysis of unsteady motions of wings and wing-tail combinations, NACA report 1188, NASA Ames, Moffet Field, Ca, USA
- [3] M. Tobak, L.B. Schiff
Aerodynamic Mathematical Modeling - Basic Concepts, 1981, AGARD-LS-114, Lect. no. 1, VKI Brussels, Belgium and NASA Ames, Moffet Field, Ca., USA
- [4] C.P. Schneider
Analytical determination of dynamic stability parameters, 1981, AGARD-LS-114, Lect. no. 12, VKI Brussels, Belgium and NASA Ames, Moffet Field, Ca., USA
- [5] C.P. Schneider, D. Nikolitsch
"Längsmomentenderivative von Flügeln bei hohen Anstellwinkeln in Unterschallströmung", 1976, BMV-FBWT 76-26
- [6] J.W.G. van Nunen, R. Roos, J.J. Meijer
Investigation of the unsteady airloads on wing-store configurations in subsonic flow, 1977, NLR MP 77025 U, Amsterdam
- [7] D.E. Hoak, R.D. Finck
DATCOM USAF Stability and Control Handbook, Wright-Patterson Air Force, Ohio, 1979, sec. 7.1-7.4
- [8] H. Fuchs, R. Kapp
Prediction of Dynamic Derivatives, March 1987, AGARD-FDP-VKI
Special Course "Missile Aerodynamics", VKI Brussels
- [9] F. Burhan
"Theoretische Bestimmung instationärer flugmechanischer Derivative von Deltaflügeln mit kleinem Seitenverhältnis", 1964, Bericht 64/43 des Instituts für Aerodynamik der DLR Braunschweig
- [10] H.C. Garner
"Multhopp's Subsonic Lifting-Surface Theory of Wings in Slow Pitching Oscillations", 1952, R&M No. 2885
- [11] H. Otto
"Theoretische Bestimmung instationärer flugmechanischer Derivative der Nickschwingung von Pfeil- und Deltaflügeln", Braunschweig, 1967, DLR-Forschungsbericht 67 - 26
- [12] K. Gersten
"Nichtlineare Tragflächentheorie insbesondere für Tragflügel mit kleinem Seitenverhältnis", Ing.-Archiv, Bd. 30, 1961, S. 431 - 452
- [13] J.D. Bird
Some Theoretical Low-Speed Span-Loading Characteristics of Swept Wings in Roll and Sideslip
1950, NACA TR 969

- [14] J. De Young
Theoretical Antisymmetric Span Loading for Wings of Arbitrary Plan Form at Subsonic Speeds 1951, NACA TR 1056
- [15] Anon.:
Royal Aeronautical Society Data Sheets-Aerodynamics, Vol. III (Aircraft S.06.03.01), 1957
- [16] S.M. Harmon und I. Jeffreys
Theoretical Lift and Damping in Roll of Thin Wings with Arbitrary Sweep and Taper at Supersonic Speeds. Supersonic Leading and Trailing Edges, 1950, NACA TN 2114
- [17] F.S. Malvestuto Jr., K. Margolis und H.S. Ribner
Theoretical Lift and Damping in Roll at Supersonic Speeds of Thin Sweptback Wings of Arbitrary Taper and Sweep at Supersonic Speeds. Subsonic Leading Edges and Supersonic Trailing Edges, 1950, NACA TR 970
- [18] L.H. Jorgensen
"Prediction of Static Aerodynamic Characteristics for Space-Shuttle-Like, and other Bodies at Angles of Attack from 0° to 180°", 1973, NASA-TN-D6996
- [19] H. Fuchs, E. Schmidt und F.-J. Niezgodka
Experimental and Theoretical Prediction of Dynamic Derivatives of Missiles, AGARD CP-336, 1982, p. 25-1 to 25-13
- [20] H. Fuchs
Dynamische Derivativa von Flugkörpern (Phase II) Auswertung der Windkanalmessungen und Vergleich mit theoretischen Ergebnissen, 1981, Dornier-Bericht 81BF/15B
- [21] K.J. Orlik-Rückemann
Review of Techniques for Determination of Dynamic Stability Parameters in Wind Tunnels, 1981 AGARD-LS 114, p. 3.1 - 3.28
- [22] E.S. Hanff
Direct Forced-Oscillation Techniques for the Determination of Stability Derivatives in Wind-Tunnels, 1981, AGARD-LS 114, p. 4.1 - 4.23
- [23] E. Schmidt
"Über die Erprobung der AVA-Derivatивawaage mit einem Alpha Jet Modell im Göttinger 3m-Windkanal", 1978, BMFT-FB W78-07
- [24] H. Fuchs
"Dynamische Derivativa von Flugkörpern (Phase I), Auswertung der Windkanalmessungen und Vergleich mit theoretischen Ergebnissen", Friedrichshafen, 1979, Dornier-Bericht Nr. Do 79/18
- [25] E. Schmidt
Introductory remarks on a new high-load oscillatory derivative balance for the DFVLR transonic wind tunnel 1981, AGARD-LS-114, comment to Lect. no. 4, VKI Brussels, Belgium
- [26] S.E. Gudmundson, L. Torngren
"Supersonic and Transonic Wind Tunnel Tests on a Slender Ogive-Cylinder Body Single and in Combination with Cruciform Wings and Tails of Different Sizes", 1971, FFA-Report AV-772
- [27] F.J. Niezgodka, H. Emunds
"Nickdämpfungsmessungen an mehreren Flugkörperkonfigurationen" Köln, 1980, DFVLR-Bericht Nr. IB 351-79/K1
- [28] X. Hafer
"Wind Tunnel Testing of Dynamic Derivatives in W. Germany"

J. v.d. Decken, E. Schmidt, B. Schulze
"On the Test Procedures of the Derivative Balances Used in W. Germany", AGARD CP-235, 1978, p. 5-1 to 6-17
- [29] O. Determann
"Ermittlung von dynamischen Derivativen der Längs- und Seitenbewegung mit der mobilen oszillierenden Derivatивawaage und systematische Untersuchungen zum Einfluß einiger Parameter auf die Ergebnisse", Darmstadt, 1978, DGLR-paper 78-115
- [30] O. Jacob
"Untersuchungen zur Flugkörperwirbelinterferenz (Phase I), Zusammenfassung und Auswertung der Ergebnisse", Friedrichshafen, 1978, Dornier-Bericht Do 78/19B
- [31] St. Hitzel, J. Muijlaert
"Untersuchungen zur Flugkörper-Wirbelinterferenz (Phase II)", Friedrichshafen, 1981, Dornier-Bericht 81 BF/10 8
- [32] K.J. Orlik-Rückemann, E.S. Hanff
"Dynamic Stability Parameters at High Angles of Attack", 1980, ICAS-80-7.1

- [33] G.N. Malcom
"Impact of High-Alpha Aerodynamics on Dynamic Stability Parameters of Aircraft and Missiles", 1981, AGARD-LS-114, Lect. no. 2
- [34] E. Schmidt, H. Fuchs
"Rolldämpfungsmessungen an zwei Flugkörper-Konfigurationen im Transkanal der DFVLR-AVA Göttingen", DGLR-Jahrestagung 1985, Vortrag Nr. 85-90, Bonn
- [35] M. Gad-el-Hak, Ch. Ho
"The pitching Delta Wing", 1985, AIAA Journal, Vol. 23, No. 11
- [36] H. Triebstein
"Steady and Unsteady Transonic Pressure Distributions on NACA 0012", 1986, J. Aircraft, Vol. 23, No. 3
- [37] W. Geissler
"Unsteady Boundary-Layer Separation on Airfoils Performing Large-Amplitude Oscillations - Dynamic Stall -", 1985, AGARD-CP-386
- [38] J.M. Walker, H.E. Helin, J.H. Strickland
"An Experimental Investigation of an Airfoil Undergoing Large-Amplitude Pitching Motions", 1985, AIAA Journal, Vol. 23, No. 8
- [39] R.G. den Boer, A.M. Cunningham, Jr.
"A Windtunnel Investigation at Low Speed of the Flow about a Straked Delta Wing, Oscillating in Pitch", 1987, AIAA paper

9. APPENDIX

2nd order Taylor series expansion of function $L(u, w, q, \dot{u}, \dot{w}, \dot{q})$ with respect to small perturbations:

$$\begin{aligned}
 L(u+\Delta u, w+\Delta w, q+\Delta q, \dot{u}+\Delta \dot{u}, \dot{w}+\Delta \dot{w}, \dot{q}+\Delta \dot{q}) &= L(u, w, q, \dot{u}, \dot{w}, \dot{q}) + \\
 &+ \underbrace{\frac{\partial L}{\partial u} \Delta u + \frac{\partial L}{\partial w} \Delta w + \frac{\partial L}{\partial q} \Delta q}_{= \frac{\partial L}{\partial \alpha} \Delta \alpha} + \underbrace{\frac{\partial L}{\partial \dot{u}} \Delta \dot{u} + \frac{\partial L}{\partial \dot{w}} \Delta \dot{w} + \frac{\partial L}{\partial \dot{q}} \Delta \dot{q}}_{= \frac{\partial L}{\partial \dot{\alpha}} \Delta \dot{\alpha}} + \\
 &+ \frac{1}{2} \frac{\partial^2 L}{\partial u^2} \Delta u^2 + \frac{1}{2} \frac{\partial^2 L}{\partial w^2} \Delta w^2 + \frac{1}{2} \frac{\partial^2 L}{\partial q^2} \Delta q^2 + \frac{1}{2} \frac{\partial^2 L}{\partial \dot{u}^2} \Delta \dot{u}^2 + \frac{1}{2} \frac{\partial^2 L}{\partial \dot{w}^2} \Delta \dot{w}^2 + \frac{1}{2} \frac{\partial^2 L}{\partial \dot{q}^2} \Delta \dot{q}^2 + \\
 &+ \frac{1}{2} \frac{\partial^2 L}{\partial \alpha^2} \Delta \alpha^2 + \frac{1}{2} \frac{\partial^2 L}{\partial \dot{\alpha}^2} \Delta \dot{\alpha}^2 + \\
 &+ \frac{\partial^2 L}{\partial u \partial w} \Delta u \Delta w + \frac{\partial^2 L}{\partial u \partial q} \Delta u \Delta q + \frac{\partial^2 L}{\partial u \partial \dot{u}} \Delta u \Delta \dot{u} + \frac{\partial^2 L}{\partial u \partial \dot{w}} \Delta u \Delta \dot{w} + \frac{\partial^2 L}{\partial u \partial \dot{q}} \Delta u \Delta \dot{q} + \\
 &+ \frac{\partial^2 L}{\partial w \partial q} \Delta w \Delta q + \frac{\partial^2 L}{\partial w \partial \dot{u}} \Delta w \Delta \dot{u} + \frac{\partial^2 L}{\partial w \partial \dot{w}} \Delta w \Delta \dot{w} + \frac{\partial^2 L}{\partial w \partial \dot{q}} \Delta w \Delta \dot{q} + \\
 &+ \frac{\partial^2 L}{\partial q \partial \dot{u}} \Delta q \Delta \dot{u} + \frac{\partial^2 L}{\partial q \partial \dot{w}} \Delta q \Delta \dot{w} + \frac{\partial^2 L}{\partial q \partial \dot{q}} \Delta q \Delta \dot{q} + \\
 &+ \frac{\partial^2 L}{\partial \dot{u} \partial \dot{w}} \Delta \dot{u} \Delta \dot{w} + \frac{\partial^2 L}{\partial \dot{u} \partial \dot{q}} \Delta \dot{u} \Delta \dot{q} + \\
 &+ \frac{\partial^2 L}{\partial \dot{w} \partial \dot{q}} \Delta \dot{w} \Delta \dot{q}
 \end{aligned}$$

equation A.1

	STATIC DERIVATIVE		DYNAMIC DERIVATIVE				
	$\Delta \alpha$	$\Delta \dot{\alpha}$	Δq	$\Delta \dot{q}$	$\Delta a \Delta q$	$\Delta \dot{q}$	$\Delta \ddot{q}$
Absolute term	k_1	k_1	-	-	k_1	-	-
$\sin \omega t$	k_1	k_1	-	-	k_2	-	-
$\cos \omega t$	k_1	k_1	-	-	k_2	-	-
$\sin 2\omega t$	k_2	k_2	-	-	k_1	-	-
$\cos 2\omega t$	k_2	k_2	-	-	k_1	-	-

Table A.3: Structure of the derivative coefficient matrix terms due to k_1 , k_2 and terms due to θ ($= K$)

	C_{Z_q}	$C_{Z_{\dot{\alpha}}}$	$C_{Z_{\alpha q}}$	$C_{Z_{\dot{q}}}$	$C_{Z_{q^2}}$	Right hand sides
Absolute-	-	-	$\omega^* \left[\frac{1}{2} (\theta_{\cos}^2 + k_1 \omega \theta_{\sin}) \theta_{\sin} - \frac{1}{2} k_R (\theta_{\sin}^2 + \theta_{\cos}^2) \theta_{\cos} \right] F^2$	-	$\frac{1}{4} \omega^* (\theta_{\sin}^2 + \theta_{\cos}^2) F^2$	R_0
sin ωt -	$-\omega^* \theta_{\cos} F$	$-\omega^* \theta_{\cos} F$	$\frac{3}{8} k_R \omega^* (\theta_{\sin}^2 - \theta_{\cos}^2) \theta_{\cos} F^2$	$-\omega^* \theta_{\sin} F$	-	R_1
cos ωt -	$\omega^* \theta_{\sin} F$	$\omega^* \theta_{\sin} F$	$\frac{3}{8} k_R \omega^* (\theta_{\sin}^2 - \theta_{\cos}^2) \theta_{\sin} F^2$	$-\omega^* \theta_{\cos} F$	-	R_2
sin $2\omega t$ -	-	$\omega^* k_R (\theta_{\sin}^2 - \theta_{\cos}^2) F$	$\omega^* \left[\frac{1}{2} (\theta_{\sin}^2 - \theta_{\cos}^2) - k_1 \omega \theta_{\sin} \theta_{\cos} \right] F^2$	-	$-\omega^* \theta_{\sin} \theta_{\cos} F^2$	R_3
cos $2\omega t$ - terms	-	$2\omega^* k_R \theta_{\sin} \theta_{\cos} F$	$\omega^* \left[\theta_{\sin} \theta_{\cos} + \frac{1}{2} k_1 \omega (\theta_{\sin}^2 - \theta_{\cos}^2) \right] F^2$	-	$\frac{1}{2} \omega^* \theta_{\sin}^2 - \theta_{\cos}^2 F^2$	R_4

With $F = \frac{180}{\pi}$, $G = \frac{g}{q=S}$ and the right hand sides according to:

$$\begin{aligned}
 R_0 &= G \cdot \Delta Z_0 - f_{01}(k_R, \theta_{\sin}, \theta_{\cos}) C_{Z_{\alpha}} - f_{02}(k_1, k_R, \theta_{\sin}, \theta_{\cos}) C_{Z_{\alpha'}}, \\
 R_1 &= G \cdot \Delta Z_{\sin}^1 - f_{11}(k_1, \theta_{\sin}, \theta_{\cos}) C_{Z_{\alpha}} - f_{12}(k_1, k_R, \theta_{\sin}, \theta_{\cos}) C_{Z_{\alpha'}}, \\
 R_2 &= G \cdot \Delta Z_{\cos}^1 - f_{21}(k_1, \theta_{\sin}, \theta_{\cos}) C_{Z_{\alpha}} - f_{22}(k_1, k_R, \theta_{\sin}, \theta_{\cos}) C_{Z_{\alpha'}}, \\
 R_3 &= G \cdot \Delta Z_{\sin}^2 - f_{31}(k_R, \theta_{\sin}, \theta_{\cos}) C_{Z_{\alpha}} - f_{32}(k_1, k_R, \theta_{\sin}, \theta_{\cos}) C_{Z_{\alpha'}}, \\
 R_4 &= G \cdot \Delta Z_{\cos}^2 - f_{41}(k_R, \theta_{\sin}, \theta_{\cos}) C_{Z_{\alpha}} - f_{42}(k_1, k_R, \theta_{\sin}, \theta_{\cos}) C_{Z_{\alpha'}}.
 \end{aligned}$$

Eq. A.2: System of equations for higher order MOO data evaluation

$$\begin{aligned}
 a_{11} &= \frac{1}{2} (\theta_{\cos}^2 - \theta_{\sin}^2) F & a_{12} &= \frac{1}{4} (1+k_1 \omega^*) (\theta_{\cos}' - \theta_{\sin}') F^2 & a_{13} &= \frac{3}{16} (\theta_{\cos}^* + \theta_{\sin}^* - 2\theta_{\sin}' \theta_{\cos}') F \\
 a_{21} &= \frac{1}{2} (\theta_{\cos}^2 - \theta_{\sin}^2) F & a_{22} &= 0 & a_{23} &= \frac{3}{8} (\theta_{\cos}^* + \theta_{\sin}^* - \frac{2}{3} \theta_{\sin}' \theta_{\cos}') F
 \end{aligned}$$

Eq. A.4: Coefficients a_{ij} for determination if k , according to eq. 6.6

10. ILLUSTRATIONS

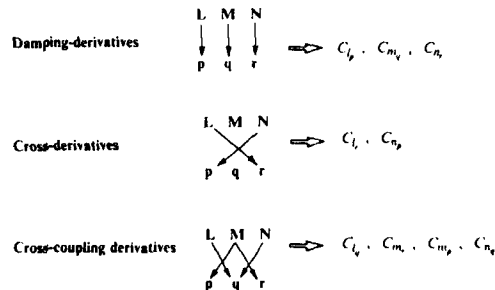


Fig. 2.1: The classification of dynamic derivatives

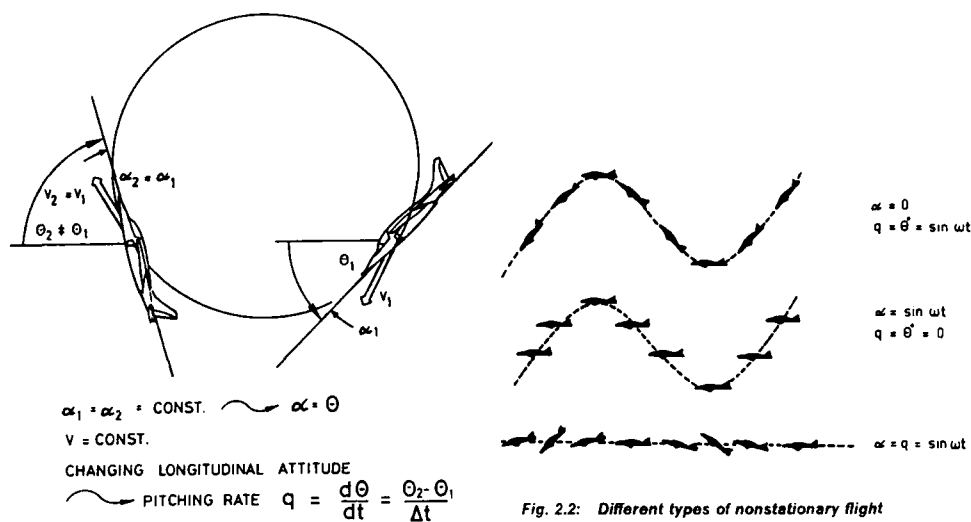
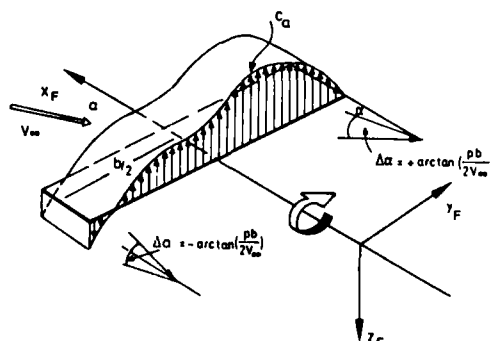


Fig. 2.2: Different types of nonstationary flight

WING SHAPE		F2	F2 exp	L2	L2 exp
l	60	50	3.50	2.50	
Δ	1.0	0.857	1.17	0.857	
λ	0.33	0.4	0.286	0.4	

DERIVATIVE	WING / TAIL	SLENDER BODY THEORY (NIELSEN)	DATCOM	SLENDER BODY THEORY (BURHAN)	GARNER	GERSTEN-SCHNEIDER-NIKOLITSCH
C_{zq}	F2	-85.3	-33.0	-104.0	-132.0	-105
	L2	-26.2	-4.7	-23.0	-25.4	-22
	F2 exp.	-52.0	-21.1	-53.0	—	—
	L2 exp	-6.5	-2.4	-6.6	—	—
C_{mq}	F2	-170.7	-51.7	-183.0	196.7	204
	L2	-41.3	-4.1	-23.8	22.0	-25
	F2 exp	-112.7	-33.0	-83.0	—	—
	L2 exp	-7.0	-2.1	-5.2	—	—

Fig. 3.1: Wing-alone contributions according to different theoretical methods

Fig. 3.2: Roll-rate induced wing lift distribution c .

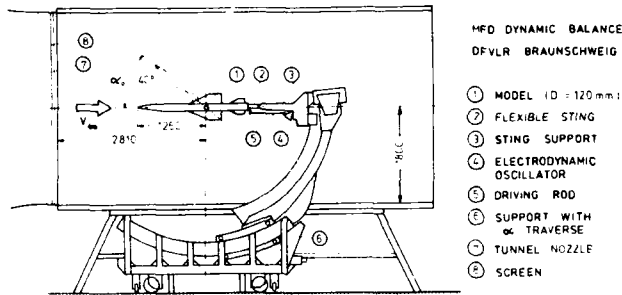


Fig. 4.1: The MFD dynamic test rig of the DFVLR Braunschweig

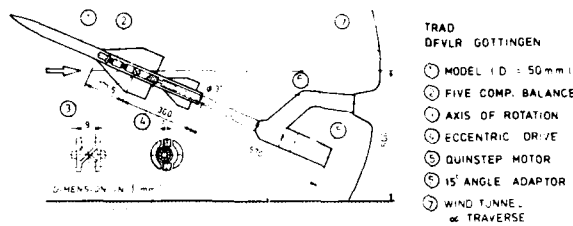


Fig. 4.2: The high-load derivative balance TRAD of the DFVLR-AVA Göttingen

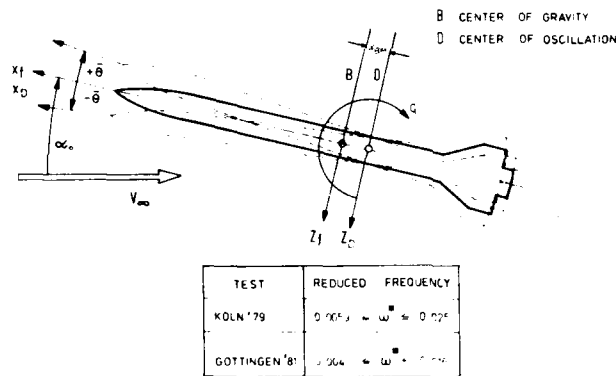


Fig. 4.3: The principle of 1-dof pitching mode

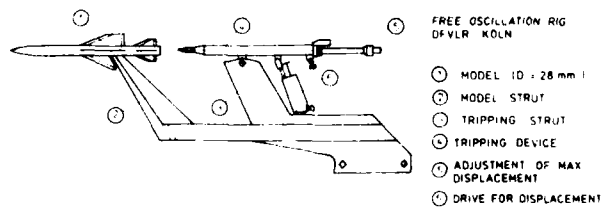


Fig. 4.4: The free oscillation type balance of DFVLR Cologne

Fig. 4.5: The mobile oscillation derivative balance MOD

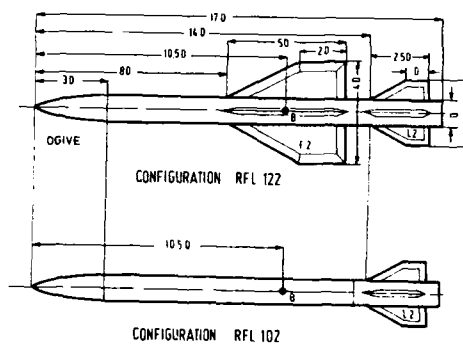


Fig. 5.1: The Dornier standard missile configurations

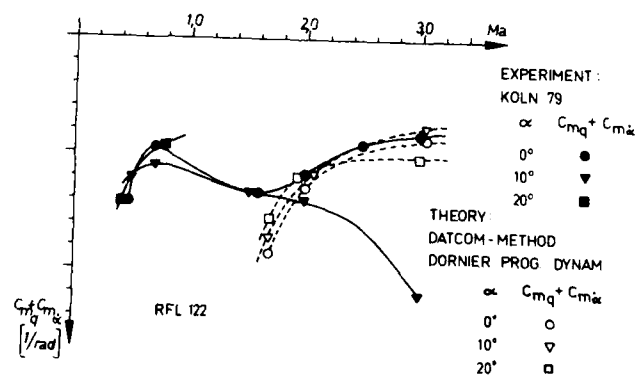


Fig. 5.2: Pitching moment results $C_{m_{\alpha}} + C_{m_{\dot{\alpha}}}$ of the Dornier conf. RFL122 with free oscillation tests at the supersonic wind tunnel of the DFVLR Cologne

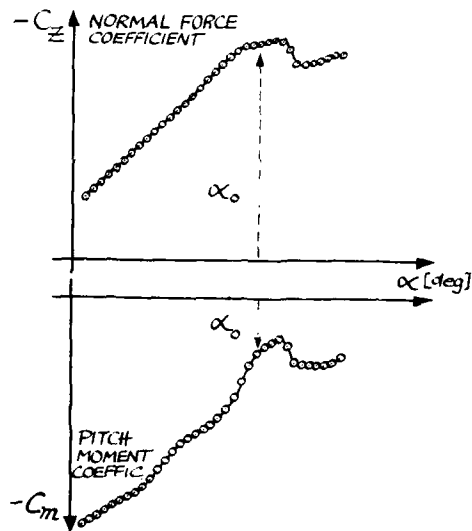
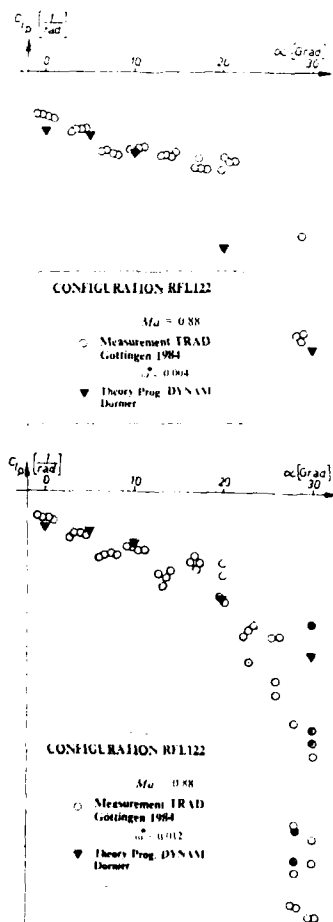
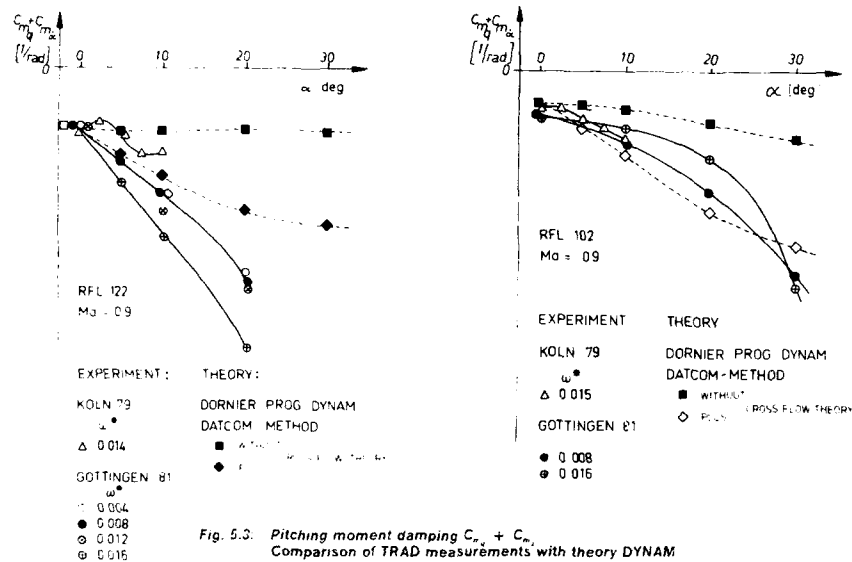


Fig. 6.1: Typical lift- and pitch moment curve of a modern delta wing fighter aircraft

Fig. 5.4: Roll damping $C_{l\dot{\alpha}}$ of Dornier config. RFL122 (at left)
 Comparison of TRAD measurement with theory
 Different reduced frequency ω assumed

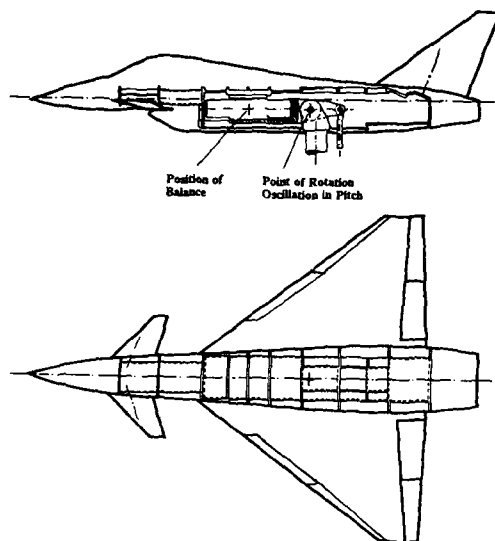


Fig. 6.2: Predesign configurations of the new Eurofighter



Fig. 6.3: Fighter aircraft configuration at the TRAD test setup in the Dornier wind tunnel

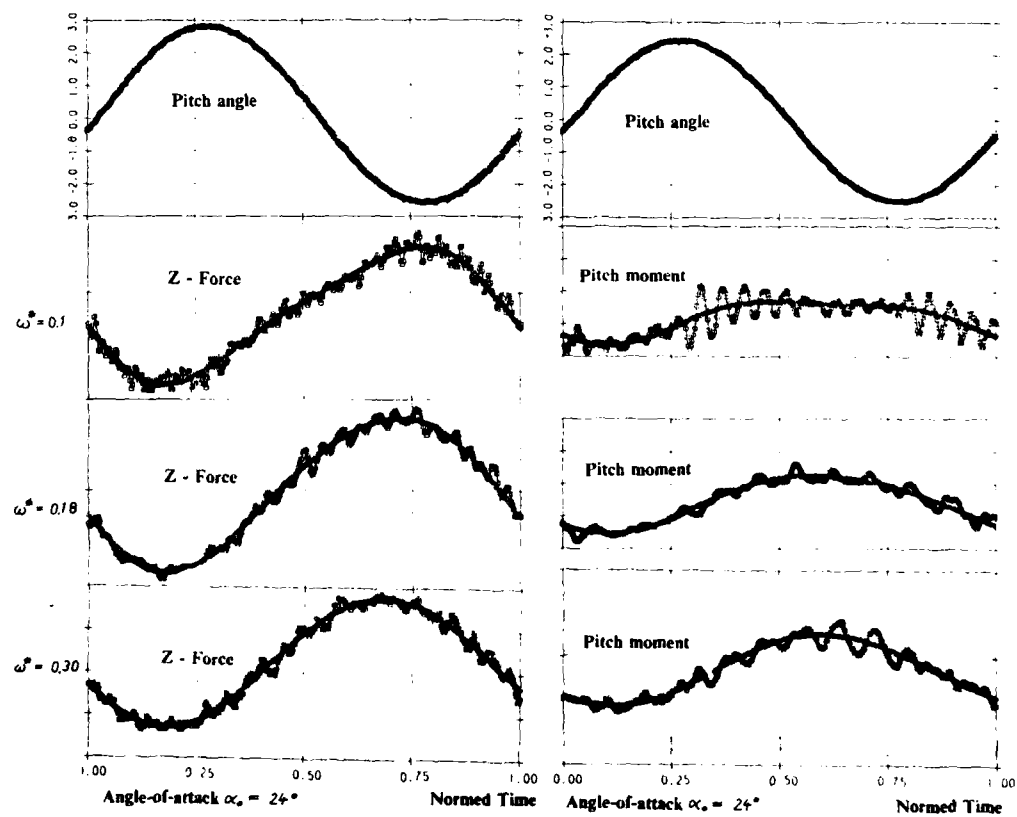


Fig. 6.4: Lift- and pitching moment variation of a fighter aircraft configuration at harmonic pitching oscillations (amplitude $A = 2.5$ deg)

DYNAMIC DERIVATIVES OF EFA CONFIG.
MOD TEST-RIG, DORNIER WINDTUNNEL
ALPHA = 24 DEGS, AMPL = 2.5 DEGS,
CANARD-ANGLE = -20 DEGS

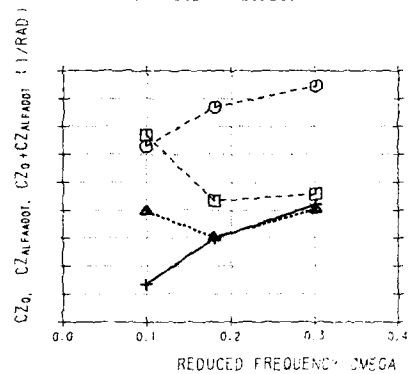


Fig. 6.5: Dynamic derivatives $C_{z_0} + C_{z_0}\omega$ of a fighter aircraft configuration undergoing motions at $\alpha_s = 24$ deg. Comparison of linear and nonlinear data evaluation

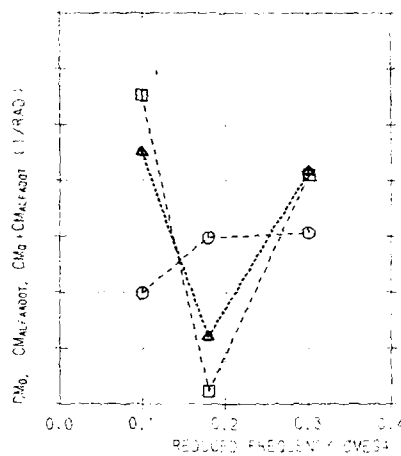


Fig. 6.6: Dynamic derivatives $C_{m_0} + C_{m_0}\omega$ of a fighter aircraft configuration undergoing motions at $\alpha_s = 24$ deg. Comparison of linear and nonlinear data evaluation amplitude $A = 2.5$ deg. $\omega = 0.1 - 0.3$

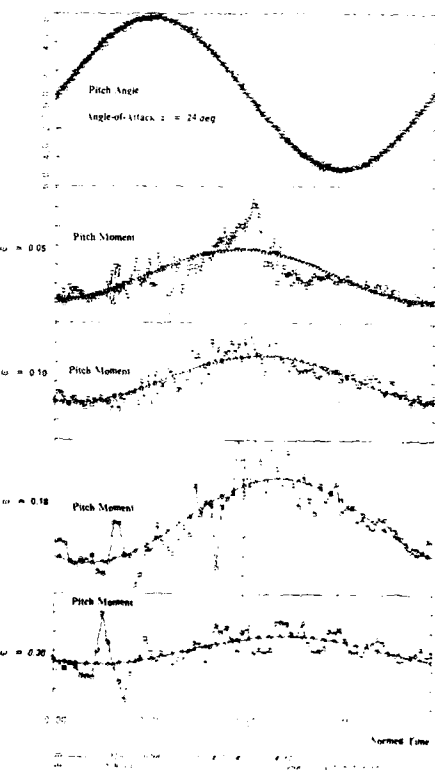
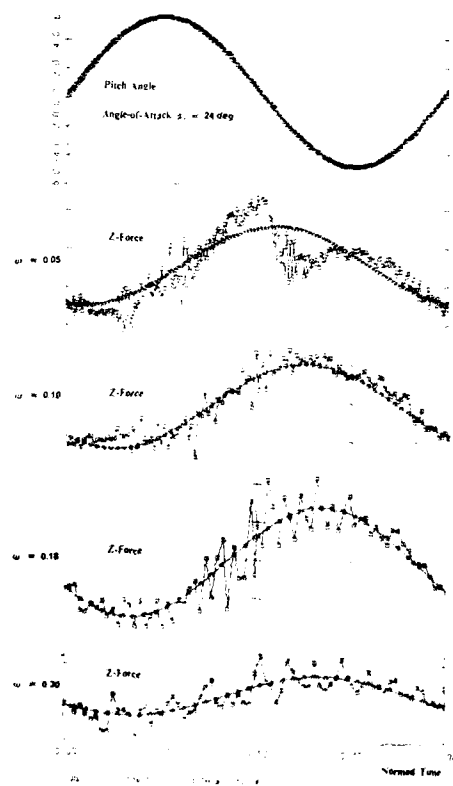


Fig. 6.7: LIFT- and pitching moment variation of a fighter aircraft configuration at harmonic pitching oscillations (amplitude $A = 5.25$ deg)

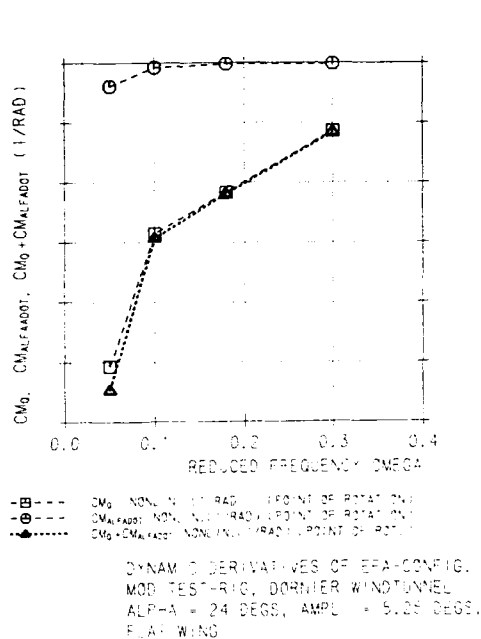


Fig. 6.8: Dynamic derivatives $C_{\dot{\alpha}} + C_{\dot{\alpha}}$ of a fighter aircraft configuration undergoing motions at $\alpha_s = 24$ deg. Comparison of linear and nonlinear data evaluation amplitude $A = 5.25$ deg, $\omega' = 0.05 - 0.3$

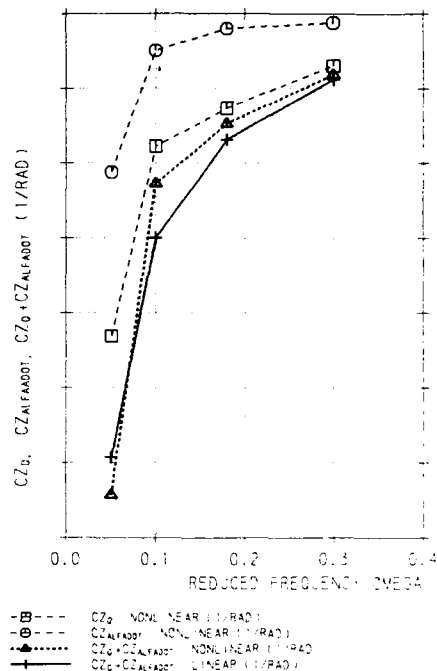


Fig. 6.9: Dynamic derivatives $C_{\dot{\alpha}} + C_{\dot{\alpha}}$ of a fighter aircraft configuration undergoing motions at $\alpha_s = 24$ deg. Comparison of linear and nonlinear data evaluation amplitude $A = 5.25$ deg, $\omega' = 0.05 - 0.3$

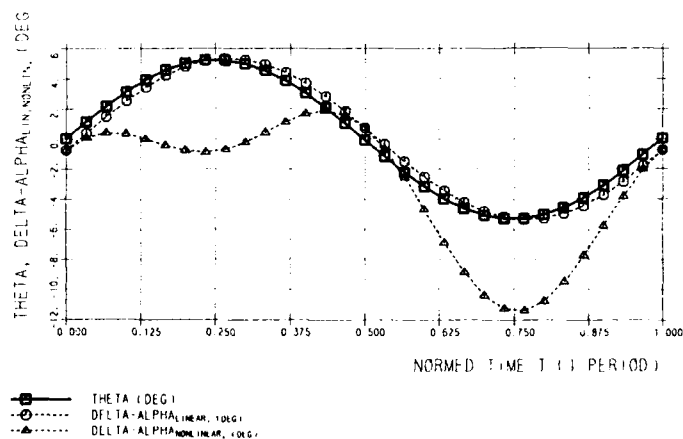


Fig. 6.10: Time-history of induced $\Delta\alpha$ according to eq.(6.3) for the pitching fighter aircraft ($A = 5.25$ deg, $\omega' = 0.05$)

PREDICTION OF TACTICAL MISSILE DYNAMICS

L. E. Ericsson
Lockheed Missiles & Space Company, Inc.
Sunnyvale, California, USA

Abstract

The aerodynamic information needed for preliminary design of tactical missiles has always been obtained through the combined use of theory and experiments. In regard to the static aerodynamics this has resulted in a prediction capability that often is satisfactory for preliminary design. However, the vehicle dynamics cannot be predicted with the same confidence, especially not at the high angles of attack where high performance missiles often must operate. In this case we are still dependent upon continuous efficient interaction between theoretical and experimental methods. The paper delineates the limitations of both methods and describes how to circumvent them in order to predict tactical missile dynamics over the required range of operational parameters.

Nomenclature

c reference length, $c = d$ except $c = d_B$ or $c = l$ for cones and ogives
 D, d cylinder diameter in 2D and 3D flow, resp.
 d_B base diameter
 l total body length
 l_0 sharp cone body length
 l' cross-sectional lift: coefficient
 $c_l = l' / (\rho_\infty U_\infty^2 / 2) D$
 M Mach number
 M_p pitching moment, coefficient $C_m = M_p / (\rho_\infty U_\infty^2 / 2) (\pi c^2 / 4) c$
 N normal force, coefficient $C_N = N / (\rho_\infty U_\infty^2 / 2) (\pi c^2 / 4)$
 P static pressure: coefficient $C_p = (P - P_\infty) / (\rho_\infty U_\infty^2 / 2)$
 \dot{D} rotation or spin rate
 q rigid body pitch rate
 Re Reynolds number, usually $Re = Re_c = U_\infty c / \nu_\infty$ or $Re_D = U_\infty D / \nu_\infty$
 t time
 U_∞ freestream velocity
 U_w wall velocity
 x axial distance from nose
 Y sideforce: coefficient $C_Y = Y / (\rho_\infty U_\infty^2 / 2) (\pi c^2 / 4) c$; $c_Y = dC_Y / d\epsilon$
 α angle of attack
 γ tilt angle of symmetric vortex couple (Fig. 28)
 Δ increment and amplitude
 θ body perturbation in pitch
 θ_A apex half angle
 θ_C cone half angle

- ν kinematic viscosity of air
 ξ dimensionless x-coordinate, $\xi = x/c$
 ρ density of air
 σ total angle of attack (Fig. 28)
 φ peripheral angle, $\varphi = 0$ at the stagnation point
 ψ coning angle

Subscripts

- A apex
 AV asymmetric vortices
 B base
 c cone
 CG center of gravity
 F flare or fins
 SV symmetric vortices
 tr transition
 UV unsteady vortices
 v vortex
 W wall
 ∞ free stream conditions

Superscripts

- i induced, e.g. $\Delta^i C_{m\alpha}$ = transition-induced contribution to $C_{m\alpha}$

Derivative Symbols

$$\begin{aligned}
 \dot{\alpha} &= \frac{\partial \alpha}{\partial t}, \quad \ddot{\psi} = \partial^2 \psi / \partial t^2 \\
 C_{m\alpha} &= \frac{\partial C_m}{\partial \alpha} \\
 C_{mq} &= \frac{\partial C_m}{\partial \left(\frac{q}{U_\infty}\right)}; \quad C_{m\dot{\alpha}} = \frac{\partial C_m}{\partial \left(\frac{c\dot{\alpha}}{U_\infty}\right)}; \quad C_{m\theta} = \frac{\partial C_m}{\partial \left(\frac{c\dot{\theta}}{U_\infty}\right)} \\
 C_{m\dot{\theta}} &= C_{m\dot{\alpha}} + C_{mq}; \quad \text{integrated mean value measured in a dynamic test}
 \end{aligned}$$

INTRODUCTION

Extensive efforts have been made during recent years to develop rapid computational means for design of tactical missiles. They have almost entirely been concerned with the static aerodynamics, the goal being to develop a missile DATCOM program that can provide the aerodynamic characteristics by using component build-up techniques, e.g. as is described in Ref. 1. The unsteady aerodynamics have received much less attention, although rapid computational means have been developed for conventional missile geometries for the case that viscous flow effects are of insignificant magnitude (Ref. 2).

When viscous flow effects are important, experimental and theoretical methods are usually combined to provide the build-up of the static aerodynamic characteristics. It is the purpose of the present paper to outline how a similar build-up of the dynamic characteristics can be accomplished. As the static aerodynamic components usually are available through the efforts to provide the missile designer with the static loads, and as it is exceedingly difficult and expensive to obtain the dynamic component build-up through the use of experiments, the method described here builds on the use of available static components in an analysis that relates the unsteady aerodynamics to the static aerodynamic characteristics. The required use of experimental results, obtained on subscale models, brings on the usual problems of support interference (Refs. 3 and 4) and

Reynolds number scaling (Refs. 5-8). In addition to reviewing the present state of the art in the prediction of tactical missile dynamics, the present paper is aimed at extending the guidelines of Ref. 7 to include the high angles of attack where the aerodynamics are highly nonlinear and often exhibit strong cross-coupling between lateral and longitudinal degrees of freedom even at zero sideslip (Ref. 9).

DISCUSSION

With some exceptions, i.e., when the nose is very blunt (Ref. 10) or the base has a rounded shoulder (Refs. 11 and 12), viscous flow effects are usually negligible for perturbations around $\alpha=0$. Consequently, inviscid flow concepts can be used to obtain the needed vehicle dynamics.

Inviscid Flow

In order to improve the accuracy of the prediction of the pitch damping of tactical missiles (Ref. 13) a study was performed (Ref. 14) in which slender body and Newtonian theories were modified to provide rapid computational means for axi-symmetric, finned bodies. The modified slender body theory (Ref. 15) provides prediction in the speed range $0 < M_\infty < 5$ and a generalization (Ref. 16) of the embedded Newtonian theory (Ref. 17) in the range $M_\infty < M_\infty < \infty$, where M_∞ is the lower limit for application of embedded Newtonian flow concepts. A straight line fairing is used between $M_\infty = 1$ and $M_\infty = M_\infty$.

In Figs. 1-5 the predictions provided by this theory, denoted PRESENT THEORY, are compared with experimental results and other theoretical predictions for axi-symmetric bodies of various geometries. The rapid prediction by the "present theory" (Ref. 14) obviously gives a satisfactory prediction of the measured pitch damping. According to the experimental results (Ref. 18) in Fig. 5, the predictions for $\alpha = 0$ apply to a substantial angle-of-attack range around $\alpha = 0$. Not until forebody flow separation occurs at higher α , with associated free body vortices, will the nonlinear flow effects become substantial. No systematic nonlinear effect can be discerned above the data scatter in Fig. 5.

Lifting-Surface Effects

In Ref. 14 rapid computational means are derived for the effect of low aspect ratio lifting surfaces on the inviscid unsteady aerodynamics at $\alpha = 0$. Figures 6 and 7 show that the predictions are in good agreement with experimental results at subsonic (Ref. 18) and supersonic (Ref. 19) Mach numbers, respectively. Even in the case of rather non-conventional (tactical missile) geometries does the prediction agree rather well with experiment, as is illustrated in Fig. 8 for the MK76 Practice Bomb (Ref. 20) and in Fig. 9 for the MK82 Mod 2 Bomb (Ref. 21). The deviation at $M_\infty = 1$ in Fig. 9 between inviscid prediction and experiment is probably caused by separated flow on the boat-tailed aft body, induced by the strong shocks generated by the cruciform fins.

Nonlinear Inviscid Flow Effects

At high supersonic and hypersonic speeds the nose-bluntness-induced bow shock curvature generates an inviscid non-uniform flow region, the "entropy-wake", in which the aft body is embedded (Ref. 17 and Fig. 10). Figure 11 shows a comparison between the predicted (Refs. 16 and 22) and measured (Ref. 23) effect of nose-bluntness on slender cone pitch damping at $M_\infty = 6.85$. The figure shows that a dramatic reduction of dynamic stability occurs for the 10° cone when the nose bluntness is increased from 10 to 20 percent. It is obvious from the flow sketch in Fig. 10 that aerodynamic characteristics, such as the pitch damping, will vary nonlinearly with angle of attack, as is also verified by both theory (Ref. 16) and experiment (Ref. 23) according to the results in Fig. 12a for a 20° blunt 10° cone and in Fig. 12b for a cylinder-flare body, the hyperballistic shape (HBS) model.

Viscous Flow Effects at Low Alpha

At high subsonic and transonic speeds, nose bluntness can generate a viscous non-uniform flow field, a viscous wake similar to the "entropy wake" discussed earlier (Ref. 10 and Fig. 13). In both cases the high radial velocity gradients in the wake cause large forces to be generated on the embedded aft body through a change of its location in the wake. This wake-induced aft body force is statically stabilizing. However, because of the time lag Δt occurring before a translation of the nose at time $t - \Delta t$ has resulted in a change of the wake relative to the aft body (see inset in Fig. 14), the wake-induced force component ΔC_{NF} on the aft flare is dynamically destabilizing (Ref. 10). In contrast to the case of the entropy wake, the viscous wake effect cannot yet be computed by theoretical means. Consequently, static experimental results are used to determine the magnitude of ΔC_{NF} before the unsteady aerodynamic pitch derivatives can be determined (Ref. 10). The prediction obtained in this manner is in good agreement with dynamic experiment. Especially noteworthy is the prediction of the separation-induced negative pitch damping at subsonic speeds (Fig. 14). In similar fashion the loss of dynamic stability at $M_\infty = 0.9$ of a hemisphere-cylinder body, observed experimentally (Ref. 24), could be predicted (Ref. 25 and Fig. 15), in contrast to what is the case for a purely theoretical method (Ref. 26).

Effect of boundary layer transition

A more subtle viscous flow effect is that of boundary layer transition, which has been found to be surprisingly large, as is illustrated by experimental results for a pointed 10 deg. cone (Ref. 27 and Fig. 16). When transition occurs on the aft body (aft of C.G.), it generates a negative normal force component (ΔC_N) which causes a decrease of the static stability. Due to the effect of the convective flow time lag, the dynamic effect is of the opposite sign, as was the case for the nose-induced flow separation effect (see inset in Fig. 14), and ΔC_N causes an increase of the dynamic stability. Using the experimentally determined transition movement (Ref. 27 and Fig. 17), the measured static effect of transition could be predicted by considering the different growth rates for turbulent and laminar boundary layers (Refs. 28 and 29). By accounting for the convective time lag effect, the measured (Ref. 27) maximum effect of transition on the pitch damping could be predicted (Ref. 29 and Fig. 18). That the transition-induced effect on the pitch damping inferred from experimental results, such as those in Fig. 16, is indeed correct is confirmed by direct measurements for a 15% blunt 7 deg. cone (Ref. 30 and Fig. 19).

Similar transition-induced effects have been observed for ogive-cylinder bodies (Ref. 31 and Fig. 20). At these supersonic Mach numbers the boat-tail does not have any significant effect (Ref. 11), as is also verified by the experimental results (Ref. 32) in Fig. 21. The data points marked by x are the plateau-values below the Re-range for transition in Fig. 20. They agree well with inviscid theory (Refs. 14 and 15).

Following standard engineering practice the experimental results (Ref. 32) in Fig. 21 were used to formulate computational means by which the aerodynamics of future, similar missile designs could be predicted (Ref. 33). This so-called Spinner code gives, of course, predictions that are in agreement with the experimental results (Ref. 25) for the $l/d = 5$ ogive-cylinder (Fig. 22a), as it was the data base used to develop the Spinner code. However, when applied to a shorter, $l/d = 3$, ogive-cylinder, the Spinner code greatly overpredicts the experimentally observed pitch damping (Fig. 22b). The reason for this is that the short body never experienced any boundary layer transition effects (Ref. 34).

The fact that the inviscid theory (Refs. 14 and 15) overpredicts the measured damping at subsonic speeds could also be caused by transition effects. Based upon the results (Ref. 35) in Fig. 23 one would expect transition on the 10 deg. sharp cone to move forward of the oscillation center when going from supersonic to subsonic Mach numbers. In that case the transition effect is reversed (Ref. 36 and Fig. 24) and decreases rather than increases the pitch damping.

In Refs. 14 and 15 a straight line fairing is used between the slender body value at $M_\infty = 1$ and the lowest supersonic Mach number to which the hypersonic embedded Newtonian theory (Ref. 16) can be extended. Consequently, there is a need for a theory, such as the one presented in Ref. 37, which specifically addresses the problem of predicting the vehicle dynamics at low to moderate supersonic Mach numbers. Based upon the comparisons made in Fig. 25 between experimental results (Ref. 32) and theoretical predictions (Refs. 14, 15, 37 and 38), one is, however, reluctant to substitute the approximation used in Ref. 15 with the computational method presented in Ref. 37.

Viscous Flow Effects at High Alpha

As a slender body of revolution is pitched through the angle-of-attack range from 0 to 90 deg, it experiences four distinct flow patterns that reflect the diminishing influence of the axial flow component (Refs. 39-41 and Fig. 26). At low angles of attack ($0 \leq \alpha < \alpha_{sv}$), the axial flow component dominates, and the flow is attached, although the cross-flow effects will generate a thick viscous layer on the leeside. If the nose is blunt, however, so-called nose-induced separation of the axial flow will occur (Ref. 10). This closed-type of flow separation, which often is associated with standing, tornado-like vortices (Ref. 42), creates reattaching flow on the aft body, thereby delaying the development of the open-type flow separation on the aft body with associated body vortices (Ref. 43). At intermediate angles of attack ($\alpha_{sv} \leq \alpha < \alpha_{vv}$), the crossflow separates and rolls up into a symmetric vortex pair. In the angle-of-attack range of asymmetric vortex shedding ($\alpha_{vv} \leq \alpha < \alpha_{vy}$), the axial flow component is still sufficiently large to produce steady vortices. However, the vortices become asymmetric and produce a side force and yawing moment at zero sideslip. Finally, at very high angles of attack ($\alpha_{vy} \leq \alpha < 90^\circ$) the axial flow component has less and less influence and the vortex shedding converts to the unsteady type, starting on the aft body and progressing toward the nose with increasing angle of attack. That is, the leeside flow resembles the wake of a two-dimensional (2D) cylinder normal to the flow.

As α_{sv} for a pointed slender nose (Ref. 41), on the 10 deg. half-angle conic nose in Fig. 27 one expects symmetric body vortices to start occurring when $\alpha > 10^\circ$. Thus, it is reasonable to assume that the measured (Ref. 44) sharp change in the aerodynamic characteristics at $\alpha > 10^\circ$ is caused by symmetric body vortices. Based upon the results shown in Fig. 5, and similar results for wing-body configurations, one expects viscous flow effects to be negligible for $|\alpha| < 10^\circ$.

With this in mind, one can estimate the vortex-induced effect as the change between $\alpha \approx 10^\circ$ and $\alpha = 0$. That is, $(\Delta C_m)_v = 8.3$ and $\Delta(C_m + C_{m\alpha})_v = -80$ from Fig. 27. According to experiment with body vortices (Ref. 48) and analysis of boundary layer vortices (Ref. 29), it is the flow conditions at the body apex that determine the vortex-induced aerodynamic effects. As the nose-induced change of the body vortices can be assumed to convect downstream with free stream speed, the time lag occurring before the fin surfaces experience the nose-induced change is simply $\Delta t = (x_F - x_A)/U_\infty$. Using Taylor expansion one can express the vortex-induced effect as follows:

$$\begin{aligned}\Delta^i C_m(t) &= \Delta^i C_{m\alpha} \alpha(t - \Delta t) \\ &= \Delta^i C_{m\alpha} \alpha - \Delta^i C_{m\alpha} \dot{\alpha} \Delta t\end{aligned}$$

Thus,
$$\Delta^i C_{m\dot{\alpha}} = \frac{\partial \Delta^i C_m}{\partial (\frac{\dot{\alpha}}{U_\infty})} = -\Delta^i C_{m\alpha} \frac{x_F - x_A}{c}$$

With $(x_F - x_A)/c = 10 - 0.46 = 9.54$ one obtains $\Delta^i C_{m\dot{\alpha}} = -9.54 \Delta^i C_{m\alpha}$. That is, with $\Delta C_{m\alpha} = 8.3$ one obtains $\Delta^i C_{m\dot{\alpha}} = -79.2$, which is in excellent agreement with the experimental results. Thus, if one obtains the static vortex-induced loads, e.g., through comparison between static experiment and inviscid theory, as was done here, to get $(\Delta C_{m\alpha})_v$, one can predict the vortex-induced effect on the damping in pitch.

The tilting of the symmetric vortex pair through an angle γ , where $\gamma = \tan^{-1}(x_{cc}/U_\infty)$, observed for ogive-cylinders (Ref. 45) and slender pointed cones (Ref. 46), can produce significant nonplanar motion effects on the pitch damping of a body in free flight (Ref. 47 and Fig. 28).

At higher angles of attack, $\alpha > 20^\circ$ (Ref. 41), or $\alpha > 20^\circ$ in Fig. 27, asymmetric forebody flow separation occurs, generating one vortex close to the top surface, and near the body centerline, while the other vortex is lifted high off the body (Ref. 41). The associated loss of tail lift, due to the inboard vortex movement, is reflected in the loss of the vortex-induced statically stabilizing moment contribution, $(\Delta C_{mq})_v$ (Fig. 27). The absence of any change in the pitch damping derivative could possibly be due to compensating moving wall effects on the forebody flow separation (Ref. 48). At still higher angles of attack, $\alpha > 30^\circ$ in Fig. 27, multiple asymmetric vortices (Ref. 41) could be responsible for the large variation with angle of attack of both static and dynamic stability.

Moving wall effects

"Moving wall" effect as used in the present paper refers to the unsteady boundary condition at the body surface between flow stagnation and separation points. A rotating circular cylinder presents a well known case of moving wall effects in stationary flow, and the experimental results presented by Swanson (Ref. 49) will be used as the starting point and reference when discussing other types of moving wall effects. The wall-jet-like effect of the moving wall is illustrated in Fig. 29 (for the case $U_w/U_\infty = 1$). On the top side, downstream moving wall effects fill out the boundary layer velocity profile, thereby delaying flow separation, whereas on the bottom half upstream moving wall effects promote separation. The upstream moving wall effects are by far the strongest, as is demonstrated by comparing the Magnus lift for laminar (subcritical) (Fig. 30) and turbulent (supercritical) (Fig. 31) flow conditions. (The nomenclature refers to the initial boundary layer conditions existing at $p = 0$). In the laminar case, the Magnus lift is generated mainly by the downstream moving wall effect on the top side, moving the separation from the subcritical towards the supercritical position (Fig. 30). On the bottom side, the separation is already of the subcritical type at $p = 0$, and the upstream moving wall effect does not have much leverage for its separation-promoting action. In the turbulent case (Fig. 31), however, the situation is reversed. The main effect is that of the upstream moving wall on the bottom side, promoting separation, moving it from the supercritical towards the subcritical position. The difference in Magnus lift slopes, the turbulent one being three times as large as the laminar one, reflects the fact that the adverse (upstream) moving wall effect is the largest, as would be expected.

These moving wall effects on laminar and turbulent flow separation are rather straightforward and explain the positive Magnus lift slopes. The negative slopes, the so called Magnus lift reversals, are caused by the moving wall effect on boundary layer transition. In the laminar case (Fig. 30), when $p > p_{crit}$, the upstream moving wall effect on the bottom side causes transition to occur before separation, changing it from the subcritical toward the supercritical type. This effect completely overpowers the regular moving wall effects and causes a more or less discontinuous loss of lift, (Fig. 30). In the turbulent case (Fig. 31), it is the downstream moving wall effect on the top side that delays transition, causing it to move downstream of the separation point, thereby changing the separation from the supercritical towards the subcritical type. This also generates a more or less discontinuous loss of lift.

In both cases of Magnus lift reversal just discussed, the changes were towards, but not all the way to, the subcritical or supercritical types, the full change being restricted by the "regular" moving wall effects. However, at critical flow conditions these restrictions are no longer present. As a result, the lift loss is

larger and is generated immediately when p changes from $p = 0$ to $p > 0$ (Fig. 32). In the critical Reynolds number region the flow separation is dominated by the presence of a laminar separation bubble. The laminar flow separation develops near the lateral meridian ($\psi = 90^\circ$) and is followed by transition in the lifted shear layer, which causes flow reattachment. The reattaching "freshly" turbulent boundary layer is able to withstand the adverse pressure gradient until $\psi \approx 140^\circ$ before separation occurs. This is far aft of the separation location for a fully turbulent boundary layer, $\psi \approx 100^\circ$, resulting in a "drag bucket" for the critical Reynolds number region (Ref. 50 and Fig. 33).

When the Reynolds number is increased, transition moves forward in the raised shear layer forming the bubble. This generates a fuller turbulent flow profile in the reattaching shear layer, resulting in a delay of the final turbulent flow separation. This amplification of the beneficial effects of increasing Reynolds number will continue until transition reaches its most forward location on the top of the bubble. Transition will remain there until the Reynolds number has been increased enough to overcome the transition delay caused by local accelerated flow effects. The minimum drag plateau in Fig. 33 would result from such momentary arrest of the forward transition movement with increasing Reynolds number. When transition is increased further, transition jumps forward of the bubble, wiping it out. The resulting supercritical type separation increases with increasing Reynolds number and associated increased boundary layer thickness, resulting in increased drag (Fig. 33).

The first part of the critical flow region in Fig. 33, with its sharp drop of C_D with increasing Reynolds number until the minimum drag plateau is reached, corresponds to the Reynolds number region in Fig. 32 giving the negative Magnus lift slope. In the case of a rotating circular cross-section (Fig. 34b), the boundary layer turbulence generated by upstream moving wall effects causes a forward movement of transition in the lifted shear layer forming the laminar separation bubble. As is sketched in Fig. 34b, the resulting separation delay produces increased suction, generating negative lift. A similar contribution to the negative Magnus lift in Fig. 32 is generated by the transition delay caused by the downstream moving wall effects on the opposite side (Fig. 34). This promotes flow separation and causes a loss of suction.

The results shown in Figs. 29 through 34 are going to be used in what follows to explain the observed moving wall effects in three-dimensional flow. It is obvious from the discussion above that one can expect the moving wall effects to have a large influence also in the high- α three-dimensional flow case illustrated in Fig. 26. Even a modest spin rate has a large effect on the developed side force (Refs. 51, 52 and Fig. 35). Test results for an ogive-cylinder with a spinning nose tip (Ref. 53) give a very vivid demonstration of how powerful the moving wall effects can be (Fig. 36). At $\alpha = 55^\circ$, the crossflow conditions on the nose tip were apparently of the critical type shown in Figs. 32 and 34. Thus, even an infinitesimally small spin rate will cause reversal of the flow separation, and it is the direction rather than the rate of spin that determines the vortex-induced side force. For a more direct comparison of the three-dimensional flow case with the two-dimensional one in Figs. 29-34, the reader is referred to Figure 20 of Keener's flow visualization report (Ref. 54). The data in Fig. 36 show motion hysteresis effects similar to those measured by others. The critical condition shown in Fig. 36 has also been realized by an ogive-cylinder body in pitch-up motion (Ref. 55), with associated large effects on the unsteady aerodynamics (Ref. 56). The experimental results (Ref. 57) in Fig. 37 show that the three-dimensional moving wall effects can be powerful also for purely laminar flow conditions. The authors describe how only a slight push was needed to establish the coning motion in one direction or the other, regardless of the fact that the measured static yawing moment was biased in one direction due to nose microasymmetries (Refs. 39-41). The cone-cylinder body reached very nearly equal steady state coning rates in positive and negative rotation directions (Fig. 37). That is, the motion dominated over the static asymmetry, locking-in vortex asymmetry in the direction of the body motion, driving it. In the case of a coning motion, the moving wall effects act as follows on the translating cross-section (Ref. 58 and Fig. 38). The lateral motion of the circular cross-section causes the flow separation to be delayed on the advancing side and promoted on the retreating side, the important moving wall effects being those generated near the flow stagnation point. Thus, the motion produces a force that drives it until an equilibrium coning rate is reached, where the separation-induced driving moment is balanced by the drag-generated damping moment. This occurs also in the case of coning at $\alpha = 90^\circ$, the flat-spin case (Ref. 59) described in Ref. 60.

At critical flow conditions the flat spin motion controls completely the flow separation asymmetry, as is illustrated by the results (Ref. 61) in Fig. 39. This is not too surprising, as in the free-to-spin case, which Fig. 39 simulates, the flat spin rate reaches magnitudes for which the moving wall velocity at the tip exceeds the free stream velocity (Refs. 59 and 60). Although the flat spin is initiated by a subcritical/critical separation asymmetry with nonsymmetric spanwise distribution (Refs. 60-62), the very large moving wall effects cause a change to the critical/supercritical separation asymmetry illustrated in Fig. 40b before the final, limiting spin rate is reached. It is shown in Ref. 61 how the measured two-dimensional moving wall effects (Ref. 49 and Figs. 29-32) can be used to predict the experimentally observed limiting flat spin rate of circular canisters (Ref. 61).

On an axisymmetric body the moving wall effects on transition at high angles of attack, $\alpha > 30^\circ$, are very much the same as in two-dimensional flow (Refs. 39-41). This provides a simple explanation (Ref. 63) of the wing rock observed for a wing-body configuration looking very much like a tactical missile (Ref. 64 and Fig. 41). The Reynolds number of the test, $Re = 0.3 \times 10^6$, is in the critical region (see Fig. 32), providing the following scenario (Ref. 63 and Fig. 42). At $t=t_1$ the upstream moving wall effect causes boundary layer transition to occur in the forebody crossflow before separation occurs. This changes the portside flow separation from the subcritical towards the supercritical type. In absence of time lag effects, the vortex geometry sketched at $t=t_1$ would result. Due to time lag effects, similar to those present in the case of slender wing rock (Ref. 65), this vortex geometry (only the lower vortex is shown as only it will induce significant loads on the wing-body) is not realized until $t=t_1 + \Delta t$. At $t=t_2$, when the roll rate reaches its maximum in the opposite direction, another forebody switch of separation asymmetry occurs. Because of the time lag effect (Ref. 65), the vortex geometry at the (now horizontal) wing has not changed, but will be of the type shown for $t=t_1 + \Delta t$, in agreement with the vortex behavior observed through smoke flow visualization (Ref. 64).

Similar moving wall effects on transition can explain the oscillatory coning behavior observed experimentally for a cone-cylinder body flying backwards (Ref. 57 and Fig. 43). The mirror symmetry of the limiting coning rates is very similar to that obtained for the regular nose-forward orientation (Fig. 37). However, in this case no exterior push was needed to change the coning direction. The measured acceleration and coning rates are shown in Fig. 44. It can be seen that, when a certain limiting coning rate is reached, the acceleration suddenly switches sign. The fluid mechanical process can be described as follows (Ref. 58), with the aid of the inserted flow sketches: Initially, flow asymmetry or minute surface irregularities set the separation asymmetry, initiating the coning motion. The coning-induced moving wall effects delay the laminar separation on the advancing side, resulting in positive coning velocity and spin acceleration ($\dot{\psi} > 0$ and $\dot{\psi} > 0$). However, the adverse upstream moving wall effect eventually causes boundary layer transition on the retreating side, the effect being very similar to the one observed for the rotating cylinder (Ref. 49 and Fig. 30). This reverses the separation asymmetry and the coning motion starts to decelerate ($\dot{\psi} > 0$, $\dot{\psi} < 0$). Eventually, this results in accelerated coning in the opposite direction ($\dot{\psi} < 0$ and $\dot{\psi} < 0$). The coning reversal moves transition back into the wake on the new advancing side, and asymmetric laminar separation is reestablished. Eventually, transition occurs on the retreating side to cause critical/subcritical separation asymmetry, reversing the vortex asymmetry and decelerating the coning motion ($\dot{\psi} < 0$, $\dot{\psi} > 0$). The process continually repeats itself, resulting in a self-reversing, oscillatory coning motion.

Apparently, the test Reynolds number was not high enough to establish the necessary high laminar flow conditions on the conic nose (Ref. 57 and Fig. 37). One can see, however, how with increasing Reynolds number the successive establishment on the nose of the flow conditions illustrated in Figs. 31, 33, and 32 is possible, generating variations of the self-reversing coning conditions illustrated in Figs. 43 and 44. Thus, for a missile in free flight one can foresee a strong coupling between wing rock and coning. As the vortex strength (and flow separation extent) will depend strongly upon the angle of attack, one can indeed expect a strong coupling to exist between the three angular degrees of freedom, as has been pointed out by Orlik-Rückemann (Ref. 9).

In view of the strong interplay between Reynolds number and moving wall effects just demonstrated, Champigny's experimental results (Ref. 66 and Fig. 45) give cause for the concerns expressed in Refs. 41, 56 and 58 that in full scale flight a vehicle maneuver could lock-in the single cell flow separation asymmetry along the full length of a missile or aircraft forebody.

Obviously, in order to predict the high-alpha missile dynamics heavy reliance has to be placed upon experimental means. The use of experimental data to predict full scale missile dynamics, in addition to the usual problems of support interference (Refs. 3 and 4) and scaling (Refs. 5-8), is complicated greatly by two types of flow unsteadiness effects; one is the motion-dependent unsteady effect discussed above, the other is the motion-independent flow unsteadiness discussed in Refs. 67 and 68.

The intermittent, unsteady character of asymmetric forebody vortices was observed already by Allen and Perkins (Ref. 69), who found that the asymmetry changed between its two extremes in an aperiodic manner. Further investigations by Gowen (Ref. 70) showed that the lateral pressure difference $\Delta C_p = C_p(t) - C_{p, \text{mean}}$, at $\phi = \pm 15^\circ$ on the leeside, varied in a random, aperiodic manner (Fig. 46). More recent test results (Refs. 71 and 72) show similar intermittent, asymmetric vortex characteristics. Figure 46 illustrates the relation between the static, time-average value of the side force and the maximum, instantaneous one.

Besides presenting a possible forcing function of the buffet type, the unsteadiness of the asymmetric vortices also indicates a certain proneness for the coupling with vehicle motion discussed earlier. A similar concern was expressed already by Gowen and Perkins (Ref. 73): "It is realized that for full-scale vehicles in flight there exists the possibility of coupling between the shedding of the wake vortices and the movement of the aircraft". How the angle of attack

affects the vortex unsteadiness is discussed at length in Ref. 67.

In regard to the problem of wind tunnel tests at high alpha, the experimental results (Ref. 72) in Fig. 47 show that a reduction of the free stream turbulence from the 0.7% level of the Bristol tunnel (Fig. 47a) to the 0.01% of the R.A.E. tunnel (Fig. 47b) eliminated the intermittent "flipping" of the vortex asymmetry. However, eliminating this high turbulence level did not change the effect of roll angle (Fig. 48), contrary to the authors' expectation (Ref. 72). They concluded that this effect is caused by micro-asymmetries (Refs. 39-41) and persists even in presence of high turbulence levels. Combining this with the results in Figs. 35-45 one gets some appreciation of the power of the moving wall effect; which also has been demonstrated for non-circular cross-sections (Refs. 74 and 75).

The conclusion to be drawn from the discussed experimental results is that great care has to be exercised when attempting to use static high-alpha test results for analysis of full scale flight characteristics. It appears that one would need to use test rigs that allow coning and/or rolling motions in order to obtain "static" test results that can be applied to a full scale vehicle that describes maneuvers that produce (even low) coning and/or spin rates.

CONCLUSIONS

Results of analytic developments since the early sixties have been reviewed and summarized. The following conclusions can be drawn:

I. Low angles of attack

- o The developed fast computational method can determine the inviscid unsteady missile aerodynamics over the complete Mach number range $0 < M_\infty < \infty$ with the accuracy needed for preliminary design. This is documented by comparison between predicted and measured pitch damping for a great variety of missile configurations in cases where viscous flow effects are not significant.
- o Viscous flow affects the vehicle dynamics to a significant degree in the following cases:
 1. A blunt nose and/or an aft body flare causing extensive flow separation at transonic and high subsonic speeds.
 2. A slender body experiencing aft body boundary layer growth and/or asymmetric transition due to forebody crossflow effects.
 3. A model support causing distortion of the aft body flow field at hypersonic low density test conditions and/or at transonic and high subsonic speeds. When the base has a bulbous shape, the viscous flow effects can be large even in free flight.

II. High angles of attack

- o The only significant nonlinear aerodynamics of inviscid origin are those caused by the non-uniform flow field, the "entropy wake", generated by the nose-bluntness-induced bow-shock-curvature at high supersonic and hypersonic speeds. The developed fast computational means based upon the embedded Newtonian concept can determine these nonlinear effects with the accuracy needed for preliminary design, as is documented by comparison with experimental results obtained at flow conditions where viscous effects are insignificant.
- o Flow separation generally affects the missile dynamics to a significant degree in all cases where $\alpha > 30^\circ$, and in the following special cases.
 1. A pointed slender nose causing forebody flow separation and free body vortices, symmetric at $\theta_A < \alpha < 2\theta_A$ and asymmetric at $\alpha \geq 2\theta_A$.
 2. A model support interacting with the vortex wake.
 3. Free stream turbulence and/or model vibration causing the time-average forces and moments measured in static tests to be of little practical use.

III. Prediction methodology

- o The inviscid computer program is completely general, within the geometric constraints of axisymmetry and low aspect ratio lifting surfaces, and the only inputs required are the geometry and the desired test or flight condition. However, the existing computational means for viscous flow effects on the vehicle dynamics require static experimental data as an input and are, therefore, much less mechanized than the inviscid computer program. Additionally, it is in many cases not sufficient to know the

separation-induced static effects in order to determine the flow separation effects on the vehicle dynamics, because of the dominant role played by so called moving wall effects. Further analysis could, however, lead to the development of the needed prediction capability using an approach similar to that resulting in successful prediction of the maximum flat spin rate for a circular cylinder.

- o The most severe problem in regard to the prediction of full scale high alpha dynamics at the present is the total dependence on experimental data obtained on subscale models. Because of the existing problems of Reynolds number scaling and support interference, aggravated by flow unsteadiness effects, a thorough understanding of the physical flow phenomena is needed before reliable use can be made of the experimental results.

REFERENCES

1. Vukelich, S. R. and Jenkins, J. E., "Missile Datcom; Aerodynamic Prediction of Conventional Missiles Using Component Build-Up Techniques", AIAA Paper 84-0388, Jan. 1984.
2. Ericsson, L. E., "Rapid Computation of Missile Dynamics", AIAA Paper 84-0341, Jan. 1984.
3. Ericsson, L. E. and Reding, J. P., "Review of Support Interference in Dynamic Tests", AIAA Journal, Vol. 21, No. 12, Dec. 1983, pp 1652-1666.
4. Ericsson, L. E. and Reding, J. P., "Dynamic Support Interference in High Alpha Testing", J. Aircraft, Vol. 23, No. 12, Dec. 86, pp 889-896.
5. Ericsson, L. E. and Reding, J. P., "Scaling Problems in Dynamic Tests of Aircraft-Like Configurations", Paper 25, AGARD-CP-227, Feb. 1978.
6. Ericsson, L. E. and Reding, J. P., "Reynolds Number Criticality in Dynamic Tests", AIAA Paper No. 78-166, Jan. 1978.
7. Ericsson, L. E. and Reding, J. P., "Practical Solutions to Simulation Difficulties in Subscale Wind Tunnel Tests", Paper No. 16, AGARD-CP-348, Sept. 1983.
8. Ericsson, L. E., "Reflections Regarding Recent Rotary Rig Results", J. Aircraft, Vol. 24, Jan. 1987, pp 25-30.
9. Orlik-Rückemann, K. J., "Aerodynamic Aspects of Aircraft Dynamics at High Angles of Attack", J. Aircraft, Vol. 20, No. 9, Sept. 1983, pp 737-752.
10. Ericsson, L. E., "Unsteady Aerodynamics of Separating and Reattaching Flow on Bodies of Revolution", Recent Research on Unsteady Boundary Layers, Vol. 1, IUTAM Symposium, Laval University, Quebec, May 24-28, 1971, pp 481-512.
11. Ericsson, L. E. and Reding, J. P., "Aerodynamic Effects of Bulbous Bases", NASA/CR-1339, Aug. 1969.
12. Ericsson, L. E. and Reding, J. P., "Effects of Bulbous Bases on Re-entry Vehicle Dynamics", Paper 6, Vol. II, Transactions of the 3rd Technical Workshop on Dynamic Stability Problems, NASA Ames Research Center, Moffet Field, Calif., Nov. 4-7, 1968.
13. Moore, F. G. and Swanson, R. C., Jr., "Aerodynamics of Tactical Weapons to Mach Number 3 and Angle of Attack 15", Part 1 - Theory and Application", NSWC/DLTR-3584, Feb. 1977.
14. Ericsson, L. E., "Modification of Aerodynamic Predictions of the Longitudinal Dynamics of Tactical Weapons," Lockheed Missiles & Space Co., Inc., Sunnyvale, Calif., LMSC-D646354, Contract N60921-77C-A294, June 1979, Addendum, LMSC-D646354A, Aug. 1979.
15. Ericsson, L. E., "Effect of Mach number on Slender Vehicle Dynamics", J. Spacecraft and Rockets, Vol. 18, No. 1, Jan-Feb, 1981, pp 18-23.
16. Ericsson, L. E., "Generalized Unsteady Embedded Newtonian Flow", J. Spacecraft and Rockets, Vol. 12, No. 12, Dec. 1975, pp 718-726.
17. Ericsson, L. E., "Unsteady Embedded Newtonian Flow", Astronautica Acta, Vol. 18, Nov. 1973, pp 309-330.
18. Shadow, T. O., "Investigation of the Half-Model Reflection-Plane Technique for Dynamic Stability Testing at Transonic Mach Numbers", AEDC-TR-76-165, Jan. 1977.

19. Shantz, I. and Groves, R. T., "Dynamic and Static Stability Measurements of the Basic Finner at Supersonic Speeds", NAVORD Report 4516, Sept. 1960.
20. Regan, F. J., "Wind Tunnel Investigation of the MK76 Practice Bomb", NAVORD Report 6772, Sept. 1964.
21. Boyle, W. and Mantler, M., "The Effects of Configuration Sensitivity on Ballistics of Bombs, Final Report, Part I - Aerodynamic Math Model and Tolerances", Contract N60921-C-A076, Northrup Services, Inc., Huntsville, Alabama, Nov. 1978.
22. Tong, B. G. and Hui, W. H., "Unsteady Embedded Newton-Busemann Flow Theory", J. Spacecraft and Rockets, Vol. 23, No. 2, March-April 1986, pp 129-135.
23. East, R. A. and Hutt, G. R., "Hypersonic Static and Dynamic Stability of Axisymmetric Shapes, A Comparison of Prediction Methods and Experiment", Paper No. 28, AGARD CP-428, April 1987.
24. Shadow, T. O. and Paulk, R. A., "Dynamic Stability Characteristics of Bluff Bodies of Revolution at Transonic Mach Numbers", AEDC-TR-72-110, Aug. 1972.
25. Ericsson, L. E. and Reding, J. P., "Approximate Slender Vehicle Dynamics at All Speeds", Paper 4, 11th Navy Symposium on Aeroballistics, NADC, Warminster, Pennsylvania, 22-24 Aug. 1978.
26. Hsieh, T., "Unsteady Transonic Flow Over Blunt and Pointed Bodies of Revolution", AIAA Paper 78-21, Jan. 1978.
27. Ward, L. K., "Influence of Boundary Layer Transition on Dynamic Stability at Hypersonic Speeds", Transactions of the Second Technical Workshop on Dynamic Stability Testing, Paper 9, Vol. 11, April 1965, Arnold Engineering Development Center, Arnold Air Force Station, Tenn.
28. Ericsson, L. E., "Effects of Boundary Layer Transition on Vehicle Dynamics", J. Spacecraft and Rockets, Vol. 6, No. 2, Dec. 1969, pp 1404-1409.
29. Ericsson, L. E., "Effect of Transition on Slender Cone Pitch Damping", AIAA Paper 87-0493, Jan. 1987.
30. Uselton, B. L. and Cyran, F. B., "Sting Interference Effects as Determined by Measurements of Dynamic Stability Derivatives, Surface Pressure, and Base Pressure for Mach Numbers 2 through 9", AEDC-TR-79-89, Oct. 1980.
31. Ward, L. K., Private, communication of unpublished experimental results, Feb. 1972.
32. Uselton, B. L. and Shadow, T. O., "Dynamic Stability Characteristics of 3- and 5-Cal Army-Navy Spinner Projectiles at Mach Numbers 0.2 through 1.3", AEDC-TR-70-115, July 1970.
33. Whyte, R. H., "'Spinner' - A Computer Program for Predicting the Aerodynamic Coefficients of Spin-Stabilized Projectiles", G.E. Technical Information Service, Class 2, 69APB3, Aug. 1969.
34. Ericsson, L. E., "Viscous Effects on Missile Aerodynamics at Low Angles of Attack", J. Spacecraft and Rockets, Vol. 18, No. 5, Sept.-Oct. 1981, pp 401-405.
35. Mack, L. M., "Linear Stability Theory and the Problem of Supersonic Boundary-Layer Transition" AIAA Journal, Vol. 1, No. 3, March 1975, pp 273-289.
36. Ericsson, L. E., "Transition Effects on Slender Vehicle Stability and Trim Characteristics", J. Spacecraft and Rockets, Vol. 11, No. 1, Jan. 1974, pp 3-11.
37. Liu, D. D., Garcia-Fogeda, P., and Chen, P. C., "Oscillating Wings and Bodies with Flexure in Supersonic Flow-Applications of Harmonic Potential Panel Method", Paper ICAS-86-2.9.4, The 15th ICAS Congress, London, UK, Sept. 7-12, 1986.
38. Garcia-Fogeda, P., Communication of theoretical prediction for the $l/d = 3$ ogive-cylinder body, 1 April 1987.
39. Ericsson, L. E. and Reding, J. P., "Review of Vortex-Induced Asymmetric Loads-Part I", Z. Flugwiss. Weltraumforsch., 5 (1981), Heft 3, pp. 162-174.
40. Ericsson, L. E. and Reding, J. P., "Review of Vortex-Induced Asymmetric Loads-Part II", Z. Flugwiss. Weltraumforsch., 5 (1981), Heft 6, pp. 349-366.
41. Ericsson, L. E. and Reding, J. P., "Asymmetric Vortex Shedding from Bodies of Revolution", Chapter VII, Tactical Missile Aerodynamics, Vol. 104, Progress Astro. and Aero. Series, M. J. Hemmich and H. N. Nielson editors, 1986, pp 243-296.

42. Hsieh, T., "Low Supersonic Flow Over Hemisphere-Cylinder at Incidence", *Journal of Spacecraft and Rockets*, Vol. 14, Nov. 1977, pp 662-668.
43. Hall, I. M., Rogers, E. W. E., and Davies, B. M., "Experiments with Inclined Blunt-Nosed Bodies at $M = 2.45$ ", *Aeronautical Research Council*, Great Britain, ARC R&M 3129, Aug. 1957.
44. Uselton, B. L. and Uselton, J. C., "Test Mechanism for Measuring Pitch Damping Derivatives of Missile Configurations at High Angles of Attack", AEDC TR-75-43, May 1975.
45. Tobak, M., Schiff, L. B., and Peterson, F. L., "Aerodynamics of Bodies of Revolution in Coning Motion", *AIAA Journal*, Vol. 7, Jan. 1969, pp 95-99.
46. Schiff, L. B. and Tobak, M., "Results from a New Wind-Tunnel Apparatus for Studying Coning and Spinning Motions of Bodies of Revolution", *AIAA Journal*, Vol. 8, Nov. 1970, pp 1953-1958.
47. Ericsson, L.E. and Beyers, M.E., "Nonplanar Motion Effects", *AIAA Paper* 88-0215, Jan. 1988.
48. Ericsson, L. E., "Dynamic Omnipresence of Moving Wall Effects", *AIAA Paper* 87-0241, Jan. 1987.
49. Swanson, W. M., "The Magnus Effect: A Summary of Investigations to Date", *J. Basic Eng.*, Vol. 83, Sept. 1961, pp 461-470.
50. Achenbach, E., "Influence of Surface Roughness on the Cross Flow Around a Circular Cylinder", *J. Fluid Mech.*, Vol. 46, Part 2, 1971, pp 321-335.
51. Atraghji, E. E., "The Influence of Mach Number, Semi-Nose Angle and Roll Rate on the Development of the Forces and Moments over a Series of Long Slender Bodies of Revolution at Incidence", *NAE Data Report 5x5/0020*, 1967, *National Research Council*, Ottawa, Canada.
52. Kruse, R. L., "Influence of Spin Rate on Side Force of an Axisymmetric Body", *AIAA Journal*, Vol. 12, No. 7, July 1974, pp 1003-1005.
53. Fidler, J. E., "Active Control of Asymmetric Vortex Effects", *J. Aircraft*, Vol. 18, No. 4, April 1981, pp 267-272.
54. Keener, E. R., "Flow-Separation Patterns on Symmetric Forebodies", *NASA TM* 86016, Jan. 1986.
55. Smith, L. H., "Aerodynamic Characteristics of an Axisymmetric Body Undergoing Uniform Pitching Motion", *Ph.D. Thesis*, *Naval Post-Graduate School*, Monterey, California, Dec. 1974.
56. Ericsson, L. E. and Reding, J. P., "Steady and Unsteady Vortex-Induced Asymmetric Loads on Slender Vehicles", *J. Spacecraft and Rockets*, Vol. 19, No. 2, March-April 1981, p 97-109.
57. Yoshinaga, T., Tate, A., and Inoue, K., "Coning Motion of Slender Bodies at High angles of Attack in Low Speed Flow", *AIAA Paper* 81-1899, Aug. 1981.
58. Ericsson, L. E. and Reding, J. P., "Dynamics of Forebody Flow Separation and Associated Vortices", *J. Aircraft*, Vol. 22, No. 4, April 1985, pp 329-335.
59. Yoshinaga, T. and Tate, A., "Flat Spin of Slender Bodies near the Critical Reynolds Number Region", to be published; private communication, Dec. 20, 1985.
60. Ericsson, L. E., "Flat Spin of Axisymmetric Bodies in the Critical Re-Region", *AIAA Paper* No. 86-2083-CP, Aug. 1986.
61. Kubota, H., Irai, I., and Matsuzaka, M., "Wind Tunnel Investigations for the Flat Spin of Slender Bodies at High Angles of Attack", *J. Spacecraft and Rockets*, Vol. 20, No. 2, March-April 1983, pp 108-114.
62. Ericsson, L. E., "Flat Spin of Axisymmetric Bodies in the Critical Re-Region", *AIAA Paper* 86-2083, Aug. 1983.
63. Ericsson, L. E., "Wing Rock Generated by Forebody Vortices", *AIAA Paper* 87-0268, Jan. 1987.
64. Brandon, J. M. and Nguyen, L. T., "Experimental Study of Effects of Forebody Geometry on High Angle of Attack Static and Dynamic Stability", *AIAA Paper* 86-0331, Jan. 1986.
65. Ericsson, L. E., "The Fluid Mechanics of Slender Wing Rock", *J. Aircraft*, Vol. 21, No. 5, May 1984, pp 32-328.

66. Champigny, P., "Reynolds Number Effect on the Aerodynamic Characteristics of an Ogive-Cylinder at High Angles of Attack", AIAA Paper 84-2176, Aug. 1984.
67. Ericsson, L. E. and Reding, J. P., "Vortex Unsteadiness of Slender Bodies at High Incidence", J. Spacecraft and Rockets, Vol. 24, No. 4, July-Aug. 1987, pp 319-326.
68. Ericsson, L. E., "Flow Unsteadiness Considerations in High Alpha Tests", AIAA Paper 89-0057, Jan. 1988.
69. Allen, H. J. and Perkins, E. W., "Characteristics of Flow Over Inclined Bodies of Revolution", NACA RMA50L07, March 1951.
70. Gowen, F. E., "Buffeting of a Vertical Tail on an Inclined Body at Supersonic Mach Numbers", NACA RMA53A09, March 1953.
71. Lamont, P. J. and Hunt, B. L., "Pressure and Force Distributions on a Sharp-Nosed Circular Cylinder at large Angles of Inclination to a Uniform Stream", J. Fluid Mech., vol. 76, part 3, 1976, pp 519-559.
72. Hunt, B. L. and Dexter, P. C., "Pressures on a Slender Body at High Angle of Attack in a Very Low Turbulence Level Air Stream", Paper 17, AGARD CP-247, Jan. 1979.
73. Gowen, F. E. and Perkins, E. W., "A Study of the Effects of Body Shape on the Vortex Wakes of Inclined Bodies at a Mach Number of 2", NACA RM A53117, Dec. 1, 1953.
74. Malcolm, G. N. and Clarkson, M. H., "Wind Tunnel Testing with a Rotary-Balance Apparatus to Simulate Aircraft Spin Motions", Proceedings of the AIAA 9th Aerodynamic Testing Conference, June 1976, pp 143-146.
75. Ericsson, L. E., "Aerodynamic Characteristics of Noncircular Bodies in Flat Spin and Coning Motions", J. Aircraft, Vol. 22, No. 5, May 1985, pp 397-392.

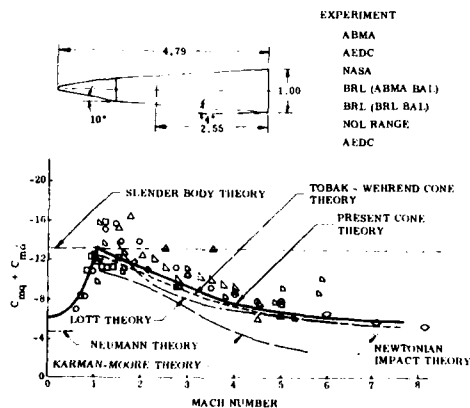


Fig. 1. Comparison between theoretical predictions and experimental results for pitch damping of a slender vehicle (Ref. 15)

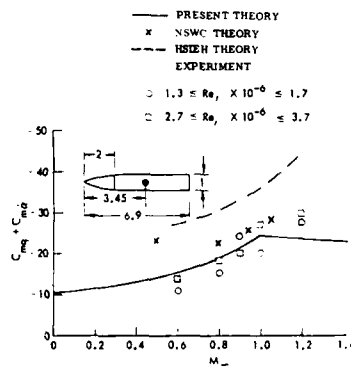


Fig. 2. Predicted and measured pitch damping of an ogive-cylinder body (Ref. 15)

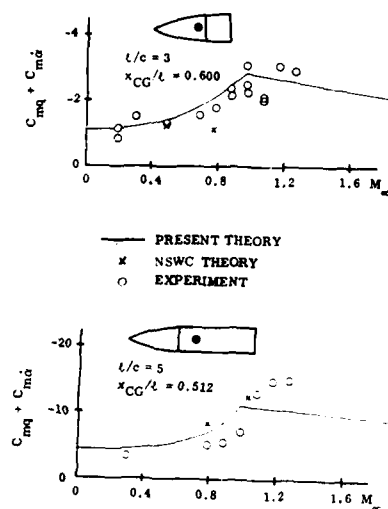


Fig. 3. Predicted and measured pitch damping of two ogive-cylinder bodies (Ref. 14)

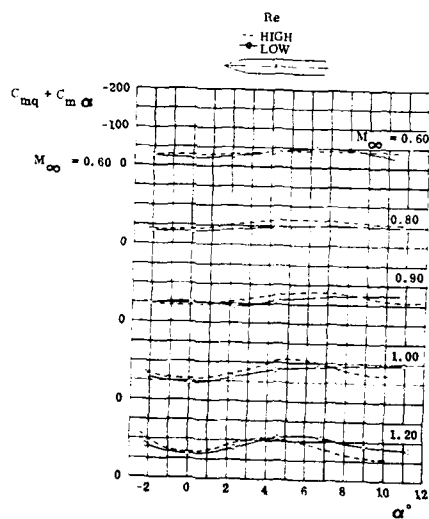


Fig. 5. Effect of angle of attack on the measured pitch damping of an ogive-cylinder body (Ref. 17)

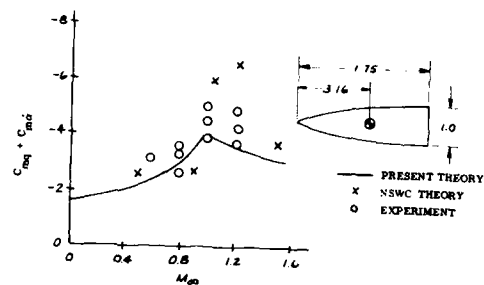


Fig. 4. Predicted and measured pitch damping of a tangent-ogive body (Ref. 14)

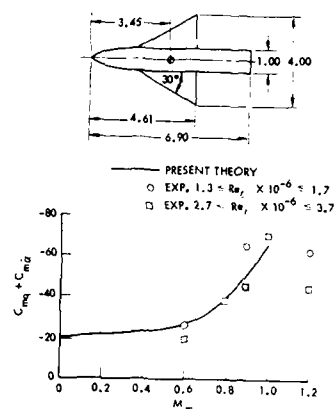


Fig. 6. Predicted and measured subsonic pitch damping of an ogive-cylinder body with a delta wing.

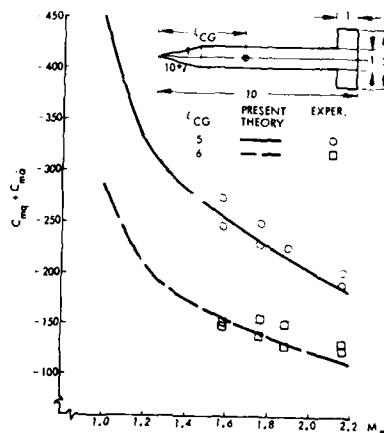


Fig. 7. Predicted and measured supersonic pitch damping of the "Basic Finner".

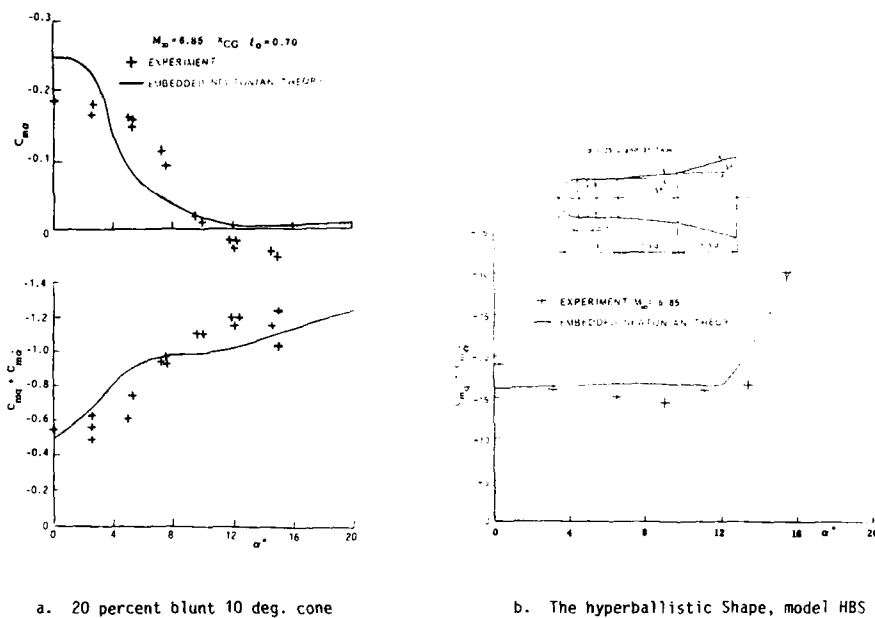


Fig. 12. Comparison of embedded Newtonian and experimental pitch damping derivatives versus angle of attack (Ref. 25)

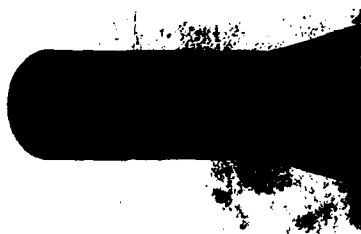


Fig. 13. Nose-induced flow separation

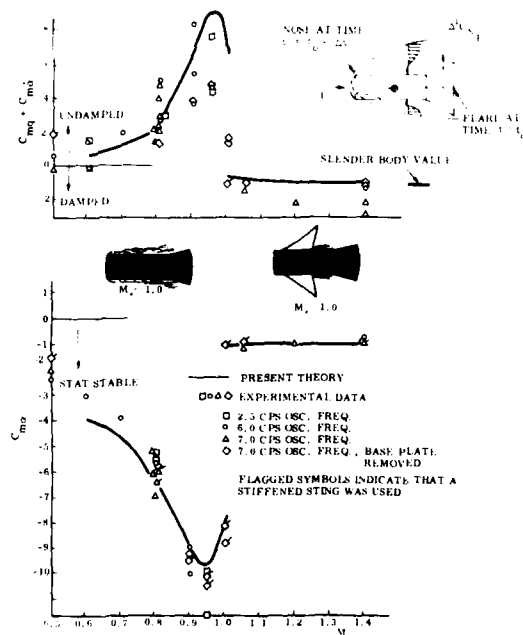


Fig. 14. Pitch stability derivatives of a blunt cylinder-flare body at $\alpha = 0$ (Ref. 10)

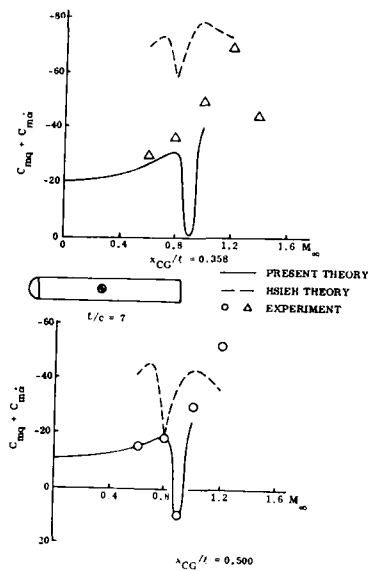


Fig. 15. Predicted and measured pitch damping of a hemisphere-cylinder at transonic speeds.

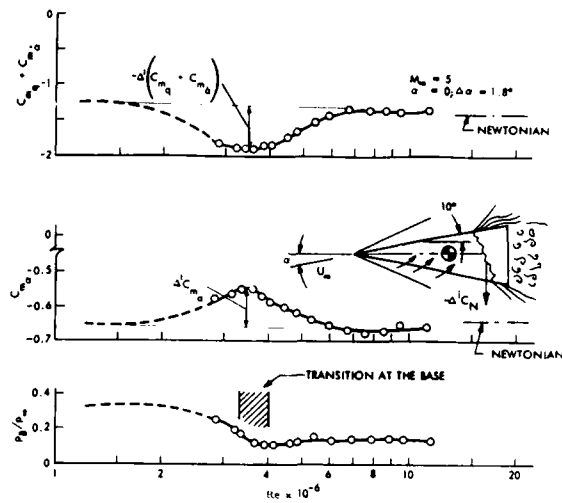


Fig. 16. Effect of Reynolds number on the aerodynamic characteristics of a 10 deg. sharp cone (Ref. 30).

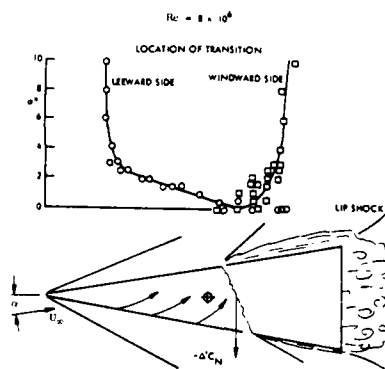


Fig. 17. Effect of angle of attack on transition location (Ref. 30).

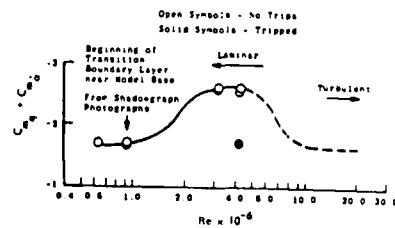


Fig. 19. Effect of boundary layer trip on slender cone pitch damping at $\alpha=0$ and $M_\infty=5$ (Ref. 33).

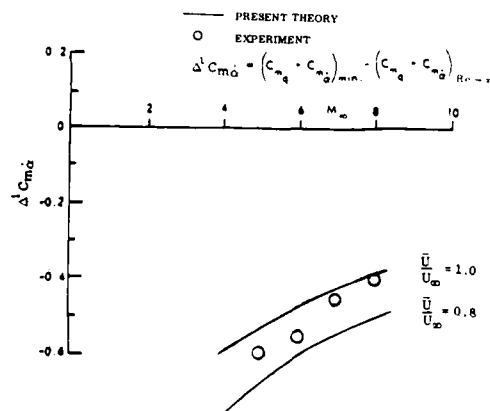


Fig. 18. Comparison between predicted and measured effect of transition on the pitch damping of a 10 deg. sharp cone (Ref. 32).

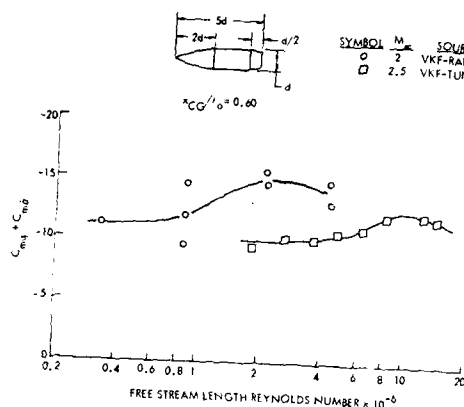


Fig. 20. Effect of transition on the pitch damping of an ogive-cylinder body (Ref. 34).

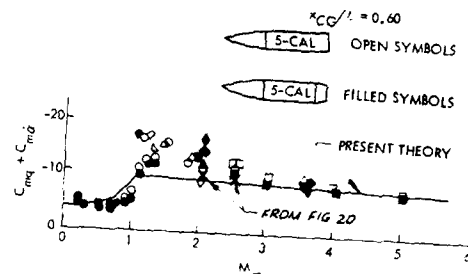


Fig. 21. Comparison between experiment and inviscid prediction (Ref. 36).

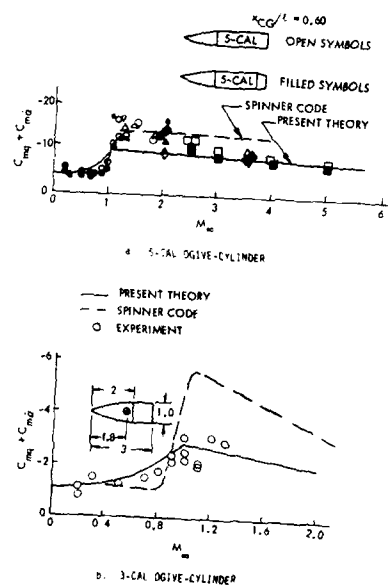


Fig. 22. Comparison between inviscid theory and experiment for two ogive-cylinder bodies (Ref. 36).

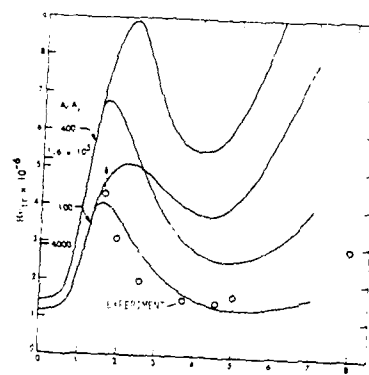


Fig. 23. Flat plate transition as predicted by linear stability theory (Ref. 37).

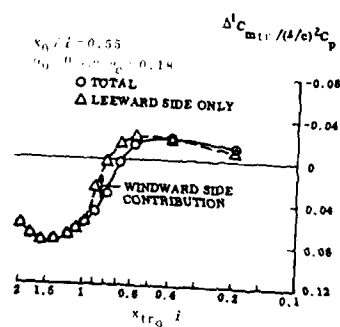


Fig. 24. Effect of transition location on the induced static stability increment (Ref. 38).

Figure 1 is a graph showing the dependence of the coefficient $C_{eq} + C_{ind}$ on the Mach number M . The x-axis represents M and ranges from 0 to 2.0. The y-axis represents $C_{eq} + C_{ind}$ and ranges from 0 to -0.6. Experimental data points (open circles) are plotted for M values between 0.4 and 1.2. Two theoretical curves are shown: a solid line labeled 'THEORY, REF. 14' and a dashed line labeled 'THEORY, REF. 39'. An inset diagram shows a cross-section of a blunt-nosed body with a rectangular cavity. The dimensions of the body are indicated: a total height of 2, a base radius of 1.0, and a rectangular cavity with a width of 1.8 and a height of 0.3.

Fig. 25. Comparison of inviscid theory and experiment in regard to ogive-cylinder pitch damping.

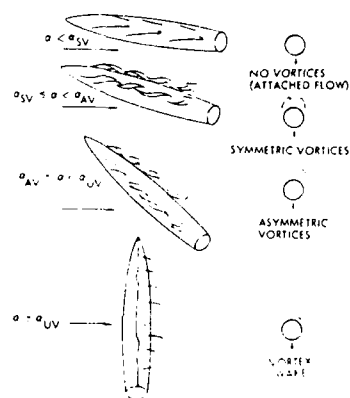
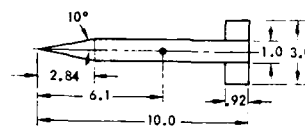


Fig. 26. Effect of angle of attack on the leeside flow field of a slender body (Ref. 44)



— — PRESENT THEORY
EXPERIMENT

He 0.187 $\times 10^6$

Sym	st. day	st. day	st. day
0	12	12	0
1	12	0	18
2	18	0	18
3	0	0	18
4	18	0	18
5	18	0	18

Strut Support: $M_{st} = 0$ $\theta = 0$ $\delta = 0$ $\Delta = 0$

$W = 1.2 \times 20 = 2.4 \times 10^3 \text{ lb}$

$W = 1.2 \times 1.2 \times 10^3 = 1.44 \times 10^3 \text{ lb}$

57 BR 100 31400-205 $x_p = 0.1$ Range Date 5 - 10/10/84 - 10/10/84
9 - 11/10/84

Ex. A SWC (RM) of $M_{25} = 2.26$, $M_{25} = 0.45 \times 10^6$, $\epsilon_L = 0.5$, $\mu = 1.2$ cm.
 $n = 4$ day, 1.6 verse had support

Fig. 27. Effect of angle of attack on static and dynamic stability of the "Basic Finner" (Ref. 44).

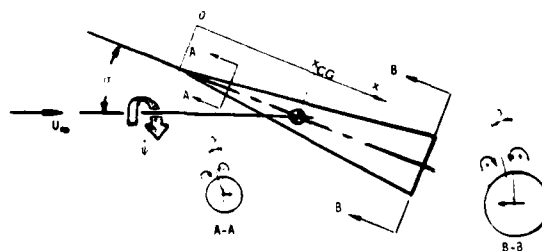


Fig. 28. Body vortices on a pointed slender cone in coning motion (Ref. 47).

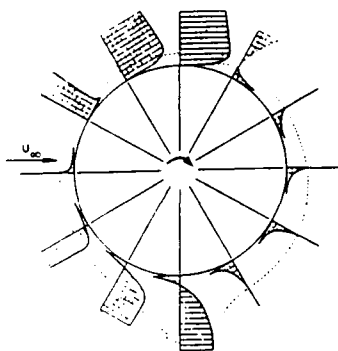


Fig. 29. Computed boundary-layer profiles on a circular cylinder rotating with $U_W = U_{\infty}$ (Ref. 49).

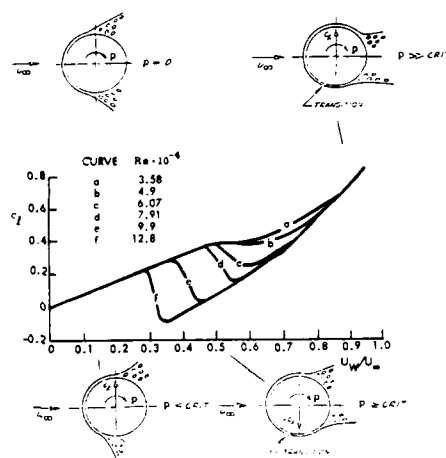


Fig. 30. Magnus lift characteristics for initially subcritical flow conditions (Ref. 49).

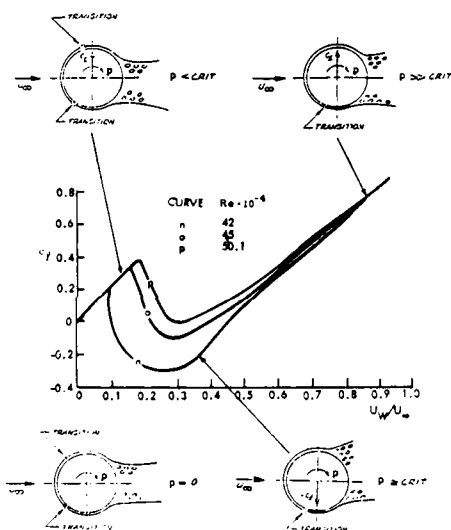


Fig. 31. Magnus lift characteristics for initially supercritical flow conditions (Ref. 49).

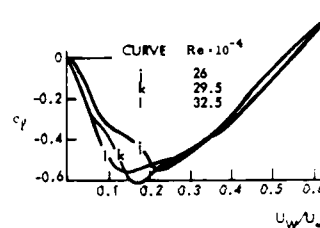


Fig. 32. Magnus lift characteristics in the critical flow regime (Ref. 49).

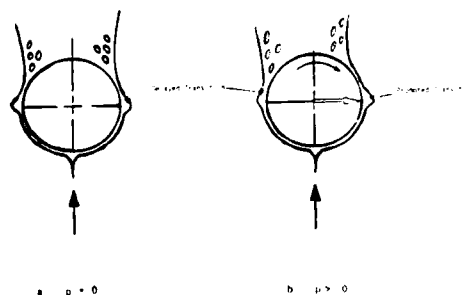


Fig. 34. Moving wall effects on a rotating cylinder at critical flow conditions (Ref. 48).

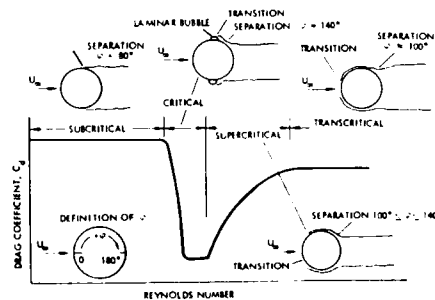


Fig. 33. Flow regions for a circular cylinder (Ref. 50).

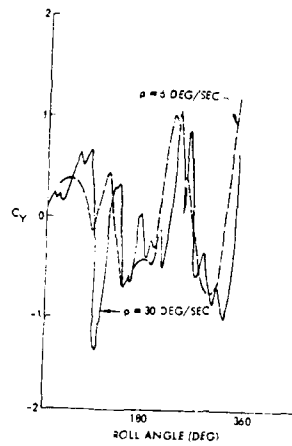


Fig. 35. Effect of roll angle and roll rate on the vortex-induced side force on a cone-cylinder (Ref. 510)

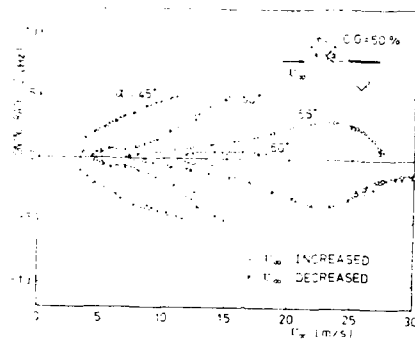


Fig. 37. Coning characteristics of a cone-cylinder (Ref. 57).

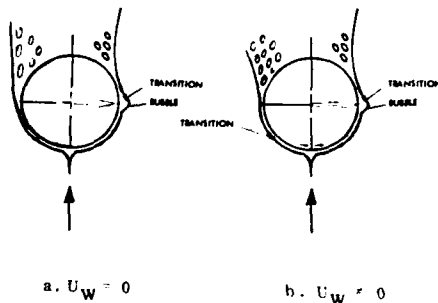


Fig. 40. Moving wall effects on a translating circular cross-section at critical flow conditions (Ref. 48)

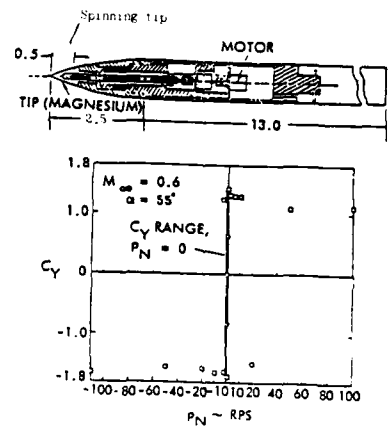


Fig. 36. Effect of spinning nose tip on the vortex-induced side force (Ref. 53).

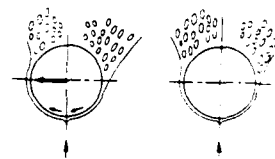


Fig. 38. Coning-induced translational moving wall effects (Ref. 48)

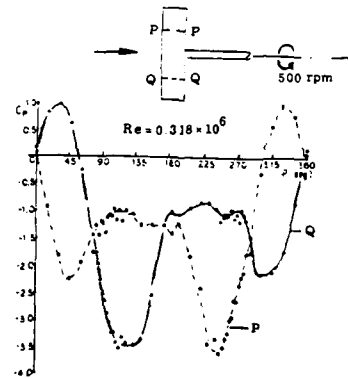


Fig. 39. Measured pressure distributions on a circular cylinder in flat spin (Ref. 63)

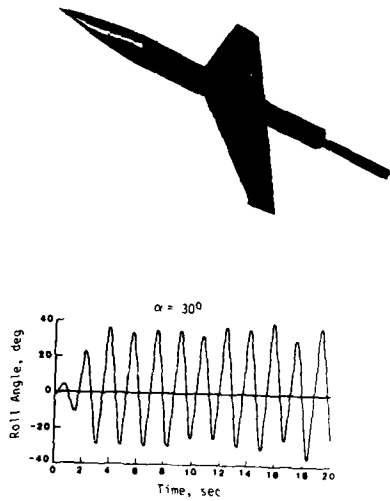


Fig. 41. Wing rock build-up at $\alpha = 30$ deg. (Ref. 66).

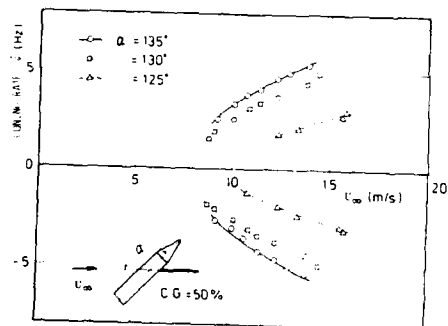


Fig. 43. Coning rates of a cone-cylinder at $\alpha > 90$ deg. (Ref. 57).

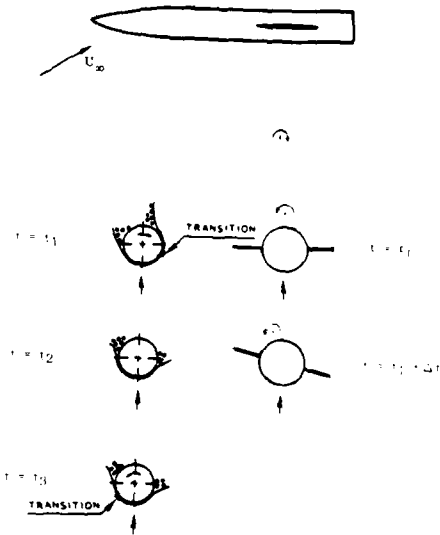


Fig. 42. Conceptual flow mechanism for wing-body rock (Ref. 65).

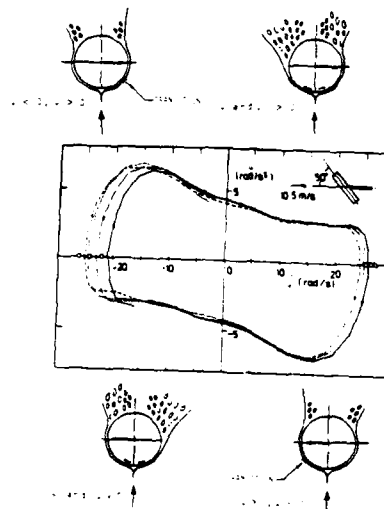


Fig. 44. Acceleration-rate, time history for a flat-faced circular cylinder coning at $\alpha = 50$ deg. (Ref. 48).

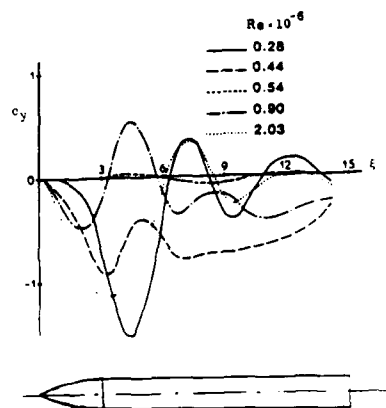


Fig. 45. Side force distribution at $\alpha = 50$ deg. on an ogive-cylinder through the critical Reynolds number range (Ref. 69).

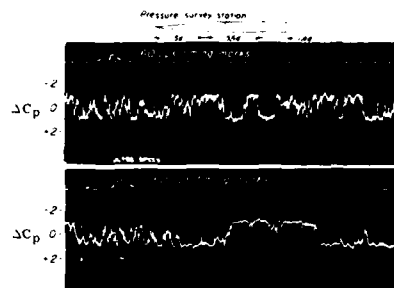


Fig. 46. Differential pressure coefficient at $\varphi \pm 157^\circ$ and $\xi = 10.6$ on a cone-cylinder body at $\alpha = 23.7^\circ$, $M_\infty = 1.45$, and $Re = 0.5 \times 10^6$ (Ref. 73).

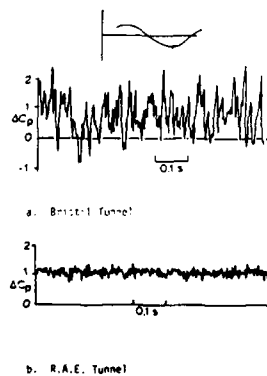


Fig. 47. Lateral leeside pressure differential at $\xi = 5$ on an ogive-cylinder at $\alpha = 60^\circ$ and $Re = 0.11 \times 10^6$ (Ref. 75).

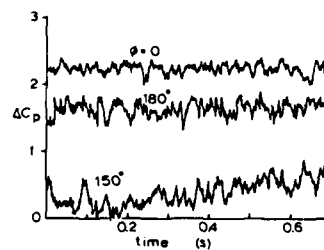


Fig. 48. Effect of roll angle on lateral pressure differential at $\xi = 4$ on ogive-cylinder at $\alpha = 50^\circ$ and $Re = 0.10 \times 10^6$ (Ref. 75).

VORTEX INDUCED CHARACTERISTICS OF MISSILES IN UNSTEADY MANEUVERS

by
Michael R. Mendenhall, Vice President
Stanley C. Perkins, Jr., Senior Research Engineer
Nielsen Engineering & Research, Inc.
510 Clyde Avenue
Mountain View, California 94043 USA

SUMMARY

A preliminary design method to predict the nonlinear aerodynamic characteristics of tactical missiles in unsteady maneuvers at high angles of attack in subsonic flow is described. The approach is based on the accurate representation of the complex flow phenomena in the vicinity of the missile, including effects of forebody vortex shedding and lifting surface trailing vorticity. For specified motion of the missile, the time-dependent forces and moments on all missile components are calculated, including hysteresis effects due to vortex lag and the history of the motion, without the need for empirical information. This provides a capability to predict the stability and control characteristics of advanced missile configurations for preliminary design analysis. When possible, comparison of experiment and theory are presented to validate the method.

SYMBOLS

AR	aspect ratio
\bar{c}	mean aerodynamic chord
C_{m_f}	fin alone pitching moment coefficient, based on fin area and \bar{c}
C_{N_f}	fin alone normal force coefficient, based on fin area
C_p	pressure coefficient
D	maximum equivalent diameter of fuselage
l	reference length
p,q,r	angular rotation rates about x,y,z-axes, respectively
q_∞	free stream dynamic pressure
Re _D	Reynolds number based on D
t	time
u,v,w	velocity components in x,y,z-directions, respectively
U_c	velocity component along inertial x_0 axis
V_∞	free stream velocity
x,y,z	body-fixed coordinate system with origin at missile nose
x_0,y_0,z_0	inertial coordinate system
z_m	maximum amplitude in heaving motion, Fig. 9
α	angle of attack
α^*	average angle of attack in oscillating flow
Γ	vortex strength
$\Gamma_{f_i,t}$	strength of fin trailing vortex at spanwise station "i" at time "t"
$\Gamma_{m,t}$	strength of forebody vortex shed at axial station "m" at time "t"
$\Delta\alpha$	maximum perturbation angle of attack
Δt	time increment
Δx	axial length increment
θ	circumferential angle; $\theta=0^\circ$ for horizontal fin, Figure 6.
λ	fin taper ratio
ϕ	phase angle
Φ	velocity potential
ω	frequency
ω'	reduced frequency; $\frac{\omega l}{U_c}$ for pure heave and pitch motions
$\dot{(\)}$	time rate of change
$(\)_s$	steady
$(\)_u$	unsteady

1. INTRODUCTION

Future advanced tactical missiles have mission requirements which include rapid maneuvers at low speeds and high angles of attack. Under these flight conditions, the missile operates in a flow regime in which the aerodynamic and stability and control characteristics are dominated by nonlinear effects induced by separation and vortex shedding. For example, induced roll on a missile is caused by interference of shed body vortices and canard trailing vortices on tail control surfaces. The dynamic and time-dependent effects of these nonlinear flow phenomena contribute significantly to the flight capability of the missile during extreme maneuvers; therefore, it is essential that undesirable flow regimes be considered during the preliminary design phase of a new missile.

Traditional aerodynamic prediction methods are not applicable to these unsteady and nonlinear flow conditions, and modern computational techniques (Euler, Navier-Stokes, etc.) which could possibly handle extreme flight conditions are not generally available nor practical for preliminary design and analysis. Wind tunnel and flight testing are available, but difficult, for examination of unsteady aerodynamic characteristics, and the high cost prohibits consideration of a large number of configurations during early design phases. A prediction method applicable to the unsteady and nonlinear flight conditions associated with maneuvering at high angles of attack will permit evaluation of a large number of configurations during the conceptual design at a fraction of the cost required for testing. Given this added preliminary design capability, the number of configurations carried to the testing phase is reduced to a reasonable and manageable level at less cost. The purpose of this paper is to document results from such a prediction method for tactical missiles in subsonic flow.

The prediction method is based on the accurate representation of the physics of the flow around the missile in a maneuver at high angles of attack. It is applicable to simple missile configurations with multiple lifting surfaces, and it is not dependent on existing empirical information. The technology from which the method has been developed for missiles has been used successfully for similar predictions for fighter aircraft (Ref. 1) and submersible vehicles (Ref. 2). The work described in this report is an extension of the body-alone method presented in Reference 3.

2. GENERAL DISCUSSION

A missile maneuvering at high angles of attack experiences nonlinear aerodynamic characteristics dominated by vortex effects. Preliminary design of modern missiles and their control systems must consider these extreme flow conditions which result as part of normal mission requirements, or unexpected forces and moments beyond the capability of the control system may threaten the success of the flight. The following sections describe the type of prediction methods needed, the flow phenomena of interest, and the general approach for the prediction technique.

2.1 Technical Requirements

Preliminary design and analysis of missile configurations in rapid maneuvers involving high angles of attack requires a prediction method which is easy and economical to use and is not dependent on a priori knowledge of aerodynamic characteristics. Traditional prediction methods based on potential flow models are very useful at low angles of attack when flow separation and vortex shedding have little or no effect. Though these methods, often using a surface paneling approach, provide good linear aerodynamic analysis capability, they generally do not include nonlinear vortex-induced effects. As demonstrated by this author (Ref. 4) and others, vortex effects can be included in panel methods; however, the resulting prediction method is often too expensive to apply to time dependent maneuvers during preliminary design or parametric studies. Their use in later design phases is unquestioned.

The aerodynamic prediction capability envisaged for preliminary design and analysis of missiles in unsteady time-dependent flows should be relatively fast and economical to use, but it must include the dominant nonlinear effects. It is important that the method represent the flow phenomena associated with missiles at high angles of attack. The method should have several levels of applicability. First, it should adequately predict the steady aerodynamic characteristics of missile configurations in both static and steady maneuvering flight conditions. Second, it should be applicable to time-dependent motions of the missile when the motion is prescribed. This latter condition arises under forced oscillation testing in a wind tunnel or tow tank. Finally, the aerodynamic prediction method can be coupled with a six-degree-of-freedom equation-of-motion solver to predict flight trajectories and transient performance. This capability should include effects of control inputs. One added capability of significant value is the prediction of dynamic stability derivatives in nonlinear flight regimes.

In all the above applications, the method should provide detailed information on the character of the flow field in the vicinity of the missile at any point in the maneuver. This information is very useful in diagnostic analysis of induced flow problems; for example, induced roll or roll reversal is often better understood when the strength and position of the shed vortex field relative to the tail fins is known.

2.2 Flow Phenomena

A modern tactical missile at high angle of attack is surrounded by an extensive wake region which can have a dominant effect on the induced nonlinear aerodynamic characteristics. This wake is made up of body vortices shed from the forebody, trailing vortices from a wing or canard, afterbody vortices, and tail trailing vortices. A familiar sketch of forebody vortex shedding is shown in Figure 1.

In unsteady maneuvers involving time history of the translation (u, v, w) and angular rotation (p, q, r) of the missile, the presence of the wake introduces memory into the flow problem. The forces and moments on the missile and its control surfaces depend on the history of the motion and the wake development. For example, shed vorticity from the nose will pass downstream to influence the induced loads on the wing and tail surfaces; however, the position of this vorticity depends on the missile motion between the time it was shed and the time it passes the lifting surfaces. Accurate prediction of the unsteady vortex-induced forces and moments requires construction of the time-varying vortex field representing the unsteady wake.

At very high angles of attack, the body vortex shedding from the nose becomes asymmetric, leading to lateral or out-of-plane forces and moments during a pure pitching maneuver (Ref. 5). For the analysis considered in this paper, only symmetric vortex shedding is considered. This effectively limits the useful angle of attack range of the prediction method to less than 35 degrees.

2.3 Prediction Techniques

A number of prediction techniques are available to apply to various aspects of a missile in unsteady motion; however, when high angles of attack are considered, many of the traditional methods are no longer applicable because of nonlinear effects. Several different flow models have been combined to develop a unified prediction method to apply to the problem described.

For purposes of this analysis, an axisymmetric missile body is considered, and axis singularity distributions of sources, sinks, and doublets (Ref. 4) are selected. The lifting surfaces are represented with a vortex lattice panel method.

Beginning at the missile nose, the forebody vortex shedding is represented by a vortex cloud or discrete vortex model (Ref. 4) in which individual vortices form the feeding sheet and rolled-up vortex on the lee side of the missile (Fig. 1). The steady vortex wake model for missile bodies alone was extended to unsteady motions in References 3 and 6. The unsteady influence of forebody vortices on lifting surfaces has been studied for fighter aircraft (Ref. 1) and submersible configurations (Ref. 2); therefore, this technology is available for application to missiles in unsteady flow.

2.4 Calculation Procedure

As described elsewhere (Refs. 2, 3, and 4), the calculation of the nonlinear aerodynamic characteristics of a missile configuration in static and steady flow is carried out with a marching procedure. Beginning at the missile nose, vorticity is formed by boundary layer fluid leaving the body at separation lines on both sides of the missile. The vorticity is represented by discrete vortices which are added to the lee side flow field at axial stations along the body length. The trailing vorticity from the lifting surfaces is included in the flow field as vortex filaments which are permitted to interact with the body vorticity as part of the marching process.

In unsteady flow, the calculation procedure is slightly more complex. The initial conditions must be steady, and they are computed in the usual manner described above. Assuming some motion of the missile, either specified or predicted, the flow conditions change with time. The vortex wake is allowed to move downstream under the influence of the changing local flow conditions during some small time interval, and the modified flow field influences the pressure distribution on the missile and subsequent separation. New vortices are added to the field, new forces and moments are computed, and the calculation procedure continues. The vortex wake represents the historical lag in the flow field which relates to the aft portion of the missile what happened at an earlier time on the forward portion. The starting conditions are eventually swept downstream past the base of the vehicle, and their effect on the induced loads is lost forever. Details of the flow models and calculation procedure are presented below.

3. TECHNICAL APPROACH

A summary of the flow models and calculation procedures making up the prediction method are presented in this section.

3.1 Geometry

For the simplified missile configurations considered in this investigation, the fuselage is defined as a body of revolution. This axisymmetric body is represented by a distribution of sources and sinks on the body axis (Ref. 4). This three dimensional volume representation of

a body in a uniform flow provides a potential flow model for calculating velocities at flow field points outside the body and for calculating surface pressure distributions. The prediction technique is applicable to noncircular cross sections using conformal mapping procedures or surface panel models; however, in the interest of economy, these methods are not considered herein.

The surface pressure distribution on the body is required to calculate forces and moments and to predict separation locations. The pressure coefficient at a point on the body in unsteady motion is

$$C_{p_u} = C_{p_s} - \frac{2}{V_\infty^2} \frac{\partial \phi}{\partial t} \quad (1)$$

where C_{p_s} is the instantaneous steady pressure coefficient. This result is obtained by a transformation of the Bernoulli equation from an inertial coordinate system to a body-fixed system. The last term is the unsteady term caused by the motion of the missile and associated changes in the flow field. Calculation of this unsteady term is described in Reference 3.

The prediction method permits two regions of lifting surfaces on the missile, each region containing multiple surfaces. Each individual surface is represented by a distribution of vortex lattice panels with the strength of each vortex obtained by satisfying the flow tangency condition at control points on the panels. The boundary condition includes induced effects from the total flow field made up of the vortex wake, the fuselage, angular rotation, and mutual interference from adjacent lifting surfaces. This simple approach is well documented, and its use in unsteady motion is described in References 1 and 6.

3.2 Vortex Wake

A major nonlinear effect on a missile at high angles of attack in both steady and unsteady flow conditions is the separation vortex wake on the lee side of the body. At moderate angles of attack, the body vorticity rolls up into a symmetrical vortex pair (Fig. 1) which can have a dominating effect on the induced forces and moments on the missile forebody. As demonstrated by a number of investigators (Refs. 7-10) under steady flow conditions, a successful model for this wake is a cloud of discrete vortices.

The vortex cloud model requires the separation location on the body at each cross section be known to specify the strength and position of the shed vortices. The circumferential pressure distribution on the body is predicted using Equation (1) including unsteady terms, and Stratford's separation criteria using predicted pressure distributions are utilized to predict either laminar or turbulent separation depending on the Reynolds number. At each axial station on the body, the strength of the shed vortex is obtained by integrating the vorticity flux across the boundary layer assuming no slip at the surface. Details of the pressure distribution and separation calculations are described in Reference 4.

Vortices shed at a given axial station are tracked to the next station along the body by integrating their equations of motion. At the next station they influence the pressure distribution and the resulting separation location. As the calculation continues downstream, vortices are added to the flow field, and they form a discretized wake representing the lee side vortex wake associated with bodies at high angles of attack.

Lifting surfaces contribute to the vortex wake via the trailing wake associated with their loading. This portion of the wake is made up of two parts, (1) the traditional trailing vortices representing the potential attached loading on the wing as represented by the vortex lattice model, and (2) the vorticity associated with separation from swept sharp leading edges and side edges. In an effort to simplify the leading edge vortex model, the approach described in References 11 and 12 is used for this investigation. Aft of the lifting surface trailing edge, these vortices are added to the vortex field from the body to complete the wake. Mutual interaction of all the wake vortices is considered for tracking purposes, and the entire wake is considered for loading and separation calculations on the afterbody and other lifting surfaces near the base of the missile.

The above wake model has proved to be a reasonable representation of a complex flow phenomena in steady flows. Some modifications are required for unsteady or time-dependent flows, and these are described in the next section.

3.3 Unsteady Calculation Procedure

An unsteady wake calculation requires a steady wake (described above) as a starting point. The time-dependent flow conditions on the missile can be specified, or they can be calculated as a result of the trajectory prediction. The steady initial conditions to start an unsteady computation cause a transient behavior which is removed as the calculation proceeds and the initial wake is transported downstream out of the field of influence of the vehicle.

The separation vortex field on a missile fuselage at $t = 0$ is shown schematically in Figure 2(a) where only the forebody is considered for this discussion. The discrete body separation vortex positions are shown as dots at each axial station, and their trajectories are

denoted as dashed lines. The individual vortices are identified as $\Gamma_{m,t}$, where the first subscript represents the axial station at which the vortex is shed, and the second subscript represents the time interval in which it was shed. The initial conditions at $t = 0$ in Figure 2(a) are analogous to steady flow conditions described previously. The unsteady calculation begins with the specification of new flow conditions at $t_1 = t_0 + \Delta t$ where the axial integration interval, Δx , is related to the time interval Δt .

Given the new flow conditions at t_1 , the existing vortex wake is allowed to move downstream under the influence of the average local flow conditions during the interval Δt . The motion of the body vortex field is shown schematically in Figure 2(b). Comparison of parts (a) and (b) of this figure shows the axial motion of individual vortices; however, during this interval, motion in the crossflow planes is also occurring. In essence, the entire vortex field existing at t_0 has been transported downstream a distance Δx . Under the influence of the average flow conditions during the interval and the modified vortex field, the body pressure distribution is predicted, loads are calculated, and a new separation calculation is conducted to add new vortices to the field. The final flow field at t_1 is illustrated in Figure 2(c) with the new vortices included in the cloud.

The unsteady loading on a lifting surface produces a more complex trailing vortex field than that discussed above. Changing loading on the surface requires a spanwise vortex be shed to represent the change in bound vortex strength on the lifting surface between t_0 and t_1 . This situation is illustrated in Figure 3 where spanwise vortex filaments are included as part of the trailing vortex field from the fin. The axial filaments are free to move in y - z planes normal to the body axis, and the spanwise filaments are always attached to the axial filaments; therefore, the spanwise filaments remain in the planes normal to the axis. The shed vortex ring (or quadrilateral) illustrated by $\Gamma_{F2,1}$ in Figure 3(c) moves with the total vortex flow field but keeps its identity.

The unsteady procedure is repeated for each time interval to the end of the maneuver or until the aerodynamic characteristics begin to repeat in the case of cyclic motions. The vortex wake described above forms the historical lag in the flow field which relates to the aft portions of the missile what happened at an earlier time on the forward portions. As time passes, the wake shed at an earlier time is swept downstream past the base of the missile, and its effect on the vehicle is lost forever. Results from an unsteady calculation are the forces and moments on the missile at each instant in time including the effects of changing flow conditions and control surface deflections, if considered.

3.4 Aerodynamic Characteristics

The singularity models described above provide a means to calculate the induced velocity field on or near the missile. The induced velocity field, when combined with the velocities associated with the motion of the missile, is used to predict the distribution of loads on the missile components. The derivation of the equations for the velocity field and surface pressure distribution on the missile is presented in Reference 3 and will not be repeated in this paper. It should be noted that each singularity in the flow model is changing with time in an unsteady calculation; therefore, each contributes to the unsteady term in the Bernoulli equation for surface pressures.

The forces on the lifting surfaces are a combination of the forces on the horseshoe vortices on the lattice panels and a leading edge and side edge suction force represented by the Polhamus suction analogy (Refs. 11 and 12). The unsteady effects are included through the interference of the time dependent body vorticity and fin trailing vorticity. In this preliminary version of the prediction method, the nonlinear lift associated with leading edge separation is allowed to change with time and changing flow conditions, but a hysteresis or lag effect is not included. A discussion of this effect is presented in Reference 1.

At high angles of attack, the flow separates from the lifting surface, and the attached flow vortex lattice model no longer represents the correct loading. As described in Reference 1, stall of the lifting surface is approximated by reducing the lift on the wing when the predicted section lift coefficient exceeds some specified value. The lift and associated horseshoe vortex strengths are reduced accordingly, and the total surface loads are recomputed with the modified local loadings. This model has proved to be a reasonable approximation to wing stall, and it permits use of the vortex lattice to angles of attack beyond the linear range.

3.5 Trajectory Analysis

The prediction method described contains the capability to consider both prescribed and predicted motions. When the motion is prescribed, the missile trajectory and flow conditions are determined by harmonic variation of the flow characteristics or by specification of the time history of the missile velocity and acceleration. In either case, the flow condition is specified at each instant in time, and the method produces the time history of the forces and moments on the missile configuration based on the history of the motion prior to that instant.

Coupling the unsteady aerodynamics prediction method with a six-degree-of-freedom equation-of-motion solver provides a means to predict the missile trajectory. The aerodynamic prediction model supplies the instantaneous forces and moments on the missile which are used

to calculate the translational and rotational accelerations which go directly into the equations of motion. Stability derivatives are not needed in this formulation (described in Refs. 1 and 3); therefore, it is possible to predict missile trajectories in nonlinear flight regimes when stability derivatives are not available.

The results presented in this paper will consider only prescribed motion of the missile.

4. RESULTS

The prediction method described above has been applied to a number of different simplified missile configurations for a wide range of flow conditions, both steady and unsteady. In an effort to evaluate the strengths and weaknesses of the method, comparisons with experiment are presented when possible; however, little experimental data are available for unsteady flows. In the results to follow, a series of comparisons of measured and predicted static forces on a fin on a body are described to demonstrate the prediction of vortex-induced effects. This is followed by predicted results on the same fin with the missile in unsteady motion. These results are designed to illustrate unexpected control problems which can develop on a typical missile configuration in steady and unsteady motions involving high angles of attack. Since the prediction method has been demonstrated for bodies alone for a variety of steady and unsteady flow conditions (Refs. 2, 3, and 4), these will not be repeated in this paper.

4.1 Static

Measured forces on individual fins of a cruciform arrangement on an ogive-cylinder body of revolution are described in Reference 13. These data consider a large number of fins over a wide range of angles of attack and roll angle, but total configuration forces are not available. For the comparisons to follow, a rectangular planform fin (Fig. 4) with aspect ratio 2 is selected. The fin exposed semispan is equal to the body radius, and the fin leading edge is 10.4D from the missile nose. Fin deflection is not considered. Though the experimental results are for a subsonic Mach number of 0.8, compressibility effects are not included in the theoretical results.

Static normal force coefficients on a single fin in the $\theta = 0^\circ$ position are shown in Figure 5. It appears the fin begins to stall near 10 degrees angle of attack, but the loading recovers above 15 degrees and continues to increase at a lower rate. The stall model described above represents the wing loading up to 20 degrees angle of attack, but the slope of the curve after stall does not agree with experiment and the level of predicted lift is well under that measured at angles above 20 degrees.

Since the tail fins are located more than 10 diameters aft of the nose, a large body vortex is developed in the region of the fins above 10 degrees angle of attack. The predicted body vortex represented by a cloud of discrete vortices is shown at the leading edge of the tail fins in Figure 6 for $\alpha = 15$ and 20 degrees. The strength of the vortex at $\alpha = 20$ degrees is more than double the strength at 15 degrees, and it appears to be broader in extent on the lee side of the missile. These vortices will have a large effect on the fin loadings as the fin moves through the vortex wake.

The induced effects of the body vortex on the normal force coefficient on a single fin of a cruciform set as the body rolls through 360 degrees is shown in Figures 7(a) and (b) for $\alpha = 15$ and 20 degrees, respectively. The predicted results, shown as the solid curve in the figures, are in very good agreement with experiment, even in the region of maximum vortex interference on the body lee side. The vortex-induced effects are further illustrated by the comparison with potential flow results with no body separation included. The vortex-induced effects on the windward side of the body are small, and potential flow results are in good agreement with experiment.

4.2 Dynamic

Though dynamic experimental data are not available on the missile configuration considered above, this same body tail model is examined theoretically under various dynamic motions to illustrate the unsteady prediction capability and typical unsteady vortex phenomena. Two different motions are considered below. The first is a heave maneuver, and the second is an oscillatory heaving motion.

In the first unsteady maneuver, the model begins at a steady angle of attack of 5 degrees. At $t = 0$, the model begins to heave such that the angle of attack increases at a constant rate of 10 deg/sec (reduced frequency = 0.2) to an angle of attack of 10 degrees. This angle is held constant, and the unsteady solution continues until the results converge to the static result. The history of the angle of attack and predicted results on the fin alone are presented in Figure 8 where the dashed curve represents the static results obtained from a converged solution. Note that time is shown in seconds for these results, and the calculation was carried out at a free stream velocity of approximately 5D/sec. At this velocity, a vortex shed from the nose reaches the tail fins in two seconds. In both the normal force and pitching moment results, the unsteady characteristics of the fin lag the static results because of the influence of the unsteady wake from the fin. At the low angles considered in this case, neither body vortex shedding nor fin stall have a significant effect on the predicted results.

The heaving motion next considered is obtained from a sinusoidal variation of angle of attack with amplitude $\Delta\alpha$ around a nominal angle of attack α^* . The model experiences no rotation or pitch rate during this motion, and a sketch of the motion (from Ref. 14) is shown in Figure 9. The prediction method produces a time history of the forces and moments on the model, and each calculation is continued until the cyclic aerodynamic characteristics are in agreement with the previous cycle. In most cases, only one quarter cycle is required for the transient behavior to disappear. In the unsteady results to follow, a number of flow conditions are selected to illustrate the different interference effects of importance.

The predicted normal force on a single fin (Fig. 4) in the $\theta = 0$ position is shown in Figure 10. The heave flow conditions are such that the model heaves around $\alpha^* = 10$ degrees with $\Delta\alpha = 5$ degrees at a reduced frequency $u' = 0.2$. Body vortex shedding is suppressed for this case. In this fin position, the loading on the fin is high, and the fin stall model begins to reduce the fin loading near $\alpha = 9$ degrees. Though the effect is small, there is a well defined hysteresis loop for the fin normal force in the unstalled region. In the stalled region, the two legs of the loop are identical, though there is a small lag in the angle of attack at which stall affects the loading.

The predicted normal force coefficient on the same fin during a similar heaving maneuver with $\alpha^* = 15$ degrees, $\Delta\alpha = 5$ degrees, and a reduced frequency $u' = 0.2$ is shown in Figure 11. In this case, the body is rolled 60 degrees from the horizontal as shown in the sketch. No body vortex separation is considered; therefore, this result is linear, and its purpose is to demonstrate the hysteresis effect of the unsteady loading on the fin. The direction of motion is shown by the arrows on the theoretical curve. The initial transient disappears after approximately 1 degree of motion, and the solution repeats periodically. The change in the fin normal force with time is also shown in this figure. Note that the time scale is dimensional, and the time interval for the calculation is 0.1 seconds at a free stream velocity of 15.2 in/sec.

The induced effect of body vortex shedding for the same flow condition and configuration described above is shown in Figure 12. A significant body vortex is shed from this missile body at angles of attack above 15 degrees, and as shown in Figure 7 for static flow conditions, the vortex reduces the loading on the fin when the fin is rolled to the $\theta = 60$ degree position. In Figure 12(a), the unsteady normal force coefficient on the single fin as the missile heaves between 10 and 20 degrees angle of attack is shown as the solid curve. These predicted results are smoothed to remove some numerical roughness in the calculation caused by the large Δx increment chosen for this case. The smoothing is accomplished to simplify the discussion of vortex induced effects, and the degree of roughness in the results is shown in Figure 12(b) where the actual fin normal force coefficient at each time step is shown.

Arrows illustrate the direction taken by the unsteady calculation in Figure 12(a), and predicted static results are presented as symbols for comparison purposes. The first item to note in these results is that the hysteresis loop moves in the opposite direction from the linear results in Figure 11(a). The second important point is that the fin loading is less at $\alpha = 20$ degrees than it is at $\alpha = 15$ degrees. The latter result is caused by the significantly stronger body vortex at the higher angle and its stronger influence on the fin loading as illustrated in Figures 6 and 7. The former result is best explained by examining in detail the unsteady vortex field in the vicinity of the tail fin.

The predicted vortex field shed from the missile fuselage ahead of the tail fin is shown in Figure 13 at various times in the unsteady calculation. The tail fin at $\theta = 60$ degrees is placed in each sketch to illustrate the relative positions of the wake and the fin. Beginning at $t = 0$ and $\alpha = 15$ degrees, the steady vortex field is shown at the top of the figure. Except for the slightly different axial station, this result is nearly identical to the result in Figure 6(a). As the motion starts, the missile heaves upward such that the angle of attack decreases toward a minimum value of 10 degrees as shown in Figure 12. The strength of the vortex field at $\alpha = 10$ degrees is approximately one half the strength of the starting field, and as seen in Figure 12(a), the entire initial vortex field has been swept past the base of the missile and the periodic unsteady behavior has been achieved. As the missile heaves downward with increasing angle of attack and passes through $\alpha = 15$ degrees, the resulting vortex field in the vicinity of the fin at this time is weaker than the initial static result; therefore, the vortex induced effects on the fin are weaker, and the fin loading is greater than the static value. This is seen in Figure 12(a). The vortex field near the fin is weaker in this case because the vorticity was shed at an earlier time when the angle of attack was less than the current value.

The motion continues and the angle of attack increases to a maximum value of 20 degrees. The vortex field is slightly weaker than the static result shown in Figure 6(b) for the same reasons described above. The normal force on the fin is higher than the static result because of reduced vortex interference.

The angle of attack begins to decrease, and at $\alpha = 15$ degrees the vortex strength is now stronger than both the static result and the previous unsteady result. This is because the vorticity was shed from the body when the angle of attack was higher than 15 degrees. Since the motion is periodic, the vortex field and associated fin normal force repeats with time.

5. CONCLUSIONS

A method to predict the aerodynamic characteristics of missile configurations in steady and unsteady maneuvers involving angles of attack above the linear range is described. Prediction of body separation and lifting surface shed vorticity and its contribution to the induced nonlinear loads on the body and tail fins is an integral part of the method. The vortex cloud model of the body vorticity provides a means to calculate nonlinear interference effects and a capability to predict details of the flow phenomena associated with specified flight conditions. Unsteady effects of vortex lag and hysteresis associated with changing and periodic flow conditions are considered.

Comparisons of measured and predicted tail fin loads under the direct influence of body separation vorticity illustrate the capability to predict nonlinear static loads at moderate angles of attack. Induced roll on missiles caused by vortex-induced loading reversals on the fins on the body lee side is quantified, and a better understanding of the flow phenomena causing these nonlinearities is now available.

The feasibility of the technical approach for unsteady flows is demonstrated; however, experimental data are not available for verification purposes. Analysis of the predicted results indicate the method has the capability of modeling the proper physics of the complex flow phenomena associated with unsteady motions.

The prediction method presented in this paper can be used to predict the aerodynamic characteristics of generic missile configurations over a wide range of flight conditions including high angles of attack and rapid maneuvers in subsonic flow. The method is applicable during the preliminary design and analysis phase of a new missile to investigate the nonlinear time-dependent phenomena which are difficult to obtain using traditional methods. Results from the method are the time history of the forces and moments on the missile and the detailed flow field associated with the unsteady motion.

Given the capability demonstrated in this paper, a proposed missile configuration can be analyzed for aerodynamic and stability and control characteristics at high angles of attack when vortex-induced effects dominate the flow field. Undesirable nonlinearities can be investigated early in the design phase of the missile, and, provided with the knowledge of the flow field, modifications to the configuration or proposed flight profile can be considered before wind tunnel or flight tests are conducted.

Though only used herein for specified motion of the missile, the prediction method also has application as part of a trajectory calculation procedure. It is possible to couple the nonlinear aerodynamics prediction method with a six-degree-of-freedom equation-of-motion solver to calculate flight trajectories. Control inputs and thrust requirements can be specified at each instant in time for a realistic flight simulation. This capability is currently reliable for flight conditions at high angles of attack prior to massive stall on lifting surfaces.

6. REFERENCES

1. Mendenhall, M. R. and Perkins, S. C., Jr.: Analysis of Dynamic Maneuver Performance of Fighter Aircraft at High Angles of Attack. NLR TR 350, March 1988.
2. Mendenhall, M. R. and Perkins, S. C., Jr.: Prediction of the Unsteady Hydrodynamic Characteristics of Submersible Vehicles, Fourth International Conference on Numerical Ship Hydrodynamics, National Academy of Sciences, Washington, D. C., Sept. 24-27, 1985.
3. Mendenhall, M. R., Perkins, S. C., Jr., and Lesieutre, D. J.: Prediction of the Nonlinear Aerodynamic Characteristics of Maneuvering Missiles, Journal of Spacecraft and Rockets, Vol. 24, No. 5, Sept.-Oct. 1987, pp. 394-402.
4. Mendenhall, M. R. and Perkins, S. C., Jr.: Vortex Cloud Model for Body Vortex Shedding and Tracking. Tactical Missile Aerodynamics, Vol. 104 of Progress in Astronautics and Aeronautics, ed. by M. J. Hemsch and J. N. Nielsen, AIAA, 1986.
5. Ericsson, L. E. and Reding, J. P.: Asymmetric Vortex Shedding from Bodies of Revolution. Tactical Missile Aerodynamics, Vol. 104 of Progress in Astronautics and Aeronautics, ed. by M. J. Hemsch and J. N. Nielsen, AIAA, 1986.
6. Mook, D. T. and Nayfeh, A. H.: Application of the Vortex-Lattice Method to High-Angle-of-Attack Subsonic Aerodynamics. SAE 851817, Oct. 14-17, 1985.
7. Angelucci, S. B.: A Multivortex Method for Axisymmetric Bodies at Angle of Attack. Journal of Aircraft, Vol. 8, Dec. 1971, pp. 959-966.
8. Marshall, F. J. and Deffenbaugh, F. D.: Separated Flow Over Bodies of Revolution Using an Unsteady Discrete-Vorticity Cross Wake. Part I - Theory and Applications. NASA CR-2414, June 1974.
9. Wardlaw, A. B.: Multivortex Model of Asymmetric Shedding on Slender Bodies at High Angles of Attack. AIAA 75-123, Jan. 1975.

10. Mendenhall, M. R., Spangler, S. B., and Perkins, S. C., Jr.: Vortex Shedding from Circular and Noncircular Bodies at High Angles of Attack. AIAA 79-0026, Jan. 1979.
11. Mendenhall, M. R. and Nielsen, J. N.: Effect of Symmetrical Vortex Shedding on the Longitudinal Aerodynamic Characteristics of Wing-Body-Tail Combinations. NASA CR 2473, 1975.
12. Polhamus, E. C.: A Concept of the Vortex Lift of Sharp-Edged Delta Wings Based on a Leading Edge-Suction Analogy. NASA TN D-3767, 1966.
13. Lesieur, D. J., Mendenhall, M. R., Nazario, S. M., and Hensch, M. J.: Prediction of the Aerodynamic Characteristics of Cruciform Missiles Including Effects of Roll Angle and Control Deflection. NEAR TR 360, Aug. 1987.
14. Goodman, A., Brown, C. E., and Altmann, R. J.: An Experimental Study to Determine the Flow and the Subsonic Static and Dynamic Stability Characteristics of Aircraft Operating at High Angles-of-Attack. AIAA 87-2580, Aug. 1987.

7. ACKNOWLEDGEMENT

The analysis reported in this paper was funded under a Nielsen Engineering & Research IR&D project.

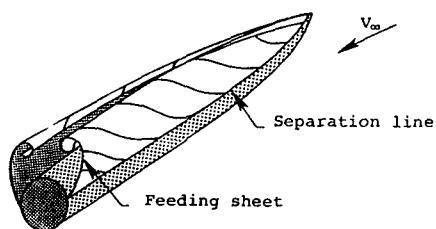


Fig 1 Lee side vortex formation.

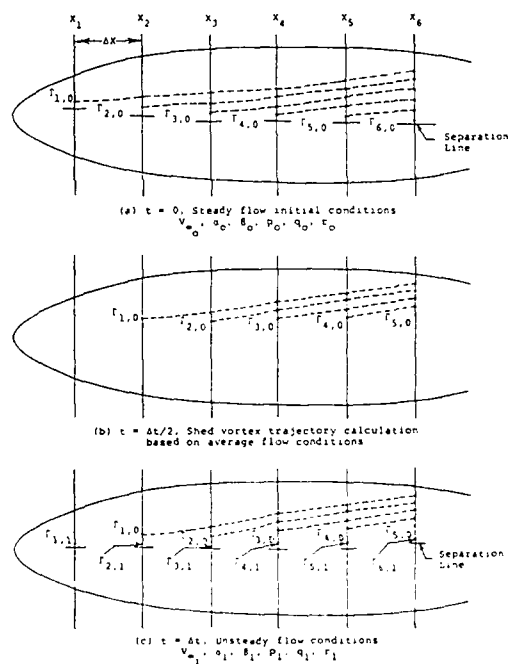


Fig 2 Unsteady vortex wake calculation procedure on a missile forebody.

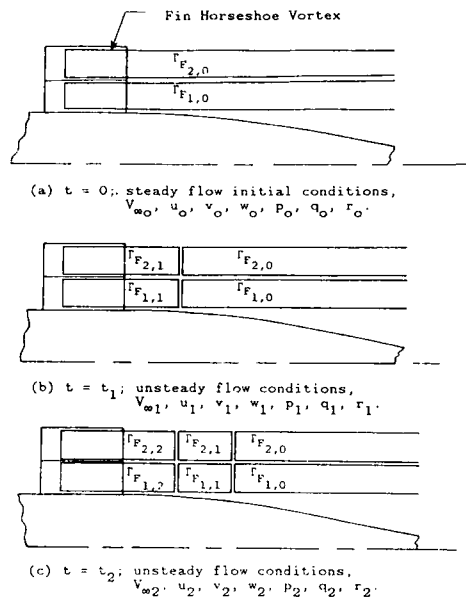


Fig 3 Unsteady vortex wake calculation procedure on a lifting surface.

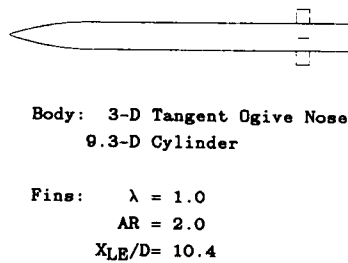


Fig 4 Missile configuration with cruciform tail fins.

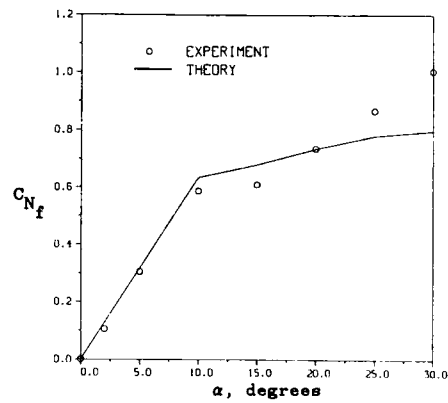


Fig 5 Measured and predicted fin normal force coefficients, $\theta = 0$ deg.

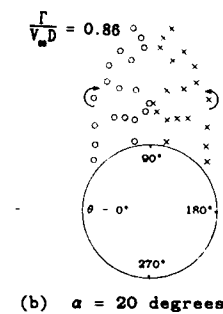
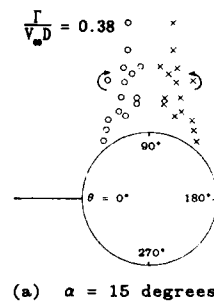


Fig 6 Predicted body vortex field near the tail fins, $x/D = 10.4$.

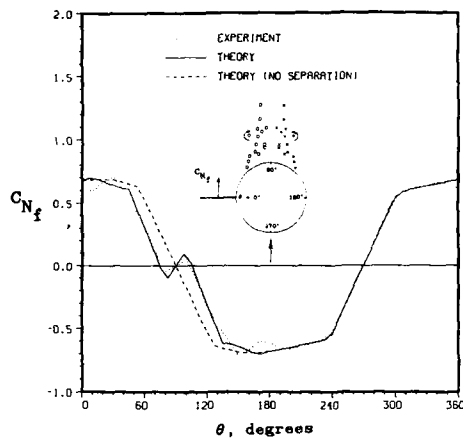
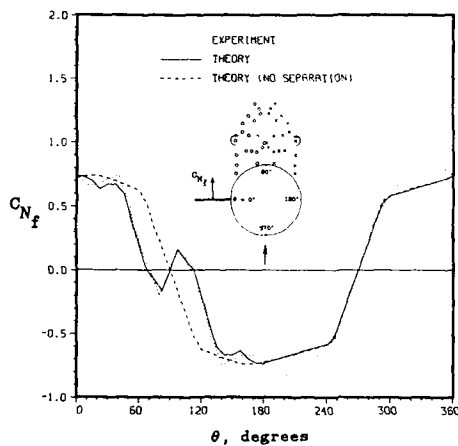
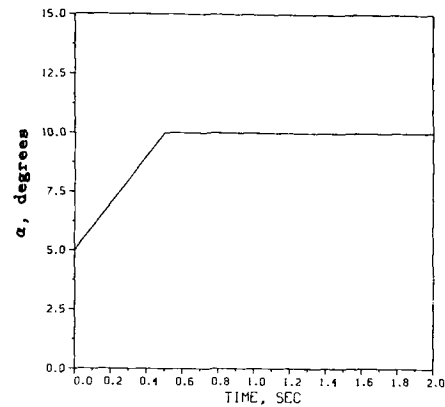
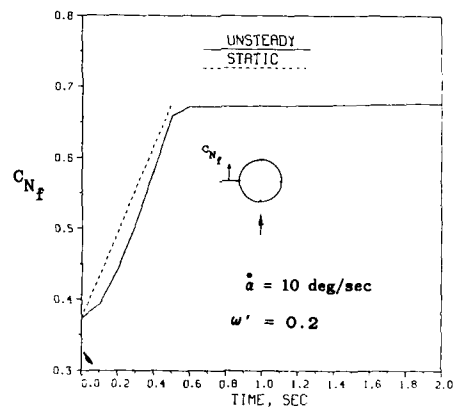
(a) $\alpha = 15$ degrees(b) $\alpha = 20$ degrees

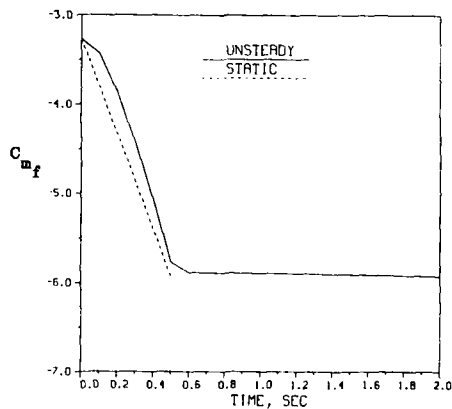
Fig 7 Measured and predicted normal force coefficient on a tail fin under the influence of body vorticity.



(a) Angle of attack history



(b) Normal force coefficient



(c) Pitching moment coefficient

Fig 8 Predicted unsteady aerodynamic characteristics of a tail fin on a missile in heaving motion.

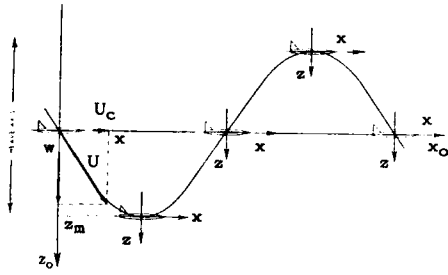


Fig 9 Missile configuration in pure heaving motion, $\alpha^* = 0$ deg.

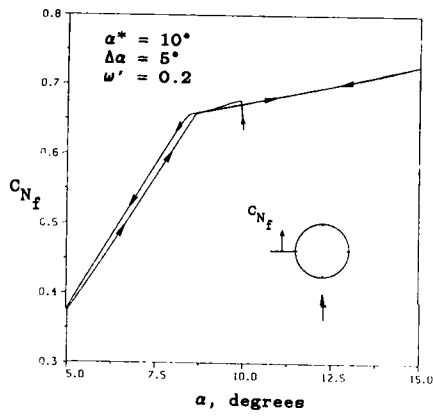
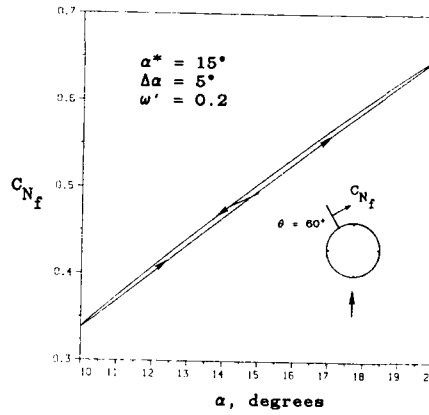
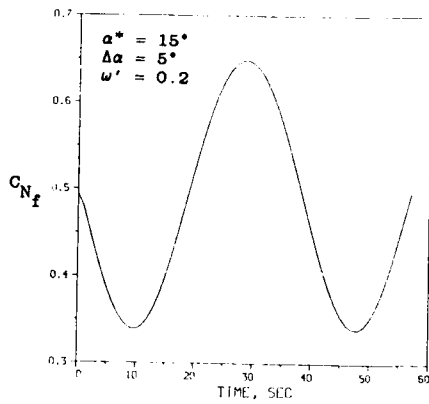


Fig 10 Predicted unsteady normal force coefficient on a single fin on a body-fin configuration in heaving motion, $\alpha^* = 10$ deg, $\Delta\alpha = 5$ deg, $\omega' = 0.2$, $\theta = 0$ deg.



(a) C_{N_f} vs α



(b) C_{N_f} vs time

Fig 11 Predicted unsteady normal force coefficient on a single fin on a body-fin configuration in heaving motion, no vortex shedding, $\alpha^* = 15$ deg, $\Delta\alpha = 5$ deg, $\omega' = 0.2$, $\theta = 60$ deg.

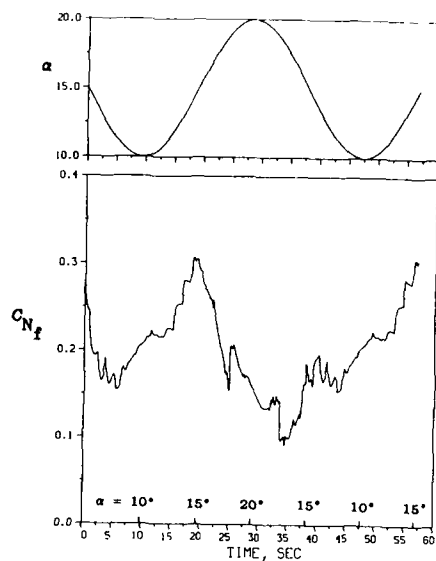
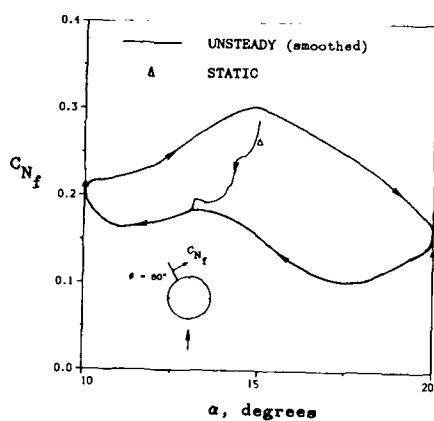
(a) C_{N_f} vs time(b) C_{N_f} vs α

Fig 12 Predicted unsteady normal force coefficient on a single fin on a body-fin configuration in heaving motion, $\alpha^* = 15$ deg, $\Delta\alpha = 5$ deg, $\omega' = 0.2$, $\theta = 60$ deg.

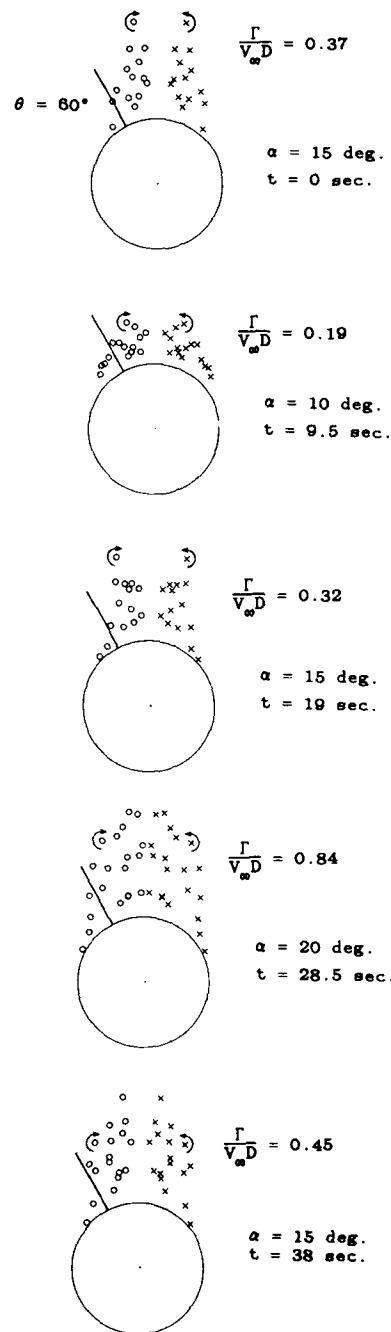


Fig 13 Predicted body vortex field near the tail fins of a missile in heaving motion, $\alpha^* = 15$ deg, $\Delta\alpha = 5$ deg, $\omega' = 0.2$, $x/D = 10.2$.

AEROELASTIC TAILORING PROCEDURE FOR CONTROLLING FIN HINGE MOMENTS

by

M. F. E. Dillenius
Director of Missile and Store Separation Aerodynamics
Nielsen Engineering & Research, Inc.
510 Clyde Avenue
Mountain View, California 94043-2287 USA

and

S. C. McIntosh, Jr.
President
McIntosh Structural Dynamics, Inc.
887 Warren Way
Palo Alto, California 94303 USA

Summary

A combined static aeroelastic and optimization design method is presented which is aimed at controlling the center of pressure acting on a missile control fin made of composite material. Specifically, the material principal-axis directions of various segments of an orthotropic fin are varied in order to influence the chordwise location of the center of pressure through elastic fin deformation under nonlinear supersonic aerodynamic loading. The design problem is posed as an optimization problem, where the principal-axis directions are the design variables, and the objective is the difference between the current center of pressure location and its desired location. Constraints on flutter speeds, displacements, and natural frequencies are permitted, and the design variables have upper and lower bounds. Consistent fin deformations are obtained by iterating between the aerodynamic load and the fin displacement calculations. Results obtained by the present method are presented for a hypothetical supersonic missile control fin. An antisymmetric angle-ply layup of graphite fibers and epoxy is used for the fin material. The variation of chordwise center of pressure location with material principal-axis direction is mapped, and operation of the optimizer, with and without constraints, is demonstrated. The results demonstrate that locally optimum center of pressure locations can be calculated.

Symbols

C_N	fin normal force coefficient, $F_N/(q_\infty S_{ref})$
C_{RMB}	fin root bending moment coefficient, $moment/(q_\infty S_{ref} L_{ref})$
c_r	fin root chord
F_N	fin aerodynamic normal force, lbs
L_{ref}	reference length, ft
M_∞	freestream Mach number
q_∞	freestream dynamic pressure, lbs/ft^2
S_{ref}	reference area, ft^2
x_{cp}	chordwise location of center of pressure on the fin, measured aft from fin root chord leading edge
x, y, z	fin coordinate system
θ	principal-axis orientation angle measured from y or x axes, see Fig. 5

Introduction

This paper describes a new concept in the design procedure of control fins for supersonic missiles. An aerodynamic paneling technique is combined with a structural analysis and an optimization scheme to control the chordwise location of the center of pressure location of a missile control fin by aeroelastic tailoring. This is accomplished by taking advantage of the design flexibility offered by composite materials and using the fin deformation under aerodynamic loading to affect the chordwise pressure distribution in a desirable way. The advantages offered by this concept include reduced actuator power requirements and the possibility of controlling fin loads. Another possibility is the extension of the design procedures to other goals, such as the reduction of spanwise bending moments. Highly maneuverable tactical missiles are expected to benefit most, since they generate large nonlinear aerodynamic loads and can be subject to severe limitations on actuator size and complexity.

The design process is divided into four discrete tasks:

- (1) In the finite element modeling task, an initial model is constructed with particular material principal-axis orientations as design variable(s), an updated model is obtained when the design variables are changed, and structural gradient information is calculated.

- (2) Aerodynamic loading calculations are required for given fin shape and flow conditions; results include aerodynamic force distribution and center of pressure location, and a procedure is included for transformation of aerodynamic forces from aerodynamic control points to structural nodal points.
- (3) Displacement, frequency, and flutter calculations are performed for constraint evaluation and gradient calculations.
- (4) In the fourth task, an optimization scheme is aimed at satisfying an objective (controlling chordwise center of pressure location) subject to certain constraints.

All of the tasks summarized above are tied together by an executive routine which handles input and output and schedules the various tasks. The requirements for each task are described below.

Approach

The following discusses in general terms what is required of each segment of the design procedure. First, the fin structure must be modeled. Material properties and a layup or construction scheme are selected in advance and remain unchanged, as do the fin planform geometry and structural node layout. The material principal-axis orientation will be varied as part of the design procedure. Only the stiffness matrix will vary with changes in material principal-axis orientation. Hence, this matrix must be updated as the design changes, and derivatives of this matrix must be calculated for sensitivity and gradient information.

To determine the objective, the fin center of pressure is calculated for a given set of flow conditions. As with the fin structural model, geometric data such as fin paneling details are fixed in the beginning and are not changed. However, the fin can deform arbitrarily subject to constraints. Since the aerodynamic calculation depends on fin slopes and is nonlinear, an iterative means is used to arrive at a consistent displacement and load distribution. Since the aerodynamic control points and the structural node points do not in general coincide, fin loads must be transformed from one set of points to the other.

The derivatives of the center of pressure location with respect to the material principal-axis orientations are determined. Evaluation and derivative calculations for constraints on flutter speed, frequencies, and displacements are also performed as required.

The optimization task includes a procedure capable of handling multiple constraints. The optimization is gradient-based. All of these tasks are organized by the executive routine.

Technical Description

This section contains descriptions of the structural model, the aerodynamic model with the load prediction method and force conversion procedure, the method of analysis, and the optimization scheme.

Structural Model

The structure is modeled by finite elements. For simplicity, a very restricted collection of elements is incorporated. The elements available are:

- (1) A nonconforming triangular bending element, which can be isotropic or orthotropic, or sandwich (without shear effects).
- (2) A beam bending element (without shear effects).
- (3) A torsion element.

The orthotropic bending element provides the modeling capability for the portion of the structure that is to be tailored. The stiffness matrix for this element is derived as in Chapter 5 of Ref. 1, with the addition of an orthotropic stress-strain relationship as given in Ref. 2. Consider now the element illustrated in Fig. 1. The local y axis lies along the edge defined by nodes 1 and 2, and the material principal axes (x' , y') are offset from the local axes by the angle θ . Its stiffness matrix can be written as follows (Ref. 3).

$$[K] = [C^{-1}]^T \left(\int_A [Q]^T [D] [Q] dx dy \right) [C^{-1}] \quad (1)$$

Here A is the element of the area, $[D]$ is the constitutive matrix for plate bending, $[C]$ is the matrix of coefficients in the polynomial representation of the plate displacement, and $[Q]$ is made up of derivatives of the polynomial terms (Ref. 1).

The matrix $[D]$ takes the following form when written with respect to the principal axes:

$$[D'] = \begin{bmatrix} D_x & D_1 & 0 \\ D_1 & D_y & 0 \\ 0 & 0 & D_{xy} \end{bmatrix} \quad (2)$$

If the local coordinate axes do not coincide with the principal axes, then $[D]$ is given by the transformation

$$[D] = [T]^T [D'] [T] \quad (3)$$

with

$$[T] = \begin{bmatrix} \cos^2\theta & \sin^2\theta & -2\sin\theta\cos\theta \\ \sin^2\theta & \cos^2\theta & 2\sin\theta\cos\theta \\ \sin\theta\cos\theta & -\sin\theta\cos\theta & -\sin^2\theta + \cos^2\theta \end{bmatrix} \quad (4)$$

The element stiffness matrix thus becomes

$$[K] = [C^{-1}]^T \left(\iint_A [Q]^T [T]^T [D'] [T] [Q] \, dx dy \right) [C^{-1}] \quad (5)$$

The idea of tailoring involves manipulating the principal-axis directions for a given layout or structural configuration. For sensitivity or gradient calculations, the derivatives of $[K]$ with respect to θ are needed. In Eq. (5), only $[T]$ depends on θ , so differentiating Eq. (5) with respect to θ gives

$$[\partial K / \partial \theta] = ([C^{-1}]^T) \left(\iint_A [Q]^T [\partial D / \partial \theta] [Q] \, dx dy \right) ([C^{-1}]) \quad (6)$$

with

$$[\partial D / \partial \theta] = [\partial T / \partial \theta]^T [D'] [T] + [T]^T [D'] [\partial T / \partial \theta] \quad (7)$$

Note that the derivative matrix is formed in much the same way as the stiffness matrix itself.

Aerodynamic Model and Load Prediction

The aerodynamic model used in this work applies to a fin attached to an axisymmetric body. Subject to specified body angle of attack, flight Mach number (supersonic), and a set of local fin displacements calculated for the structural model described above, the objective of the aerodynamic calculation includes the determination of the following aerodynamic parameters:

1. Distribution of aerodynamic forces acting normal to the fin at aerodynamic control points.
2. Chordwise and spanwise location of the aerodynamic center of pressure.
3. Total normal force acting on the fin.

The method used in the aerodynamic model is extracted from the detailed missile aerodynamics prediction computer program NWCDM-NSTRN (Ref. 4). The aerodynamics model is based on representing the missile components by distributions of singularities derived from supersonic linear theory (wave equation) (Ref. 5). The missile body is modeled with linearly varying supersonic line sources and line doublets to account for volume and angle of attack effects, respectively. In a finned section, the lifting surfaces and the body portion spanned by the lifting surfaces (i.e., the interference shell) are modeled with planar supersonic lifting panels called constant u-velocity panels. If required, fin thickness can be included by engaging planar source panels. The strengths of the body and lifting surface panels are obtained from a matrix solution based on satisfying the flow tangency condition at a set of control points, one for each panel. The body solution is performed first and the panel solutions for the finned sections follow. In this process, body-on-fin interference is included, and fin-on-body lift carryover is modeled by the interference shell positioned on the body surface next to the fins.

As described in detail in Ref. 5, the calculated fin loads include nonlinear augmentations due to fin leading and side edge flow separation which can occur at high angles of attack. These additional aerodynamic forces are assumed to act slightly inboard of the fin edges. Their nonlinear contributions are included in the force distributions calculated for the fin. In addition, the nonlinear effects induced by vortices formed on the forebody, provided the forebody length is sufficiently long (greater than 6 diam) and the angle of attack sufficiently high (greater than 10 deg), are also included in the canard fin loading.

Routines were added to fit a smooth surface through the fin displacement coordinates and to compute the slopes of the surface in a direction parallel to the fin root chord for use in the flow tangency condition applied at the control points. After the panel strengths have been

determined, the program proceeds to compute pressures acting on the panels and, consequently, the aerodynamic normal forces at the panel centroids. In this process, the fin surface is assumed planar, and the local fin deformation is included in the flow tangency condition only.

The conversion of aerodynamic forces acting at the panel centroids on the fin to aerodynamic forces acting at the specified structural nodal points is performed by module NASCON. The main requirement for the force conversion process is to retain the essential characteristics of the force distribution on the fin, and, additionally, to insure conservation of the total force and moments acting on the fin.

The fin loading calculation routines of NWCDM-NSTRN compute pressure coefficients, based on the compressible Bernoulli pressure-velocity relationship, at the aerodynamic control points. There is one such control point for each constant u-velocity panel. The pressures are assumed to be uniform over a given panel, and a local aerodynamic normal force coefficient is formed by multiplying the pressure coefficient by the corresponding panel area. The local normal forces are assumed to act at the panel centroid points. In what follows, these points are also categorized as aerodynamic control points. Nonlinear fin edge forces are added to the normal forces acting on the panels nearest to the edges.

In NASCON, the local normal force coefficients are converted to forces, and a smooth surface is fitted to the distribution of the aerodynamic forces acting at the panel centroids on the fin. Note that the panel centroid points lie on the interior of the fin; that is, there are no points on the fin edges. The interpolated aerodynamic forces acting at the specified structural nodal points on a given fin are obtained from the surface fit. For grid points on the fin edges, the aerodynamic forces are set equal to zero. The interpolated normal forces are then scaled by an unknown multiplier. The value of the unknown constant is obtained by equating the sum of the absolute values of the interpolated and scaled normal forces, to the sum of the absolute values of the original local aerodynamic fin forces, calculated by program NWCDM-NSTRN.

For cases with clustered structural nodal points on a given fin, the scaling procedure can be applied separately to partitions on the fin as an option. In any event, the original features of the normal force distribution on the fin(s) are preserved (for example, where the forces are positive and negative) even for local high density nodal point layouts.

The final conditioning of the interpolated and scaled normal forces at the specified structural nodal points makes use of conserving the aerodynamic forces and moments for the given fin. The final normal force is first related to the interpolated and scaled normal force using the expression below, which is linear in the local fin coordinates x and y . Here x is the distance aft along the fin root chord measured from the leading edge. Coordinate y lies in the plane of the fin, positive outboard.

$$F_{N,i} = F_{\text{ints},i} + D_1 + D_2 x_i + D_3 y_i \quad (8)$$

where

F_N final fin local normal force
 F_{ints} interpolated and scaled fin local normal force
 $()_i$ i'th structural analysis grid point
 x_i, y_i fin coordinates
 D_1, D_2, D_3 .. unknown constants

The values of the three unknown constants are obtained from conservation of the normal force and of the moments taken about the fin root chord (root bending moment) and about the leading edge of the root chord (pitching moment) using the original aerodynamic forces calculated by program NWCDM-NSTRN.

The end product consists of a set of normal aerodynamic forces acting at a set of specified structural nodal points on a given fin. The forces are set equal to zero for grid points on the fin edges including the root chord.

Analysis

The analyses to be discussed here are those to compute the objective (that is, the quantity to be minimized) and the constraints and their derivatives with respect to the design variables. The ultimate goal of this work is to control hinge moments. This can be accomplished for a given set of flow conditions by moving the chordwise location of the center of pressure in a desired direction. This is performed in three steps.

First, the structural model is updated by calculating the stiffness matrix for the current values of the design variables (the structural principal-axis orientation angles). Then, the location of the center of pressure is calculated. This must be done iteratively, as illustrated in Fig. 2. The nodal load vector from the last objective calculation, or an initial estimate if this is the first time through, is used as the right-hand side for the solution of the linear problem $[K]\{s\} = [F]$. The displacement vector $\{s\}$ is then passed to the aerodynamic load prediction module, which computes a new load vector $\{F\}$. The displacements are then recalculated and compared with those previously calculated. If the displacements at any node differ by more than a selected amount, the displacements are updated and the load calculation is repeated. Once satisfactory convergence is obtained, the resulting value of x_{cp} is used in the third step to

define the objective as

$$OBJ = |x_{cp}/\bar{x}_{cp} - 1.0| \quad (9)$$

As shown in Fig. 2, underrelaxation is employed in updating the displacements in order to enhance convergence. Minimizing the objective in the dimensionless form given above minimizes the difference between x_{cp} and its desired location, \bar{x}_{cp} .

The derivatives of the objective are calculated by finite differencing. The step size for the finite differencing is determined by a multiplicative factor, with a lower limit on magnitude to ensure accuracy.

Three sets of constraints are permitted: displacements, natural frequencies, or flutter speeds. A full technical description of the techniques employed to calculate these constraints and their derivatives can be found in Ref. 3; their principal features are discussed here.

A displacement constraint is formulated as

$$G = z_r/\bar{z}_r - 1.0 \quad (10)$$

where z_r is the r 'th member of the displacement vector found from solution of

$$[K]\{z\} = \{F\} \quad (11)$$

Negative values of G mean that z_r is less than its upper bound \bar{z}_r .

The nodal force vector $\{F\}$ is fixed. Up to four displacement constraints can be imposed. These can be four different nodal displacements for a given load condition, single displacements at different node points for four different load conditions, or any combination in between. The derivatives of these constraints are calculated analytically; see Ref. 3 for details.

For dynamic constraints, inertia properties are also required for the structural model. For tailoring applications, the inertia properties do not vary. The mode shapes of the initial design are used to define generalized coordinates, so the inertia matrix remains diagonal. The generalized stiffness matrix is recomputed for each design with the modal matrix and the updated discrete stiffness matrix. Data needed for the present work are obtained from dynamic analyses performed separately.

The frequency constraint function is written as

$$G = 1.0 - \omega_r/\bar{\omega}_r \quad (12)$$

where ω_r is the frequency of the r 'th mode and $\bar{\omega}_r$ is its lower bound. The frequencies of up to four modes may be constrained. The derivatives of this constraint function are also calculated analytically; the details are in Ref. 3.

For a flutter constraint, the constraint function is simply

$$G = g_r - \bar{g}_r \quad (13)$$

where g_r is the damping parameter of the r 'th mode, and \bar{g}_r is its upper bound. This constraint is enforced at a fixed value of airspeed. As the design changes, this root of the flutter equations occurs at different values of reduced frequency, so an iterative procedure is used to find the value of reduced frequency that yields the required airspeed. The generalized aerodynamic forces are interpolated on reduced frequency, so no unsteady aerodynamic computations need to be performed during the optimal tailoring search. A complete description of this procedure, as well as the procedure for calculating analytical derivatives of the flutter constraint function, can be found in Ref. 3. Four flutter constraints are permitted, which can range from four separate V-g points on a single branch to V-g points on different branches for four separate sets of flow conditions.

In summary, the analysis function is concerned with either evaluation or derivative calculation of the objective or the constraints. The procedures of Ref. 3 have been taken over directly for the constraints; for present purposes, the inertia matrix is constant, and the derivative of the stiffness matrix is computed as described above.

Optimization

The optimization problem is posed as follows: minimize OBJ given by Eq. (9), subject to constraints

$$G_j(\theta_i) \leq 0, \quad j = 1, 2, \dots, N_c; \quad i = 1, 2, \dots, N_d \quad (14)$$

Here N_c is the number of constraints and N_d is the number of design variables. Upper and lower bounds on the design variables may also be specified. Expressing the constraints in the form above means that upper bounds are being imposed on displacements and dampings, and lower bounds on frequencies.

The optimal search is based on the method of feasible directions. The computer code CONMIN (Ref. 6) is used to implement this search scheme.

Executive

As mentioned earlier, the executive function controls input and directs program execution. There is an option for analysis and gradient calculations without optimization that can be used to check that the input and other auxiliary files are being read properly before an optimal search is attempted. The executive is called program TAILOR.

Results

Aerodynamic Predictions

The methodology incorporated in the aerodynamic prediction program NWCDM-NSTRN (Ref. 4) includes computationally fast supersonic panel and line singularity methods. Models are included to account for the important nonlinear effects of fin and body vorticity on downstream missile components and to account for effects of nonlinear compressibility associated with high supersonic flight Mach numbers (Ref. 5).

In Ref. 5 good to excellent comparisons with experimental chordwise pressure distributions on rectangular and delta wings are shown for Mach numbers up to 4.6 and for angles of attack up to about 21 deg. The cited reference also contains comparisons with NASA/Langley Research Center experimental longitudinal and lateral-directional aerodynamic data for a canard-tail missile configuration including forward pitch and roll control. An example of zero-control canard normal force is shown in Fig. 3 as a function of angle of attack at $M_\infty = 2.5$. Ref. 7 also contains comparisons with hinge and root bending moments. Agreement between prediction and experiment is good.

Comparisons with tail normal force and root-bending moment coefficients are shown in Fig. 4 for the tail control configuration (Ref. 8) shown at the top of the figure. These comparisons also show good to excellent agreement for cases with and without fin deflection.

Controlling Center of Pressure on a Fin

Analysis and optimization results for a hypothetical fin are presented next. The objective is to control the chordwise center of pressure by varying the directions of the structural principal axis.

Example Structural Model. The hypothetical fin chosen for the example calculations is made of a laminated graphite-fiber composite. The layup and the structural nodal layout are illustrated in Fig. 5. Each quadrilateral in the figure is comprised of two triangular bending elements; the thickness of each element is given by the average of the fin thicknesses at the three nodes defining the element boundary. Each element constitutive matrix $[D']$ (Eq. (2)) is computed by lamination theory from the basic lamina properties (Ref. 9). The nodes for each element are ordered so that its orientation angle θ is consistent with the global definition given in Fig. 5. The fin hinge line is at the midpoint of the root chord; a beam-rod at this point connects the fin to a fixed point and is sized to provide realistic root-restraint conditions. More details concerning the layup used for this model may be found in Ref. 3.

For the initial design, the direction of the "zero-deg" plies is in the same direction as the global y axis. In the two inboard segments of the fin, the principal-axis directions are allowed to vary independently; these are the two design variables, θ_1 and θ_2 . In the outboard section, the principal-axis direction is held fixed. This portion of the fin, along with the beam-rod at the root, is inactive for design purposes. For the initial model, therefore, θ_1 and θ_2 are zero.

Aerodynamic Description. The flight conditions and the body/fin aerodynamic modeling details associated with the example problem are described next. The following conditions were chosen as being reasonably realistic for an air to air missile in steady flight with zero rotational rates:

α_c	= included angle of attack	= 15.4 deg
ϕ	= angle of roll	= 0 deg
M_∞	= flight Mach number	= 1.6
H	= flight altitude	= 30,000 ft

The example case concerns a hypothetical canard fin mounted on an idealized axisymmetric body as shown in Fig. 6. The fin is undeflected. There is a vertical plane of symmetry so that there are actually two fins, one on each side of the body in the horizontal plane. The body consists of an ogive nose up to the leading edge of the fins.

The body is modeled by 10 supersonic line sources and doublets. The fin has one break in the leading edge and is modeled by a 4 chordwise by 8 spanwise layout of constant u-velocity panels. (One panel is indicated in Fig. 6.) An interference shell is placed around the body over the length of the fin root chord. It contains a layout of 4 lengthwise by 8 circumferential constant u-velocity panels for lift carryover.

In the above aerodynamic modeling specifications, fin thickness details are not included. In the effort reported in this paper, the main purpose was to demonstrate the feasibility of controlling center of pressure location by altering the structural properties of the fin. For the sake of simplicity and reduced computer running time, the effects of fin thickness were omitted. In addition, the nonlinear fin normal force augmentation on the leading edge was zero because the leading edge is supersonic for the Mach number considered. Effects of vortices shed from the forebody were also neglected. For the nose length shown in Fig. 6 and the angle of attack considered here, forebody vortex effects should be small.

Constraints. A flutter constraint was the only one considered. This is the most important constraint and the most complex in terms of its being incorporated into the optimization. The methods used for all the constraints, and much of the code itself, have been validated in previous work.

A flutter analysis was performed for the initial design at a Mach number of 1.4. The V-g and V-w curves at the match-point altitude of 43,500 ft are given respectively in Figs. 7 and 8. Structural damping of 3% is assumed, which means that the match-point flutter speed is given by the $g = 0.03$ crossover of the first-mode branch in Fig. 7. The flutter constraint is imposed by requiring that the damping parameter g be less than 0.03 at this speed.

Parametric Survey. For a clearer understanding of the behavior of the fin as the principal-axis orientations are varied, the analysis-only option of TAILOR was exercised to compute the variation of the fin center of pressure location. Angles θ_1 and θ_2 were varied identically, thereby reducing the number of design variables in effect to unity. Figure 9 displays the variation of x_{cp} . Given the nature of the transformation matrix $[T]$ for each element (Eq. (4)), the harmonic nature of this variation is not surprising. With the particular layup and flow conditions used, the chordwise center of pressure location does indeed vary, albeit over a limited range.

Figure 10 presents views of the deformed fins for values of θ between -90 deg and 90 deg. The view in these figures is outboard in the x-y plane, so that the undeformed fin would be seen as a single straight line. It can be seen that there is a clear correspondence between chordwise flexibility and center of pressure location. With θ near +45 deg or -45 deg, chordwise flexibility is near maximum. Contrary to what might be expected, however, the fin chordwise bending is concave, rather than convex, with respect to the load direction, which reduces the aerodynamic loads near the leading edge and leads to an aft shift in the location of the center of pressure. The most forward locations of the center of pressure correspond to the fins with the most chordwise rigidity. Note that for all these examples, there is a nose-down rigid body rotation about the hinge line. This rotation is included in the perspective plots of the deformed fins. Figure 11 presents perspective plots of the aerodynamic load distributions corresponding to the deformed fins in the previous group of figures. These plots show quite clearly the reduction in loads near the leading edge with chordwise bending.

The layup selected here produces chordwise bending that reduces loads near the leading edge. To move the center of pressure forward, nose-up bending is required. This can be accomplished with a different layup scheme. In particular, an unbalanced layup, where lamina oriented forward of the "zero-deg" plies are not matched by lamina oriented aft at the same angle, provides additional bending-torsion coupling that can be tailored to give the desired chordwise bending characteristics. This enhanced control of the bending-torsion coupling is not available with a balanced layup. It also requires a full constitutive matrix $[D']$ in Eq. (2), which cannot be modeled in the present version of the structural code.

It is interesting to note that the total load generated by the fin is also affected and varies in much the same manner as x_{cp} does. The cambering of the leading edge that leads to aft movement of the center of pressure also reduces the total load generated by the fin in comparison with the total load generated for the forward center of pressure locations. Thus, tailoring will affect not only the pressure distribution but also the total load generated by the fin for a given rigid-fin angle of attack.

Finally, consider what happens when θ_1 and θ_2 are allowed to be independent. For this two-design-variable case, the curve of Fig. 9 can be viewed as the intersection of the $\theta_1 = \theta_2$ plane with the x_{cp} surface. This surface was not mapped extensively, but enough analyses were performed to show that the surface resembles that of an egg carton: the minima of x_{cp} in Fig. 9 are the bottoms of valleys, and the maxima are the tops of peaks.

Optimization. The following calculative results are described in detail in Ref. 10. For the first optimization example, θ_1 and θ_2 are linked to form a single design variable. The desired value of x_{cp} (measured from the fin root chord leading edge) is set to 60% of the root chord, and the initial value of the single design variable θ is set to 0.7 rad, or 40.1 deg. The flutter constraint, fixing the critical first-mode crossover at 43,500 ft at Mach 1.4, is also imposed. The iteration history for this example is shown in Fig. 12. In five iterations, the minimum at $\theta = 3.43$ deg is found. This result corresponds very well with the curve of x_{cp} vs θ in Fig. 9. The flutter constraint remained satisfied, which means that varying θ from approximately 0 deg to 40 deg or so has little effect on the critical flutter altitude at Mach 1.4. On the other hand, attempts to find the minimum near $\theta = 90$ deg with the flutter constraint included were not successful. As θ is increased beyond 45 deg or so, the flutter characteristics deteriorate and effectively bar the optimization procedure from increasing θ any further.

For the next optimization example, θ_1 and θ_2 are unlinked, and the flutter constraint is removed. The initial values of θ_1 and θ_2 are 0 deg and 45 deg, respectively. Convergence is achieved in five iterations, with θ_1 at 0.334 deg and θ_2 at 1.53 deg. This result essentially reproduces the minimum found in the first example; the iteration history is shown in Fig. 13.

The third optimization example is an attempt to find a neighboring valley in the two-design-variable space. The starting point was at $\theta_1 = 10$ deg, $\theta_2 = 70$ deg, and no constraints were imposed except for upper and lower bounds on the design variables. In six iterations, a different minimum was found at $\theta_1 = 2.20$ deg, $\theta_2 = 92.5$ deg. This example illustrates the fact that an optimal search procedure can find only a local minimum. Figure 14 presents the iteration history for this example.

The final optimization example has a single design variable and no constraints. The optimal search was begun at $\theta = 57.3$ deg, and a minimum at $\theta = 94.0$ deg was found in five iterations. The iteration history is shown in Fig. 15.

From these results, it can be seen that the design with the most favorable (i.e., most forward) center of pressure location is ironically the design initially modeled, with the "zero deg" plies in the spanwise direction. Other local minima exist that have less favorable center of pressure locations; these minima are excluded, however, if the flutter constraint is imposed.

One question that may arise concerns the use of optimization with such a small number of design variables. While it is true that a parametric survey is very easy to do for one or two design variables, it must be remembered that the ultimate application will involve several different aerodynamic flow conditions and a variety of constraints, including perhaps aeroelastic and displacement constraints for different flow and load conditions. Under these circumstances, optimal search procedures are far more efficient than any alternative approach.

Conclusions and Recommendations

The following conclusions can be drawn from this study:

- (1) A nonlinear supersonic aerodynamic load prediction code has been successfully integrated with a finite element modeling code and an optimization code.
- (2) These codes have demonstrated the ability to alter the material principal-axis directions in a fin structural model in an optimal search procedure and to find the directions that result in the most favorable center of pressure locations. Constraints on displacements, natural frequencies, and flutter speeds can be imposed; an optimal solution with a flutter constraint was found.

Further details of the work and additional results are described in Ref. 10.

Now that the operation of the codes has been successfully demonstrated, it is planned to incorporate improvements and to design a fin that is suitable for testing. Some suggested improvements are listed below:

- (1) Incorporate improvements and added capabilities including (a) modeling anisotropic materials (such as unbalanced layups), (b) constraining the total aerodynamic load, and (c) considering multiple aerodynamic flow conditions, with a corresponding expanded definition of the objective. Another important phenomenon that needs to be modeled is the airgap that can exist between the body surface and the control fin root chord with large control deflection. The distribution of aerodynamic loading on the inboard portion of the fin and thus the center of pressure location will be affected by the airgap. The aerodynamic model can be extended to provide a representation of the airgap effect.
- (2) Exercise fully the improved codes in the design of a fin that can be built and tested. The goal here is to demonstrate the reduced hinge moments that can be achieved with a tailored fin in comparison with a fin of conventional construction.
- (3) Construct and test the fins in a wind tunnel. Compare the experimental results with the theoretical predictions.

References

1. Przemieniecki, J. S., Theory of Matrix Structural Analysis, McGraw-Hill, New York, 1968.
2. Zienkiewicz, O. C., The Finite Element Method, McGraw-Hill (UK), London, 1977.

3. McIntosh, S. C., Jr., "Optimization and Tailoring of Lifting Surfaces with Displacement, Frequency, and Flutter Performance Requirements. Theoretical and User's Manuals," Naval Weapons Center, China Lake, CA, TP 6648, Apr. 1987.
4. Dillenius, M. F. E., Perkins, S. C., Jr., and Lesieutre, D. J., "Modified NWCDM-NSTRN and Supersonic Store Separation Programs for Calculating NASTRAN Forces Acting on Missiles Attached to Supersonic Aircraft," Naval Weapons Center, China Lake, CA, TP 6834, Sep. 1987.
5. Dillenius, M. F. E., "Program LRCDM2, Improved Aerodynamics Prediction Program for Supersonic Canard-Tail Missiles with Axisymmetric Bodies," NASA Contractor Report 3883, Apr. 1985.
6. Vanderplaats, G. N., "CONMIN - A Fortran Program for Constrained Function Minimization, User's Manual," NASA TM X-62,282, Aug. 1973; Addendum, May 1978.
7. Blair, A. B., Jr., Allen, J. M., and Hernandez, G., "Effect of Tail-Fin Span on Stability and Control Characteristics of a Canard-Controlled Missile at Supersonic Mach Numbers," NASA Technical Paper 2157, Jun. 1983.
8. "Final Report - Tail Control Sparrow Wind Tunnel Test (U) at NASA/Ames Research Center - January, 1976," Raytheon Co., Waltham, MA, Apr. 1976.
9. Jones, R. M., Mechanics of Composite Materials, Scripta Book Co., Washington, 1975.
10. McIntosh, S. C., Jr. and Dillenius, M. F. E., "Aeroelastic Tailoring Procedure for Reduction of Fin Hinge Moments," Nielsen Engineering & Research, Inc., Mountain View, CA, TR 374, Feb. 1987.

Acknowledgements

The work described in this paper was performed as a Phase I Small Business Innovation Research (SBIR) project sponsored under U.S. Navy NAVAIR Contract N00019-86-C-0032.

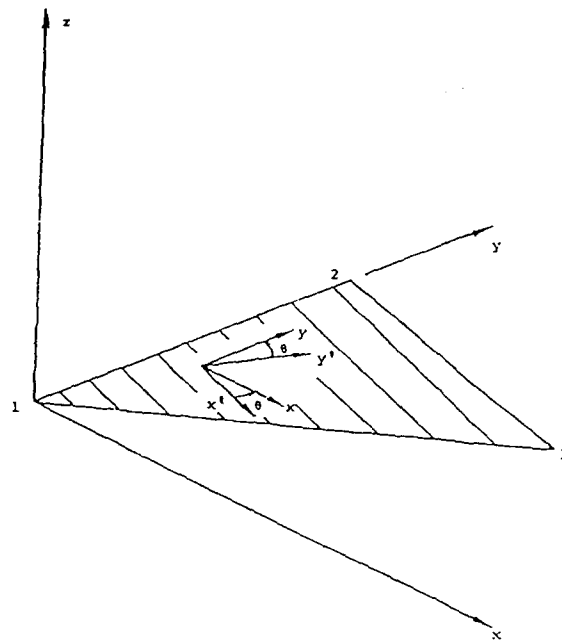


Fig. 1.- Orthotropic bending element.

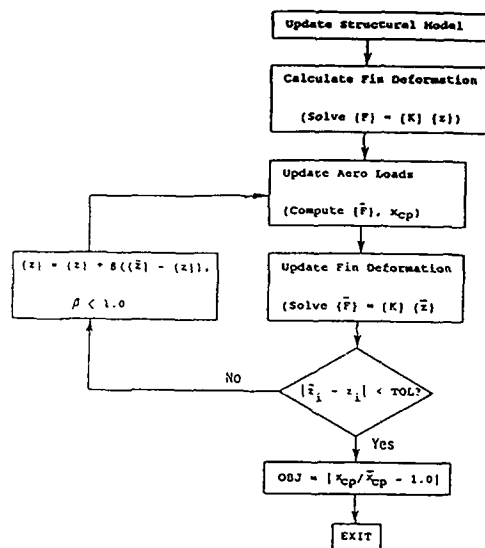
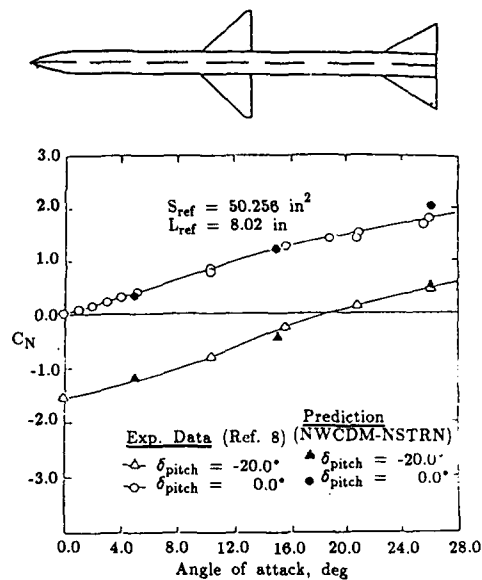
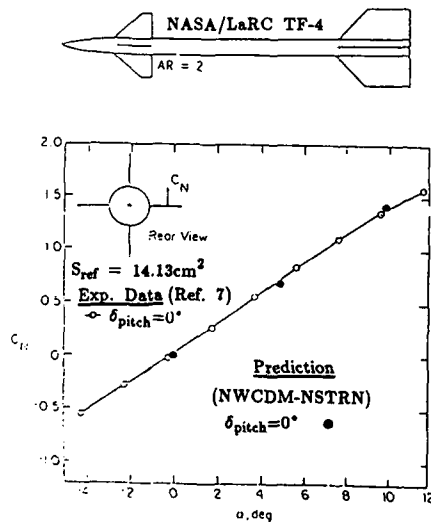
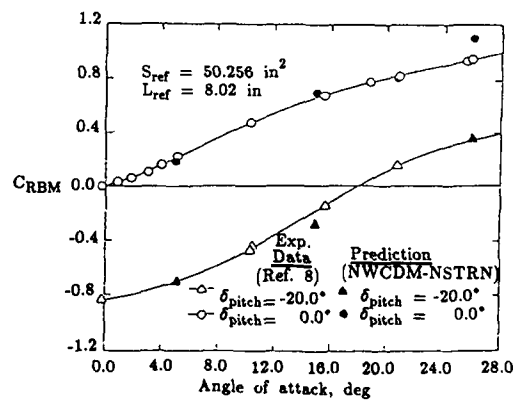


Fig. 2.- Block diagram of objective calculation.

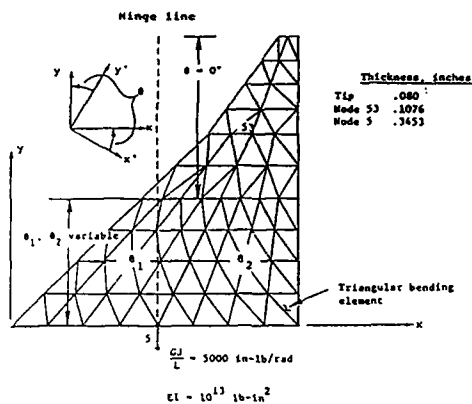


(a) Fin normal-force coefficient

Fig. 3.- Normal force on horizontal canard fin ($AR = 2$) of TF-4, $M_\infty = 2.5$, $\phi = 0$.

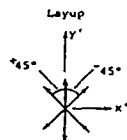
(b) Fin root-bending moment coefficient

Fig. 4.- Loads acting on left horizontal tail fin with tail pitch control; $\phi_{roll} = 0 \text{ deg}$, $M_\infty = 1.6$.



Ply	Thickness, in
+45	12.5
-45	12.5
0	50.0
+45	12.5
-45	12.5

graphite
fiber comp.
with epoxy
matrix



Double wedge chordwise

Fig. 5- Structural layout of hypothetical fin. Principal-axis directions are defined by x' and y' .

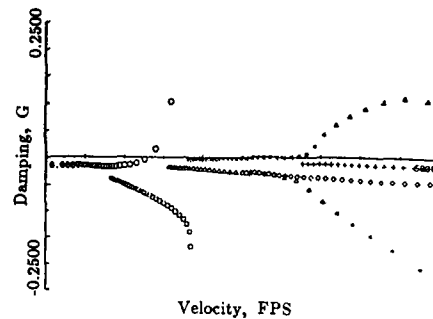


Fig. 7- Flutter velocity-damping plots for composite fin, $\theta_1 = \theta_2 = 0$ deg.

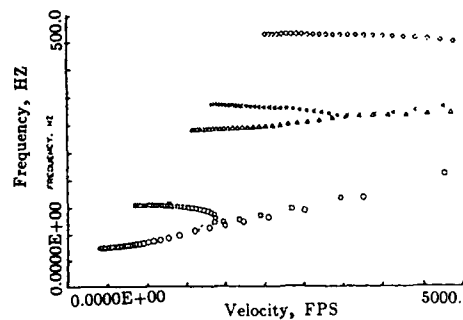


Fig. 8- Flutter velocity-frequency plots for composite fin, $\theta_1 = \theta_2 = 0$ deg.

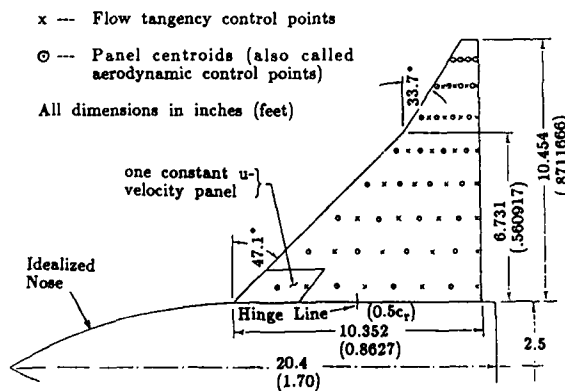


Fig. 6- Missile fin mounted on axisymmetric body.

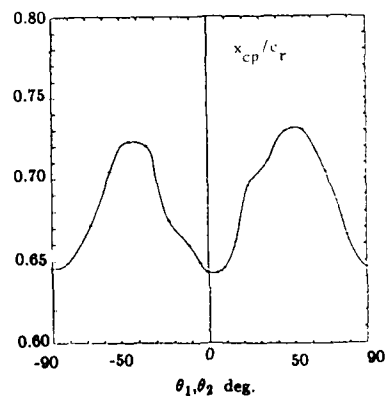


Fig. 9- Center of pressure location, in root chords, vs. θ . (a) $\theta_1 = \theta_2 = -90$ deg.

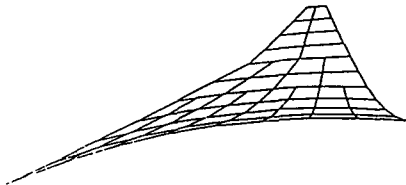
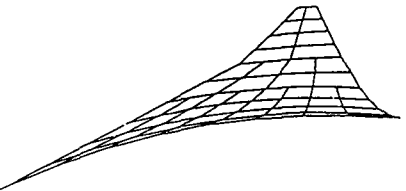
(a) $\theta_1 = \theta_2 = -90$ deg(b) $\theta_1 = \theta_2 = -45$ deg(c) $\theta_1 = \theta_2 = 0$ deg(d) $\theta_1 = \theta_2 = 45$ deg(e) $\theta_1 = \theta_2 = 90$ deg

Fig. 10.- Spanwise view of deformed composite fin.

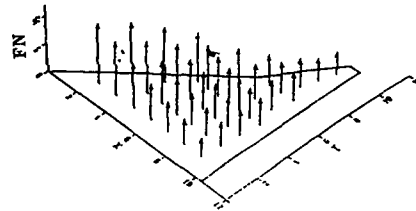
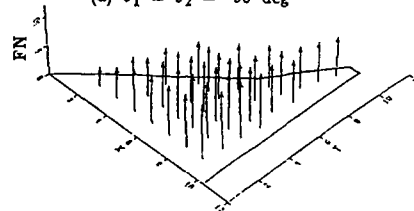
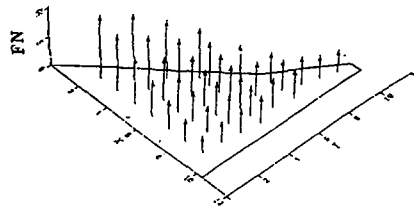
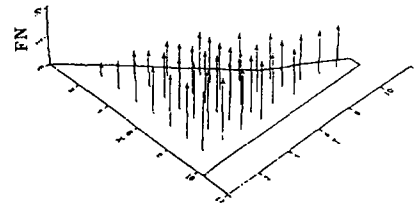
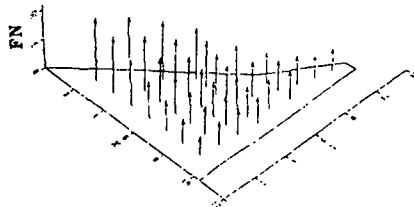
(a) $\theta_1 = \theta_2 = -90$ deg(b) $\theta_1 = \theta_2 = -45$ deg(c) $\theta_1 = \theta_2 = 0$ deg(d) $\theta_1 = \theta_2 = 45$ deg(e) $\theta_1 = \theta_2 = 90$ deg

Fig. 11.- Forces on deformed fin.

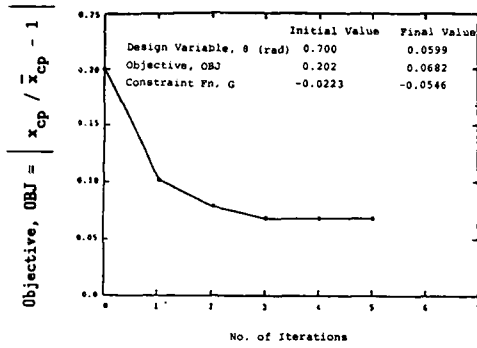


Fig. 12.- Iteration history for optimization example 1.

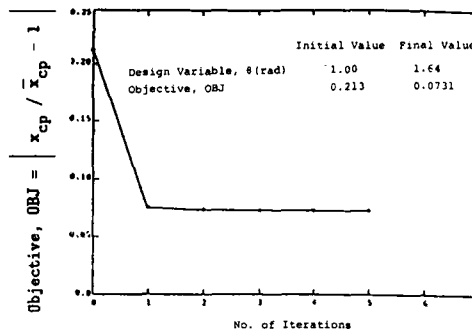


Fig. 15.- Iteration history for optimization example 4.

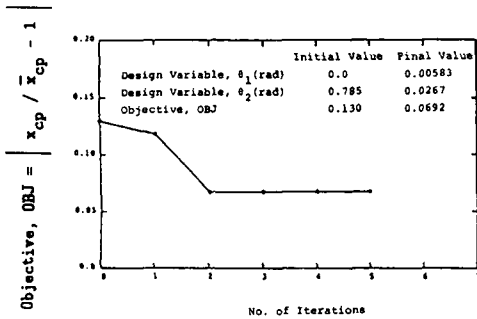


Fig. 13.- Iteration history for optimization example 2.

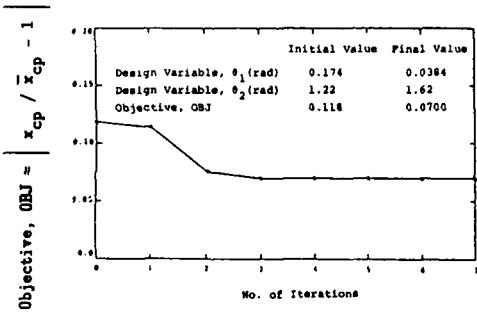


Fig. 14.- Iteration history for optimization example 3.

ALTERNATIVE POLAR HOMING STRATEGIES

Dr. M.S. Gate and R.S. Randall
Systems Support Dept.
British Aerospace Dynamics Division
Hatfield Hertfordshire England

SUMMARY

The coupled lateral and roll requirements are considered for a "twist-to-track" missile which is constrained by the seeker to maintain the sight line at an approximately fixed polar angle from the body. Two alternative approaches, one based on roll profile optimisation and the other on adopting a non-cruciform missile configuration, are described.

1. INTRODUCTION

The polar homing problems addressed here are those which arise when for some reason we wish to design a missile system with a seeker which has limited rollwise field of view. While it is possible to design a system in which the missile spins continuously and the guidance is designed to operate with only intermittent looks at the target, the concern here is with systems in which the missile is roll controlled so as to follow the target throughout. Such systems have been termed "Twist-to-Track" or TTT.

The motivation for designing twist-to-track systems comes about in two ways. Firstly, in a case such as a small high speed Infra-Red missile, a larger speed envelope can be readily engineered if the aperture is sited away from the nose tip of the missile which suffers intense kinetic heating. This also allows the nose to be more streamlined so that higher speeds may be maintained with a given motor size. Secondly or additionally, the seeker design may be simplified or indeed made feasible by restricting the rollwise field of view - for instance it is not difficult to produce a look angle coverage to beyond the beam if only a small rollwise segment is covered at large look angles, but very difficult to engineer if full all-round coverage is required. Even when feasibility is not in doubt, rollwise restriction of the field of view will produce a smaller, lighter and generally cheaper arrangement.

In order to obtain the benefits of twist-to-track, the missile is required to perform a rapid roll response to navigational demands, so that maintenance of tracking may be reconciled with guidance requirements perpendicular to the look plane. Because of low roll inertia, the provision of adequate physical control power is typically not difficult, but the system has to be designed to avoid so far as possible the various coupling effects which will degrade the homing performance from that which would be achieved without the necessity to roll.

The design of a twist-to-track system for a particular project soon becomes quite complex and particularised to the characteristics of the seeker and its stabilisation scheme, and to the form of control and aerodynamics. In this paper the results of two studies at a relatively simplified level are given. The first of these concerns finding a suitable twist-to-track law by use of optimisation theory and the second refers to easing the situation by altering other features of the problem.

2. APPROXIMATION TO OPTIMAL TWIST-TO-TRACK LAW

2.1 Derivation of a Cost Function

The requirements on the law are that the lateral navigation should be maintained, the target should remain within the field of view, and that the roll motion should be minimised, since it is this which leads to coupling problems and increased noise sensitivity.

In order to express these requirements mathematically, we take a quadratic cost function of look angle and roll rate which is to be minimised for a given trajectory of lateral navigation. The cost function, illustrated by Figure 1, is given by:

$$J = \frac{1}{T} \int (\dot{\phi}^2 + \gamma_T^2 F^2 (\phi_E)) dt; \quad \frac{\partial J}{\partial \phi_E} > 0 \quad \text{Eq.(1)}$$

where: ϕ_E = roll of look from the major look plane in the missile = $\phi - \phi_T$

γ_T = total look angle

ϕ = missile roll in unspun axes

and where F is defined by the field of view boundary which is of the form:

$$\gamma_T F = \text{constant} \quad \text{Eq.(2)}$$

2.2 Differential Equation

The integrand in the cost function is of the same form as the Lagrangian of a conservative system having a time varying negative potential field deflecting the motion of a "point mass".

Hence the differential equation for the motion may be written down:

$$\ddot{\phi} = \gamma_T^2 F \frac{\partial F}{\partial \phi_E} \quad \text{Eq.(3)}$$

2.3 Expression as a Control Law

It may be found by substituting simple cases that the differential equation has both stable and unstable solutions, of which we are of course only interested in the stable ones. (The unstable ones are believed to correspond to J being stationary at a maximum rather than a minimum).

The stable solutions must be expressible in a form equivalent to the loop shown in Figure 2, i.e. the missile roll must in the long term be driven round to coincide with that of the sight line. The optimality condition is then expressed by the variation of the forward path control function g .

The control law equivalent to Figure 2 is:

$$\dot{\phi} = -g(\phi_E, t) \quad \text{Eq.(4)}$$

and substituting this into the optimal differential equation gives:

$$\frac{\partial g}{\partial \phi_E} = \frac{\partial}{\partial \phi_E} \left\{ \frac{1}{T} (\dot{\phi}^2 - \gamma_T^2 F^2) + g \phi_T \right\} \quad \text{Eq.(5)}$$

2.4 Form of Solution of the g Equation

As would be expected by comparison with control optimisation equations derived by dynamic programming techniques, the g equation is unstable if solved in forward time but stable if solved in backward time (since it is future costs, not past ones, which are influenced by actions now).

The case of interest is when the target passes close to the origin "0" in Figure 1, and then moves back out to a condition where roll rate is small and hence so is g . Because of the stability of the backwards integration this means that numerical solutions for the optimising gain g can be easily calculated for windows which can be expressed by Equation 2.

2.5 Solutions with a Linear Look Function F

As an illustrative example to show typical numerical forms of the g function the case is taken of a linear relation for the look function F. This gives the window shape shown in Figure 3. Thus we have:

$$F = k \cdot \phi_E \quad \text{Eq.(6)}$$

In this case the partial differential equation is separable. Put:

$$g = k \cdot a \cdot \phi_E - b \quad \text{Eq.(7)}$$

where a and b are functions of time. Then substituting this and Equation 6 into Equation 5 gives:

$$k \cdot \phi_E (\dot{a} - k \cdot a^2 + k \cdot \gamma_T^2) = \dot{b} - k \cdot a(b - \phi_T) \quad \text{Eq.(8)}$$

This is satisfied for all ϕ_E if:

$$\dot{a} = k \cdot (a^2 - \gamma_T^2) \quad \text{Eq.(9)}$$

$$\text{and } \dot{b} = k \cdot a \cdot (b - \phi_T) \quad \text{Eq.(10)}$$

2.6 Definition of Target Trajectories

In cases where good target track is maintained the bandwidth of the roll motion will be higher than that of the lateral manoeuvre, so we can get a good impression of the effect of the optimal law by defining a target trajectory sweeping linearly across the unspun field of view, as shown in Figure 4.

By referring time and roll angle to the point of closest approach of the target to the missile nose, and then scaling distance and speed to give unity γ_T and ϕ_T at this point, Equations 9 and 10 become normalised to a single-parameter family of curves:

$$\dot{a}_N = k_N \cdot \{a_N - (1 + t_N^2)\} \quad \text{Eq.(11)}$$

$$\dot{b}_N = k_N \cdot a_N \cdot \{b_N - 1/(1 + t_N^2)\} \quad \text{Eq.(12)}$$

2.7 Parametric Family of Solutions

Solutions for a and b are shown in Figure 5 and 6 for a range of values of k_N . The $k_N = \infty$ case corresponds to the limiting condition when roll costs are insignificant compared with field of view costs. In this case a bias (actually equal to ϕ_T) is applied to ensure near perfect open loop tracking, and the gain is proportional to γ_T . This latter relationship makes the controller evenly sensitive to target position noise as γ_T changes, which is a desirable feature.

When k_N is reduced the bias becomes more predictive, causing the missile to roll over in preparation for the fast roll excursion as the target passes near the origin. In this case the gain is comparatively higher when the target is near the origin, although it is lower earlier on when the anticipatory bias is being applied.

2.8 Typical Trajectory in Missile Axes

Finally, the form of trajectory of the target in the missile field of view is shown in Figure 7. The missile starts to roll before the target gets near to the singularity, thus showing the expected anticipatory action of rolling the missile over early within the limits of the field of view. The trajectory is symmetric reflecting the original conservative motion analogy.

2.9 Review of Optimisation

We have shown how to find "closed" solutions to the non-linear problem of trading off missile roll rate and one-sided field of view constraints. The simple window case solved numerically here is close to a practical window design, although the method is not limited to any particular shape, as the law would be implemented by fits for a_N and b_N as a function of target trajectory which could as well be derived for alternative window shapes.

Because of the non-linear and predictive nature of the law the system requires some reasonably reliable input of what the manoeuvre will be at a future time. Such data is not available in a case when the homing bandwidth is designed by the miss due to random noise, but is available when the homing bandwidth is constrained by aberration or other parasitic loop considerations, or by lateral autopilot bandwidth. Thus the scheme has greater and more straightforward applicability in the latter cases, and if it is to be used the homing dynamic design may with advantage be tuned accordingly.

3. COMBINATION OF TWIST-TO-TRACK WITH BANK-TO-TURN

3.1 Background

An alternative approach to twist-to-track arose out of a proposal for a ground attack missile having a strongly down-curving terminal trajectory, in order to reach the target from a level cruise course with a relatively short acquisition range.

It was desired to use a single axis seeker for this missile, with a large field of view in pitch but very restricted in yaw. In a nominal flight the target would appear at acquisition below the missile nose and then sweep up to a position above the nose at intercept, the look angle then being equal to the missile incidence associated with the curved trajectory.

However, difficulties with this scheme begin to appear as soon as conditions away from this simple case are considered, for instance the effects of sidewind or of target motion. We have to decide whether the missile is to roll through half a turn as the look angle passes through zero, as for the system which was the subject of the optimisation study above, or whether it is to roll through only small angles and allow the look to traverse through the nose of the missile to the other side. In either case a large and probably unacceptable disturbance to the system will occur at a crucial part of the homing, because of one or more of very high roll rates, loss (at least temporarily) of tracking, and inability to follow the required azimuth course.

Therefore the scheme described here was proposed. This uses the large systematic manoeuvre together with a change from a cruciform aerodynamic configuration to ease the problems.

3.2 Manoeuvre Relationships for an Anisotropic (Bank-to-Turn) Missile

Given a missile with differing lift slopes (a_p , a_y) in pitch and yaw, the kinematic conditions during homing can be expressed as in Figure 8, in which the motion is related to the fly-plane, defined here as the plane containing the sight line and the missile velocity vector. Treating for clarity all angles except roll about the sight line as small, it can be found that the out-of-plane aerodynamic manoeuvre is given by:

$$f_y = a_p L \sin \phi - (a_p - a_y) \lambda \sin 2\phi / 2 \quad \text{Eq. (13)}$$

where L = Look angle

λ = Lead angle

ϕ = Roll of missile about the sight line

For a symmetric cruciform missile $a_p = a_y$ and the second term disappears, so that f_y cannot effectively be controlled when L is required by the in-plane navigation to be near zero.

However, if a_p and a_y are different then the point of control ineffectiveness is removed to other values of L and λ . To the first order in ϕ ,

$$\begin{aligned} f_y / \phi &= a_p L - (a_p - a_y) \lambda \\ &= a_p \alpha + a_y \lambda \end{aligned} \quad \text{Eq. (14)}$$

where α = the in-plane incidence, $\alpha = \lambda - L$

Thus control effectiveness by rolling is zero when the lead to in-plane incidence ratio equals the pitch to yaw lift slope ratio. For a missile similar to the ground attack missile for which this system was proposed, the lead at the start of the turning down phase of flight is about 2.5 times the in-plane incidence required to reach the target, and removal of the vertical wing surfaces reduces lift slope by a factor of approximately five. Hence the point of zero control effectiveness can be removed from the terminal phase.

This situation is illustrated in Figure 9 in which the slope of out-of-plane manoeuvre with roll about the sight line is sketched as a function of time for both the original cruciform missile and the anisotropic missile.

3.3 Twist-to-track Control Law

In order to implement the navigation, a law has to be found which causes the manoeuvre to converge onto that required, while simultaneously driving any yaw look towards zero. This may be done by finding the body rates which correspond to a desired rate of change of manoeuvre and yaw look angle and then using a fast inner rate loop to drive towards these values.

We have, for body rates p, q, r , sight line unit vector s_x, s_y, s_z and incidence α, β in pitch and yaw, a rate of change of manoeuvre due to incidence, in non-rolling axes instantaneously aligned with the body given by:

$$\dot{f}_v = -\alpha \dot{\beta} - f_w \dot{p} \quad (15) \quad \text{Eq. (15)}$$

$$\dot{f}_w = -\alpha \dot{\alpha} + \dot{f}_v \dot{p} \quad (16) \quad \text{Eq. (16)}$$

and for the contribution to yaw look angle rate, \dot{s}_y , which is due to body rotation:

$$\dot{s}_y = -s_x \dot{r} + s_z \dot{p} \quad (17) \quad \text{Eq. (17)}$$

We also have for the rate of change of incidence:

$$\dot{\alpha} = q + f_w/V - \beta \dot{p} \quad (18) \quad \text{Eq. (18)}$$

$$\dot{\beta} = -r + \dot{f}_v/V + \alpha \dot{p} \quad (19) \quad \text{Eq. (19)}$$

where V = Missile Speed

Having determined a rate of change of manoeuvre and of yaw look angle consistent with the desired homing and tracking response, the above equations may be solved to yield the corresponding demanded body rates:

$$\dot{p}_d = -(\alpha \dot{s}_y + (f_v + \alpha \dot{f}_v/V) s_x)/D \quad (20) \quad \text{Eq. (20)}$$

$$\dot{q}_d = -\dot{f}_w/\alpha p + f_w/V + (\beta + \dot{f}_v/\alpha p) \dot{p}_d \quad (21) \quad \text{Eq. (21)}$$

$$\dot{r}_d = (s_z \dot{p}_d - \dot{s}_y)/s_x \quad (22) \quad \text{Eq. (22)}$$

$$\text{where } D = s_x(\alpha \dot{\alpha} + \dot{f}_w) - \alpha \dot{s}_z \quad (23) \quad \text{Eq. (23)}$$

Because we wish to work in the regime of negative f_y/ω (as plotted in Figure 9), the values of α and f_w used in evaluating D are taken to correspond to this region. These may be taken as the demanded values or, at some expense in course biases due to the approximation, as constant values estimated at the start of terminal homing.

3.4 Modelled Form of Trajectory

The form of trajectory and time histories of various major parameters are shown in Figures 10 and 11. Figure 10 shows the response to sidewind (or target lateral velocity) and Figure 11 shows the response to an initial azimuth offset.

These runs show that a smooth homing course is achieved by the system after the initial convergence onto the navigation law, which is PN with the addition of an up bias to shape the elevation trajectory.

4. CONCLUDING DISCUSSION

On the other hand, provided that a systematically high level of terminal manoeuvre exists (or can be contrived by suitable navigation design) and an anisotropic configuration is possible, then the alternative approach of removing the twist-to-track singularity from regions of interest may be followed.

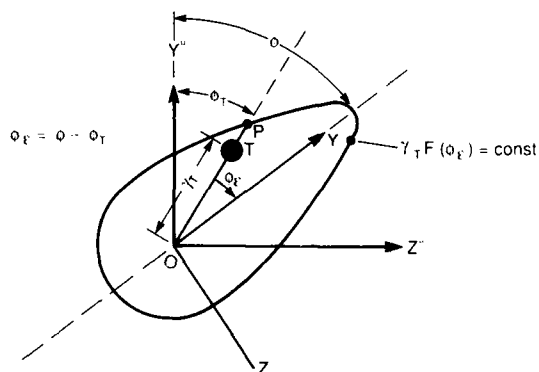


Figure 1 Definition of Cost Function

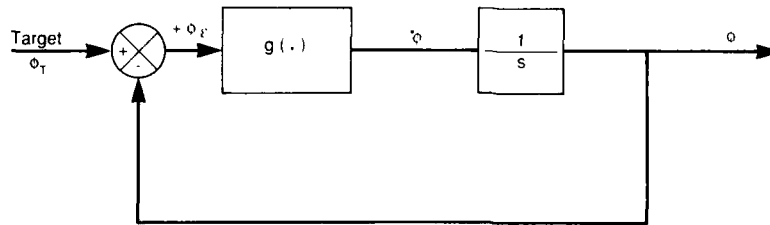


Figure 2 Stable Solutions in Feedback Form

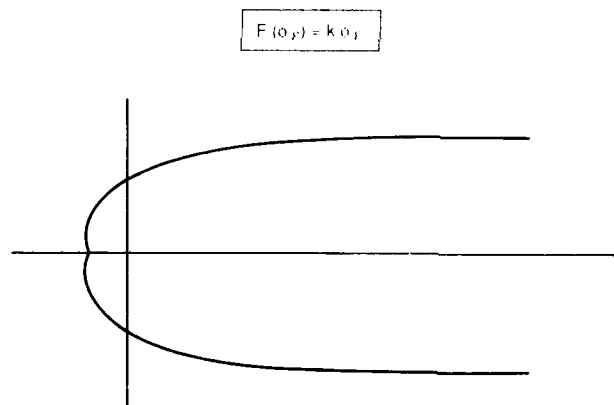


Figure 3 Linear Cost Function

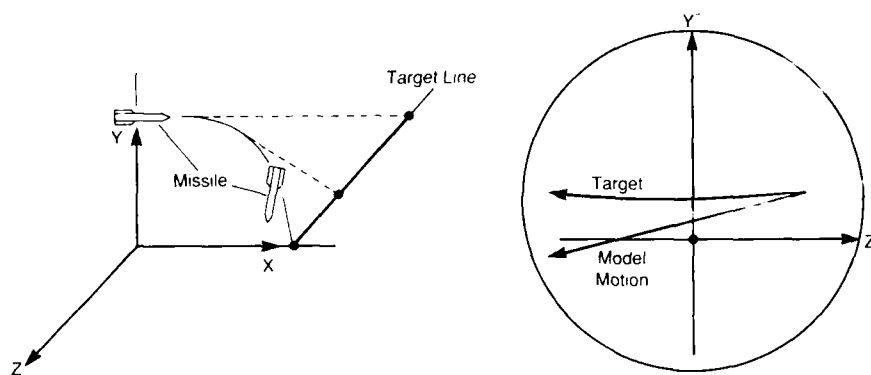


Figure 4 Typical Target Motion

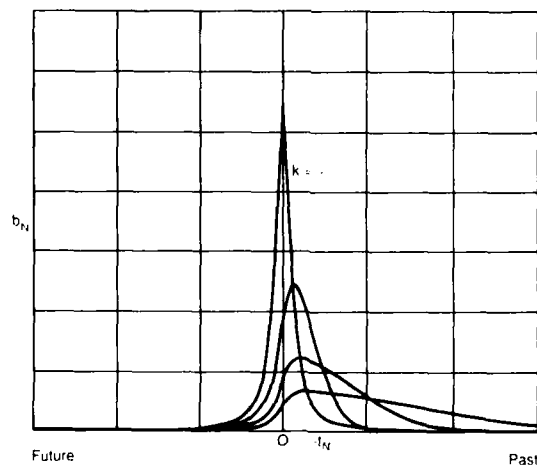


Figure 5 Scaled Bias Function

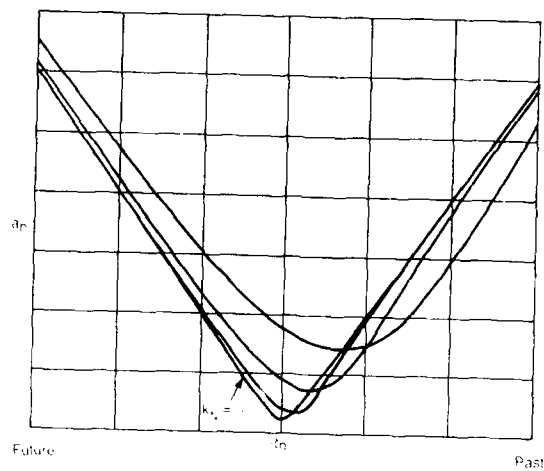


Figure 6 Scaled Gain Function

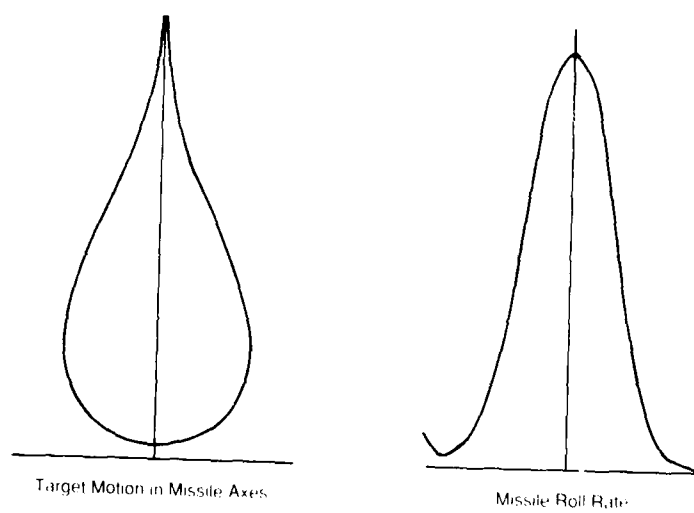


Figure 7 Typical Solution Trajectory

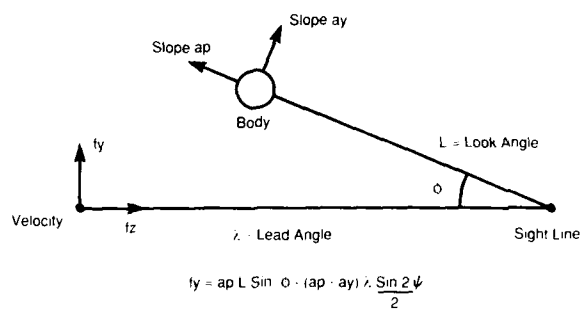


Figure 8 Manoeuvre Achieved During Twist-To-Track

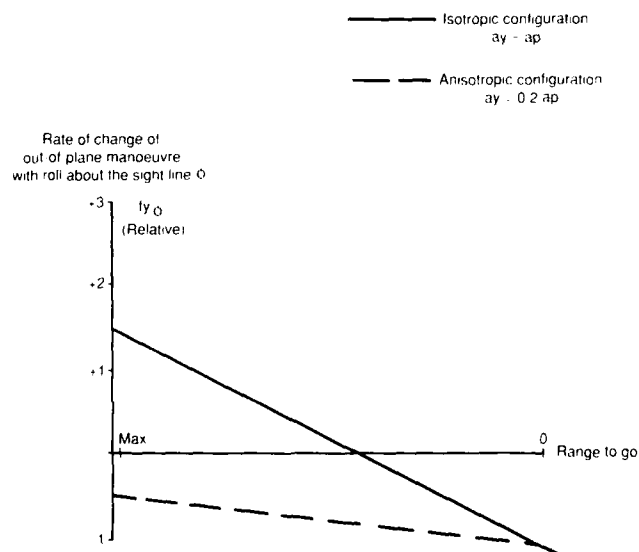


Figure 9 Manoeuvre Slope with Roll about the Sight Line

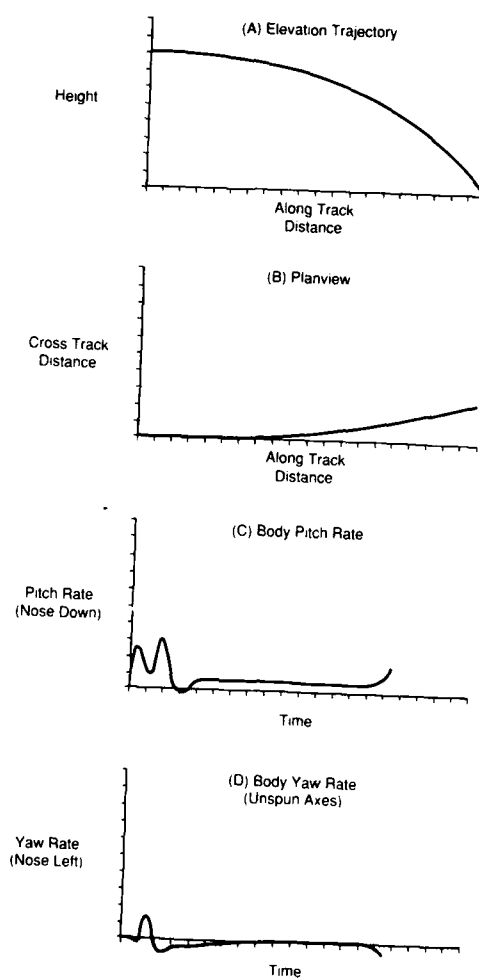


Figure 10 Response to Target Velocity - Part 1

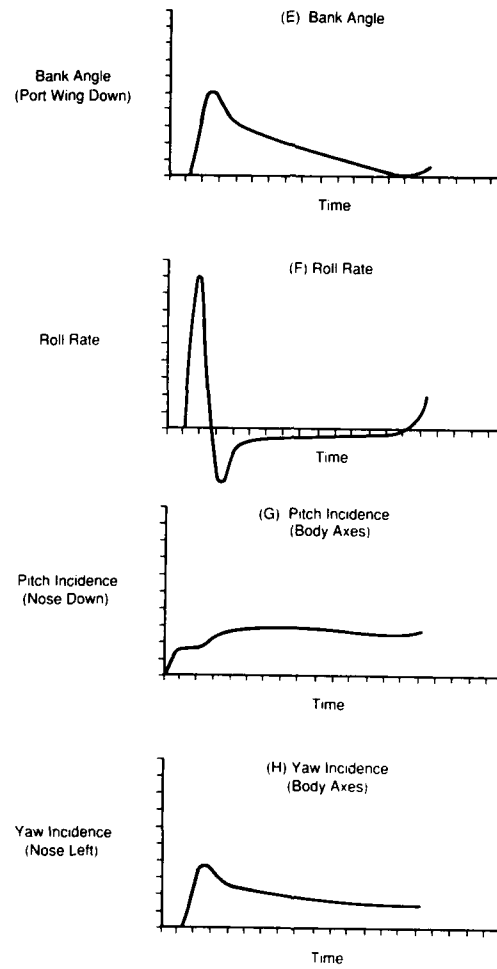


Figure 10 Response to Target Velocity - Part 2

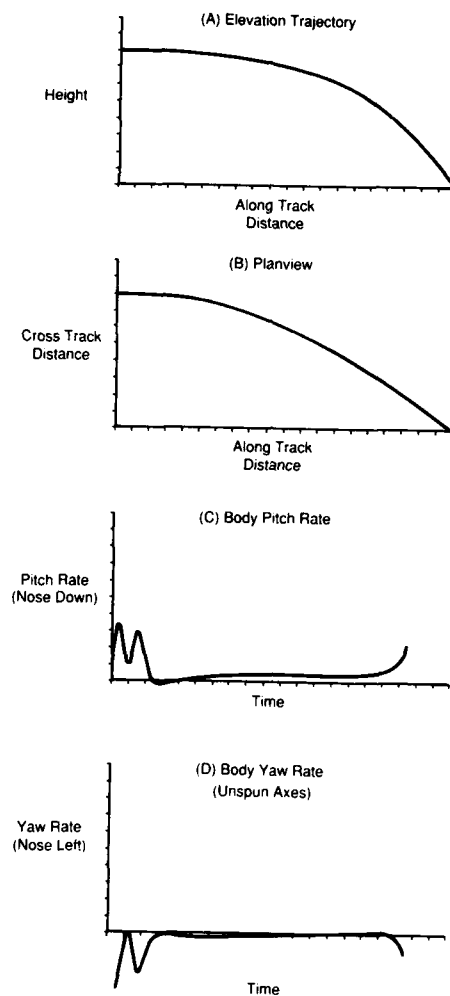


Figure 11 Response to Lateral Aiming Error - Part 1

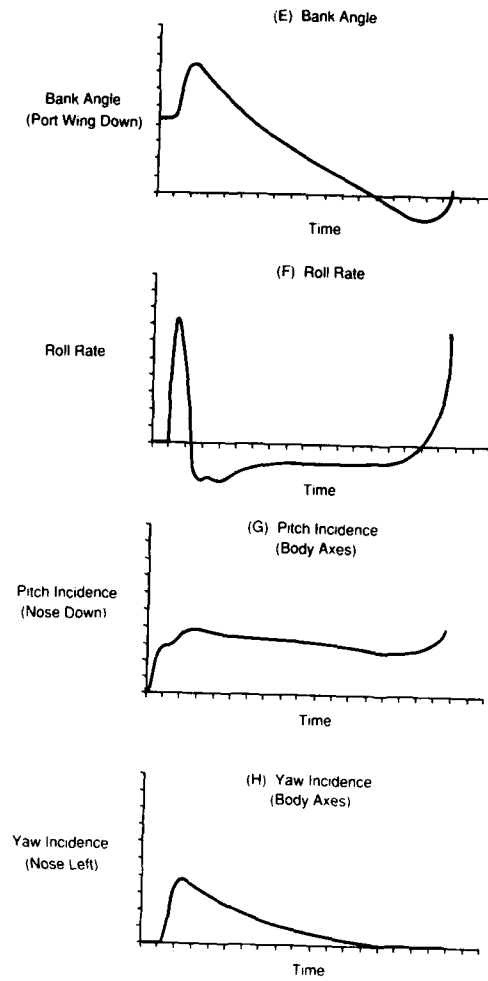


Figure 11 Response to Lateral Aiming Error - Part 2

HOW TO CONTROL UNSTABLE MISSILE AIRFRAMES: METHODOLOGY AND LIMITATIONS

DR. A. GAZZINA

Selenia S.p.A. - Missile System Division
Via Tiburtina Km 12,400 - POB 1083
00131 - ROMA - Italy

1. SUMMARY

This paper deals with the problem of controlling static unstable airframes of tactical missiles through the proper choice both of gains and of the autopilot configuration.

Unlike other excellent treatments of the subject, the paper tries to simplify to the extreme the analytical description of the problem in order to shorten the gap between the aerodynamicist and the control system designer.

Classical feedback paths are described highlighting the key features of each of them and a method of direct synthesis is presented valid for both stable and unstable airframes. The maximum allowable instability of the airframe is derived.

2. INTRODUCTION

The problem of controlling unstable airframes is not new or unusual. This requirement was dictated in the past by the need to accommodate an acceptable trade off to the center of gravity excursions during the boost phase and to compensate for the center of pressure shifts throughout all the flight situations encountered by the missile during its mission.

More recently the need for developing missiles with very fast response time suggests that this requirement could be more easily fulfilled by deliberately designing unstable airframes.

Consequently it is of practical interest for the missile designer to know what are the limits to the static instability of an airframe; this involves determining what is the maximum instability that can still be controlled by the autopilot, what are the physical or technological constraints, and what are the most relevant parameters affecting the problem.

This paper tries to give an answer to this general problem using the tools of classical control theory.

Further on, unlike other excellent papers on the subject, an effort has been made to simplify to the maximum possible extent the analytical description in order to better highlight the physical aspects of the problem and to present the results in a way more familiar to the aerodynamic designer.

3. OPEN LOOP AIRFRAME

With reference to fig. 1 and considering the airframe in an initial TRIM situation, the equations of small perturbations about the TRIM are (REF. 1) (a tail controlled tactical missile is considered here):

$$\dot{\gamma} = Z_{\alpha} \alpha + Z_{\delta} \delta \quad (1)$$

$$\ddot{\theta} = M_{\alpha} \alpha + M_{\delta} \delta + M_{\dot{\delta}} \dot{\delta} \quad (2)$$

$$\theta = \gamma + \alpha \quad (3)$$

where:

$$\dot{\gamma} = \frac{n_L}{V} \quad (4)$$

$$Z_{\alpha} \delta = f C_{N\alpha} \delta \quad (5)$$

$$M_{\alpha} \delta = g C_{m\alpha} \delta \quad (6)$$

$$M_{\dot{\theta}} = g \left(\frac{C}{2V} \right) C_{m\dot{\theta}} \quad (7)$$

$$g = \frac{95c}{J}, \quad f = \frac{95}{mV}$$

m = mass

J = pitch/yaw moment of inertia

n_L = normal acceleration of Center of Gravity

V = missile speed

$q = \frac{1}{2} \rho V^2$ dynamic pressure

The so called "damping term" $M_{\dot{\theta}}$ is usually small, but of some significance for a bare airframe, whereas when an autopilot is present, it provides much larger artificial damping so that this term can be neglected.

Further on in the force equation (1) the term $Z_{\delta} \delta$ can also be neglected with respect to $Z_{\alpha} \alpha$; this is to say that control panels generate only moments but not forces; this assumption is generally acceptable for canard and tail control, less for wing control.

With the above simplifications the equations become:

$$\dot{\gamma} = Z_{\alpha} \alpha \quad (1a)$$

$$\ddot{\theta} = M_{\alpha} \alpha + M_{\delta} \delta \quad (2a)$$

$$\theta = \alpha + \gamma$$

From these equations it is easy to derive the main (for stability analysis) aerodynamic transfer functions $\dot{\theta}/\delta$:

$$\frac{\dot{\theta}}{\delta} = M_{\delta} \frac{s + Z_{\alpha}}{s^2 + Z_{\alpha} s - M_{\alpha}} \quad (8)$$

In the denominator of the transfer function the damping term Z_{α} is very small (usually the corresponding γ is less than 0.1); again it can be neglected when compared to the artificial damping provided by the autopilot so that (8) finally becomes:

$$\frac{\dot{\theta}}{\delta} = M_{\delta} \frac{s + Z_{\alpha}}{s^2 - M_{\alpha}} \quad (8a)$$

This is the key equation for the stability analysis. In (8a) only and all the "essential" terms are included, that are:

M_{α} representing the static stability

M_{δ} representing the control authority

Z_{α} representing the turning rate capability, or its inverse $\frac{1}{Z_{\alpha}}$, sometimes called the incidence time lag".

As is well known, three possibilities exist:

($C_{m\alpha}$) $M_{\alpha} < 0$ this means STABLE AIRFRAME
 ($C_{m\alpha}$) $M_{\alpha} = 0$ this means ASTABLE AIRFRAME
 ($C_{m\alpha}$) $M_{\alpha} > 0$ this means UNSTABLE AIRFRAME

A stable airframe means that a restoring moment is generated in response to a perturbation in α , the angle of attack. This occurs when the center of gravity is closer to the nose of the missile than the center of pressure.

An unstable airframe means that the missile exhibits a growing response to a perturbation in α . This is due to the center of pressure being ahead of the center of gravity. The stable airframe, which in fact is not a practical situation, is the boundary between stable and unstable airframes. All three situations are depicted in the sketch of fig. 2 together with a plot of the pole-zero configuration of the transfer function θ/δ .

In the remaining part of the paper only the case of unstable airframes will be considered and analyzed ($M_\alpha > 0$). Nevertheless it is important to remark that many of the conclusions derived for this particular case are also applicable to stable airframes.

4. CLOSED LOOP AIRFRAME

An unstable missile will exhibit a growing response to a perturbation in α , unless a suitable control system is present to prevent such degenerative behavior. A very general approach to the control philosophy is to measure the angular rate $\dot{\theta}$ of the missile, from which to derive appropriate commands to the movable panels; these in turn will generate an aerodynamic moment (this is the term M_δ) that eventually will counteract the destabilizing effects of M_α . The control loop is depicted in fig. 3. The control law may take three different basic forms or a combination of them:

angular acceleration feedback	$\delta = K_a \ddot{\theta}$
angular rate feedback	$\delta = K_R \dot{\theta}$
attitude feedback	$\delta = K_\theta \theta$
rate plus attitude feedback	$\delta = K_R \dot{\theta} + K_\theta \theta$

4-1. Angular acceleration feedback

The control law $F(s)$, the open loop transfer function F_{OL} and the corresponding characteristic equation C.E. are:

$$F(s) = \frac{\delta}{\theta} = K_a s \quad (9)$$

$$F_{OL} = K_a M_\delta \frac{s(s+Z_\alpha)}{s^2 - M_\alpha} \quad (10)$$

$$\text{C.E.} = (1+K_a M_\delta) s^2 + K_a M_\delta Z_\alpha s - M_\alpha = 0 \quad (11)$$

According to Pouth's criterion the "minus" sign in the characteristic equation shows the existence of at least one root with positive real part, implying that the system is unstable. The same conclusion is easily derived from examination of the root loci plot (see fig. 4a).

4-2. Angular rate feedback

In this case the three relations are:

$$F(s) = K_R \quad (9a)$$

$$F_{OL} = K_R M_\delta \frac{s + Z_\alpha}{s^2 - M_\alpha} \quad (10a)$$

$$\text{C.E.} = s^2 + K_R M_\delta s + (K_R M_\delta Z_\alpha - M_\alpha) = 0 \quad (11a)$$

From inspection of the characteristic equation and the root loci (fig. 4b) it is easy to see that the system can be made stable, and that a necessary and sufficient condition for stability is:

$$K_R M_\delta > \frac{M_\alpha}{Z_\alpha} \quad (12)$$

4-3. Attitude feedback

The three relations are:

$$F(s) = \frac{\delta}{\theta} = \frac{K_\theta}{s} \quad (9b)$$

$$F_{OL} = K_\theta M_\delta \frac{s + Z_d}{s(s^2 - M_d)} \quad (10b)$$

$$C.E. = s^3 + (K_\theta M_\delta - M_d)s + K_\theta M_\delta Z_d = 0 \quad (11b)$$

Inspection of the C.E. shows that a necessary condition for stability is:

$$K_\theta M_\delta > M_d \quad (13)$$

But this relationship is of little interest because the plot of the root loci (fig. 4c) shows that a branch of the locus is completely in the right plane; this means that the system is always unstable whatever the value of the electronic gain K_θ .

4-4. Rate + attitude feedback

This very popular control algorithm is also referred as: rate + synthetic stability control. The equations are:

$$F(s) = K_R + \frac{K_\theta}{s} = K_R \frac{s + W_I}{s} \quad (9c)$$

$$F_{OL} = K_R M_\delta \frac{(s + Z_d)(s + W_I)}{s(s^2 - M_d)} \quad (10c)$$

$$C.E. = s^3 + K_R M_\delta s^2 + [K_R M_\delta (Z_d + W_I) - M_d]s + K_R M_\delta Z_d W_I = 0 \quad (11c)$$

$$\text{where: } W_I = \frac{K_\theta}{K_R}$$

From the C.E. a necessary condition for stability can still be found:

$$K_R M_\delta (Z_d + W_I) > M_d \quad (14)$$

Unfortunately this condition, being only necessary, is not very helpful because even if it is satisfied the control designer does not know if the system is stable or not.

In some extent the root loci (see fig. 4d) is of valid assistance. At least it shows that with a proper choice of the control parameters K_R and W_I the system can be made stable. The condition for stability is given by the crossover of the root locus with the $j\omega$ axis.

In the appendix to this paper the analytical relation for the root to be in the left plane has been found. It is:

$$K_R M_\delta > \frac{M_d + \psi Z_d^2}{(\psi + 1) Z_d} \quad (15)$$

$$\text{where: } \psi = \frac{W_I}{Z_d} = \frac{K_\theta}{K_R Z_d}$$

A conclusion on the different control algorithms can now be derived:

- It is not possible to stabilize a statically unstable airframe with angular acceleration feedback alone or with an attitude feedback alone. The

key feedback to achieve this objective is the rate feedback, alone or in combination with the other two.

5. HIGH FREQUENCY ANALYSIS

In the analysis performed in the previous paragraph the high frequency terms due to the autopilot component dynamics have been deliberately neglected. This assumption led to find the stability condition for two different control algorithms (Eq. 12 and 15); this condition is: in order to stabilize an unstable airframe the gain of the control loop $K_R M_\delta$ must be kept sufficiently high. No upper limit seems to exist and this would lead to the conclusion that it is always possible to find a proper value of the electronic gain to compensate for any value of aerodynamic instability. This is not true; a limit to the gain does exist and it is dictated by the autopilot component dynamics, mainly by the bandwidth of the actuator system.

In REF. 1 a comprehensive model of the system including all significant high frequency term is described. It is an 11th order model that also includes the 3rd order model previously described in this paper. Fig. 5 taken from REF. 1 shows the frequency response of the 3rd order model compared with the 11th order model. This figure shows that if the gain is increased above certain limits high frequency instability will occur.

It is not easy to express the instability condition in a simple analytical way for such a complex model. On the other hand inspection of the frequency response diagram suggests a possibility for major simplification of the high frequency contributors, through the introduction of the "equivalent actuator". In fact the only important effect of the high frequency terms is to add a phase lag near the phase crossover frequency ω_{EA} ; there is only a small influence on the phase in the low frequency region and no influence at all on the gain in the overall frequency domain of interest.

This behavior is due to the fair separation that exists, at least in tactical missiles, between the airframe frequencies Z_α and $\sqrt{M_\alpha}$ and the frequencies of the autopilot components; typically this separation is of the order of one to five or one to ten. In this situation the whole of the high frequency terms can be approximated by a 2nd order transfer function that is:

$$F_{EA}(s) = \frac{1}{1 + \frac{2\zeta_{EA}}{\omega_{EA}}s + \frac{s^2}{\omega_{EA}^2}} \quad (16)$$

where the value of ζ_{EA} must be put equal to 0.5 in order to keep the gain as flat as possible and ω_{EA} is the frequency at which the phase lag of all high frequency terms is 90 degrees. It is the same as having an autopilot without structural filter and inertial sensors dynamics but with an actuator whose bandwidth is lower than that of the actual actuator; this is called an "equivalent actuator". Fig. 5 shows the kind of approximations introduced with the use of the equivalent actuator (dashed line).

With this simplification the complete open loop transfer function of the system becomes:

- Rate feedback alone

$$F_{OL} = K_R M_\delta \frac{s + Z_\alpha}{(s^2 - M_\alpha) \left(1 + \frac{1}{\omega_{EA}}s + \frac{s^2}{\omega_{EA}^2}\right)} \quad (17)$$

- Rate plus attitude feedback

$$F_{OL} = K_R M_\delta \frac{s + \omega_I}{s} \frac{(s + Z_\alpha)}{(s^2 - M_\alpha) \left(1 + \frac{1}{\omega_{EA}}s + \frac{s^2}{\omega_{EA}^2}\right)} \quad (18)$$

As stated above there is a great separation between ω_{EA} and the airframe frequencies; further more the zero ω_I in the control law (9c) must be kept reasonably low in order not to introduce an additional phase lag near ω_{EA} . Typically it should be:

$$\omega_I \leq \frac{\omega_{EA}}{10} \quad (19)$$

It follows that in the high frequency region, near ω_{EA} , the two transfer functions (17) and (18) can be approximated with:

$$(F_{OL})_{H.F.} \approx \frac{K_R M_\delta}{s \left(1 + \frac{1}{\omega_{EA} s} + \frac{s^2}{\omega_{EA}^2}\right)} \quad (20)$$

The gain at the crossover frequency ω_{EA} , where the phase lag is 180° , is:

$$G = \frac{K_R M_\delta}{\omega_{EA}} \quad (21)$$

In order for the system to be stable G must be < 1 that is:

$$\boxed{K_R M_\delta < \omega_{EA}} \quad (22)$$

This relationship synthesizes all the constraints imposed by the component dynamics. Once this condition is satisfied the study of the system may be limited to the 3rd order model.

6. OVERALL STABILITY CONDITIONS

6-1. Rate feedback

Merging the condition for stability at low frequency (12) with the high frequency condition (22) leads to the overall stability relationship:

$$\omega_{EA} > K_R M_\delta > \frac{M_\delta}{Z_\delta} \quad (23)$$

Obviously it also must be the case that:

$$\omega_{EA} \gg \frac{M_\delta}{Z_\delta} \quad (24)$$

This means that the limits to the controllability of unstable airframes are dictated by the bandwidth of the actuators (mainly), that in turn is limited by current technologies and cost.

It is also possible to make a quantitative estimate of above limits and to express the instability of the airframe in terms more familiar to the aerodynamicist. For this purpose a gain margin of 10 dB is assumed for both low and high frequency sides. The (24) becomes:

$$\omega_{EA} = \frac{M_\delta}{Z_\delta} + 20 \text{ dB} \quad (25)$$

that is:

$$\omega_{EA} = 10 \frac{M_\delta}{Z_\delta} \quad (25a)$$

Recalling the expressions (5) and (6), and introducing the arm b_α of the aerodynamic force, due to a perturbation in α (see also fig. 2) we obtain:

$$\frac{M_\alpha}{Z_\alpha} = \frac{C_{m\alpha} c mV}{C_{N\alpha} J} = \frac{b_\alpha mV}{J} = \frac{b_\alpha V}{R^2} \quad (26)$$

where $R = \sqrt{J/m}$ is the radius of inertia of the missile. There is a quite constant relationship between R and the length L of the missile. It is:

$$R \cong \frac{L}{10} \quad (27)$$

Hence the overall stability condition becomes:

$$\beta_L = w_{EA} \frac{L}{V} \quad (28)$$

where $\beta_L = b_\alpha/L \times 100$ represents the "unstable" arm of the aerodynamic force, expressed in percentage of the missile length. It may now be concluded that: "The maximum static instability (relative to missile length), that can be controlled with a rate feedback loop is:

- proportional to the actuator bandwidth (equivalent)
- proportional to the missile length
- inversely proportional to the missile speed.

Fig. 6 is a plot of β_L versus V for typical values of w_{EA} and L . It shows that, for missile speeds exceeding 500 m/sec, instabilities of less than one per cent of the missile length can be controlled by a rate autopilot alone.

6-2. Rate + attitude feedback

In this case the overall stability condition is, from (15) and (22):

$$w_{EA} > K_R M_\delta > \frac{M_\alpha + \Psi Z_\alpha^2}{(\Psi + 1) Z_\alpha} \quad (29)$$

For typical values of Z_α and for quite large instabilities, an approximate expression can be derived for the low frequency condition. It is:

$$K_R M_\delta > \frac{1}{\Psi} \frac{M_\alpha}{Z_\alpha} \quad (30)$$

where: $\Psi = \frac{w_I}{Z_\alpha}$

The overall stability condition becomes:

$$w_{EA} \gg \frac{1}{\Psi} \frac{M_\alpha}{Z_\alpha} \quad (31)$$

Assuming the same gain margin of 10 dB the allowable instability becomes:

$$\beta_L = \Psi w_{EA} \frac{L}{V} \quad (32)$$

That is, the insertion of the attitude feedback (also referred to as a synthetic stability loop) increases the maximum allowable instability by a factor of Ψ . Typical values of Ψ may be in the range of 5 to 10 (at sea level).

6.3 Acceleration feedback

The purpose of a flight control system is to quickly and accurately generate the accelerations called for by the guidance algorithm. This means that the primary control loop of an autopilot is the acceleration feedback and that the gyro loops are added only to provide stability.

A block diagram of a complete 3 loop pitch/yaw autopilot is shown in fig. 7. Its 3rd order model is shown in fig. 8, together with the most significant transfer functions of the airframe (complete and simplified). A question arises whether the conclusions derived for the gyro loops alone are still valid or not.

To answer, let us consider separately the high frequency and low frequency performance.

6-3-1 High frequency analysis

In the proximity of ω_{EA} , typically for frequencies of 100 rad/sec, the gains of the acceleration path and gyro path are:

$$G_{ACC \text{ H.F.}} \approx \frac{K_A M \delta Z \alpha V}{s^3} \quad (33)$$

$$G_{GYRO \text{ H.F.}} \approx \frac{K_R M \delta}{s} \quad (34)$$

The ratio between these gains is:

$$R_g = \frac{G_{ACC}}{G_{GYRO}} = \frac{K_A Z \alpha V}{K_R} \frac{1}{s^2} \quad (35)$$

Typical values of the above parameters for a tactical missile flying at sea level at supersonic speed are:

$$\begin{aligned} K_A &= 5 \times 10^{-3} \frac{\text{rad sec}^{-1}}{\text{m sec}^{-2}} \\ Z \alpha &= 2 \text{ sec}^{-1} \\ K_R &= 0.1 \text{ sec} \end{aligned}$$

Considering a speed $V = 750 \text{ m/s}$ and a frequency $s = 100 \text{ rad/sec}$, we find:

$$R_g = 7.5 \times 10^{-3}$$

This means that in the frequency region near ω_{EA} , the contribution of the acceleration path is negligible compared to the gyro path. Therefore all the conclusions found in para 5 are still valid, namely the high frequency stability equation (22):

$$K_R M \delta > \omega_{EA}$$

6-3-2 Low frequency analysis

Considering the 3rd order model of fig. 8 it is worthwhile to remark that the accelerometer has been put at the center of gravity station. This situation does not happen very often, never the less it may be shown that with the present control algorithm, to move the accelerometer from the C. of G. station is perfectly equivalent to changing the gain of the rate loop K_R , and, further, this change is negligible compared to the values of K_R .

In fact; if Δx is the longitudinal distance of the accelerometer from the C. of G., we have:

$$n_A = n_L \pm \Delta x \ddot{\theta}$$

where n_A and n_L are the normal accelerations at the accelerometer station and at the C. of G. station.
The control law of the acceleration path is:

$$\delta = -\frac{K_A}{s} n_A \quad (36)$$

It follows that:

$$\delta = -\frac{K_A}{s} n_L + K_A \Delta x \dot{\theta} \quad (37)$$

It is the same of having the accelerometer put at the C. of G. station and the gain K_R changed by the amount:

$$\frac{\Delta K_R}{K_R} = \frac{K_A}{K_R} \Delta x \quad (38)$$

A typical value for Δx is 1 meter, leading to:

$$\frac{\Delta K_R}{K_R} \approx 0.05$$

In conclusion, for the purpose of the present analysis it is perfectly acceptable to put the accelerometer at the C. of G. station.

From the block diagram of fig. 8 the open loop transfer function is derived (loop broken at δ):

$$F_{OL} = \frac{K_R M \delta (s + W_I) (s + Z_d) + K_A M \delta Z_d V}{s (s^2 - M_d)} \quad (39)$$

It is not easy to find an analytical expression for the stability condition using the same procedure used in the Appendix.

Whereas the method of direct synthesis developed by Nesline and presented in REF 1 is of valuable support. This method is briefly reported here-in. The characteristic equation of the system is:

$$\begin{aligned} \text{C.E.} &= 1 + F_{OL} = \\ &= s^3 + K_R M \delta s^2 + [K_R M \delta (Z_d + W_I) - M_d] s + M \delta Z_d (K_R W_I + K_A V) \end{aligned} \quad (40)$$

Introducing the gain crossover frequency:

$$W_{CR} = K_R M \delta \quad (41)$$

(44) becomes:

$$\begin{aligned} \text{C.E.} &= s^3 + W_{CR} s^2 + [W_{CR} (Z_d + W_I) - M_d] s + W_{CR} Z_d (W_I + \frac{K_A}{K_R} V) \\ &= s^3 + W_{CR} s^2 + a s + b \end{aligned} \quad (42)$$

where:

$$a = W_{CR} (Z_d + W_I) - M_d \quad (43)$$

$$b = W_{CR} Z_d (W_I + \frac{K_A}{K_R} V) \quad (44)$$

The roots of the 3rd order equation are typically characterized by a real pole ($\frac{1}{\tau}$) and a quadratic pair of poles (W_n, ζ) that is:

$$\begin{aligned} \text{C.E.} &= (s + \frac{1}{\tau}) (s^2 + 2\zeta W_n s + W_n^2) = \\ &= s^3 + (2\zeta W_n + \frac{1}{\tau})s^2 + (W_n^2 + \frac{2\zeta W_n}{\tau})s + \frac{W_n^2}{\tau} \end{aligned} \quad (45)$$

Equations (42) and (45) are in fact the same equation. In (42) the coefficients are expressed in terms of autopilot gains and aerodynamics whereas in (45) the same coefficients are expressed in terms of closed loop roots.

By equating the coefficients of Equations (42) and (45):

$$W_n = \frac{W_{CR} \tau - 1}{2\zeta \tau} \quad (46)$$

$$a = W_n + \frac{2\zeta W_n}{\tau} \quad (47)$$

$$b = \frac{W_n^2}{\tau} \quad (48)$$

Moreover from the (43) and (44):

$$W_I = \frac{a + M_\delta}{W_{CR}} - Z_\delta \quad (49)$$

$$K_A = \frac{K_R}{V} \left(\frac{b}{W_{CR} Z_\delta} - W_I \right) \quad (50)$$

An autopilot design procedure can now be defined; this procedure is general and not restricted to unstable airframes only.

Once the natural frequency W_{EA} of the equivalent actuator has been evaluated, the high frequency gain margin M_G should be chosen. This leads to define the upper limit of W_{CR} :

$$W_{CR} = \frac{W_{EA}}{M_G} \quad (51)$$

and of K_R :

$$K_R = \frac{W_{CR}}{M_\delta} \quad (52)$$

where for M_δ the highest value expected in the region where the gains are used must be used.

The second step is to define the desired values for τ and ζ , from which to compute the parameters a and b with (47) and (48). Finally the two remaining gains W_I and K_A are evaluated through (49) and (50).

An iterative process may be necessary mainly if the constraints of this analysis are violated, i.e. if W_I results too large with respect to W_{EA} .

Coming back to the main purpose of present analysis, that is to find a mathematical relationship for stability in the low frequency region, it is to be remarked that the limit condition for stability is $\zeta = 0$. Introducing this value into (46) (47) (48) leads to the equation:

$$a w_{CR} = b \quad (53)$$

That is, from (47) and (48):

$$w_{CR} = \frac{M\alpha + Z_\alpha w_I}{Z_\alpha + w_I} + \frac{K_A Z_\alpha V}{K_R (Z_\alpha + w_I)} \quad (54)$$

Equation (54) represents a limit situation ($\delta = 0$). For the stability of the system, that is for $\delta > 0$, it must be true that:

$$w_{CR} > \frac{M\alpha + \psi Z_\alpha^2}{(\psi + 1) Z_\alpha} + \frac{K_A V}{K_R (\psi + 1)} \quad (55)$$

For large airframe instabilities and for typical values of autopilot parameters the second term in the right side of equation (55) can be neglected so that the condition stability becomes the same found in para 6-2, equation (29).

It can be concluded that the contribution of the acceleration path to the stability conditions for both low and high frequency sides may be neglected; therefore all the results and comments of para 6-1 dealing with the gyro path alone remain still valid.

7. COMMENTS TO THE RESULTS

Recalling the equation (32), that synthesizes the results of the study:

$$\beta_L = \psi w_{EA} \frac{L}{V}$$

it is interesting to remark that ψ is not a constant factor but:

$$\psi = \frac{w_I}{Z_\alpha} \quad (56)$$

As said in par. 5, w_I cannot be made as large as desired but there is a limitation coming (once more) from the equivalent actuator bandwidth w_{EA} . This is:

$$w_I = \frac{w_{EA}}{10} \quad (57)$$

Moreover, from (5) the expression of β_L becomes:

$$\beta_L = K \frac{L}{g} \left(\frac{w_{EA}}{V} \right)^2 \quad (58)$$

$$K = \frac{m}{5 C_{N\alpha} S}$$

It may be concluded that: "THE MAXIMUM ALLOWABLE INSTABILITY" (relative to missile length):

- IS PROPORTIONAL TO MISSILE LENGTH;
- INCREASES WITH ALTITUDE;
- HAS A QUADRATIC DEPENDANCE ON w_{EA} AND V .

In fig. 9 a plot of β_L versus speed is presented for a typical missile (AMRAAM class).

This diagram emphasizes the strong influence of missile dynamic pressure on allowable instability; at sea level and with a missile speed exceeding 500 m/sec an instability of only a few percent of missile length can be tolerated.

Fortunately the two protagonists of aerodynamic stability that are the Center of Gravity and the Center of Pressure exhibit a quite favorable behavior with respect to missile speed. In fact as the speed increases during the boost phase the C. of G. moves forward while in general the Centre of Pressure tends to move backward when speed increases (at least for wing-body-tail configurations).

However, even if this beneficial effect can alleviate the problems of the high speed regimes, this still remains the most critical situation and the only way to increase the allowable instability will be to increase the "equivalent actuator" bandwidth.

To achieve this purpose three levels of increasing complexity may be envisaged, at least in the author opinion. The first and probably simplest action is to increase the natural frequency of inertial sensors. Second action would be to increase the missile stiffness and hence the body bending frequencies. The third and probably heaviest technological effort would be to increase the bandwidth of the actual actuator.

8. CONCLUSION

- In order to control unstable airframes the best autopilot configuration is the "rate + attitude feedback".
- The limits to the maximum allowable instability are mainly dictated by the bandwidth of the actuator system.
- The maximum allowable instability increases with missile length and decreases with dynamic pressure.

REFERENCES

1. F. William Nesline and Mark L. Nesline, "How autopilot requirements constrain the aerodynamic design of homing missiles".
2. F.W. Nesline, B.H. Wells, and P. Zarehan, "A combined Optimal/Classical approach to robust missile autopilot design" AIAA Guidance and Control Conference, Aug. 1979 - Paper No. 79 - 1731.
3. James W. Carter, Thomas J. Monteodorisio, "System design requirements for separation of tactical air-launched missiles".

APPENDIX - STABILITY CONDITION FOR A RATE + ATTITUDE FEEDBACK CONFIGURATION

The open loop transfer function is (para 4-4):

$$F_{OL} = K_R M \frac{(s + Z_\alpha)(s + W_1)}{s(s^2 - M_\alpha)} \quad (A1)$$

The corresponding root loci is depicted in fig. 4 d. The limit condition for stability occurs when the locus crosses the $j\omega$ axis (for $w = \bar{w}$). By definition, the root loci are the points of the complex plane where:

$$1 + F_{OL} = 0 \quad (A2)$$

that is:

$$F_{OL} = -1 + j0 \quad (A3)$$

This means that the phase of $F_{OL}(s)$ has to be 180° .

Since along the imaginary axis it is always: $s = j\omega$, in order to find the crossover frequency $\bar{\omega}$, it will be sufficient to find the phase of the frequency transfer function $F_{OL}(j\omega)$ and to put it equal to -180 degrees. This transfer function is:

$$F_{OL}(j\omega) = \frac{(Z_d + j\omega)(W_I + j\omega)}{j\omega [(j\omega)^2 - M_d]}$$

The phase contribution of the denominator of eq. (A4) is -270 degrees; in order for the phase shift of F_{OL} to be -180 degrees, the numerator must give a phase shift of $+90$ degrees, that is:

$$\text{tg}^{-1} \frac{\bar{\omega}}{Z_d} + \text{tg}^{-1} \frac{\bar{\omega}}{W_I} = 90 \quad (A5)$$

that can also be written as:

$$\text{tg}^{-1} \frac{\frac{\bar{\omega}}{Z_d} + \frac{\bar{\omega}}{W_I}}{1 - \frac{\bar{\omega}^2}{Z_d W_I}} = 90 \quad (A6)$$

that is satisfied for:

$$\bar{\omega} = \sqrt{Z_d W_I} = Z_d \sqrt{\Psi} \quad (A7)$$

where:

$$\Psi = \frac{W_I}{Z_d} \quad (A8)$$

In order for the system to be stable the root must lie in the left halfplane; this implies that:

$$|F_{OL}(j\omega)| > 1 \quad (A9)$$

that is:

$$K_R M_d > \frac{\bar{\omega} (M_d + \bar{\omega}^2)}{\sqrt{(Z_d^2 + \bar{\omega}^2)(W_I^2 + \bar{\omega}^2)}} \quad (A10)$$

and finally:

$$K_R M_d > \frac{M_d + \Psi Z_d^2}{(\Psi + 1) Z_d} \quad (A11)$$

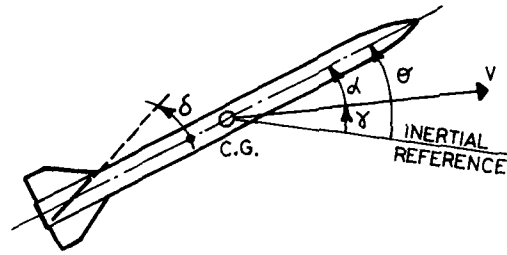


FIG. 1 AIRFRAME

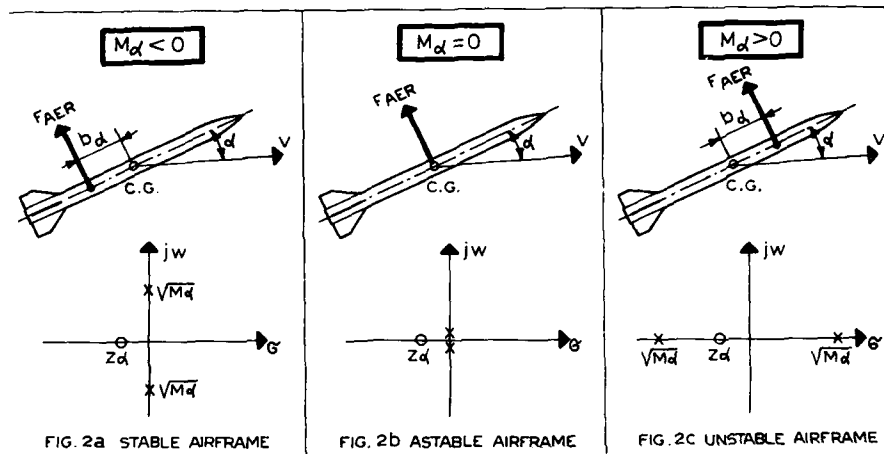
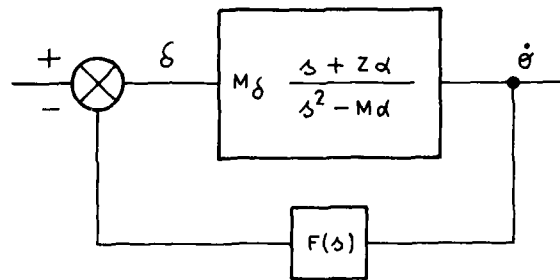


FIG. 2 STABILITY SITUATIONS



CONTROL LAW :

$$F(s) = K_a s \quad (\text{ANGULAR ACCELERATION FEEDBACK})$$

$$F(s) = K_R \quad (\text{ANGULAR RATE FEEDBACK})$$

$$F(s) = \frac{K_\theta}{s} \quad (\text{ATTITUDE FEEDBACK})$$

$$F(s) = K_R + \frac{K_\theta}{s} \quad (\text{RATE + ATTITUDE FEEDBACK})$$

FIG. 3 AUTOPILOT STABILITY LOOP

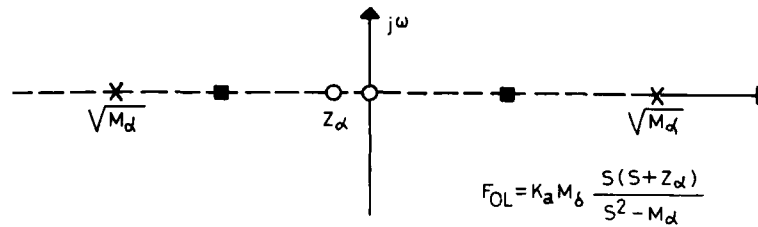


FIG. 4 a ANGULAR ACCELERATION FEEDBACK

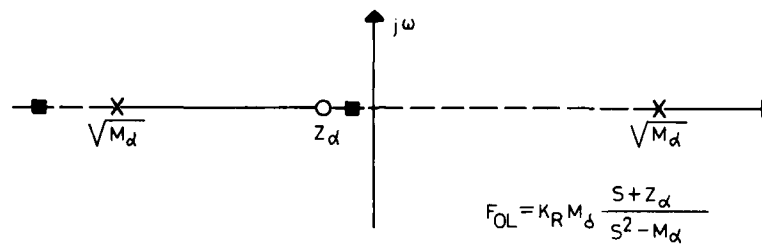


FIG. 4 b ANGULAR RATE FEEDBACK

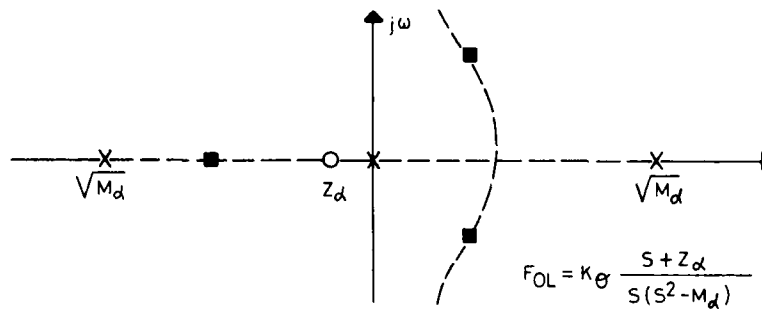


FIG. 4 c ATTITUDE FEEDBACK

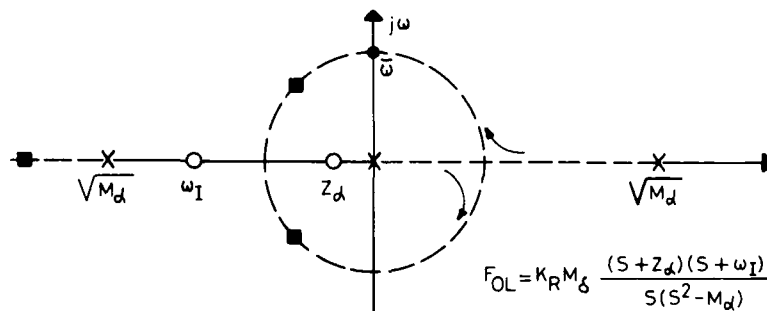


FIG. 4 d RATE + ATTITUDE FEEDBACK

X POLES ■ ROOTS
O ZEROES --- ROOT LOCI

FIG. 4 ROOT LOCI OF DIFFERENT FEEDBACK CONFIGURATIONS

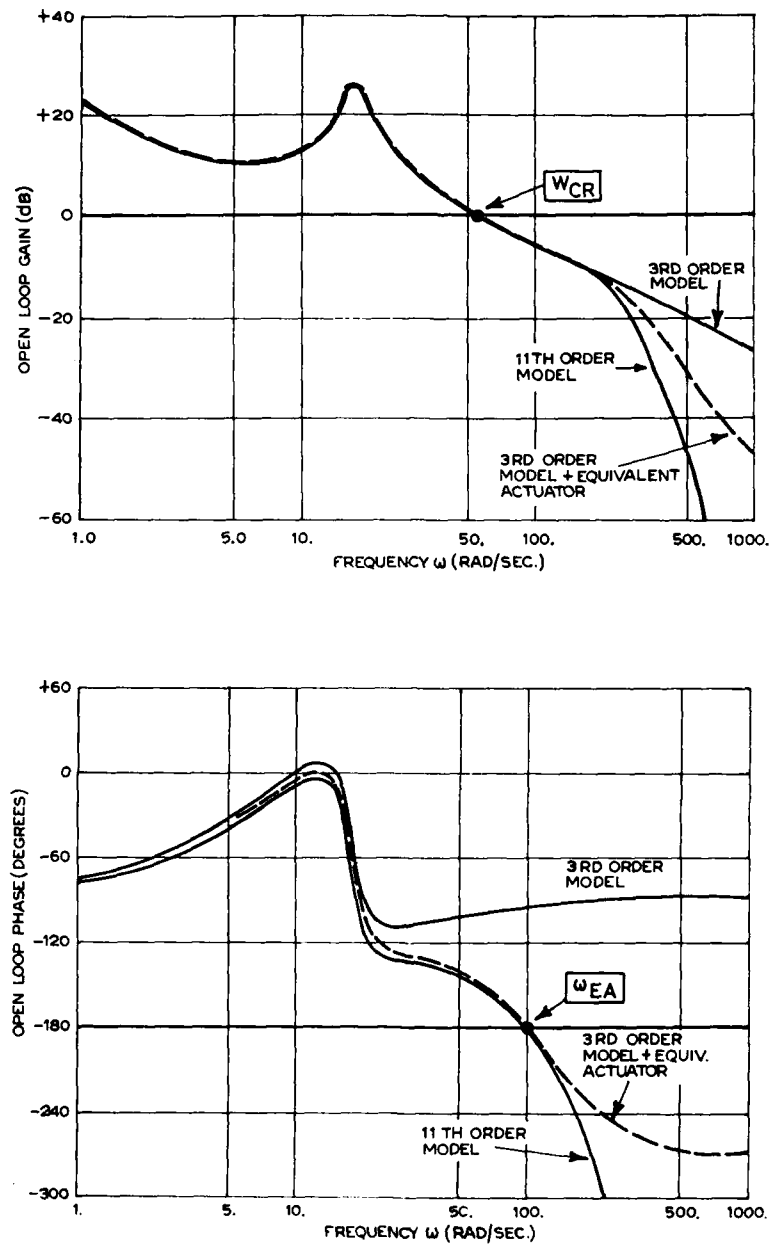


FIG. 5 OPEN LOOP FREQUENCY RESPONSE.

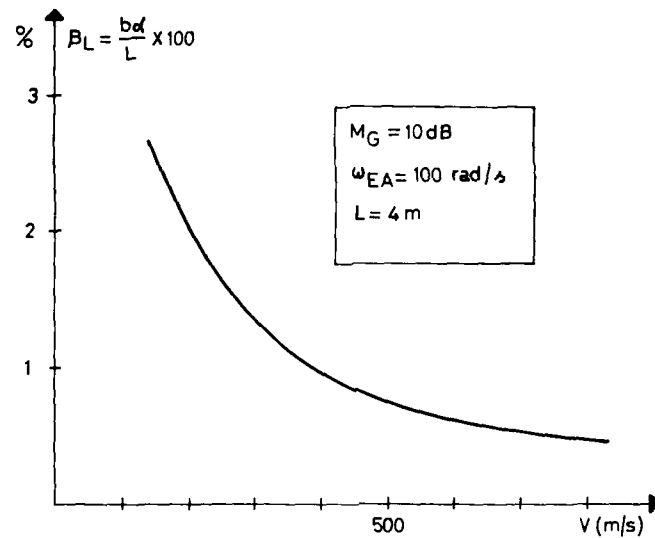


FIG. 6 MAXIMUM ALLOWABLE INSTABILITY WITH A RATE FEEDBACK ALONE.

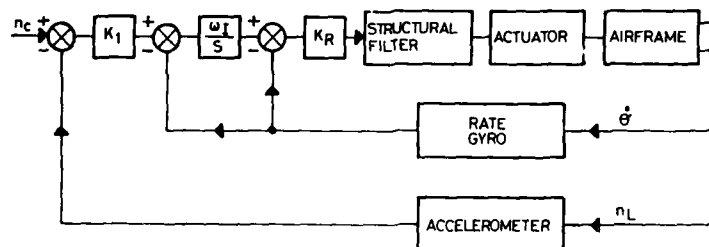
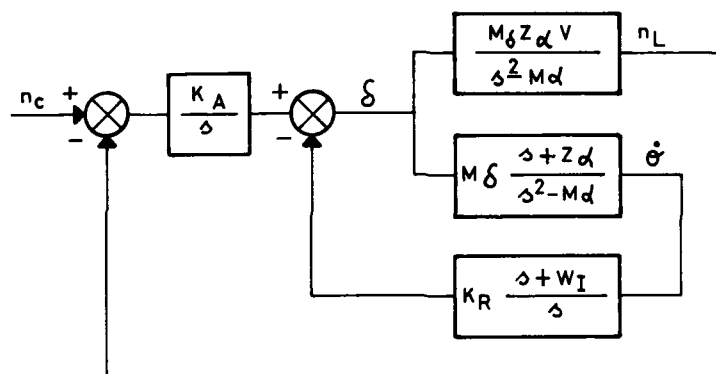


FIG. 7 BLOCK DIAGRAM OF A COMPLETE 3-LOOP AUTOPILOT.



$$\frac{n_L}{\delta} = V \frac{Z_\alpha s^2 - (M_\delta Z_\alpha + M_\alpha Z_\delta)}{s^2 + Z_\alpha s - M_\alpha} \approx \frac{M_\delta Z_\alpha V}{s^2 - M_\alpha}$$

$$\frac{\dot{\theta}}{\delta} = \frac{M_\alpha Z_\alpha + M_\delta Z_\alpha + M_\delta s}{s^2 + Z_\alpha s - M_\alpha} \approx M_\delta \frac{s + Z_\alpha}{s^2 - M_\alpha}$$

$$\frac{\alpha}{\delta} = \frac{M_\delta + Z_\delta s}{s^2 + Z_\alpha s - M_\alpha} \approx \frac{M_\delta}{s^2 - M_\alpha}$$

FIG. 8 3RD ORDER MODEL OF THE 3-LOOP AUTOPILOT.

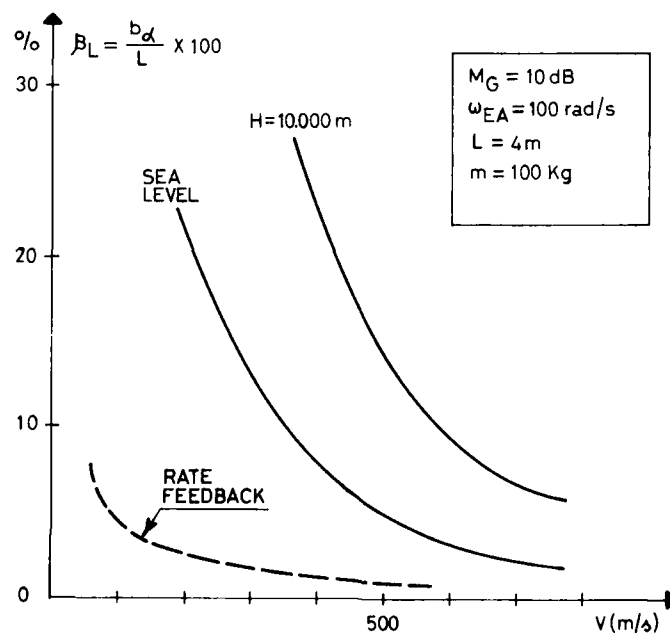


FIG. 9 MAXIMUM ALLOWABLE INSTABILITY WITH A RATE + ATTITUDE FEEDBACK.

GYROMETRE LASER TRIAXIAL MINIATURISE

par

Serge PETIT

Société Française d'Equipeement pour la Navigation Aérienne (SFENA)

BP 231

86101 CHATELLERAULT CEDEX FRANCE

RESUME

Après avoir présenté à la Conférence AGARD-CP-431 d'Athènes en Mai 1987 [1] le concept de bloc gyrométrique triaxial, les essais de faisabilité et la définition d'un gyromètre laser triaxial monobloc de petite dimension pour application missile, nous présentons aujourd'hui les performances gyrométriques obtenues sur deux maquettes.

1. INTRODUCTION

L'activité de SFENA dans le domaine de l'inertie à composants liés à base de gyrolasers va de la Navigation autonome pour avions d'armes aux blocs senseurs pour le guidage et le pilotage de missiles en passant par le système de référence inertiel pour le lanceur ARIANE 4.

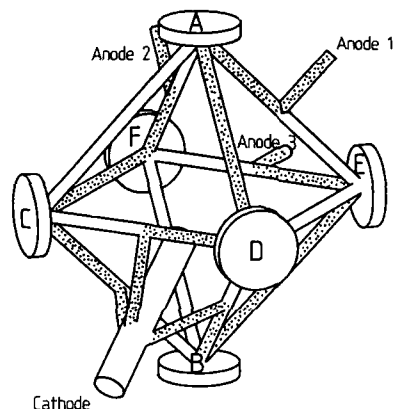
Concernant le guidage et le pilotage de missiles tactiques de moyenne portée (Diamètre < 250 mm), les travaux de SFENA se sont concrétisés en 1986 par la qualification d'un bloc senseur d'une masse de 3,5 Kg. Les gyromètres qui équipent ce type de bloc senseurs sont des gyrolasers monoaxes triangulaires de 12 cm de périmètre pour lesquels les travaux de développement ont débuté en 1981.

Plus tard, un besoin nouveau est apparu pour des missiles de plus petite taille (diamètre environ 160 mm) comme par exemple les missiles anti-missiles ou les torpilles lourdes. Le bloc senseur doit avoir un volume inférieur à 2 litres pour une masse de 2,5 Kg et les performances nécessaires à un missile moyenne portée.

SFENA répond à ce besoin grâce à un capteur gyrolaser triaxial qui pour une masse de 400 g offre des performances meilleures que celles qui peuvent être obtenues avec des capteurs mécaniques.

La suite de cet exposé présentera :

- 1 - LES PRINCIPES DE FONCTIONNEMENT ET LES AVANTAGES DU CONCEPT GYROLASER TRIAXIAL
- 2 - UNE DESCRIPTION TECHNOLOGIQUE DU CAPTEUR TRIAXIAL DEVELOPPE POUR LE BESOIN MISSILE DE PETITE TAILLE
- 3 - LES PERFORMANCES OBTENUES SUR LES PREMIERES MAQUETTES
- 4 - POUR FINIR, APRES UNE PRESENTATION SUCCINCTE DU CAPTEUR ACCELEROMETRIQUE MINIATURE DEVELOPPE PAR AILLEURS A SFENA, NOUS DONNERONS LES CARACTERISTIQUES D'UN BLOC SENSEUR CONSTRUIT A PARTIR DE CES CAPTEURS.

2. PRINCIPES DE FONCTIONNEMENT ET AVANTAGES DE LA SOLUTION TRIAXIALE

SCHEMA DE PRINCPE D'UN GYROLASER TRIAXIAL
Brevet N° 80-06298

Le concept de bloc gyrométrique triaxial a été breveté par SFENA en 1980.

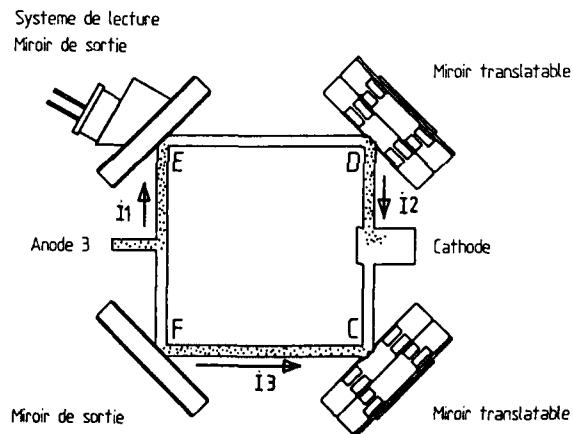
La principale originalité du concept consiste à imbriquer trois cavités laser carrées dans un bloc gyrométrique triaxial compact à 6 miroirs.

Les 6 miroirs placés au sommet d'un octaèdre régulier définissent trois cavités orthogonales entre elles et chaque miroir participe à deux cavités laser.

La seconde originalité du concept concerne les circuits de décharge.

En effet, sur les capteurs gyrolasers, la stabilité du biais dépend très fortement de la compensation des effets de décharge. Il faut que chacune des ondes contrarotatives voit des bras de décharge dans le même sens. C'est pour cela que les gyrolasers monoaxes fonctionnent avec deux bras de décharge symétriques. Transposer cette symétrie au laser triaxial aurait conduit à implanter 7 électrodes sur le bloc.

Or, la configuration adoptée dans l'octaèdre qui consiste comme on le voit sur la figure 1, en 3 décharges installées entre 1 cathode commune et 3 anodes ne nécessite que 4 électrodes et produit dans chaque cavité la symétrie souhaitée.



GYROLASER TRIAXIAL : REPRESENTATION D'UNE CAVITE

Ainsi, comme cela est montré ici, dans chaque cavité carrée, chaque onde voit un bras de décharge dans un sens et deux demi bras dans l'autre sens.

A part cela, chacun des gyromètres du bloc triaxial ressemble beaucoup à un gyrolaser monoaxe avec :

- même milieu amplificateur
- présence d'un miroir de sortie et d'un dispositif de mélange des faisceaux laser prélevés
- présence de deux miroirs translatables équipés de transducteurs piézo électriques pour accorder chaque cavité.

Les technologies acquises et qualifiées par ailleurs sont donc applicables.

En sus des avantages liés à la technologie gyrolaser qui sont entre autre les performances potentielles, l'insensibilité mécanique, la fiabilité et la plus grande dynamique de mesure possible, la solution triaxiale divise environ par deux les grandeurs suivantes : masse, encombrement, consommation électrique et prix.

La réduction de masse est due à la compacité du bloc optique et à la suppression de deux modules d'activation car le gyromètre triaxial peut être activé par un seul mouvement autour de sa bissectrice.

La diminution de consommation électrique est à imputer à la diminution du nombre de bras de décharge et de régulation (3 au lieu de 6).

La réduction sur le prix de revient est due à la diminution du nombre de pièces et à la simplification de certains travaux d'usinage et de montage.

L'amélioration de la fiabilité du trièdre gyrométrique est elle aussi due à la diminution du nombre de pièces.

Et, finalement, le concept de bloc gyrolaser triaxial supprime les dérives coniques induites par les mésalignements d'axes non stables.

Grâce au soutien des Services Officiels Français, SFENA a pu démontrer la faisabilité du concept de gyromètre triaxial en vérifiant et en validant ses principes sur des maquettes de 21 cm de périmètre.

Puis, toujours sur contrat des Services Officiels Français, SFENA a défini, réalisé et évalué deux maquettes de plus petite taille pour application missile.

Ce sont ces maquettes et leurs performances que nous présentons ci-après.

3. PRESENTATION TECHNOLOGIQUE ET FONCTIONNELLE

Le gyromètre est constitué d'un bloc laser triaxial de 14 cm de côté, pincé entre les deux roues du dispositif d'activation.

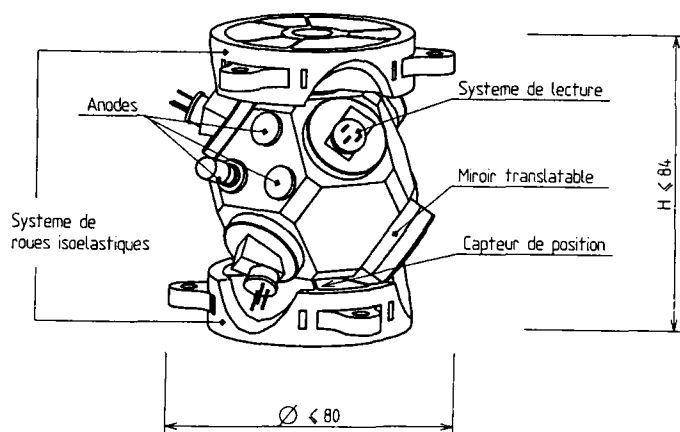
Les technologies utilisées sont éprouvées et qualifiées par SFENA dans des domaines de hautes performances (Avion d'arme) et d'environnement sévère (Ariane IV, Missile Anti navire).

On notera plus particulièrement l'excitation du mouvement d'activation par céramiques piézo-électriques, le capteur de position qui repère la position du laser par rapport au support et permet la soustraction du mouvement d'activation et la présence d'une seconde roue qui rend le dispositif d'activation isoélastique et qui supprime la résonance mécanique de basculement.

Ces technologies permettent un bon fonctionnement dans des conditions :

- d'accélération ou de choc jusqu'à 140 g
- de vibration jusqu'à 0,04 g²/Hz entre 20 et 2500 Hz
- de température entre - 40°C et + 100°C

Enfin, l'ensemble du gyromètre rentre dans un cylindre de 80 mm de diamètre et de 84 mm de haut et a une masse de 400 g.

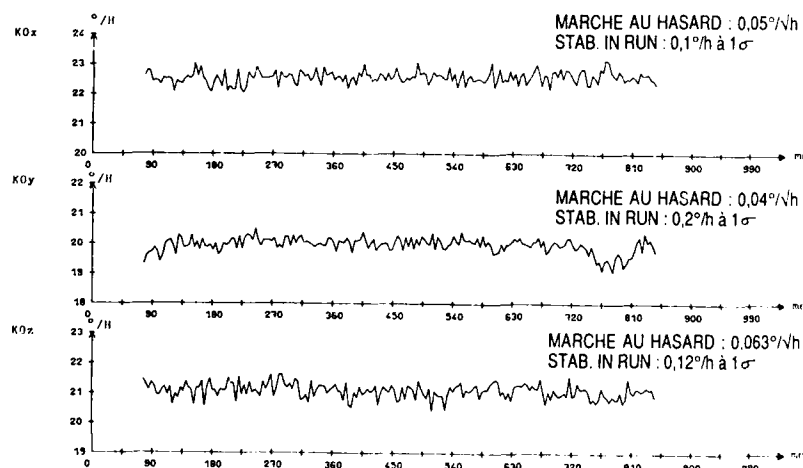


GYROLASER TRIAXIAL : VUE D'ENSEMBLE

4. RESULTATS GYROMETRIQUES

Les essais gyrométriques ont été conduits pour caractériser le biais et le facteur d'échelle de chaque voie des deux gyromètres réalisés.

La caractérisation du biais est faite à partir d'une série d'essais de longue durée (10 à 16 heures) comme celui qui est présenté figure suivante.



MESURE LONGUE DUREE DU BIAIS SUR LE GYROMETRE N°2 (Acquisitions de 240 secondes)

Sur chaque essai, sont relevés :

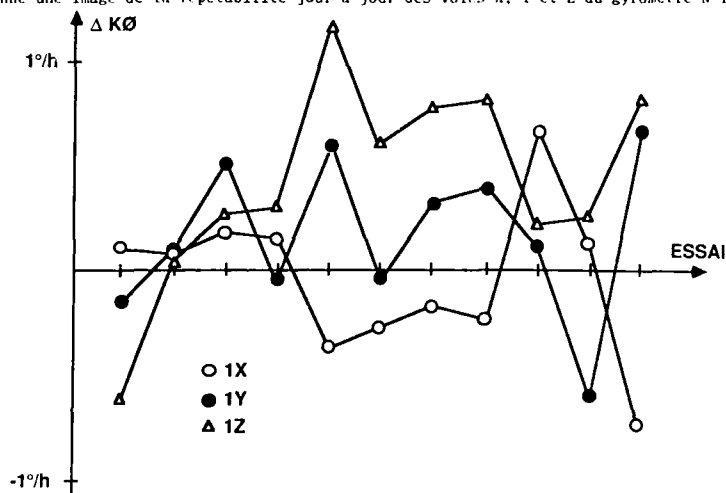
- la marche au hasard : ici $5 - 4$ et $6,3 \cdot 10^{-2} \cdot \sqrt{h}$
- le biais moyen ici $22,6 - 20$ et $21,1^\circ/h$
- la stabilité à moyen terme du biais (ou "in run stability") qui est ici de $0,1 - 0,2$ et $0,12^\circ/h$ à 10
- les variations du biais à la mise sous tension

A partir de ces quatre paramètres mesurés sur une grande série d'essais, nous avons pu déterminer pour chaque gyromètre :

- une statistique sur la marche au hasard
- la répétabilité jour à jour du biais (run to run stability)
- une statistique sur la stabilité in run
- une répétabilité à la mise sous tension.

4-1 Répétabilité du biais

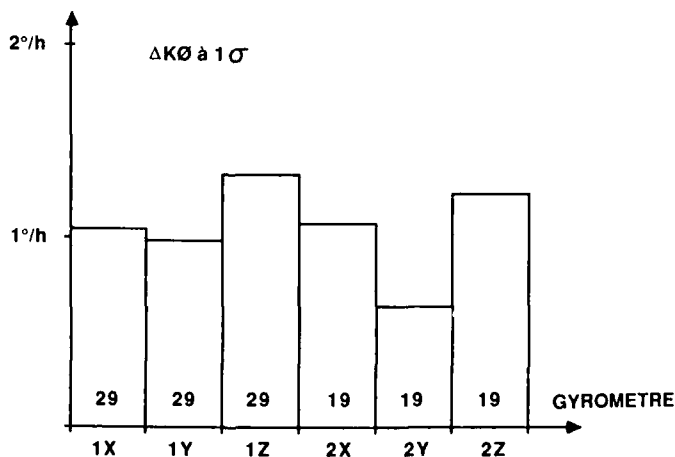
Sur la figure 5, ont été portés les biais moyens mesurés sur onze essais de longue durée consécutifs. Cela donne une image de la répétabilité jour à jour des voies X, Y et Z du gyromètre N°1.



REPÉTABILITE DU BIAIS MOYEN DU GYROMETRE N° 1

On peut constater que, sur ces onze essais, la répétabilité crête à crête du biais est inférieure à $2^\circ/h$ sur chacune des voies.

La répétabilité jour à jour à température ambiante du gyromètre laser triaxial 14 cm peut être bien appréhendée par la synthèse présentée sur l'histogramme de la figure 6.



REPÉTABILITE DES BIAIS MOYENS (RUN TO RUN)

Pour chaque voie de chaque gyromètre nous avons calculé la dispersion à 1σ sur le biais moyen à partir de toutes les mesures disponibles à savoir 29 essais sur le gyromètre N°1 et 19 essais sur le N°2. La répétabilité du biais moyen est de $1,3 \text{ } ^\circ/\text{h}$.

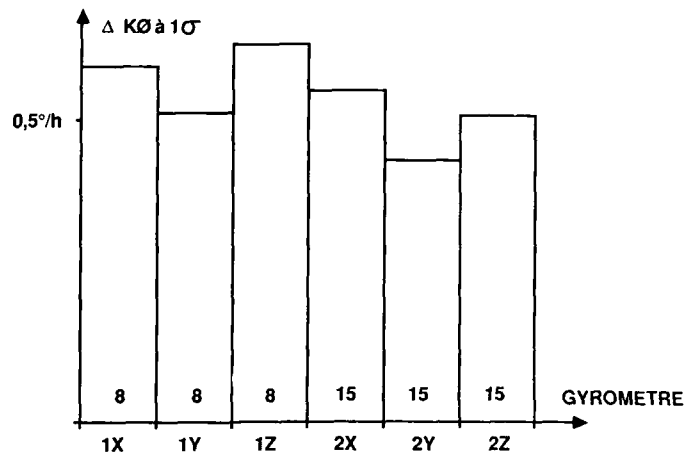
4-2 Marche au hasard

Le même type de traitement statistique a été effectué sur les valeurs de marche au hasard relevées. Sur 120 valeurs mesurées, 90 % sont inférieures à $0,07 \text{ } ^\circ/\sqrt{\text{h}}$.

4-3 Stabilité du biais ("IN RUN STABILITY")

Enfin, ce type de traitement a aussi été effectué sur la stabilité en fonctionnement du biais mesurée pendant certains essais de longue durée.

Ces stabilités prises à 1σ sont de l'ordre de $0,5 \text{ } ^\circ/\text{h}$ comme le montre cet histogramme.



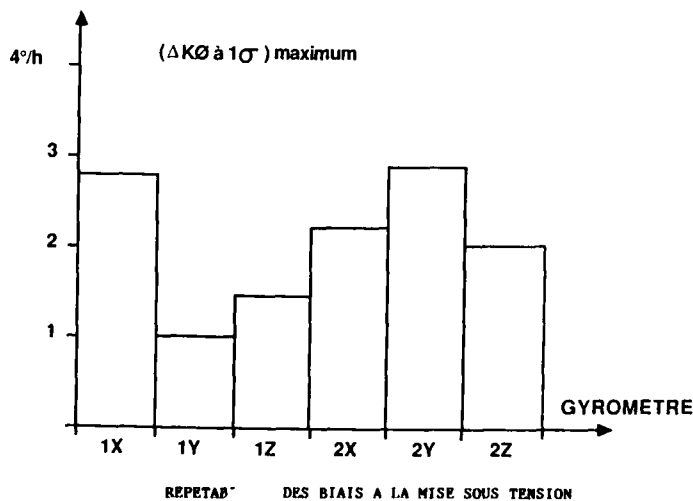
STABILITE DES BIAIS (IN RUN)

Ceci signifie que, pour 90 % des essais, la stabilité "in run" des gyromètres à température ambiante est inférieure à $0,5 \text{ } ^\circ/\text{h}$.

4-4 Répétabilité des biais à la mise sous tension

Pour évaluer la répétabilité du biais des gyromètres à la mise sous tension, nous avons procédé de la manière suivante. Pour chaque gyromètre, 30 essais de mise sous tension ont été compilés pour obtenir la courbe moyenne du Biais en fonction du temps et la dispersion à 1σ autour de cette courbe moyenne.

Nous représentons ici, pour chaque axe de chaque capteur la dispersion à 1σ maximale observée pendant la première heure de fonctionnement.

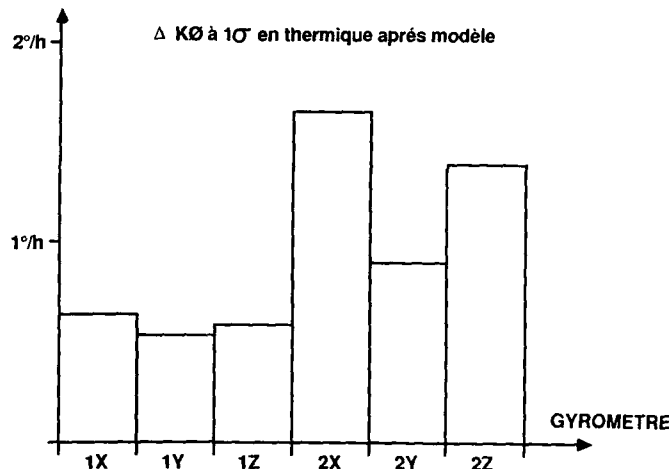


Le résultat obtenu est voisin de $3^{\circ}/h$, ce qui signifie que, pendant la phase de mise sous tension, les variations des biais peuvent être modélisées et que le résidu de modélisation est de $3^{\circ}/h$ à 10 .

4-5 Répétabilité thermique des biais

Pour évaluer la répétabilité thermique du biais, nous avons réalisé pour chaque gyromètre plusieurs mesures de biais longue durée à des températures stabilisées entre $-40^{\circ}C$ et $-70^{\circ}C$.

A partir des valeurs de biais moyens mesurées sur ces paliers de température, nous avons établi par régression un modèle thermique. Puis chaque mesure est comparée au modèle et c'est la valeur à 10 de l'écart par rapport au modèle que nous avons porté sur l'histogramme de la figure 9 pour chaque axe de chaque gyromètre triaxial.



REPETABILITE DES BIAIS EN THERMIQUE

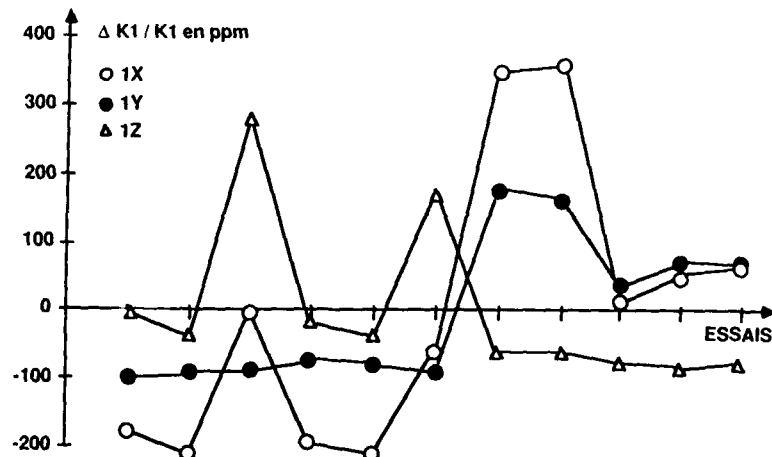
La valeur obtenue est de l'ordre de $1,5^{\circ}/h$ ce qui veut dire que les résidus après modélisation thermique sur les biais des triaxes sont dans 90 % des cas inférieurs à $1,5^{\circ}/h$.

4-6 Facteur d'échelle

La caractérisation du facteur d'échelle s'est faite en relevant des courbes complètes qui représentent les variations du facteurs d'échelle en fonction de la vitesse d'entrée appliquée au gyromètre. De chaque courbe on peut extraire un facteur d'échelle moyen ($K1$ moyen) et une erreur de modélisation σ qui représente l'écart type des écarts par rapport au modèle $K0 = K1 \times \Omega$.

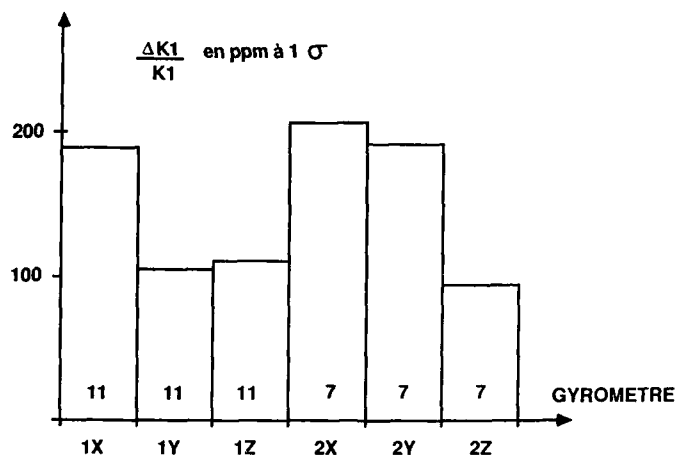
Le facteur d'échelle moyen est de $964 \text{ Hz}/^{\circ}/s$ soit $3,7''$ d'arc par pulse, l'erreur de modélisation est de l'ordre de 100 ppm.

Sur la figure 10 sont représentées en ppm les fluctuations des $K1$ moyens mesurés lors de 11 essais sur le gyromètre N°1. Tous les essais sont faits à température ambiante mais entre chaque essai le gyromètre a subi des séquences marche arrêt et des passages en température.



REPETABILITE DU FACTEUR D'ECHELLE DU GYROMETRE N°1 SUR 11 ESSAIS CONSECUTIFS

Cet histogramme montre une statistique sur tous les K1 moyens relevés sur les deux gyromètres.



REPETABILITE DES FACTEURS D'ECHELLE

Il apparaît que la répétabilité jour à jour prise à la du facteur d'échelle moyen est de l'ordre de 100 à 200 ppm.

4-7 Récapitulatif des performances

Ce dernier tableau récapitule les valeurs que nous venons de mettre sur chaque type de performance au vu des résultats des deux maquettes.

PERFORMANCES		RELEVÉES	OBJECTIVES
MARCHE AU HASARD SUR LE BIAIS	°/√h	<0,07	0,05 1 à 3°/h
STABILITE A MOYEN TERME DU BIAIS	°/h	≈ 0,5	
REPETABILITE JOUR A JOUR DU BIAIS	°/h	≈ 1,3	
REPETABILITE DU BIAIS EN THERMIQUE	°/h	≈ 1,3	
REPETABILITE DU BIAIS A LA MST	°/h	≈ 2,7	
REPETABILITE J.A.J. DU FACTEUR D'ECHELLE	ppm	200	300
NON LINEARITE DU FACTEUR D'ECHELLE	ppm	300	
CARACTERISTIQUES PHYSIQUES :			
	masse encombrement	450 g < ø80 mm x h84 mm	400 g < ø80 mm x h84 mm

Le capteur gyrolaser triaxial miniature peut donc être considéré aujourd'hui comme étant de la classe des 4 à 5°/h.

Mais, pendant ces essais d'évaluation, certains phénomènes limitants ont été identifiés et la prochaine définition y remédiera.

C'est pourquoi, nous pensons que l'objectif de performance globale de 1°/h sera atteint par ce capteur dans un avenir proche et pour une masse de 400 g.

4. CONCLUSION

Parallèlement à ces travaux sur le triaxe, SFENA développe actuellement un capteur accélérométrique miniature original [2]. La masse pendulaire ainsi que les lames de rappel sont réalisées par micro usinage dans une plaque de quartz de quelques mm de côté.

Cette technologie permet aujourd'hui en version asservie d'obtenir des performances globales sur le domaine d'environnement meilleures que 0.01 G pour un encombrement de 4 cm³ et pour un prix rendu compétitif par une fabrication collective.

Grâce à ces deux capteurs, SFENA peut proposer un bloc senseur inertielle pour missile de petite taille.

Suivant les spécifications demandées, les caractéristiques physiques d'un tel bloc senseur pourraient être :

Volume 1,3 à 1,5 litre
plus faible dimension 90 mm
masse approximativement 2 Kg
coût approximatif 35000\$ avec traitements et compensations, suivant spécifications particulières et quantités.

REFERENCE

- [1] GYROMETRE LASER TRIAXIAL DE PETITE DIMENSION
S. PETIT - M. PERRET (SFENA)
CONF. AGARD - CP - 431 MAI 87 ATHENES
- [2] ACCELEROMETRE A QUARTZ MINIATURE (AQM)
A. BOURA - O. ANJAY - J.L. BOST (SFENA)
46 Sym. AGARD GCP MAI 88 GELLO (NORVEGE)

**NEW TEST TECHNIQUES TO EVALUATE NEAR FIELD EFFECTS FOR
SUPERSONIC STORE CARRIAGE AND SEPARATION**

by

Wallace C. Sawyer
Assistant Chief, Advanced Vehicles Division
and

Robert L. Stallings, Jr., Floyd J. Wilcox, Jr.
A. B. Blair, Jr., William J. Monta
Aerospace Engineers, Supersonic/Hypersonic Aerodynamics Branch
High-Speed Aerodynamics Division
and

Elizabeth B. Plentovich
Aerospace Engineer
NTF Operations Branch, Transonic Aerodynamic Division

NASA Langley Research Center
Hampton, VA 23665-5225
USA

SUMMARY

Store separation and store carriage drag studies have been conducted at the NASA Langley Research Center. A primary purpose of the studies is to develop new experimental methods to evaluate near field effects of store separation and levels of store carriage drag associated with a variety of carriage techniques for different store shapes and arrangements. Flow field measurements consisting of surface pressure distributions and vapor screen photographs are used to analyze the variations of the store separation characteristics with cavity geometry. Store carriage drag measurements representative of tangent, semi-submerged, and internal carriage installations are presented and discussed. Results are included from both fully metric models and models with only metric segments (metric pallets) and the relative merits of the two are discussed. Carriage drag measurements for store installations on an aircraft parent body are compared both with prediction methods and with installations on a generic parent body.

NOMENCLATURE

A	=	model reference area $\pi d^2/4$
C_m	=	pitching-moment coefficient, pitching moment/ $q_\infty A Z$
C_N	=	normal force coefficient, normal force/ $q_\infty A$
C_p	=	pressure coefficient, $(p-p_\infty)/q_\infty$
d	=	store-model diameter
D	=	cavity depth
Z	=	store-model length
L	=	cavity length
M	=	free-stream Mach number
P	=	local measured static pressure
P_∞	=	free-stream static pressure
q_∞	=	free-stream dynamic pressure
s	=	wing span
S_C	=	surface length on cavity ceiling relative to cavity front face
S_{FF}	=	surface length on cavity front-face relative to flat plate surface
S_{RF}	=	surface length on cavity rear-face relative to cavity ceiling
t	=	time relative to store ejection
w	=	cavity width
x,y	=	store model coordinates relative to nose tip
Z	=	perpendicular distance from splitter plate surface
X	=	longitudinal surface distance
Y	=	lateral surface distance

- α = angle of attack relative to flat plate surface
 δ_e = wing control deflection (negative denotes leading-edge down)
 C_A = axial-force coefficient, $\frac{\text{Axial force}}{qA}$
 ΔC_D = increment in store drag coefficient
 C_D = store drag coefficient, $\frac{\text{Drag force}}{qA}$

INTRODUCTION

A primary purpose of the store carriage and separation studies conducted at NASA Langley Research Center is to develop new experimental methods to evaluate near field effects of store separation and levels of store carriage drag associated with a variety of carriage techniques for different store shapes and arrangements.

In order to realize full advantage of the aircraft supersonic flight speeds, it is desirable to have the capability of releasing the stores at supersonic speeds. Although there is considerable information available in the literature concerning acoustic measurements in cavities and bomb bays, there is very little information available concerning the aerodynamic characteristics of stores during separation from conformal and internal carriage configurations at supersonic speeds. Therefore, a series of wind tunnel test were initiated to determine the near-field separation characteristics of a store configuration from cavities of various shapes and depths.

Approach

• Generic parent body

- Facilitates extraction of carriage drag increment
- Simplifies methodology development
- Readily accommodates metric pallets or cavities
- More general application

• Variety of store geometries

Figure 1.- Experimental carriage and separation studies.

The approach shown in figure 1 for obtaining the information is primarily experimental since analytical or CFD methods are difficult to apply to the complex, three dimensional flow fields resulting from interactions between the store flow field and by parent body surface. For most of the fundamental studies, the complexity of the parent body flow field is simplified by using a generic parent body. For tangent store installations the generic parent body is simply a flat surface and for semi-submerged or internal store installations it is a flat surface with a cavity to accommodate the store. A flat-plate type generic parent body readily accommodates metric pallets or metric cavities which greatly improve the data resolution of the carriage drag measurements. This improved data accuracy is particularly important for low drag carriage shapes, for empty cavity drag corresponding to semi-submerged carriage installations, or for measuring interference drag levels for various store groupings.

SUPERSONIC STORE SEPARATION STUDIES

The initial store separation studies by NASA Langley Research Center were conducted using an existing vertical flow splitter plate to simulate the parent body and an existing 1/7-scale wing control store model. The store model was attached to the tunnel model support system and could therefore be remotely positioned relative to the splitter plate. These exploratory tests (ref. 1) were conducted primarily to investigate the effects of the store/plate interactions on the store aerodynamic characteristics when the store was in close proximity of the plate surface.

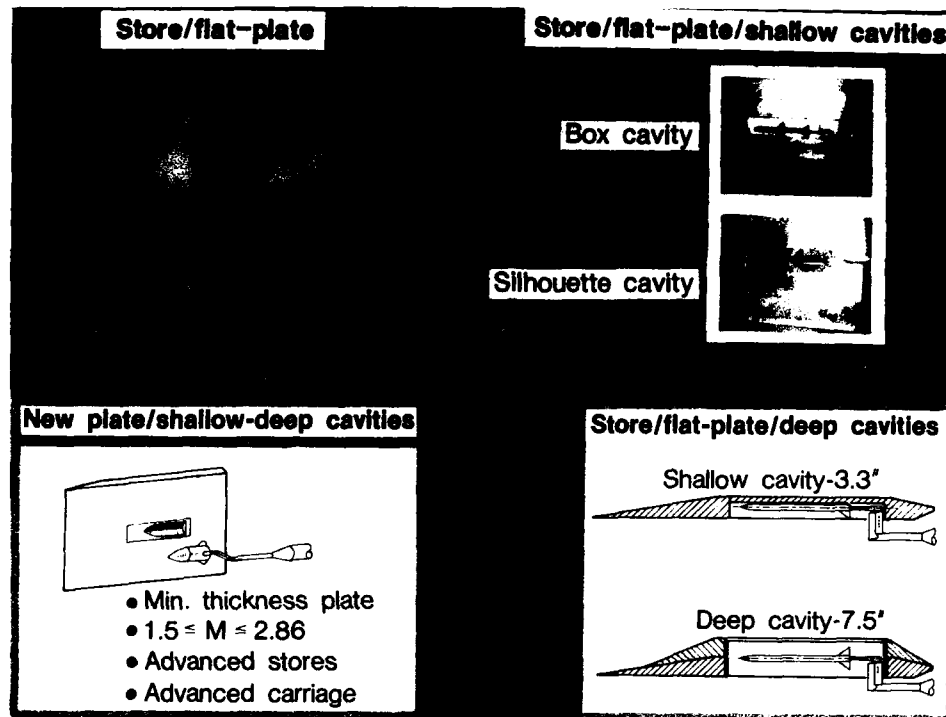


Figure 2(a).-- Development of supersonic store separation studies.

As shown in figure 2(a), subsequent to the flat plate tests, the plate surface was modified to accommodate cavities representative to internal or semi-submerged carriage configurations. The cavity configurations consisted of a box cavity and a silhouette cavity (figure 2(b)). The cutout in the plate for the silhouette cavity matched the

STORE SEPARATION STUDIES

Cavity configurations

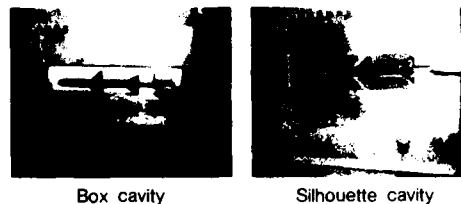


Figure 2(b).-- Cavity configuration.

silhouette of the store plus a nominal clearance gap of 20 percent of the store diameter. The plate was further modified to increase the cavity depth from approximately 3 to 6 store diameters. Tests results from these cavity configurations showed that cavity shape and depth had a large effect on the store separation aerodynamics and sample results from ref. 2 will be shown in the next figure.

The initial studies were expanded with the construction of a new splitter plate. The new minimum thickness plate was designed to reduce test section blockage to permit testing at Mach numbers down to 1.5. The blockage from the plate used in the previous studies limited testing to $M_{\infty} > 2.36$. The new plate accommodated either tangent or semi-submerged carriage configurations for non-conventional store shapes. Because of the minimum thickness design criterion, the flat plate surface would be configured to represent additional parent body surface shapes to simulate a more realistic parent body flow field environment.

STORE SEPARATION STUDIES

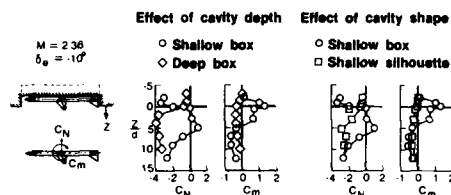


Figure 3.- Effect of cavity depth and shape.

Presented in figure 3 are force balance measurements showing typical effects of cavity geometry on store separation characteristics. The effect of cavity depth is shown on the left-hand side of the figure, and the effect of cavity shape is shown on the right-hand side. Normal force coefficients and pitching moment coefficients are presented as a function of store separation position relative to the flat plate surface for $M = 2.36$ and a wing control deflection of -10° . For the case of the shallow box cavity, shown as the circular symbols, the store experiences large positive pitching moments as it leaves the cavity. Also, within this region the store normal force is slightly positive even though the wing has a -10° control deflection. This combination of large positive pitching moments and positive normal force could result in undesirable separation conditions. For the case of the deep box cavity, the store pitching moment remains slightly negative during separation and the normal force coefficient reaches a negative value resulting from the negative control deflection. This combination of pitching moment and normal force should result in favorable separation characteristics. The large differences in store separation characteristics for the shallow and deep box cavities results from a change in the cavity flow field from "closed" cavity flow to "open" cavity flow which will be discussed in more detail.

The effect of changing the cavity shape from a shallow box to a shallow silhouette is shown on the right-hand side of the figure. The shallow box cavity data are again shown as the circular symbols. The data from the silhouette cavity are similar to the results shown for the deep box cavity and should result in favorable store separation conditions. These data clearly show that cavity shape and depth can have large effects on store separation characteristics.

SUPERSONIC STORE CARRIAGE DRAG STUDIES

Store carriage drag increments for specific aircraft configurations has historically been determined by using totally metric models. These drag increments are determined by subtracting the drag force measurements of the clean aircraft model from the drag force measurements of the aircraft model with stores attached. Since the force balance must be sized to accommodate the overall model forces, its accuracy may not be sufficient to provide the desired data resolution for measuring the drag of stores attached to the airplane in a low drag carriage configuration or to determine the various interference factors between multiple stores or between aircraft and stores. The complex flow field of a specific aircraft parent body also makes it difficult to analyze these interference factors or to generalize the results for applications to other configurations.

In order to improve the data resolution of carriage drag measurements and to provide more generalized data, two generic parent bodies with only segments of the bodies being metric were built and tested (figure 4). One of the bodies, referred to as the internal carriage model, contained a metric cavity and was designed to accommodate internal carriage installations (ref. 3).

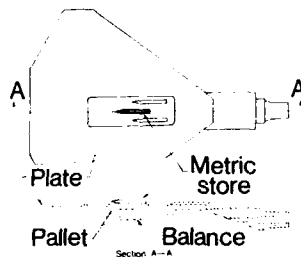
The other body, defined as the external carriage model, contained a metric pallet and was designed for testing tangent and semi-submerged installations. This model was part of a cooperative NASA/Industry carriage drag program. For each model, the metric segment was attached to an existing six-component force and moment balance and the balance load ratio was selected based on the anticipated forces on the metric segment rather than the overall model load. Results obtained from these models will be shown and discussed later.

Aircraft parent body

Total metric

Generic parent bodies**Internal carriage****External carriage
NASA/Industry co-op**

- Metric pallets
- Conventional 6-component balance
- Flat surfaces

Current tests

- Metric pallet, generic parent body
- New dedicated drag balance
- Cavity drag
- Store on store interference
- Advanced carriage

Figure 4.- Development of supersonic store carriage studies.

Current test on a newly constructed generic parent body provides even better data resolution than was obtainable with the previously tested generic parent bodies. This model also has a metric pallet which is attached to a new one-component drag balance that is not only much more sensitive than the existing six-component balance but it also eliminates problems related to pallet deflections inherent with existing six-component cantilevered force balances. The improved resolution of this new balance permitted accurate measurements of empty low drag cavity configurations designed to accommodate semi-submerged blended store configurations (ref. 4 and 5). These dedicated generic cavities allowed for the development of numerous diagnostic

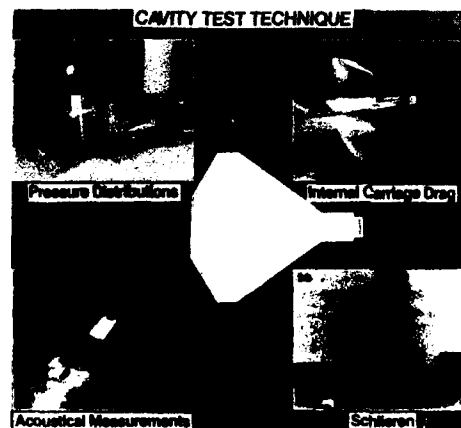


Figure 5.- Cavity diagnostic studies.

studies. As shown in figure 5, the cavity can be instrumented to acquire pressure distributions, drag and acoustical measurements, and schlieren photography.

Figure 6 shows some typical results obtained from the internal carriage drag model, including results for both empty cavities and cavities with stores. The empty

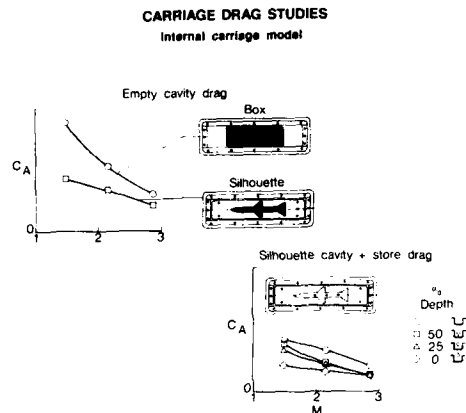


Figure 6.- Drag studies for internal carriage.

cavity results show that the box cavity throughout the test range of Mach number has greater drag than a silhouette cavity of equal length and equal depth. The cavity and store results are for the store model at various positions in a silhouette cavity ranging from the edge of the cavity to 50 percent of its depth. Results from the empty silhouette cavity (circular symbols) are also shown for comparison. These data show that the cavity and store drag levels are less than the empty cavity and that as the store is positioned from inside the cavity toward the edge of the cavity, the cavity and store drag level decrease.

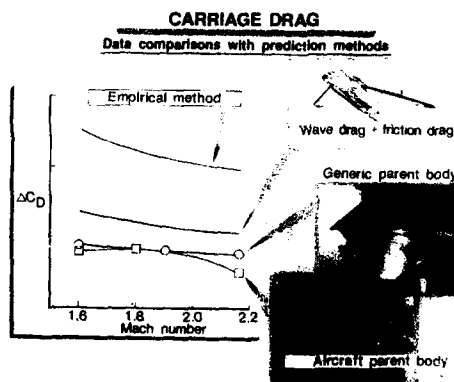


Figure 7.- Drag studies for external carriage.

Figure 7 shows comparisons of store drag measurements obtained using the external carriage generic parent body with several prediction methods and with measured values for the same store mounted on a totally metric model of an aircraft parent body. The aircraft parent body results were obtained as part of a cooperative government/industry program to determine drag levels of conventional stores attached to aircraft in non-conventional carriage configurations. The store drag measurements for the two parent bodies are in good agreement, the disagreement shown being less than the accuracy of the totally metric model. This agreement suggests that carriage drag measurements at supersonic speeds obtained using generic parent bodies can be used for defining carriage drag levels for tangent or semi-submerged type carriage installations on supersonic cruise-type aircraft configurations.

Both the empirical method (refs. 6 and 7) and the wave drag prediction method (ref. 8) overpredict the experimental data with the wave drag prediction providing the best agreement.

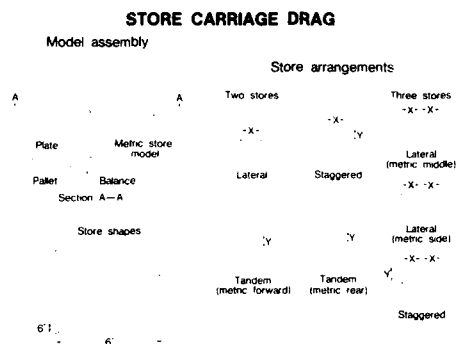


Figure 8.- Store drag interference study.

Shown in figure 8 is information related to the carriage drag program using the newly constructed generic parent body and a new high-resolution one-component drag balance. The generic stores investigated have nose and afterbody shapes consisting of ogives, hemispheres and flat-faces (ref. 5). Various two- and three-store arrangements were tested for a range of lateral and longitudinal spacing between the stores as illustrated. The position of the metric store within the array of stores was varied to determine the individual drag levels of a store in the center, side, forward, and aft positions. Cavity drag levels of a family of empty cavity configurations representative of semi-submerged shapes for non-conventional stores were also investigated.

CAVITY PRESSURE TESTS AND FLOW FIELD STUDIES

Shown in figure 9 are cavity pressure distributions that were obtained by instrumenting with pressure orifices the box cavity shown in figure 2. Several inserts

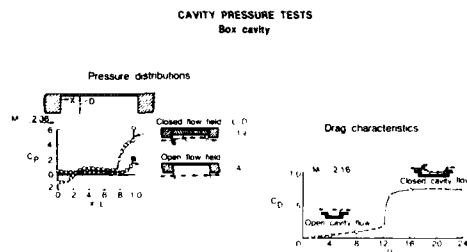


Figure 9.- Open and closed cavity pressure tests.

of various thicknesses were also instrumented with pressure orifices and placed inside the cavity to vary the cavity depth. The results shown in this figure are for cavity length-to-depth ratios (L/D) of 19 and 4. For the shallow cavity ($L/D = 19$), the pressure distributions are indicative of closed cavity flow. The flow field for this case, as illustrated in the sketch, expands over the cavity leading edge, attaches to the cavity ceiling and exits from the cavity ahead of the rear face. The pressure distributions resulting from these large turning angles of the local flow field contain several large pressure gradients as shown by the circular symbols. For the case of the deep cavity ($L/D = 4$), the flow simply bridges the cavity and impinges on the outer edge of the rear face. This type cavity flow field is generally referred to as open cavity flow and results in a relatively uniform pressure distribution over the cavity ceiling as shown by the square symbols.

The identification of the type of cavity flow field from the cavity pressure distributions offers an explanation for the effect of cavity depth on the aerodynamic characteristics of a store separating from a box cavity as shown in figure 3 concerning the effects of cavity depth and shape on store separation characteristics. For the case of a shallow cavity with a closed flow field, the nose of the store is located in an upwash region and its tail is located in a downwash region and therefore large pitching moments as were measured would be expected to occur. For the case of the deep cavity with the open flow field, the local flow had very small turning angles and would therefore not be expected to have any significant adverse effects on the store separation characteristics.

Also shown in figure 9 is the effect of cavity length-to-depth ratio on cavity drag coefficient. The drag coefficients were determined by integrating pressure measurements over the front and rear faces of cavities of constant depth and varying lengths. At $L/D = 12$ there is an abrupt increase in C_D with increasing L/D resulting from the cavity flow field going through a transition from open cavity flow to closed cavity flow. The larger drag coefficients for the closed cavity flow result from a decrease in pressure on the cavity front face due to the flow expanding into the cavity and an increase in pressure on the cavity rear face associated with the turning of the flow as it exits from the cavity. Through the test range of Mach number from 1.5 to 2.86, the critical value of L/D at which the flow switched from one type to the other remained approximately constant.

Figure 10(a) and (b) shows vapor screen photographs of open and closed cavity flow fields over a box cavity. The vapor screens depicted are in a plane perpendicular to

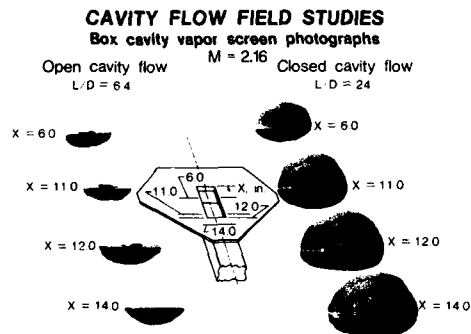


Figure 10(a).- Cavity flow field studies at $M = 2.16$.

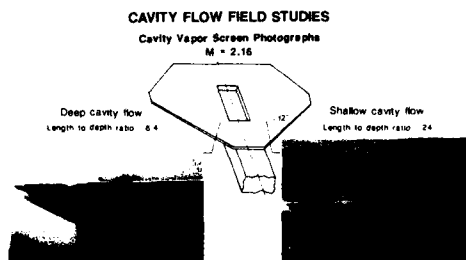


Figure 10(b).- Vapor screen photographs at cavity near face, $M = 2.16$.

the flat plate surface and were taken with a camera positioned above and behind the cavity. Photographs were taken of the vapor screen at several longitudinal positions downstream of the cavity leading edge. The overall length of the cavity was 12 inches and the cavity length-to-depth ratio (L/D) was varied by varying cavity depth. For the $L/D = 24$ cavity the cavity flow field is of the closed cavity type and the vapor screen photographs show a very complex flow field including the formation of a pair of well-defined vortices on the edges of the cavity. These vortices exit from the cavity at $X = 12$ inches and continue downstream. For $L/D = 6.4$ cavity, an open cavity flow field exists and the vapor screen photographs indicate a less complex flow field than was apparent for closed cavity flow. These vapor screen photographs also clearly demonstrate the complexity and three-dimensionality of the closed cavity flow field and suggest that in order for it to be described theoretically, three-dimensional computational procedures will be required.

SUMMARY

In summary, the results presented in this review show that the generic parent body approach of estimating the aerodynamic characteristics for store carriage and separation are in good agreement with more conventional methods. Particular results from the series of experimental tests are as follows:

1. From the store separation studies, store force and moment measurements have shown favorable separation characteristics for deep box cavities and for both deep and shallow silhouette cavities. Unfavorable separation characteristics were obtained for the shallow box cavities.

2. From the carriage drag studies, store carriage drag measurements for tangent installations on generic and specific aircraft parent bodies were in good agreement. The experimental drag measurements were consistently less than predictions. Cavity drag measurements showed that cavity drag levels are sensitive to both cavity shape and cavity depth.

REFERENCES

1. Stallings, Robert L., Jr.: Aerodynamic Characteristics of a Sparrow III Missile Model in the Flow Field of a Generalized Parent Body at Mach 2.86. NASA TM-85713, 1984.
2. Stallings, Robert L., Jr.: Store Separation From Cavities at Supersonic Flight Speeds. J. Spacecraft and Rockets, vol. 20, no. 2, pp. 129-132, March-April 1983.
3. Blair, A. B., Jr.; and Stallings, Robert L., Jr.: Supersonic Wind-Tunnel Investigation of the Axial Force Characteristics of External and Internal Store-Carriage Configurations of a Simulated Generic Parent Airplane. NASA TM-86343, 1985.
4. Blair, A. B., Jr.; and Stallings, Robert L., Jr.: Supersonic Axial-Force Characteristics of a Rectangular-Box Cavity with Various Length-to-Depth Ratios. NASA TM-87659, 1986.
5. Wilcox, Floyd, J., Jr.: Drag Measurements of Blunt Stores Tangentially Mounted on a Flat Plate at Supersonic Speeds. NASA TP-2742, 1987.
6. USAF Stability and Control Datcom. Contracts AF33(616)-6460 and F33615-76-C-3061, McDonald Douglas Corporation, October 1960. Rev. April 1978.
7. Hoerner, Sigward F.: Fluid-Dynamic Drag. Hoerner Fluid Dynamics (Brick Town, New Jersey), 1965.
8. Craidon, Charlotte B.: User's Guide for a Computer Program for Calculating the Zero-Left Wave Drag of Complex Aircraft Configurations. NASA TM-85670, 1983.

REMOTE CONTROL MISSILE MODEL TEST

by

Jerry M. Allen

David S. Shaw

Aerospace Engineers, Supersonic/Hypersonic Aerodynamics Branch
and

Wallace C. Sawyer

Assistant Chief, Advanced Vehicles Division

NASA, Langley Research Center

Hampton, VA 23665-5225

USA

SUMMARY

An extremely large, systematic, axisymmetric-body/tail-fin data base has been gathered through tests of an innovative missile model design which is described herein. These data were originally obtained for incorporation into a missile aerodynamics code based on engineering methods (Program MISSILE3), but can also be used as diagnostic test cases for developing computational methods because of the individual-fin data included in the data base. Detailed analysis of four sample cases from these data are presented to illustrate interesting individual-fin force and moment trends. These samples quantitatively show how bow shock, fin orientation, fin deflection, and body vortices can produce strong, unusual, and computationally challenging effects on individual fin loads. Comparisons between these data and calculations from the SWINT Euler code are also presented.

NOMENCLATURE

C_{HM}	- fin hinge moment coefficient
C_N	- normal force coefficient on complete configuration
C_{NF}	- fin normal force coefficient
L	- body length
M_∞	- free stream Mach number
x	- axial coordinate measured from body nose
α	- model angle of attack
δ	- fin deflection angle
ϕ	- model roll angle measured from windward meridian
$\frac{\partial C_{NF}}{\partial \delta}$	- fin control effectiveness parameter

1. INTRODUCTION

In the early 1980's, NASA Langley entered into a cooperative agreement with the three service branches of the United States Department of Defense, and with industry (Nielsen Engineering and Research, Inc.) to develop a systematic, high quality, body/tail-fin force and moment data base to be used in high-angle-of-attack missile aerodynamics computer programs based on engineering methods - specifically, Program MISSILE3 (Reference 1). The objective of this cooperative program is shown in Figure 1. Since an extremely large body of data was needed for this task, a unique model was designed and constructed to allow this quantity of data to be obtained in a reasonable time frame. The model has been named the Langley "Remote Control Missile Model." The sketch in this figure illustrates the envelope of fin data that was needed for inclusion into the MISSILE3 code compared to that which existed prior to this program. The data set defined by this envelope has been termed the "Triservice Missile Data Base."

The contributions of each of these participants in this cooperative agreement are shown in Figure 2. All three branches of the U.S. military services - Army, Navy, and Air Force - participated in the funding of this project. Thus, the origin of the name "Triservice Missile Data Base." Nielsen Engineering and Research, Inc. designed the fins for this project and organized the data in the form of a data base which was incorporated into a high-angle-of-attack engineering prediction method which they had developed. Preliminary versions of the code that had been developed before the acquisition of this extended data base were called Programs MISSILE1, MISSILE2, and MISSILE2A (References 2 through 4, respectively). The final version of the code containing the Triservice Missile Data Base is called Program MISSILE3. NASA Langley modified an existing remote control missile model to accept the fin balances necessary for this project, and designed and fabricated the three-component fin balances. NASA also provided the wind tunnel facilities and testing time, and conducted the wind tunnel tests.

Objectives: To develop a systematic, high quality, body/tail-fin force and moment data base for use in missile aerodynamic computer codes based on engineering methods

Approach: Use innovative model design techniques to allow large quantities of experimental data to be obtained

Need: Individual tail-fin loads data to cover an extended aspect-ratio/Mach-number envelope

Bonus: Individual fin data can be used as diagnostic test cases for developing computational methods

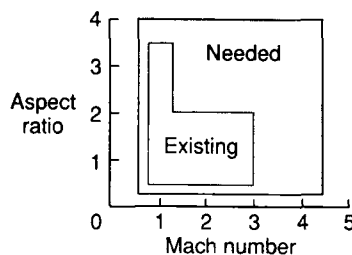


Figure 1.- Introduction.

- U.S. Department of Defense
 - Navy, Army, and Air Force involved
 - Provided funds for model
 - Provided funds for data analysis
- Industry
 - Nielsen Engineering and Research, Inc.
 - Designed fins
 - Organized data into data base
 - Incorporated data base into Program MISSILE 3
- NASA
 - Constructed fin balances
 - Constructed model
 - Provided wind tunnel testing time
 - Conducted wind tunnel tests

Figure 2.- Participants in triservice missile program.

The outline of this paper is shown in Figure 3. A description of the Remote Control Missile Model will be presented first. This will be followed by a review of the wind tunnel tests that were conducted to gather the data. Selected examples from these data will then be analyzed to highlight some of the interesting data trends that have been discovered, and which would not have been possible to observe without the unique features of this model. The data analyzed will be in the following categories: (1) the effects of the body bow-shock wave interacting with the fins; (2) fin control effectiveness over the range of model roll orientations; (3) fin-on-fin interference effects for a deflected fin; and (4) body vortex interference effects on fins. This presentation will conclude with some comparisons between these data and computational results from an Euler code specialized for use in analyzing supersonic missiles.

- Description of remote control missile model
- Review of Triservice tests
- Analysis of selected data
 - Bow-shock/fin interaction
 - Fin control effectiveness
 - Fin deflection interference
 - Body-vortex/fin interaction
- Comparison between data and Euler code computations

Figure 3.- Outline of presentation.

2. MODEL DESCRIPTION

A schematic of the missile model body used in this project is shown in the top part of Figure 4. As can be seen, the body was assembled from six separate sections, with each section serving a separate and unique function. The nose section contained an internal roll mechanism, which rotated the entire model about the main balance, whose orientation remained fixed. This internal roll capability served two purposes: (1) It simplified the main balance data reduction process since the balance always remained upright, and (2) It allowed this model to be tested in wind tunnels which do not have model roll capability. The motor section contained the four drive motors for the remote control fins. The balance section housed the main balance which measured the overall loads on the model. Along this section were located longitudinal slots for mounting fins. The wiring section contained harnesses for connecting the electrical wiring for the motors and fin balances, and for routing these wires down the inside of the sting. The control section contained the mounting arrangements for the remotely deflectable fins, which were operated through drive shafts from the motor section. The afterbody was the only section which did not contain hardware necessary for the operation of this model. It should be emphasized that, with the exception of the nose and afterbody sections, each section of this model was interchangeable so that the remote control fins could be mounted at various locations along the body length. This is illustrated in the lower part of this figure in which typical canard-control, tail-control, and wing-control configurations are pictured.

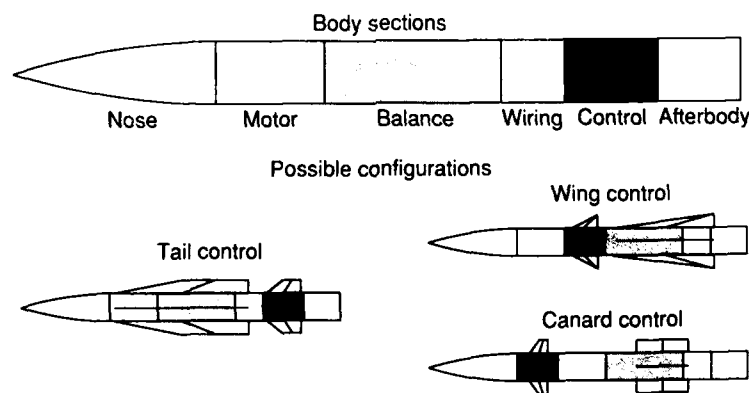


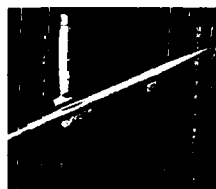
Figure 4.- Remote-control missile model.

Only body/tail-fin data were needed for this project. Therefore, the full capabilities of this model for providing interchangeable fin locations were not used. The photograph in the top part of Figure 5 shows a typical configuration for this project. The key features of this model were the remote-control fins, the internal roll capability, interchangeable fin locations, and the ability to measure individual fin loads. Once a set of fins has been installed on this model, all attitude parameters (angle of attack, roll angle, and fin deflection angle) could be changed during testing without interrupting the wind tunnel operation. Thus, this Triservice configuration offered the potential of obtaining the extremely large quantity of body/tail-fin data required for this project.

As shown at the bottom of this figure, nine sets of cruciform fins were designed and constructed for this project. The fin planforms were selected to have a wide and systematic variation of aspect ratio and taper ratio. As seen in the sketches, the fins varied in aspect ratio from 1/4 to 4, and in taper ratio from 0 to 1. All fins had a semi-span equal to the body radius. A two-digit labeling system, as shown in the figure, was used for fin identification and will be used in this paper.

The five fins shown on the right in this figure are movable and were designed to be mounted on the control section of the body. The four fins on the left were designed to mount in the slots in the balance section of the body, as previously described, and thus were not movable. They had their own fin balances, however.

All of the Triservice missile tests were conducted with single sets of cruciform fins located as tail fins near the base of the model as illustrated by the model photograph in this figure.



Key features

- Internal roll capability
- Multiple fin mounting locations
- Remote control fin deflections
- Individual fin loads

Fin planforms

Aspect ratio					Taper ratio
0.25	0.50	1.0	2.0	4.0	
	31		51		0
12	32	42	52	62	0.5
	33		53		1.0

Figure 5.- Triservice missile configuration.

3. DESCRIPTION OF TESTS

Figure 6 shows a summary of the key features of the Triservice missile tests. The low Mach number tests (Mach numbers of 2.0 or less) were conducted in the NASA Ames 6 X 6 Wind Tunnel, whereas the high Mach number tests (Mach numbers of 2.5 or greater) were conducted in the NASA Langley Unitary Plan Wind Tunnel (test section number 2). Because of the volume of data gathered, these tests required multiple tunnel entries over a 5-year time period ending in 1985.

The model angle of attack of these tests ranged from about -5 to 45 degrees in 5-degree increments, the roll angle ranged through 180 degrees in 10-degree increments and the fin deflection angle of the control fins ranged from -40 to +40 degrees in 10-degree increments. Fins were always mounted in a cruciform arrangement. For the fin deflection tests all four fins were present, but only one fin was deflected. Fin loads were measured for all four fins, however.

Over 60,000 individual data points were recorded in this project, with each point containing 25 measured quantities. This resulted in the incredible total of about 1.5 million quantities measured in this program. All data were recorded on magnetic tape. The data base needed for Program MISSILE3 has been compiled and has been incorporated into the code. References 5 and 6 contain analyses of missile configurations using the MISSILE3 code. References 7 through 10 contain aerodynamic analyses using parts of the Triservice data base. Publication of the complete tabulated data is currently underway at NASA Langley.

Tunnels: Ames 6 x 6
 Langley UPWT
 Mach numbers: 0.6 to 2.0 (Ames)
 2.5 to 4.5 (Langley)
 Angle of attack: -5° to 45°
 Roll angle: 0° to 180°
 Fin deflection: -40° to $+40^{\circ}$
 Features: 60 000 data points
 25 measured quantities per point
 Status: Tests have been completed
 Data analysis is underway
 Data base incorporated into Program MISSILE 3
 Complete tabulated data being published

Figure 6.- Triservice missile test conditions.

4. ANALYSIS OF SELECTED DATA

During the acquisition and preliminary analysis of these data, many interesting data patterns were observed in the individual fin data. Four of these cases have been selected for more detailed analysis in this paper. A subsequent wind tunnel entry into Langley's Unitary Plan Wind Tunnel was made to obtain vapor screen photographs of the flow patterns for these cases so that flow visualization data would be available to interpret the trends observed in the force and moment data.

4.1 Body Shock-Wave/Fin Interaction

The first case involves the effects of a fin being intersected by the body bow-shock wave. As seen in Figure 7, the configuration analyzed here is the body with fin 12. Since this is one of the fixed fins, no fin deflections were involved. The data to be shown is for Mach 2.0 and 4.5 at angles of attack from 20 to 40 degrees. Fin data are shown as the fin rolls from windward to leeward as indicated in the cross-section sketch in this figure. The solid line represents the fin whose data are shown in subsequent figures. The dashed lines of the other three fins indicate that these fins were present on the body during testing, but that their data are not being presented.

At the lower supersonic Mach number, the bow shock does not intersect the fin even at the highest angle of attack. As the Mach number increases to 4.5 the bow shock intersects the fin at the highest angle of attack, as illustrated by the model sketch in this figure. Thus, if any effect of this shock wave on the fin loads is present, it will occur at the highest Mach number and the highest angle of attack.

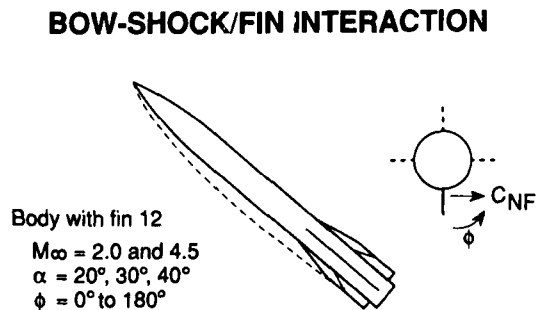


Figure 7.- Schematic of bow-shock/fin interaction.

Fin loads for these conditions are shown in Figure 8, where the effect of roll angle and angle of attack on the fin normal force and hinge moment are shown for both Mach numbers. The normal force trends for all conditions, seen at the top of this figure, are smooth and reasonable with the expected zero normal force on both the leeward and windward meridians. As the roll angle increases, the normal force increases and reaches a maximum at about 60 degrees from the windward meridian and decreases thereafter. The negative normal force near the leeward meridian in some cases will be examined in a subsequent section of this paper. Notice that the normal force increases with angle of attack, as would be expected. However, note that the maximum force at each angle of attack does not occur in the horizontal plane but at about 30 degrees windward from this plane.

Corresponding hinge moment data are shown at the bottom of the figure. Fin hinge moment is essentially the pitching moment of the individual fin about its hinge line, which for this fin is located at about the 55 percent root chord station. The trends again appear reasonable for the Mach 2.0 data, with the maximum hinge moment occurring about 30 degrees leeward from the horizontal plane.

The hinge moment data at Mach 4.5, however, show an irregular variation at the highest angle of attack. Schlieren photographs taken on this model confirm that this is the only condition shown in which the bow-shock intersected the fin. Two unusual aspects of these data can be seen. The first is the sharp negative peaks which occur near the windward meridian and just leeward of the horizontal plane. Since positive hinge moment refers to a tendency to bend the leading edge upward, these negative peaks indicate a sharp rearward movement of the aerodynamic center of the fin in a region where there is smoothly varying normal force. The second aspect is the minimum in hinge moment which is seen to occur in the region just windward of the horizontal plane. Note that this is the region where the fin normal force reaches a maximum.

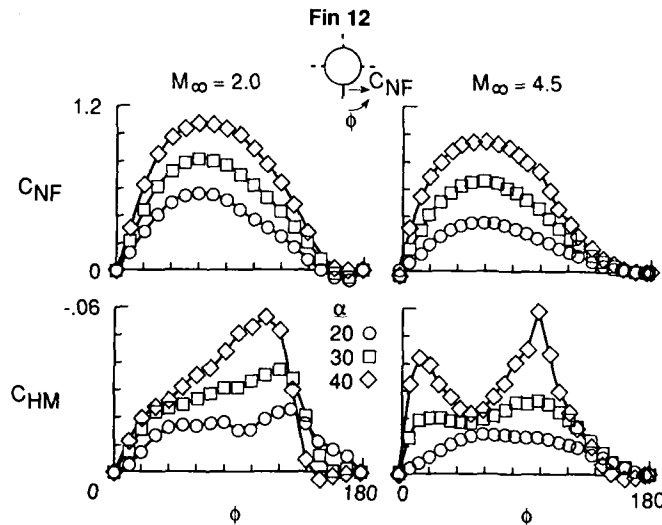


Figure 8.- Effect of bow shock interaction on fin loads.

4.2 Fin Control Effectiveness

The next data trend examined, as detailed in Figure 9, is the effectiveness of control fin deflections as the fin is rolled from windward to leeward. In this case the conditions are: body with fin 52, Mach 2.0 and 4.5, 20 degrees angle of attack, and fin deflection angles of -40 to +40 degrees.

The effect of fin deflection angle and roll angle on fin normal force is presented in the lower part of this figure. Positive deflection means leading edge upward. Positive deflection thus increases the effective angle of attack of the fin, which increases the fin normal force at all roll angles as would be expected. At the lower Mach number, the normal force on the fin experiences only a small change as the fin is rolled from windward to leeward. However, a steady decrease in the effect of fin deflections is seen to occur at the higher Mach number. On a large part of the leeward side of the body at this Mach number the fin control authority essentially disappears. An often-observed trend in missile aerodynamics is that fins become ineffective when shielded from the free stream flow at high Mach numbers. These data clearly show that the reason for this loss of control authority is that there is little force on the leeward fins.

The fin control effectiveness parameter calculated from these data is shown in Figure 10 for angles of attack of 0 and 20 degrees. The zero angle of attack results, of course, contain no effect of roll angle at either Mach number. At the higher Mach number, there is a very large fin effectiveness near the windward meridian, and a large variation of control authority with fin orientation compared to the lower Mach number results. This figure shows quantitatively the almost complete lack of control authority on the leeward side of the body at the higher Mach number.

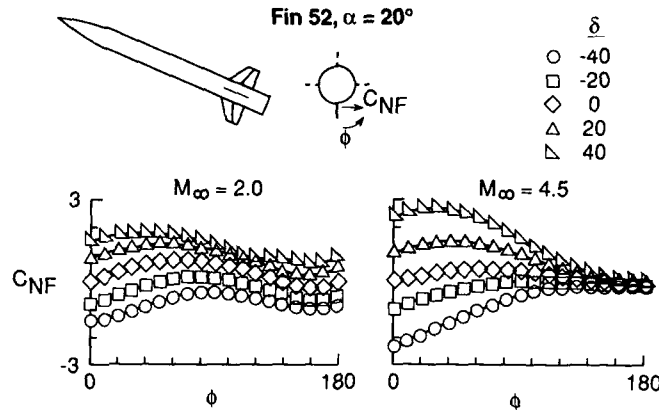


Figure 9.- Effect of fin orientation on fin loads.

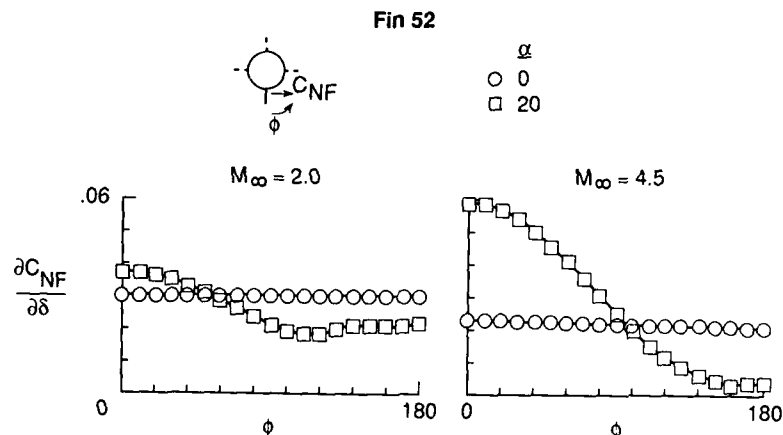


Figure 10.- Fin control effectiveness.

4.3 Fin Deflection Interference

The next case examined is the interference that can occur between a highly deflected fin and the other three fins in a cruciform arrangement. As seen in Figure 11, these results are for fin 42, Mach 3.0, angles of attack of 0 and 20 degrees, and fin deflection angles from -40 to +40 degrees. The effects of fin deflection on both the overall missile normal force and the individual fin normal forces are examined.

This figure presents these data at both 0 and 20 degrees angle of attack as the lower fin only is deflected. The small data plots near each fin in the sketch show the resulting normal force on that fin. At the left in this figure, a noticeable increase in normal force occurs on the model at both angles of attack when the fin deflection angle becomes very large, both positive and negative. Since the fin, even when deflected, is in the vertical plane, the fin normal force could not produce an upward component. It was at first speculated that the deflected fin had caused an increase in the pressures on the body in the vicinity of the fin, resulting in the increased normal force; however, as discussed below, this speculation was not correct.

Examining the forces on the individual fins in this case reveals a very interesting pattern. The lower fin - the deflected fin - naturally shows a very large and systematic variation of normal force with deflection angle. Remember that fin normal force is always normal to the plane of the fin regardless of its angular orientation.

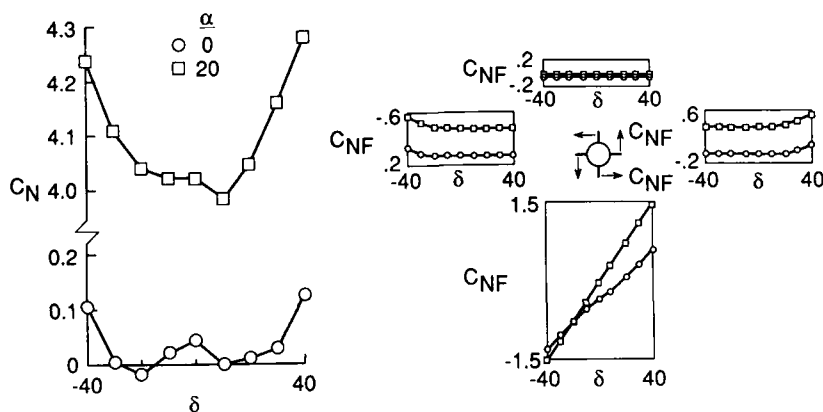
Fin 42, $M_\infty = 3.0$, $\phi = 0^\circ$ 

Figure 11.- Fin-on-fin interference for windward fin deflection.

At zero angle of attack very small fin forces would be expected from the undeflected fins. The top fin indeed shows very little force. The horizontal fins also show very little force for the small deflection angles. However for the larger deflection angles, there occurs a noticeable increase in normal force on these fins, but not at the same time. The force on the right fin increases for large positive deflection angles, and, conversely, the left fin becomes loaded for large negative deflection angles. In either case the force increases on the fin which is nearest to the trailing edge of the deflected fin. The level of the induced forces on the horizontal fins, when converted to overall normal force form, are about the same magnitude as the induced model normal forces shown on the left side of this figure. Thus the increased normal force on the missile is a result of induced forces on the fins, not on the body.

Figure 12 shows results similar to those of Figure 11 except that the top fin is deflected instead of the bottom fin. At zero angle of attack a trend very similar to that shown by the bottom fin in Figure 11 is seen except that all the induced forces are downward, as would be expected. When the leeward fin is deflected at 20 degrees angle of attack the induced forces virtually disappear. Note also that the forces on the deflected fin are also much less than in the windward case due to the body shielding effect discussed earlier.

In reviewing these results it can be concluded that a large yaw deflection of both fins, that is, the windward and leeward fins both deflected in the same direction, should produce very little induced rolling moment on the configuration at zero angle of attack since the induced forces on the horizontal fins would be approximately equal but in opposing directions to cancel each other. However, at 20 degrees angle of attack the lower fin would produce a much larger induced force than would the leeward fin, and an induced rolling moment would result.

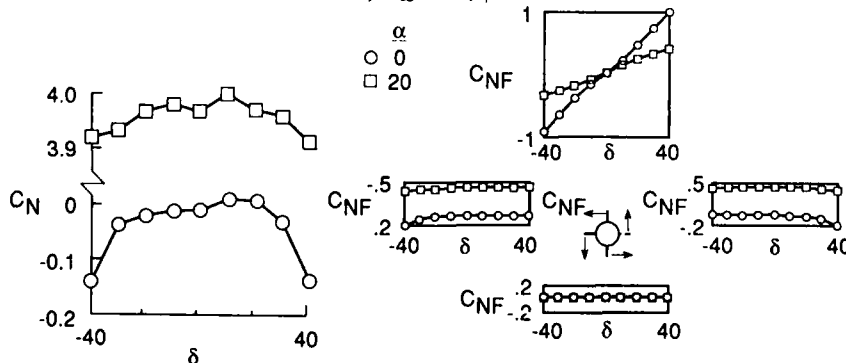
Fin 42, $M_\infty = 3.0$, $\phi = 180^\circ$ 

Figure 12.- Fin-on-fin interference for leeward fin deflection.

4.4 Body-Vortex/Fin Interference

The last data pattern analyzed in this paper is the effect of body vortices on fin loads. As shown in the model sketch in Figure 13, vortices which develop on the body could be located, for certain flow conditions, in a position to directly influence the loads on fins on the leeward side of the missile. The individual-fin data from this project permit this phenomenon to be investigated. Shown in this figure are fin normal-force data for fin 42 at Mach 2.0 at low to high angles of attack with no fin deflections. Fin normal force is shown as the fin is rolled from windward to leeward.

The vortex pattern shown in this figure was sketched from a vapor-screen photograph taken near the downstream end of this model at about 20 degrees angle of attack. At this angle the body vortices are located in a position to pass directly over the fins on the leeward side of the body. Notice that the expected trend with roll angle is observed until the fin approaches the leeward meridian, where the normal force becomes negative in the region of about 40 degrees from leeward, with the largest negative value occurring at about 20 degrees from the leeward meridian. With the sign convention used in this paper, this means that the force on the fin is actually in the downward direction, even though the configuration is at 20 degrees angle of attack. It should be emphasized that no fin deflections are involved here.

This force reversal does not occur at either the low or high angles of attack, 5 and 35 degrees, respectively. At the low angle, vapor screen photographs show that no body vortices are present, and at the high angle the vorticity has been diffused over such a large area that the force reversal does not occur. This reversal occurs only when the fin is rolled into the flow field of a tightly-wound vortex.

Figure 14 shows that this force reversal is still present at Mach 2.0 when the angle of attack is reduced to 10 degrees. However, this reversal effect is noticeably reduced at Mach 4.5 and 10 degrees angle of attack, and vanishes entirely at 20 degrees angle of attack. This result at the higher Mach number should not be surprising based on the loss of fin control effectiveness on the leeward side of the body that was shown in Figures 9 and 10.

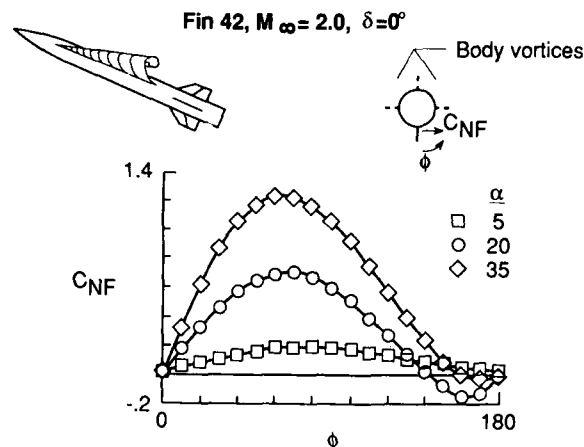


Figure 13.- Effect of angle of attack on fin force reversal.

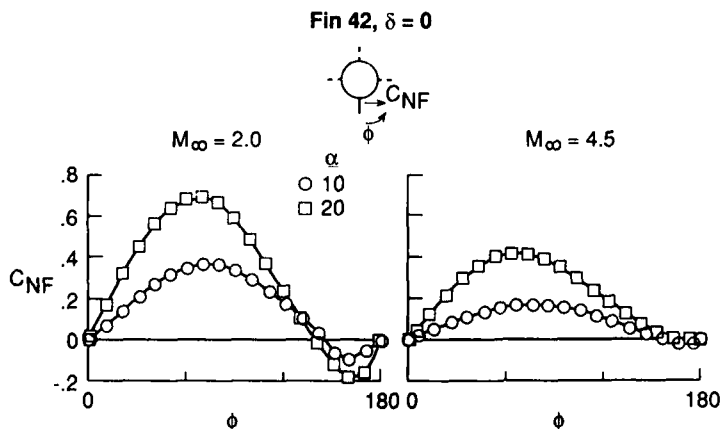


Figure 14.- Effect of Mach number on fin force reversal.

5. DATA COMPARISONS WITH THE SWINT EULER CODE

One of the most valuable aspects of the Triservice Missile Data Base is that it provides a very large, high quality, systematic set of diagnostic data that can be used to evaluate the computational accuracy of developing engineering prediction methods. One such method that has become widely used recently is the SWINT code (Reference 11). SWINT is an Euler code which has been specialized for use in supersonic missile applications. This final section of the paper will show comparisons of computational results from the SWINT code with the body-vortex/fin interference data which were analyzed in the previous section of this paper.

Figure 15 shows a comparison between data and computation for fin normal force at Mach 2.0 at 10 degrees angle of attack, and Mach 4.5 at 10 and 20 degrees angle of attack. No computational results were obtained for the lower Mach number at 20 degrees angle of attack. The overall agreement is fairly good, with the normal force being somewhat overpredicted at Mach 2.0 and underpredicted at Mach 4.5. However, notice that the SWINT code does not predict the force reversal trend near the leeward meridian that is shown in some of the data. The reason for this can be seen in Figure 16 where a vapor screen photograph and the computational crossflow velocity field for the same flow conditions are shown. The vapor screen photograph shows the presence of a well-developed, tightly-wound vortex; whereas the SWINT flow field shows no evidence of a vortex. The computed crossflow velocities continue to expand around the body, which is indicated by the length and direction of the arrows, and do not separate from the body surface. Since the computational results do not contain the vortex, there is no mechanism for calculating the normal force reversal seen in the data.

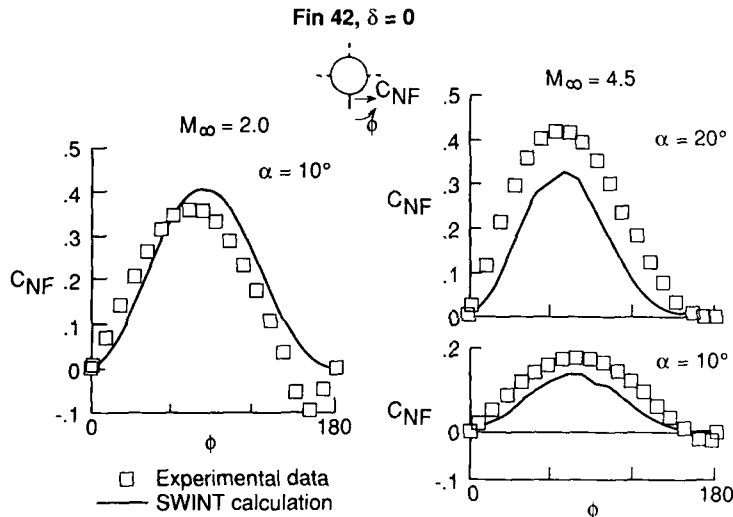


Figure 15.- SWINT/data fin normal force comparisons.

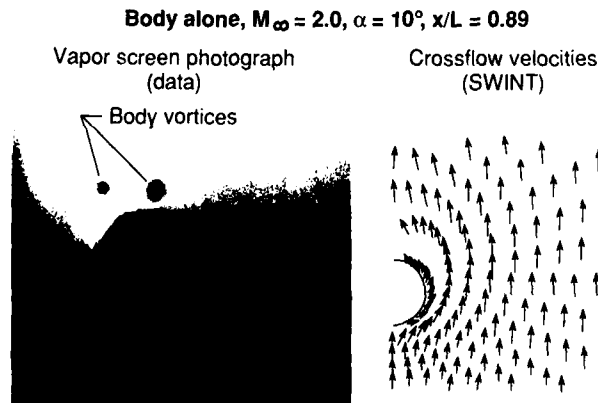


Figure 16.- SWINT/data flowfield comparisons.

Cumulative force and moment buildups on the complete configuration are available over the entire length of the body from the SWINT computed results. An interesting way of visualizing the contribution of different components of the configuration is to plot the running sum of the forces over the entire length of the configuration. Such a plot is shown in Figure 17 in which the running sum of computed normal force over the length of the body is shown for Mach 2.0 and 4.5, zero roll angle, at angles of attack of 10 and 20 degrees. Computations are shown for both body-alone and body-fin configurations. For comparison purposes the symbols on this plot are the measured values of overall configuration normal force for these conditions, which should correspond to the computed results at the end of the body.

As mentioned previously no complete 20-degree angle-of-attack body/tail solution was obtained at Mach 2.0, which explains why the SWINT results in the figure do not extend to $x/L = 1.0$. The effects of the tail fins on the computed normal force can be clearly seen from this type of plot. The agreement between data and theory is fairly good. Notice that both data and theory show a much smaller effect of the tail fins at Mach 4.5 than is seen in the Mach 2.0 case.

Fin 42, $\delta = 0^\circ$, $\phi = 0^\circ$

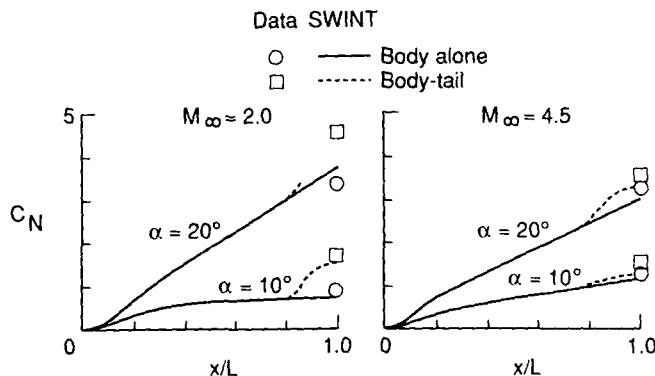


Figure 17.- SWINT/data normal force comparisons.

6. CONCLUDING REMARKS

An extremely large, systematic, axisymmetric-body/tail-fin data base has been gathered through tests of an innovative missile model design which is described herein. These data were originally obtained for incorporation into a missile aerodynamics code based on engineering methods (Program MISSILE3), but can also be used as diagnostic test cases for developing computational methods because of the individual-fin data included in the data base. Detailed analysis of four sample cases from these data are presented to illustrate interesting individual-fin force and moment trends. These samples quantitatively show how bow shock, fin orientation, fin deflection, and body vortices can produce strong, unusual, and computationally challenging effects on individual fin loads. Comparisons between these data and calculations from the SWINT Euler code are also presented.

7. REFERENCES

1. Lesieur, D. J., Mendenhall, M. R., Nazario, S. M., and Hemsch, M. J.: Prediction of Aerodynamic Characteristics of Cruciform Missiles Including Effects of Roll Angle and Control Deflection. NEAR TR 360, Aug. 1986.
2. Nielsen, J. N., Hemsch, M. J., and Smith, C. A.: A Preliminary Method for Calculating the Aerodynamic Characteristics of Cruciform Missiles to High Angles of Attack Including Effects of Roll Angle and Control Deflections. NEAR TR 152, Nov. 1977.
3. Smith, C. A., and Nielsen, J. N.: Prediction of Aerodynamic Characteristics of Cruciform Missiles to High Angles of Attack Utilizing a Distributed Vortex Wake. NEAR TR 208, Jan. 1980.
4. Hemsch, M. J., and Mullen, J., Jr.: Analytical Extension of the MISSILE1 and MISSILE2 Computer Programs. NEAR TR 272, Mar. 1982.

5. Lesieur, D. J., Mendenhall, M. R., Nazario, S.M., and Hensch, M. J.: Aerodynamic Characteristics of Cruciform Missiles at High Angles of Attack. AIAA-87-0212, Jan. 1987.
6. Lesieur, D. J., Mendenhall, M. R., and Dillenius, M. F. E.: Prediction of Induced Roll on Conventional Missiles with Cruciform Fin Sections. AIAA-88-0529, Jan. 1988.
7. Nielsen, J. N., Goodwin, F. K., Dillenius, M. F. E., and Hensch, M. J.: Prediction of Cruciform All-Movable Control Characteristics at Transonic Speeds. AIAA-84-0312, Jan. 1984.
8. Hensch, M. J., and Nielsen, J. N.: Extension of Equivalent Angle-of-Attack Method for Nonlinear Flowfields. Journal of Spacecraft, vol. 22, no. 3, May-June 1985, pp. 304-308.
9. Hensch, M. J.: Nonlinear Applications of Slender-Body Theory to Missile Aerodynamics. AIAA-85-1775-CP, Aug. 1985.
10. Nielsen, J. N.: Supersonic Wing-Body Interference at High Angles of Attack with Emphasis on Low Aspect Ratios. AIAA-96-0568, Jan. 1986.
11. Wardlaw, A. B., Hackerman, L. B., and Baltakis, F. P.: An Inviscid Computational Method for Supersonic Missile Type Bodies - Program Description and Users Guide. NSWC TR 81-459, Dec. 1981.

WIND TUNNEL TESTS:
THE ROLE OF THE MODEL

BY

Dr. Eng. S. MAZZUCA, Mr. B. PIACENTINI
SELENIA S.p.A.
MISSILE SYSTEMS DIVISION
VIA TIBURTINA Km. 12.400 - FOB. 7083
00131 ROME - ITALY

1. SUMMARY

This paper highlights the role of the model in the overall wind tunnel test program.

Depending on the specific task to be achieved (i.e. improvement of an existing missile or a new missile development), the cost-effectiveness analysis leads to the best solution in terms of:

- . scale of the model;
- . number of configurations to be tested;
- . degree of likelihood;
- . wind tunnel facilities to be used;
- . interoperability among different test sites;
- . overall test time;
- . test time of each subphase.

A further very important role is related to the test philosophy adopted in order to minimize the number of measurements while retaining the capability to obtain from the test useful information.

A proper design of the model can fulfil these constraints, minimizing overall test time and the related costs.

2. INTRODUCTION

Defining a missile, one of the main fields of investigation regards the determination of the aerodynamic data.

These are generally requested for the subsequent analysis in two different forms: linear or derivatives and non linear coefficients.

The linear form is used to assess the airframe stability characteristic and to verify the performances of the couple airframe - autopilot.

The non linear coefficients are used to establish the maneuverability and controllability boundaries of the couple airframe - autopilot.

Of course these analysis can be performed by means of a suitable mathematical model of the missile dynamic.

Many other technological areas require the use of the aerodynamic data as input for the design; this is synthesized in fig. 1 [ref. 1].

The sources of the aerodynamic coefficients are available, during the process of the development of a missile, according to the following schedule:

- a) coefficients from predictive calculation;
- b) coefficients from wind tunnel tests;
- c) coefficients from flight tests.

Each of the above sources have a specific use, cost and reliability as summarized in the tables 1), 2), and 3), [ref. 2].

The repartition of the cost of the aerodynamic predictive means of point a) and b) is summarized in fig. 2 [ref. 1].

This paper analyzes how derive the aerodynamic coefficients from wind tunnel tests for a typical program of:

- a) improvement of an existing missile;
- b) development of a new missile.

For these programs the role of the fisic model is highlighted.

3. HOW TO PLAN A WIND TUNNEL TEST PROGRAM

A wind tunnel test program is established to simulate, with the maximum degree of likelihood, the aerodynamic behaviour of a missile in particular areas that need to be investigated.

The main factors that realize this simulation correctly, with reference to a fig. 3 [rif. 3], are:

- a) the wind tunnel facilities;
- b) the physical model of the missile;
- c) the test program.

The main objectives of a wind tunnel test programme, with reference to a table 2), are to:

- Check of the theorethical calculation.
- Direct the measurement of the aerodynamic coefficients in areas where theoretical calculation is unreliable (high incidence or high deflections of control surfaces).
- Data extraction with presentation suitable for direct analysis and subsequent handling.

To be consistent with these objectives, the wind tunnel test program must define:

- Areas to be investigated.
- Test sequence and modalities.
- Suitable test facilities.

3-1. Areas to be investigated

The identification of the areas to be investigated is the first and the most important activity to be performed in order to find the experimental data that permit the solution of the specific question.

For instance for an exiting missile could be important to know the aerodynamic characteristic of the control surfaces as they become from production.

In this case the main area to be analized is the determination of the correlation between the hinge moment and the geometric production tolerance that could change the center of pressure location, while the other aerodynamic characteristics are expected to be less influenced by production process.

For a new missile all the aerodynamic coefficients of the control surfaces need to be measured. That means measure normal force, hinge moment, bending moment, drag etc; furthermore the whole aerodynamic pressure field must be determined in order to perform the mechanical project and the flutter analysis.

3-2. Test sequence and modalities

In order to define a suitable test program, after the specification of the aerea to be investigated, it is necessary to identify the key parameters governing the physical process.

These parameters must be ordered in a hierarchical manner, and a proper range of each one must be assessed. Since the measurements must be done with a prefixed value of the key parameters, they need to be discretized; the size of the step depends on the correlation between parameter and process.

The product of the number of the steps of each parameter between themselves give the maximum size of the test program; by elimination of the repetition and meaningless combination and taking in account the symmetries, the final test program is defined.

For instance a multirole missile with a cartesian control requires the determination of the six main aerodynamic coefficients function of six key parameters in the form:

$$C = C(\text{Mach}, \alpha_T, \varphi_{\alpha_T}, \delta_R, \varphi', \delta_a)$$

where, with reference to fig. 4.

Mach = Mach number
 α_T = total incidence
 φ_{α_T} = bank angle of the wing respect to plane of the incidence
 δ_R = total command deflection (pitch + yaw)
 φ' = angle of the command with respect to plane of the incidence
 δ_a = differential command (roll).

By discretization we obtain:

Mach = 0 : 4, step 0,3 13 steps
 α_T = -5 : +25°, step 1° 31 steps
 φ_{α_T} = -180° : +180°, step 22°,5 17 steps
 δ_R = 0 : 28°, step 7° 5 steps
 φ' = -180° : +180°, step 30° 13 steps
 δ_a = -28° : +28°, step 28° 3 steps

The total number of the points to be measured is 1.335.945.

Choosing to measure with α_T traverse we need 43095 polars. Instead with φ_{α_T} traverse we need 78585 polars, so α_T traverse are less numerous.

Tacking in to account the configuration's simmetries we can reduce φ_{α_T} steps for a cruciform missile, to five and the α_T traverse will become 12.675; further when $\delta_R = 0$ the key parameter φ' becomes meaningless and we obtain a minimum number of α_T traverse of 11700.

If we expect a slow dependence of the coefficients from Mach number we can obtain other savings by reduction of Mach's steps and so for the others parameters.

However the resulting program is a "mass program" requiring a long time for the execution with associated high cost.

In order to achieve the maximum of flexibility the program needs a good management; in this respect the test modalities play the principal role. These modalities consists at least in:

- Phase 1) Suitability of the set up assessed by comparison with theoretical data or previous measurement.
- Phase 2) Escalation of the main program obtained starting from the less complicated up to the more difficult (to predict) combination of the key parameters.
- Phase 3) Final check, made by a repetition of few reference measurement, or by verification that the response of the set up and the model are not deteriorated beyond the specifications.

To avoid waste of time and money all the above steps must be performed with the continuous supervision of the head of the experimental activities and generally cannot be completely delegated to the facilities people.

3-3. Suitable test facility

Once the areas to be investigated are defined and the final test program is selected it is possible to make a preliminary search among the candidate test facilities. Their characteristics must be analyzed and ordered in relation to the capability to fulfil the program's requirements.

Afterwards the test facilities must be consulted in order to obtain the information on the following fields:

- a) Capability to perform the test program.
- b) Model requirements.
- c) Waiting list.
- d) Overall test time.
- e) Estimation of the cost.

These information must be checked with the requirements of the main program both in terms of schedule and budget.

Should any conflict arise, it will be necessary to make a trade-off analysis between:

- test program;
- model's specification;
- total test time (i.e. staggering);
- total costs.

All the activities aforesaid must be performed in order to make at least a minimal test program because, in general terms, it is better to have a small amount of measured data instead to having none.

3-4. Specification of the test model

The purpose of this activity is to define the general criteria for the design and manufacturing of the physical model by which measuring the aerodynamic data in a wind tunnel facility

A typical specification of a test model contains at least the following paragraphs:

- Object; containing a brief description of the entire model and the scope of the activities.
- Applicable documentation; defining the guide lines for the design of the test model, the list of the referenced documents, and priority between them.
- Configuration; containing the complete detailed description of the test model including body, wings, excrescences, ogive, boattail, and remote control devices if any.
- Measurement devices; are defined by type, location, range, precision, redundancy, and calibration requirements.
- General requirements; divided into, mechanical, electrical, functional, handling, interoperability between different test sites, transportability and storage.

4. ROLE OF THE MODEL

The typology of the physical model and the related options are consequence of the areas that must be investigated.

Among the options we will choose the model in order to maximize the likelihood of the measured data and minimize the test time and total cost.

This concept will be illustrated by bringing two practical examples.

4-1. Improvement of an existing missile

The activity is addressed to obtain the reduction of the exposed span of the control surfaces of a cruciform missile with cartesian control system.
The key parameters are:

- a) Geometrical configuration well defined from the geometrical point of view: excrescences, harness covers, hooks or lugs, external rugosity as becomes from production processes, etc., etc.
In many cases it is possible to test the production items.
- b) Range of test parameters is known "before hand" being that of the existing missile.
- c) Test program is generally conceived to obtain an high number of data through the combination of the test parameters. It is a "mass program" as per para 3.2.

The areas to be investigated are the measurement of the characteristics and boundaries of controllability of the entire configuration. The test program is tailored to examine the influence of key parameters as control surfaces deflections, incidence, Reynolds numbers, Mach numbers.

The test modalities need to begin with a comparison between existing data and reference measurement before extending the program to the following activities:

- Take exact measurements of the aerodynamic characteristics with low incidence and small control deflections.
- Extend the measurements up to boundaries of controllability.

With a preliminary test program a certain number of wind tunnel facility can be selected with the following capability:

- Large working section to permit high incidence with big scale of the model.
- Pressurized working section to obtain high Reynolds numbers.
- Closed loop and high speed of data acquisition system to ensure high productivity.
- Capability to test the entire span of Mach number.

At this point it is possible to issue the specification of the model taking into account the following guidelines:

- Maximum of geometrical likelihood with reference to the existing weapon.
- Scale as large as possible.
- High speed of changement of controls positions.
- Interoperability between differents tests facilities.
- Measurement and control devices accessibility.
- Simplicity of handling and maintainability.

If we look at the fig. 5 [ref. 4], we know the time distribution for a typical test of three large wind tunnel; model changes constitute about the 50% of the occupancy with only 13% dedicated to data acquisition process. It is evident that a drastic reduction of the time devoted to a model's configuration changes is highly desirable.

The test model at the end of optimization proces will be generally a model with a big scale (half scale up to full scale).

The control surfaces will be operate via remote control by the computer which manages the wind tunnel and that execute automatically the test program.

This model is costly by itself; on the other hand its high productivity lowers the test time and the cost of the overall program.

4-2. Development of a new missile

The activity is addressed to issue the specification of the aerodynamic configuration of new tactical missile.

The key parameters are:

- a) Geometrical constraints consisting in the overall dimensions and attachment systems.
- b) Typical performances required in terms of speed envelope, g capabilities and altitude range.
- c) Test program is conceived to select among several aerodynamic configurations the best compromise for the point b).

The areas to be investigated are the measurements of the performances, mainly in the incidence plane, taking also into account the out of plane disturbances. The test program is tailored to examine the influence of the geometrical configuration and the choice of the control system (Cartesian or Bank to Turn), size the wing panels and the location of control panels on the axis (Canard, wing or tail configuration).

The test modalities need to begin with a configuration to be taken as reference in order to check all the equipments of the wind tunnel, mainly balance loads, traverse system, Mach numbers, pressure measurement taps and Reynolds capability.

The program must continue with the other configurations to assess the influence of the geometric change in comparison with the reference configuration on the entire envelope of the key parameters.

At this point it is possible to issue a preliminary test program and select the wind tunnel facility with the following characteristics:

- Pressurized working section to obtain high Reynolds number.
- High speed of data acquisition system to ensure high productivity.
- Closed loop with a by-pass system and large access door to allow quick change of configuration.
- Capability to test all mach numbers.

The specification of the model will take into account the following guidelines:

- Define the geometrical aspect with the maximum likelihood within the available informations.
- Interoperability between different test facilities.
- Define a scale as large as possible.
- High speed of change of the aerodynamic configuration and setting of the control surfaces.
- Simplicity of handling, accessibility and maintainability.

The test models at the end of optimization process will be generally a model with a small scale (about a-tenth of the real scale). The control surfaces will be operated manually with an appropriate system of setting that minimizes the time required for the change of configuration.

The model will be able to accommodate different wing panels on the same body, in order to avoid the dismantling of the body and consequent calibration of the balance.

In consequence the design will be done thoroughly and so will its construction to meet the requirements of flexibility and easiness of handling.

5. CONCLUSION

A wind tunnel test program is established to simulate, with the maximum degree of likelihood, the behaviour of the missile flying in the particular areas that need to be investigated. The main factors that realize correctly this simulation, with reference to a rig. | 3 |, are:

- a) the wind tunnel facilities;
- b) the physical model of the missile;
- c) the test program.

The characteristics of the wind tunnels not being modifiable, the appropriate choice and definition of the physical model allow to obtain, together with a good test program, the right and significant answers, within minimum time and cost.

6. REFERENCE

- /1/ VON KARMAN INSTITUT - "An introduction to tactical missile aerodynamics" R.G. LACAU - AEROSPATIALE - BRUXELLES 1987.
- /2/ ACARD - Symposium on Missile System Flight Mechanics - Paper n° 38 F. Gasperini - S. Mazzuca - Selenia - "Flight tests for control system validation of a tactical missile" London 1979.
- /3/ MICHAEL HUSSEY "The MAN-MADE WORLD" Technology Foundation Course 1972 by the Open University, Bletchley.
- /4/ J. CHRISTOPHE ONERA "Productivity: The economic aspect of cryogenic wind tunnel design and use".

COMPUTED AERODYNAMIC COEFFICIENTS

TYPE	USE	COMMENTS
LINEAR $CY(d), CZ(d)$ OR CY_d, CZ_d $CMY(d), CMZ(d)$ OR CMY_d, CMZ_d $CX_0(\delta)$ $CY(\delta), CZ(\delta)$ OR CY_δ, CZ_δ $CMX(\delta_\alpha)$ CMX_{δ_α}	AERODYNAMIC CONFIGURATION SELECTION MASS CENTER LOCATION AUTOPILOT PARAMETERS SELECTION AUTOPILOT STABILITY CHECK	- HIGH SPEED OF COMPUTATION - ENOUGH ACCURATE FOR ALL MACH NUMBERS - EASY EXAMINATION OF MANY AERODYNAMIC CONFIGURATIONS - LOW COST
NON LINEAR $CX \left\{ \begin{matrix} (M, \alpha, \varphi_d, \delta_R, \varphi_R, \delta_\alpha) \\ (M, \alpha, \varphi_d, \delta_R, \varphi_R, \delta_\alpha) \end{matrix} \right.$ $CY \left\{ \begin{matrix} (M, \alpha, \varphi_d, \delta_R, \varphi_R, \delta_\alpha) \\ (M, \alpha, \varphi_d, \delta_R, \varphi_R, \delta_\alpha) \end{matrix} \right.$ $CMX \left\{ \begin{matrix} (M, \alpha, \varphi_d, \delta_R, \varphi_R, \delta_\alpha) \\ (M, \alpha, \varphi_d, \delta_R, \varphi_R, \delta_\alpha) \end{matrix} \right.$ $CMY \left\{ \begin{matrix} (M, \alpha, \varphi_d, \delta_R, \varphi_R, \delta_\alpha) \\ (M, \alpha, \varphi_d, \delta_R, \varphi_R, \delta_\alpha) \end{matrix} \right.$ $CMZ \left\{ \begin{matrix} (M, \alpha, \varphi_d, \delta_R, \varphi_R, \delta_\alpha) \\ (M, \alpha, \varphi_d, \delta_R, \varphi_R, \delta_\alpha) \end{matrix} \right.$	MAXIMUM MANOEUVRE CHECK CONTROLLABILITY CHECK HINGE MOMENT CHECK STRUCTURAL DESIGN CHECK	- LOW SPEED OF COMPUTATION - HIGH ACCURACY FOR $M > 1$ - POOR ACCURACY FOR $M \leq 1$ - EMPIRICAL DATA NEED - EXAMINATION CONFINED TO FEW AERODYNAMIC CONFIGURATION - HIGH COST

TAB. 1

WIND TUNNEL TESTED AERODYNAMIC COEFFICIENTS

TYPE	USE	COMMENTS
$CX \left\{ \begin{matrix} (M, \alpha, \varphi_d, \delta_R, \varphi_R, \delta_\alpha) \\ (M, \alpha, \varphi_d, \delta_R, \varphi_R, \delta_\alpha) \end{matrix} \right.$ $CY \left\{ \begin{matrix} (M, \alpha, \varphi_d, \delta_R, \varphi_R, \delta_\alpha) \\ (M, \alpha, \varphi_d, \delta_R, \varphi_R, \delta_\alpha) \end{matrix} \right.$ $CZ \left\{ \begin{matrix} (M, \alpha, \varphi_d, \delta_R, \varphi_R, \delta_\alpha) \\ (M, \alpha, \varphi_d, \delta_R, \varphi_R, \delta_\alpha) \end{matrix} \right.$ $CMX \left\{ \begin{matrix} (M, \alpha, \varphi_d, \delta_R, \varphi_R, \delta_\alpha) \\ (M, \alpha, \varphi_d, \delta_R, \varphi_R, \delta_\alpha) \end{matrix} \right.$ $CMY \left\{ \begin{matrix} (M, \alpha, \varphi_d, \delta_R, \varphi_R, \delta_\alpha) \\ (M, \alpha, \varphi_d, \delta_R, \varphi_R, \delta_\alpha) \end{matrix} \right.$ $CMZ \left\{ \begin{matrix} (M, \alpha, \varphi_d, \delta_R, \varphi_R, \delta_\alpha) \\ (M, \alpha, \varphi_d, \delta_R, \varphi_R, \delta_\alpha) \end{matrix} \right.$ $CZW \left\{ \begin{matrix} (M, \alpha, \varphi_d, \delta_R, \varphi_R, \delta_\alpha) \\ (M, \alpha, \varphi_d, \delta_R, \varphi_R, \delta_\alpha) \end{matrix} \right.$ $CMXW \left\{ \begin{matrix} (M, \alpha, \varphi_d, \delta_R, \varphi_R, \delta_\alpha) \\ (M, \alpha, \varphi_d, \delta_R, \varphi_R, \delta_\alpha) \end{matrix} \right.$ $CMYW \left\{ \begin{matrix} (M, \alpha, \varphi_d, \delta_R, \varphi_R, \delta_\alpha) \\ (M, \alpha, \varphi_d, \delta_R, \varphi_R, \delta_\alpha) \end{matrix} \right.$	- AUTOPILOT STABILITY CHECK - MAXIMUM MANOEUVRE CHECK - CONTROLLABILITY CHECK - HINGE MOMENT CHECK - MECHANICAL STRENGTH CHECK - AEROELASTIC CHECK	- TEST - SOME MODELS NEED SCALE EFFECTS ON REYNOLD NUMBER (WING STALL, DRAG COEFFICIENT) - GOOD ACCURACY - LIMITED MACH ENVELOPE - LIMITED CONFIGURATIONS - VARIANT - HIGH COST - TIME CONSUMING

TAB. 2

FLIGHT TESTED AERODYNAMIC COEFFICIENTS

TYPE	USE	COMMENTS
LINEAR $CY_d, CZ_d, CM_{\dot{\alpha}}, Cn_d$ $CM_{\dot{\alpha}d}, CMZ_d, Cm_{\dot{\delta}}, Cn_{\dot{\delta}}$ $CX_0, C\ell_{\delta_\alpha}$	- AERODYNAMIC MODEL CHECK AND IMPROVEMENT - AIRFRAME - AUTOPILOT PERFORMANCE CHECK - MAXIMUM MANOEUVRE CHECK - PROPER CONTROL CHECK	- PROPER DYNAMIC MATHEMATICAL MODEL NEED - PROPER TELEMETRY LINK NEED - IDENTIFICATION PROCEDURE SLOW AND EXPENSIVE - GOOD OVERALL ACCURACY
NON LINEAR $CX \left\{ \begin{matrix} (M, \alpha, \varphi_d, \delta_R, \varphi_R, \delta_\alpha) \\ (M, \alpha, \varphi_d, \delta_R, \varphi_R, \delta_\alpha) \end{matrix} \right.$ $CY \left\{ \begin{matrix} (M, \alpha, \varphi_d, \delta_R, \varphi_R, \delta_\alpha) \\ (M, \alpha, \varphi_d, \delta_R, \varphi_R, \delta_\alpha) \end{matrix} \right.$ $CZ \left\{ \begin{matrix} (M, \alpha, \varphi_d, \delta_R, \varphi_R, \delta_\alpha) \\ (M, \alpha, \varphi_d, \delta_R, \varphi_R, \delta_\alpha) \end{matrix} \right.$ $CMX \left\{ \begin{matrix} (M, \alpha, \varphi_d, \delta_R, \varphi_R, \delta_\alpha) \\ (M, \alpha, \varphi_d, \delta_R, \varphi_R, \delta_\alpha) \end{matrix} \right.$ $CMY \left\{ \begin{matrix} (M, \alpha, \varphi_d, \delta_R, \varphi_R, \delta_\alpha) \\ (M, \alpha, \varphi_d, \delta_R, \varphi_R, \delta_\alpha) \end{matrix} \right.$ $CMZ \left\{ \begin{matrix} (M, \alpha, \varphi_d, \delta_R, \varphi_R, \delta_\alpha) \\ (M, \alpha, \varphi_d, \delta_R, \varphi_R, \delta_\alpha) \end{matrix} \right.$ $CZW \left\{ \begin{matrix} (M, \alpha, \varphi_d, \delta_R, \varphi_R, \delta_\alpha) \\ (M, \alpha, \varphi_d, \delta_R, \varphi_R, \delta_\alpha) \end{matrix} \right.$ $CMXW \left\{ \begin{matrix} (M, \alpha, \varphi_d, \delta_R, \varphi_R, \delta_\alpha) \\ (M, \alpha, \varphi_d, \delta_R, \varphi_R, \delta_\alpha) \end{matrix} \right.$ $CMYW \left\{ \begin{matrix} (M, \alpha, \varphi_d, \delta_R, \varphi_R, \delta_\alpha) \\ (M, \alpha, \varphi_d, \delta_R, \varphi_R, \delta_\alpha) \end{matrix} \right.$		

TAB. 3

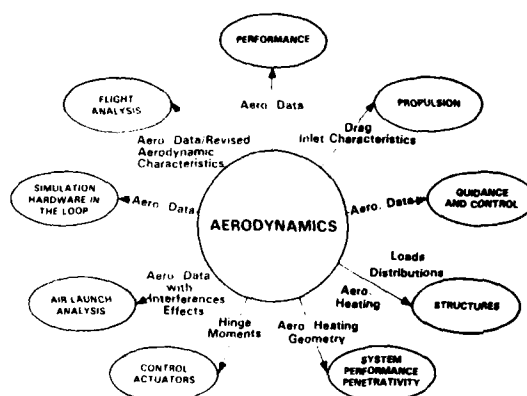


Fig. 1 - CONNECTIONS BETWEEN AERODYNAMICS AND THE OTHER TECHNOLOGY AREAS

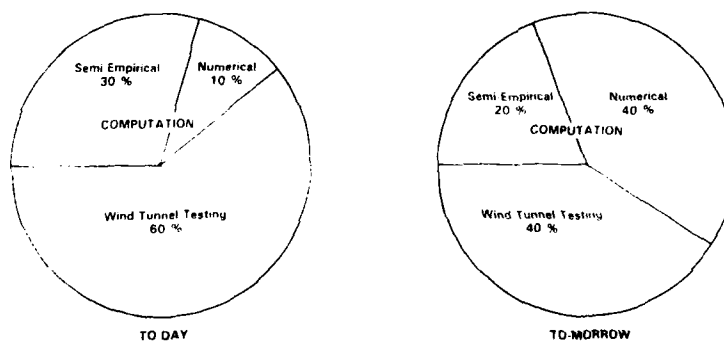


FIG. 2 COST OF AERODYNAMIC PREDICTIVE MEANS.

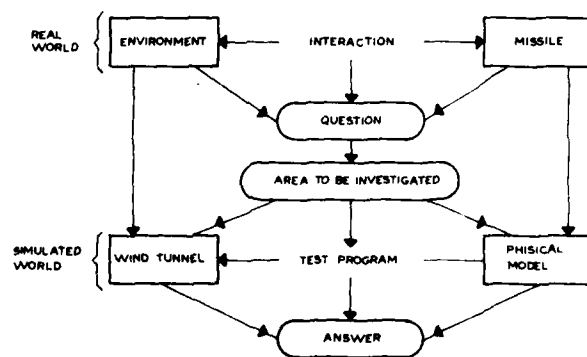


FIG. 3 MODELLING PROCESS .

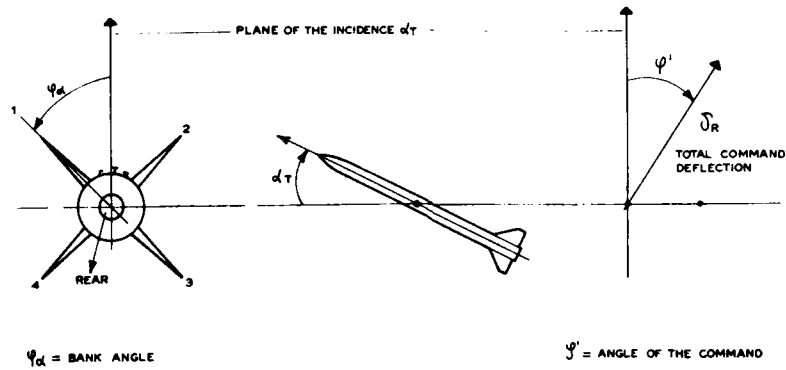


FIG. 4 AERODYNAMIC PARAMETER

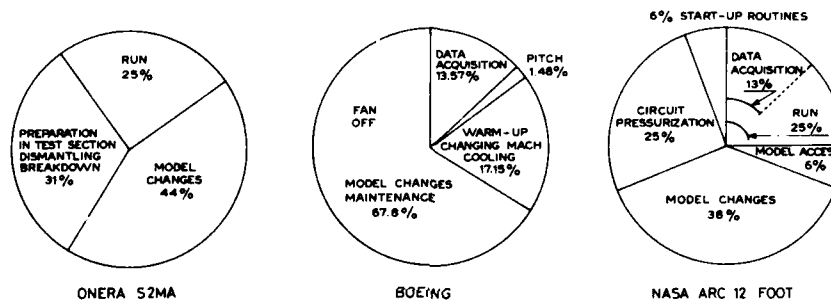


FIG. 5 OCCUPANCY TIME DISTRIBUTION.

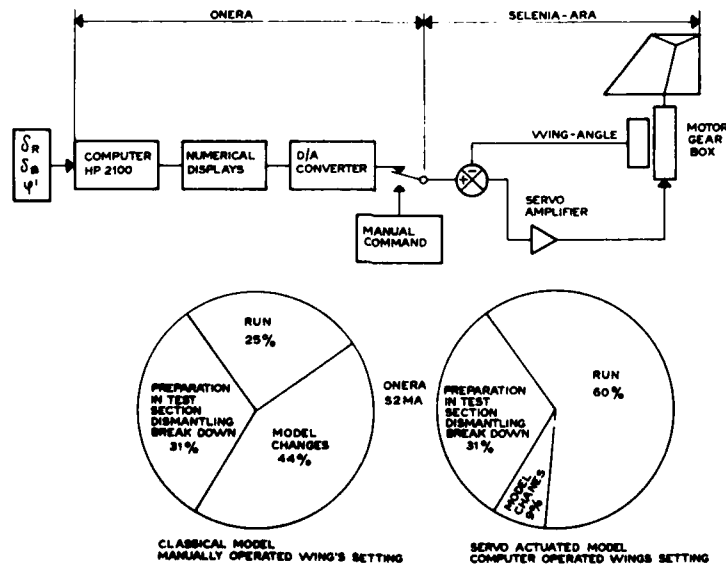


FIG. 6 CHANGE IN OCCUPANCY TIME DISTRIBUTION.

IDENTIFICATION OF STABILITY AND CONTROL PARAMETERS OF A BRILLIANT AMMUNITION

K.-F. Doherr & G. Lehmann
DFVLR - Institut für Flugmechanik
Flughafen
D-3300 Braunschweig
West Germany (FRG)

H. Schilling
Rheinmetall GmbH
Ulmenstr. 125
D-4000 Düsseldorf
West Germany (FRG)

SUMMARY

The efficient defense against armoured ground vehicles depends heavily on precisely delivered warheads. New terminal guided warheads are under development presently which improve the hit accuracy and therefore the effectiveness drastically. One example is EPHRAM which employs a sophisticated detection and control system in order to achieve optimal results.

A considerable part of the development of a brilliant ammunition is spent on the determination of its aerodynamic and control characteristics. For EPHRAM static and dynamic wind tunnel experiments were performed. A recoverable instrumented version was developed for the validation of the concept and the identification of aerodynamic parameters and thrust interference effects from flight tests.

The test vehicle was dropped several times from a helicopter-lifted platform. During these first tests with reduced sensor equipment, which focused on the performance of EPHRAM, the desired footprint was achieved. An analysis of one of these flights confirmed the static wind tunnel results at low angle of attack.

For the system identification at high angle of attack more flight tests are scheduled with complete instrumentation and selected thrust programs to fully excite the vehicle dynamics.

SYMBOLS

Symbols have been used according to ISO 1151/1 Flight Mechanics Standards [1]. In Chapter 3.2 the terminology common in the literature on parameter estimation has been adopted. Other symbols are explained in the text.

1. INTRODUCTION

During the last few years new so-called "brilliant" or "smart" ammunition has been under development. With the help of terminal guided warheads the hit accuracy can be increased significantly. The effectiveness is raised due to special maneuvers in the terminal phase by which impact at an optimum angle is achieved (top-attack capability).

One example of such newly developed ammunition is the EPHRAM system. EPHRAM is the German acronym for "Autonomous Precision Guided Munition". The terminal guided flight is controlled by a sophisticated jet reaction control system using lateral thrusters [2]. These lead to aerodynamic interferences which cannot be simulated well enough in a usual wind tunnel environment. Moreover, simulations showed the need for an estimation of the dynamic aerodynamic coefficients, which cannot be obtained with sufficient quality (or even not at all) in wind tunnel tests. Therefore, it was decided to use the method of nonlinear system identification in order to quantify the desired data. The necessary mathematical model is based on wind tunnel results and on recent experience with the identification of rotating ammunition in the high velocity range.

In this paper some typical characteristics of the EPHRAM system are discussed first. Then the results of static and dynamic wind tunnel measurements are reported, which were required to obtain the basic nonlinear aerodynamic model. Descriptions follow of the nonlinear parameter identification method, the mathematical model and the instrumented flight test version of EPHRAM, which will be used to identify the desired stability and control parameters from flight tests scheduled in May 1988.

So far, based on an analysis of one of the performance tests with reduced instrumentation, the location of the center of pressure and the normal force gradient at small angle of attack were estimated.

2. E P H R A M BRILLIANT AMMUNITION

2.1 Technical Concept

In several US and European programs the feasibilities and the advantages of different concepts for "intelligent" or "brilliant" submunition are explored. The concepts rely on the already high hit probability of the artillery improved by terminal-phase autonomous

flight of the submunition. In addition, top-attack capability promises high effectiveness also against heavily armoured targets, which cannot be attacked successfully by conventional kinetic energy or shaped charge warheads.

One example is the EPHRAM system, presently under development. Fig. 1 shows a sketch of the projectile structure with the outer thinwall shell, the inner shell (canister), and the submunition. For ballistic similitude to conventional artillery projectiles, the shape of the EPHRAM projectile is identical to that of the well known M483A1, therefore having the same aerodynamic characteristics. To get the same dynamic flight behaviour, weight, moments of inertia, and center of gravity have to be chosen properly.

In Fig. 2 a cut through the EPHRAM submunition shows main components like MMW seeker, jet reaction control system [2], autopilot, instrumentation package, and shaped charge warhead. The overall projectile is a modular delivery system with a modular submunition payload.

The function of the system is explained in Fig. 3. The complete EPHRAM projectile is fired like a conventional artillery round. Its initial flight is a ballistic trajectory. When first stage separation takes place, the thinwall canister is pushed out and proceeds on its ballistic trajectory. At this point typical speed is around Mach 1 and spin rate approximately 200 Hz, both being much too high for a safe function of the submunition. Therefore, a parachute is used to decelerate the canister down to 150 m/s and stabilize it at the same time, while spin brakes at the front and at the rear of the canister decrease the spin rate to about 10 Hz.

When suitable flight conditions have been reached, the submunition is pulled out of the canister. For initial stabilization the parachute remains attached until the wings of the submunition have been deployed and guarantee stable flight with almost vanishing spin rate.

Then the rear part of the canister is separated, and the submunition can start its controlled terminal maneuver. This includes the following sequence of actions: Initiation of vertical acquisition, attitude adjustment, search acquisition, tracking, seeker inhibition, impact on target.

The vertical plane is established by special MMW seeker algorithms. As soon as ground is located, the seeker starts a circular scan about a fixed axis. The trace on the ground is an ellipse. Its minor and major axes can be calculated from the radar range data. By this time the flight path is known and the autopilot is fully operating in its strapdown mode. The actuator squibs are fired, the thrusters are on full power, and the submunition is in controlled flight.

Now the submunition enters the attitude adjustment phase. It is travelling at 125 to 150 m/s, rolling less than 1 Hz and descending at a flight path inclination angle of -40° to -70° . At this point a variety of flight paths can be commanded; the particular one chosen depends on the seeker performance characteristics.

Search mode is now in progress, the submunition is held on an ideal flight path by the autopilot, and the MMW seeker scans for targets. Once a target has been detected, the seeker switches from search to track mode. The autonomous autopilot gyros play a key role, making significant trajectory variations possible and, with the aid of range information from the seeker, steering the submunition in for a top attack.

The submunition is controlled by a lateral blowing jet reaction control system. Its thrust forces cause changes in pitch and yaw and, consequently, angle of incidence. This results in high lift from eight large wings, sufficient to fly the desired terminal maneuvers and achieve optimal footprints.

For the control system three principal approaches were reviewed. Moving fins and canards, with their many moving parts, are not space efficient and cost effective enough. The explosive charge steering system warranted serious consideration and consumed much detailed analysis. However, this scheme is new for projectile maneuvering, and its extremely non-linear control behaviour places serious design constraints on the autopilot. In the end, the decision to use a jet reaction control actuator system was made by considering which technology does not only meet today's performance requirements, but also has the potential for next generation designs. It offers a growth path to higher performance, longer flight time as propellants will improve, and increased cost effectiveness by application of fluidic vortex amplifier arrangement.

2.2. Aerodynamic Characteristics

To model the aerodynamic characteristics of the EPHRAM submunition in the expected flight regime, preliminary theoretical calculations were carried out first, providing the static aerodynamic coefficients in the linear angle-of-attack range as well as an estimation of the nonlinear aerodynamic characteristics.

Then, to prove the results of the analysis, a number of static and dynamic wind tunnel tests were performed in the 3 m x 3 m low speed wind tunnel of the DFVLR in Braunschweig (MWB) and the 1 m x 1 m low speed facility (MUB) of the same institute. The large wind tunnel guaranteed an almost perfect simulation with results very close to reality. The smaller tunnel was useful because of its lower costs; however, the wind tunnel correc-

tions had to be established experimentally.

In the first series of wind tunnel tests a large variety of geometric variations was tested in order to confirm and improve the calculated aerodynamic data especially in the nonlinear range. The final configuration has 8 wings and a hemispherical nose. In Fig. 4, typical results for the coefficients of the tangential force, the normal force, and the pitching moment with respect to the submunition base are shown for two different roll orientations. One can see the extremely suitable behaviour of the submunition in general. The tangential force, Fig. 4a, is rather small due to the use of a NACA 0012 profile for the wings. The difference between the two roll orientations is significant only for angles of attack greater than 10 to 15°.

The normal force coefficient, Fig. 4b, shows an almost linear behaviour up to approximately 6°. For larger angles of attack, due to the large number of wings, flow separation effects result only in a lower gradient of the normal force (not in a breakdown!). This transition region ends at about 15°. Then the increase becomes almost linear again, however, the gradient remains smaller than in the beginning. The effect of roll orientation is rather small and can be neglected in the simulations, another advantage of the EPHRAM multi-wing concept. The pitching moment, Fig. 4c, has characteristics very similar to the normal force.

In the next step the dynamic roll coefficients had to be established. The EPHRAM concept requires very low roll rate due to seeker requirements. Therefore, the roll damping derivative is of considerable interest. As expected, the influence of the roll rate on the static coefficients turned out to be small enough to be negligible. Fig. 5 shows the EPHRAM configuration in the DFVLR wind tunnel mounted on a dynamic spin balance. Fig. 6 presents a typical result of the roll damping coefficient vs. angle of attack. Gradually increasing values in the beginning are followed by a sharp decrease and again a constant behaviour afterwards. It could be shown by detailed 6-DoF-simulations that the stationary roll rate of the submunition would stay well below the permitted limits. This result was confirmed during the field tests.

It is well known that, due to aerodynamic interference, lateral forces of supersonic missiles are almost doubled (jet spoiler effect [3-5]). To see whether this holds true also in the subsonic case, additional wind tunnel tests with working thrusters had to be performed. The result was that, indeed, a small benefit due to aerodynamic interference can be expected.

In order to learn more about the system, it was decided to apply system identification methods and extract the relevant static and dynamic characteristics from flight test data. To estimate the actual flight conditions, besides accelerations and angular rates, the angle of attack, angle of sideslip and velocity of the submunition have to be measured. For this the hemispherical nose can be used as a five-hole-probe. An additional test series has been performed in the wind tunnel for the calibration of this probe.

2.3. Simulation and Field Tests

During the development of the EPHRAM system, first the performance of the overall system had to be demonstrated under real field conditions. The field tests proved that the EPHRAM projectile, fired with the 8th charge, had full function as described above (projectile, canister with parachute and spin brakes, submunition with rear spin brakes and parachute, submunition dummy with wing deployment).

Parallel to these gun hardening tests, drop tests were performed in order to demonstrate the stable flight of the submunition on the one side and to develop a launch system for programmed flights on the other side. It could be shown that the aerodynamic wind tunnel results were correct and that the EPHRAM submunition had a very suitable flight behaviour. These drop tests were accompanied by numerous detailed 6-DoF flight simulations which helped to specify the gyros and accelerometers for the programmed flight.

A sketch of the EPHRAM programmed flight is shown in Fig. 7. To provide the necessary accuracy of the initial flight data, EPHRAM is dropped from an instrumented helicopter-lifted platform. After a free fall of approximately 1.000 m the submunition reaches its design environmental conditions, the jet reaction control system begins to work, and the submunition flies a controlled terminal maneuver. After the burn-out of the control actuator system a recovery system is activated for a soft landing of the submunition.

The tests were prepared by Monte Carlo simulations which gave an impression of the influence of possible system errors on the point of impact on the ground. Fig. 8 shows typical results. Looking in detail at the different error sources, one realizes that the error due to wind has the greatest influence. Without wind the impact point of the submunition shows only very small dispersion. From these simulations a footprint in the order of 500 m could be expected.

Fig. 9 provides typical results of a programmed flight (cinotheodolite data). It can be seen that the EPHRAM system works very well and is able to deliver the desired footprint which is indeed in the order of 500 m as the calculations had shown.

In order to identify the actual system and control parameters, additional programmed flights are planned. Their results shall be evaluated applying identification methods. In the following an introduction to this method is given and the efforts are described which have been made so far towards the scheduled identification flight tests.

3. NONLINEAR PARAMETER IDENTIFICATION CONCEPT

3.1 General Background

At the Institute for Flight Mechanics of DFVLR Maximum Likelihood Estimation methods and the corresponding computer programs are developed for the identification of general linear and non-linear systems. The systems may be non-linear in the state and control variables as well as in the parameters to be estimated [6 - 17].

Two major application are:

- Estimation of the flight mechanic parameters of aircraft, helicopter etc. [18 - 20];
- flight path reconstruction based on kinematic consistency checking of the flight test data [13].

At the same Institute sophisticated flight test instrumentation is developed to measure the required data [21,22]. Graphical work stations and a user-oriented software package are available to assist processing and a thorough analysis of the flight test data [23,24] before parameter estimation routines are applied.

Based on this experience the identification of less conventional vehicles, like sounding rockets, rotating shells or brilliant ammunition, is now undertaken [25 - 28]. For EPHRAM a study revealed the kind of instrumentation needed to identify the non-linear aerodynamic characteristics and thrust interference effects [27].

3.2 Maximum Likelihood Estimation Method

It is assumed that the system to be identified (Fig. 10) can be described by the general nonlinear dynamic equations [13]:

$$(3.2.1) \quad \dot{x}(t) = f(x(t), u(t) - \Delta u, \beta); \quad x(0) = x_0$$

$$(3.2.2) \quad y(t) = g(x(t), u(t) - \Delta u, \beta) + \Delta z$$

$$(3.2.3) \quad z(k) = y(k) + v(k) \quad k = 1, \dots, N$$

where x is the state vector, u is the control input vector, β is the vector of unknown system coefficients, y is the observation vector (model response) and $z(k)$ is the measurement vector sampled at N discrete time points. The measurement noise vector, v , is assumed to be Gaussian with zero mean and covariance matrix R .

In general, the initial values of the state variables x_0 , are unknown. Also the measurements of both, the control and output variables usually contain systematic errors Δu and Δz , respectively, so that the parameter estimation problem amounts to the determination of the parameter vector θ :

$$(3.2.4) \quad \theta^T = (\beta^T \quad x_0^T \quad \Delta u^T \quad \Delta z^T).$$

Maximum likelihood estimates of the parameters follow from minimization of the negative logarithm of the likelihood function

$$(3.2.5) \quad L = 1/2 \sum_{k=1}^N (z(k) - y(k))^T R^{-1} (z(k) - y(k)) + N/2 \ln |R|$$

with respect to θ , where

$$(3.2.6) \quad R = 1/N \sum_{k=1}^N (z(k) - y(k)) (z(k) - y(k))^T.$$

Differentiation of L with respect to θ and quasi linearization leads to a system of linear equations for the changes in parameter values $\Delta \theta$:

$$(3.2.7) \quad ((\partial y / \partial \theta)^T R^{-1} (\partial y / \partial \theta)) \Delta \theta = \sum_k (\partial y / \partial \theta)^T R^{-1} (z - y).$$

The cumbersome evaluation of the sensitivity matrix $\partial y / \partial \theta$ from partial differentiation of the system equations can be avoided if $\partial y / \partial \theta$ is approximated by numerical differences

$$(3.2.8) \quad \partial y / \partial \theta = (y(\theta + \delta \theta) - y(\theta)) / \delta \theta,$$

where $\delta \theta$ represents a small perturbation in θ . Information about the accuracy of the estimated parameter is given by the information matrix

$$(3.2.9) \quad J = \sum_k (\partial y / \partial \theta)^T R^{-1} (\partial y / \partial \theta).$$

The inverse of J provides an approximation for the estimation error covariance matrix of the parameters.

3.3 Mathematical Model of EPHRAM

3.3.1 State Equations

Six state equations follow from the Euler equations of motion in rotating coordinates x, y, z (Fig. 11):

$$\begin{aligned} \dot{u} &= vr - wq + g (\cos\theta_{in} \cos\psi_{in}) + \frac{\rho}{2} V^2 \frac{S}{m} C_X \\ (3.3.1) \quad \dot{v} &= wp - ur + g (\sin\theta_{in} \sin\theta_{in} \cos\psi_{in} - \cos\phi_{in} \sin\psi_{in}) + \frac{\rho}{2} V^2 \frac{S}{m} C_Y + \frac{1}{m} F_Y \\ \dot{w} &= uq - vp + g (\cos\phi_{in} \sin\theta_{in} \cos\psi_{in} + \sin\phi_{in} \sin\psi_{in}) + \frac{\rho}{2} V^2 \frac{S}{m} C_Z + \frac{1}{m} F_Z \end{aligned}$$

$$\begin{aligned} \dot{p} &= \frac{\rho}{2} V^2 \frac{SD}{I_x} C_l \\ (3.3.2) \quad \dot{q} &= \frac{\rho}{2} V^2 \frac{SD}{I_q} C_m + (1 - \frac{I_x}{I_q}) pr - \frac{x_T}{I_q} F_z \\ \dot{r} &= \frac{\rho}{2} V^2 \frac{SD}{I_q} C_n - (1 - \frac{I_x}{I_q}) pq + \frac{x_T}{I_q} F_y \end{aligned}$$

where the aerodynamic forces and moments are modelled by $C_X, C_Y, C_Z, C_l, C_m, C_n$, and the thrust control forces are contained in F_y and F_z (see Table 1, p.6).

Six more state equations are given for the trajectory in earth fixed coordinates x_{in}, y_{in}, z_{in} and the Euler angles $\psi_{in}, \theta_{in}, \phi_{in}$ (Fig. 12), respectively:

$$\begin{aligned} \dot{x}_{in} &= u T_{11} + v T_{21} + w T_{31} \\ (3.3.3) \quad \dot{y}_{in} &= u T_{12} + v T_{22} + w T_{32} \\ \dot{z}_{in} &= u T_{13} + v T_{23} + w T_{33} \end{aligned}$$

with transformation matrix T

$$(3.3.4) \quad T = \begin{bmatrix} \cos\theta_{in} \cos\psi_{in} & \cos\theta_{in} \sin\psi_{in} & -\sin\theta_{in} \\ \sin\phi_{in} \sin\theta_{in} \cos\psi_{in} & \sin\phi_{in} \sin\theta_{in} \sin\psi_{in} & \sin\phi_{in} \cos\theta_{in} \\ -\cos\phi_{in} \sin\psi_{in} & +\cos\phi_{in} \cos\psi_{in} & \\ \cos\phi_{in} \sin\theta_{in} \cos\psi_{in} & \cos\phi_{in} \sin\theta_{in} \sin\psi_{in} & \cos\phi_{in} \cos\theta_{in} \\ +\sin\phi_{in} \sin\psi_{in} & -\sin\phi_{in} \cos\psi_{in} & \end{bmatrix}$$

and

$$\begin{aligned} \psi_{in} &= (q \sin\phi_{in} + r \cos\phi_{in}) / \cos\theta_{in} \\ (3.3.5) \quad \theta_{in} &= q \cos\phi_{in} - r \sin\phi_{in} \\ \phi_{in} &= p + (q \sin\phi_{in} + r \cos\phi_{in}) \tan\theta_{in} \end{aligned}$$

During the flight tests EPHRAM is dropped vertically. If the vehicle's attitude was described by the usual Euler angles ψ, θ, ϕ relative to earth fixed coordinates x_g, y_g, z_g (Fig. 12), the initial value of θ would be $\theta(0) = -90^\circ$. This would cause numerical problems in Eqn. 3.3.5, which can be avoided by choosing x_{in}, y_{in}, z_{in} as earth fixed reference coordinates, respectively.

The relations between the trajectory data in both coordinate systems are given by

$$\begin{aligned} x_g &= -z_{in} ; \quad \dot{x}_g = -\dot{z}_{in} \\ (3.3.6) \quad y_g &= y_{in} ; \quad \dot{y}_g = \dot{y}_{in} \\ z_g &= x_{in} ; \quad \dot{z}_g = \dot{x}_{in} \end{aligned}$$

3.3.2 Aerodynamic Model

With its eight wings EPHRAM possesses almost rotational symmetry. In the case of rotational symmetry and for small roll rates the resultant aerodynamic force would lie in the x, V -plane. Therefore, the aerodynamic coefficients are described first in a coordinate system x_s, y_s, z_s in which no sideslip occurs (Fig. 11), and the velocity vector has the components

$$(3.3.7) \quad \mathbf{V}^T = (u_s, v_s, w_s)^T = (u, 0, \sqrt{v^2 + w^2})^T,$$

and the angle of incidence δ is

$$(3.3.8) \quad \delta = \arctan(w_s / u_s).$$

δ corresponds to the angle of attack α of the wind tunnel experiments (Fig. 4).

Neglecting the effects of roll angle and Mach number, the aerodynamic coefficients in body fixed coordinates are modelled by

$$C_X = C_{Xs0}$$

$$(3.3.9) \quad C_Y = C_{Ys0} \frac{v}{w_s}$$

$$C_Z = C_{Zs0} \frac{w}{w_s}$$

$$C_l = C_{l0} + C_{lp} p^*$$

$$(3.3.10) \quad C_m = C_{ms0} \frac{w}{w_s} + C_{mq} q^* + C_{m\delta} \frac{w}{w_s} \delta^*$$

$$C_n = -C_{ns0} \frac{v}{w_s} + C_{nq} r^* - C_{n\delta} \frac{v}{w_s} \delta^*.$$

Subscript s refers to the "s"-coordinate system, 0 to zero angular rates. Superscript $*$ refers to non-dimension angular rates:

$$(3.3.11) \quad p^* = p \frac{D}{2V}, \quad q^* = q \frac{D}{2V}, \quad \text{etc.}$$

3.3.3 Thrust Model and Systems Inputs

To identify the non-linear aerodynamics at high angles of incidence suitable thrust programs (Fig. 13) have been selected from 6 DoF-simulations for the identification flights. During a total flight time of 22 s, after a free fall phase of 5 to 10 s, thrust will be applied for 10 s. Therefore, identification is possible in both phases, with and without thrust, providing information about the thrust effects.

During the controlled flight phase thrust perpendicular to the body axis x is generated by gas expelled through nozzles into the directions $+y, -y, +z, -z$. The length of the thrust pulses is 8 ms followed by interrupts of 8 ms duration with zero thrust. The nozzles are positioned at distance x_T below the center of gravity (Table 1) of the flight test vehicle (Fig. 14).

length	l	0.570	m
diameter	D	0.144	m
reference area	S	$\pi/4 D^2$	m ²
mass	m	23.14	kg
center of gravity position	x_S	0.2615	m
thruster nozzle position	x_T	0.1695	m
moment of inertia	I_x	0.0837	kg m ²
moment of inertia	I_q	0.5621	kg m ²

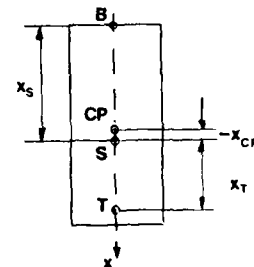


Table 1: EPHRAM flight test vehicle data

3.4 Flight Test Instrumentation

3.4.1 Measurement Concept

To be able to identify the system, sufficient information about each state and parameter of interest must be contained in the measured data. Either all state variables or their rates have to be measured. To compensate for integration errors rate data must be supported by measurements of the corresponding states, which may be sampled less frequently. An analysis of what was needed and what could be technically realized, led to the following measurement concept [27,28] (Table 2):

On-board instrumentation

1 accelerometer in x-direction	a_{x1}
2 accelerometers in y-direction	a_{y2}, a_{y4}
2 accelerometers in z-direction	a_{z3}, a_{z5}
3 rate gyros	p, q, r
3 pressure transducers (α, β, V -sensor)	$\alpha, \beta, \rho/2 V^2$
data acquisition and processing system	thrust on/off status

External measurements

radar / cinetheodolites	x_g, y_g, z_g
wind balloon	$V_w(z_g), T(z_g), P(z_g)$
launch platform, initial data	$\psi(0), \theta(0), \phi(0)$

Table 2: Required data for parameter identification

The translational states are observed by three accelerometers positioned near the center of gravity with their sensitive axes parallel to the body fixed axes. They are supported by α, β, V -measurements and x_g, y_g, z_g -data from radar tracking. For the determination of V the density ρ is to be computed from known atmospheric data T, P as a function of altitude.

The rotational states are observed by three highly accurate rate gyros for p, q and r , which are also needed for the thrust control system of EPHRAM, and by two additional accelerometers, positioned forward at some distance from the center of gravity, looking into the y - and z -directions. The angular position has to be computed by integration with no more supporting information. Therefore, it is essential to measure the initial attitude at release, $\psi(0), \theta(0), \phi(0)$, from which $\psi_{in}(0), \theta_{in}(0)$ and $\phi_{in}(0)$ follow.

Since the initial velocity of the test vehicle is almost zero at release, the wind velocity vector plays an important role during the first seconds of free fall. For the identification it would be optimal to have only small atmospheric disturbances.

The on-board digital data acquisition and processing system is capable of storing all data in memory for up to 30 s of flight time at a sampling rate of up to 250 Hz. The resolution is 12 bit. Parallel, the data are transmitted to a ground station by PCM-telemetry.

3.4.2 α, β, V -Sensor

The α, β, V -Sensor (Fig. 15) was calibrated in the low speed wind tunnel at the DFVLR Braunschweig [29]. Measured were the pressure signals P_1 through P_5 at 5 positions, the static pressure P and the dynamic pressure $\rho/2 V^2$, respectively. The pressure coefficients

$$(3.4.1) \quad C_{PA} = \frac{P_1 - P_3}{P_5 - P}; \quad C_{PB} = \frac{P_4 - P_2}{P_5 - P}; \quad C_{PT} = \frac{P_5 - P}{\rho/2 V^2}$$

are nonlinear functions of α, β and V , but become linear for small angles of incidence. Some representative results of the calibration are given in Fig. 16. To solve for α, β and V the calibration data can be approximated by polynomials.

Although some errors are to be expected during drop tests due to temperature drifts of the pressure signals, the information gained should be sufficient to reconstruct v and w for the identification.

3.4.3 Launch Platform

The EPHRAM test vehicle is launched from an instrumented platform, hanging 50 m below a helicopter (Fig. 17). The signals from a high precision three-axis magnetometer and a gyro for pitch and roll angle (Fig. 18) are registered with a resolution of 12 bits at a sampling rate of 250 /s. From these data the micro-processor system on the platform immediately computes pitch, roll and heading [22]. This information is transferred to the helicopter and to the EPHRAM control computer for the programmed flight. On board the helicopter the data are stored and displayed for the test engineer.

Special emphasis was put on the accuracy of the platform measurements. The resolution and the linearity of the gyro resulted in an accuracy of $\pm 1/2^\circ$ in pitch and roll. The error in the heading from magnetic field measurement does not exceed $\pm 1^\circ$. To get also this error down to $\pm 1/2^\circ$, a more extensive calibration procedure was performed, applying laser instrumentation to measure the misalignment between the axes of the gyro, the magnetometer and the EPHRAM test vehicle. Also a high precision inertial reference system was used during the calibration of the launch platform after all sensors were assembled.

Fig. 19 shows an example of the small heading measurement error $\Delta\psi$ which was achieved after application of an higher order error model [30].

3.5 Observation Equations

In some cases the states can be measured directly, in other cases complicated non-linear functions of the states are registered.

Accelerometers

$$\begin{aligned}
 a_{x1m} &= a_{xS} - (q^2 + r^2) x_1 + (pq - \dot{r}) y_1 + (pr + \dot{q}) z_1 \\
 a_{y2m} &= a_{yS} + (pq + \dot{r}) x_2 - (p^2 + r^2) y_2 + (qr - \dot{p}) z_2 \\
 (3.5.1) \quad a_{z3m} &= a_{zS} + (pr - \dot{q}) x_3 + (qr + \dot{p}) y_3 - (p^2 + q^2) z_3 \\
 a_{y4m} &= a_{yS} + (pq + \dot{r}) x_4 - (p^2 + r^2) y_4 + (qr - \dot{p}) z_4 \\
 a_{z5m} &= a_{zS} + (pr - \dot{q}) x_5 + (qr + \dot{p}) y_5 - (p^2 + q^2) z_5
 \end{aligned}$$

where $(a_{xS}, a_{yS}, a_{zS})^T$ is the acceleration that would be measured at the center of gravity S

$$\begin{aligned}
 a_{xS} &= \dot{u} - (vr - wq) - g (\cos\theta_{in} \cos\psi_{in}) \\
 (3.5.2) \quad a_{yS} &= \dot{v} - (wp - ur) - g (\sin\phi_{in} \sin\theta_{in} \cos\psi_{in} - \cos\phi_{in} \sin\psi_{in}) \\
 a_{zS} &= \dot{w} - (uq - vp) - g (\cos\phi_{in} \sin\theta_{in} \cos\psi_{in} + \sin\phi_{in} \sin\psi_{in})
 \end{aligned}$$

and $(x_j, y_j, z_j)^T$ is the position vector of the jth accelerometer.

Rate gyros:

$$(3.5.3) \quad p_m = p; \quad q_m = q; \quad r_m = r$$

α, β, V -Sensor:

$$(3.5.4) \quad \tan \alpha_m = w/u; \quad \tan \beta_m = v/\sqrt{u^2 + w^2}; \quad V_m^2 = u^2 + v^2 + w^2$$

Radar:

$$(3.5.5) \quad x_{gm} = -z_{in}; \quad y_{gm} = y_{in}; \quad z_{gm} = x_{in}$$

Initial data:

$$\begin{aligned}
 \tan\psi_{in}(0) &= -\sin\psi(0) \tan\theta(0) \\
 (3.5.6) \quad \sin\theta_{in}(0) &= \cos\psi(0) \cos\theta(0) \\
 \tan\phi_{in}(0) &= \frac{\sin\phi(0) \sin\theta(0) \cos\psi(0) - \cos\phi(0) \sin\psi(0)}{\cos\phi(0) \sin\theta(0) \cos\psi(0) + \sin\phi(0) \sin\psi(0)}
 \end{aligned}$$

During the identification bias terms are to be added to the measurement equations as discussed in chapter 3.2.

3.6 Verification of the Identification Concept

Before the expensive flight test instrumentation was built and calibrated, the identification concept, described above, was verified by an estimation of the nonlinear aerodynamic characteristics from simulated data [28]. For this, several 6 DoF-simulations were made based on the EPHRAM wind tunnel data from static and dynamic tests. Each aerodynamic coefficient was approximated as a function of δ by broken lines. Then, simulated experimental data were generated, adding noise, biases and sensor errors to the observation equations in chapter 3.5. Finally, Maximum Likelihood estimation was applied for the flight path reconstruction and the estimation of the aerodynamic coefficients. As an example the force coefficient $C_{z\delta 0}(\delta)$ and the pitching moment coefficient $C_{m\delta 0}(\delta)$ about the center of gravity are shown in Fig. 20. The solid lines are the wind tunnel coefficients, the dashed lines the coefficients identified from simulated data.

4. ANALYSIS OF A FLIGHT TEST WITH REDUCED SENSOR PACKAGE

4.1 Flight Path Reconstruction

On one of the functional flight tests measurements were taken by the accelerometers, gyros and cinetheodolites (Fig. 21). The vehicle (Table 1) was dropped from 2203 m above ground. The wind varied between 6 and 10 m/s, which caused a considerable initial disturbance.

A flight path reconstruction yielded the following results:

- The quality of the gyroscopic data is high enough to determine the angular accelerations by differentiation of the filtered measured rates until thrust is applied (Fig. 22):

$$(4.1.1) \quad \dot{p} = \dot{p}_m; \quad \dot{q} = \dot{q}_m; \quad \dot{r} = \dot{r}_m$$

- There is considerable scatter and bias in \dot{q} and \dot{r} , as computed from the signal differences of the corresponding accelerometers

$$(4.1.2) \quad \begin{aligned} \dot{q} &= pr + [-(a_{z5}-a_{z3}) + (qr+\dot{p})(y_5-y_3) - (p^2+q^2)(z_5-z_3)] / (x_5-x_3) \\ \dot{r} &= -pq + [(a_{y4}-a_{y2}) + (p^2+r^2)(y_4-y_2) - (qr-\dot{p})(z_4-z_2)] / (x_4-x_2) \end{aligned}$$

- From Eqns. (3.5.1), (3.5.3) and (4.1.1) the accelerations at the center of gravity a_{xS} , a_{yS} , a_{zS} can be determined.
- The total velocity V can be estimated from the cinetheodolite and wind data.
- Since neither initial data nor α and β were recorded, it was not possible to reconstruct the direction of the velocity vector and the angular position with any degree of confidence. Therefore, no attempt was made for a full parameter estimation. But, from an analysis of the free fall phase the position of the center of pressure, x_{CP} , and the average normal force derivative, $C_{N\alpha} = -C_{Z\alpha} = -C_{Z\beta}$, at low angle of incidence can be evaluated.

4.2 Center of Pressure

After release, due to the initial disturbances, EPHRAM began to roll and to oscillate (Fig. 21). A cross plot of $q(r)$ in Fig. 23 reveals that after $t = 6$ s EPHRAM performed a coning motion with decreasing amplitude, while rolling slowly at about -30° per oscillation period.

Until thrust is applied the motion is governed by mass and aerodynamic forces only. Angular accelerations are caused by aerodynamic and gyroscopic moments. For sufficiently small roll rate, the gyroscopic moments can be neglected. Thus,

$$(4.2.1) \quad \begin{aligned} a_{yS} &= \frac{\rho}{2} V^2 \frac{S}{m} C_Y; & a_{zS} &= \frac{\rho}{2} V^2 \frac{S}{m} C_Z \\ \dot{q} &= \frac{\rho}{2} V^2 \frac{SD}{I_q} C_m; & \dot{r} &= \frac{\rho}{2} V^2 \frac{SD}{I_q} C_n \end{aligned}$$

In Fig. 24 cross plots of $\dot{q}(a_{zS})$ and $\dot{r}(a_{yS})$ for $t = 6$ to 10 s indicate an almost linear dependence, therefore, in the mean

$$(4.2.2) \quad \begin{aligned} \bar{C}_m &= k_m \frac{I_q}{Dm} \bar{C}_Z; & \text{with } k_m &= 0.75 \text{ [1/m]} \\ \bar{C}_n &= k_n \frac{I_q}{Dm} \bar{C}_Y; & \text{with } k_n &= -0.80 \text{ [1/m]} \end{aligned}$$

Setting

$$(4.2.3) \quad \bar{C}_m = -\frac{x_{CP}}{D} \bar{C}_Z; \quad \bar{C}_n = \frac{x_{CP}}{D} \bar{C}_Y$$

leads to

$$(4.2.4) \quad x_{CP} / D = -0.156 \text{ to } -0.166$$

and

$$(4.2.5) \quad x_{CP} = -0.022 \text{ to } -0.024 \text{ [m]}.$$

This means that during the coning motion the position of the center of pressure CP was between 22 and 24 mm behind the center of gravity S, which is in good agreement with the results from static wind tunnel measurements (Fig. 25).

4.3 Aerodynamic Derivatives

The normal force derivative and the pitch damping coefficient are estimated from the frequency and the damping of the coning motion, which can be described by a linear combination of two planar motions. Assuming rotational symmetry, it is sufficient to focus on the motion in the x, z -plane. Neglecting roll ($p = 0$, $\phi_{in} = 0$), then for small angles of attack and pitch ($\alpha = w/V$, $\sin \theta_{in} = \theta_{in}$, $\cos \theta_{in} = 1$, $u = V$), the equations of motion become

$$\begin{aligned} \dot{w} &= Vq + g \theta_{in} + \frac{\rho}{2} V^2 \frac{S}{m} C_{Z\alpha} \frac{w}{V} \\ (4.3.1) \quad \dot{q} &= \frac{\rho}{2} V^2 \frac{SD}{I_q} \left(-\frac{x_{CP}}{D} C_{Z\alpha} \frac{w}{V} + C_{mq} \frac{D}{2V} q \right) \\ \dot{\theta}_{in} &= q \end{aligned}$$

For constant velocity V this is a system of homogeneous linear differential equations for the displacements of w , q , θ_{in} from vertical descent, which has solutions of the type $w = w_0 e^{\lambda t}$ with complex exponent $\lambda = \zeta \pm i\omega$.

The characteristic polynomial

$$(4.3.2) \quad \lambda^3 + a_2 \lambda^2 + a_1 \lambda + a_0 = 0,$$

where

$$\begin{aligned} a_2 &= -\frac{\rho SV}{2m} \left(C_{Z\alpha} + \frac{mD^2}{2I_q} C_{mq} \right) \\ (4.3.3) \quad a_1 &= \frac{\rho SDV^2}{2I_q} C_{Z\alpha} \left(\frac{x_{CP}}{D} + \frac{\rho SD}{4m} C_{mq} \right) \\ a_0 &= \frac{\rho SDV^2}{2I_q} \frac{g}{V} \frac{x_{CP}}{D} C_{Z\alpha} \end{aligned}$$

has one real root λ_1 and a pair of complex roots $\lambda_{2,3} = \zeta_2 \pm i\omega_2$. Introducing the system parameters (Table 1) into Eqn. (4.3.3) and neglecting terms of lesser importance, first order approximations emerge for the roots:

$$\begin{aligned} \lambda_1 &= -a_0/a_1 = -g/V \\ (4.3.4) \quad \zeta_2 &= -(a_2 + \lambda_1)/2 = \frac{\rho SV}{4m} \left(C_{Z\alpha} + \frac{mD^2}{2I_q} C_{mq} + \frac{2mg}{\rho SV^2} \right) \\ \omega_2^2 &= a_1 = \frac{\rho SDV^2}{2I_q} \frac{x_{CP}}{D} C_{Z\alpha} \end{aligned}$$

Eqn. (4.3.4) can be solved for $C_{Z\alpha}$ and C_{mq} , with ζ_2 and ω_2 being the damping and the frequency of the coning motion. C_{mq} and $C_{Z\alpha}$ are both negative and contribute to the damping, while the ratio of the weight to the dynamic pressure reduces the damping. Thus, for small velocity, the coning motion is less damped. The square of the frequency is proportional to $x_{CP} C_{Z\alpha}$.

The next step is to determine ζ_2 and ω_2 . Two difficulties arise: Firstly, during the drop test, the vehicle's speed increased from $V = 46.9$ to 80.3 m/s between 6 to 10 s. This caused corresponding variations in ζ and ω and contradicts the assumption of linearity in Eqn. (4.3.1). Secondly, taking ζ_2 from either q or r is not possible in a straight forward way. The amplitudes of q and r decrease due to damping and additionally vary, because the angular velocity vector Ω is projected on and measured in rotating coordinates. Therefore, in the time history plot (Fig. 26), the yaw rate r seems to be less damped than the pitch rate q .

The effect of roll becomes obvious in the following simplified case: If the components of Ω in earth fixed coordinates were

$$(4.3.5) \quad p_{in} = p_0; \quad q_{in} = q_0 \sin \omega t e^{\zeta t}; \quad r_{in} = r_0 \cos \omega t e^{\zeta t}$$

then its components in a coordinate system, which rotates only at constant rate p_0 about x_{in} , are given by

$$\begin{aligned} p &= p_0 \\ (4.3.6) \quad q &= (q_0 \sin \omega t \cos p_0 t - r_0 \cos \omega t \sin p_0 t) e^{\zeta t} \\ r &= (q_0 \sin \omega t \sin p_0 t + r_0 \cos \omega t \cos p_0 t) e^{\zeta t} \end{aligned}$$

Roll is eliminated from

$$(4.3.7) \quad (q^2 + r^2)^{1/2} = (q_0^2 \sin^2 \omega t + r_0^2 \cos^2 \omega t)^{1/2} e^{\zeta t}.$$

Therefore, ω_2 and ζ_2 are determined from $(q_m^2 + r_m^2)^{1/2}$, which oscillates at frequency 2ω , see Fig. 26. The mean values and standard deviations over the time interval from 6 to 10 s are:

$$(4.3.8) \quad \begin{aligned} \zeta_2/V &= -0.0028 [1/m] \pm 36 \% \\ \omega_2/V &= 0.080 [1/m] \pm 2.3 \% . \end{aligned}$$

From this follows

$$(4.3.9) \quad C_{Z\alpha} = \frac{1}{x_{CP}} \frac{2 I_q}{\rho S} \frac{\omega_2^2}{V^2} = -16.8 \text{ to } -20.1 .$$

The gradient of the pitching moment about the wind tunnel reference point B (Fig. 25) becomes

$$(4.3.10) \quad C_{m\alpha}(B) = -C_{Z\alpha} (x_B + x_{CP})/D = 27.7 \text{ to } 33.4 .$$

Both results match well with the corresponding static wind tunnel coefficients at small angles of attack (Fig. 4).

The pitch damping coefficient C_{mq} cannot be determined with the same accuracy. Taking mean values of $C_{Z\alpha}$, ζ_2/V and V leads to $C_{mq} = +2.4$, which has the wrong sign and is not in agreement with the result from theoretical considerations ($C_{mq} = -7$). But, assuming $C_{mq} = -7$, then from Eqn. (4.3.4) $\zeta_2/V = -0.0035$ is computed, which lies well within the experimental scatter of ζ_2/V .

5. CONCLUSIONS

In a common effort of Rheinmetall and DFVLR an approach was made towards the identification of the EPHRAM brilliant ammunition system with aerodynamic and thrust control forces. The necessary methods, a flight test vehicle, and the instrumentation have been developed. During flight tests with reduced sensor equipment the desired trajectory was flown. An analysis of one of these tests verified static wind tunnel results at small angle of attack. It also showed that, for the scheduled identification tests, the full sensor equipment, including an α, β, V -sensor, is required.

6. REFERENCES

- [1] N.N.: "LN9300, Blatt 1: Flugmechanik", Normenstelle der Luftfahrt, 7022 Laufelden, December 1970.
- [2] Peller, H., Buechele-Buecher, S.: Advances in Guidance and Control Systems and Technology. AGARD CP-411, 1986.
- [3] Heyser, A., Maurer, F.: Experimentelle Untersuchungen an festen Spoilern und Strahlspoilern bei Machzahlen von 0,6 bis 2,8. Z. Flugwiss. 10 (1962).
- [4] Gilman, B.G.: Control Jet Interaction. J. Spacecraft 4 (1971), pp. 334-339.
- [5] Spring, D.J.: An Experimental Investigation of the Interference Effects Due to a Lateral Jet Issuing from a Body of Revolution over the Mach Number Range of 0.8 to 4.5. U.S. Army Missile Command, Redstone Arsenal, Alabama, Rep. No. RD-TR-68-10, 1968.
- [6] Plaetschke, E.: Parameter Identification: Its Purpose, Methods, and Resulting Requirements for Flight Test Instrumentation. AGARD-Cranfield-DFVLR Short Course on "Flight Test Instrumentation", June 1977, Paper No. 14.
- [7] Hamel, P.G. (Editor): Parameter Identification. AGARD LS-104, Papers 1-10, 1979.
- [8] Plaetschke, E. and Schulz, G.: Practical Input Signal Design. AGARD Lecture Series No. 104 "Parameter Identification", 1979, Paper No. 3.
- [9] Koehler, R., Marchand, M., Plaetschke, E., Kaletka, J., Rohlf, D. and Doherr, K.-F.: Systemidentifizierung am Institut für Flugmechanik. DFVLR Institut für Flugmechanik, Braunschweig, Dec. 1980.
- [10] Hamel, P.G.: Determination of Aircraft Dynamic Stability and Control Parameters from Flight Testing. AGARD LS-114, Paper 10, 1981.

- [11] Plaetschke, E., Mulder, J.A. and Breeman, J.H.: Flight Test Results of Five Input Signals for Aircraft Parameter Identification. IFAC Identification and System Parameter Estimation 1982, Washington D.C., USA, 7-11 June 1982, pp. 1149-1154.
- [12] Plaetschke, E., Mulder, J.A. and Breeman, J.H.: Results of Beaver Aircraft Parameter Identification. DFVLR-FB 83-10, 1983.
- [13] Jategaonkar, R.V. and Plaetschke, E.: Maximum Likelihood Estimation of Parameters in Nonlinear Flight Mechanics Systems. IFAC Identification and System Parameter Estimation 1985, York, UK, 3-7 July 1985, pp. 663-668.
- [14] Plaetschke, E. and Weiß, S.: Aircraft System Identification - Determination of Flight Mechanics Parameters. In: "Application of System Identification in Engineering" (Ed. H.G. Natke). International Centre for Mechanical Sciences, CISM, Courses and Lectures No. 296, Springer, 1988.
- [15] Jategaonkar, R.V. and Plaetschke, E.: Maximum Likelihood Estimation of Parameters in Linear Systems with Process and Measurement Noise. DFVLR-FB 87-20, 1987.
- [16] Hamel, P.G.: Techniques for Model Identification and Design of Model Following Control Systems. Academie Nationale de L'Air et de L'Espace, O.N.E.R.A.-CERT, International Symposium on Stability, Paris, 3-5 November 1987, pp. 257-283.
- [17] Hamel, P.G.: Flight Vehicle System Identification, Status and Prospects. In: Systemidentifikation in der Fahrzeugdynamik, SFB 212 "Sicherheit im Luftverkehr", Paper 5, DFVLR-Mitt. 87-22, 1987.
- [18] Krag, B., Labarrere, M., Foster, G.W. and Breeman, J.H.: Application of Complementary Parameter Identification Techniques to Flight Test Data of Transport Aircraft. SFTE 18th Annual Symposium "Flight Testing, World Wide", 28 Sept.-2 Oct. 1987, Amsterdam.
- [19] Tischler, M.B. and Kaletka, J.: Modeling XV-15 Tilt Rotor Aircraft Dynamics by Frequency and Time-Domain Identification Techniques. AGARD CP-423, Paper 9, 1987.
- [20] Brockhaus, R. and Doherr, K.-F. (Editors): Systemidentifikation in der Fahrzeugdynamik. SFB 212 "Sicherheit im Luftverkehr", DFVLR-Mitt. 87-22, 1987.
- [21] Hanke, D. and Bouwer, G.: DFVLR In-Flight Simulators ATTAS and ATThES for Flying Qualities and Flight Control Research. AGARD CP-408, Paper 23, 1986.
- [22] Gandert, R.: IDES: Ein System zur Ermittlung der flugmechanischen Lagewinkel einer Plattform mit Hilfe eines kreiselgestützten Magnetometertripels. Internal Report DFVLR-IB 111-87/15, 1987.
- [23] Doherr, K.-F. and Wulff, G.: Interactive Data Analysis. DFVLR-Mitt. 86-07, 1986.
- [24] Doherr, K.-F. and Wulff, G.: DIVA-Flugversuchsauswertung für ATTAS. DFVLR-Jahresbericht 1986, ISSN 0070-3966, 1987.
- [25] Subba Raju, P.V. and Plaetschke, E.: Trajectory Reconstruction and Parameter Estimation from Flight Data of a Satellite Launch Vehicle Using Maximum Likelihood Method. Internal Report DFVLR-IB 111-87/54, 1987.
- [26] Doherr, K.-F., Hammelrath, F., Plaetschke, E. and Saliaris, C.: Durchführbarkeitsstudie über Parameteridentifizierung bei EPHAG. Internal Report DFVLR-IB 111-84/8, 1984.
- [27] Hammelrath, F. and Saliaris, C.: Parameteridentifizierung für EPHRAM. Internal Report DFVLR-IB 111-86/20, 1986.
- [28] Weiß, S., Hammelrath, F. and Saliaris, C.: Parameteridentifizierung für EPHRAM: Verifizierung des Identifizierungskonzepts. Internal Report DFVLR-IB 111-87/12, 1987.
- [29] Mastreiter, W.: Eichung eines EPHRAM-Modells für Strömungsrichtungsmessung; 4. Meßabschnitt. Internal Report DFVLR-IB 19111-87C06, 1987.
- [30] Moch, H.: Programm zur Berechnung des flugmechanischen Gierwinkels Psi mit Hilfe eines kreiselgestützten Magnetometertripels in Echtzeit. Internal Report DFVLR-IB 111-87/18, 1987.

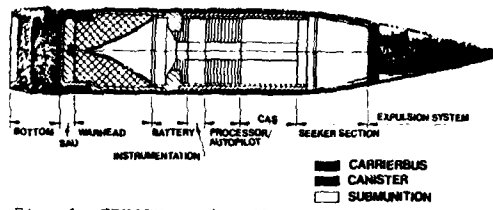


Fig. 1: EPHRAM projectile

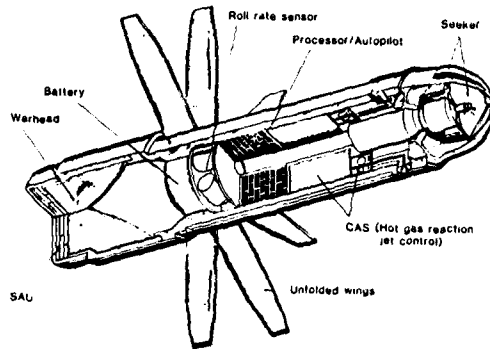


Fig. 2: EPHRAM submunition

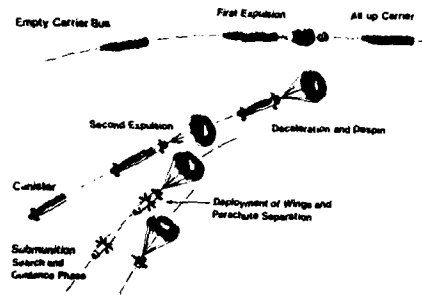


Fig. 3: EPHRAM functional sequence

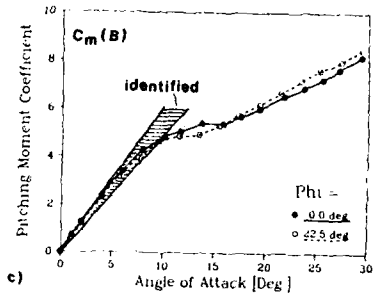
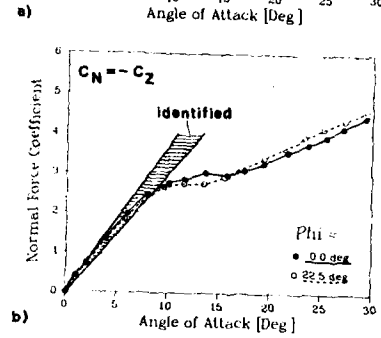
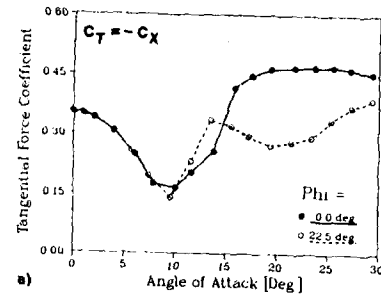
Fig. 4: Aerodynamic coefficients from static wind tunnel tests for two different roll angles Φ ; C_m about B at base of model^m (Fig 6)

Fig. 5: Dynamic wind tunnel test set-up

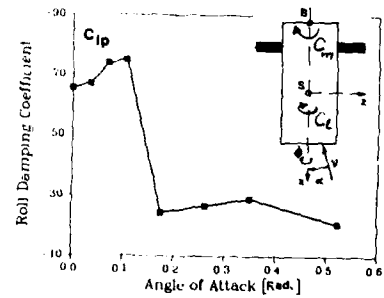


Fig. 6: Roll damping coefficient

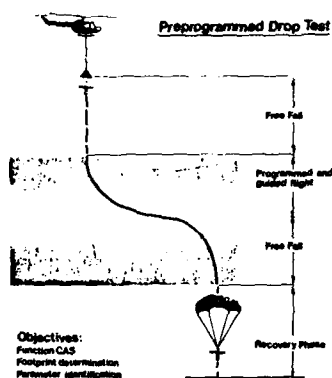


Fig. 7: EPHRAM programmed flight profile

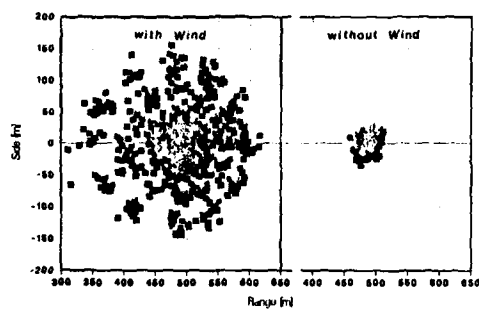


Fig. 8: Monte Carlo simulation results for the programmed flight

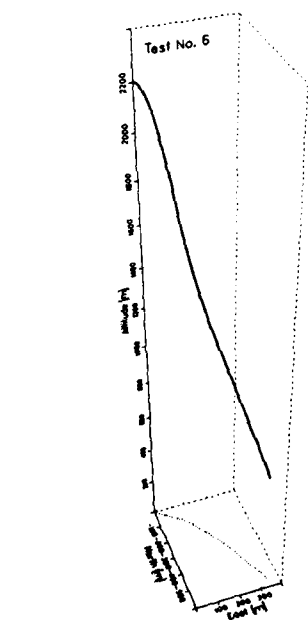


Fig. 9: Trajectory of programmed flight

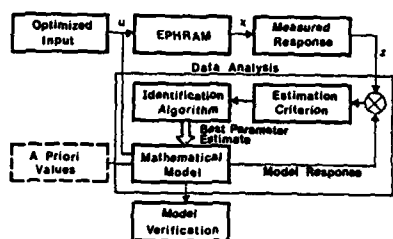


Fig. 10: Parameter identification concept

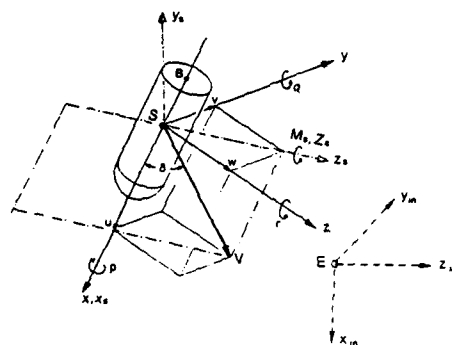


Fig. 11: Coordinate systems

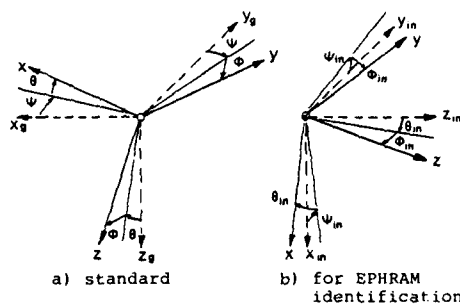


Fig. 12: Euler angles and Earth fixed coordinates

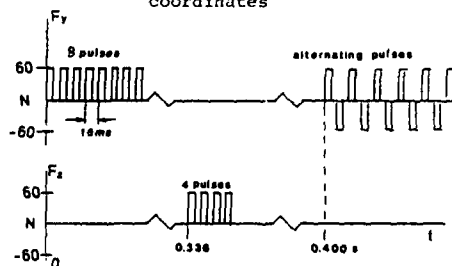


Fig. 13: Example of thrust control program for identification flights

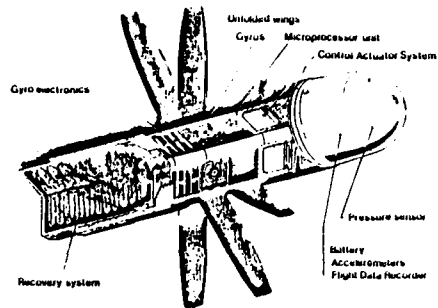


Fig. 14: EPHRAM munition test vehicle

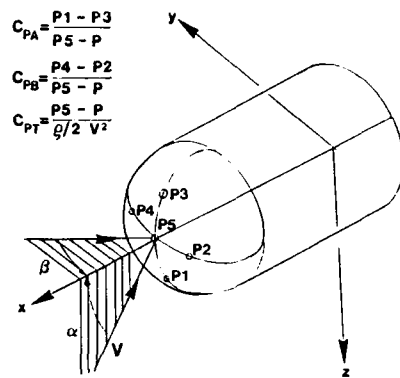
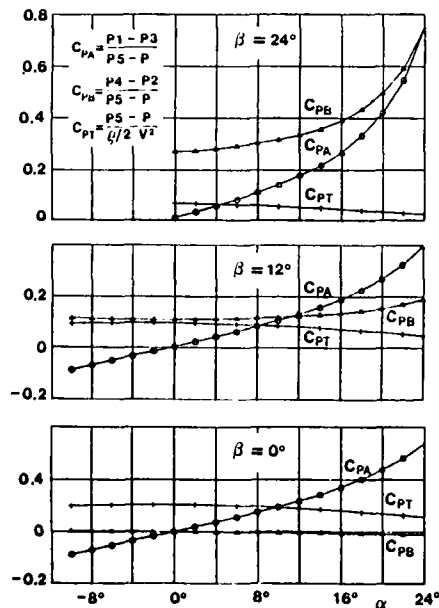
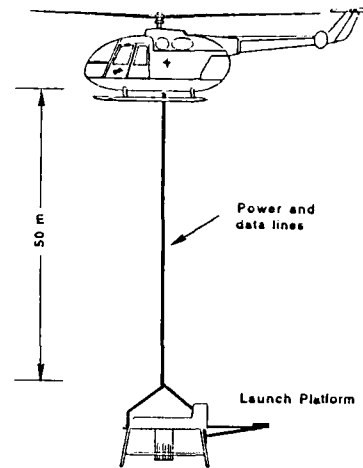
Fig. 15: α, β, V -sensorFig. 16: Calibration of the α, β, V -sensor

Fig. 17: Drop test arrangement

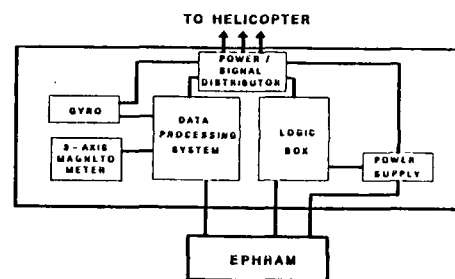


Fig. 18: EPHRAM launch platform instrumentation

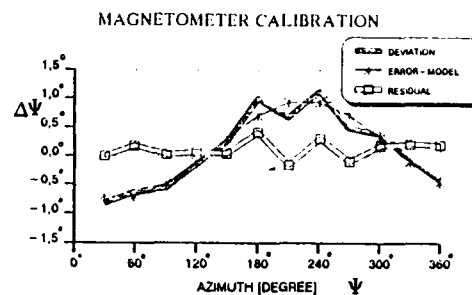


Fig. 19: Heading error of launch platform

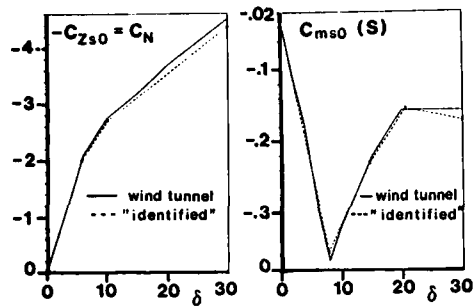


Fig. 20: Aerodynamic coefficients from static wind tunnel and "identified" from noise corrupted simulated data

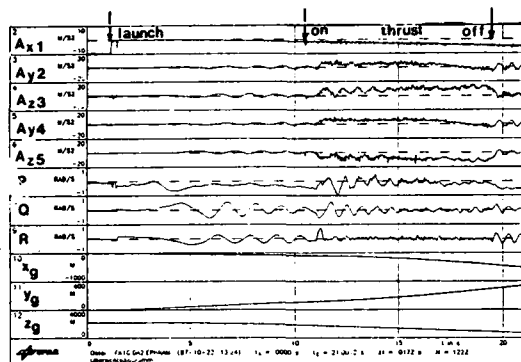


Fig. 21: Recorded data of flight test No. 6

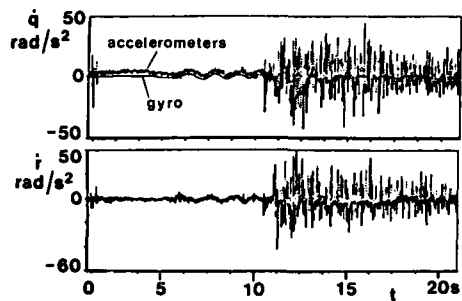


Fig. 22: Reconstructed angular rates

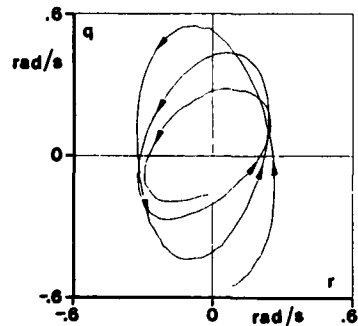


Fig. 23: Coning motion from $t = 6$ to 10 s

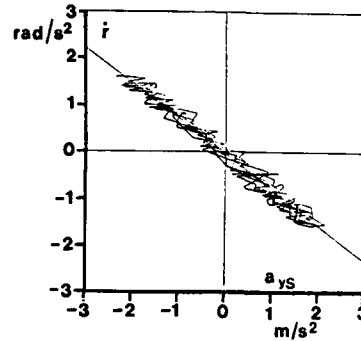
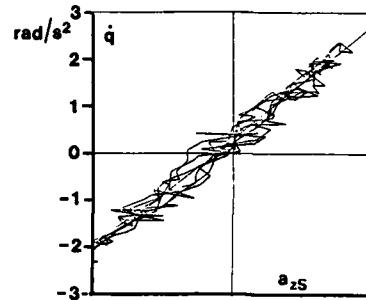


Fig. 24: Angular vs. translational accelerations for $t = 6$ to 10 s

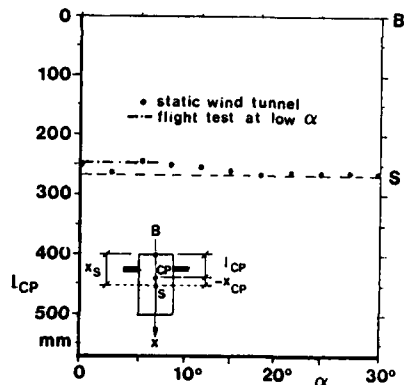


Fig. 25: Distance of center of pressure l_{CP} (a) from base (B)

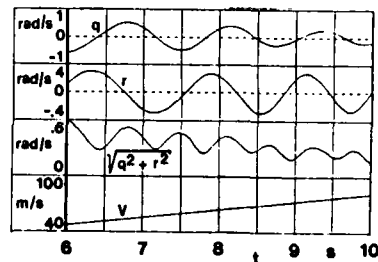


Fig. 26: Damped coning motion

VALIDATION OF MISSILE SIMULATION

by

Werner Bub
MESSERSCHMITT-BÖLKOW-BLOHM GmbH
Defense Systems Division - AS53
P.O. Box 80 11 49
8000 München 80
Federal Republic of Germany

SUMMARY

One of the key findings of AGARDograph No. 279 "Survey of Missile Simulation and Flight Mechanics in NATO" was that very little effort was expended in missile simulation validation. No standard or well-defined techniques were in use adequate to communicate confidence in missile simulations to persons not directly involved in the process of simulation development. Therefore the AGARD FMP formed Working Group 12 to examine missile simulation validation and confidence building techniques. The group recommended a simulation terminology that should simplify the validation process. In addition a hierarchical model representation called "CLIMB" was recommended in order to organize and document the knowledge base for simulation development as well as the data bases used for simulation validation.

1. BACKGROUND

During the late 1970s/early 1980s AGARD's Flight Mechanics Panel was investigating the feasibility of the cooperative use of NATO community facilities for the simulation, test and evaluation of missile systems and subsystems. Therefore the FMP sponsored a survey of missile simulation facilities which was conducted by Willard M. Holmes of the US Army Missile Command at Redstone Arsenal and which was reported in AGARDograph No. 279, "Survey of Missile Simulation and Flight Mechanics Facilities in NATO". A basic prerequisite of cooperative use of simulation facilities is a certain commonality and coherence in simulation methodology. One of the key findings in the survey was that very little effort was being expended especially in missile simulation validation and, furthermore, validation techniques themselves are generally not standard, often being ill-defined or undocumented. This fact motivated the formation of FMP Working Group 12 "Validation of Missile System Simulation", of which the author was a member. This paper is an invited summary of the Working Group's findings as documented in AGARD Advisory Report No. 206, "Final Report on FMP Working Group WG-12 on Validation of Missile System Simulation".

2. THE PROBLEM

There is abundant literature available on simulation verification/validation techniques. These are mostly mathematical and also heuristic methods to compare two different sets of data. The most prominent ones are depicted in Figure 1.

These methods are supplemented by procedures assuring that the computerized simulation model works correctly, as known from software engineering.

In actual practice the team of engineers which actively establishes a system simulation submits it to numerous tests, changes the model and executes it again until a certain "good feeling" about the simulation has grown up within the participating persons. To a large extent this is a psychological process. It is supported by model characteristics such as coherence to relevant theory and past experience and the model being able to produce "useful answers" with respect to the model developers' views of the modelled reality. As soon as a "good feeling" is achieved the simulation is considered "valid". In general, and especially with regard to cooperative and mutual use of simulation capabilities, the question is very important, how this "good feeling" can be communicated to a non-developer or third party user of the model or facility.

The working group concluded that the most important objective was to find a method of organizing simulation validation techniques rather than producing another collection of actual methods. The objective therefore was to develop a method that was suitable to communicate such an abstract, non-technical and more psychological item as is "confidence". Therefore it was attempted to find a new kind of "organization of thought" which resulted in the process called CLIMB and which is described in section 4.

3. TERMINOLOGY

3.1 INTRODUCTION

To provide a proper framework to review the credibility of a simulation, it is convenient to divide the simulation environment into elements as depicted in Figure 2. The dashed arrows describe the processes which relate elements to each other and the bold arrows refer to the procedures which evaluate the credibility of these processes.

3.2 DESCRIPTION OF TERMINOLOGY

REALITY	An entity, situation, or system which has been selected for analysis.
CONCEPTUAL MODEL	The CONCEPTUAL SYSTEM MODEL represents the model builder's perception and understanding of the system to be simulated. It consists of a hypothetical complete explanation of how the system functions. It often takes the form of verbal description, complemented by block diagrams, flow charts and systems specifications. In most cases, the large complexity of the conceptual model precludes its consideration as a possible simulation model. In view of the requirements of the intended simulation studies, the modeler establishes the complexity of the simulation model and degree of detail necessary. This information, generally in descriptive (verbal) form, complemented by block diagrams and flow charts constitutes the CONCEPTUAL SIMULATION MODEL or abbreviated to CONCEPTUAL MODEL. At the same time, this represents the requirements on the FORMAL SIMULATION MODEL.
FORMAL MODEL	provides the technical description of the simulation model. It takes the form of mathematical equations, adequate description of logic flow and model data, complemented by the necessary detailed text.
THEORETICAL MODEL	Both the CONCEPTUAL and the FORMAL MODEL together form the THEORETICAL MODEL.
DOMAIN OF INTENDED APPLICATION	Prescribed conditions for which the FORMAL MODEL is intended to match REALITY.
COMPUTERIZED MODEL	An operational computer program which implements a FORMAL MODEL.
IMPLEMENTATION	The process of programming the FORMAL MODEL on an adequate computer. It is recommended to apply software engineering methods such as top-down design, structured programming, top-down implementation and testing, etc.
MODEL VERIFICATION	The process of showing that the proposed THEORETICAL MODEL is an adequate and consistent representation of the system to be simulated as represented by the CONCEPTUAL SYSTEM MODEL, all in view of the intended application. The method used is basically expert critique, which makes use of expertise and past experience in order to assess the adequacy of the CONCEPTUAL SIMULATION MODEL and the derivation of the FORMAL MODEL. Suitable documentation should allow following and understanding the ideas of the model builder in deriving the THEORETICAL MODEL.
PROGRAM VERIFICATION	The process of demonstrating that the FORMAL MODEL has been correctly implemented on the computer. This includes source code inspections, code walk throughs and tests of the model behaviour predicted on the basis of the THEORETICAL MODEL (analytical solutions, behaviour for small signals, etc.).
MODEL VALIDATION	The process of demonstrating through objective testing that the FORMAL MODEL and its associated COMPUTERIZED MODEL form an adequate representation of the system to be simulated, judged in view of the DOMAIN OF INTENDED APPLICATION. Model generated output data are being compared against actual data obtained by experiments performed on the real system.
DOMAIN OF APPLICABILITY	Prescribed conditions for which the COMPUTERIZED MODEL has been tested, compared against REALITY to the extent possible, and judged suitable for use (by MODEL VALIDATION, as described above).
RANGE OF ACCURACY	Demonstrated agreement between the COMPUTERIZED MODEL and REALITY within a stipulated DOMAIN OF APPLICABILITY.

4. CONFIDENCE LEVELS IN MODEL BEHAVIOUR (CLIMB)

4.1 INTRODUCTION

The greater part of the working group's effort was spent to discuss and to evaluate the scheme called Confidence Levels in Model Behaviour (CLIMB), an idea which originally was launched and largely influenced by Willard M. Holmes. CLIMB is a five level hierarchical process for representing information about a model such that a third party user can readily develop confidence in the model's behaviour.

4.2 KNOWLEDGE BASES

An important issue with CLIMB is the term "knowledge base". As used here (ref. Figure 3) it includes two components, each associated with a particular model and its domain of intended application: (a) facts and (b) heuristics.

Whereas the facts associated with a particular model currently are reasonably well documented, there is a big gap as far as the heuristics component is concerned. Heuristics are "educated guesses" or rules of good practice acquired by the experienced modeler over years of experience in developing and implementing simulation models. The experienced simulationist uses them as a guide in making many decisions during the model development process. Seldom if ever are the heuristics of the modeler included in the model documentation. This results in an inadequate knowledge base for establishing model credibility since all model developers have their own "rules of thumb" for solving particular simulation design and modelling problems. Establishing credibility with second and third party users of a model requires that in addition to the hard facts also the heuristics, such as the assumptions made in developing and implementing the model as well as the assumptions made about the domain of intended application be documented.

4.3 DATA BASES AND MODEL VERIFICATION/VALIDATION

As mentioned above, during the processes of model verification and validation two different data bases are compared. In particular the model generated data base is compared against a reference data base which can be either data generated on a theoretical basis or real world data. It is essential to distinguish between reference data which have been used for model development and such that have not been used for model development. In the first case the model generated data base is not independent of the reference data base, whereas in the second case it is independent. In view of this we supplement the definition of two terms given in section 2:

MODEL VERIFICATION : The two data bases to be compared are dependent, i.e., the reference data base has been used for model development.

MODEL VALIDATION : The two data bases to be compared are independent, i.e., the reference data base has not been used for model development.

4.4 LEVELS OF MODEL CREDIBILITY

The basic issues in developing confidence in simulation models are

- the knowledge base of the model
- the nature of the reference data bases.

The model either represents a theoretical system or a real world system. The real world system is associated with laboratory test data, hardware-in-the-loop operation and real world data (ref. Figure 4). If a theoretical model produces data for which no real world system exists, then only a limited confidence level could be established in the model's behaviour.

However, if the model produced data that could be compared with real world systems or other validated models, an increased level of confidence in model behaviour is established. Additionally, if model generated data compares with results produced from a hardware-in-the-loop simulation, then another increase in level of confidence can be established. This process continues until multiple sets and sources of real world system data are compared with model generated data, producing an even higher level of confidence in model behaviour. The process of relating confidence levels and data bases is graphically depicted in Figures 4 and 5.

4.5 THE CLIMB PROCESS

The CLIMB scheme can be viewed as a process for capturing knowledge about a model, sufficient to develop levels of confidence in the behaviour of the model in question for a particular domain of application. It uses three components:

- Documentation Format
- Requirements for knowledge base description
- Guide for generation of simulation data during model development and the requirements for the reference data bases to be used for validation

In accordance with the typical stages of model development and validation CLIMB considers five stages or levels of information necessary to communicate five levels of model credibility:

- (1) Model summary information, results and conclusions
- (2) The analytical model and its verification
- (3) Subsystem testing and subsystem model validation
- (4) Hardware-in-the-loop operation
- (5) Real world system testing with model updates and validation

Conclusions can be drawn about the use of CLIMB in two areas:

- (1) Development of new models

The most efficient and effective uses of CLIMB are in the areas of establishing a basic framework for new model development and validation efforts. The knowledge required for desired confidence levels will be available during development with straightforward documentation resulting.

- (2) Existing models

Investing the manpower and computer resources for the application of CLIMB to developed or existing simulation models will be most effective in areas where:

- (a) the model will be used and may be updated by third parties not involved in the development, e.g., international transfer of models and
- (b) the model will be used over extended periods where the developer would not be available to establish confidence in the model behaviour, i.e., models of operational weapon systems that require modelling and analysis support from different groups over the life of the system.

4.6 SUMMARY OF THE CLIMB PROCESS

CLIMB LEVEL 1: Model Summary, Results and Conclusion

This level includes information on the objective of the simulation, model developer, function of the model, domain of application, major assumptions made in model development, criteria for model validation and the results of model application. At this level, only functional diagrams with major subsystems and critical variables are identified. The overview nature of the information here is intended to give the potential model user sufficient information to take the first step in reviewing the model capability without getting lost in details. Expert opinion is typically the major tool for confidence building at this level with descriptive rather than technical documentation. The information should be structured in the following way:

1. Model Origin And Related Information
2. Objectives In Developing The Simulation Model
3. Model Summary
4. Functional Model
5. Model Application
6. Validation Philosophy
7. Summary Comments On Simulation Implementation
8. Studies Or Areas Where Model Has Been Used
9. Comments On Model Performance
10. Applicable Documents

CLIMB LEVEL 2: System Models and Submodels theoretical and indirect Data Bases

Simulation model and submodel performances are compared with theoretical models and/or existing appropriate validated simulation models. Methods of comparing model performances are identified and results given at the level of visual inspection, expert opinion and plot overlays. Analysis methodology with assumptions and deficiencies are identified. The information should be structured in the following way:

1. System Model Elements
2. Implementation Description
3. System Model Verification
4. Validation Of System Model's Stochastic Components
5. Validation Against Other Existing Models
6. Subsystem Characterization And Brief Description Of Subsystem
7. Benchmark Test Case
8. Computer Programs
9. Program Verification
10. Applicable Documents

CLIMB LEVEL 3: Subsystem Real World Data Base

This level includes real world data for at least one major subsystem to be compared with the simulation model generated data. Documentation is provided for the total complex model including benchmark results. Data collection and validation methods are described. The information should be structured in the following way:

1. Real World Subsystem Data
2. Experimental Test Environment
3. Methods And Techniques Used In Collecting Real World Data
4. The Approach Used For Validating The Submodel Using The Real World Data
5. Technical Documentation For Excitation Methods (excitation sources may be different for submodel and real world subsystems)
6. User Instruction For Test Set Up
7. Benchmark For Test Set Up
8. Applicable Documents

CLIMB LEVEL 4: Hardware-in-the-Loop Operation

A data base is available from a Hardware-in-the-Loop (HIL) simulation with major subsystem models being replaced with actual hardware operation. Methods of data base comparisons are identified along with criteria for subsystem model validation. Specifics on the computer configuration for HIL operation is also given. The information should be structured in the following way:

1. Description Of Hardware-In-The-Loop (HIL) System
2. Partitioned Model For HIL Operation
3. Results Of Hardware-In-The-Loop Operation
4. Computer Program
5. Applicable Documents

CLIMB LEVEL 5: Total Real World Systems Operations

A data base is available from the real world system test and operation. As a minimum, the critical variables are compared with corresponding system data. Results of validation of system variables are given along with methods of validation according to established validation criteria. The information should be structured in the following way:

1. Conclusions And Comments On Model Validation Effort Using Real World System Test Results
2. Descriptive Summary Of Real World Test Conditions And Test Results
3. System Test Environment
4. Description Of Test Scenario Used To Stimulate The Real World System
5. Real World System Performance Reconstruction
6. Structuring Of Simulation Model For System Test Conditions
7. Analysis Of Simulated Model Generated Data And System Test Results
8. Identify And Explain Discrepancies Between Adjusted Model Generated Data And Real World System Test Results
9. Recommendation For Model Improvement
10. Applicable Documents

5. REFERENCES

1. Holmes, Willard M.
"Survey of Missile Simulation and Flight Mechanics Facilities in NATO" AGARDograph No. 279, April 1983
2. "Final Report on FMP Working Group WG-12 on Validation of Missile System Simulation"
AGARD ADVISORY REPORT No. 206, November 1985

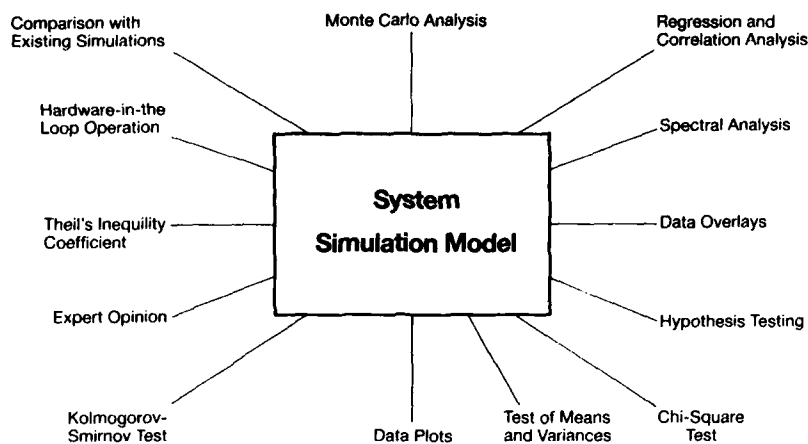


Fig. 1 Developing Simulation Model Credibility Using the Random Tool Box Approach

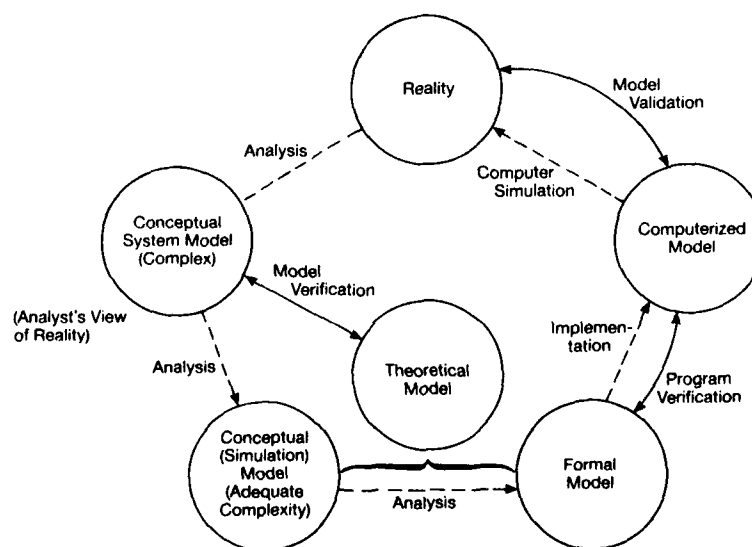


Fig. 2 Model/Simulation Credibility Framework

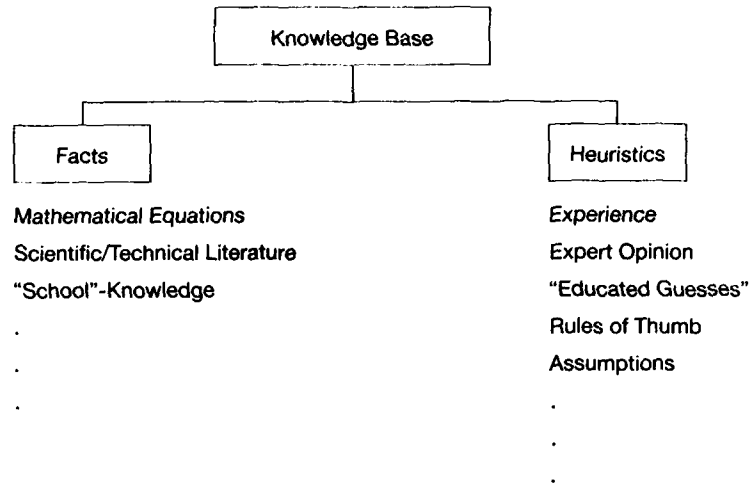


Fig. 3 Knowledge Base in Model Development

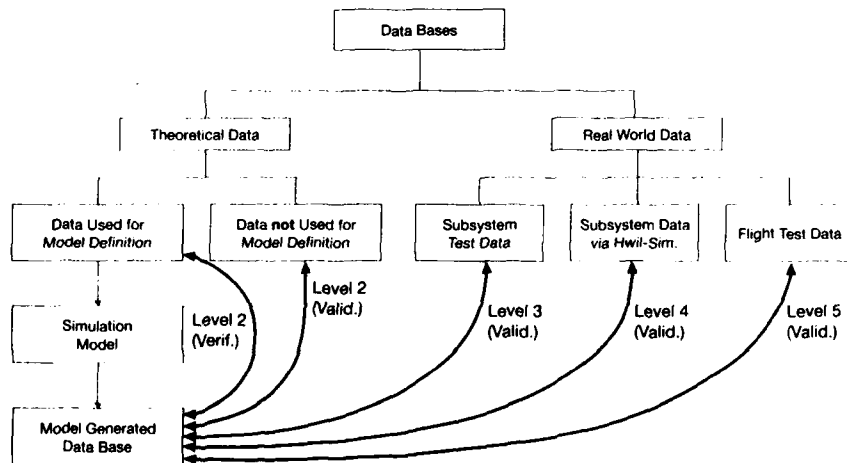


Fig. 4 Data Bases and Levels of Model Validation

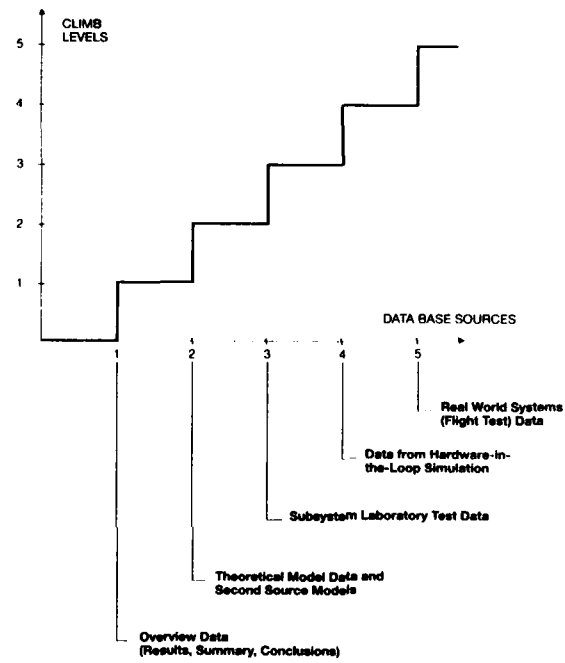


Fig. 5 CLIMB Process for Developing Model Credibility

INVESTIGATIONS OF THRUST VECTOR CONTROL FOR HIGH-ALPHA PITCHOVER

by

A. O. Danielson

R. B. Dillinger

Propulsion Control Technology Program

Naval Weapons Center

China Lake, California, 93555-6001

USA

SUMMARY

Historically, thrust vector control (TVC) system investigations at the Naval Weapons Center have touched on a wide variety of technologies. Emphasis in this paper is on two technologies, the movable-nozzle and the jet-vane TVC, whose performance capabilities demonstrate the significant maneuvers achievable by thrust vector controlled missiles. Investigations have revealed an especially notable result of testing in the high-alpha vertical-launch pitchover environment; that is, despite high-performance TVC capability, missile subsystems such as seeker, airframe, actuation, autopilot, and rocket motor can limit the potential benefits otherwise offered by thrust vectoring. Some lessons learned in approaching such limits are delineated and referenced to assist systems engineers and designers of tactical missile airframes and control systems.

INTRODUCTION

The intent of this paper is to summarize results derived from investigations at the Naval Weapons Center (NWC), China Lake, into TVC systems for missile maneuver control. Major successes, as well as some significant problems, are noted. Investigations summarized include significant flight tests and static firings of experimental and developmental systems examined over the past 20 years at NWC.

A key point demonstrated by NWC flight tests was that practical propulsion-derived flight control devices could be made to function and that means have been worked out to exploit these devices for the high-alpha missile pitchover. This is especially important in view of long-standing concerns over yaw-induced forces that can make control difficult in such a maneuver. This concern has been pointed out in References 1 and 2. Indeed, in spite of practical flight successes, these references identify areas in which the knowledge base is limited. Attempting to model and understand the many complex processes that must occur while a missile executes the thrust-vector-controlled pitchover is more of a problem than the availability of the technology suggests.

In this paper, detailed discussions are concentrated on two systems, the movable-nozzle technique and the jet-vane TVC technique. Including the extensive amount of information available on the subject of TVC is beyond the scope of this document; however, some important sources of further information are referenced. It is believed that awareness of the technology investigations, coupled with the bibliographic reference data, will assist designers in planning for new systems and in comparing development problems. A tabulation of TVC capabilities provides general details to help the system engineer evaluate which TVC options should be examined for specific applications.

BACKGROUND

The use of vertical launchers by the U. S. Navy during the latter half of the 1980s is the primary reason for adding TVC capability to missile systems. Some of the advantages of vertical launchers over trainable launchers include reliability, quick response, targeting effectiveness, and stowage efficiency, including protection of the weapon load. Reference 3 is an informative, nontechnical article that includes a discussion on a few advantages of such launcher systems.

The use of vertical launchers has required product modifications to adapt existing missiles to the launch method. In many cases this requires retrofit interfacing, product improvements, and, most importantly, fitting with some kind of TVC system. As a

Further dissemination only as directed by Naval Weapons Center, China Lake, California, Code 3273; 25 April 1988; or higher DOD authority.

minimum, vertical launch has necessitated some rethinking about methods of boost-phase control and shaping of missile trajectories. Existing aerodynamic controls are not generally efficient users of boost-phase propulsion because of the nature of an aerodynamic turn. Some of the end-performance results are unacceptably high apogee and time losses. Figure 1 qualitatively identifies relative gains achievable by jet-vane TVC over conventional aerodynamic controls. (The trajectories shown in Figure 1 represent flyouts to the same target.) The TVC capitalizes on propulsion system thrust to more efficiently execute the initial trajectory; hence, both time loss and apogee are kept low. A velocity vector control law is an integral part of the pitchover flyout that makes TVC even more effective in the maneuver. The end results limit radar-detection improving survivability for both the missile and the ship and also minimize the time needed to get on trajectory. However, the related control optimization problem is not trivial. (Some features of this problem are discussed in Reference 4.)

Since at least 1963, NWC's Propulsion Control Technology Program has included the investigation of TVC techniques. A primary objective of this ongoing effort has been to investigate the potential and assess the risks of developing TVC systems that will fulfill current and future propulsion and control requirements in surface-launch missile applications. Technology investigations and demonstrations under this program have spanned a broad TVC spectrum, including various types of secondary injection, jet interaction, several movable nozzle concepts, gimbaled rocket motors for ejection seats, jet vanes, nozzle boundary layer techniques, and many others.

Mission specific requirements will dictate which TVC technology might work best for an application. At NWC, numerous trade-off investigations have been done to determine which method might best be employed for specific missions. This is essential when it comes to understanding the TVC problem. The variables are so many that quick solutions do not generally exist. Consequently, numerous experiments have proved to be a most effective means of reducing the concepts to practice. Often analysis and in-depth understanding have lagged behind because of the quickness of the experimental methods.

The ongoing efforts under exploratory development funding at NWC continue to stress this aspect of the pitchover problem when seeking to examine other TVC methods or to further understand existing techniques.

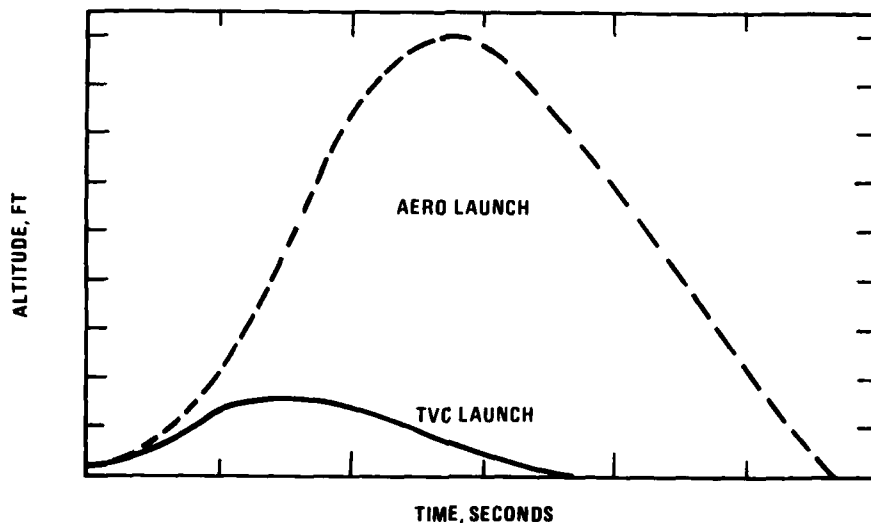


FIGURE 1. Comparison of Jet Vane TVC and Aero-Controlled Pitchovers (6-Degree-of-Freedom Simulation).

SCOPE OF DISCUSSION

Portraying detailed descriptions of all the TVC systems that have been investigated is beyond the scope of this paper. Table I summarizes current and past efforts in which NWC has had direct experience. Many have involved close coordination with contractors to explore new aspects of TVC. Table II summarized a number of TVC technologies. Their general attributes are listed with regard to perceived complexity, costs, control effectiveness, and other features.

The two TVC techniques chosen for more detailed discussion in this paper are the movable nozzle (see, for example, the ball-in-socket nozzle illustrated in Figure 2) and the jet-vane TVC (Figure 3). These were chosen because, in terms of performance, they represent control capabilities most likely to be achieved by use of TVC apparatus. They, or their derivatives, are methods most often being examined by NWC for system use. Discussions of these TVC options include function, problems, and current areas of technical interest. (Reference 5 discusses details of movable nozzle TVC and related development work, and Reference 6 has further details on jet vane TVC testing at NWC.)

Beyond the basic reasons for using vertical launch, as previously noted, systems engineers must recognize many surrounding factors in the application of TVC technology. Therefore, in this paper, particular attention will be given to considerations of integration within the missile system, major TVC components, subsystem-imposed limits on the TVC capability, and tools found exceptionally useful for TVC design. Where known, references are included that bear on particular aspects of these technologies such as materials problems or advances, actuation and torque problems, heat transfer analysis techniques, modeling methods, and current issues or advances.

Finally, aspects of two exploratory projects, QuickTurn, for the movable nozzle, and Vertical-Launch Technology, for jet-vane TVC, are described, and some system concerns related to these two TVC options are noted. These project efforts have progressed to flight testing. (The authors' experience lies almost exclusively in jet-vane TVC design, test, and analysis, including some association with system developments. However, many discussions with those involved in the QuickTurn project and others working in the TVC area have provided much information on the movable-nozzle and vane TVC techniques.)

TABLE I. Summary of NWC TVC Experience.

System	Contractor	Dates (fiscal year)
Liquid secondary injection (LSITVC)	NWC Honeywell	63-67 72-73
Hot gas secondary injection (HGSITVC)	NWC/Philco Ford Thiokol-Wasatch	65-66 71-73
Gimbal nozzle TVC	Thiokol-Wasatch	69-73
Flexseal nozzle TVC	LPC	69-70
Trapped ball nozzle TVC	Thiokol-Wasatch	74
Techroll nozzle TVC	United Technologies Corp	72-74
Jet-tab TVC	TRW	72-74
Jet-vane TVC	NWC	72-present
Boundary layer TVC	CEC	72-present
Forward jet reaction control (JRC)	Moog/NWC	72-73
Hot gas roll control	Thiokol-Wasatch	70-73
Warm gas roll control	Thiokol-Wasatch	72-74
Jet interaction (JI) control	McDonnell Douglas	68-70
Projectile jet reaction control	Philco Ford	72-73
Underwater Thiovec (Hydrovec)	Thiokol-Huntsville	73-74
Underwater gimbal nozzle TVC	Thiokol-Elkton	72-73
Gimbal spherical motor TVC	NWC	72-73
High vector angle systems (> 45 degrees) (studies)	Rocketdyne Thiokol-Wasatch Lockheed	73-74
Pintle thrust magnitude control; DAN thrust magnitude control	Aerojet Rocketdyne	69-73

TABLE II. TVC Techniques.

Device	Nominal capability (vector angle, degrees)	Design limitations	Design virtues	Developmental status
HGSITVC	7-9	Duty cycle; materials limited; packaging; fairly short burn time; valve limitations	Small power supply; does not require separate injectant	Static test
LSITVC	5-6	Duty cycle dependent; packaging	Simplicity	Flight test
Gimbal nozzle	~20	High cost; splitline and fluid transfer problem	High performance; moderate torque	Flight test
Flexseal	~20	High torques; environment sensitivity	High vector angle; seal simplicity	Flight test
Thiovec	~15	Low-frequency response and torque	Simple and low cost	Static test
Jet tabs	10-12	Axial thrust losses; tab duty cycle limited	Simple; moderate cost	Static test
Jet vanes	6-8	Limited to short burn times; axial thrust losses	Roll control capability	Flight test
Trapped ball nozzle	~20	Possible high or variable torques	High performance; simplicity	Static test
Techroll	~20	Relatively unknown	Potential for low cost	Static test
Boundary layer TVC	~10	Altitude and chamber pressure dependent; large nozzles	Very low cost; simple	Static test
Hot gas forward reaction control	Relatively moderate side force	Valving duration and side force levels; mission sensitive; packaging	Independent of main propulsion	Flight test
Jet interaction	Relatively moderate side force	Aerodynamic sensitivity	Amplification possible under proper flight regimes	Flight test
Hot gas roll control	High torques	Duty cycle and duration limited	High performance	Static test
Warm gas roll control	Low torques	Duty cycle limited because of supply	Moderate cost; ease of handling warm gas	Flight test
Gimbal motor TVC	~20	Only valid for very low motor length/diameter ratio	No hot gas sealing required	Flight test
Underwater gimbal nozzle	~20	High cost; splitline and fluid transfer problem	High performance; moderate torque	Flight test

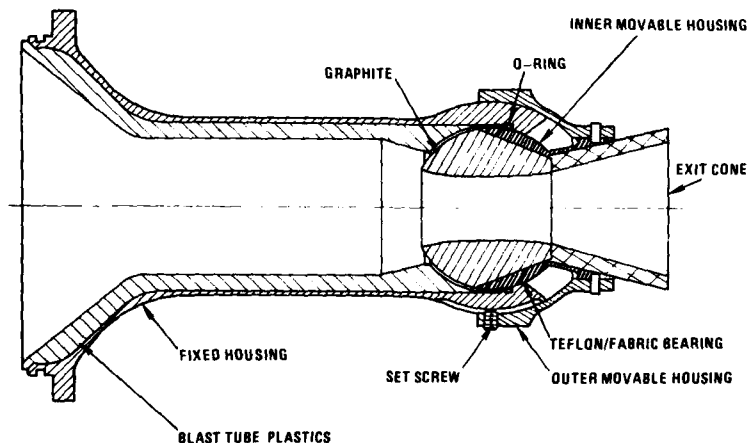


FIGURE 2. The Ball-in-Socket Nozzle TVC Technique.

MOVABLE-NOZZLE TVC

The QuickTurn project at NWC provides an example of the movable-nozzle TVC capability. QuickTurn was the culmination of advances that led to current ball-in-socket nozzle TVC technology. This method of control, in single or multiple nozzle sets, is a major choice when it comes to TVC for missile systems 8 inches or more in diameter.

The QuickTurn test vehicle was not specifically designed for vertical launch. However, this vehicle is mentioned in the context of vertical launch because, in flight

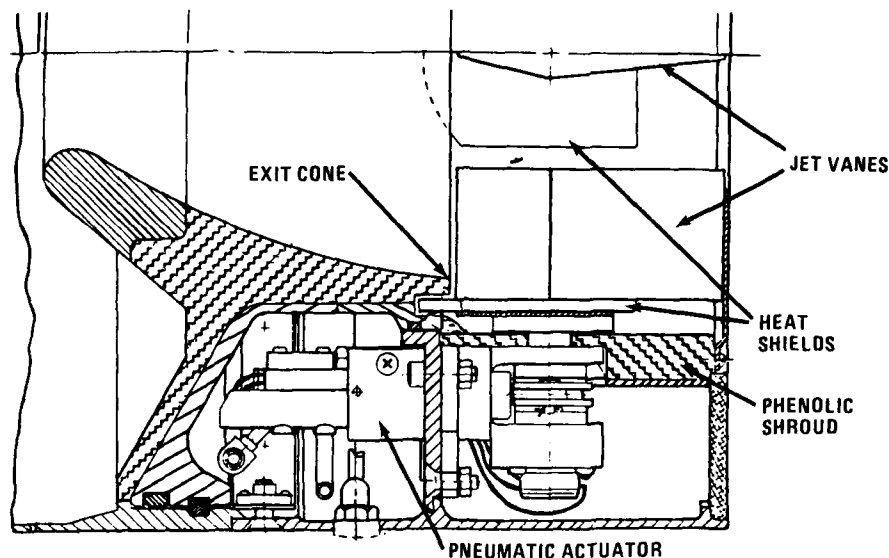


FIGURE 3. Typical Jet-Vane TVC Control System.

tests at NWC, QuickTurn was launched from the ground in a near vertical aspect to achieve initial maneuver conditions that duplicated air launch. In-flight preprogrammed commands produced controlled turns that achieved angles of attack greater than 90 degrees. The results of the landmark tests were excellent, with TVC control demonstrated in all the flights. As expected, induced yaw was observed in the flights. During those portions of flight, control was maintained even during thrust tailoff of the rocket motor.

The QuickTurn test results are highly relevant to the concerns of the system engineer in an assessment of the vertical launch application of movable nozzle TVC technology. Current movable-nozzle TVC systems use operationally similar technology. The QuickTurn demonstration project confirmed the effectiveness of this TVC technique through the flight test studies. Through this development, gimbal-nozzle TVC produced the desired maneuver capability. A discussion of the developments that led to its success are beyond the scope of this paper. However Reference 5 provides details on many of the TVC development features.

Functionally, the large omni-axis thrust vector angles (± 20 degrees) produced by movable nozzles provide superior control capability. However, technical concerns occur in several areas, as described below.

Propulsion Limits on TVC Control

The TVC approach is entirely dependent on rocket motor thrust. For the movable nozzle, this technical limitation was met, during the QuickTurn project, with technology investigations of a combination TVC system capable of producing aerodynamic control after motor burnout. Several aero/TVC methods, including a jet-interaction/aero-steering technique were tested; this included extensive wind tunnel work. These techniques later led to a system in which aero-control tail fins and a movable nozzle were driven off a common actuator (see Reference 7). If torque requirements could be matched between fins and nozzle, the combined system would maintain stability. Otherwise, controller gain switching would be necessary. Six degree-of-freedom flight simulations offered an effective way to sort out gain-derived control problems such as this, provided adequate aerodynamic data were incorporated into the model.

Aerodynamic Data

The need for good aerodynamic data that also support TVC work (a significant cost driver for system development) was one of the major system concerns for the QuickTurn

flight test vehicle. The intent was to design a vehicle that would be stable at launch, that required minimum control force to pitch and hold the vehicle at high angle-of-attack, and that had extremely low levels of aerodynamically induced roll and yaw. Initial wind tunnel tests covered an angle-of-attack range from 0 to 90 degrees and Mach numbers from 0.4 to the low supersonic regime. Simulations of free-flight Reynolds numbers covering a range of altitudes were especially necessary to observe the desired vehicle aerodynamics. Induced side forces and plume-airframe interactions were also specifically examined during wind tunnel testing at angles of attack up to 180 degrees by flowing gas through the nozzle (Reference 8 and 9).

Roll Control

A second consideration for movable-nozzle techniques is the lack of roll control. For tactical missile systems this is a significant concern. Several means of addressing this were implemented in the QuickTurn project. A straightforward approach was to design the airframe so that no active roll control would be required. The QuickTurn airframe was designed to be wingless with a rotating tail fin assembly far aft around the TVC section. Free-rotating mounts were designed to allow the tail fin assembly to turn freely to decouple roll-inducing forces on the fins from the airframe. Wind tunnel tests and flight tests showed that this method was effective. The airframe was otherwise smooth, without cable raceways, to minimize yaw and roll moment coupling. Additionally, special attention was paid to the polar mass balance of the system. Finally, the attitude-control section was mounted to roll freely inside the missile so that it could maintain a constant reference with the TVC nozzle assembly for suitable attitude control. (For larger diameter missiles, roll control needs are typically met with multiple movable-nozzle TVC systems.)

Actuation Torque

A major problem with the movable nozzle technique is the relatively high torque required to drive the system (nominally 500 in-lb running torque for the QuickTurn gimbal ring nozzle). For the ball-in-socket TVC system, which is typically used today, the torques may run twice as high and, more importantly, they can vary widely due to minor differences in the quality of the mating spherical parts and in the type of load-bearing surface materials used. For current ball-in-socket TVC, low-friction loading pads are typically made from a Teflon/glass matrix material.

In QuickTurn TVC work, the Teflon matrix materials were first found in studies of drag in the spherical bearings of the gimbal mount that supported the nozzle ball. First tested around the nozzle ball were O-ring seals of Teflon, silicon rubber, and Viton A. The silicon rubber was found most satisfactory for the design. But when gimbal bearing surface materials from different suppliers were studied, the most effective were found to use a Teflon/glass weave. As shown in Reference 10, many sources of uneven torques were found in the buildup of systems for test. The Teflon/glass materials were later exploited for the load-bearing pads of the ball-in-socket TVC, a more effective design. Careful use of materials and exacting fabrication methods were used to derive a successful TVC technology. A problem of current interest is pad attachment to substrate steel supports.

Adding to the torque problem, the type of split-line design between the nozzle and the surrounding mount affects the torque required. In tests following QuickTurn this was evidenced by a tendency for contamination by aluminum from motor propellant. A new rocket motor boost-sustain profile provided evidence that the boost chamber pressure load would initially open up the split line, during which time aluminum would deposit, and then it would close down in the reduced-pressure sustain phase. At this point nozzle torque would increase. Split-line insulation materials that had swelled during boost also contributed to the problem. Later use of different insulator materials was one means of solving this problem. This was a design problem requiring significant test experience to address effectively. Among possible solutions, low aluminum in the propellant can diminish the effects, but the trade-off is lower specific impulse. Shaping of the throat entrance region and use of labyrinth-type seals are two other approaches for reducing this problem.

Relating to the split-line problem, a concern lies in the O-ring seal used to block high-pressure gas from escape around the nozzle ball joint. These parts require sufficient hot gas protection to eliminate potential for damage by hot gas impingement. Because this is so similar to the split-line problem, it has a similar solution. However, heat-resistant zinc-chromate putty provides added O-ring protection.

A final problem related to the need for high actuator torques is the comparatively higher volume required to package the actuation and power supply system. This is a system concern because the additional volume is generally subtracted from propellant volume unless a smaller seeker or warhead can provide the necessary space. The large volume required for nozzle actuator and power supply is partially offset by improved thrust and control.

Cost Considerations

Another significant system consideration is the cost of the movable nozzle. Cost-driving items can include the mating nozzle and support parts. Nozzle throat cracking is a problem giving rise to cost concerns in systems using 4D carbon-carbon materials. The less costly graphite materials, used for the QuickTurn nozzle, did not exhibit significant cracking problems even with the long burn rocket motor. The nozzle throat, however, is not a TVC-related cost driver.

Actuation and Control

As experienced in the QuickTurn Project at NWC, actuation and attitude-control limitations brought forth system performance concerns. Actuation response needs were met by use of a stiff hydraulic system with bandwidth response greater than 30 hertz. Even at that performance level, flight tests demonstrated evidence of phase lag and destabilizing characteristics. Furthermore, missile roll, induced by the high-alpha maneuver, was evident in spite of specific efforts to build features into the system to minimize roll.

Status of Movable-Nozzle TVC

Despite functional problems and fabrication difficulties, the performance potential of the current ball-in-socket nozzle is exceptional. It is noteworthy that, as evidenced by QuickTurn, the functionally similar gimbal-nozzle system was made to work very effectively in flight tests at NWC. Technology development went through several cycles of test activities on earlier heavy-weight designs before the final QuickTurn flight TVC system was developed. Subsequently, the ball-in-socket nozzles were introduced to add improvements in packaging to similar control effectiveness.

Although the TVC system and test vehicle flights at NWC were successful, application of this technology to the air-to-air mission did not occur. The technology continued to change with improvement in rocket motor case weight and stiffness by the use of composite materials. The gradual advance of technology in pulse motors, the expanded performance demonstrated with the aero-TVC system technology, and the newer ball-in-socket TVC technology are all factors that continue to improve the possibilities for a second-generation system should the need arise.

JET-VANE TVC TECHNOLOGY

The jet-vane TVC technique predates movable-nozzle TVC, beginning with work on early liquid-fuel rockets more than 60 years ago. The first operational application was with the German V-2 missile. Newer, high-temperature vane technology is typically considered at NWC for use on medium-diameter (9-14 inches) vertical launch missiles in which roll control is a requirement. Vanes also are a good retrofit candidate to equip existing missiles with vertical launch capability. For such systems, especially those in which a complex airframe may feature a multitude of external aero surfaces or obstructions, vane-derived roll control is generally necessary for the pitchover. The typical configuration can be seen in Figure 4 on a modular booster investigated at NWC for vertical launch application. Application of vanes to missiles begins to become difficult for airframes with a large length-to-diameter ratio (~24), since sideforce requirements remain high while packaging volume shrinks due to the greater actuation duty cycle and associated larger power supply requirements. More limitations are imposed by the thermal exposure limits of the vanes and the usual TVC limit imposed by the rocket motor burn time.

System Performance Prediction

Methods of predicting TVC performance are more difficult for vane-based systems. At NWC, predictions are based on DATCOM charts for double-wedge airfoils in supersonic flow. These, when applied carefully, give reasonable results within 5% for the linear

control region. Although the basic aerodynamic analysis methods are fully described in the USAF DATCOM (Reference 11), the application to jet-vane TVC is not. However, the analysis is not difficult provided the techniques are worked judiciously and backed up by test. The techniques used at NWC are described below in general terms.

The vane is idealized as a two-dimensional double-wedge airfoil in supersonic flow with no significant heat transfer or edge effects in the model. Beyond the geometry of the vane, the significant need is to locate a representative effective aerodynamic condition over the surface of the vane. The chosen condition has the effect of accounting for edge effects and nonlinearities in the complex flowfield about the vane. The conical, expanding flow with some internal and some external flow regions as well as shock interactions is in this way idealized to a simple uniform external flow. Remarkably, the resultant model works with sufficient accuracy for design prediction.

Without a proper definition of the effective aerodynamic condition about the vane, the model will not predict a reliable result. The effective aerodynamic condition used will differ for each application but can be approximated by conditions at the 20% chord location for unshrouded vanes and 12.5% chord for shrouded vanes. The theoretical center of pressure is typically in the 25-35% chord range for a symmetrical double wedge jet vane cross section in uniform flow. A sketch of typical TVC exhaust gas flow is shown in Figure 5. For accurate roll torque prediction, a spanwise aerodynamic center of pressure is required (generally the 45-50% spanwise location referenced from the vane root).

Regardless of the chosen vane chord location, inside or outside the rocket nozzle exit plane, the effective flow condition about the vane is computed using nozzle design computations and associated rocket motor design parameters. This requires use of an appropriate plume ratio of specific heats, generally in the 1.17-1.21 range, and the expected maximum thrust and chamber pressure. It also requires use of a flow area that corresponds to an imaginary exit plane at the vane chordwise location determined for the aerodynamic evaluation. Since this generally does not match the area of the physical nozzle exit plane, it is a source of potential errors when the technique is used to predict vane forces. Ultimately, test comparisons are used to calculate an effective diameter for model flow condition matching. The nominal diameter at the desired exit plane may be geometrically predicted by extending the existing nozzle expansion angle to the appropriate vane chord location and picking off an imaginary nozzle diameter at that point. The presence of interior nozzle flow separation, vane base plate heat shields, and/or supersonic blast tubes about the vanes may impose the use of a different exit diameter for prediction of the desired flow condition.

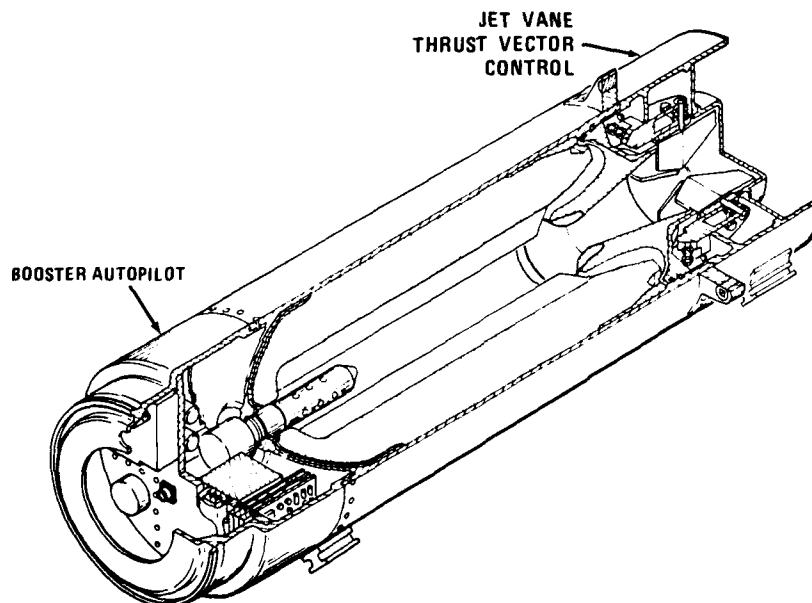


FIGURE 4. Jet-Vane TVC Controlled Booster.

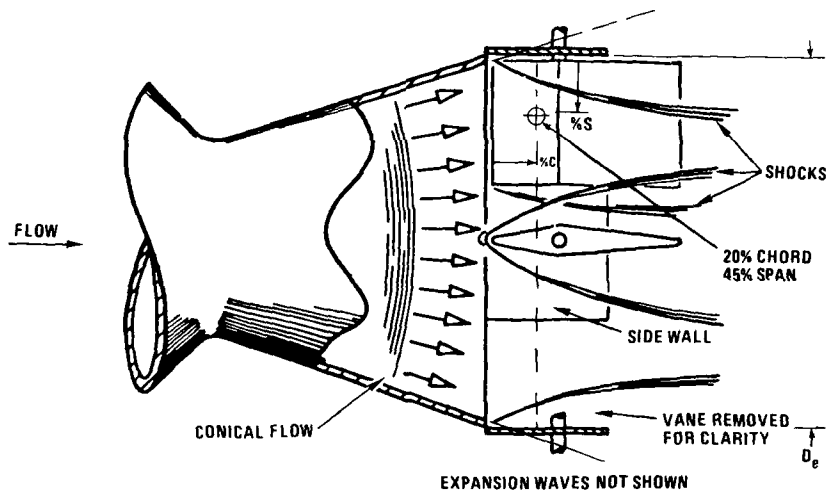


FIGURE 5. Vane Aerodynamic Force Evaluation.

Generally, the resultant model will work well for vane deflection angles to about 15-18 degrees or less. Beyond that, nonlinear shock interaction effects become evident. The linear vane side force coefficient, in pounds per degree of vane deflection, begins to roll off at vane deflection angles above 15 degrees.

The final requirement for side force predictions is an appropriate summation of vane-derived lift forces to predict maximum side thrust and the associated vector angle for pitchover control. The maximum force is obtained for four vanes, 90 degrees apart, oriented in the cross (X) configuration such that all four vanes contribute 70.7% (45-degree) lift components to the total sideforce. The minimum force orientation is the plus (+) configuration in which two vanes contribute 100% lift components to total side force.

Vane TVC Problem Areas

Jet vanes provide significantly less vector angle capability than the movable nozzle, up to 6-8 degrees omni-axial, but offer the option of roll control. Additionally, vanes contribute continuous drag-related system energy losses, typically at least 4% above the cosine thrust losses common to all TVC techniques. The need for control is significant for the high-angle-of-attack pitchover. In design work, control margins are set with enough side force to offset pitch and yaw moments by at least a factor of two, typically three. Predicting moments is difficult without good aerodynamics, which includes special attention given to matching the Reynolds number in wind tunnel tests. Good 6-degree-of-freedom flight simulations, using the wind-tunnel-derived aerodynamics, can then predict the desired control force margins.

Control Margins

Adequate control is a major design problem for all TVC-controlled airframes. Often, the best answer to the question of margins is the flight test of a developmental system backed up by previous static firings of the TVC system and rocket motor. The variables are so many that generalizations rarely can satisfy the need for satisfactory application specific answers. Static test requirements dictated by the nature of the system impose a need for the full 6-degree-of-freedom test stand. Better still is the flight test; unfortunately, flights can generate more questions than answers.

Development flight tests at NWC enabled a comparison of control margins met by four-vane and three-vane systems. In the very early exploratory development tests that predated the later three-vane flight test program, successful flights of a four-vane

vehicle for vertical launch were made (Reference 12). Later, flights of a three-vane control system configuration were made, and some of these flights produced failures in which the control effectiveness of three vanes was overcome by large adverse aero moments generated by small airframe defects. However, even though it was confirmed that lower control margins were a characteristic of three vanes, later successful flight tests verified that, had airframe defects not occurred, the flights would have been successful. This kind of flight failure indicates the need for good aerodynamic studies to support TVC system developments. The realism required in the wind tunnel tests includes adequate model scale to duplicate the vehicle micro-configuration variables, transonic Reynolds number simulation, and wind tunnel model sting influence on vortex formation and shedding. The combination of variables was such that several causes contributing to flight failure had to be sorted out.

Airframe Effect on Control

Certain airframe characteristics were postulated to influence control margins in the two flights of the three-vane TVC system that experienced control difficulty. These included evidence of nose cap separation and/or misalignment, the number and design of cable raceways (strakes) on the rocket motor, the combined raceway orientation with respect to vane orientation, the related vane control policy, the initial missile roll orientation at the start of pitchover, and strake loosening in flight. External aerodynamic asymmetries and obstacles such as the cable raceways and V-band coupler joints with large unsymmetrical attachment nodes were other factors influencing system development and aerodynamic performance.

Generally, a cumulative effect of many of the above-mentioned factors were able to induce loss of control in three-vane flight tests. Marginal vane control, autopilot/TVC response, and marginal control policy (which placed the airframe in a position during the pitchover for maximum generation of adverse aero forces and, simultaneously, minimum generation of TVC control forces) were all system design features that enabled natural force buildups caused by unique airframe asymmetries to supersede missile control. Correction of these problems by a combination of data analysis, more wind tunnel tests, and verifying flight tests have resulted in successful flight tests of the three-vane TVC system and the subsequently reinstated four-vane system.

Actuation Systems

Pneumatic actuators are typically used for jet-vane TVC actuation, although some difficulties can occur. Compared to other methods, such as electric and hydraulic, pneumatic actuators are normally lower in cost. However, some situations, such as retro-fits, dictate the use of hydraulic or electric systems.

Problems with pneumatic actuators include slower and more erratic response and power supply capacity limits. Low leakage null-state solenoid valves are a system design feature that can reduce the power supply capacity size. Another problem with the power supply is finding a way to determine whether a supply is full without inducing a pressure vessel leak. A generic control problem is system stiffness due to gas compressibility. If fast, accurate response is needed, controller electronic compensation and mechanical damping are needed. Frequency response is nominally 17 to 30 hertz, depending heavily on the development effort and end application requirements. The 30-hertz pneumatic actuator system is considerably harder to achieve than an equal-bandwidth hydraulic actuator.

Airframe Stiffness

Certain externally derived control system factors were revealed during technology studies leading to the first four-vane vertical launch technology demonstration flight tests. Vibration-tested V-band joint designs on the airframe revealed reduced stiffness to the point that low-frequency airframe harmonic modes would affect the control system. These were studied in detail at NWC in vibration tests (Reference 13). Control system notch filtering was used to address this situation. Complicating this was a low frequency bandwidth typical of the moderately compensated pneumatic actuators.

Materials Issues

Other difficulties have been encountered in the areas of materials for vanes, materials for the support shaft, vane durability in erosive (aluminized) plumes, heat shielding, and sealing.

Almost exclusively, the best performing vane materials are forms of tungsten refractory metals. Powdered, pressed, and sintered tungsten forms a base matrix into which copper is infiltrated. Work with these materials at NWC actually occurred very early in liquid rocket nozzle development. Transpiration cooling was the process exploited for that work (see, for example, Reference 14). Subsequent vane work benefitted by this early experience at NWC. The copper-infiltrated tungsten material works well when the high-cost grade of high-density tungsten/low-percentage copper is used. Not all suppliers of such materials provide the quality required for the TVC application. The material works well for several reasons. The copper decreases thermal stress through high conductivity and evaporates to cool by sweating. Copper also improves machinability in fabrication, but notch sensitivity is still a concern.

The copper-infiltrated tungsten refractory material provides substantially greater durability than any other material, considering overall performance, cost, availability, and manufacturing. However, some associated system problems are high cost and heavy weight. As an aid to manufacturing cost reduction, considerable work went into a manufacturing technology program, contracted by NWC, which explored ways to reduce waste and costs in the vane fabrication process (References 15 and 16). With respect to weight reduction, carbon-fiber-reinforced carbon and silicon carbide matrix composite materials are of current interest. Reference 17 describes work with materials similar to those used at NWC and illustrates typical development problems; Reference 6 describes related early work in vane material studies and vane technology developments at NWC.

Thermal Durability

The problem of keeping vanes working long enough to effect a pitchover is significant from the perspective of heat transfer. The major factors are the amount of time spent exposing vanes to plume impingement before pitching begins and the duty cycle in the pitchover. Soak time can easily amount to 25% of the action time of the vanes. The action time duty cycle can be reduced by adjustment of the velocity vector control commanded attitude, use of higher thrust in the rocket motor for more effective vane control, or larger vanes. In any case the TVC-related trade-off is durability due to heating against effective control derived from greater thrust. (Greater thrust also imposes stresses on the airframe and results in a higher apogee although time to target can improve since pitching can begin sooner.) For a given configuration, the desirable greater thrust is developed by a higher mass flow or, typically, a larger nozzle throat area at constant chamber pressure. This results in a lower expansion ratio and higher exit plane pressure.

High exit plane pressure frequently contributes to destructive hot gas flows into the actuator, the vane support shaft, bearings, and related sensitive TVC system areas. The trade-off between high thrust for quicker pitchover, better use of vanes, and the associated high exit pressure thermal durability problems remains to be fully explored. The overall trends are apparent when the results of system static test activities at NWC are examined. For the system designer, two convenient parameters can be used as indicators of expected difficulties. These are the product of the ratio of exit plane pressure to ambient pressure and Mach number, $(P_e/P_a)M_e$, and the percentage of propellant aluminum. The higher these numbers are the more difficult and costly will be the development of an effective vane TVC system. Successes have been achieved for the 0% aluminum propellants and for $(P_e/P_a)M_e = 7.268$ or less.

Significant problems with steel vane support shafting were experienced in early technology investigations of jet-vane TVC systems at NWC (see, for example, Reference 6). Solutions include cooling methods, such as a PTFE sleeve about the shaft for sublimation cooling; use of TZM refractory metal shaft material, and zirconia-coated vanes. However, the material and fabrication costs for these approaches are high. The costly ceramic coatings, such as yttria-stabilized zirconium oxide, are also routinely used to retard erosion and heat transfer into the support shaft location.

Recent Work

Recent technology program work at NWC has been directed toward alternative solutions to the vane support shaft problem. The use of an integral vane-shaft is one approach. Better understanding of the heating process is another. Another solution, retraction of the vane, is a relatively simple mechanical approach that has generated spinoffs in the acquisition of data for further study beyond producing a solution to the support problem (see, for example, Reference 18).

In addition to incorporating new solutions to the vane shaft durability, the retraction system (a test shown in Figure 6) has been used to gather information concerning the relative thermal durability of various vane shapes. Another test spinoff has been measurement of internal vane temperatures (Figure 7). It is also now possible that, by retracting the vane during a test, surface temperature distributions can be measured to gather heat transfer data for design and model verification purposes. Beyond the data-gathering utility of the retraction system, the scope is widened for application of jet-vane TVC to retrofit on performance-driven systems in which previously derived vanes would not survive a highly aluminized plume.

To better understand the process of vane heating, empirical methods have been exploited to build models of the vane shaft heating process. These techniques use a combination of subscale and full-scale test data, parametric system identification analysis, and direct simulation to generate vane heating time-temperature profiles, related lumped-parameter heat transfer models and associated linearized network transfer function expressions (see Reference 19).

Materials limitations to propellant aluminum have been investigated. Subscale test motor firings were used to build a data base on vane material erosion and shaft temperature-time history to feed into the empirical modeling effort.

Many of the design tools for work with vanes, materials data, and empirical equations describing vane forces, including interactive or crosstalk forces, are described in Reference 20, a result of NWC cooperative work through The Technical Cooperation Program with Canada and Australia.



FIGURE 6. Vane Retractor Test.

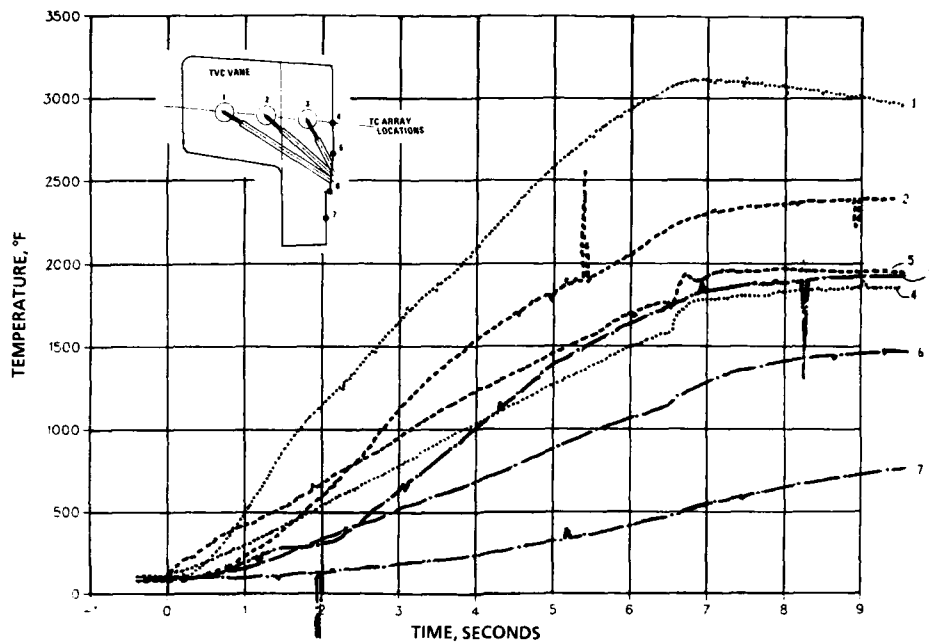


FIGURE 7. Vane Internal Temperature Measurements. (Sketch shows integral TVC vane and shaft design; numbers indicate thermocouple locations.)

REFERENCES

1. J. Peter Reding and Lars E. Ericsson, "Maximum Vortex-Induced Side Force," *AIAA J. of Spacecraft*, Vol. 15, No. 4, July-August 1978, pp. 201-207.
2. P. J. Lamont, University of Manchester, England, "Pressure Distributions on an Ogive-Cylinder at High Angles of Attack with Laminar, Transitional, and Turbulent Separation." Paper presented at the AIAA Atmospheric Flight Mechanics Conference, Danvers, Massachusetts, 11-13 August 1980. (AIAA-80-1556-CP)
3. Capt. J. W. Kinnier, "Vertical Launch: Up and At 'Em," *Surface Warfare*, March 1980, pp. 16-19.
4. H-O. Jonsson and G. Malmberg, "Optimal Thrust Vector Control for Vertical Launch of Tactical Missiles," *AIAA J. of Guidance*, Vol. 5, No. 1, January-February 1982, pp. 17-21.
5. L. H. Erickson, Thiokol/Wasatch Division, for the Naval Weapons Center, China Lake. *Low Cost Flightweight Trapped Ball TVC Nozzle Development, Final Report*. July 1982. (NWC TP 6162)
6. M. J. Ripley-Lotee, S. M. O'Neil, and D. R. Blue, Naval Weapons Center, China Lake. *Jet Vane TVC Development Testing*. June 1985. (NWC TP 6415)
7. N. L. Purcell, Naval Weapons Center, China Lake. *Aero TVC Demonstration*. April 1983. (NWC TP 6339)
8. R. K. Shigeno, McDonnell Douglas Astronautics Company. *Agile Extreme Incidence Wind Tunnel Tests*. Huntington Beach, Calif., MDAC, February 1973. (MDC G4310 for the Naval Weapons Center)
9. W. H. Clark, J. R. Peoples, and M. M. Briggs. "Occurrence and Inhibition of Large Yawing Moments During High-Incidence Flight of Slender Missile Configurations," *Journal of Spacecraft and Rockets*, Vol. 10, No. 8, August 1973, pp. 510-519.

10. M. R. Wolfson, R. D. Ulrich, D. P. Wirtz, and W. H. Thielbahr, Naval Weapons Center, and J. M. Simonsen, Brigham Young University. *Agile Gimbal Nozzle Mechanics Investigation*. Paper presented at the AIAA/SAE 9th Propulsion Conference, 5-7 November 1973. (AIAA Paper No. 73-1205)
11. McDonnell Douglas Astronautics Company for the Air Force Flight Dynamics Laboratory, Wright-Patterson Air Force Base. *USAF Stability and Control Datcom*. Revised 1974.
12. S. M. O'Neil, P. W. Bowen, and J. J. Ripley-Lotee, Naval Weapons Center, China Lake. *Vertical Launch ASROC Prototype Demonstration*. China Lake, Calif., NWC, June 1979. (NWC TP 6092)
13. Naval Weapons Center, China Lake. *Vertical Launch ASROC Modal Survey Using High Input Forces and Various Clamp Band Tensions*, by Jim McManigal and Tim Hofer. August 1987. (NWC TM 6075)
14. A. T. Robinson, R. L. McAlexander, J. D. Ramsdell, and M. R. Wolfson, "Transpiration Cooling With Liquid Metals," *AIAA Journal*, Vol. 1, No. 1, January 1963, pp. 89-95.
15. J. H. Peterson and K. E. Meiners, Battelle, Columbus Laboratories. *Fabrication of Copper Infiltrated Tungsten Jet Vanes. Final Report*. 30 September 1981.
16. M. J. Ripley-Lotee and S. M. O'Neil, Naval Weapons Center. *Powdered Metal Sintering of Jet Vanes*. February 1982. (NAVSEA MT Report S-587-79)
17. D. Kamps, A. Weiss, R. H. Schmucker, Solid Rocket Company, Ottobrunn, Germany. "Material Problems in Jet Vane Thrust Vector Control Systems." Paper presented at the 53rd Propulsion and Energy Panel Meeting, 1979. (AGARD Conference Proceedings 259, *Solid Rocket Motor Technology*)
18. A. O. Danielson, Naval Weapons Center. "Development of a Stowable Jet Vane TVC System at NWC." Paper presented at the 1987 JANNAF Propulsion Meeting, December 1987.
19. Robert H. Nunn, Naval Postgraduate School, Monterey, California. *TVC Jet Vane Thermal Modeling Using Parametric System Identification*. March 1988. (NPS69-88-001)
20. A. O. Danielson, Naval Weapons Center, for The Technical Cooperation Program. "USA Final Report Submittal for TTCP WTP-4 KTA-9; Thrust Vector and Magnitude Control Technology-An Assessment." 20 November 1987.

A STRUCTURED SINGULAR VALUE APPROACH TO MISSILE AUTOPILOT ANALYSIS II

Dr. G. A. Hewer
Naval Weapons Center
Code 39102
China Lake, CA 93555

Richard Klabunde
Naval Weapons Center
Code 3912
China Lake, CA 93555

Dr. Charles Kenney
Naval Weapons Center
Code 3807
China Lake, CA 93555

ABSTRACT

A state space model for additive errors that is algebraically and dynamically equivalent to Doyle's structured singular value is presented. Using this theory a new algorithm based on a Monte Carlo eigenvalue search is presented. Some examples are included that illustrate the convergence properties of the Monte Carlo technique

1 INTRODUCTION

Since plant perturbations can destabilize a nominally stable system, the term robustly stable refers to the extent to which a model of the open-loop system may be changed from the nominal design without destabilizing the overall closed-loop feedback system. What is really desired is a robustness analysis that will apply to simultaneous independent, not necessarily small, perturbations. There is a certain range, due to neglected nonlinearities and unmodeled system dynamics where the model and system may behave in grossly different ways. Unfortunately, this range is implicit in the technology that the model approximates and so any general theory must encompass a variety of perturbations. Robustness issues are not new in control system design. Presently, robustness theory requires a set of model errors combined with a suitable notion of "nearness to instability". Standard techniques for single-input single-output control systems employ graphical means (e.g. Bode, Nyquist, root locus, inverse Nyquist, Nichols plots) to assess stability. These graphical stability tests have the added advantage that the plots themselves can be used to determine the minimum change that will lead to instability. In fact for standard single-input, single-output (SISO) systems the gain and phase margins are basically measures of how close the Nyquist plots come to encircling the -1 point [Franklin, 8, p. 256]. The importance of obtaining robustly stable feedback control has long been recognized by designers in classical SISO servomechanism designs, robustness specifications are often specified by gain margin and phase margin requirements. Even for SISO systems, gain and phase margins do not exhaust all the robustness issues. For multiple-input, multiple-output (MIMO) control systems general robustness measures are a significant theoretical challenge and are a major theme in current MIMO research.

Recently, a promising analysis tool called structured singular values has been proposed by Doyle [Doyle, 4; Doyle et al, 5] that can be used to non-conservatively calculate stability margins in feedback loops with real or complex variations. A key observation in Doyle's structured singular value theory is that a linear interconnection of inputs, outputs, transfer function, parameter variations and perturbations can be rearranged to isolate all perturbations in a feedback block similar to Figure 1.

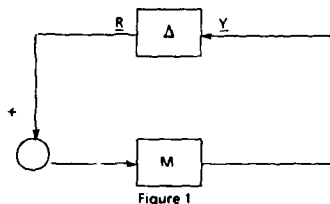


Figure 1

The transfer function matrix M represents the nominal plant and the block diagonal matrix Δ represents the perturbations with its only non-zero entries on the main diagonal block. The block diagonal elements of Δ are bounded, but otherwise unknown real or complex variables or even bounded transfer matrices. The papers by deGaston [1] and Hewer [9] discuss a common example illustrating this technique. In the first sections a state space model for real additive perturbation errors that is algebraically and dynamically equivalent to Doyle's structured singular value is introduced. The proofs of these results will appear in [10]. Based on this theory the problem can be described as a spectral assignment problem using output feedback, where the variable feedback matrix is constrained to the block diagonal elements represented in Figure 1. Using this theory it is shown that the structured singular value is equivalent to solving an eigenvalue problem. Next, a link between root locus and structured singular values is established. To demonstrate this theory a Monte Carlo search algorithm is combined with some graphical convergence strategies to compute μ for third order systems. The Monte Carlo algorithm was used by Hewer, Klabunde and Kenney [9] to compute the structured singular values for the autopilot example first studied by de Gaston-Safonov [2] with general numerical agreement. For the de Gaston example, the Monte-Carlo algorithm yields sharper bounds than the Fan-Tits algorithm [6] and Doyle's estimates [4], which is consistent with the well known fact that their estimates are valid for both complex and real perturbations. The newer Fan and Tits algorithm [7] was unavailable for computational comparison.

2 STRUCTURED SINGULAR VALUES

In order to introduce Doyle's structured singular value μ , the block structure in Figure 1 is defined. The perturbation matrix Δ is a block diagonal matrix, which can be written as $\Delta = \text{diag} \{ \Delta_1, \Delta_2, \dots, \Delta_p \}$ where each block diagonal matrix element is not necessarily a square matrix. Nonsquare perturbations can be accommodated by augmenting the interconnection structure with rows and columns of zero. The block diagonal matrices are member of a set Q that includes elements with family members like

$$Q = (\text{diag}(d, I_k), \text{ or } \text{diag}(\Delta_j))$$

where d is a complex (real) variable and I_k is a $k \times k$ identity matrix and Δ_j is a square complex (real) valued matrix. Reducing the members to a uniform norm bound typically requires that the scaling matrices be absorbed into the interconnection structure. Two particular families of norms that are used in the sequel are the Frobenius norm of a square matrix E defined by [11, p. 358],

$$\|E\|_F^2 = \text{trace}(E^T E)$$

(here E^T denotes the conjugate transpose of E) and the spectral norm [11, page 365] (2-norm) defined by

$$\|E\|_2 = \sup_{\|x\|_2 = 1} \|Ex\|_2$$

The subset Q_δ of the set Q is the family of norm bounded elements

$$Q_\delta = \{\Delta \in Q \mid \|\Delta\| \leq \delta\}$$

$$BS(M, \delta) = \{\Delta \in Q_\delta \mid \det(I - M\Delta) = 0\} \quad (2.1)$$

If $BS(M, \delta)$ is nonempty then Doyle defined the following optimization problem

$$\mu(M) = \sup_{\Delta \in BS(M, \delta)} \frac{1}{\|\Delta\|}$$

By the definition of the determinant, the algebraic equation that is defined by the formula in (2.1) is a polynomial in the n variables Δ . This means that the optimization problem defined by (2.1) can have multiple local maxima which are not global.

Doyle [3] derived the following bounds for μ

$$\rho(M) \leq \mu(M) = \mu(DMD^{-1}) \leq \|M\|_2 \quad (2.2)$$

The block diagonal matrix D must be compatibly dimensional with the members of Q and commute with the members of Q . The spectral radius $\rho(M)$ is the maximum modulus of the eigenvalue of M .

3 A LINEAR SYSTEM MODEL FOR ADDITIVE ERRORS

Consider the following linear dynamical system.

$$\dot{x} = Ax + [B_1, B_2] \begin{bmatrix} r_1 \\ r_2 \end{bmatrix} \quad (3.1)$$

$$\begin{bmatrix} y_1 \\ y_2 \end{bmatrix} = \begin{bmatrix} C_1 \\ C_2 \end{bmatrix} x \quad (3.2)$$

The matrices A , B_1 , B_2 , C_1 , C_2 are $n \times n$, $n \times 1$, $n \times k$, $p \times n$, $k \times n$ dimensional matrices, respectively. The state vector x , the input vectors r_1 and r_2 and the output vectors y_1 and y_2 are compatibly dimensioned.

After taking the Laplace transform of (3.1) - (3.2) with the complex variable s and imaginary component $j\omega$, we obtain the two port $(p+k) \times (l+k)$ block matrix

$$\begin{bmatrix} Y_1 \\ Y_2 \end{bmatrix} = \Gamma(s) \begin{bmatrix} R_1 \\ R_2 \end{bmatrix} = \begin{bmatrix} G_{11}(s) & G_{12}(s) \\ G_{21}(s) & G_{22}(s) \end{bmatrix} \begin{bmatrix} R_1 \\ R_2 \end{bmatrix}$$

with the transfer matrices $G_{ij}(s) = C_{ij}(sI-A)^{-1}B_j$, $i = 1, 2$, $j = 1, 2$.

The triple (A, B_1, C_1) ((A, B_2, C_2)) is a minimal realization of the transfer matrix $G_{11}(s)$ ($G_{22}(s)$). The transfer matrix $G_{11}(s)$ is exponentially stable (exp. st.) [3] iff it is proper (i.e. bounded at infinity) and has all of its poles in the open left-half-plane.

The $n \times n$ loop transfer matrix $G_{11}(s)$ incorporates both open-loop plant dynamics and any compensation employed. The $n \times n$ additive real-valued perturbation matrix ΔA is represented by a product of matrices $\Delta A = B_2 S \Delta C_2$. The matrix S is a $k \times k$ real valued diagonal scaling matrix and Δ is a $k \times k$ member of Q .

The state space counterparts of the spectral set $BS(M, \delta)$ and the real valued function μ are introduced. Define the spectral set

$$\Theta(\delta) = \{\Delta \in Q_\delta \mid \det(j\omega I - A + B_2 \Delta C_2) = 0\}$$

and let $\mu_\Theta(A, B_2, C_2)$ be the real-valued function

$$\mu_\Theta(A, B_2, C_2) = \sup_{\Delta \in \Theta(\delta)} \frac{1}{\|\Delta\|}$$

While the scaling matrix can be used to reduce the members of Q to a uniform bound, it also determines whether the structured singular values represents a relative or absolute robustness margin. The next proposition makes the distinction

between the margins explicit and compares the two margins. Let S be a fixed nonsingular diagonal scaling matrix and consider the two spectral sets:

$$ae(\delta) = (\Delta c Q_1 S^{-1} \delta) \det(j\omega I - A + B_2 \Delta C_2) = 0$$

$$re(\delta) = (\Delta c Q_2 \delta) \det(j\omega I - A + B_2 S \Delta C_2) = 0.$$

Proposition 2.1 If the spectral set $re(\delta)$ is nonempty and if S is a nonsingular diagonal matrix such that $S \Delta c Q$ for every member of Q , then

$$\mu_{ae}(A, B_2, C_2) \leq \|S^{-1}\| \mu_{re}(A, B_2, C_2)$$

Proof: Since the two spectral sets are equal, the following equations are valid.

$$\begin{aligned} \mu_{re}(A, B_2, C_2) &= \sup_{\delta \in re(\delta)} \frac{1}{\|\Delta c\|} = \sup_{\delta \in re(\delta)} \frac{1}{\|\Delta c a e(\delta)\| \|S\|} = \\ &= \sup_{\delta \in re(\delta)} \frac{1}{\|\Delta c a e(\delta)\| \|S\|} \\ &\geq \|S^{-1}\|^{-1} \sup_{\delta \in re(\delta)} \frac{1}{\|\Delta c\|} = \|S^{-1}\|^{-1} \mu_{ae}(A, B_2, C_2) \end{aligned}$$

The explicit distinction between the two types of margins will be omitted unless it is required.

4 STATE SPACE SINGULAR VALUES

The following theorem, which will be proved in [10], is a state space robust stability theorem. The corollaries establish the basic link between the frequency derived structured singular values and eigenvalue based structured singular values.

Theorem 4.1 Let (A, B_1, C_1) be an exp. st. system, assume that $e(\delta)$ is nonempty and assume that $(A + \Delta A, B_1, C_1)$ is a minimal system for every $\Delta c Q_2$. The system (3.1) - (3.2) is exp. st. with respect to the real perturbation set Q_2 iff

$$\mu_e(A, B_2, C_2) < 1.$$

The following corollary depends on the following well-established identity. Let W and Z be $n \times l$ and $l \times n$ dimensional matrices, respectively then

$$\det(I_n + ZW) = \det(I_l + WZ).$$

Corollary: 4.1 For every s with real part of $s \geq 0$ and every $\Delta c e(\delta)$

$$\mu_e(A, B_2, C_2) = \mu(C_2 (sI - A)^{-1} B_2).$$

Proof: Since A is exp. st. the matrix $(sI_n - A)$ is nonsingular, whenever $\text{Re } s \geq 0$. The following identity clearly establishes the claim

$$\det(sI_n - A + B_2 \Delta C_2) = \det(I_n + C_2 (sI_n - A)^{-1} B_2 \Delta) \times \det(sI_n - A)$$

These results show that the additive perturbation structure outlined above gives a workable and rigorous model that yields a nonconservative state space test for real perturbations. The first corollary can be used to develop a Monte Carlo based algorithm that reduces the computation of μ_e to an eigenvalue search. Corollary 4.1 forms the basis for the Monte Carlo search algorithm outlined in Appendix 1, it reduces the computation of μ to an eigenvalue problem. The Monte Carlo eigenvalue search is proposed as a heuristic tool to supplement other algorithms.

5 ROOT LOCUS

In this section the link between root locus and structured singular values is sketched. Next the stability margins predicted by root locus for second and third order polynomials are compared with the stability margins predicted by structured singular values. For second order polynomials they are identical, but for third order systems they are divergent.

Let $g(s)$ denote a strictly proper (i.e. $g(\infty) = 0$) n th degree transfer function. Let (A, b_2, c_2) be the minimal control-canonical form realization such that

$$g(s) = c_2 (sI - A)^{-1} b_2$$

Using the basic matrix identity the following equation is easily derived which relates root locus and the spectral set $e(\delta)$, for some parameter λ

$$\det(sI_n - A + \lambda b_2 c_2) = \det(I_1 + \lambda c_2 (sI_n - A)^{-1} b_2) \times \det(sI_n - A)$$

for every s for which $sI_n - A$ is nonsingular.

Any polynomial subject to additive perturbations can be represented as a dynamical control system where A is the companion matrix and b is the controllable canonical column vector and the nonzero coefficients in the row vector c represent the additive perturbations of A . Thus, as an additive robustness measure root locus represents a uniform affine shift of all perturbed coefficient.

Consider the third order stable polynomial $q(s) = s^3 + a_2 s^2 + a_1 s + a_0$ and the canonical form

$$A = \begin{bmatrix} 0 & 1 & 0 \\ 0 & 0 & 1 \\ -a_0 & -a_1 & -a_2 \end{bmatrix}, \quad b_2 = \begin{bmatrix} 0 \\ 0 \\ 1 \end{bmatrix}, \quad c_2 = [-a_0, -a_1, 0] \quad (5.1)$$

Let the perturbed polynomial be $q_p(s) = s^3 + a_2 s^2 + a_1(1 + \Delta_1)s + a_0(1 + \Delta_0)$

The Hermite matrix [11, p. 465] for the third order perturbed polynomial is

$$H_p(\Delta) = \begin{bmatrix} a_0(1 + \Delta_0) & a_1(1 + \Delta_1) & 0 & a_0(1 + \Delta_0) \\ 0 & a_1(1 + \Delta_1) & a_2 - a_0(1 + \Delta_0) & 0 \\ a_0(1 + \Delta_0) & 0 & a_2 & 0 \end{bmatrix}$$

Since the original polynomial is stable it follows that the perturbed polynomial is stable iff the matrix $H_p(\Delta)$ is positive definite. Equivalently, the leading principle minors of H_p are all positive.

The perturbation matrix ΔA for root locus is $b_2 c_2$ and the perturbation matrix ΔA for the structured singular values is $\Delta A = B_2 \Delta C_2$

$$B_2 = \begin{bmatrix} 0 & 0 \\ 0 & 0 \\ 1 & 1 \end{bmatrix}, \quad C_2^t = \begin{bmatrix} 1 & 0 \\ 0 & 1 \\ 0 & 0 \end{bmatrix}$$

with scaling matrix S and diagonal matrix Δ

$$\Delta = \text{diag}(\Delta_0, \Delta_1) \text{ and } S = \text{diag}(-a_0, -a_1).$$

By Hermite's test $q_p(s)$ is unstable when the first leading principle minor in $H_p(\Delta)$ is zero. Root locus would predict a gain margin of one at $\omega = 0$. The structured singular value spectral set $\sigma(\delta)$ would contain the matrix $\Delta = \text{diag}(1, 1)$, which is not necessarily the minimum element. Next consider the second leading principle minor of $H_p(\Delta)$, it can vanish whenever the linear equation is satisfied $\Delta_0 = m\Delta_1 + m - 1$, where m is the positive real variable $m = a_1 a_2 / a_0$

$$\text{The matrix } \Delta = \text{diag} \left(\frac{-1}{m+1}, \frac{-m}{m+1} \right)$$

is always a member of $\sigma(\delta)$.

Moreover, the maximum singular value of Δ is always less than 1. Thus, root locus and the structured singular value test are never equal even for this simple problem.

Retracing these steps for the second order polynomial $q(s) = s^2 + a_1 s + a_0$ it is easy to see that $\mu_{re}(A, b, c)$ is always equal to the root locus value provided the 2-norm is used for comparison.

6 A MONTE CARLO COMPUTATION

As an application of this theory the Monte Carlo search algorithm is used to compute a $\mu_p(A, B_2, C_2)$ for a third order system. The system matrices have the same form as equation (5.1) with $a_0 = 1, a_1 = 2, a_2 = 2$.

Figure 2 is a graph of Doyle's inequalities defined in equation (2.2). The ordinate and abscissa are log scales. The spectral radius and singular value plots were computed using standard eigenvalue routines. The upper bound $\mu_{DMD}^{1/2}$ is computed using a balancing algorithm. The paper by Osborne [12] discusses balancing theory.

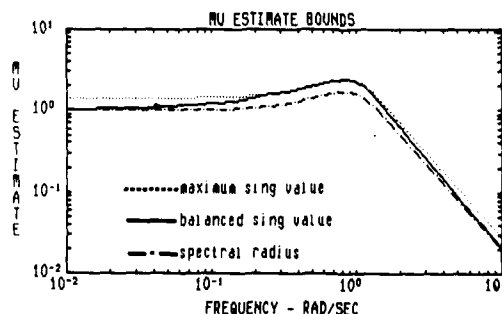


FIGURE 2

Since these inequalities are valid for real and complex perturbations, they will be generally conservative for real perturbations. Nevertheless, they do identify the following range where the robustness margins are smallest. Also, they provide a useful guide to the variation in the robustness margin as function of frequency.

The Monte Carlo robustness margins predict $\Delta\mu = .7268$ at the frequency $\omega = .7678$. Doyle's inequality predicts $\mu = 2.3789$ at the frequency $\omega = .8214$. This can be converted to a comparable delta by taking the reciprocal of μ which is .42036 and computing $\text{diag}(.42036, .42036) \mu = .5945$.

Figures 3 and 4 are graphical aids that monitor the convergence behavior of the Monte Carlo search algorithm. Figure 3 is a histogram that compares the number of times a Monte Carlo search produces a member of the spectral set e_{re} with the μ estimate.

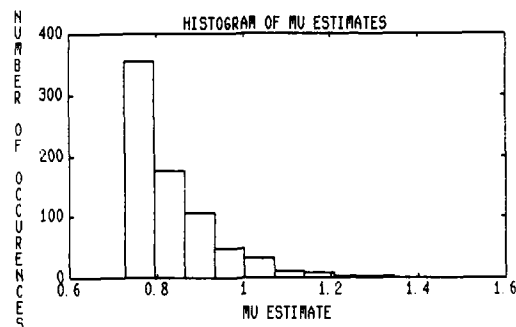


FIGURE 3.

The Monte Carlo search used the F-norm, which represents a 2-sphere for the Q_{set} that describes the robustness region.

Figure 4 is a plot of the convergence history of the Monte Carlo search. It represents a heuristic empirical estimate of convergence that can be used to justify a stopping time for the search.

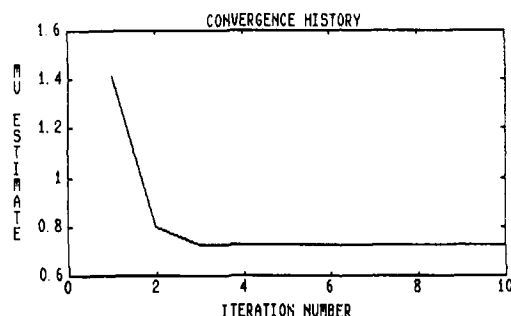


FIGURE 4

These same Monte Carlo techniques were used to compute the robustness margin in the Hewer-Klabunde-Kenney paper. The example is a typical SISO autopilot problem. These examples strongly suggest that the Monte Carlo search algorithm can be used to find μ for interesting control problems. However, the Monte Carlo search is only a heuristic tool that should only be used to augment other algorithms. It is always subject to the caveat that a reasonable result has been delivered but not necessarily the supremum.

7. A MONTE CARLO ANALYSIS FOR SECOND ORDER SYSTEMS

The histogram in Figure 5 represents the density function that describes the members of $e(\mu)$ for the second order example:

$$A = \begin{bmatrix} 0 & 1 \\ -2 & -3 \end{bmatrix} \quad B_1 = \begin{bmatrix} 0 \\ 1 \end{bmatrix} \quad C_1 = [1, 0]$$

$$B_2 = \begin{bmatrix} 0 & 0 \\ 1 & 1 \end{bmatrix} \quad C_2 = \begin{bmatrix} 1 & 0 \\ 0 & 1 \end{bmatrix}$$

Let θ be a random variable that is uniformly distributed in the interval $(-\pi, \pi)$ and let $\Delta = \text{diag}(r \sin \theta, r \cos \theta)$ where r is a scaling parameter such as $\Delta p(\delta)$. The characteristic equation for this problem is the random polynomial

$$\lambda^2 + (3 - r \sin \theta) \lambda + (2 - r \cos \theta) = 0.$$

Now $\Delta \mu(\delta)$ iff the following two cases occur:

- (i) $\lambda = 0$ and $r \cos \theta = 2$
- (ii) $\lambda = \pm \beta_j$ and $r \cos \theta = 3$.

These equations define a random variable $r(\theta)$ which is a member of $p(\delta)$ on the interval $[2, 3/\cos(\arctan(2/3))]$. The cumulative distribution function for the random variable can be derived using standard transformation formulas in Papoulis. Upon integrating we find

$$P(r(\theta) \leq d) = f(2) \quad 2 \leq d \leq 3, \quad P(r(\theta) \leq d) = 2/n \arccos(3/d) + f(2) \quad 3 \leq d \leq 3.6056$$

where $f(u) = 1 - 2/n \arcsin(u/d)$.

The density function for this random variable has a discontinuity at $d = 2$ and $d = 3$ and is superimposed on the histogram in Figure 5.

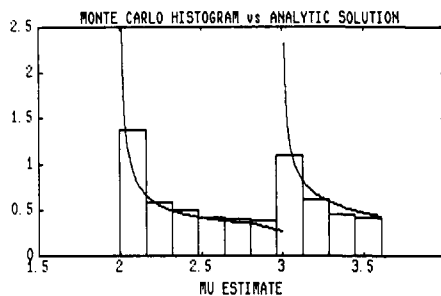


FIGURE 5.

CONCLUSIONS

A state space theory of additive errors has been outlined. An algebraic equivalence between an eigenvalue equation and Doyle's structured singular value has been derived. This equivalence has been combined with a Monte Carlo search algorithm that was used to compute the structured singular value. Until a numerically robust and efficient algorithm is demonstrated for μ computations the Monte Carlo search algorithm combined with graphical convergence tools presents a viable method that can be used to augment the Doyle bounds and the deGaston-Safonov and the Fan-Tits algorithms.

REFERENCES

1. R. R. E. de Gaston, *Nonconservative Calculation of the Structured Singular Value*, Ph. D Dissertation, Univ. of Southern California, (1985)
2. R. R. E. de Gaston and M. G. Safonov, "Exact Calculation of the Multiloop Stability Margin", *IEEE Trans. Auto. Control*, AC-33, (1988), pp. 156-171.
3. C. A. Desoer and W. S. Chan, *The Feedback Interconnection of Lumped Linear Time-Invariant Systems*, J. of Franklin Inst. Vol. 300, (1975), pp. 335-351.
4. J. C. Doyle, "Analysis of Feedback and Systems with Structured Uncertainties", *IEEE Proceedings*, Part D, 129, (1982), pp. 242-250.
5. J. C. Doyle, J. E. Wall and G. Stein, "Performance and Robustness Analysis with Structured Uncertainty", in *Proc. 21st IEEE Conf. Decision Control*, (1982), pp. 629-636.
6. M. Fan and A. Tits, "Characterization and Efficient Computation of the structured Singular Value", *IEEE Trans. Auto. Control*, AC-31, (1986), pp. 734-743.
7. M. Fan and A. Tits, "Toward a Structured Singular Values", *Proc. 26th Conf. on Decision and Control*, IEEE Service Center, Piscataway, N.J., (1987).
8. G. F. Franklin, J. D. Powell and A. Emani-Naeini, *Feedback Control of Dynamic Systems*, Addison-Wesley: Reading, Mass. (1986).
9. G. A. Hewer, R. Klabunde and C. Kenney, "A Structured Singular Value Approach to Missile Autopilot Analysis", *Proceedings of the SCC Multi-Conference on Aerospace Simulation III*, San Diego, Calif. (1988).
10. G. A. Hewer, C. Kenney and R. Klabunde, "A State Space Theory of Structured Singular Values, To appear.
11. P. Lancaster and M. Tismenetsky, *The Theory of Matrices*, Second Edition, Academic Press: New York, (1985).
12. E. E. Osborne, *On Preconditional Matrices*, *JACM* 7, (1960), pp. 338-345.
13. A. Papoulis, *Probability, Random Variables and Stochastic Processes*, McGraw-Hill, New York, (1965).

Appendix

COMPUTING MU BY THE MONTE CARLO METHOD

The equivalence between the spectral set $e(\delta)$ and BS (M, δ) that has been established means that a Monte Carlo eigenvalue routine can be used to compute $\mu_e(A, B_2, C_2)$. The procedure used in this paper is now outlined.

Procedure: Find a Δ $e(\delta)$.

Step 1: Generate Δ uniformly and randomly such that

$$\sum_{l=1}^k \Delta_l^2 = 1,$$

step 2: Start with known upper bound α for $e(\delta)$, reset $\alpha = 2 \times \alpha$ until either:

- a) $A + \alpha B_2 \Delta C_2$ has an eigenvalue with a positive real part and use bisection to get an α such that $A + \alpha B_2 \Delta C_2$ has an eigenvalue in a disk centered on the imaginary axis
- b) if α is greater than some cutoff value go to step 3

Step 3: Same as step 2 but search using negative scaling

Step 4: Save the minimum computed values of Δ and repeat

24-4

5. REFERENCE

- [1] R. Deslandes, A. Eberle
Characteristic Flux Averaging Approach to the Solution of Euler's Equations
Part I: Pseudo Unsteady Approach
Part II: Time Accurate Techniques
MBB/LKE12/S/PUB/313, 6.10.1987

Acknowledgement:

The movie shown during the presentation was originally recorded on a PS390 station of 'Evans & Sutherland'. Due to the conversion from video into a 16 mm film the brilliant quality has been considerably degraded.

ABBREVIATIONS AND SYMBOLS

g	Gravitational constant (=9.81 m/s ²)
ρ	Air density
l, m, n	Momentum of an particle
e	Specific total energy of an air particle
x, y, z	Local body velocities along the store surface
p	Pressure within a fluid
U	Velocity vector of the store
u, v, w	Velocity components of a fluid particle
V	Finite volume of a cell
E, F, G	Homogenous Euler-Fluxes
M	Mach number
$\alpha, AOA, A1fa$	Angle of attack
$\beta, Beta$	Sideslip
C_z	Rolling moment coefficient

6. FIGURES

ANALYSIS AND TESTING OF A HIGH PERFORMANCE AIR-AIR MISSILE

Gerald L. Stevens
Dynamics and Control Branch
Naval Weapons Center China Lake, California 93555-6001, U.S.A.

SUMMARY

This paper addresses hardware-in-the-loop (HWIL) testing of air-air missiles at the Naval Weapons Center (NWC), China Lake. To illustrate the procedures, this presentation follows a highly maneuverable flight test vehicle from initial hardware testing, through the launch, to the subsequent postflight analysis. HWIL testing combines a real-time simulation with flight hardware. The purpose of the dynamic simulation is to validate stability and controllability of the missile system, debug flight hardware, help to characterize the missile subsystems and test interfaces used throughout the hardware. The simulation that results helps to characterize the air-air missile and its capabilities.

INTRODUCTION

A method of testing air-air missiles has evolved at NWC, in which missile hardware is an integral part of a simulation. This talk will describe the HWIL procedures used at NWC for testing new missiles. To illustrate the benefits and pitfalls of this method, we will draw on experience gained in preparing a tail controlled missile for flight.

The air-air missile (Figure 1) that is discussed here was a tail controlled, nonguided round. The missile was programmed to make predetermined maneuvers to demonstrate stability and controllability of the system. The tail controlled missile program represented a cooperative effort between the U.S. Navy and industry. Most components of this missile represented new technology.

Components were: (Figure 2)

- a) a rocket motor built and donated by U.S. industry,
- b) a low-volume, high-bandwidth, 4-axis, cold-gas actuator built under contract for NWC,
- c) a telemetry system designed by the Navy's Pacific Missile Test Center,
- d) aluminum silicon carbide metal matrix fins (which have high-strength at high temperatures) designed by the Naval Weapons Surface Center.

The airframe for this missile, the interface electronics, the autopilot, the digital test sequencer, the sensor package, and the destruct package were built at NWC. Integration, preflight checkout and launching of the missile also took place at NWC.

Before the missile could be flown a number of issues had to be addressed. The types of problems which were studied using the HWIL simulations were stability verification, hardware debugging and electronic interface checks. Some of the more urgent issues were as follows:

- Determine if the cold-gas actuator had sufficient bandwidth to stabilize the missile in pitch and roll.
- Determine if there was enough reserve in the cold-gas reservoir to sustain the actuators during a flight.
- Determine the robustness of the autopilot to deviations from the approximate aerodynamics, and the autopilot's ability to handle deadbands and delays in the actuators.
- Check the electrical interfaces between the autopilot, the sensor package, the telemetry unit, and the actuators. Any of the above problems could have caused the missile to fail during flight.

HARDWARE-IN-THE-LOOP

Computer Equipment

The computers and equipment used at NWC for HWIL simulations has been evolving. Six years ago hybrid equipment which combined a general purpose digital computer with an analog computer was the heart of the simulators. For the work presented here (Figure 3) a high-speed digital computer, the AD10, was used for the first time. More recently, the AD10 computers have been replaced with the more advanced system, the AD100 computer. The HWIL simulation was composed of an AD10 digital computer which drove a flight table (CARCO), and had DACs, ADCs, sensors and control lines for communicating with the missile hardware.

The AD10's, made by Applied Dynamics, replaced the digital/analog hybrid systems. This high-speed digital computer used a 16-bit integer arithmetic. The analyst had the same problems with scaling and dynamic range that were associated with programming of analog computers (Figure 4). The advantages of this computer over the analog computers were that it was self-documenting, that is, a program listing could be obtained, and machine problems were usually apparent. On analog equipment computer problems could go unnoticed, but on the AD10 computer problems were generally catastrophic. The use of a fixed point arithmetic led to many problems including noise due to round off and lack of dynamic range in the program variables. It was not certain when we started the simulation that the AD10 would be fast enough to host a 6-degree of freedom simulation (6-DOF) while completing tasks associated with driving the flight table and communicating with the hardware. In this

simulation, after optimizing the code for speed, a frame time of 387 microseconds was achieved. This meant that the integrals could be updated every 1.16 milliseconds. Because of time constraint we were not able to incorporate body bending, data logging or the complex actuator model into the digital program while hardware was in the loop. Strip chart recorders were used for recording data, and a body bending study was addressed in an all computer simulation.

Digital Simulations

Two 6-DOF simulations were built for use in the design and analysis of the tail controlled missile. One program written in FORTRAN was used in autopilot design and aerodynamic modeling. The other simulation was implemented on the AD10 computer for use in doing high-speed runs and testing hardware. High-speed runs become necessary when producing performance envelopes and doing parametric studies. The FORTRAN program was hosted on a VAX 11/780 and ran 50 times slower than real-time. The AD10-hosted program ran in real-time when hardware was used in the simulation and faster than real-time when the simulation was operated alone. A 20-second flight simulated in FORTRAN took about 15 minutes. The same flight took about 10 seconds on the AD10. The simulations were built by different people starting from different equations and using different integration methods. For example, the FORTRAN program used Euler equations for transformations and a fourth-order Runge-Kutta integrator. The other simulation used quaternions and Adams-Bashforth third-order integrators. The two programs were of the same complexity and modeled subsystems with the same detail. We hoped that the final products would produce the same results. Over a month of comparative studies of the two simulations led to computer programs that had detailed agreement. This time was well spent. Debugging of both programs was accomplished and confidence in both simulations increased greatly.

Hardware-In-The-Loop Simulation

The HWIL simulation was designed to interchange hardware for software modules easily. Modules which could be switched were the autopilot, the actuators, the rate gyro sensor package and the commands programmer (Figure 5). The flight table could be driven by the simulation. Models solved only on the computer were the airframe model, aerodynamics, missile geometries, thrust profile and the accelerometers. Hardware that was tested but not modelled on the computer were the telemetry package and the built in test sequencer.

SUBSYSTEM TESTING WITH THE HARDWARE-IN-THE-LOOP SIMULATION

Testing Of The Autopilot Brassboard

The first set of hardware used in the simulation was a preliminary implementation of the autopilot (Figure 6). This brassboard autopilot needed verification before flight ready hardware was built. The HWIL simulation was the tool chosen for this purpose. The simulation had a model of the autopilot developed in an analysis effort by the Dynamics and Control branch. The brassboard was also an implementation of this model. The hardware autopilot consisted of a hybrid system composed of a microprocessor which did the timing and calculated gains, and analog circuits which formed the acceleration and rate loops. The approach to debugging the hardware was to run the simulation with the hardware autopilot in the loop and then to run the simulated autopilot. Strip chart traces of important simulation variables were examined. Differences between the two sets of traces pointed to problems that needed to be resolved.

As might be expected, the first experiment showed vast differences in the hardware autopilot and the all-up simulation. These differences were traced to mismarked resistors, the digital program in the microprocessor selecting incorrect gains as a function of altitude and velocity, and different conventions used in determining the signs of the outputs and inputs. Two weeks of intense work were spent debugging the brassboard autopilot after which the two sets of traces started resembling each other. As mentioned above, the HWIL had been verified against the FORTRAN program used in the autopilot study. Thus, by default, problems which arose were ascribed to the hardware.

After debugging the hardware brassboard, we were able to start examination of the autopilot implementation. The first problem that caught our attention was a glitch in the airframe model at autopilot enable. Autopilot enable closed the acceleration loop 4 seconds after launch. The flight table was being driven in parallel with the simulation so an observer could get a feel for the response of the airframe to this transient. It was found that biases built up quickly in the accelerometer feedback path when the circuit was opened. These biases caused the airframe transient. The glitch was not going to be a problem for the unguided test vehicle to be fired. However, looking toward a future guided round we decided to solve the problem now. The digital program was rewritten to ramp the "K1" gain from zero to its nominal value in a half second after enable. This change smoothed out the transient on the airframe. G-bias being added for an air-launched shot would have aggravated this airframe transient before ramping the closure of the autopilot loop.

After the first session the brassboard autopilot was left in the simulation laboratory for use in future HWIL tests. The "go ahead" was now given to start building the flight ready autopilot boards.

Testing With The Sensor Package Mounted On The Flight Table

Next a sensor package consisting of the craft gyros and accelerometers was mounted on the flight table (Figure 8). The accelerometers were not used. The rate gyro outputs of this package could be switched by the digital simulation as inputs to the brassboard autopilot or to the simulated autopilot. Biases, scale factors and sign conventions were determined from these tests. The interface from the sensor package to the hardware autopilot was verified. Checking that the rate gyros are mechanically mounted properly and that the autopilot does not incorrectly invert the signs of the feedback sensors is one of the more important checks that can be accomplished in a HWIL simulation. Early in my career I was part of a team that fired a surface-to-surface missile with the roll rate gyro hooked up backwards. That missile firing was one of the more spectacular events that I have witnessed.

With the rate gyro in the loop, the characteristics of the flight table became important. The flight table added a phase lag to the feedback of the lateral autopilot loops and the roll autopilot loop. If uncompensated this phase lag caused the HWIL simulation to become unstable at high gains. The gains of the simulation are associated with the dynamic pressure on the missile which increases as the square of the missile velocity. At 4 seconds into a run, the flight table would start to chatter and not stop until near the end of the run. To prevent these oscillations, second-order lead-lag compensators were wired on the analog computers and used to filter the flight table commands (Figure 9). The compensators stopped the oscillations due to phase lags.

but they increased a buzz on the table by amplifying the 60 Hertz noise. The 60 Hertz noise is an unpreventable side effect of the laboratory power supplies.

Testing of the Actuator Package

The next hardware to be tested using the simulation was the cold-gas actuator unit (Figure 10). There had been bench tests of the unit by the contractor prior to delivery of the subsystem. The company had plotted step responses and phase-gain data from tests using several hinge moment loads. However, whether the unit had sufficient bandwidth to stabilize the missile was still a question. Our first priority was to resolve this issue. The roll control loop was the highest gain loop in the missile system. The polar to transverse moment of inertia ratio was on the order of 1:100. It was in the roll loop that we expected difficulty. The actuators were pressurized from an external dry helium source and were electrically commanded by the digital computer. The simulated autopilot produced fin position commands. There were potentiometers mounted on the axes of all four fins that measured the angular position of the fins. Also, each axis was restrained with a torsion bar that applied a returning moment proportional to the angular displacement of the fin. The bars could be held fixed at various lengths which provided different simulated aero loads. The output of the potentiometers was fed back to the digital simulation where they were used to determine the control force on the airframe.

After several false starts we got the hardware talking to the simulation and were able to run a simulated flight. Upon examination of the strip charts several facts were evident. The flight was not wildly oscillatory and the flight trajectory was about as planned. There was severe noise on both the lateral channel and the roll channel. Both lateral and roll channels sustained limit cycles (Figure 11). The amplitude of the roll limit cycle was on the order of ± 2 degrees and the lateral channels experienced excursions of ± 0.2 degree. As had been predicted, deadbands in the actuators were the cause of the limit cycle. What was not expected was that all four axes had different size deadbands and different frequency responses. After 15 minutes of intermittent testing the simulation degraded as the actuators failed.

The actuator unit was returned to the contractor for examination and repair. They found that the solenoid valve seats that stopped the flow of gas into and out of the piston chambers failed as a result of the high-duty cycle. The high-duty cycle of the solenoids was a result of the limit cycle of the missile. Other problems that the company undertook to correct were a reworking of the electronics to get minimum deadband out of all axes, changing the power supply wiring of the unit to decrease noise on the fin position pots, and free up some locking pins that were sticking. The results of this first series of test were positive even with all the problems that emerged. It had been shown with the help of the HWIL simulation that this low-volume, cold-gas actuator design could be used to control a missile.

System Testing

The actuator unit was returned and designated for use with the HWIL simulation. The simulation now had a full complement of hardware at its disposal. We were able to undertake several tasks for the next several months. Important among these tasks were characterization of the actuator unit, verification of simulation models against the hardware, and study of the stability of the missile system.

Open-loop and HWIL tests were used to characterize the actuators. The nonlinearities associated with the unit were as important as the bandwidth and damping. Flights were run with several simulated aerodynamic loads on the fins. We needed to verify that the missile would be stable throughout the regime of aerodynamic hinge loads that would be seen during normal flight. The result of these studies was a complex model of the actuators that was implemented on the high-speed digital computer (Figure 12). This model slowed the frame time of the simulation by 30% and was not normally used when other hardware was in the loop.

Concurrent with the above study, was an attempt to decrease the amplitude of the limit cycles on the lateral and roll channels. The roll limit cycle might have caused apparent smearing of a target on a future guided round. Component changes on the brassboard autopilot were arrived at which increased the frequency of the roll limit cycle and decreased its amplitude. Independent autopilot analysis confirmed that these changes were acceptable (Figure 13). The changes were added to the flight ready autopilot hardware. The problems that were being encountered in the HWIL simulation due to actuator characteristics were communicated to the contractor. It was hoped that future iterations of the actuator design could improve the characteristics of the unit. The limit cycle phenomena could only be demonstrated in a dynamic simulation. Bench tests of the actuators could not produce the effects of the deadbands and delays. Thus, the HWIL simulation was used to rewrite the specifications on future actuator designs.

The aerodynamics model for the tail controlled missile was approximate. Wind tunnel testing for this missile would have been expensive in terms of time and cost. The gains for the autopilot had been determined using the approximate aerodynamics. Using the simulation with the hardware switched into the loop the aerodynamics were increased and decreased from the nominal values by 30%. The simulated missile flew reasonably well with these deviations in aerodynamics. We were gaining more confidence in the robustness of the missile system.

Blowdown Tests

As mentioned before, determining if the cold-gas reservoir had the capacity to sustain a flight, was a prime concern (Figure 14). Calculations had been made by the contractor of the gas flow needed to operate the actuator unit assuming a given duty cycle and a given duration of flight. However, the calculations did not include fin movements due to limit cycles or other noise sources and did not account for gas leakages which had been observed in the HWIL testing. By switching all of the hardware into the simulation and pressurizing the actuators from the cold-gas reservoir, gas usage could be determined. The reservoir was opened with an explosive device and was not refilled locally. So we had one attempt at determining gas usage. The pressure in the gas regulator was monitored as were the normal simulation variables. A drop in pressure at the regulator indicated when the gas bottle had been exhausted. The test was conducted by running a flight, resetting the hardware and the computer and then repeating the same flight. The bottle sustained two entire flights similar to the proposed launch before a decrease in pressure was observed. One more major hurdle had been overcome.

BODY BENDING STUDY

The body bending modes of the tail controlled missile were determined from an experimentally validated analytical model. These modes were too high in frequency for the model to be run on the high-speed computer when hardware was in the

loop. Separate hardware and software studies were undertaken to determine if body bending might be a problem. A linear analysis of the missile system with body bending modeled showed some ringing in response to step inputs at high dynamic pressures (Figure 15). This ringing quickly died out. Studies using the high-speed simulation indicated that the missile could ring at body bending frequencies but that the deadbands in the actuators effectively stopped these modes. The deadbands did not allow small amplitude oscillations to be passed by the actuators.

A hardware test was devised to detect body bending modes in which the missile was suspended from elastic cords. With the missile suspended, the autopilot, sensors and actuators were energized. The missile was then struck with a rubber mallet to see if body bending modes could be initiated on the airframe (Figure 16). Accelerometers externally mounted on the airframe picked up any induced frequencies. This test would show if body bending modes could be sustained in the airframe-sensor-autopilot-actuator loop. The strip charts showed no signs of ringing. It was felt that body bending if it were a factor would die out quickly.

PREFLIGHT CHECKOUT

The preflight system check is where the flight ready hardware is brought together and tied into the HWIL simulation. This is the last chance to catch errors that might have crept into the harness wiring, autopilot electronics, telemetry circuits or any of the many interfaces. The engineers responsible for the various pieces of the missile generally assemble in the simulation facility around the hardware. This is a stressful environment due to time constraints and one of a kind hardware undergoing dynamic testing. However, it is in this environment that many problems are solved.

The hardware involved in the preflight testing were the autopilot, digital programmer, built-in-test (BIT) sequencer, cold gas actuator unit, craft sensors, and the wire harnesses used throughout the missile (Figure 17). This was all new flight ready hardware that had not previously been part of the HWIL simulation.

The telemetry (TM) unit was used to monitor the outputs of the sensors, the autopilot, the actuators, and various battery voltages. These same signals were directly monitored on strip chart recorders as were the important simulation variables. A magnetic tape was used to record the data stream of the TM unit. At the end of a flight the TM tape was played back through a demodulation unit and the monitored variables were stripped out. By comparison with recordings taken during the simulated flight we were able to verify that the correct data was being received by TM and that the correct scaling had been used. As is normal, all of the tests did not proceed smoothly. While debugging an interface between the autopilot and TM unit, electronic circuits in the autopilot boards were damaged. There was a spare set of flight ready autopilot boards which were inserted and the testing proceeded. The TM tape of one of the runs was sent to the data reduction facility for processing. The scale factors and biases for the TM channels were also sent and plots were made of telemetry data using engineering scaling. After several iterations we were convinced that the telemetry unit was working and that TM data could be satisfactorily reduced.

The accelerometers in the sensor package could not be used in the simulation. However, tests were contrived during preflight checkout that allowed verification of the accelerometer polarities. By using gravity as the measured acceleration and watching the resulting motion of the fins, we were able to check alignment. One of the accelerometer outputs had to be inverted.

The flight profile for the tail controlled missile had been decided earlier (Figure 18). It consisted of commanded accelerations in the pitch and yaw planes and rates commanded about the roll axis. The flight was designed to last about 50 seconds. Maneuvers occurred during the first 13 seconds and drag data was to be collected during the remainder of the flight. At 50 seconds from launch, a command to destruct would be issued and the airframe caused to breakup. This last precaution was to keep the flight on the NWC ranges. The maneuvers consisted of independent pitch and yaw plane accelerations followed by a combined plane acceleration. The combined plane maneuver would cause induced roll and test the accuracy of the roll autopilot. A final maneuver was to command a roll rate of 45 degrees/seconds for 1 second and then reverse the command for the next second. This caused the missile to roll 45 degrees and then return to its original orientation.

The commands were downloaded into the digital programmer. A BIT sequencer served as a master timer and enabler for the various prelaunch functions of the missile. The BIT sequencer monitored the battery voltages and would not allow the squib for the gas bottle or the motor squib to fire unless all conditions were correct. Of course, the motor was not in the simulation facility but the firing pulse was monitored. This firing pulse was used to start the digital simulation. The first time the sequencer was used to control the HWIL simulation nothing worked. The program used by the BIT sequencer had errors which were wrong out at this time. Finally the BIT sequencer started the simulation and data was taken.

The data taken during the preflight checkout served to document the flight hardware and the expected flight environment. After launching the missile we would return to this data for comparison. If a problem occurred during flight this preflight documentation and data would be a starting point for understanding the problem.

FLIGHT

The tail controlled missile was launched on 8 November 1985 (Figure 19). The telemetry channels were demodulated and stripped out on a chart recorder during the flight. Watching the strip chart recordings was an experience. The charts came up properly but soon showed a high-frequency oscillation which gradually started to disappear. TM transmission ceased long before was expected (Figure 10). We knew immediately that there was going to be long nights ahead to make sense of the data. From the charts taken during the flight it was determined that the tail controlled missile had sustained body bending oscillations and that the cold-gas reservoir which powered the actuator unit had been exhausted before the expected end of flight. The rest of the story had to await radar plots of the trajectory and reduction of the data from the telemetry recordings.

The radar plots which came in later that morning showed that the missile had performed the proper trajectory during the first part of the flight but had started to tumble 19 seconds from launch (Figure 21). It appeared that the body bending oscillations had imposed a high duty cycle on the actuator unit. This high duty cycle exhausted the cold-gas reservoir before the end of flight. With the gas reservoir exhausted the actuators no longer responded as necessary. Lack of controllability led to the instability of the missile. The question remained as to how well the tail controlled missile had performed while the actuator unit was fully pressurized. This flight was a challenge to the analysts. There was information that needed to be recovered but it was masked by noise and dominated by a high frequency oscillation.

There were several receiving sites which recorded the TM data stream. All of the sites suffered from obscuration during some part of the firing. The obscuration problem resulted in TM dropouts. However, we were able to concatenate the data from two sites to produce a relatively clean launch record. The data was digitized and dumped onto the digital computers for

further processing. It was up to the analysts to recover as much information from the launch as possible. Graphics based programs were written to review the telemetry data. These programs were also used to delete TM dropouts and remove biases from the accelerometer and rate gyro data. The high-speed simulation and experience gained from the HWIL testing was used in the postflight analysis.

POST FLIGHT ANALYSIS

Postflight analysis was begun by separating the body bending frequencies from the rigid body motion of the missile. The work also divided along those lines. One effort tried to determine the mechanism for the body bending problem and the other effort tried to document the rigid body characteristics of the missile.

Rigid Body Motion

There was a factor of 10 difference between the body bending and maximum rigid body frequencies. So, a second-order digital low pass filter was used to remove the body bending modes from the airframe motion. The rate gyro and accelerometer outputs now started looking similar to the data gathered during the preflight testing. The fin positions, however, appeared to be off by a factor of 2 in amplitude from the HWIL results. The preflight TM tapes were again compared with the strip charts taken during that session to verify the TM scale factors. There was agreement and the smaller amplitude deflections were accepted as real.

To upgrade the aerodynamics for the tail controlled missile model we needed to derive the angle of attack, angle of sideslip and aerodynamic wind angle. These variables along with the fin deflections, Mach number and accelerations were used to determine aerodynamic coefficients. A mathematical procedure was derived for obtaining the angles (see Appendix). The method involved using the rate gyro and accelerometer data to calculate the inertial to missile transformation and subsequently compute the components of the velocity vector in missile coordinates. By comparison of the results of this procedure with range data gathered from camera coverage of the flight, we were able to adjust out the biases. In the end the technique had reproduced from the TM data all of the variables monitored in the preflight simulation. We were now ready to overlay plots from the simulation and plots derived from the telemetry data.

The pitching moment coefficient C_m was adjusted to account for the observed differences in fin deflections. The induced roll moment was found to be higher than predicted. The induced roll appeared primarily during the combined plane maneuver and the moment produced was about 50% higher than predicted. Changes to the aerodynamic models and an updated thrust curve were implemented in the simulation. The simulation now reproduced the flight test data quite well. The degradation of the pressure to the actuators due to the exhaustion of the cold-gas reservoir was also modeled in the simulation. We tried to replicate the degradation of the actuator bandwidths and the subsequent instability of the missile (Figures 22 through 24).

Body Bending Study

Studies into the mechanism for the body bending went in two directions. The first line of inquiry checked the bandwidth of sensors and actuators to see if the airframe-sensor-autopilot-actuator loop could have accounted for the problem. The second effort was to determine if there was a mechanical or aerodynamic effect that accounted for or help sustain the bending modes. The first effort led to cross correlation techniques using fast Fourier transforms of the data to determine the transfer function between inputs and outputs. The cross correlation method was used on the actuator commands and fin positions. This helped us get a feel for the bandwidths of the actuators during flight. The four actuators differed markedly and two of the bandwidths were much higher than the other two. Cross correlation is a linear technique and in the presence of nonlinearities such as deadbands is not completely valid. However, we were able to use the information to vary the actuator models in the simulation.

The second approach led to an unbalance term in the fins. The center of the gravity of the fin was a half-inch aft of the hinge line. The offset was small and had been disregarded for two reasons, the carbide matrix metal was hard to machine, and an unbalance fin was thought to help prevent fin flutter. In the presence of the unbalance term it was found that the body bending amplitudes were strongly a function of the aerodynamic hinge moments. Without wind tunnel data on the fins the hinge moments could not be accurately predicted.

We were able to demonstrate the body bending problem in both a linear analysis and the high-speed simulation with the introduction of the unbalance term and larger hinge moments (Figure 25). Extending the bandwidth of two of the actuators also exacerbated the problem. If the models are correct then balancing the fins and placing notch filters in the autopilot would eliminate the effects of the bending modes.

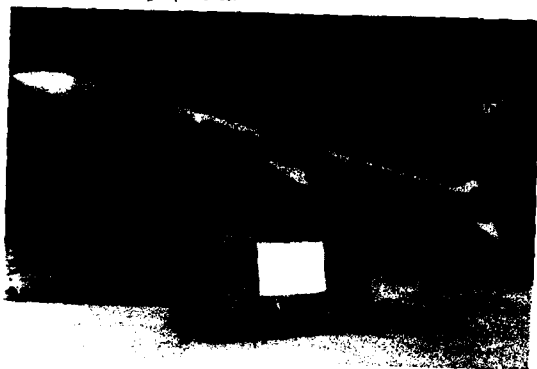
By matching the flight data a simulation was produced which helped to document the missile and the missiles capabilities. The model can be used with greater confidence to predict missile performance and help in improving that performance. We also now have a tool which by comparison can be used to measure the performance of other air-air missiles.

CONCLUSIONS

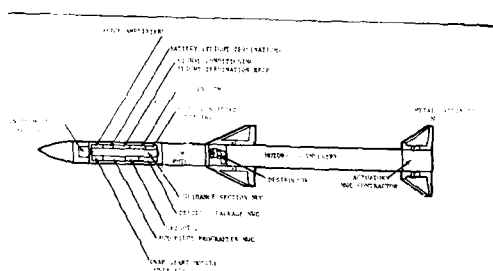
Our conclusions from this experience are that a simulation capable of testing missile HWIL is an invaluable tool. The simulation gives the design engineers a chance to see how their missile subsystems perform in a dynamic environment. The simulation is a tool for debugging flight hardware and proving the controllability and stability of the flight system. One of the most valuable aspects of this testing is that all the engineers are brought together in one place, at one time with all the subsystems interfaced and operating. This proves to be a very stressful situation but also is a very creative environment for the engineer. Problems are quickly solved which otherwise might take considerable time. Some problems might surface only during the flight. The flight test itself is extremely necessary. In a new missile design many guesses are made in the areas of aerodynamics, body bending, actuator performance, and motor performance. These guesses are the foundations upon which the simulation and analysis efforts inevitably rest. Our experience is that every flight test produces new data which the analyst will have to spend days to understand.

After the firing of the tail controlled missile and subsequent postflight analysis we felt that several major technical accomplishments had been achieved. The program had demonstrated the airframe controllability. The rocket motor had performed flawlessly. A cost effective, cold-gas actuator had been packaged within the required volume and the actuators had been shown to have the necessary bandwidth to control the missile. The BIT sequencer and digital programmer had worked well. The autopilot design and implementation performed as required to stabilize the rigid body motion of the airframe. The

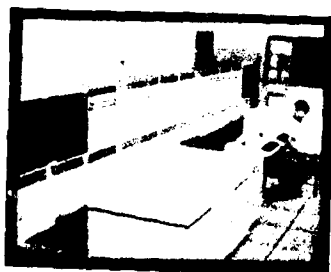
TM system performance was proven. The Carbide-matrix fins had been flown and the airframe integrity was demonstrated. The firing had also shown that we needed to do more homework in some areas. We had to control the body bending modes and we needed to reject or improve the effects of the nonlinearities in the actuators. As analysts the tail controlled missile program had been a valuable learning experience.



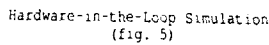
Tail Controlled Missile
(fig. 1)



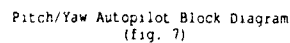
Components - Tail Controlled Missile
(fig. 2)



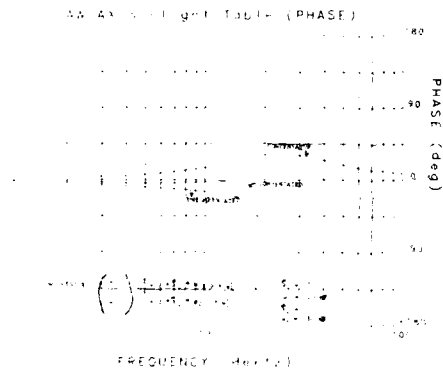
Simulation Laboratory - Naval Weapons Center
(fig. 3)



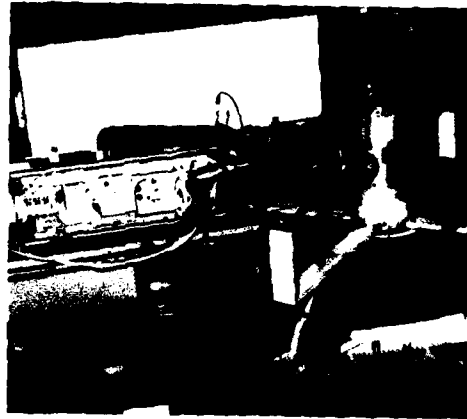
A black and white photograph showing a person in a dark, industrial or laboratory setting. The person is wearing a dark jacket and is positioned in the foreground, looking towards the right. A large, bright, curved object, possibly a piece of machinery or a large container, is visible in the background. The scene is dimly lit, with a strong light source creating a bright area on the right side of the image.



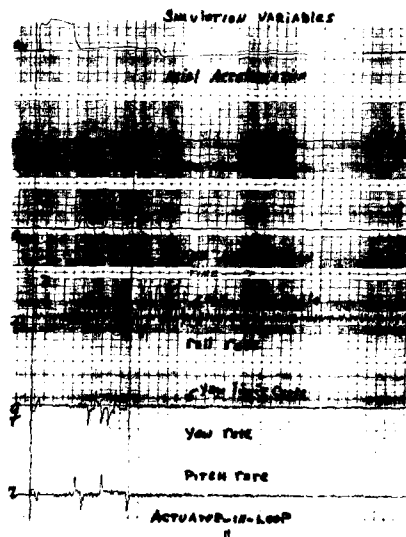
Sensor Package Mounted on the Flight Table
(fig. 8)



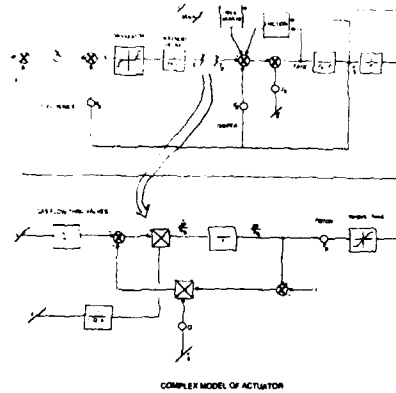
Compensating the Yaw Axis of the Flight Table
(fig. 9)



Testing the Cold Gas Actuator Unit
(fig. 10)



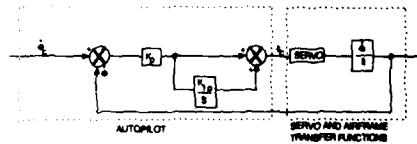
Strip Charts of Computer Variables from Actuator Testing
(fig. 11)

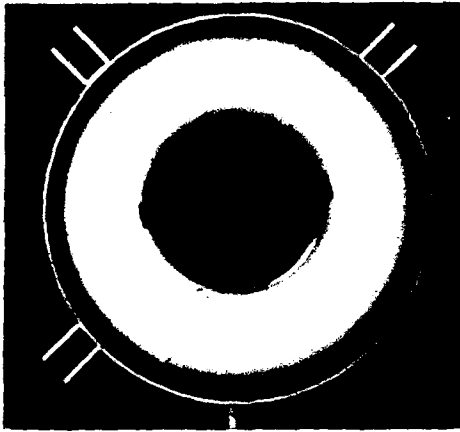


Complex Model of One Axis of the Actuator
(fig. 12)

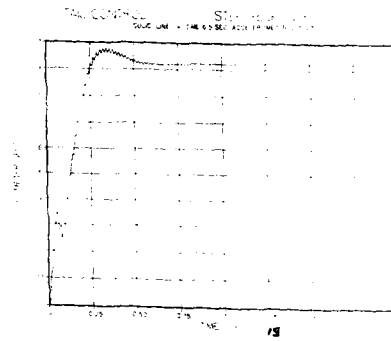
TAIL CONTROL
ROLL AUTOPILOT BLOCK DIAGRAM FOR ANALYSIS

Roll Autopilot Block Diagram
(fig. 13)





Cold Gas Reservoir for the Actuator Unit
(fig. 14)



Step Response from Linear Model of Missile
Showing Body Bending Frequencies
(fig. 15)

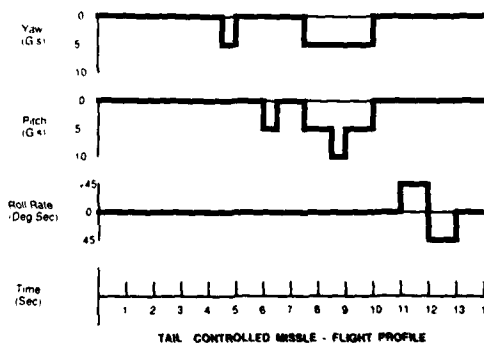


Missile Suspended from Elastic Cords
Body Bending Tests
(fig. 16)



Preflight Checkout
(fig. 17)

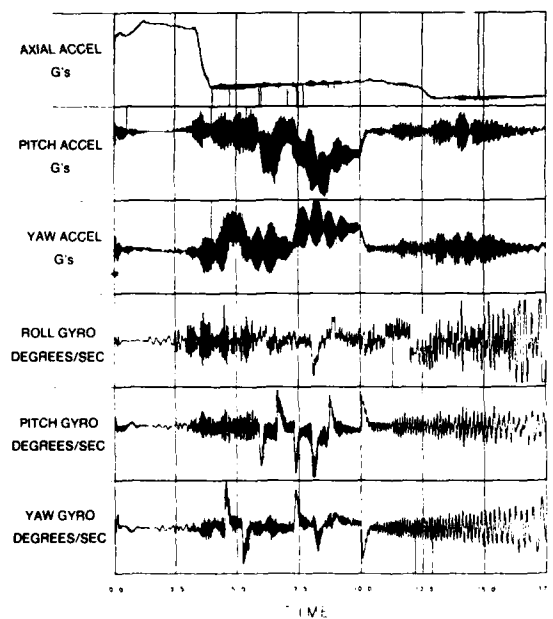
Flight Profile
(fig. 18)



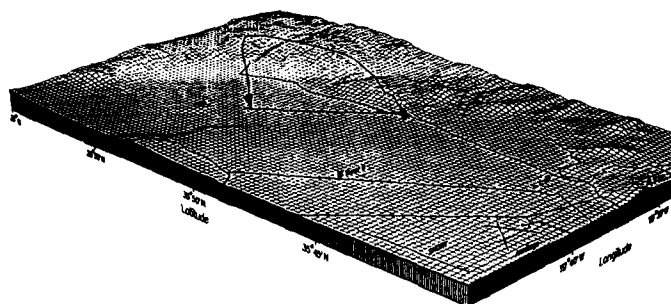


Launch of the Tail Controlled Missile
(fig. 19)

Tail Controlled Missile
Live Firing Data
8 November 1985

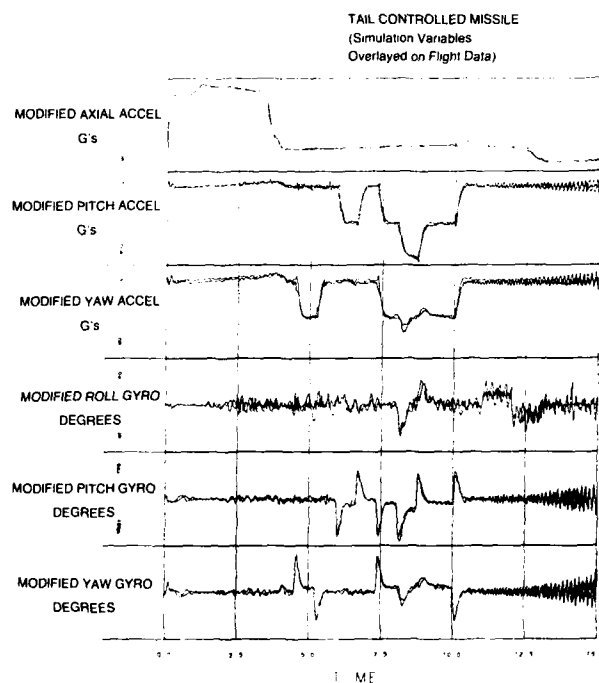


Telemetry from the Missile Firing
(fig. 20)

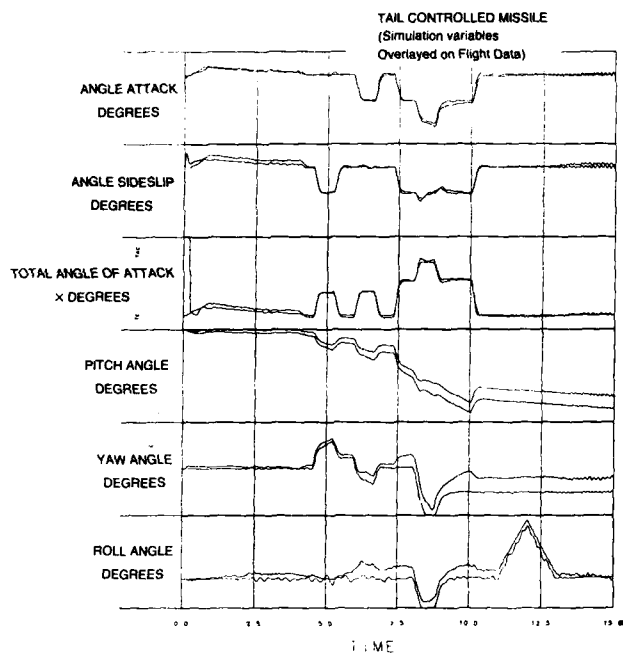


NAVAL WEAPONS CENTER, G RANGE
CHINA LAKE, CALIFORNIA
DATE: 8 November 1955

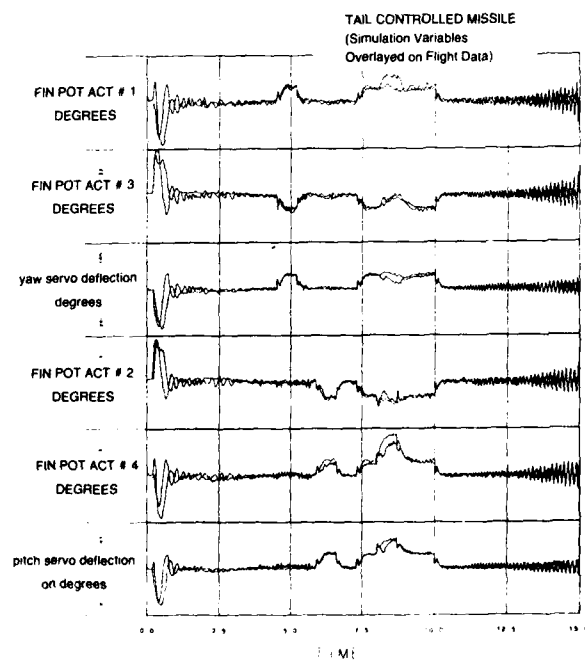
Trajectory from Radar Data
(fig. 21)



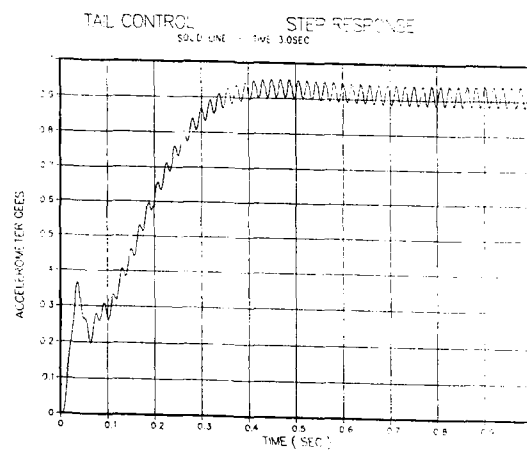
Overlay of Accelerometer and Rate Gyro
Data from Firing and Simulation
(fig. 22)



Overlay of Angles of Attack and Euler Angles
Derived from Firing with Data from Simulation
(fig. 23)



Overlay of Fin Deflection from Firing
and Simulation
(fig. 24)

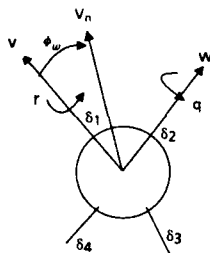


Plot from Postflight Body Bending Analysis
(fig. 25)

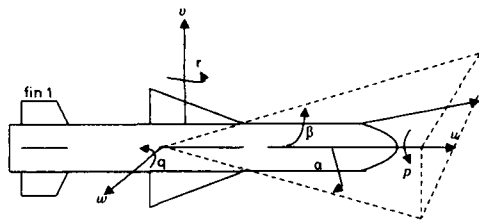
Appendix

MATHEMATICAL PROCEDURE FOR DERIVING DATA

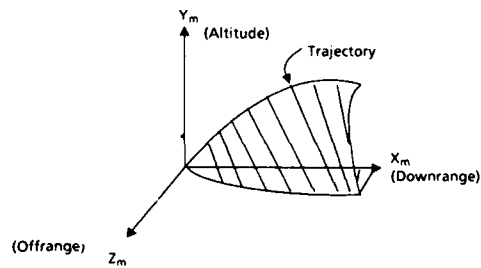
The coordinate systems and nomenclature for the variables plotted in enclosure (2) are:



Body fixed coordinates
from aft looking forward



Body fixed coordinates



Inertial coordinates

$$\alpha = \tan^{-1} \left(\frac{-V}{U} \right)$$

$$\beta = \tan^{-1} \left(\frac{-W}{U} \right)$$

$$\phi_w = \tan^{-1} \left(\frac{-W}{V} \right)$$

Accelerometers:

ax = axial accelerometer
ay = pitch accelerometer
az = yaw accelerometer

Rate gyros:

p = roll rate gyro
q = pitch rate gyro
r = yaw rate gyro

Derived angles:

α = angle of attack
 β = angle of sideslip
 α_T = total angle of attack
 ϕ_w = aerodynamic wind angle

Inertial angles:

θ = pitch angle
 ψ = yaw angle
 ϕ = roll angle

Equations for the derivative of the quaternion is calculated from the output of the rate gyros:

$$\begin{aligned} \dot{e}_1 &= 5^* (-p^* e_4 - r^* e_3 - q^* e_2) + \text{err}^* e_1 \\ \dot{e}_2 &= 5^* (r^* e_4 - p^* e_3 + q^* e_1) + \text{err}^* e_2 \\ \dot{e}_3 &= 5^* (-q^* e_4 + p^* e_2 + r^* e_1) + \text{err}^* e_3 \\ \dot{e}_4 &= 5^* (q^* e_3 - r^* e_2 + p^* e_1) + \text{err}^* e_4 \end{aligned}$$

where

$$\text{err} = 1 - (e_1^* e_1 + e_2^* e_2 + e_3^* e_3 + e_4^* e_4)$$

The quaternion (e1,e2,e3,e4) results from the integration of the above derivatives and initialization:

$$\begin{aligned} e1(0) &= \cos(\phi/2) \cdot \cos(\theta/2) \cdot \cos(\psi/2) - \sin(\phi/2) \cdot \sin(\theta/2) \cdot \sin(\psi/2) \\ e2(0) &= \cos(\phi/2) \cdot \sin(\theta/2) \cdot \cos(\psi/2) - \sin(\phi/2) \cdot \cos(\theta/2) \cdot \sin(\psi/2) \\ e3(0) &= \cos(\phi/2) \cdot \cos(\theta/2) \cdot \sin(\psi/2) + \sin(\phi/2) \cdot \sin(\theta/2) \cdot \cos(\psi/2) \\ e4(0) &= \cos(\phi/2) \cdot \sin(\theta/2) \cdot \sin(\psi/2) + \sin(\phi/2) \cdot \cos(\theta/2) \cdot \cos(\psi/2) \end{aligned}$$

The transformation matrix from inertial to missile coordinates is:

$$\begin{bmatrix} a11 & a12 & a13 \\ a21 & a22 & a23 \\ a31 & a32 & a33 \end{bmatrix}$$

where:

$$\begin{aligned} a11 &= e1 \cdot e1 - e2 \cdot e2 - e3 \cdot e3 + e4 \cdot e4 \\ a12 &= 2 \cdot (e3 \cdot e4 + e1 \cdot e2) \\ a13 &= 2 \cdot (e2 \cdot e4 - e1 \cdot e3) \\ a21 &= 2 \cdot (e3 \cdot e4 - e1 \cdot e2) \\ a22 &= e1 \cdot e1 - e2 \cdot e2 + e3 \cdot e3 - e4 \cdot e4 \\ a23 &= 2 \cdot (e2 \cdot e3 + e1 \cdot e4) \\ a31 &= 2 \cdot (e2 \cdot e4 + e1 \cdot e3) \\ a32 &= 2 \cdot (e2 \cdot e3 - e1 \cdot e4) \\ a33 &= e1 \cdot e1 + e2 \cdot e2 - e3 \cdot e3 - e4 \cdot e4 \end{aligned}$$

The inertial angles (l,ψ,φ) are calculated from the quaternion:

$$\begin{aligned} \theta &= \text{atan2}(a12, a11) \\ \psi &= \text{atan2}(-a13, \sqrt{a11^2 + a12^2}) \\ \phi &= \text{atan2}(a23, a33) \end{aligned}$$

The components of gravity in missile coordinates are:

$$\begin{aligned} Gx &= -g \cdot a12 \\ Gy &= -g \cdot a22 \\ Gz &= -g \cdot a32 \end{aligned}$$

The derivatives of the velocity components along missile axes are:

$$\begin{aligned} \dot{u} &= g \cdot ax + Gx \cdot r \cdot w + q \cdot v \\ \dot{v} &= g \cdot ay + Gy \cdot q \cdot u + p \cdot w - l \cdot q \\ \dot{w} &= g \cdot az + Gz \cdot p \cdot v + r \cdot u + l \cdot r \end{aligned}$$

where the lq and lr terms are due to the accelerometers being placed forward of the C.G. by 4.63 feet q and r are differentiated numerically.

Integrating the above derivatives and initializing produces the velocity components along missile axes (u,v,w)

$$\begin{aligned} u(0) &= 0 \\ v(0) &= 0 \\ w(0) &= 0 \end{aligned}$$

The aerodynamic angles are derived from the velocities:

$$\begin{aligned} \alpha &= \text{atan}(-v/u) \\ \beta &= \text{atan}(-w/u) \\ \phi_w &= \text{atan}(w/v) \end{aligned}$$

Inertial velocities are found by rotating the body fixed velocities (u,v,w) using the transformation matrix:

$$\begin{aligned} \dot{x}_m &= a11 \cdot u + a21 \cdot v + a31 \cdot w \\ \dot{y}_m &= a12 \cdot u + a22 \cdot v + a32 \cdot w \\ \dot{z}_m &= a13 \cdot u + a23 \cdot v + a33 \cdot w \end{aligned}$$

Finally, we get inertial position by integrating the above derivatives and initializing:

$$\begin{aligned} x_m(0) &= 0 \\ y_m(0) &= 2888.5 \text{ ft} \\ z_m(0) &= 0 \end{aligned}$$

Since the above is an open loop procedure, small biases can cause the derived variables to drift. Where possible these offsets must be carefully removed.

Marginal Release Disturbances on Advanced Missiles

by

Ronald Deslandes
Messerschmitt-Bölkow-Blohm GmbH, FE121
P.O. Box 801160
D-8000 Munich 80, FRG

SUMMARY

Today's store separation analysis is more and more confronted to marginal clearance situations due to increasing requirements imposed by the aircraft operators.

In fact, that an advanced missile has to be perfectly released during arbitrary aircraft manoeuvres and variable installations affords the accurate knowledge of the missile's motion during tip-off.

The engineering task is therefore no longer focussed exclusively on the analysis of safety aspects of separation, but is now to be extended on the consideration of compatibility between operator's requirements to allow any strength of release disturbances and the missile control system to overcome such situations. The results expected from such an analysis is an accurate indication of any marginal limitation respective to safety or to controllability.

Based on simulations performed with a powerful 6-DOF code developed at MBB during the last decade, this paper deals with such inconsistencies implicated by excessive roll or pitch-motions during different rail-launch situations. After a short description of the basic algorithms, computed results involving data from flight test movie will be displayed by 3D-video, in order to prove that the problem area is well handled.

1. INTRODUCTION

The main objective of a separation analysis, when integrating an advanced missile system on a modern combat aircraft, is to ensure all safety requirements for the aircraft and the missile for a successful operational delivery or in emergency cases.

Depending on the missile type under consideration the envelopes to be provided for such operations may be defined as follows:

- 0.5g to 2g for air to surface
- 0.5g to 4g for air to ground
- 1g to 7g for air to air operation

Within these zones of operation any physical contact between separation stores and aircraft has to be strictly omitted. At the same time, thermal interferences occurring between the plume of the missile and sensitive parts of the aircraft have to be monitored in order to prevent structural damages or losses of the engine performance in the case of gas ingestion.

Normally these aspects can easily be matched by the definition of appropriate specifications for the launcher characteristics, or preventions to be used during separation.

Even then, a major area of problems remains unsolved, if within such envelopes the delivery accuracy requirement is violated by the intensity of the release disturbance.

In such situations, where the limitations of the missile flight control system may be overridden by excessive rate-inputs to the gyro's of the missile or by excessive angular disorientation of the seeker-head, the release disturbance is considered to be marginal.

Any further deviation introduced by the leading parameters of the missile such as misalignment or failure of control devices, failure of the flight control system itself, may increase the release disturbance within the nearfield of the aircraft, and therefore cause a further degradation of the operational success.

In order to overcome such incompatibilities a new set of specifications for the control system design should be provided by the separation analysts.

Therefore, the topic of this paper will be to demonstrate the effects of such kind of marginal aircraft release disturbances and to give an indication for the determination of the leading parameters for such design specifications.

In order to proceed in this way a six-degree-of-freedom-code will be used to simulate the missile motion, taking into account all previously mentioned dominant interference effects. After briefly describing the basic algorithm of this code, some concrete examples will be picked up showing typical cases of marginal release disturbances expected at level flight and during a high-g-maneuver.

2. THE MBB-STORE-SEPARATION-PROGRAM (SSP)

In general, such a code combines the two major engineering tasks of aerodynamics and flight mechanics within a main loop circuit as sketched in Fig. 1. The flight mechanic part includes the complete set of equations of motion necessary to describe the store translation and rotation with all non-linearities introduced by cross-coupling effects. The SSP-code, for instance, makes use of quaternion equations in order to provide an arbitrary non-linearized resolution for the store rotation.

The aerodynamic task itself is splitted in a basic subsonic approach and a supersonic extension. The basic subsonic part consists in concatenating three main families of aerodynamic loads

- aircraft flowfield interference
- dynamic effects (damping)
- reciprocal interferences

In the supersonic case these implements have to be completed by non-linearities such as:

- correct steady shock representation (detached or reflected)
- time dependent moving and reflected shocks on the separating store

The approach corresponds to a flow angularity concept as sketched in Fig. 2.

In a first step the aircraft flowfield as well as the free-flight aerodynamics of the store are evaluated separately by means of higher order Euler-solver.

In a second step the aerodynamic characteristics of the store are decomposed into sectional load-gradients for different combinations of angles of attack and sideslip.

During a trajectory calculation the velocity components resulting from the non-uniform flowfield around the aircraft, from the store translation and rotation are superposed to effective sectional flow angles. These angles of attack and sideslip are imposed to the load gradients of each store section and summed up to total store loads.

Within this representation aerodynamic damping effects are automatically captured by converting the store rotation into discrete sectional velocities.

The higher order effects however have to be separately implemented by upgrading these trajectory loads with measured installed loads and with unsteady Euler calculations in discrete store positions.

For this purpose, the Euler equations are formulated for moving control volumes which allows an accurate description of the dynamic effects of the store surface in motion. A detailed description of this theory is given in Ref. 1. Worked out into the divergence formulation this set of equations can be written as shown in Fig. 3, where ρ , l , m , n and e correspond to the conservative variables of the specific flow properties such as density momentum and total energy. The store velocity is represented by x , y and z . Using this formulation it is possible to analyse the major part of inviscid non-linearities occurring during a launch situation. Even a hot gas plume analysis can be quantitatively achieved within this description. Fig. 4 shows such a result describing the isotherms within the plume of a starting missile interfering with the fully deflected trailing edge flap of the aircraft wing.

This kind of approach affords at least 30.000 finite volumes in order to perform a reasonable calculation. Typical discretizations are shown in Fig. 5 and Fig. 6 for a missile in a semi-submerged fuselage corner installation and at a launch transient position.

Summarizing all options achievable with this code, as shown in Fig. 7, any kind of aircraft manoeuvres can be described by parameters used to define the initial release condition. Looking at the store parameters in use, any type of store may be represented taking into account all relevant items of active controls and control surface deflection.

3. DEMONSTRATION OF MARGINAL RELEASE DISTURBANCES

As already mentioned in the introduction the marginality of the release disturbances occurs whenever the missile dynamic control capability is overridden by the dynamic response of the missile induced during release.

For this purpose two relevant cases will be highlighted. The first situation will produce a gyro saturation by the roll-response at a relaxed straight and level flight condition, whereas the second example deals with a strong angular disorientation during a high g manoeuvre on a corner point of the release envelopes.

Using some of the previously described SSP options the basic release disturbance arising from the installation effects will be amplified such as to cause a complete degradation of the roll rate for the first example and an excessive angular disorientation for the high performance manoeuvre during launch. Finally this last case will be picked up to show how to overcome degradation by using attitude control during the first moments of the separation phase.

Fig. 8 is illustrating the considered configuration which is featuring a fictive arrangement of air-to-air and air-to-ground missiles. Focussing on the underfuselage carried air-to-ground missile, it is obvious that the highest risk of gyro rate saturation is expected around the axis of reference providing the lowest moment of inertia.

In that case a first indication for the nature of the dominant release disturbance may be deduced from the installed rolling moment coefficients. Such a characteristic is shown in Fig. 9, where the aerodynamic roll up moment coefficient is plotted versus the aircraft angle of attack. In this specific case at $\alpha = 4^\circ$ the rolling moment changes its sign. For greater angles of attack the missile is supposed to perform an in-board roll, whereas a small reduction of angle of attack may invert this rolling motion according to the interference effects.

As soon as the missile separates from the launcher-rail a secondary roll response will be initiated by the cross-coupling effects with the other degrees of freedom. This increment can be easily extracted by analysing the launch trajectory at $\alpha = 4^\circ$, where the installed rolling moment is nullified. Such a result is shown in the top diagram of Fig. 10, where the roll time history is plotted during the first 0.9 seconds after the begin of the first movement of the missile. Tip-off occurs in this case at 0.1 seconds. Up to 0.3 seconds the roll rate remains constant until the pitch and yaw responses cause a positive gain in roll, which is certainly supported by the non-uniformities within the flowfield. A peak of 4.5 rad/sec (250°/sec) is reached at 0.7 seconds, where the missile is considered to be outside of the aerodynamic interference field of the carrier.

Assuming a roll-gyro limitation of 400°/sec this type of release disturbance is acceptable. If however a misalignment of the rudders is superimposed to the initial condition the roll rate may be easily increased up to values beyond this limitation. Using only a few tenths of degrees of misalignment on the four rear fins of the missile such as to provide by each an additional roll increment, the roll rate is amplified up to 430°/sec (7.5 rad/sec) as shown on the left of Fig. 10. The effect of misalignment of the rudders can now be seen between 0.1 sec and 0.3 sec, whereas the further response retains the principal characteristics as before.

Finally the installation effect is accentuated for a slightly different flight condition. Using a reduction of 2 degrees in angle of attack superimposed with an adverse initial misalignment of the rudders the roll rate can be brought up to values of nearly $-600^\circ/\text{sec}$ rotating in the other direction, which again will produce a complete roll saturation. This case is shown on the right diagram at the bottom of Fig. 10.

Looking at the three corresponding trajectories comparatively plotted in Fig. 11, the overall motion of the missile does not give any indication for such drastical differences in roll. These trajectories are only documenting a perfect safe separation behaviour.

Greater differences of the overall path of separation are illustrated in Fig. 12 for an air-to-air launch during a high g manoeuvre. Here, three different missile control modes have been selected in order to induce a strong angular disorientation and to demonstrate how to overcome this kind of degradation.

The first trajectory on the top of Fig. 12 is computed for a non-guided missile with fixed wings and without any control facilities.

In the second step the missile is simulated with free-floating canards between $\pm 35^\circ$ local deflection around their hinge line. In this case the roll inputs are additionally considered to be perfectly damped.

The bottom trajectory however was evaluated by implementing an attitude control mode, which is designed to maintain the initial orientation of the installed missile position.

Looking at the iso-Mach-lines and iso-lines for the angle of attack within the non-uniform flowfield of the aircraft on Fig. 13 and Fig. 14 the strong response of the missile seems to be quite reasonable. Along the missile path the Mach-number changes from low speed at $M=0.3$ up to the freestream condition of $M=0.9$ within two missile lengths, whereas the angle of attack is alternating between -15° up to 45° according to the initial high g condition.

A better analysis is provided by the time histories of the pitch and yaw motion of the missile during launch.

Fig. 15 is documenting the pitch angle response for the three cases under consideration. Tip-off can be seen at 0.12 seconds where the angular disorientation rapidly grows to values up to 14° within 0.2 seconds for the two unguided modes. With an active attitude control mode this disorientation is minimized to values less than 4° in pitch.

As shown in Fig. 16 the yaw motion is much stronger. There, the maximum angular displacement of the missile axis reaches values up to 25° within the same time. Depending on the characteristics of the target seeker such a strong dispersion may completely degrade the system and cause a loss of the missile. However, using an attitude controlled missile, the angular disorientation will be minimized retaining an advantageous tracking path. Without an attitude control, the delivery envelope of the missile has to be confined to acceptable levels of angular dispersion.

These facts can be validated by appropriate flight test results, as demonstrated by the movie to be shown during the presentation.

4. CONCLUSION

Marginal release disturbance effects have to be strictly differentiated from the safe separation requirements during the launch of advanced missiles from an aircraft.

Ensuring safe separation is more or less a matter of defining the proper launcher characteristics such as roll length, booster and ejector forces, in order to provide a wide release envelope.

In order to ensure a successful delivery it is essential to perform a sensitive analysis on all leading parameters which affect the dynamic response during release.

Whenever soft or hardware limits of the missile are overridden the corresponding release disturbances shall be considered as critical.

For rail launch situations the dominant sources were highlighted. Depending on the missile installation marginality may arise from:

- installed aerodynamic loads
- interference flowfield close to the aircraft

in combination with:

- intended or unintended fin, wing or rudder deflections/failures

and could be considerably increased by

- slight changes of the initial conditions (M , α and β).

Different preventions can be provided in order to overcome such a marginality such as:

- detailed sensitive analysis
- definition of suitable gyro limitations
- design of a powerful subcontrol system for the separation phase
- reduction of the time for activation of the flight control system
- introduction of a special release envelope within the safe separation envelope

5. REFERENCE

- [1] R. Deslandes, A. Eberle
 Characteristic Flux Averaging Approach to the Solution of Euler's Equations
 Part I: Pseudo Unsteady Approach
 Part II: Time Accurate Techniques
 MBB/LKE12/S/PUB/313, 6.10.1987

Aknowledgement:

The movie shown during the presentation was originally recorded on a PS390 station of 'Evans & Sutherland'.
 Due to the conversion from video into a 16 mm film the brilliant quality has been considerably degraded.

ABBREVIATIONS AND SYMBOLS

g	Gravitational constant ($=9.81 \text{ m/s}^2$)
ρ	Air density
l, m, n	Momentum of an particle
e	Specific total energy of an air particle
x, y, z	Local body velocities along the store surface
p	Pressure within a fluid
U	Velocity vector of the store
u, v, w	Velocity components of a fluid particle
V	Finite volume of a cell
E, F, G	Homogenous Euler-Fluxes
M	Mach number
$\alpha, \text{AOA, Alfa}$	Angle of attack
β, Beta	Sideslip
C_L	Rolling moment coefficient

6. FIGURES

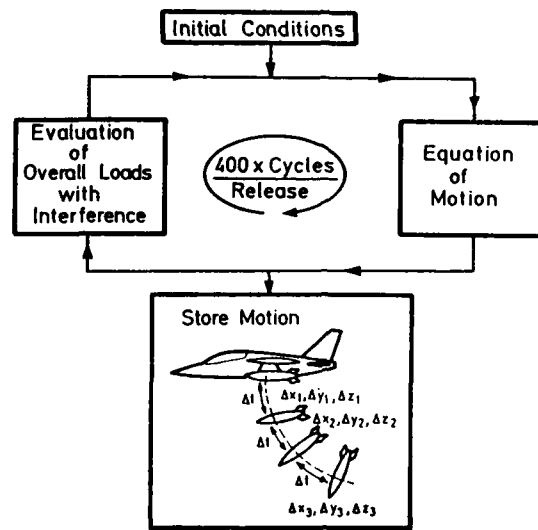


Fig. 1 Typical Program Design

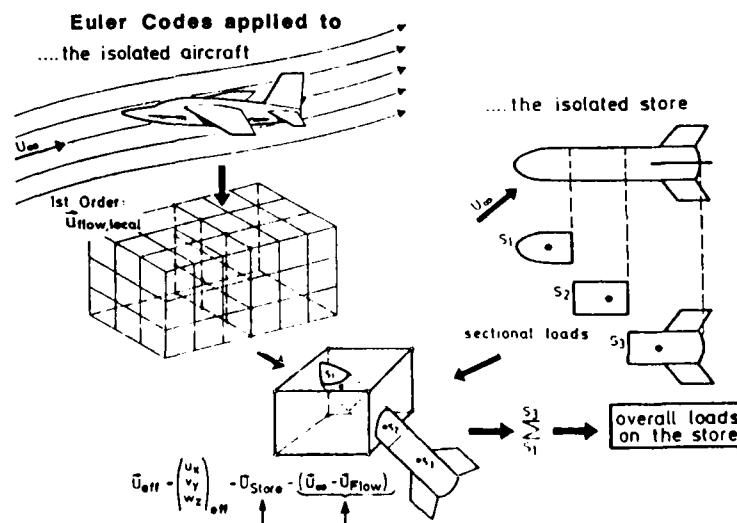


Fig. 2 Current Interference Concept (MBB-SSP)

$$\begin{aligned} \dot{\rho} + \rho(\dot{x}_x + \dot{y}_y + \dot{z}_z) + (l - \dot{x}\rho)_x + (m - \dot{y}\rho)_y + (n - \dot{z}\rho)_z &= 0, \\ \dot{l} + l(\dot{x}_x + \dot{y}_y + \dot{z}_z) + \{l(u - \dot{x}) + p\}_x + \{l(v - \dot{y})\}_y + \{l(w - \dot{z})\}_z &= 0, \\ \dot{m} + m(\dot{x}_x + \dot{y}_y + \dot{z}_z) + \{m(u - \dot{x})\}_x + \{m(v - \dot{y}) + p\}_y + \{m(w - \dot{z})\}_z &= 0, \\ \dot{n} + n(\dot{x}_x + \dot{y}_y + \dot{z}_z) + \{n(u - \dot{x})\}_x + \{n(v - \dot{y})\}_y + \{n(w - \dot{z}) + p\}_z &= 0, \\ \dot{e} + e(\dot{x}_x + \dot{y}_y + \dot{z}_z) + \{e(u - \dot{x}) + pu\}_x + \{e(v - \dot{z}) + pv\}_y + \{e(w - \dot{z}) + pw\}_z &= 0 \end{aligned}$$

$$\begin{aligned} \frac{\dot{V}}{V} &= \dot{x}_x + \dot{y}_y + \dot{z}_z & \nabla \vec{Q} \cdot \vec{Q} + \vec{Q} \cdot \nabla &= (QV)^* \\ (QV)^* + V(E_{1x} + F_{1y} + G_{1z}) &= 0, \end{aligned}$$

Fig. 3 3D Flow Equations for Unsteady Moving Boundaries

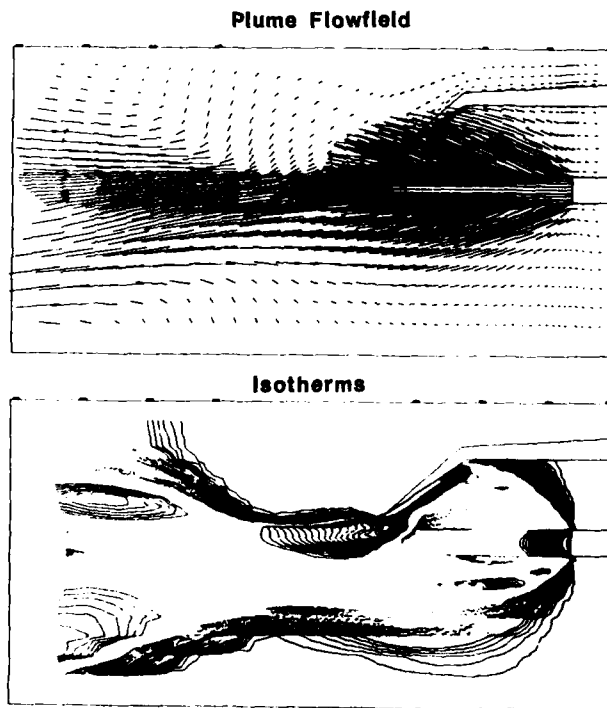


Fig. 4 Computed Plume Interferences

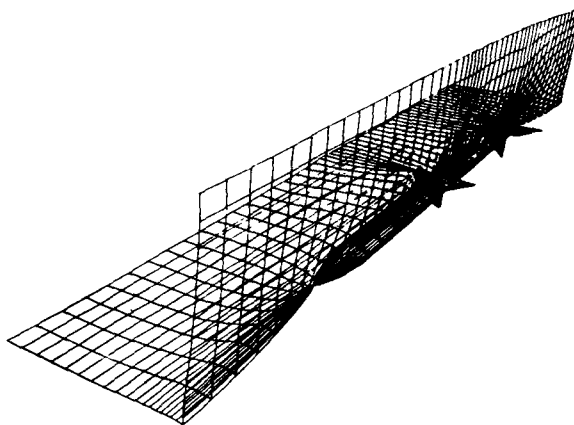


Fig. 5 Semisubmerged Installation

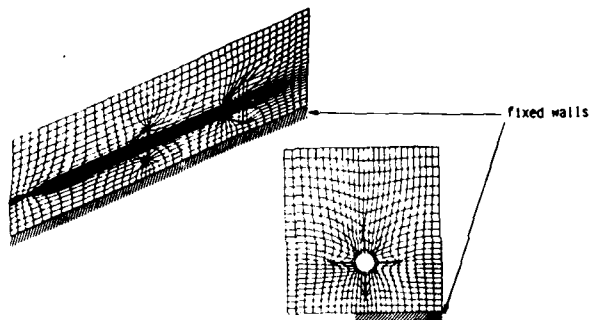


Fig. 6 Transient Droplaunch Position

① aircraft - parameters

orientation	load factor	rates	free stream conditions
		<ul style="list-style-type: none"> • pitch (1) • roll (1) • yaw (1) 	<ul style="list-style-type: none"> • Mach number • angle of attack • sideslip angle • altitude • temperature • disturbances

② Ejection Release Unit - parameters

cartridges	throttles	ERU-position
------------	-----------	--------------

③ store - parameters

type	physical characteristics	constraints
<ul style="list-style-type: none"> • missile • bomb • tank / pod • dispenser • ammunition • emergency device 	<ul style="list-style-type: none"> • mass • inertias • c.g. - location • thrust • ignition - time • release sequence • arrangement • location 	<ul style="list-style-type: none"> • rail • rear pivot • drag chute • floating fins • control deflection • wing extension • autopilot

Fig. 7 SSP-Program Options

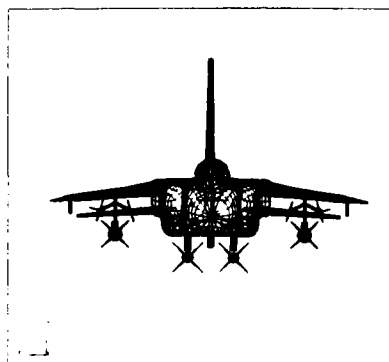
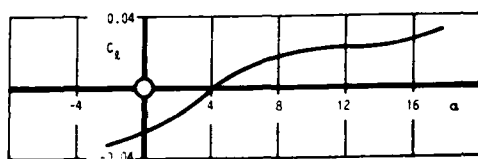


Fig. 8 Fictive Air-Air/Air-Ground Configuration



$M = 0.8$
Beta = 0

Fig. 9 Installed Rolling Moment for Underfuselage Carriage

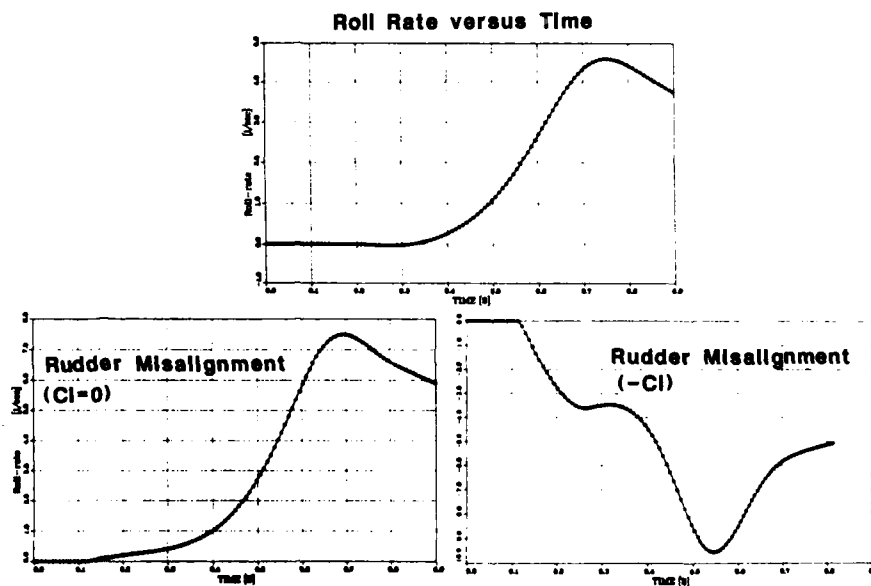


Fig. 10 Roll Analysis/Rail Launch UF Nominal Case

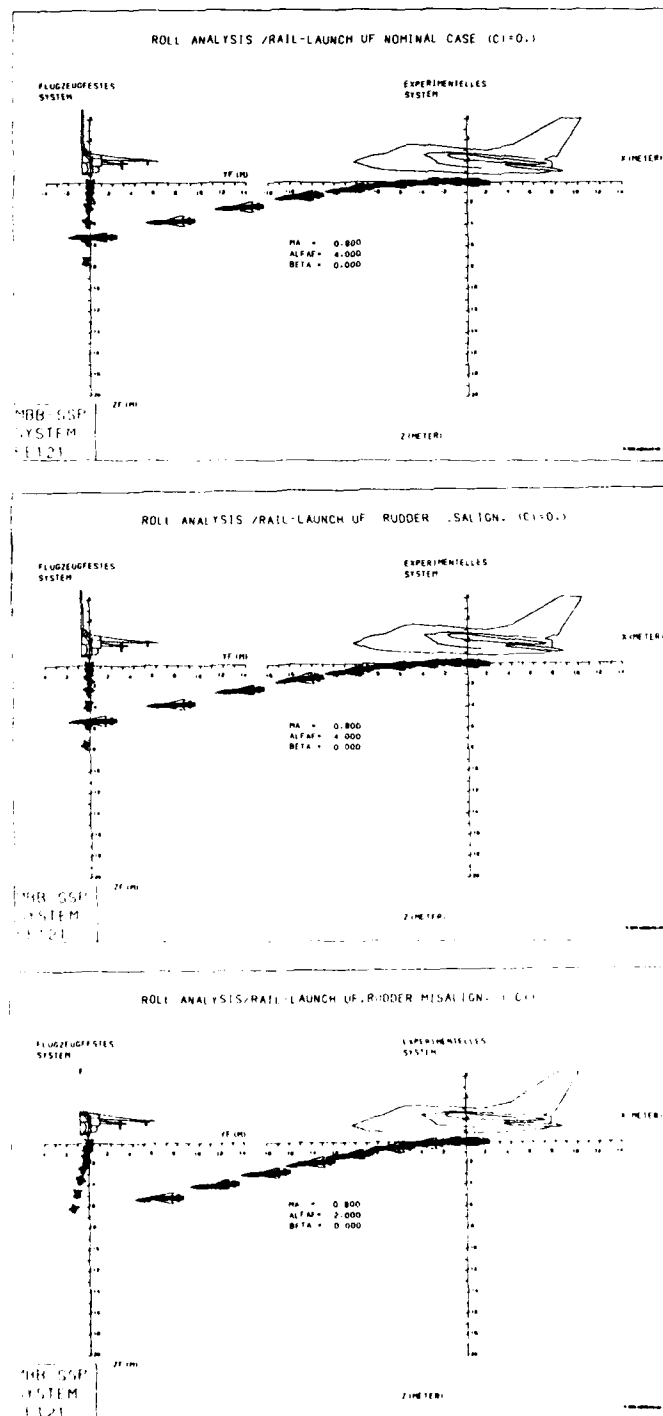


Fig. 11

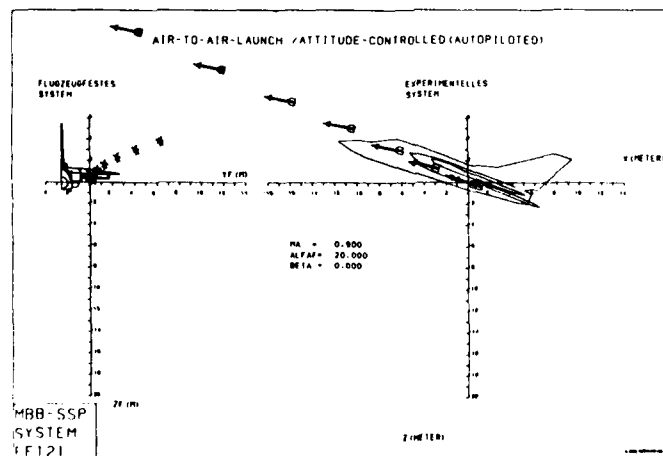
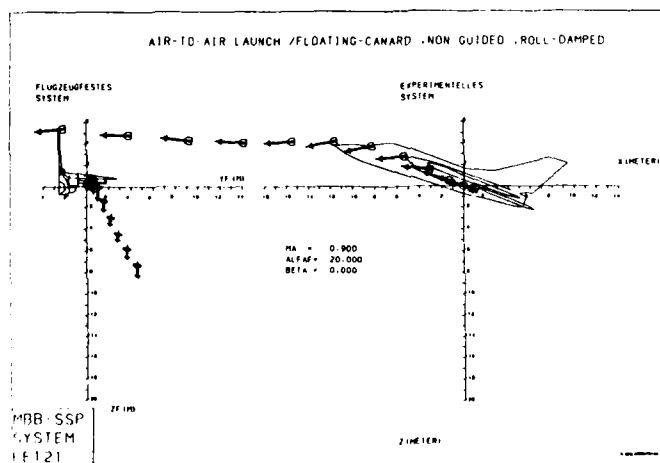
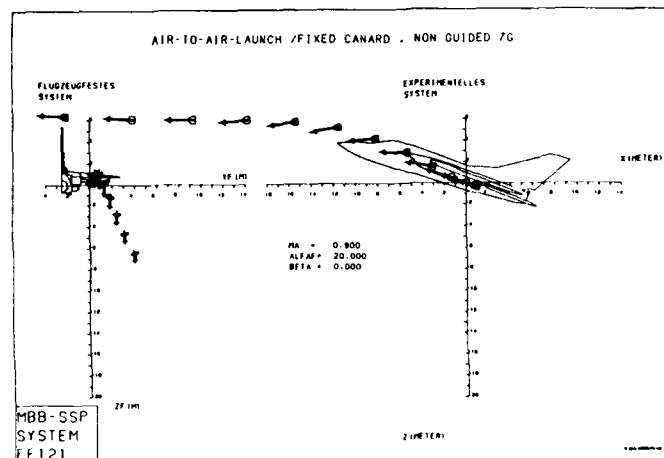


Fig. 12

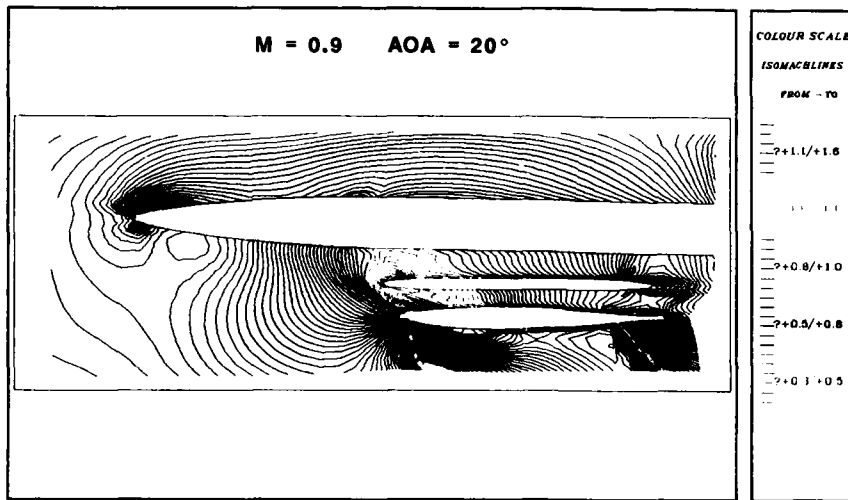


Fig. 13 Isomachlines in Non-Uniform Flowfield

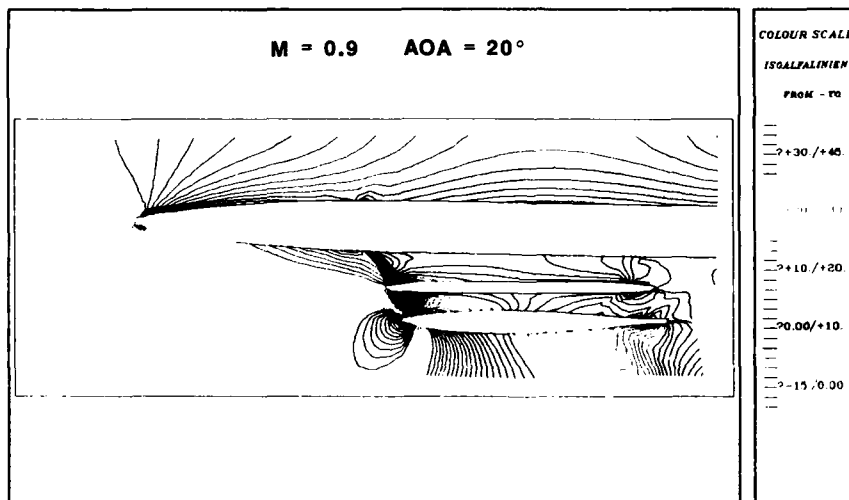


Fig. 14 Isoclinal AOA-Lines

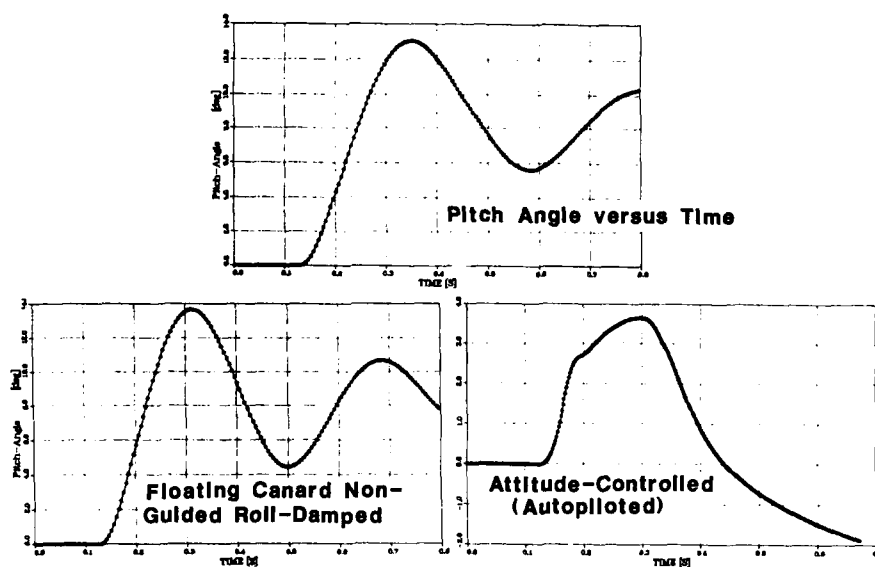


Fig. 15 Air-to-Air-Launch/Fixed Canard, Non Guided 7G

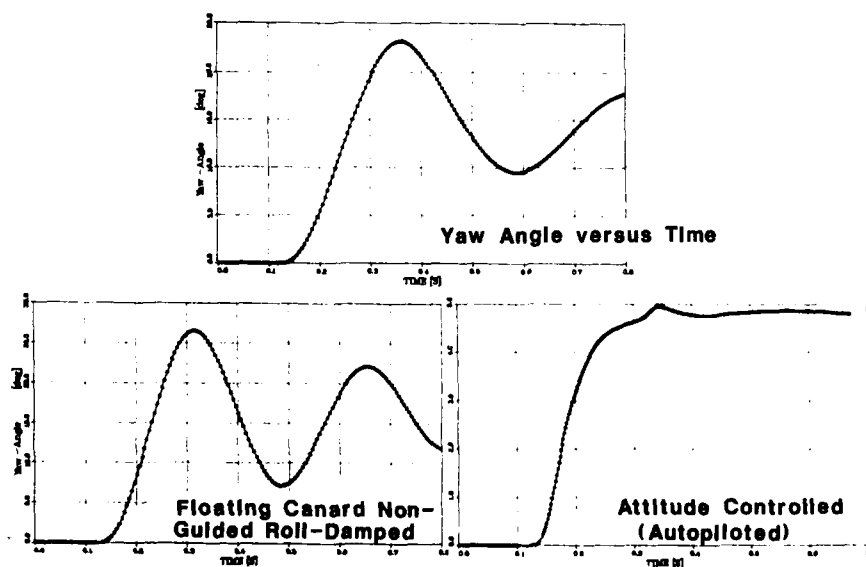


Fig. 16 Air-to-Air-Launch/Fixed Canard, Non Guided 7G

AEROELASTIC ANALYSIS OF MISSILE CONTROL SURFACES WITH STRUCTURAL NON-LINEARITY

Dr. D. Sepahy, Systems Support Dept
British Aerospace Dynamics Division
Hatfield Hertfordshire England

SUMMARY

This paper presents an aeroelastic procedure to deal with structural non-linearity of a missile control surface using the concept of linearised equivalent structural stiffness. This approach enables the use of standard software packages such as Nastran for linear aeroelastic analysis ie divergence, flutter and dynamic response analysis. An example, backed up with experimental validation, is given for a flexible control surface with structural non-linearity due to free play at the root connection. A time simulation technique is also discussed for solution of the problem.

1. INTRODUCTION

One of the factors which could influence the production of an economical and competitive aerostructure system is an acceptance of low tolerances in manufacturing of the components. Therefore it is of interest to investigate and evaluate the effect of manufacturing imperfections and lack of fit on the characteristics, performance and reliability of the system. The example taken here is a study of a mechanism for simple and quick fitting of a control surface to a body which means that a certain amount of freeplay (backlash) at the connection fitting should be allowed.

The freeplay (loose fitting) in the system makes the response behaviour of the structure highly non-linear under dynamic loading, ie the response characteristic of the control surface is a function of the oscillation amplitude and the response obtained from linear analysis cannot simply be factored to estimate performance of the system with freeplay. Structural failure of the control surface can be brought about by dynamic or static aeroelastic instability of the control surface under unsteady aerodynamic loading in subsonic, transonic or supersonic flight speeds.

The aeroelastic stability analyses are based on linear theory by the superpositioning of aerodynamic loading on the structure. The flutter or divergence speed of a control surface is found by solving the characteristic dynamic equations, the analyses are made cost effective by using a selected number of modes of vibration and constructing generalised dynamic equations which are based on the assumption of the linearity of the system. The linear theory is valid for small amplitude oscillation and characteristic equations are obtained from linearisation of minimum potential energy of the system, however with the occurrence of instability, the oscillation amplitude grows exponentially with time and violates the assumption of linearity of the system, ie the stiffness characteristic (2nd derivative of potential energy) also becomes amplitude dependent. But since the sudden growth of amplitude is followed by structural failure it is generally sufficient to limit the aeroelastic stability analysis to compute the condition of neutral stability for a perfect structure. The instability analysis is of interest if the effect of structural imperfection is to be investigated using the perturbation technique for solution of non-linear dynamic equations by expanding the minimum potential energy in the vicinity of neutral equilibrium, however this method will not be considered in this paper.

A recent treatment of structural non-linearities in pitch and roll for rigid and flexible control surfaces is given in ref [1] using a describing function technique which is more efficient than the numerical solution technique when simplified linear aerodynamics are used, however the technique can be extended to unsteady aerodynamic loads. Earlier work [2, 3] along similar lines has evaluated the influence of structural non-linearity on missile control surface flutter, but they were limited to a non-linearity of one degree of freedom for rigid control surfaces.

Structural non-linearity has been investigated by Haunstain et al [4] using an asymptotic expansion technique; three simulation techniques were compared for response of a non-linear system. A two degree of freedom non-linear aeroelastic structure was also examined by Ibrahim [5] using the Fokker-Planck equation technique.

2. METHOD

The general dynamic stability equation for a flexible control surface under oscillatory aerodynamic loading with flight speed v in generalised coordinates can be written as [6].

$$[M_{hh}p^2 + (B_{hh} - \frac{1}{2}\rho cvQ^I/k)p + (K_{hh} - \frac{1}{2}\rho v^2Q^R)]U_h = 0 \quad \text{Eq.(1)}$$

where:

- M_{hh} = modal mass matrix, usually diagonal for inertia terms
- B_{hh} = modal damping matrix. An equivalent viscous structural damping matrix is usually diagonal.
- K_{hh} = modal structural stiffness matrix usually diagonal.
- Q^I_{hh} = modal aerodynamic damping matrix, a function of reduced frequency, k and Mach number, M .
- Q^R_{hh} = modal aerodynamic stiffness matrix, a function of reduced frequency, k and Mach number, M .
- p = eigen value = $\omega (\gamma \pm i)$
- ω = circular frequency
- γ = transient decay rate coefficient
- ρ = density
- v = velocity
- c = reference chord
- k = reduced frequency = $\frac{\omega c}{2v}$
- U_h = modal amplitude vector

The aerodynamic matrices, Q , are calculated for either subsonic or supersonic flight regimes using a finite element aerodynamic model (doublet lattice or Mach box method), subsequently the aerodynamic matrices are transferred to structural coordinates using surface spline interpolation techniques and finally they are transferred to the required modal coordinates.

The structural stiffness matrices are constructed for a finite element structural model using a range of suitable elements and finally structural matrices are transferred to the generalised modal coordinates by selecting a range of suitable natural frequencies of the structure.

With the introduction of structural non-linearity due to freeplay (backlash) at the connection of the control surface with the body, although aerodynamic matrices can be constructed in the same way as before ie based on linear theory, the structural stiffness matrix is displacement dependent, see Figure 2, for the root force displacement function.

The structural non-linearity of the system violates the principle of superposition, and the following cannot be applied:

- (a) Calculation of the aerodynamic and structural coefficients separately,
- (b) The assumption of a response amplitude from a combination of normal modes.

The coupled aerostructure dynamic equation can no longer be reduced to a complex eigen value problem as formulated in equation (1) and hence flutter speed cannot simply be calculated from the stability equations in the normal way.

There are two possible alternative approaches which can be explored with the help of standard facilities available in NASTRAN [6] to solve the dynamic response equations, and to estimate the flutter flight speed.

- (a) Approach A - Time simulation
- (b) Approach B - Linearisation

The perturbation technique which could also be developed using NASTRAN DMAP facility, for the solution of non-linear equations will not be considered here.

2.1 Approach A - Time Simulation

Coupled aerostructure dynamic equations for a flexible structure, can in general be written as:

$$[A] \{\ddot{u}\} + [B] \{\dot{u}\} + [C] \{u\} = \{F(t)\} \quad \text{Eq.(2)}$$

where u = response amplitude in the physical coordinate due to force $F(t)$

\dot{u} = response velocity

\ddot{u} = response acceleration

A = mass matrix in physical coordinate

$[B] = [B_A] + [B_S]$

B_A = aerodynamic matrix in phase with response velocity

B_S = structural damping matrix

$[C] = [C_A] + [K(u)]$

C_A = aerodynamic matrix in phase with response amplitudes

$[K(u)]$ = Non linear structural stiffness matrix

The aerodynamic matrices B_A and B_S can be constructed for a given Mach number and range of reduced frequency parameters. The aerodynamic matrices are generated in the frequency domain ie. matrices Q^R and Q^I as given in equation (1). For a given Mach number and air density the matrices can be transferred to the time domain using an standard fast Fourier transformation package. With the availability of aerodynamic matrices in the time domain the transient response can proceed.

Non-linear structural stiffness can now be introduced into the problem, by supplying a load deflection curve for the freeplay of the connection and using standard elements for the rest of the structure. However, the non-linear characteristic of the connection can also be represented easily using the gap element.

2.2 Approach B - Linearisation

By considering the uncoupled aerostructure dynamic equations for the structure alone, the transient dynamic equations of the system can be expressed as:

$$[A] \{\ddot{u}\} + [B_S] \{\dot{u}\} + [k(u)] \{u\} = \{F(t)\} \quad \text{Eq.(3)}$$

B_S is a small structural damping matrix which is used to ensure the numerical stability of equation (3) under dynamic load $F(t)$.

The above equations are solved with a non-linear element to represent non-linear terms in the stiffness $K(u)$. A range of options is provided in NASTRAN using the finite difference approach for solution of equation (3).

To obtain an equivalent linearised stiffness matrix a one d.o.f non-linear dynamic equation is considered for the sake of simplicity.

$$a\ddot{u} + b\dot{u} + k(u)u = f(t) \quad \text{Eq.(4)}$$

which can be replaced by equivalent linear equation

$$a\ddot{u} + b\dot{u} + k_e u = f(t) \quad \text{Eq.(5)}$$

the displacement error due to linearisation is

$$e(t) = c r(u) - u$$

where $c = k^{-1}$ and $k(u).u = r(u)$

To minimise the error, the mean square value of the error $E[e^2(t)]$ should be small. This is done by

$$\frac{\delta}{\delta c} E[e^2(t)] = 0$$

resulting in

$$c = \frac{E[u.r(u)]}{E[r(u)^2]} \quad \text{Eq.(6)}$$

where $E[u.r(u)]$ is the mean of two uncorrelated random variables

$$= \int_{-\infty}^{\infty} u.r(u) f(u,r) du.dr$$

$$\begin{aligned} \text{And } E[r(u)^2] \text{ is mean square value} &= \int_{-\infty}^{\infty} u^2 f(u) du \\ &= \int_{-\infty}^{\infty} s(\omega) d\omega \end{aligned}$$

where spectral density is given by:

$$s(\omega) = \lim_{T \rightarrow \infty} \frac{2\pi}{T} \{ |G_T(\omega)|^2 \}$$

and Fourier transforms G_T is given by

$$G_T(\omega) = \frac{1}{2\pi} \int_{-\infty}^{\infty} u(t) e^{-i\omega t} dt$$

For the fundamental frequency this method is the same as the "describing function" technique.

For multi d.o.f equation (6) can be written in matrix form for selected points on the structure.

$$\text{ie. } [C] = [E \{r^2(u)\}]^{-1} [E\{u\} \cdot \{r(u)\}]$$

The response of the system is computed for a given step force. The response time history of the structure is obtained for a selected number of d.o.f of the structure, which can fairly describe the behaviour of the flexible control surface under dynamic load. The response amplitude time history $u(t)$'s is transformed from the time domain to frequency domain using a fast Fourier transformation routine. The equivalent linear transfer function of the system is computed and hence equivalent linear stiffness of the system is calculated. The analysis is repeated for a range of step forces with different magnitudes. An improvement in the solution of the problem can be made by applying the iteration method on each increment of the stiffness matrix, where each incremental solution produces an equivalent stiffness matrix of the non-linear system.

3. NUMERICAL EXAMPLE

The results are given for a flexible control surface with and without freeplay attachment to the body. A small amount of freeplay is allowed at the control surface root attachment.

The example displays an interesting but generally unexpected phenomenon; by introducing additional flexibility (linearised freeplay affect) at the root of the control surface the flutter speed has increased, this could be due to the additional freeplay flapping mode taking energy from the air stream but not contributing to any instability modes.

3.1 Structural Model

The flexible, control surface is modelled using isotropic plate elements 'TRIG6' and 'QUAD8'. Elements with variable thickness were used to allow for thickness variation in the control surface. Normal modes of vibration of the control surface without freeplay are shown in Figure 4, the frequencies are normalised to a base frequency.

Transient non-linear analyses were performed to obtain the response of the structure to a step force, with a range of freeplay at the root. A small value of structural damping was included in the analysis to remove extraneous noise due to numerical instability of the dynamic equations. Small time increments Δt of constant intervals were used. The time history response for a selected d.o.f was saved in a file for post processing analysis. The signals were analysed using a standard fast Fourier transformation program, a sample output for the response and spectral density function for a d.o.f is given in Figure 3. The equivalent generalised root stiffness variation with degree of freeplay is given in Figure 8.

3.2 Aerodynamic Model

The study was carried out at the supersonic flight regime, using the 'Mach Box' method. Standard NASTRAN procedure was followed using equivalent linearised structural stiffness and the surface spline option was used to transfer aerodynamic matrices to the structural coordinate, and hence to the normal mode coordinates.

3.3 Flutter Analysis

Flutter analysis was carried out for a range of Mach numbers and reduced frequency parameters.

The analyses were limited to one value of free stream air density.

Flutter analysis results with and without freeplay at the root are given in Figure 6 and Figure 7. The introduction of an extra d.o.f at the root gave an additional flapping flutter mode as shown in Figure 5. The flutter speeds were estimated from Figure 6 and Figure 7 when damping of the system became zero for a given flight speed.

The variation of flutter speed with equivalent root stiffness is given in Figure 8.

4. CONCLUSION

Cost effective flutter analysis with non-linear structural stiffness can be carried out using the concept of equivalent stiffness calculated from non-linear dynamic transient response analysis. The numerical results given here are merely to demonstrate the technique using an arbitrary model, further work is required to validate the results obtained by this method. Approach A, ie time simulation, could provide a more accurate estimate of the flutter speed of a flexible control surface with a freeplay root connection, but it requires extensive programming effort and the computer cost for analysis would also be greater.

ACKNOWLEDGEMENTS

Thanks are due to British Aerospace PLC for permission to present this report and to my colleagues who have carried out some of the computation and modelling involved.

REFERENCES

- 1 Laurensen R M Flutter analysis of missile control surfaces containing structural non-linearities, AIAA Journal vol 18 No 19 Oct 1980).
- 2 Woolston D S An investigation of effects of certain type of non-linearities on wing and control surface flutter, J Aero Sc Vol 24 Jan (1957).
- 3 Brietback E Effects of structural non-linearities on aircraft vibration and flutter AGARD-R-665 Jan (1978).
- 4 Hauenstein A J Investigation of an asymptotic expansion technique to analyse limit cycle response of aerodynamic surfaces with structural non-linearity, Airforce office of Scientific Research, Technical Report 86-0288 Jul (1985).
- 5 Ibrahim R A Stochastic non-linear flutter of aeroelastic structures. Airforce office of Scientific Research, Technical Report 85-1076 Oct (1985).
- 6 Bellinger D MSC/NASTRAN Aeroelastic Supplement Mac Neal Schwendler Corp (1980).

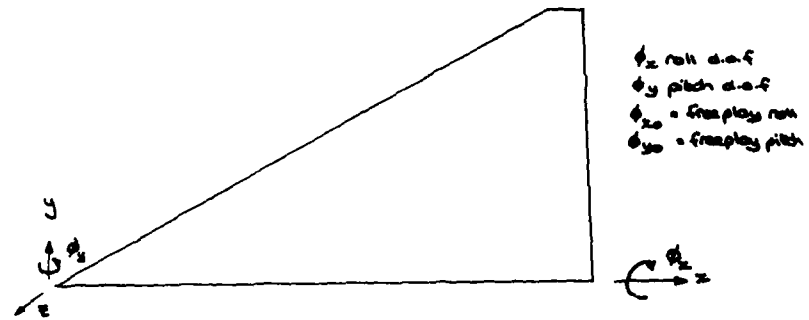


Fig. (1) Control Surface

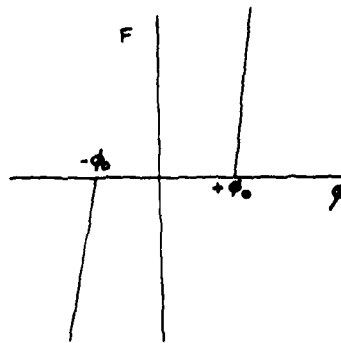
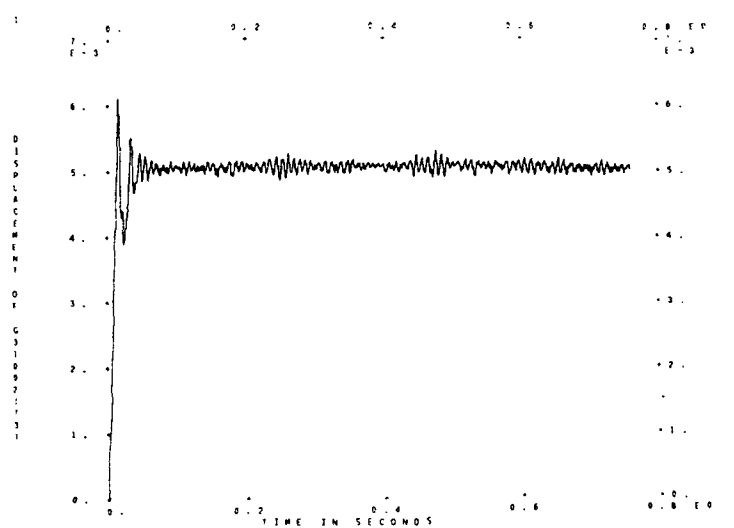
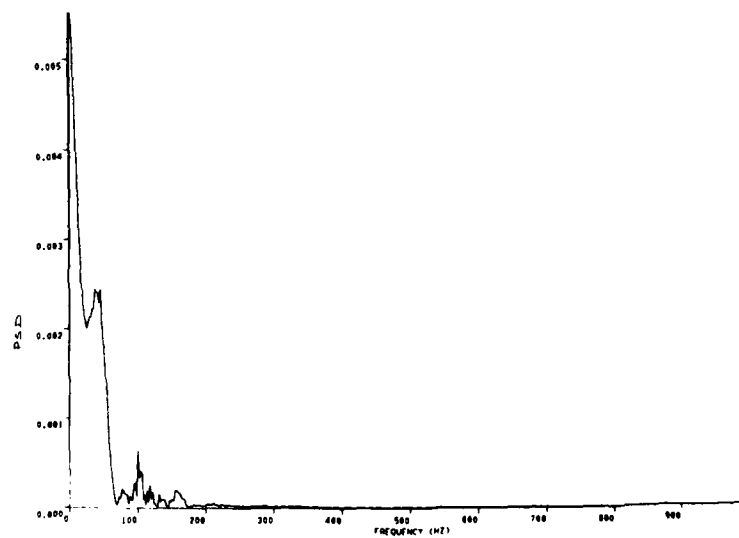


Fig. (2) Root connection : load deflection curve



Transient response of a control surface with freeplay due to a step force



Response power spectral function

Fig.(3)

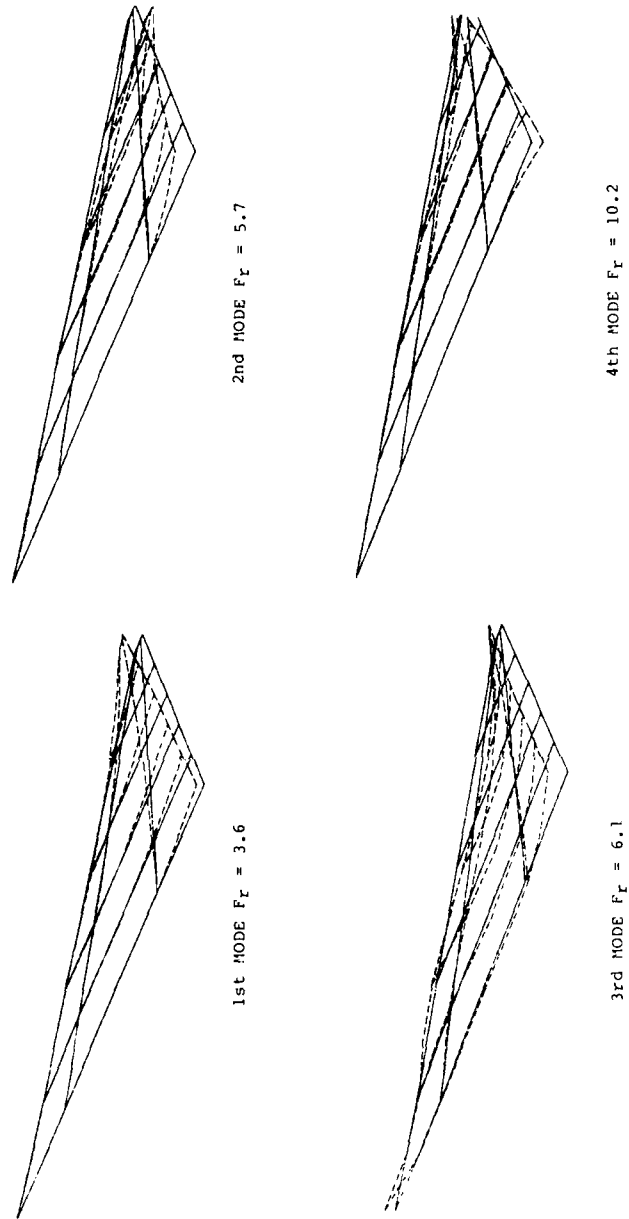
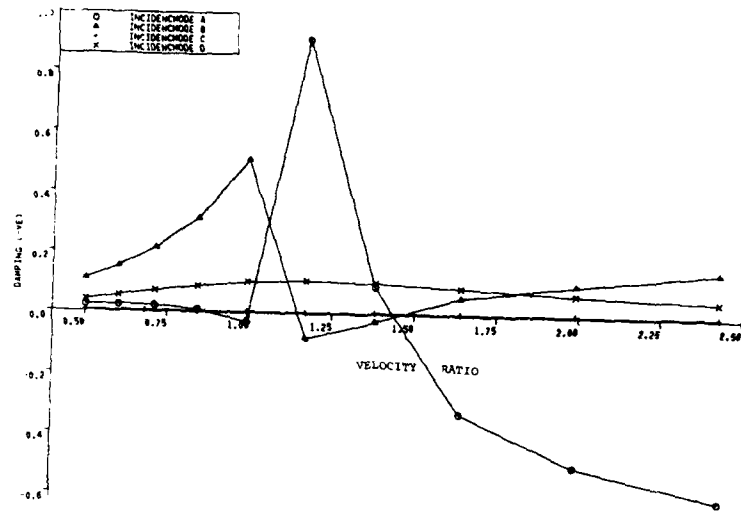


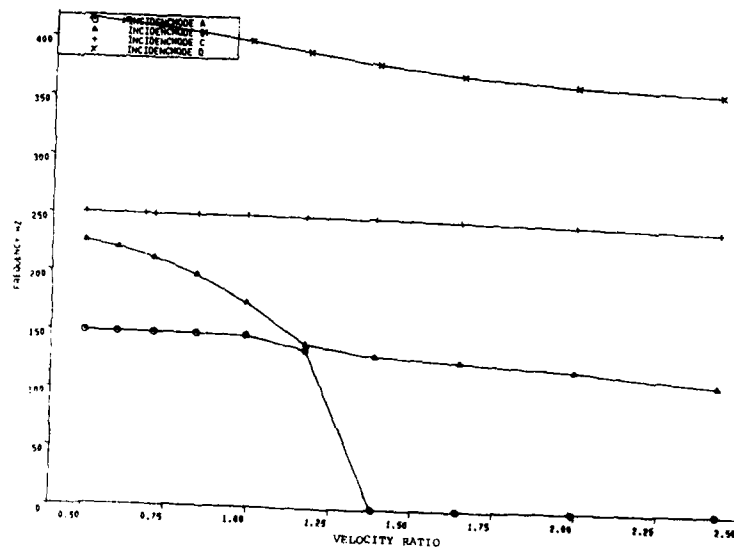
Fig.(4) Modes of Vibration Without Freeplay



Fig.(5) Modes of Vibration with Freeplay



WING WITHOUT FREEPLAY



WING WITHOUT FREEPLAY

Fig.(6)

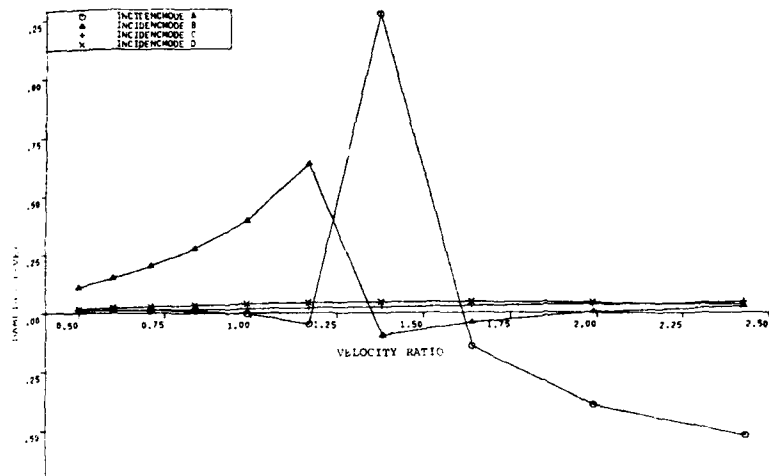
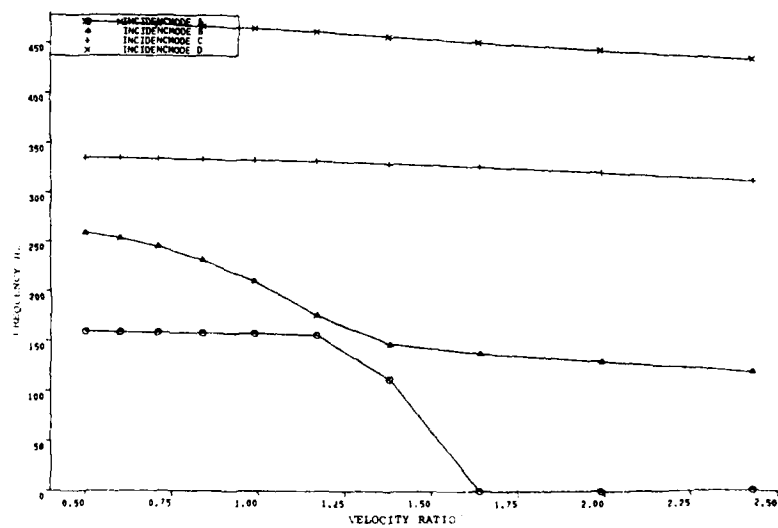
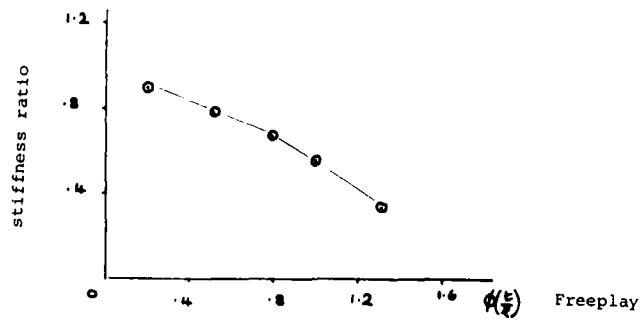
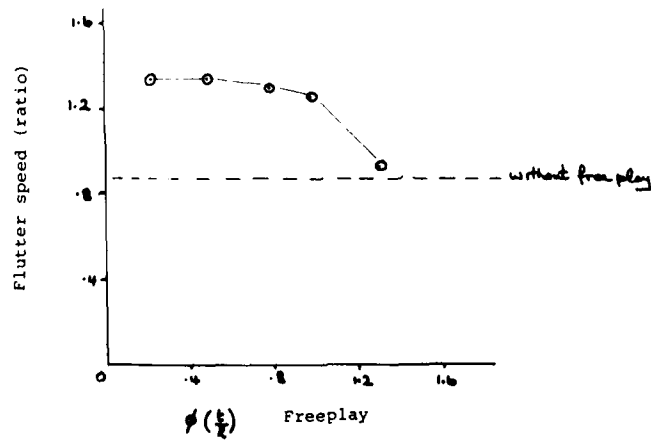
WING WITHOUT FREE PLAY $K=300$ WING WITHOUT FREE PLAY $K=300$

Fig.(7)



Variation of the generalised root stiffness with free play non-linearity at the root.

(small amplitude = 3 x freeplay).



Variation of the flutter speed with freeplay non-linearity at the root (small amplitude).

Fig. (8)

EXPERIENCE GAINED IN THE IMPROVEMENT OF THE ASPIDE AERODYNAMIC CONFIGURATION FOR THE SURFACE TO AIR ROLE

Dr. Eng. S. MAZZUCA

Selenia S.p.A. - Missile System Division
Via Tiburtina Km 12,400 - POB 1083
00131 - ROMA - Italy

1. SUMMARY

- This paper describes, from the begin to the end, the development process of the new aerodynamic version of the Aspide in the surface to air role.
- The aims, constraints and main activities of the project are reported.
- The entire decision process is also analized in great detail.
- The succesful completion of the above process, with the new configuration in full production constitutes the solid background for further improvements or new designs.

2. INTRODUCTION

The aerodynamic configuration of the multirole ASPIDE, derived from the well known Sparrow III 7E in the Air to Air role, has range of operating condition of fig.1.

Within the Nato Sea Sparrow Consortium an aerodynamic configuration for the Surface to Air role that extended the operating Mach range down to zero, including the dynamic pressure, was also developed.

The final lay-out was close to A/A with only two modifications:

- a) reduced span of tails;
- b) foldable wings with different location of hinge axis.

The modifications led to an improved maneuverability at low Mach numbers, matched the aerodynamic hinge moment with the actuation system, and achieved the capability of the launch from canisters. [fig. 2.3.4].

The Multirole Aspide retained these aerodynamic configurations for the use in systems where one to one replacement capability with the Sparrow III was required; conversely developed a totally new aerodynamic configuration for the use with SELENIA Launcher-Canister C.C.S (Cella Contenitore Standard) whose characteristic is the interoperability between land based systems (Spada - Skyguard) and ship based system (Albatros MK 5.).

3. DESIGN OF THE AERODYNAMIC CONFIGURATION

The design of the aerodynamic configuration for the Aspide in surface to Air role, compatible with C.C.S., was an optimization process where the solution represented the best compromise between the objectives and the constraints; this decision process is analized in detail in the following paragraphs.

3-1. Objectives

"To obtain an aerodynamic configuration for the ASPIDE in Surface to Air role, compatible with C.C.S., with dynamic capability similar to existing ASPIDE" was the first requirement.

"Substancially improve the reliability of the existing ASPIDE in Surface to Air role with the folding wind" was the second requirement.

"To facilitate the logistics, handling, producibility of the whole Aspide" was the last requirement.

3-2. Constraints

The objectives of the para 3.1 covered many different aspects of the ASPIDE regarded as weapon system; that seemed, at first glance, to leave a very large freedom of choice for a design process. The addition of the constraints has greatly reduced this freedom of choice in design, and we analyze how this is done in detail.

3-2-1. Geometrical constraints

The geometrical constraints are derived from the geometrical dimensions of the C.C.S. The geometrical analysis of C.C.S. cross section, rail dimensions, missile suspension systems tolerances on so on lead to a definition of the maximum allowable semispan for the wing or tail panel of 256 mm. It is important to remember that the folding wing has a semispan of 407.5 mm. Ensuring the compatibility with the last version of launchers for the NATO SEA SPARROW MISSILE SYSTEM, was also required during the development of the new configuration; the analysis performed further reduced the allowable semispan (fig. 5.6).

Within the allowable semispan and overall canister dimensions solutions with either a foldable wing or fixed wing were permitted. [fig. 7].

3-2-2. Reliability constraints

The analysis performed on the existing folding wing highlighted two important factors of poor reliability:

- a) the occurrence of "hard" or "catastrophic" failure of the wing, and of the missile mission if one of the four torsion bars fails;
- b) the relatively high number of mechanic items of a folding wing, about three times that of a non foldable wing as used in Air to Air role.

The above consideration dictates for a design with "soft" failure and/or reduction of mechanic items.

3-2-3. Logistic and producibility constraints

Being the A.M.I. (Aeronautica Militare Italiana) one of the main customer of the ASPIDE in both the Air to Air role (for the use with F104S) and the Surface to Air role (for the use with the SPADA SYSTEM), a strong push toward the unification of the wing production process becomes a new constraint.

3-2-4. Handling constraints

The M.M.I. (Marina Militare Italiana) who used the Aspide in Surface to Air role was worried with ALBATROS SYSTEM by the potential hazard to the personnel caused by the folding wings during the operation of missile loading - unloading from the launchers on the deck of ships. A recommendation to solve this problem constitutes another constraint.

3-2-5. Time and Budget constraints

The last, and in many aspects more difficult constraints were originated from the allocation of the development time and the associated cost. In this particular programme the new configuration for the S/A role was required to be used with the first delivery of SPADA system to AMI. The related cost was agreed to be at SELENIA expenses so the solution with a production cost lower than the existing version of the foldable wing was highly desirable.

3-3. Solution

Regarding to the objectives, and taking the constraints in to account, two possible ways for the solution were selected:

- 1) To design a totally new folding and opening system with "soft" failure occurrence and higher reliability;
- 2) To design a totally new wing panel, unfoldable, within the assigned semispan derived from existing wings, giving a totally new missile aerodynamic configuration with dynamic performances similar to the existing ASPIDE.

A careful analysis identified the advantages and disadvantages of each of the possible solutions.

The first one has the advantage of retaining the missile aerodynamic configuration, the autopilot, interfaces with the launching systems, logistics and so on but requires a big technological effort of design qualification and testing with great impact on the production line, and resulting to a higher cost.

The second one has the advantage of high reliability, commonality, minimum impact with the production process, low cost but leading to a totally new aerodynamic configuration requiring difficult computation, the design of a new autopilot, wind tunnel tests for accurate measurement and flight tests for the final assessment.

The final choice was toward the second solution based on the following considerations:

- a) the existence of in house developed computer code MATAM, that can compute, within the engineering accuracy, the aerodynamic coefficients of a complete missile configuration also in the range of low or very low aspect ratio;
- b) the experience of the autopilot design gained in the development of a new roll autopilot for Aspide;
- c) the expected lower cost in production for the new wing that permits the recovery of the expenses for the R & D within the projected production volume.

The final solution is a wing derived from a wing panel used for the Air to Air role having exposed span cropped and tip with sharp edges. [fig. 8].

The computed linear coefficients of this configuration are the inputs for the design/verification of the autopilot, (pitch, yaw and roll), while coefficients computed at higher incidence permit the establishment of the maneuver and controllability boundaries.

4. TEST

The activities related to the test and validation are the last, and most important step, of the process of development of a new missile configuration.

The phase of the design, described in the previous paragraph, is mainly a mental activity, supported by mathematical models whose representation of the "true world" is subject to a many simplifications and approximations; it is, in conclusion, a "software activity".

The phase of the test, analyzed in this paragraph is, by definition, a practical activity where different prototypes are immersed, at different depths, in the "real world" in order to measure the effect of this interaction and to improve the credibility of the mathematical models; it is an "hardware activity".

The phase of the validation is a "software activity" where the test data are compared with the objectives and the constraints to give an objective judgment of the final solution.

The following paragraphs detail the wind tunnel and the flight tests performed during the process of development.

4-1. Wind tunnel test

The aerodynamic configuration outlined in para 3.3 was analyzed using the MATAM code and the reference values of the aerodynamic coefficients were computed.

From these, no problems were envisaged in the area of maneuver capability and autopilot modifications, but some problems arose in the area of high incidence, mainly from the controllability point of view.

In fact, the computation showed the occurrence of unwanted disturbances and a drastic reduction of roll control derivative (a factor of three was expected) and the main question resulting was:

"Will this cause the total loss of control authority at high body incidence in presence of wing stall as it is expected in transonic and subsonic regimes?"

In order to obtain the necessary information with a high degree of reliability, a preliminary test program was issued to investigate:

- a) the effect of wing span on coefficients derivatives by parametric reduction of wing panel semispan;
- b) the effect of high and very high incidence at subsonic speed on control authority characteristics both for folding and fixed wing configuration.

These tests were considered so important that the development program would be stopped if adverse results arose.

In the following paragraphs we analyze how the complete wind tunnel test program was unrolled.

4-1-1. Development process

The formal start of the experimental program was received in October 1981 with a preliminary test program oriented to:

- 1) make subsonic tests at low incidence to measure the effect of wing span reduction on control derivatives;
- 2) make subsonic tests at high and very high incidence to assess the behaviour of the old and new configuration.

Test n° 1) was performed in March 1982 at the University of Napoli on subsonic wind tunnel with:

- three component main balance for normal force, pitching moment, roll moment measurements;
- simplified model scale 1 : 2 made by REPI
- incidence range - 6° : + 12°
- dynamic pressure 100 mm H₂O
- polars measured 45
- wing exposed span range 256 mm - 216 mm
- typical results in [fig. 9]

Test n° 2) was performed in February 1982 at Flugzeugwerk Emmen Suisse on subsonic wind tunnel with:

- six component main balance for complete determination of force and moment coefficients;
- model scale 1:1 made by SELENIA utilizing a true missile body;
- incidence range - 10° : + 35°
- Mach number 0,16
- polars measured 80
- configurations tested: folding wing and span reduced to 256 mm

With the above measured data, the verification of the autopilot designed from computed aerodynamic data was made. With minor modifications the design was frozen and accordingly two U.G.C. of Sparrow RIM 7H of M.M.I. were modified for autopiloted flight test.

The tests were performed in May 1982 and subsequent analysis allowed the continuation of the program.

A test program was issued as consequence oriented to:

- 3) extend the subsonic investigation up to maximum possible incidence;
- 4) explore the entire operating Mach range.

Test n° 3) was performed in July 1982 at Flugzeugwerk Emmen Suisse on subsonic wind tunnel with:

- six component main balance for complete determination of force and moment coefficients;

- model scale 1:1 made by SELENIA utilizing a true missile body;
- incidence range from -4° to +42°
- Mach number 0.16
- polars measured 112
- configurations tested: complete with wing span cropped and partial (body, wing body, body tail)

The extension of the test to the entire operating Mach range was a challenging problem spanning this range from Mach zero to three. The interest toward the high incidence required the minimization on the measured data of the influence of the Reynolds number so we chose a model scale near to 1:2 (0.492) and the compatibility with both the suitable wind tunnel at ARA Bedford and ONERA S2MA Modane.

With the aim to minimize the overall test cost we issued a specification for a model with remote wings control capability to enhance the wind tunnel productivity.

As result based on SELENIA specification the ARA of Bedford made the design and the construction of a very sophisticated test model, compatible with ARA TWT and ONERA S2MA facility, embedding, in the airframe, not only all the excrescences of the true missile but also four remote wing servo control and three components wing balance for the direct determination of wing's efforts. The test programme led to a measurement of the six missile aerodynamic coefficients (CX, CY, CZ, CMX, CMY, CMZ) and the three wing panel coefficients (CZW, CMXW, CMYW) with various combination of missile's bank position and pitch-yaw-roll command combination and was oriented towards to a:

- 4.1) subsonic-transonic investigation with max possible incidence
- 4.2) supersonic investigation with max possible incidence.

Test n° 4.1) was performed in January 1983 at ARA Bedford on transonic wind tunnel with:

- six component ARA main balance
- three component model wing balance
- two internal pressure ports for base correction
- incidence range from - 2° to +28°
- model scale 0.492 with remote wing controls
- Mach numbers 0.6, 0.9, 1.1, 1.3
- polars measured 390
- configurations tested: complete with wing span cropped, complete with folding wing, partial (body, wing body, body tail)

Test n° 4.2) was performed in February 1983 at ONERA Modane on supersonic wind tunnel S2MA with:

- six component ONERA main balance
- three component model wing balance
- two internal pressure ports for base correction
- incidence range from - 4° to + 20°
- model scale 0.492 with remote wing control
- Mach numbers 1.5, 2.2, 3.0 and 0.6, 0.9
- polars measured 650
- configurations tested: same as 4.1)

With the above measured data the final verification of the autopilots was made, these were finalized in the new "autopilot of banda S". Two U.C.C. Aspidre were constructed accordingly for autopilot flight test.

The tests were performed in May 1983 by SPADA system during acceptance test made by AMI and the results allowed the acceptance of the combination new aerodynamic + autopilot "banda S" for the Aspidre in Surface to Air role.

For the complete validation by numerical simulation a very accurate mathematical model of the aerodynamic was necessary, a new test program was issued to:

- 5) complete the aerodynamic file in transonic regime.

Test n° 5) was performed in October 1983 at ARA Bedford on transonic wind tunnel with:

- six component ARA main balance
- three component model wing balance
- two internal ports for base correction
- incidence range from - 2° to + 28°
- model scale 0.492 with remote wing control
- Mach numbers 0.9, 1.3
- polars measured 250
- configurations tested same as 4.1)

After these no other wind tunnel test were performed on this configuration. A complete validation was done in Apr. May 1984 with operating flight test (against flying target) on the entire system envelope.

4-2 Flight test

The aerodynamic configuration outlined in para 3.3 and the autopilot "banda S" described in para 4.1.1. are separate items that must work together. Their integration, made initially using a mathematical modelling, must be tested in a real environment by flight test.

There are various possibilities, but a logical sequence can be:

- 1) flight test with no autopilot. Permits to measure the drag coefficient;
- 2) flight test with autopilot. Permits to test, at various extent, the performance of the couple airframe - autopilot;
- 3) flight test with target. Permits to test the performance of the whole system.

In the present work phase 1) wasn't done and the development process began with phase 2.

In the following parameter we analyze how it was unrolled.

4-2-1. Development process

Being the formal start of the experimental program in the October 1981 a flight test go-ahead not was received until the completion of wind tunnel test n° 1 and n° 2 and the analysis of measured data that ended in March 1982. Two were the possible test bed:

- a) SPARROW RIM 7E
- b) ASPIDE 1A

The choice was directed towards the use of the Sparrow for these main reasons:

- 1) roll control with only two of four wings;
- 2) roll autopilot with constant gain;
- 3) use, in S/A role of the nato Sea Sparrow launcher that requires the minimum exposed wing span

By comparison the Aspide has:

- 1) roll control with four wings;
- 2) roll control with adaptive gain;
- 3) use, in S/A role, of the C.C.S. that allows an exposed wing span of 256 mm.

It is clear that the use of Sparrow maximized the technical risk, but gave safety margin to Aspide if the test was successful. Two fires were made in May 1982 from the Italian Ship SAGITTARIO with Sparrows having wings of reduced span and the new autopilot. Results were satisfactory and the programme was cleared to continue. After the wind tunnel test n° 3 and 4, the analysis of the data and the final revision of the autopilot that ended in March 1983, two ASPIDE were built in this new configuration for the use in the S/A role. Two fires were made in May 1983 from SPADA system. Results confirmed the premises and the new wings and the new autopilot were cleared to go in production. The tests of Apr. May 1984 made with the Spada system confirmed the choice from the operating point of view.

4-3. Validation

This process, as final step of a development process, can be an endless activity if the discrepancies between the mathematical model and the real world must be reduced to zero from all points of view.

In practice the likelihood demanded during the development process increases from the start to the end, but at each phase a certain amount of incertitude remains so some risk must be taken to proceed further.

As reported, this program proceeded with these milestones:

- 1) after the wind tunnel test of phase 1 and 2 and subsequent verification of the autopilot were authorized the autopiloted flight tests with Sparrow as test bed, the linear analysis was completed, the non linear behaviour only inspected;
- 2) after the Sparrow flight test and the analysis of the telemetered data, were performed the wind tunnel tests of phase 3 and 4 for the complete validation of the autopilot. As consequence the authorization to the autopiloted flight test with Aspide was done.
The non linear analysis was completed and the maximum performances estimated;
- 3) after the Aspide flight test and the analysis of the telemetered data, the wind tunnel test of phase 5 was performed in order to build the complete mathematical model of the aerodynamics of the new configuration. At the same time the cost-benefits analysis was completed and, consequently the authorization for the pilot production was done; at this point the confidence in this decision was estimated close to 95%;
- 4) the operating evaluation of the new Aspide configuration in the SPADA system against flying targets was the last milestone; successful test of total fires led to the homologation by AMI on the light that all the objectives of the work were obtained.
As important bonus the performances of the new S/A configuration are better than the old one as shown in fig. 10.

5. CONCLUSION

The improvement of the aerodynamic configuration of the SELENIA ASPIDE in the Surface to Air role was a challenging program.

The main objective, create a totally new aerodynamics with performances similar to an existing, classic and well established, within many constraints further complicated the problem.

The proposed solution was highly non conventional from the aerodynamic point of view, having moving wings in line with, and about of the same span of the tails; the feasibility of this configuration was supported by the theoretical calculations performed with the semiempirical code MATAM.

The new autopilot, designed from the computed aerodynamic data, required only minor changes after the extensive wind tunnel measurement.

Hundreds of flight tests have confirmed the choices made during the development phase and constitute the strong background where further improvements or new developments will be based on.

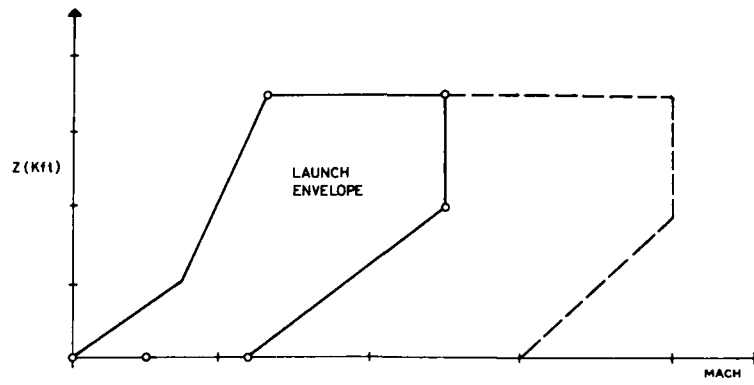


FIG. 1 TYPICAL FLIGHT ENVELOPE

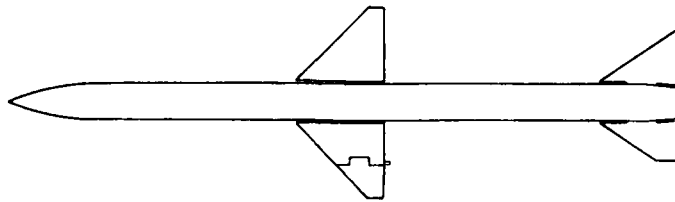


FIG. 2 CONFIGURATIONS FOR A/A AND S/A ROLE

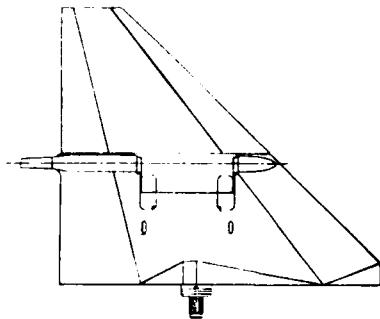


FIG. 3 FOLDING WING

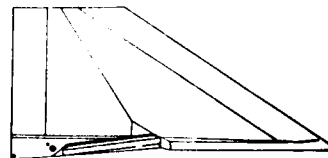


FIG. 4 CROPPED TAIL

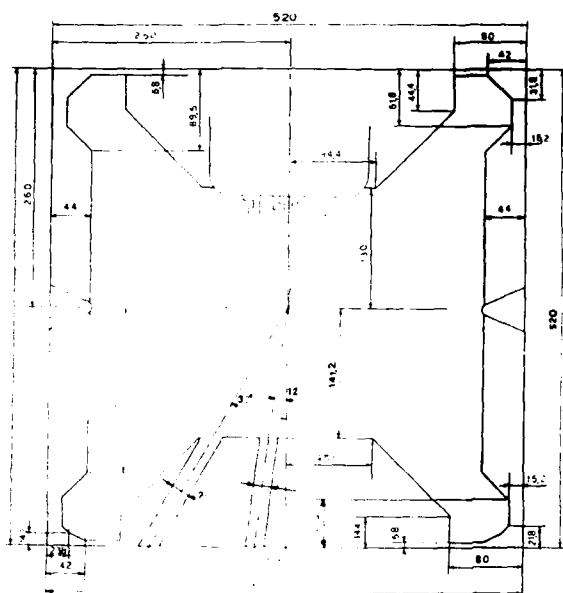


FIG 5 C C S CROSS SECTION

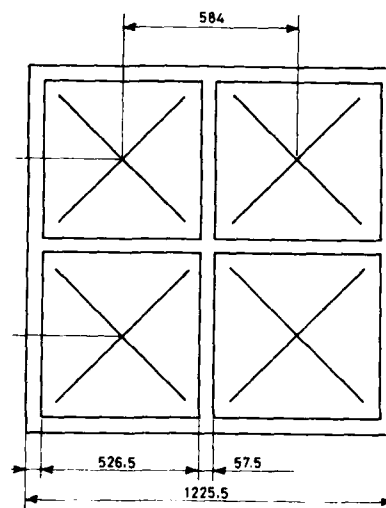


FIG 6 NSSMS

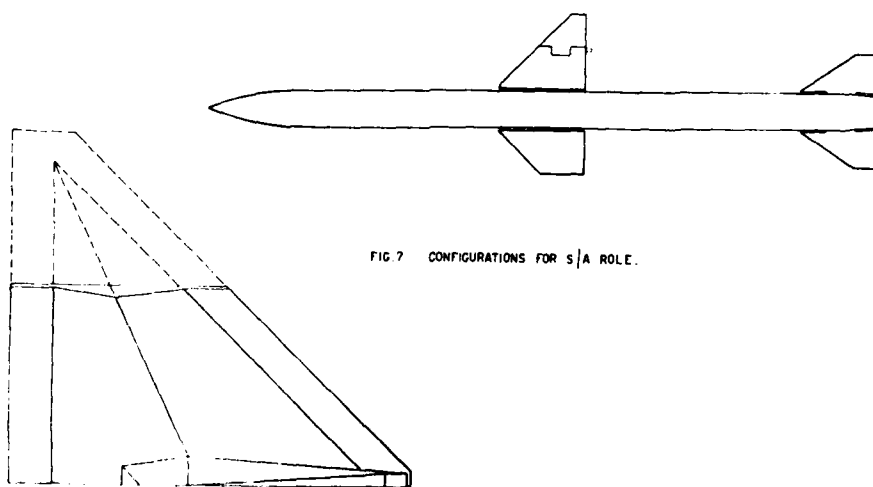


FIG 7 CONFIGURATIONS FOR S/A ROLE.

FIG 8 CROPPED WING

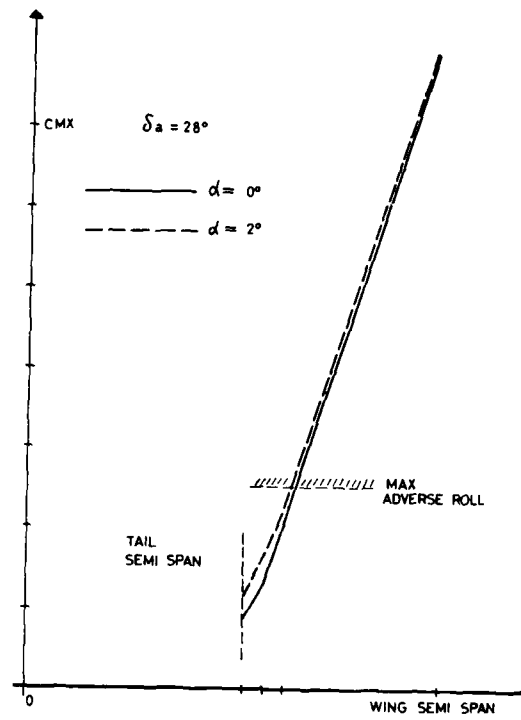


FIG. 9 ROLL CONTROL EFFECTIVENESS.

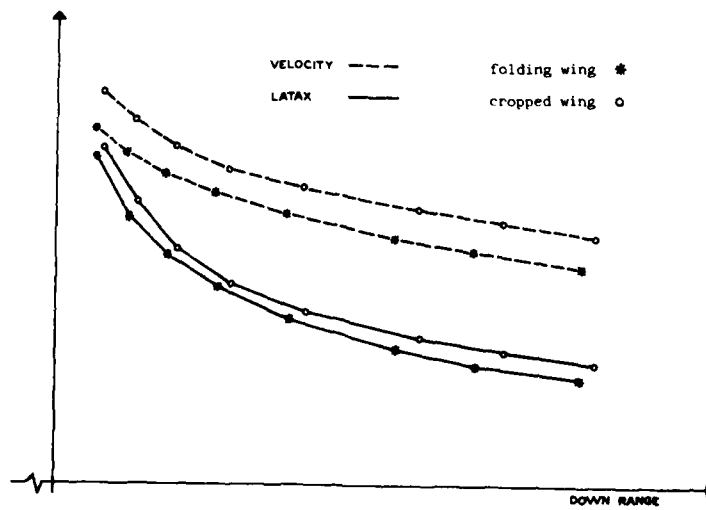


FIG. 10 COMPARATIVE MISSILE PERFORMANCES

WINGED VERSUS WINGLESS AIRFRAMES

by

DR A GAZZINA, DR S. MAZZUCA

SELENIA S.p.A.

MISSILE SYSTEMS DIVISION

VIA TIBURTINA Km 12,400 - POB 1083

00131 ROME - ITALY

1. SUMMARY

This paper describes an analytical method developed with the purpose to compare the kinematic and dynamic performance of a winged configuration with respect to a wingless configuration of a tactical anti-air missile.

A reference mission of the missile is firstly defined and the analytical method is built-up through the introduction of suitable assumptions and simplifications. The method is then applied to an actual missile for which wind tunnel results are available in its winged and wingless configuration. The peculiar aspects of both configurations are identified and highlighted.

Even if the method was developed for a specific aim it revealed suitable and accurately enough for general application mainly for a quick evaluation of a missile kinematic performance and to conduct sensitivity analysis of the mass, propulsion, and aerodynamic properties of a generic tactical missile.

List of symbols

a_o	= missile axial acceleration at launch
a_N	= missile normal acceleration
A	= aerodynamic axial force
C_N	= normal force coefficient
$C_{N\alpha}$	= C_N derivative wrt α
C_{N0}	= zero lift drag coefficient
I_{sp}	= propellant specific impulse
m	= missile mass
\dot{m}	= derivative of missile mass wrt time
m_o	= missile mass at launch
m_o	= propellant mass
M^{Dr}	= Mach number
N	= normal force
P	= missile flight path
s	= reference surface
t	= time
t_B	= end of boost phase
t_{SB}	= time when $V = V_S$ during boost phase
t_{St}	= time when $V = V_S$ during glide phase
T	= missile thrust
V	= missile speed
\dot{V}	= time derivative of missile speed
V_B	= missile speed at the end of boost phase
V_o	= missile speed at beginning of manoevered phase
V_S	= speed of sound
x_B	= distance covered by the missile at the end of the boost phase
α	= angle of attack
α_o	= angle of attack at beginning of manoevered phase
β_o	= supersonic deceleration factor in glide phase
β_B	= supersonic deceleration factor in boost phase
β_o	= subsonic deceleration factor (in glide phase)
β_B	= subsonic deceleration factor (in boost phase)
β_o	= missile mass fraction
ρ	= air density
γ	= manoevered flight factor

2. INTRODUCTION

The problem of comparing the kinematics and the dynamics of a wingless versus a winged configuration can be formulated in a quite simple way. A typical mission of a tactical antiair missile begins with a non maneuver (or low maneuver) approaching phase to the target area followed by a terminal phase characterized by strong lateral accelerations. Hence the first phase is dominated by the drag coefficient C_{x0} whereas the second by the normal force coefficient C_N or its derivative with respect to α that is $C_{N\alpha}$.

In such a mission the wingless missile, having a lower C_{x0} , will arrive into the target area with higher speed than the winged missile but it will exhibit a lower C_N during the subsequent maneuvering phase. The key question may now be formulated as:

"can the extraspeed of the wingless configuration compensate for its deficiency in the normal force coefficient, and under what circumstances?".

This paper tries to give an answer to this question through the introduction of appropriate assumptions and simplifications that allow for the direct integration of the motion equations.

In the era of computers and simulations it may appear anachronistic the attempt to find analytical solutions to the problems especially to the problem of missile motion that traditionally is an area that has gained the greatest benefits with the advent of simulations. Nevertheless closed form solutions possess two unique features: they are still faster than the fastest computers and secondly they isolate and put in evidence the key parameters affecting the results while ignoring all the minor effects.

3. MISSILE MOTION

A typical dynamic mission of a tactical antiair missile is described in fig. 1 in terms of speed versus range.

There is a rocket powered phase (boost phase), followed by a glide phase and finally the third phase, close to the target encounter that is characterized by important missile maneuvers. With reference to fig. 2 and considering the missile as a point mass the equations of motion in wind axis are:

$$m\dot{V} = (T - A) \cos \alpha - N \sin \alpha \quad (1)$$

$$ma_N = (T - A) \sin \alpha + N \cos \alpha \quad (2)$$

where the force of gravity has been neglected.

The three phases of the flight will now be considered in detail and some important assumptions will be taken in order to permit the direct integration of the motion equations.

3-1. Drag coefficient

The zero lift drag coefficient C_{x0} has the typical profile versus Mach as plotted in fig. 3. This profile can be very profitably approximated by the dashed line diagram that is:

$$\text{for Mach} \leq 1 \quad C_{x0} = C_{sb}$$

$$\text{for Mach} > 1 \quad C_{x0} = -\frac{f_x}{M}$$

where C_{sb} and f_x are properly chosen constants.

A further simplification may be introduced for the boost phase; in fact this phase is usually very short so that the speed loss due to the aerodynamic drag

is only a small percentage of the final speed; moreover this speed loss is concentrated in the supersonic part where the dynamic pressure is much larger. All this leads to the conclusion that in the subsonic part of the boost phase the aerodrag may be completely neglected, so that the C_{x0} diagram becomes as shown in fig. 4.

Another assumption used throughout all the paper is that the missile flies an horizontal path that is: $\varphi = \text{const}$.

3-2. Boost phase

For the purpose of present analysis only the long distance intercepts are of interest; moreover only the case of trainable launchers is considered here. This means that during the boost phase the missile will exhibit very small lateral maneuvers or no maneuvers at all, that is:

$$N = \alpha = 0$$

The equation (1) and (2) become:

$$m\dot{V} = T \quad \text{for } M \leq 1 \quad (3)$$

$$m\dot{V} = T - A \quad \text{for } M > 1 \quad (4)$$

where, assuming for the thrust a rectangular profile (fig. 5):

$$m = m_0 - \dot{m}t = m_0 (1 - \mu \frac{t}{t_B}) \quad (5)$$

$$A = C_{x0} \frac{1}{2} \rho V^2 S \quad (6)$$

$$C_{x0} = \frac{f_x}{M} = \frac{f_x V_S}{V} \quad (7)$$

where μ is the mass fraction of the missile.

In Appendix 1 the equations have been integrated. The most important and useful results are the missile speed and range at the end of the boost phase that represent also the initial conditions for the subsequent phase:

$$V_B = \frac{a_0}{\beta_0} \left[1 - \left(1 - \frac{\beta_0}{a_0} V_S \right) \exp \left(\frac{\beta_0 t_B}{\mu} \ln \frac{1 - \mu}{1 - \mu t_S/t_B} \right) \right] \quad (8)$$

$$X_B = \frac{V_B t_B}{2} \quad (9)$$

where t_S is the time required to reach the speed of sound V_S ($M=1$):

$$\frac{t_S}{t_B} = \frac{1}{\mu} \left[1 - \exp \left(- \frac{V_S}{I_{sp}} \right) \right] \quad (10)$$

Furthermore

$$a_0 = \frac{T}{m_0} \quad (11)$$

$$\beta_0 = \frac{f_x \rho S V_S}{2 m_0} \quad (12)$$

where a_0 is the initial axial acceleration and β_0 is called the "supersonic deceleration factor in boost" (see also para 3.3).

3-3. Glide phase

In this phase, also referred to as the midcourse phase, the task of the missile is just of approaching the target area, at least for homing guided missiles. The corrections to the trajectory are in general very small and the missile speed is large; this means that the induced drag is small compared to C_{x0} and hence it can be neglected.

As in the boost phase it is still: $N = \alpha = 0$ and the motion equation is:

$$m\dot{V} = -A \quad (13)$$

The C_{x0} profile versus Mach is approximated as in Fig. 6, so that the drag equation becomes:

$$A = -\frac{f_x S \rho V_S}{2} V \quad \text{for } M > 1 \quad (14)$$

$$A = -\frac{C_{sb} S \rho}{2} V^2 \quad \text{for } M \leq 1 \quad (15)$$

Equations (13) and (14) have been integrated (see Appendix 2) and the results are:

3-3-1. Supersonic portion of glide phase

$$V = V_B - \beta(X - X_B) \quad (16)$$

$$t = t_B + \frac{1}{\beta} \ln \frac{1}{1 - \beta \frac{X - X_B}{V_B}} \quad (17)$$

3-3-2. Subsonic portion of glide phase

This part of the flight is generally of less interest. In fact, being the glide phase followed by a strong manoeuvres situation, only starting from supersonic speed the missile is able to fulfil the manoeuvre requirements. Nevertheless for the sake of generality the motion equation:

$$m\dot{V} = -\frac{C_{sb} S \rho}{2} V^2 \quad (18)$$

has been integrated leading to:

$$V = V_S \exp \left[-\gamma(X - X_S) \right] \quad (19)$$

$$t = t_S + \frac{1}{\gamma V_S} \left[\exp \left(\gamma(X - X_S) \right) - 1 \right] \quad (20)$$

where V_S , t_S , X_S are the initial conditions of subsonic glide phase. They are easily derived from eq. (15) and (16):

$$X_S = X_B + \frac{V_B - V_S}{\beta} \quad (21)$$

$$t_S = t_B + \frac{1}{\beta} \ln \frac{1}{1 - \beta \frac{x_S - x_B}{v_B}} \quad (22)$$

The equations (15) to (20) synthesize the kinematics of the missile glide phase. It is worthwhile to remark that:

- In supersonic regime the speed decreases linearly with range while in the subsonic the law is exponential.
- Each phase is characterized by its key parameter:

SUPERSONIC GLIDE

$$\beta = \frac{f_x S \rho_S v_S}{2 m} \quad (\text{ms}^{-1}/\text{m}) \quad (23)$$

or:

$$\beta' = 1000 \beta \quad (\text{ms}^{-1}/\text{Km}) \quad (23a)$$

is the "DECELERATION FACTOR IN SUPERSONIC REGIME" and represents the loss of speed (in m/sec) per kilometer of range.

SUBSONIC GLIDE

$$\gamma = \frac{C_{sb} S \rho}{2 m} \quad (\text{m}^{-1}) \quad (24)$$

is the "DECELERATION FACTOR IN SUBSONIC REGIME"; its inverse $\lambda = 1/\gamma$ represents the range at which the speed has decreased to the 37% of its initial value (see fig. 7).

3-4. Cross-check with simulation

In order to validate the simplifications introduced in the previous analysis, the kinematics of a real missile computed with (8), (9), (16), (17), (19) and (20) have been compared with the results of a simulation model; this model included:

- the actual thrust profile
- the actual C_x profile
- the induced x_0 drag due to gravity compensation.

The results are presented in fig. 8 both for wingless and winged configuration of the same missile.

The good agreement between these results suggests that the analytical method may be used not only for comparing different configurations (differing in mass, propulsion and aerodynamic properties) but also for evaluating the kinematic performance of whatever configuration, provided of course that the analysis is performed within the limits of stated assumptions and simplifications, the most relevant of which are: horizontal flight path and no manoeuvres during the boost and glide phase.

3-5. Terminal phase

In this phase a modern anti-air tactical missile generally exhibits very strong lateral accelerations that are mainly required because of the target evasive manoeuvres. The actual time profile of this acceleration is primarily dependent on the missile guidance algorithm and on the shape of the target manoeuvres (waving, escape etc.).

For the purpose of present analysis it is not necessary to use the true profile that would also preclude the direct integration of the motion equations. A reference profile and in particular a constant profile is considered enough appropriate.

In this phase the motion equations of the missile (1) and (2) become:

$$m\dot{V} = -A \cos \alpha - N \sin \alpha \quad (25)$$

$$ma_N = N \cos \alpha - A \sin \alpha \quad (26)$$

that, for moderate values of α , can be simplified in:

$$m\dot{V} = -A - N \alpha \quad (27)$$

$$ma_N = N - A \alpha \quad (28)$$

Moreover if the missile exhibits a very strong lateral acceleration the term A in (27) and the term $A \alpha$ in (28) may be neglected leading to:

$$m\dot{V} = -N \alpha \quad (29)$$

$$ma_N = N \quad (30)$$

where:

$$N = C_{N\alpha} \frac{1}{2} \rho V^2 S \quad (31)$$

As for the case of the drag coefficient C_{x0} , the profile of the derivative $C_{N\alpha}$ versus Mach can be approximated in the supersonic regime by the law:

$$C_{N\alpha} = \frac{f_{N\alpha}}{M} = \frac{f_{N\alpha} V_S}{V} \quad (32)$$

With above simplifications the integration of equations (see Appendix 3) gives the following results:

$$V = V_0 \sqrt[3]{1 - \frac{P}{P_M}} \quad (33)$$

$$\alpha = \frac{\alpha_0}{\sqrt[3]{1 - \frac{P}{P_M}}} \quad (34)$$

$$P_M = f_{N\alpha} V_0^3 \frac{S \rho V_S}{6 ma_N} \quad (35)$$

where:

$$P = \int V dt \quad (36)$$

represents the path covered by the missile from the beginning of the maneuvered flight.

V_0 and α_0 are the initial conditions; V_0 may be evaluated with equation (16) and α_0 is the angle of attack necessary to provide the requested maneuver when the speed is V_0 :

$$\alpha_0 = \frac{2 ma_N}{f_{N\alpha} S \rho V_S} \frac{1}{V_0} \quad (37)$$

In App. 3, for the sake of completeness, the subsonic regime has also been considered and the relative equations have been integrated leading to similar results.

3-4-1. Comments to the results

The equations (33) and (34) show that, as long as the missile proceeds along its trajectory, while providing a constant normal acceleration, its speed decreases with a cubic root law and the angle of attack increases with the same law. The path covered by the missile is limited to a maximum value P_M where the speed falls down to zero and the incidence becomes infinitely large (See Fig. 9).

This is the effect of a kinematic degenerative loop whose existence is well known to the missile system designers. This loop shows its effect whenever an unpowered (non propelled) missile tries to develop a sustained maneuver (See Fig. 10). In fact to generate the required maneuver an angle of attack must be developed; this produces an induced drag that decreases the missile speed. Due to the constant maneuver requirement, α must increase and this leads to an even larger induced drag that in turn decelerates more heavily the missile speed. This degenerative process continues unless a provision for limiting the maximum incidence is introduced into the missile control algorithms; but in this case the missile will no longer develop the required maneuver and the mission will unavoidably abort.

The relationships found in present analysis characterize in a quantitative way all the features of this degenerative loop and allow for a direct and quick comparison of different configurations.

Among these features the most important to be highlighted is the parameter Ψ that represents the maximum theoretical flight path covered by the missile while exhibiting a constant lateral maneuver. In the expression of P_M , equation (35), an even more important term can be extracted. This is:

$$\Psi = \Gamma_{H\alpha} V_0^3$$

This term, called the "maneuvered flight factor" synthesizes all the maneuvering features of an aerodynamic configuration. Two configurations having the same Ψ will achieve the same P_M and will have the same dynamic capability against maneuvering targets.

Among other considerations it may be worthwhile to remark the value power of V_0^3 , that stresses the importance of the arrival speed of the missile into the target area.

4. WINGED AND WINGLESS CONFIGURATION

In the previous paragraphs, the analysis was performed many times with reference either to a winged or a wingless configuration. In this paragraph these configurations will be examined from the point of view of the aerodynamic performance.

4-1. Winged configuration

The configuration taken as example is a tactical missile with WING-BY-TAIL combination, symmetrical line layout and moving tails for the pitch-yaw-roll control.

The fig. 11 shows the geometry of this configuration with the relevant parameters of each component.

The planform, aspect ratio and thickness distribution of both wings and tails have been chosen and optimized in order to reduce the drag and achieve a normal force versus incidence free of sudden stall.

The Mach sensitivity of the aerodynamic coefficients for the wings and tails is low and the same happens for the complete configuration. (Fig. 12)

This peculiar characteristics permits a very important simplification with reference to the trim capability in the pitch plane. By accurate positioning of the wings along the longitudinal axis it is possible to design a quasi-neutrally stable configuration for the entire span of operating Mach numbers. In this manner it is possible to reach, and maintain, the incidence with zero, or near zero, deflection of the control tails.

This feature is of great benefit in the control area because larger tail deflections can be dedicated to counteract roll and yaw disturbances. In fact wind tunnel tests confirmed that enough control authority exists for incidences greater than 25 degrees.

4-2. Wingless configuration

By removing wings from the previous aerodynamic configuration we obtain a simple BODY-TAIL cruciform combination, with moving tails for the pitch-yaw-roll control.

The fig 13 shows the geometry of this configuration with the relevant parameters of each component. It must be taken into account that this configuration is a BODY-TAIL not optimized mainly from two points of view as:

- a) the location of the center of gravity with respect to the overall centre of pressure;
- b) the fineness ratio of the body.

The point a) has great influence on the amount of tails deflection required for attaining and maintaining a given incidence, while the point b) determines the incidence limit for the symmetric down-wash from the body.

To ease the comparison we neglect point b) that means to assume the same incidence capability for both the winged and the wingless configuration.

The influence of point a) is very important for the purpose of comparison and we will consider and analyze two limit situations:

- 1) Wingless configuration neutrally stable.
- 2) Wingless configuration with the center of gravity derived from the winged configuration.

Within these assumptions we obtain:

4-2-1. Wingless configuration neutrally stable

This configuration reaches the required incidence in the entire span of Mach without tails deflection and maintains the roll-yaw control authority at incidence greater than 25 degrees.

The aerodynamic coefficients of practical interest are still:

- a) the axial force coefficient CXO_{BT1} (fig. 14)
- b) the normal force coefficient CN_{BT1} (fig. 15).

4-2-2. Winged configuration with defined stability

In order to achieve the incidence in the entire span of Mach this configuration requires some tails deflection. Roll-yaw control authority is still maintained at incidence greater than 25 degrees, as it has been confirmed by wind tunnel tests.

The aerodynamic coefficients that will be used are:

- a) the axial force coefficient $CXO_{BT2} = CXO_{BT1}$;
- b) the normal force coefficient at trim CNE_{BT2} (fig. 16). This coefficient has been computed at the incidence of equilibrium as a function of the tail deflections (negative). It has to be remarked that $CN_{BT2} < CN_{BT1}$.

4-3. Kinematic performance

The kinematics of both configurations that are the WBT and the BT have been computed for the boost and glide phase using the equations derived in para 3.2 and 3.3. The results are reported in fig. 8 in terms of speed versus range. These results represent the input data for the subsequent analysis on the dynamic performance.

4-4. Maneuvering performance

As outlined in the para 3.5 an useful method for the evaluation of a missile capability is to establish the performance with constant lateral acceleration; in this respect the parameter:

P_M = distance where the initial velocity V_0 falls down to zero under the constant lateral acceleration a_N

can be chosen as key parameter. This will allow the comparison of the dynamic performance of the three aerodynamic configurations previously considered.

To give a practical sense to a comparison between the winged and the wingless aerodynamic configuration the value of P_M has been computed at the same range from launching point.

Fig. 18 is a synopsis of all data available and the analysis shows the existence of a range of distances where a wingless configuration neutrally stable has performance equal to or better than that of a winged when a constant lateral acceleration of 20g is required.

In the same range wingless configuration with defined stability has roughly half capability so we can argue that properly designed wingless configuration will lie between these limits.

5. CONCLUSION

- An analytical method has been developed that allows a quick evaluation of the aerodynamic, mass, and propulsion properties of a tactical missile in term of its kinematic and dynamic performance.
- The method is particularly good for estimating the kinematics of the missile in a non maneuvering, horizontal flight path situation.
- When applied to a maneuvering environment, the method has evidenced that, during a sustained acceleration, the useful range of the angle of attack is limited to 25 degrees. Above this limit the missile performance presents a very fast degenerative behavior.
- The method has been used to compare in a practical case a winged with respect to a wingless missile configuration. The conclusion is that the dynamic performance of the wingless configuration can be comparable to the winged.

APPENDIX A

BOOST PHASE. INTEGRATION OF THE MOTION EQUATIONS

Due to the different structure of the equations in subsonic and in supersonic regime, the integration must be performed separately:

A.1 Subsonic regime

The equation is:

$$\frac{dV}{dt} = \frac{T}{m} \quad (A1)$$

where:

$$T = \text{const}$$

$$m = m_0 - \dot{m}t = m_0 \left(1 - \gamma^u \frac{t}{t_B}\right) \quad (A2)$$

$$\gamma^u = \frac{m_{pr}}{m_0} \quad (A3)$$

then:

$$dV = \frac{T}{m_0} \frac{dt}{1 - \gamma^u t/t_B} \quad (A4)$$

and finally:

$$V - V_0 = \frac{T}{m_0} \frac{t_B}{\gamma^u} \ln(1 - \gamma^u t/t_B) = \frac{T t_B}{m_{pr}} \ln(1 - \gamma^u t/t_B)$$

By assuming $V_0 = 0$:

$$V = I_{sp} \ln(1 - \gamma^u \frac{t}{t_B}) \quad (A5)$$

$$\frac{t}{t_B} = \frac{1}{\gamma^u} \left[1 - \exp\left(-\frac{V}{I_{sp}}\right)\right] \quad (A6)$$

where I_{sp} is the specific impulse of the propellant

$$I_{sp} = \frac{T t_B}{m_{pr}} \quad (A7)$$

If t_S is the flight time when the speed reaches the speed of sound V_S , from (A6) we obtain:

$$\frac{t_S}{t_B} = \frac{1}{\gamma^u} \left[1 - \exp\left(-\frac{V_S}{I_{sp}}\right)\right] \quad (A8)$$

A.2 Supersonic regime

The equation is:

$$m\dot{V} = T - A \quad (A9)$$

where:

$$A = C_{x0} \frac{1}{2} \rho V^2 S = \frac{f_x S \rho V_S}{2} V \quad (A10)$$

and m has the same expression as in (A2).
Equation (A9) becomes:

$$\left(1 - \frac{u}{t_B}\right) \frac{dV}{dt} = \frac{T}{m_0} - \frac{f_x S \rho V_S}{2 m_0} V \quad (A11)$$

By putting:

$$a_0 = \frac{T}{m_0} \quad (A12)$$

$$\beta_0 = \frac{f_x S \rho V_S}{2 m_0} \quad (A13)$$

we obtain:

$$\int_{V_0}^V \frac{dV}{a_0 - \beta_0 V} = \int_{t_0}^t \frac{dt}{1 - u t/t_B} \quad (A14)$$

And finally:

$$V = \frac{a_0}{\beta_0} \left[1 - \left(1 - \frac{\beta_0}{a_0} V_S\right) \exp\left(\frac{\beta_0 t_B}{u} \ln \frac{1 - u t/t_B}{1 - u t_S/t_B}\right) \right] \quad (A15)$$

At the end of the boost phase that is for $t = t_B$:

$$V_B = \frac{a_0}{\beta_0} \left[1 - \left(1 - \frac{\beta_0}{a_0} V_S\right) \exp\left(\frac{\beta_0 t_B}{u} \ln \frac{1 - u}{1 - u t_S/t_B}\right) \right] \quad (A17)$$

A direct integration of (A15) in order to obtain the range X covered by the missile is quite complicated. An acceptable estimate of this quantity at the end of the boost phase is given by:

$$X_B \approx \frac{V_B t_B}{2} \quad (A17')$$

APPENDIX B

GLIDE PHASE. INTEGRATION OF THE MOTION EQUATIONS

B.1 Supersonic regime

The motion equation is:

$$m \dot{V} = -A \quad (B1)$$

where:

$$A = \frac{f_x S \rho V_S}{2} V \quad (B2)$$

Then:

$$\frac{dV}{dt} = -\beta V \quad (B3)$$

where:

$$\beta = \frac{f_x S \rho V_S}{2 m} \quad (B4)$$

Then, by integrating from the end of the boost phase to a generic time t :

$$\int_{V_B}^V \frac{dV}{V} = - \int_{t_B}^t \beta dt \quad (B5)$$

$$V = V_B e^{-\beta(t - t_B)} \quad (B6)$$

By integrating a second time:

$$\int_{X_B}^X dX = \int_{t_B}^t V_B e^{-\beta(t - t_B)} dt \quad (B7)$$

leading to:

$$X - X_B = - \frac{V_B}{\beta} [e^{-\beta(t - t_B)} - 1] \quad (B8)$$

And from eq. (B6), and (B8):

$$V = V_B - \beta(X - X_B) \quad (B9)$$

$$t = t_B + \frac{1}{\beta} \ln \frac{1}{1 - \beta \frac{X - X_B}{V_B}} \quad (B10)$$

B.2 Subsonic regime

The motion equation is still:

$$m\dot{V} = -A$$

with:

$$A = \frac{C_{sb} S \rho}{2} V^2 \quad (B11)$$

Then:

$$\frac{dV}{dt} = -\gamma V^2 \quad (B12)$$

where:

$$\gamma = \frac{C_{sb} S \rho}{2 m} \quad (B13)$$

By integrating from the end of the supersonic phase (t_{S1} , V_S , X_{S1}) to a generic time t :

$$\int_{V_S}^V \frac{dV}{V^2} = - \gamma \int_{t_{S1}}^t dt \quad (B14)$$

$$V = \frac{V_S}{1 + V_S \gamma (t - t_{S1})} \quad (B15)$$

By integrating a second time:

$$\int_{x_{S1}}^x dx = V_S \int_{t_{S1}}^t \frac{dt}{1 + V_S \gamma (t - t_{S1})} \quad (B16)$$

leading to:

$$x - x_{S1} = \frac{1}{\gamma} \ln [1 + V_S \gamma (t - t_{S1})] \quad (B17)$$

And from eq. (B15), and (B17):

$$V = V_S e^{-\gamma (x - x_{S1})} \quad (B18)$$

$$t = t_{S1} + \frac{1}{\gamma V_S} [e^{-\gamma (x - x_{S1})} - 1] \quad (B19)$$

APPENDIX C

MANOEUVER PHASE. INTEGRATION OF MOTION EQUATIONS

C.1 Supersonic regime

The motion equations are:

$$m \dot{V} = -N \alpha \quad (C1)$$

$$m a_N = N \quad (C2)$$

where:

$$N = C_{N\alpha} \alpha \frac{1}{2} \rho V^2 S \quad (C3)$$

$$C_{N\alpha} = \frac{f_{N\alpha}}{M} = \frac{f_{N\alpha} V_S}{V} \quad (C4)$$

Combining these equations:

$$\dot{V} = -a_N \alpha \quad (C5)$$

$$\alpha = \frac{2 m a_N}{f_{N\alpha} S V_S} \frac{1}{V} \quad (C6)$$

these lead to:

$$\dot{V} = -\frac{K}{V} \quad (C7)$$

where:

$$K = \frac{2 m a_N^2}{f_{N\alpha} S \rho V_S} \quad (C8)$$

By integrating (C7)

$$\int_{V_0}^V dV = -K \int_0^t dt \quad (C9)$$

$$V = (V_0^2 - 2 Kt)^{1/2}$$

By integrating a second time ($V = \frac{dP}{dt}$): (C10)

$$\int_0^P dP = \int_0^t (V_0^2 - 2 Kt)^{1/2} dt \quad (C11)$$

$$P = \frac{1}{3K} [V_0^3 - (V_0^2 - 2 Kt)^{3/2}] \quad (C12)$$

From eq. (C11), and (C13):

$$V = V_0 \sqrt[3]{1 - \frac{P}{P_M}} \quad (C13)$$

where:

$$P_M = \frac{2 V_0^3}{3K} = f_{N\alpha} V_0^3 \frac{S \rho V_S}{6 m a_N^2} \quad (C14)$$

From eq. (C6) and (C13):

$$\alpha = \frac{\alpha_0}{\sqrt[3]{1 - \frac{P}{P_M}}} \quad (C15)$$

where:

$$\alpha_0 = \frac{2 m a_N}{f_{N\alpha} S \rho V_S} \frac{1}{V_0} \quad (C16)$$

C.2 Subsonic regime

The only difference with respect to the supersonic regime is that C_N may be assumed as a constant value.

By integrating in a similar way the motion equations leads to:

$$V = V_0 \sqrt[4]{1 - \frac{P}{P_M}} \quad (C17)$$

$$\alpha = \frac{\alpha_0}{\sqrt[4]{1 - \frac{P}{P_M}}} \quad (C18)$$

$$P_M = C_{N\alpha} V_0^4 \frac{S \rho}{8 m a_N^2} \quad (C19)$$

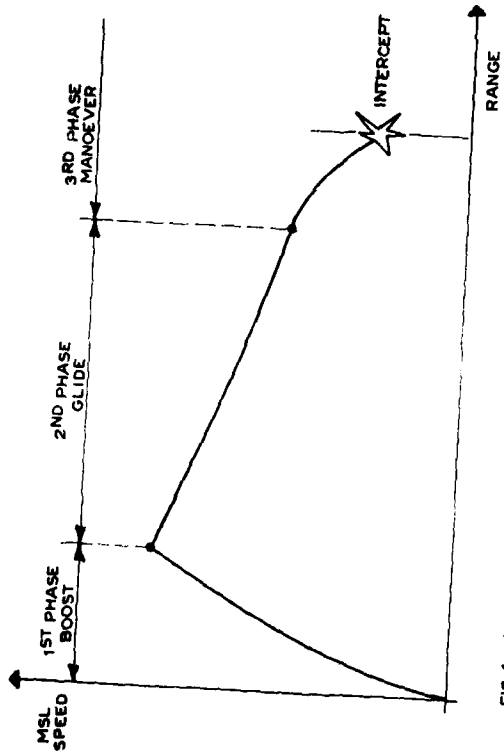


FIG. 1 SPEED PROFILE OF A TYPICAL MISSION.

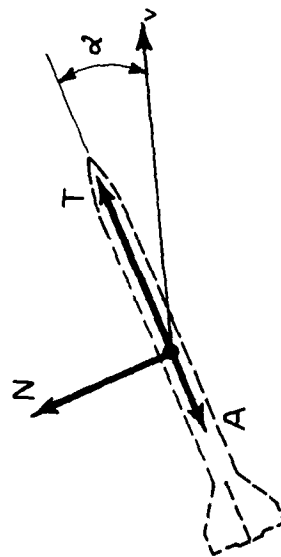


FIG. 2 MISSILE EXTERNAL FORCES

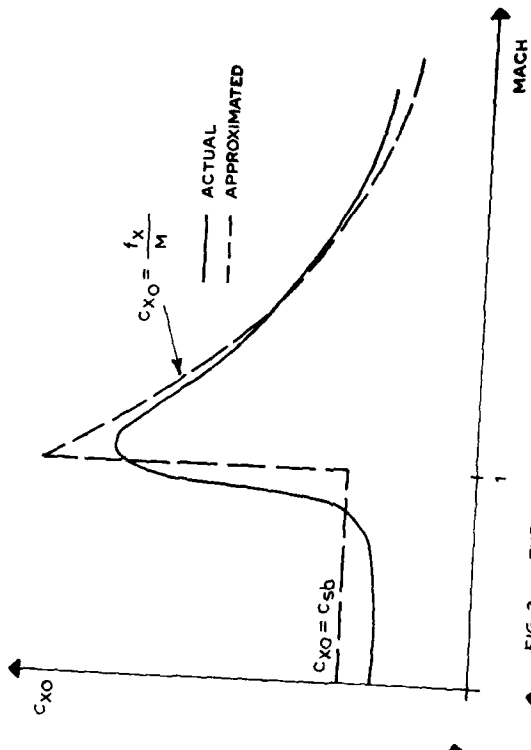


FIG. 3 TYPICAL C_{XO} DIAGRAM.

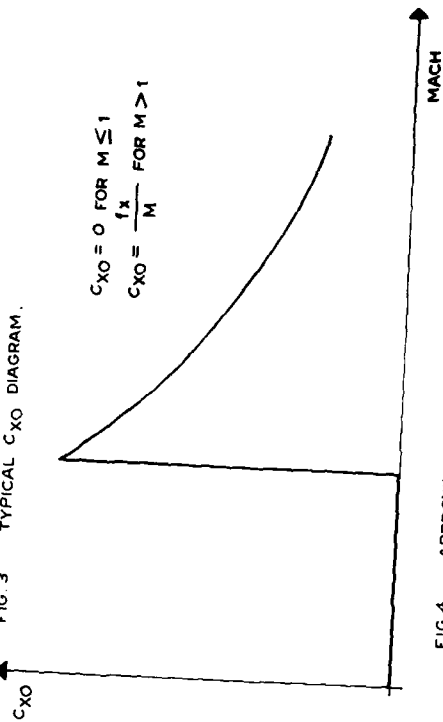


FIG. 4 APPROXIMATED C_{XO} DIAGRAM FOR THE BOOST PHASE.

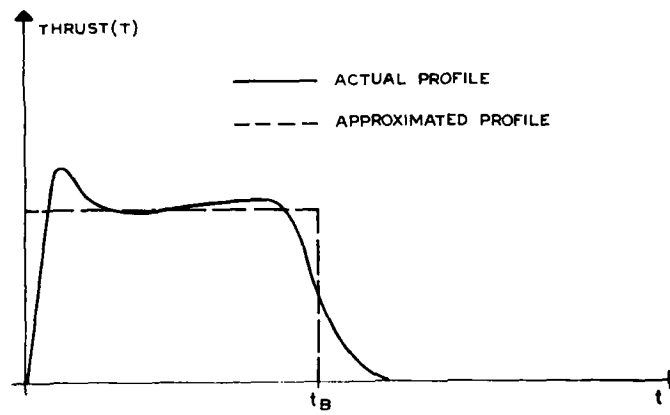


FIG. 5 THRUST PROFILE

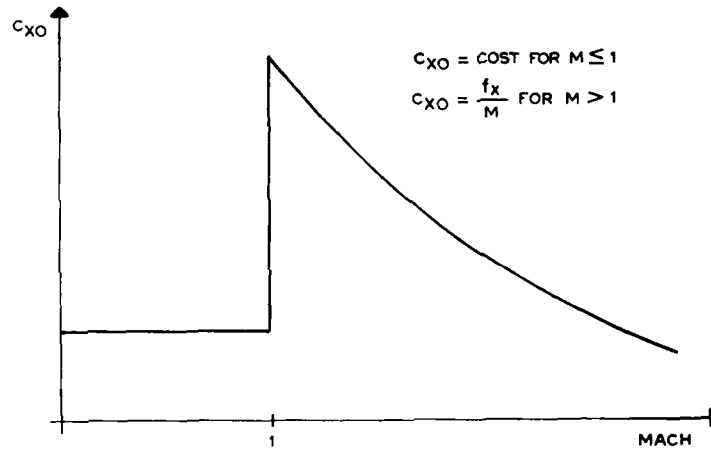
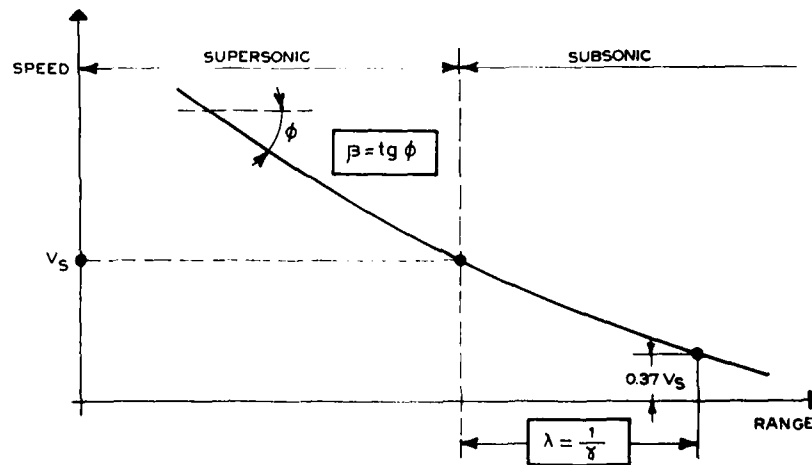
FIG. 6 APPROXIMATED C_{X0} DIAGRAM FOR THE GLIDE PHASE.

FIG. 7 MISSILE DECELERATION IN GLIDE PHASE.

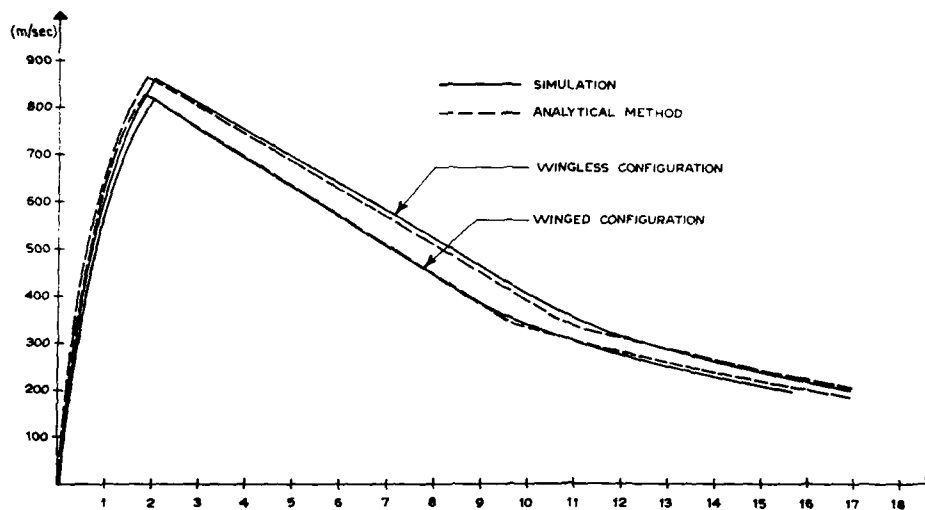


FIG. 8 COMPARISON WITH SIMULATION

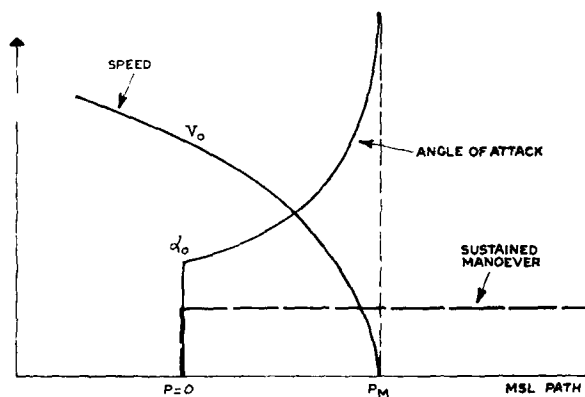


FIG. 9 SPEED AND ANGLE OF ATTACK PROFILE VERSUS MISSILE PATH.

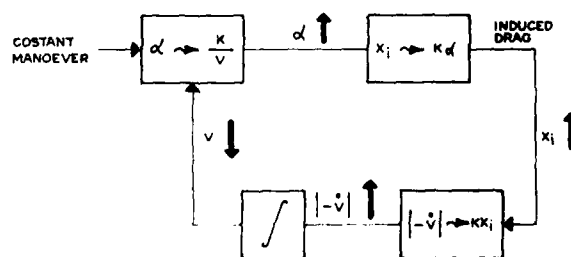


FIG. 10 INCIDENCE DEGENERATIVE LOOP.

28-18

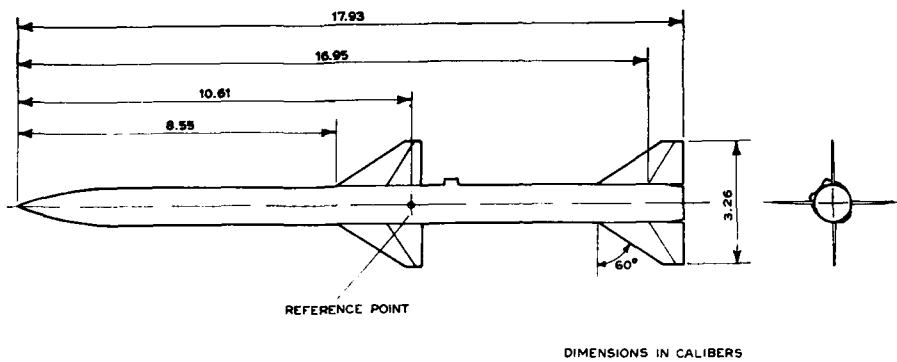


FIG.11 WING-BODY-TAIL CONFIGURATION

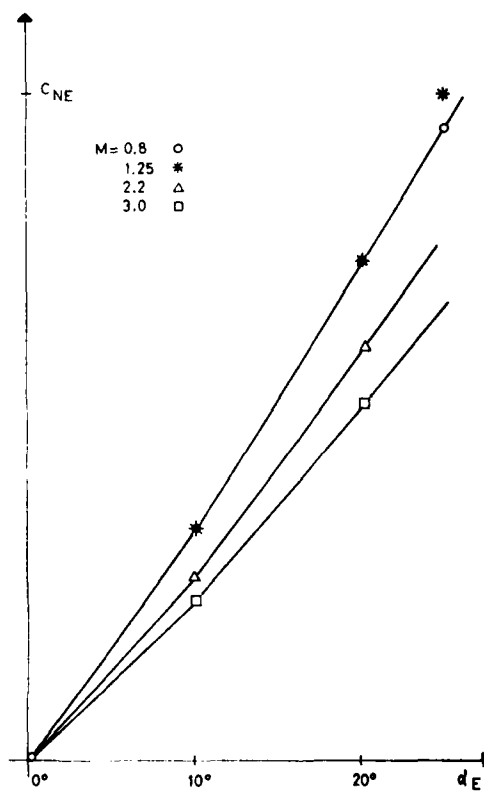


FIG.12 WBT NORMAL FORCE COEFFICIENT.

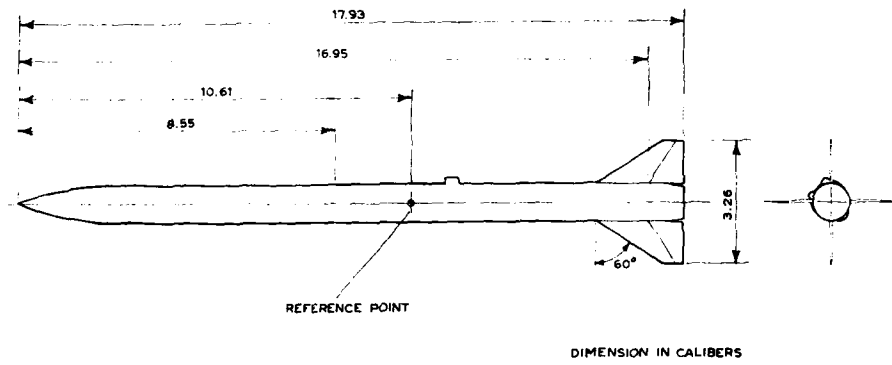


FIG. 13 BODY-TAIL CONFIGURATION

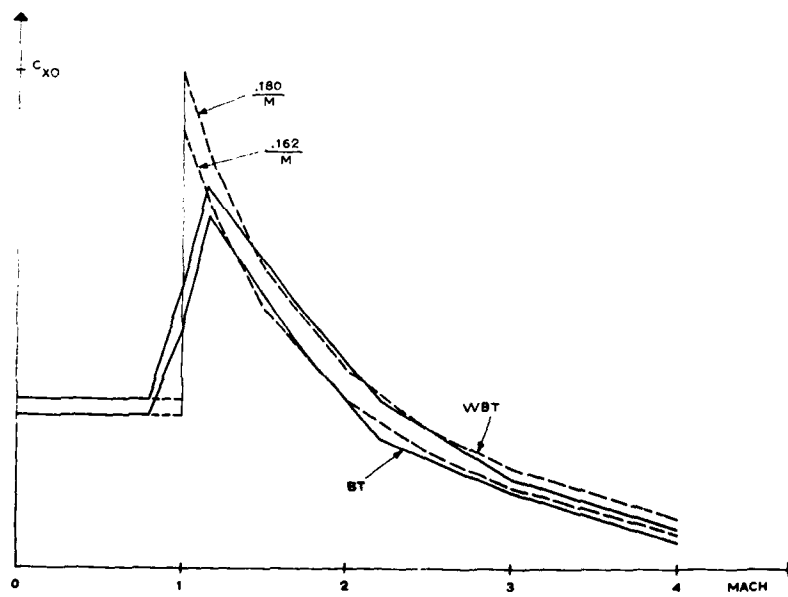


FIG. 14 AXIAL FORCE COEFFICIENT

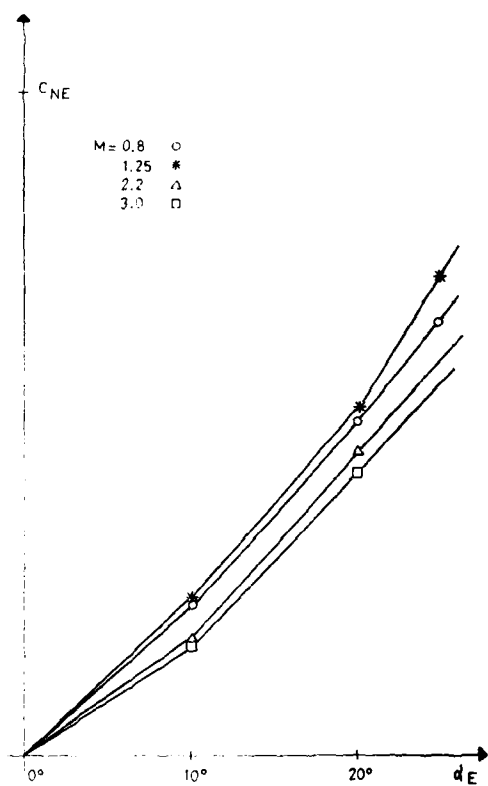


FIG 15 BT1 NORMAL FORCE COEFFICIENT.

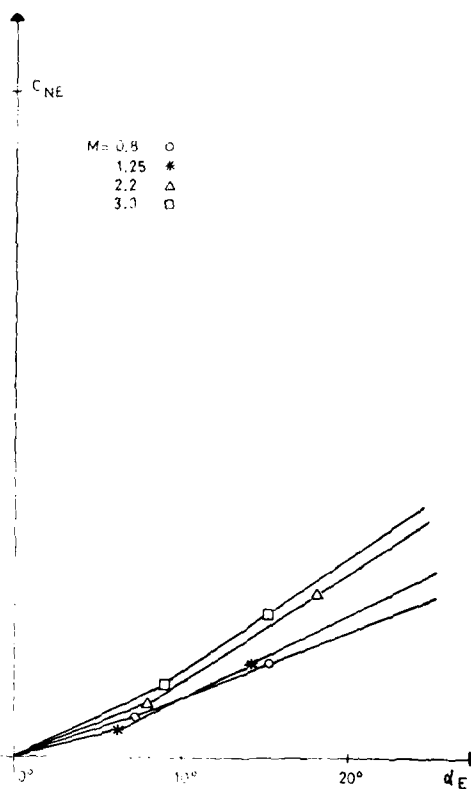


FIG 16 BT2 NORMAL FORCE COEFFICIENT.

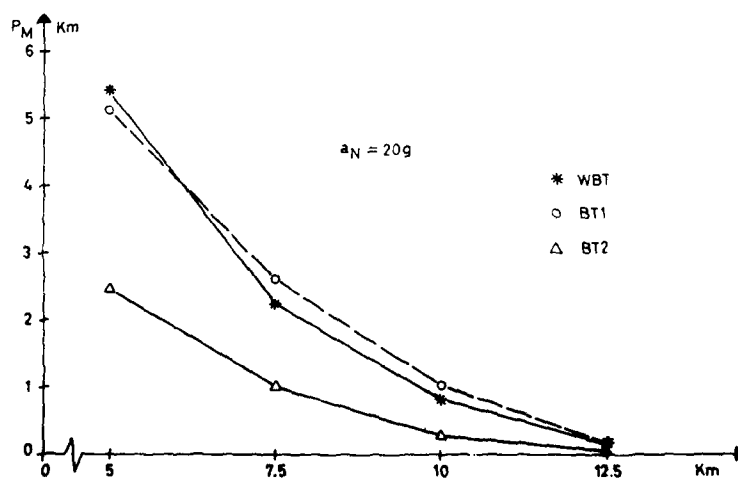


FIG 17 DISTANCE OF SUSTAINED MANOEUVRE.

REPORT DOCUMENTATION PAGE									
1. Recipient's Reference	2. Originator's Reference	3. Further Reference	4. Security Classification of Document						
	AGARD-CP-451	ISBN 92-835-0494-1	UNCLASSIFIED						
5. Originator	Advisory Group for Aerospace Research and Development North Atlantic Treaty Organization 7 rue Ancelle, 92200 Neuilly sur Seine, France								
6. Title	STABILITY AND CONTROL OF TACTICAL MISSILE SYSTEMS								
7. Presented at	the Flight Mechanics Panel Symposium held in Ankara, Turkey from 9 to 12 May 1988.								
8. Author(s)/Editor(s)	Various		9. Date March 1989						
10. Author's/Editor's Address	Various		11. Pages 336						
12. Distribution Statement	This document is distributed in accordance with AGARD policies and regulations, which are outlined on the Outside Back Covers of all AGARD publications.								
13. Keywords/Descriptors									
<table border="0"> <tr> <td>Missile control</td> <td>Air to surface missiles</td> </tr> <tr> <td>Stability</td> <td>Surface to air missiles</td> </tr> <tr> <td>Air to air missiles</td> <td></td> </tr> </table>				Missile control	Air to surface missiles	Stability	Surface to air missiles	Air to air missiles	
Missile control	Air to surface missiles								
Stability	Surface to air missiles								
Air to air missiles									
14. Abstract									
<p>These proceedings contain the papers presented at the AGARD Flight Mechanics Panel Symposium on Stability and Control of Tactical Missiles held in Ankara, Turkey from 9 to 12 May 1988.</p> <p>With recent advances in missile seekers and processors, and in the analysis of missile dynamics motions and the associated control subsystem designs, missile manoeuvre envelopes have significantly expanded. It was therefore appropriate and timely that the stability and controllability of such missiles be examined, and this symposium provided a forum for the interchange of ideas, and the different techniques currently involved in dealing with the various aspects of this subject. The presentations covered a wide selection of topics, from prediction, simulation and test, through to a look at current development experience. The subject of the symposium was deliberately limited to tactical missiles, encompassing air-to-air, air-to-ground, and ground-to-air, but not ballistic missiles.</p>									

<p>AGARD Conference Proceedings No.451 Advisory Group for Aerospace Research and Development, NATO STABILITY AND CONTROL OF TACTICAL MISSILE SYSTEMS Published March 1989 336 pages</p> <p>These proceedings contain the papers presented at the AGARD Flight Mechanics Panel Symposium on Stability and Control of Tactical Missiles held in Ankara, Turkey from 9 to 12 May 1988.</p> <p>With recent advances in missile seekers and processors, and in the analysis of missile dynamics motions and the associated control subsystem designs, missile manoeuvre</p> <p>P.T.O.</p>	<p>AGARD-CP-451</p> <p>Missile control Stability Air to air missiles Air to surface missiles Surface to air missiles</p>	<p>AGARD Conference Proceedings No.451 Advisory Group for Aerospace Research and Development, NATO STABILITY AND CONTROL OF TACTICAL MISSILE SYSTEMS Published March 1989 336 pages</p> <p>These proceedings contain the papers presented at the AGARD Flight Mechanics Panel Symposium on Stability and Control of Tactical Missiles held in Ankara, Turkey from 9 to 12 May 1988.</p> <p>With recent advances in missile seekers and processors, and in the analysis of missile dynamics motions and the associated control subsystem designs, missile manoeuvre</p> <p>P.T.O.</p>	<p>AGARD-CP-451</p> <p>Missile control Stability Air to air missiles Air to surface missiles Surface to air missiles</p>
<p>AGARD Conference Proceedings No.451 Advisory Group for Aerospace Research and Development, NATO STABILITY AND CONTROL OF TACTICAL MISSILE SYSTEMS Published March 1989 336 pages</p> <p>These proceedings contain the papers presented at the AGARD Flight Mechanics Panel Symposium on Stability and Control of Tactical Missiles held in Ankara, Turkey from 9 to 12 May 1988.</p> <p>With recent advances in missile seekers and processors, and in the analysis of missile dynamics motions and the associated control subsystem designs, missile manoeuvre</p> <p>P.T.O.</p>	<p>AGARD-CP-451</p> <p>Missile control Stability Air to air missiles Air to surface missiles Surface to air missiles</p>	<p>AGARD Conference Proceedings No.451 Advisory Group for Aerospace Research and Development, NATO STABILITY AND CONTROL OF TACTICAL MISSILE SYSTEMS Published March 1989 336 pages</p> <p>These proceedings contain the papers presented at the AGARD Flight Mechanics Panel Symposium on Stability and Control of Tactical Missiles held in Ankara, Turkey from 9 to 12 May 1988.</p> <p>With recent advances in missile seekers and processors, and in the analysis of missile dynamics motions and the associated control subsystem designs, missile manoeuvre</p> <p>P.T.O.</p>	<p>AGARD-CP-451</p> <p>Missile control Stability Air to air missiles Air to surface missiles Surface to air missiles</p>

<p>envelopes have significantly expanded. It was therefore appropriate and timely that the stability and controllability of such missiles be examined, and this symposium provided a forum for the interchange of ideas, and the different techniques currently involved in dealing with the various aspects of this subject. The presentations covered a wide selection of topics, from prediction, simulation and test, through to a look at current development experience. The subject of the symposium was deliberately limited to tactical missiles, encompassing air-to-air, air-to-ground, and ground-to-air, but not ballistic missiles.</p> <p>ISBN 92-835-0494-1</p>	<p>envelopes have significantly expanded. It was therefore appropriate and timely that the stability and controllability of such missiles be examined, and this symposium provided a forum for the interchange of ideas, and the different techniques currently involved in dealing with the various aspects of this subject. The presentations covered a wide selection of topics, from prediction, simulation and test, through to a look at current development experience. The subject of the symposium was deliberately limited to tactical missiles, encompassing air-to-air, air-to-ground, and ground-to-air, but not ballistic missiles.</p> <p>ISBN 92-835-0494-1</p>
<p>envelopes have significantly expanded. It was therefore appropriate and timely that the stability and controllability of such missiles be examined, and this symposium provided a forum for the interchange of ideas, and the different techniques currently involved in dealing with the various aspects of this subject. The presentations covered a wide selection of topics, from prediction, simulation and test, through to a look at current development experience. The subject of the symposium was deliberately limited to tactical missiles, encompassing air-to-air, air-to-ground, and ground-to-air, but not ballistic missiles.</p> <p>ISBN 92-835-0494-1</p>	<p>envelopes have significantly expanded. It was therefore appropriate and timely that the stability and controllability of such missiles be examined, and this symposium provided a forum for the interchange of ideas, and the different techniques currently involved in dealing with the various aspects of this subject. The presentations covered a wide selection of topics, from prediction, simulation and test, through to a look at current development experience. The subject of the symposium was deliberately limited to tactical missiles, encompassing air-to-air, air-to-ground, and ground-to-air, but not ballistic missiles.</p> <p>ISBN 92-835-0494-1</p>